Physik-Department

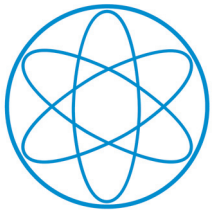

New Trends in Superconducting Circuit Quantum Electrodynamics: Two Amplifiers, Two Resonators, and Two Photons

A Not So Short Introduction to Quantum Circuits and Signals

Dissertation
of
Matteo Mariantoni

Technische Universität
München

TECHNISCHE UNIVERSITÄT MÜNCHEN

Lehrstuhl E23 für Technische Physik

Walther-Meißner-Institut für Tieftemperaturforschung
der Bayerischen Akademie der Wissenschaften

New Trends in Superconducting Circuit Quantum Electrodynamics: Two Amplifiers, Two Resonators, and Two Photons

Matteo Mariantoni

Vollständiger Abdruck der von der Fakultät für Physik der Technischen Universität München zur Erlangung des akademischen Grades eines

Doktors der Naturwissenschaften

genehmigten Dissertation.

Vorsitzender:		Univ.-Prof. Dr. P. Vogl
Prüfer der Dissertation:	1.	Univ.-Prof. Dr. R. Gross
	2.	Hon.-Prof. Dr. G. Rempe

Die Dissertation wurde am 21.09.2009 bei der Technischen Universität München eingereicht und durch die Fakultät für Physik am 07.12.2009 angenommen.

Dedicato alla mia Sasha ed a Carla e Dario

"... non vogliate negar l'esperienza,
di retro al sol, del mondo sanza gente.
Considerate la vostra semenza:
fatti non foste a viver come bruti,
ma per seguir virtute e canoscenza".

'Be ye unwilling to deny the knowledge,
Following the sun, of the unpeopled world.
Consider ye the seed from which ye sprang;
Ye were not made to live like unto brutes,
But for pursuit of virtue and of knowledge.'

[Dante Alighieri, "La Divina Commedia" (The Divine Comedy) Inferno – Canto XXVI, 116-120]

Preface

What do you want to be when you grow up? The answer to the inevitable question everyone asks you when you are a child in my case has always been "a scientist!" I have always been fascinated by the incredible world of scientific research in all its possible aspects. As if oftentimes happens, in the beginning I was highly interested in astronomy. The archetypical questions on the origin of the Universe and on the mysteries of space had represented the first steps into the development of a scientific consciousness in many civilizations. Similarly, it seems that such fundamental questions have occupied the young minds of many scientists. I remember to bother my whole family while reading out loud on a beach entire chapters of the book "L'Astronomia Pratica" by Ronan A. Colin during a summer vacation some twenty years ago and then, at night, trying to find stars and planets in the Milky Way looking through my old binocular! Besides the notions learnt at school, my first serious contact with science took place when my father gave me an issue of the popular scientific magazine "Le Scienze," the Italian translation of "Scientific American." I still jealously keep that issue at home in Italy. The article that attracted my attention was in the "Mathematical Recreations" column, which, at that time, was written by the mathematician Ian Stewart. The article dealt with Fermat's last theorem. Even if I did not understand a single line on Diophantine equations and I was mostly interested in the intriguing illustration complementing the article, I became aware, for the first time, that there were "crazy" people so motivated to spend their entire life in the search for a mathematical proof!

For their encouragement during my childhood and their continuous support during my studies, I would like to thank from the bottom of my heart both my parents, Carla Olivieri and Dario Mariantoni. My deepest gratitude goes to both of you for letting me discover with you the wonders of this world, for showing me that mathematics and physics can be fun, and for helping me to pursue my scientific career. In addition, I would like to thank my teachers of mathematics and physics during my first two years of "Liceo Scientifico" (grammar school) in Rieti, Italy, Rossella Lauretti and Agostino Maiezza, respectively. It is during their lectures that I began to appreciate the formal aspects of science, which ultimately resides in the axioms and theorems of mathematics. Also, I indirectly thank Dr. Marco Lombardi, an older alumnus of my grammar school, who, with his innate ingeniosity in mathematics and physics, inspired me through the years in grammar school.

With the time my interests shifted more and more from mathematics to physics. After being trained as an electronic engineer at the Politecnico di Milano, Italy, a choice which, in retrospective, I definitely do not regret, I eventually arrived to Chalmers University of Technology, Gothenburg, Sweden. At Chalmers, I joined the group headed by Prof. Per Delsing and, under his supervision, I worked on my Master Thesis for about a year. It is in Per's group that I had my first taste of

experimental research in physics and where I started to appreciate the beauty of *applied* quantum mechanics, a completely new experience after many years spent only studying books.

For my time at the Politecnico di Milano, I would like to thank Dr. Carlo Oleari, Prof. Amedeo Premoli, Prof. Carlo Cercignani, Prof. Carlo D. Pagani, and Prof. Sandro Salsa for giving me the strength and motivation to continue my studies in engineering with their inspirational lectures and for making me understand, with their tough examinations, that in life there is no gain without pain. For my period at Chalmers, my deepest thanks go to Prof. Per Delsing, Prof. John Clarke,[1] Dr. Alexei Kalabukov, Dr. Sergey Kubatkin, and Dr. Thilo Bauch for teaching me the rudiments of experimental physics. In addition, I thank Dr. Vitaly S. Shumeiko for making me aware that a good experimental physicist needs also to be a good theorist! It is during those years at Chalmers that my interest for quantum computing has grown and, eventually, has brought me to Munich, where I started my Ph.D. thesis at the Walther-Meissner-Institut and, jointly, at the Physik-Department of the Technical University Munich.

The beginning in Munich[2] was tough. With all the issues of a new lab to start up and the inevitable crash between the Italian and German cultures I did not have an easy life. In the search for the right motivation to bring forward the work on my Ph.D. thesis, I asked Professor Rudolf Gross, the direct supervisor of my thesis, to give me a chance to attend the annual March meeting organized by the American Physical Society in 2004. Professor Gross accepted immediately my request and in late March I went to Montreal. I vividly remember the series of four talks given by the Yale group at that meeting and, in particular, the 5.8 MHz coupling strength between a superconducting charge qubit and a resonator shown by Andreas Wallraff. The field of circuit quantum electrodynamics and its experimental implementation was born.[3] On the plane back to Munich, I could not stop thinking about those resonators and on the possibility to couple them to flux qubits, our topic of research at the Walther-Meissner-Institut. The day I got back to the institute, I knocked the door of Prof. Gross. We went to the whiteboard and started discussing about circuit quantum electrodynamics and on the possibility to start a project in that direction in the Munich research area.

I feel extremely lucky that both Prof. Dr. Rudolf Gross and Dr. Achim Marx, co-supervisor of my Ph.D. thesis, did not object to the possibility of shifting the line of research of my project from investigating π-Josephson junctions, also a very challenging research topic, to circuit quantum electrodynamics. It is because of their trust in my abilities that the adventure to be presented in this thesis had began. I am indebted to Prof. Gross and Achim for giving me the possibility to join their research group at the Walther-Meissner-Institut and for allowing me to develop my own ideas and to pursue them, both in theory and experiments. I am convinced that in many other laboratories such a pursuit would have not been possible, at least in the manner and to the extent it has been possible in Munich. The freedom I have been given at the Walther-Meissner-Institut in searching my own path constitutes the essence of my Ph.D. work. During the past years, I have learnt the importance of taking decisions, maintaining promises, aiming to reach a goal. The tutelage I

[1] Who had visited us in Sweden for a short period and helped me with my project.

[2] Garching to be precise.

[3] Theoretically, a relevant body of work already existed.

received from my advisors has helped my personal improvement and I am convinced their precious teachings will stand at the basis of my future research projects. I hope the benefit I have gained from my Munich experience has been reciprocal and also Rudolf and Achim have taken a positive advantage of it.

I use this occasion also to thank both Achim and Rudolf for investing their time in reading this fairly long manuscript! Your comments and constructive criticism has helped me a lot to improve the quality of this work.

Another important step in the development of my Ph.D. work is certainly represented by the encounter with Prof. Dr. Frank K. Wilhelm. Before moving to the Institute for Quantum Computing (IQC), Waterloo, Canada, Frank Wilhelm was leading a small group of very bright students at the Ludwig-Maximilians-Universität (LMU) in Munich. I soon became a good friend of one of his former students, Dr. Markus J. Storcz, with whom I started discussing about circuit quantum electrodynamics with superconducting flux qubits and developing architectures for the coupling of such qubits with on-chip microwave resonators.

It has been my pleasure to work with both Frank Wilhelm and Markus. The innumerous discussions in Markus' office have substantially improved my understanding of the working principles of superconducting qubits and have largely contributed to create the basis of my knowledge in this field of research.

In late 2004, Axel Kuhn, Pepijn Pinkse, and Prof. Gerhard Rempe organized at the Ringberg Castle in the south of Bavaria, Germany, a very interesting workshop on microcavities in quantum optics. Luckily, I had the possibility to attend such a workshop, where the most eminent experts in the field of cavity quantum electrodynamics gave enlightening talks. It is during that workshop that I met Prof. Dr. Enrique Solano. At that time, Enrique was a postdoctoral fellow in the groups of Prof. Igacio Cirac and Prof. Herbert Walther at the Max Planck Institute for Quantum Optics (MPQ), Garching, Germany.[4] It did not take more than a lunch sitting at the same table that Enrique and I started a collaboration which still continues and, I hope, will continue for a long time to come.

It is hard to find the appropriate adjectives to describe my gratitude to Enrique. He introduced me to the world of cavity quantum electrodynamics teaching me literally from scratch the quantum theory of atoms and photons. Enrique has always been extremely patient with me and has helped me in the good and bad times of my Ph.D. thesis. He always cheered me up when my mood was down and the work did not proceed as I wanted it and never stopped believing in my abilities as a physicist at any time. I still remember the first time he asked me to give him the "four pages," that is to write the draft of a manuscript to be submitted to the journal Physical Review Letters. Those first "four pages" were about the generation and measurement of microwave single photons. That manuscript was never accepted on any journal, perhaps for good reasons. However, it constitutes my "primary school" in circuit quantum electrodynamics. In preparing that manuscript, I learnt how to write a scientific publication at a professional level and, as painful as it is, I (we) learnt by my (our) own mistakes that circuit quantum electrodynamics is not as easy as it might seem and it cannot be regarded as a mere "copy and paste" from quantum optics. I will never regret to have written that article and I thank again Enrique for spending an insane amount of time with me to correct our mistakes and to learn a bit more about the quantum nature of microwave circuits and signals.

[4]Enrique is now professor at the Universidad del País Vasco, Bilbao, Spain.

That unpublished article substantially influenced most of the material treated in this thesis. Finally, I thank Enrique for sharing with me his Machiavellian approach to life and physics. I could have not asked for a better master than you, Kike!

I would also like to thank Dr. Henning Christ, a former graduate student of theoretical physics in the group of Prof. Igacio Cirac at the MPQ. I thank Henning for his valuable help with the development of the codes used for some of the numerical simulations reported in this thesis, for teaching me many tricks of theoretical physics, and for investing a considerable amount of time in studying with me, Markus, and Enrique the basic concepts of circuit quantum electrodynamics. Unfortunately, I think that both Markus and Henning did not get enough pay back for their time invested in this field of research. Nevertheless, I hope your professional life will always be as successful as it is now.

Again in 2004, this time during a workshop which took place in Bad Honnef, Germany, organized by Markus Storcz, Udo Hartmann, Frank Wilhelm, and Jan von Delft, I met another physicist who changed my way of interpreting microwave quantum circuits and signals, Dr. William D. Oliver. Will, who works as a staff member at the Lincoln Laboratory of the Massachusetts Institute of Technology (MIT) and as a visiting scientist at the MIT campus in the group led by Prof. Terry Orlando, has hosted me two times at MIT. The first time was in August/September 2004 and the second time in March 2005. I greatly enjoyed both my visits, during which I have been exposed to a different approach to physics as compared to the European way. In addition, Will's experience has been extremely valuable in improving my understanding of issues such as beam splitting, quantum amplification, and quantum statistics.

The activity at the Walther-Meissner-Institut was largely boosted by the arrival of Dr. Frank Deppe[5] in late 2005. Frank came with all the experience he gained during a three-year period at the Nippon Telegraph and Telephone (NTT) corporation, Japan, where he worked in the group headed by Prof. Hideaki Takayanagi and Dr. Kouichi Semba. I remember that Frank and I started having deep discussions about physics already one or two days after his arrival, in occasion of the submission of the unpublished "four pages" mentioned above. In a few weeks our discussions became a routine. Frank, I have learnt more from our discussions than reading a hundred books of physics. One day Frank came to my office with an old data set from his time in Japan. We looked at the data and thought that there could have been something particularly interesting hidden in them. It took more than two years, but we finally managed to publish those results in our first (and only for now!) Nature Physics paper. I wish that we will both keep publishing many of these kind of papers and I really hope that we will keep having our discussions, this time via Skype I assume, for a long time to come. As for Enrique, it is very hard to find the right words to thank Frank. In the past four years, we have shared our knowledge about quantum mechanics and qubits, our common interests in understanding what we are doing in the lab, we have shared good and bad times, accepted and rejected papers, and, most importantly, we have shared a great friendship which, I hope, we will continue sharing in the future.

My deepest gratitude goes also to Edwin P. Menzel with whom I carried out most of the experiments discussed in the first part of this thesis. Edwin has been of great help for me in the lab and from him I learnt to appreciate the technical aspects

[5]Still a graduate student at that time.

of experimental physics, which, indeed, are extremely important for a successful experiment. We spent many days and nights trying to measure "the cross-over" and "the nontrivial signals." It was a lot of fun. Edwin, I have no doubt that you will become an even better physicist than what you already are!

I would like to thank the entire scientific and technical staff of the Walther-Meissner-Institut. In particular, the present and former members of the qubit team: Elisabeth Hoffmann, Georg Wild, Thomas Niemczyk, Fredrik Hocke, Manuel Schwarz, Alexander Baust, Thomas Weißl, Dr. Hans Hübl and Dr. Andreas Emmert, Susanne Hofmann, Miguel Á. Araque Caballero, Heribert Knoglinger, Renke Stolle, Lars Eggenstein, Max Häberlein, Christian Rauch, Karl Madek, Tobias Heimbeck, Dr. Jürgen Schuler, and Dr. Chiara Coppi.

A special acknowledgement goes to my former officemates Dr. Leonardo Tassini, Wolfgang Prestel, and Deepak Venkateshvaran as well as to Frank Deppe's officemates (who had to suffer during the many discussions Frank and I had in the past years) Dr. Michael Lambacher and Toni Helm. I also thank Stephan Geprägs and Matthias Kath for their help in translating the exercises of the course in solid-state physics 2004-2005.

I would also like to thank Dr. Kurt Uhlig and two of the permanent guests of the Walther-Meissner-Institut, Dr. Christian Probst and Dr. Karl Neumaier. Watching them at work I started to understand what is the "art of cooling."

I thank Dr. Dietrich Einzel for his help with a few mathematical matters and Dr. Werner Biberacher for his help with burocracy matters.

I also thank the technicians Robert Müller, Dipl.-Ing. Thomas Brenninger, Helmut Thies, Christian Reichlmeier, Dipl.-Ing. Sepp Höß, and Astrid Habel for their help in manufacturing and machining components for our experimental setup.

During the years of my Ph.D. work I have visited several institutions. An incomplete list of people I interacted with in occasion of those visits follows. I would like to thank all of them. Some of the people mentioned below are now in different institutions. However, I list them according to the time of my visit.

MPQ, Germany - theory group of Prof. Dr. J. I. Cirac: Dr. Diego Porras, Dr. Juan José García-Ripoll (I am glad you are also working on circuit quantum electrodynamics now), Dr. Géza Giedke, Dr. Michael Wolf, Dr. Norbert Schuch, and Christine Muschik.

MPQ - experimental group of Prof. Dr. Gerhard Rempe: Jörg Bochmann and Barbara G. U. Englert. I thank Barbara also for the many discussions about the shelving project.

Technical University Munich, Germany - group of Prof. Dr. Steffen Glaser: Dr. Thomas Schulte-Herbrüggen (I always enjoyed our morning discussions on the 09:05 a.m. "tube!") and Dr. Andreas Spörl.

LMU, Germany - theory group of Prof. Dr. Jan von Delft: Dr. Ferdinand Helmer, Dr. Florian Marquardt, Johannes Ferber, Dr. Udo Hartmann, Dr. Michael Sindel, and Dr. Lásló Borda. In particular, I would like to thank Florian Marquardt for making me part of two of his projects. It has been my pleasure to work with you Florian. I think you are one of the smartest physicist I have ever met!

LMU - experimental group of Prof. Dr. Jörg P. Kotthaus: Dr. Stefan Ludwig and Prof. Dr. A. W. Holleitner.

University of Regensburg, Germany - theory group of Prof. Dr. Milena Grifoni: Dr. Francesco Nesi. A special acknowledgment goes to Prof. Dr. Jens "Jenzo"

Siewert with whom I had many fruitful discussions about the basic principles of superconducting qubits.

University of Augsburg, Germany - theory group of Prof. Dr. Peter Hänggi: Georg M. Reuther, Dr. David Zueco, Dr. Martijn Wubs, and Prof. Dr. Sigmund Kohler.

University of Erlangen, Germany - experimental group of Prof. Dr. Alexey V. Ustinov: Judith Pfeiffer, Dr. Jürgen Lisenfeld, Dr. Alexander Kemp, Dr. Abdufarrukh A. Abdumalikov, Jr., Dr. Alexandr Lukashenko, and Prof. Dr. Alexey V. Ustinov.

The quantronics group CEA-Saclay, France - experimental group of Prof. Dr. Daniel Esteve: Agustin Palacios-Laloy, Dr. François Mallet, Dr. Florian R. Ong, Dr. Patrice Bertet, Dr. Denis Vion, Dr. Cristian Urbina, and Prof. Dr. Daniel Esteve.

École Normale Supérieure, Paris, France - experimental group of Prof. Dr. Serge Haroche: Prof. Dr. Adrian Lupaşcu, Prof. Dr. Jean-Michel Raimond, Prof. Dr. Michel Brune, and Prof. Dr. Serge Haroche.

MIT, Boston, USA - experimental group of Prof. Dr. Terry P. Orlando: Dr. Janice C. Lee, Dr. David M. Berns, Dr. Jonathan L. Habif, Dr. William D. Oliver, and Prof. Dr. Terry P. Orlando.

University of Southern California, Los Angeles, USA: Dr. Justin F. Schneiderman, Prof. Dr. Tommaso Roscilde, and Prof. Dr. Stephan Haas.

University of Yale, New Haven, USA - experimental group of Prof. Dr. Robert J. Schoelkopf: Dr. Johannes Majer, Dr. David I. Schuster, Dr. Luigi Frunzio, and Prof. Dr. Robert J. Schoelkopf.

IQC and University of Waterloo, Waterloo, Canada: Prof. Dr. Frank K. Wilhelm, Prof. Dr. Jan B. Kycia, and Prof. Dr. A. Hamed Majedi.

University of California at Santa Barbara - experimental groups of Prof. Dr. John M. Martinis and Prof. Dr. Andrew N. Cleland: Matthew Neeley, Aaron D. O'Connell, Radoslaw "Radek" C. Bialczak, Daniel Sank, Dr. Markus Ansmann, Dr. Max Hofheinz, Dr. Martin Weides, Prof. Dr. Andrew N. Cleland, and Prof. Dr. John M. Martinis. In particular, I would like to thank John Martinis and Andrew Cleland for giving me the possibility to continue working on superconducting qubits in their laboratory as a postdoctoral fellow after the submission of this thesis! I am looking forward to this new adventure!

University of California at Berkeley: Prof. Dr. John Clarke, Prof. Dr. Irfan Siddiqi, Dr. Ofer Naaman, Dr. Emile Hoskinson, Dr. R. Vijayaraghavan, and Prof. Dr. Eli Yablonovitch.

California Institute of Technology, Pasadena, USA - experimental group of Prof. Dr. Jonas Zmuidzinas: Dr. Jiansong Gao and Prof. Dr. Jonas Zmuidzinas.

The University of Wisconsin Madison, USA - experimental group of Prof. Dr. Robert F. McDermott: S. Sendelbach, D. Hover, and Prof. Dr. Robert F. McDermott.

Last but not least, I would like to thank Yasunobu Nakamura and Prof. Dr. Franco Nori. Even if we met only once, it feels as we knew each other already. The discussions we have had via email have always been very pleasant and I hope to visit you in Japan one day and perhaps even to work with you!

These years in Munich have not only been physics and work. I have also enjoyed the culture, the music, the art, and the beauty of a city which ranks as 7th world's

top city offering the best quality of life. Most importantly, in Munich I have met my wife Alexandra Bardysheva - Sasha. Sasha, you have changed my life and I thank you from the bottom of my heart for your love and extreme patience during these stressing years of hard work. I am sure we will have a wonderful and happy life together. I will always cherish you and I will try my hardest to take good care of you.

Matteo Mariantoni, Munich, September 2009[6]

[6]Final revised edition: Fall 2010

Contents

List of Figures

List of Tables

Chapter 1

General Introduction

What is the importance of the interaction between light and matter and what is the interest in studying it? The answer to the first question lies in front of our eyes, manifesting itself in that fundamental cycle of nature which repeats itself every day: the photosynthesis.[1] Releasing oxygen as a waste product, the process of photosynthesis is vital for life on Earth. The light emitted by the Sun is absorbed by the chlorophylls contained in the photosynthetic reaction centers of the plants. Part of the sunlight energy gathered by the chlorophylls is stored as adenosine triphosphate, the rest is utilized to remove electrons from a substance such as water [1]. This light-electron interaction, which stands at the basis of the Calvin cycle, is the archetypical example of quantum electrodynamics. With such example in mind, the interest in understanding the basic mechanisms behind the interaction between light and matter is an obvious consequence!

1.1 The Light-Matter Interaction: a Historical Excursus

"When Marcellus withdrew them [the ships of the Roman fleet] a bow-shot, the old man [Archimedes] constructed a kind of hexagonal mirror, and at an interval proportionate to the size of the mirror he set similar small mirrors with four edges, moved by links and by a form of hinge, and made it the centre of the sun's beams– its noon-tide beam, whether in summer or in mid-winter. Afterwards, when the beams were reflected in the mirror, a fearful kindling of fire was raised in the ships, and at the distance of a bow-shot he turned them into ashes. In this way did the old man prevail over Marcellus with his weapons" (from John Tzetzes, Book of Histories (Chiliades) - circa 12th century AD) [2]. Whether the Archimedes heat ray (cf. Fig. 1.1) is a myth, fruit of the invention of Anthemius of Tralles, or reality, it nevertheless shows that the ancient Greeks might already have considered the interaction between light and matter as a useful topic of research. That of the great Archimedes would have been the first implementation of cavity quantum electrodynamics (QED) with direct application into everyday life, where the poor Roman vessels played the role of the atoms!

[1] The word photosynthesis comes from the ancient Greek photo-, "light," and synthesis, "placing with."

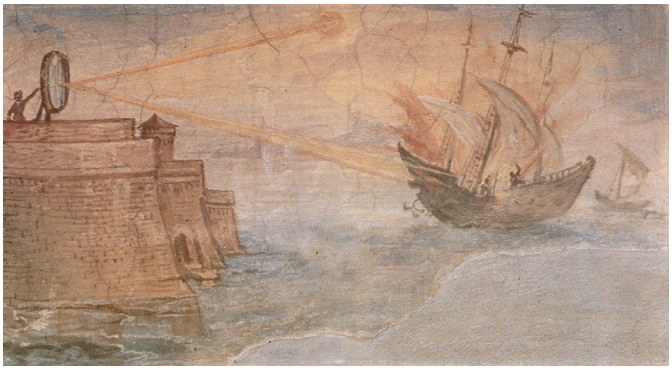

Figure 1.1: The burning mirrors of Archimedes. Wall painting from the "Stanzino delle Matematiche" in the Galleria degli Uffizi (Florence, Italy). Painted by Giulio Parigi (1571-1635) in the years 1599-1600.

The debate on light and matter continued based on more mature basis throughout the 17th and 18th centuries. In his treatise on optics [3], Newton argues about light and void and supports the hypothesis that light might consist of corpuscles, or atoms, emitted from a luminous source such as the Sun. In contrast to Newton's doctrine, a number of contemporary philosophers and mathematicians of his, such as Hobbes, Descartes, Spinoza, Huyghens, and Leibniz, asserted that light consists of a wave motion in an all-pervasive material ether.

After the theoretical and experimental developments on the concept of electromagnetic waves made by Maxwell, Hertz, and Heaviside [4–11], the discussion on the meaning of light and of its interaction with solid matter moved to Munich. In the years before World War I, Munich was the vibrant capital of a large cultural movement and one of the main hubs of research in physics. Considering that in this very moment the author is writing only a few hundred meters away from Munich's "Hofgarten," a tribute to the school of Arnold J. W. Sommerfeld is in order. Arnold Sommerfeld, who was appointed professor of theoretical physics in Munich in 1906, was undoubtedly the central figure in the "coffee meetings" at the Hofgarten, a charming garden at the Northern gates of the inner city of Munich. During Sommerfeld's time, the coffeehouse at the Hofgarten soon became one of the centers of scientific innovation in the South of Germany. The Hofgarten discussions created an entire generation of exceptional physicists. The "Sommerfeld school," a real furnace of talents, had among its ranks physicists and chemists of the caliber of Max T. F. von Laue, Werner K. Heisenberg, Peter J. W. Debye, Isidor I. Rabi, Wolfgang E. Pauli, Linus C. Pauling, and Hans A. Bethe - all Nobel Laureates but Sommerfeld [12].

Since the time of the Newton-Leibniz debate on the nature of light, eminent physicists had argued whether light behaved as a wave or a particle. Five years after Röntgen's discovery of X-rays, on 19th October 1900 Max Planck[2] presented his theory on the blackbody radiation, thus paving the way to the advent of quan-

[2]The author notices that only 36 civic numbers down the street where he lives, resides the Maximiliansgymnasium (Karl-Theodor-Straße 9, Munich), i.e., the high school where Max Planck became acquainted with astronomy, mechanics, and mathematics under the guidance of the mathematician Hermann Müller.

tum mechanics [13]. Planck's theory showed that energy is composed of individual particles in a similar way as matter is composed of atoms. In 1905, the hypothesis on the particle nature of light was strengthened by Albert Einstein's explanation of the photoelectric effect [14]. The photoelectric effect, that is the current flow and heat release occurring when light shines on a metal surface, is a beautiful example of light-matter interaction.

This was the physics background of one of the most relevant discoveries originating from the school of the Hofgarten coffeehouse. On 23rd April 1912 in the laboratories of the Ludwig-Maximilians-Universität in Munich, Walter Friedrich and Paul Knipping carried out an experiment designed by Max von Laue, where they proved the wave-like nature of X-rays and, at the same time, the space-lattice structure of crystals [15]. It started to become more clear that light or, more in general radiation, behaves both as a wave and a particle. Almost simultaneously, in 1911 Heike Kamerlingh Onnes discovered superconductivity [16].

The understanding of the physics of light advanced substantially thanks to the seminal work due to Albert Einstein on the quantum theory of radiation (1917) [17]. We remind the reader to chapter 4, Sec. 4.1 for a detailed analysis of that work. A major stir towards a complete theory of quantum electrodynamics was created by the experiment and subsequent theoretical explanation of the so-called Lamb shift (1947) [18, 19]. This phenomenon triggered the attention of Shin'ichirō Tomonaga, Julian S. Schwinger, Richard P. Feynman, and Freeman J. Dyson to develop the QED theory [20–27], which opened up a new era in the history of physics in the 20th century. In the same years the theory of QED was developed, the formal treatment of the phenomenon of superconductivity reached its climax in the theories of Ginzburg and Landau (1950) [28] and, later, of Bardeen, Cooper, and Schrieffer (BCS theory, 1957) [29].

The invention of the laser[3] in 1958 by Arthur L. Schawlow and Charles H. Townes [30], then developed and patented by Theodore H. Maiman [31], launched the research topic of quantum optics. From the theoretical point of view, quantum optics was born with the studies on optical coherence and on the states of the radiation field by Roy J. Glauber in 1963 [32, 33], which followed a large body of work on the semiclassical theory of light by Edward M. Purcell and Leonard Mandel [34–36]. In the early-mid 60's, also superconductivity witnessed a rapid sequence of experiments and theoretical achievements, which, in order, allowed a) to prove the existence of the flux quantum [37, 38], b) to predict the Josephson effect [39, 40], c) to realize the first Josephson tunnel junction [41],[4] and d) to implement the first DC and RF superconducting quantum interference devices (SQUIDs) [42, 43].

In 1977, the field of quantum optics was finally persuaded by undoubtable experimental evidence that there exists a class of light sources which cannot be explained in classical or semiclassical terms, but only by means of a fully quantum-mechanical treatment. The article on photon antibunching in resonance fluorescence by H. Jeff Kimble *et al.* [44] represents a milestone for our modern understanding of light as an entity made up of photons. Only a few years later, in the early-mid 80's

[3] Acronym for "light amplification by stimulated emission of radiation."

[4] We cannot avoid to remind the reader the title of the article by Anderson and Rowell, "Probable Observation of the Josephson Superconducting Tunneling Effect." How many articles would be accepted nowadays on the Physical Review Letters starting with the word *probable*? *Probably* none!

the experimental prove of macroscopic quantum tunneling and of the energy-level quantization in Josephson junctions [45–49] as well as the first observation of single-electron charging effects [50] opened up the avenue of quantum coherence on a chip and quantum circuits.

By the early 90's, all necessary constituents for modern applications based on atoms and light or Josephson junctions and microwave fields were available in a number of laboratories around the globe.

1.2 The Light-Matter Interaction: Modern Applications

We are now ready to appreciate the further developments in the fields of quantum optics and quantum circuits achieved in the past two decades. In particular, we focus on experimental realizations where the light is confined within a privileged environment: a cavity.

The section is organized as follows. First (cf. Subsec. 1.2.1), we briefly review the basic concepts of cavity QED distinguishing between resonant and dispersive regime and discussing the different measurement methods typically employed in experiments. We then explain the experimental apparatuses used in quantum optical cavity QED and enumerate chronologically the most important experimental achievements both for implementations at optical and microwave frequencies.

Second (cf. Subsec. 1.2.2), we present two classes of "artificial atoms" based on semiconducting and superconducting devices, respectively: quantum dots and superconducting qubits. In the case of quantum dots, we shortly introduce the most commonly used dot designs and show that it is possible to perform cavity QED experiments with them. As always, the experimental milestones reached in the field are enumerated. In addition, we make a remark on the measurement techniques used for the detection and characterization of optical photons. In the case of superconducting qubits, we delve into a detailed discussion of their working principle, define charge an flux qubits, and give a list of relevant experiments. Finally, we discuss the interaction between superconducting qubits and microwave on-chip resonators. This architecture is defined as circuit QED and constitutes one of the central topics of this thesis. Before concluding the section, we review the most important experiments realized in circuit QED in the past five years.

1.2.1 Cavity QED with Natural Atoms

Among the most fruitful playgrounds for the experimental test of quantum optical systems stands out the subfield referred to as cavity QED.

The three fundamental ingredients for the realization of a cavity QED experiment are: 1) an *atom* (or a stream of atoms); 2) a *photon* (or a beam of photons); 3) a cavity. In standard cavity QED, the atoms are let pass through the cavity, where photons are opportunely "trapped." In this sense, the cavity represents a special environment that allows the confinement of the photon-atom interaction.

If the cavity were a totally closed and lossless system, the photons would be trapped inside it forever. In real applications, we must be able to access the cavity

in order to perform an experiment. The inevitable apertures on the cavity walls[5] reduce the photon trapping time. This time is further reduced because of walls' imperfections, which give rise to radiation loss. The combined effect of the apertures and radiation loss sets the so-called *loaded quality factor*, Q_{L}, of the cavity.[6]

The presence of a cavity in a cavity QED experiment has two important consequences. The first concerns the coupling strength between photons and atoms (*(i)*) and the second the coherence properties of the system (*(ii)*).

(i) - On one hand, the electromagnetic radiation field in free space is represented by *travelling* waves. The spatial pattern of a travelling wave varies continuously in time, which makes it hard to couple, for example, to a nearby atom. In this case, the coupling strength for the atom-photon interaction cannot easily be controlled. On the other hand, due to the boundary conditions imposed by the cavity walls, the electromagnetic field inside a cavity maintains a well-define shape at all times. The waves associated with such a field are called *standing* waves and their spatial pattern is called *mode*. In this case, it is possible to engineer the photon-atom coupling strength in order to maximize it. The photon-atom coupling coefficient, defined as g, is a relevant figure of merit of a cavity QED implementation.

(ii) - The cavity behaves as an effective filter, narrowing down the energy spectrum to which an atom is coupled. The atoms used in cavity QED experiments can usually be regarded as two-level atoms, which means they are characterized by an energy groundstate, $|\mathrm{g}\rangle$, and a first excited state, $|\mathrm{e}\rangle$. These two states are separated by an energy gap, ΔE_{at}. The energy gap is oftentimes defined in terms of a wavelength, $\lambda_{\mathrm{at}} = hc/\Delta E_{\mathrm{at}}$, or a frequency, $f_{\mathrm{at}} = \Delta E/h$. The latter is called transition frequency of the atom. Here, h is the Planck constant and c the velocity of light in free space. The three-dimensional (3D) free space is characterized by a continuous energy spectrum, which corresponds to a continuum of frequencies. When an atom is placed in free space, one of the infinite frequencies f obviously equals the atomic transition frequency, $f = f_{\mathrm{at}}$. In this case, if the atom were initially in the excited state $|\mathrm{e}\rangle$, it would rapidly decay to the groundstate $|\mathrm{g}\rangle$ emitting energy into the environment in the form of a photon. The information which was once stored in the atom as an energy excitation is forever lost in the environment. This is the prototypical example of an *energy relaxation process*. The rate at which an atom decays is defined as γ, the inverse of which sets the atom lifetime. Being typically an unwanted process,[7] energy relaxation should be minimized in experiments. The presence of a cavity gives us this opportunity.

In fact, in contrast to the 3D free space, the energy spectrum inside a cavity is discrete with a discrete set of frequencies, f_i $(i = 1, 2, \ldots)$. Each of these frequencies corresponds to a cavity mode. In real applications, a cavity mode is characterized by a continuous-narrow frequency band δf_i centered around f_i, rather than a single-sharp frequency f_i only. This is due to the fact that the cavity quality factor is usually finite. The higher the quality factor, the narrower the mode frequency band, $\delta f_i \propto 1/Q_{\mathrm{L}}$. Bearing this notion in mind, two distinguished scenarios are now possible. The first is when the transition frequency of the atom equals one

[5] In reality, the cavity design is more complex than just a box with some holes! For example, cf. Figs. 1.2 and 1.3.

[6] We recall that the cavity quality factor contains the same information as the cavity finesse, which is the figure of merit mostly used when referring to optical cavities.

[7] There are several applications where it is desirable to have fast relaxation dynamics. We will not discuss these cases here.

of the cavity frequencies, $f_{\rm at} = f_i$. This case is similar to that of free space, but with an important difference. This time, the energy of an initially excited atom which decays to the groundstate is emitted in the form of a photon into a cavity mode (Purcell effect). If the quality factor of that mode is high enough, the photon remains trapped inside the cavity for a long time before being lost into the external environment via the cavity apertures or other loss mechanisms. The information which was stored in the atom does not get lost until a time on the order of the cavity lifetime, $1/\kappa = 1/\delta f_i$. The second scenario is when the transition frequency of the atom is different from any of the cavity frequencies, $f_{\rm at} \neq f_i$, $\forall i$. If the atom is in the excited state, it cannot decay into the groundstate emitting a photon because of the frequency mismatch between its transition frequency and the cavity frequencies. The atom lifetime is thus enhanced due to a mismatched environment. The enhancement is obviously more effective the further the atomic frequency is from the closest cavity mode frequencies and the narrower are the frequency bands of such modes (i.e., the higher is the cavity quality factor). This case, which does not have counterpart for an atom in free-space, clearly shows the filtering action of the cavity.

It is worth pointing out that the lifetime enhancement due to the cavity is independent of other atom loss mechanisms. In fact, atoms are not only characterized by energy relaxation processes, but also by decoherence mechanisms such as dephasing.[8] The atomic phase coherence generally does not benefit from the presence of a cavity.

It is also worth mentioning that the twofold nature of the cavity quality factor, i.e., the combined action of walls' apertures and radiation loss, gives rise to two important subcases. When the radiation loss is the dominant contribution to the quality factor, once a photon is emitted into the external environment it is practically lost anywhere in the 3D space. In contrast, when the contribution attributable to the apertures dominates over radiation loss, the photon can be guided into privileged directions defined by the geometrical shape of the apertures. In this case, the photon is not actually lost in space and the information carried by it can still be utilized for further operations.

Finally, another characteristic time scale of cavity QED implementations in quantum optics is the limited dwell time of an atom inside the cavity. Atoms are generated outside the cavity and then let pass through it. As a consequence, they interact with the photons inside the cavity only for a finite, usually short transit time, $t_{\rm trans}$. As we shall show later, major experimental efforts have been realized in order to keep an atom trapped inside a cavity under stable conditions and for a long time.

Resonant and Dispersive dynamics

Our discussion on photon emission into a cavity mode and atom lifetime enhancement opens the way to the description of the photon-atom dynamics in cavity QED. The dynamics associated with a cavity QED system can be distinguished into two major categories: the resonant and dispersive regime.[9]

[8] As we will show later, this issue is more important for "artificial atoms." We mention it here for completeness.

[9] Obviously, the transition between these two regimes is smooth and there are intermediate cases. For simplicity, we will not focus on those in the present discussion.

The resonant regime occurs when the atomic transition frequency is equal to one of the cavity frequencies, $f_{\rm at} = f_i$. Let us assume a high quality factor cavity initially prepared with a single photon and a long-lived atom prepared in the groundstate $|{\rm g}\rangle$. Before being emitted into the external environment, the photon remains trapped inside the cavity long enough to be absorbed by the atom, which, thus, gets populated to the excited state. While decaying to the groundstate, the atom then emits a photon into the cavity mode. The photon is again absorbed by the atom, giving rise to an emission-absorption process which continues at a rate set by the photon-atom coupling coefficient g. The larger the g, the higher the number of oscillations the photon-atom system undergoes within the minimum of the cavity and atom lifetimes, $\min\{1/\kappa, 1/\gamma\}$. Such oscillations are called vacuum Rabi oscillations and g is defined as the vacuum Rabi frequency.[10]

The dispersive regime occures when the atom transition frequency is largely detuned from the closest of the cavity frequencies. Mathematically, it is expressed by the condition $|f_{\rm at} - f_i| \gg g$. In this case, no photon-atom oscillations can take place because of the large frequency mismatch.

We can try to understand the dispersive regime by means of a simple Gedanken experiment. Let us consider an empty cavity, with no atoms. For simplicity, we assume the cavity to be made of a pair of semitransparent parallel mirrors, positioned one in front of the other. If we shine a laser beam towards the left mirror, part of the beam will be reflected by the mirror and part transmitted. The transmitted portion of the beam will then continue towards the right mirror, where, again, it will be partially reflected and partially transmitted. The reflected portion will now go back to the left mirror where it will be partially reflected and partially transmitted and so on and so forth until a standing wave is established inside the cavity. The electromagnetic path followed by the light beam is defined by the distance between the two mirrors or, in other terms, by the cavity resonance frequency. If we now place an atom inside the cavity, in the resonant regime this will give rise to a sort of amplitude modulation of the light beam, which ultimately results in the Rabi oscillations described above.[11] In the dispersive regime, instead, the presence of the atom modifies the reflection/tranmsission properties of the cavity. That is, if we shine a light beam through the cavity, the beam will not only be reflected and transmitted by the cavity mirrors, but also by the atom. The atom behaves as if it were an additional "mirror" inside the cavity. Since the light bounces back and forth more times in the presence of an atom, it is clear that the corresponding effective electromagnetic path is longer than in the case of an empty cavity. A longer electromagnetic path results in a redshift of the resonance frequency of the cavity! In reality, the direction of the shift and, thus, whether the effective electromagnetic path is longer or shorter, depends on which state the atom is prepared and on the sign of the cavity-atom detuning.

In summary, the relevant energy scales in a cavity QED experiment are: a) the atom transition frequency, $f_{\rm at}$ and b) the cavity resonance frequency f_i closer to $f_{\rm at}$. The relevant rates are: 1) the photon-atom coupling strength, g; 2) the

[10] In this general introduction, we will not be picky on possible factors of 2 or π in the definition of g and on possible global phases. These issues will be properly addressed throughout the rest of this thesis.

[11] This is a highly simplified representation of the vacuum Rabi dynamics in analogy to classical electronics. Basically, a high frequency carrier, the light beam at frequency $f_{\rm at}$, is amplitude-modulated (AM) by the low frequency Rabi dynamics at frequency g.

cavity decay rate, κ; 3) the atom lifetime, γ; 4) the inverse atom transit time, $1/t_{\text{trans}}$. If the atom transit time is long compared to all the other time scales of the system, we can neglect it from the discussion. In the resonant regime, $f_{\text{at}} = f_i$, and under strong coupling conditions, $g \gg \max\{\kappa, \gamma\}$, a large number of vacuum Rabi oscillations can occur before the photon-atom excitation relaxes. In the dispersive regime, $|f_{\text{at}} - f_i| \gg g$, the cavity resonance frequency is shifted by the presence of the atom. The magnitude of the shift depends on the coupling strength g and its sign (redshift or blue-shift) on the state of the atom and on the sign of the detuning.

A formal treatment of the resonant and dispersive regime of cavity QED will be given in chapter 2, Subsec. 2.3.3.

The Measurement Dilemma: Photons or Atoms?

Since there are two main actors on the stage of a cavity QED experiment, the photon and the atom, the question whether it is more suitable to measure the first or the second in order to obtain information on the total system naturally arises.

As a matter of fact, both the photon and the atom encode the same amount of information about a cavity QED system, even if, for real applications, it makes a considerable difference which one is measured. Depending on the frequency of operation, in the past three decades two main types of experiments have been developed. For cavity QED implementations at optical frequencies (i.e., for wavelengths on the order of 1000 nm) the light emitted by the cavity is directly detected and/or manipulated. The two major groups actively working in this direction are those headed by Gerhard Rempe at the Max Planck Institute for Quantum Optics (MPQ), Garching, Germany, and by H. Jeff Kimble at the California Institute of Technology, Pasadena, USA. Figure 1.2 shows a standard cavity QED experimental setup employed in the Rempe group (courtesy of Alexander Kubanek). For implementations at microwave frequencies (on the order of 50 GHz) the atoms are typically detected. The two groups actively working in this direction are those of Serge Haroche, Jean-Michel Raimond, and Michel Brune at the École Normale Supérieure (ENS), Paris, France, and of Ben T. H. Varcoe at the University of Leeds, UK. Historically, there has been another important group involved in cavity QED at microwave frequencies: the group of H. Walther, also at the MPQ in Garching. Figure 1.3 shows the experimental setup of the Paris group (courtesy of Jean-Michel Raimond and Michel Brune).

Optical Experiments. The cavities employed in a typical experiment at optical frequencies consist of a pair of spherical dielectric mirrors with ultra-high reflectivity. The cavity lateral dimension is approximately 0.1 mm and its finesse is on the order of 4×10^5. The distance between the mirrors can be adjusted by means of a piezoceramic tube in order to tune the cavity frequency. Several holes allow the atoms to enter the volume enclosed by the two mirrors.

The atoms used are usually cold rubidium or cesium atoms. The preparation principle is that of the "atomic fountain," where the cold atoms are launched into the cavity with light forces. After being trapped by means of a magneto-optical trap (MOT), the atoms are cooled first by an optical molasses and, then, by frequency detuning. The detuning also allows the vertical acceleration of the atoms, which are finally directed into the cavity.

The photons emitted by the cavity are usually detected by means of photodiodes characterized by a quantum efficiency of approximately 50 %. Depending on

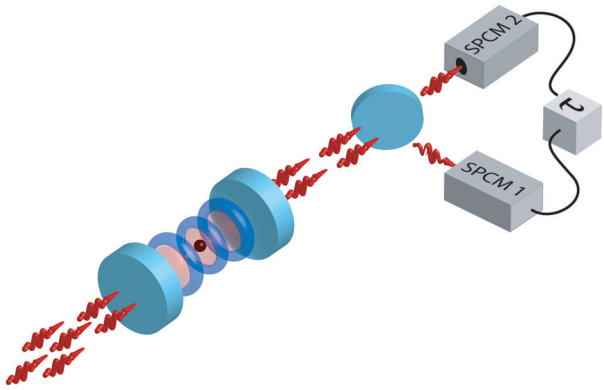

Figure 1.2: Quantum-optical cavity QED at optical frequencies: the setup of the MPQ group (courtesy of Alexander Kubanek; cf. also Ref. [51]). From left to right: A laser beam (red arrows) is sent through a cavity (blue mirrors), where it interacts with an atom. The cavity can be made highly asymmetric such that, after interacting with the atom, the photons are emitted in one special direction, e.g., to the right side. The emitted photons are splitted with an optical beam splitter and then detected by means of, e.g., single photon counting modules (SPCM 1 and 2). The time-correlation properties (τ) of the two stream of photons are finally obtained.

the specific implementation, also photomultiplier tubes or single photon counting modules can be used [51].[12]

The first observation of the normal-mode splitting due to the photon-atom interaction in optical cavity QED was realized in 1992. In that year, R. J. Thompson, G. Rempe, and H. J. Kimble were able to resolve the vacuum-Rabi splitting by investigating the spectral response of a small collection of atoms strongly coupled to a cavity under weak excitation conditions (a sort of low-level spectroscopy at optical wavelengths) [52].

Since that experiment, a tremendous progress has been realized in quantum-optical cavity QED. Here is a short list of the most important achievements: (1) A one-atom laser in the regime of strong coupling has been experimentally realized [53]; (2) an atom has been trapped inside a cavity for several tens of seconds [54]; such an experiment has made possible to overcome the short transit time issue of an atom in a cavity and (3) has allowed the implementation of a single photon server with one atom [55]; (4) the photon blockade in an optical cavity with one trapped atom has been observed [56]; (5) the quantum nature of the photon-atom interaction has been proved beyond any doubt by studying the nonlinear spectroscopy response of a cavity where a single atom is illuminated with two photons [57];[13] (6) this has also made possible the realization of a two-photon gateway [58] and can eventually lead to a single photon transistor. Recently, the possibility to study two independent cavity QED systems via two-photon quantum interference has been envisioned and

[12]The author thanks Jörg Bochmann for his detailed explanation of the optical cavity QED setup in occasion of a visit at the MPQ in Garching in early 2009.

[13]This experiment is highly related to our two-photon experiment in circuit QED to be discussed in chapter 8, Sec. 8.3.

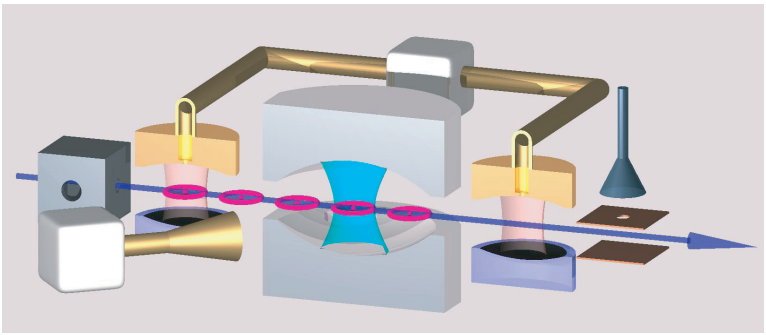

Figure 1.3: Quantum-optical cavity QED at microwave frequencies: the setup of the Paris group (courtesy of Jean-Michel Raimond and Michel Brune; cf. also Ref. [60]). From left to right: Circular Rydberg atoms [magenta (middle grey) circles] are prepared one at a time and fly at thermal velocities (100 to 500 ms^{-1}) through the apparatus. Before and after interacting with the superconducting cavity (depicted in the center), the atoms are manipulated in the so-called classical Ramsey zones (left and right of the cavity). The cavity state can be prepared by means of a classical microwave source (front left). After passing through the second Ramsey zone, the atoms are detected by a state-selective field ionization detector (last device on the right).

is being realized in the laboratory [59]. We find this advanced implementation of cavity QED based on two cavities an intriguing research area, which goes along the lines of our pioneering studies on two-resonator circuit QED (cf. chapters 5 and 6) and correlation homodyne detection at microwave frequencies (cf. chapters 3 and 4).

Microwave Experiments. There are two types of cavities employed in cavity QED experiments at microwave frequencies: closed superconducting cavities and open Fabry-Perot superconducting cavities. The former were used at the MPQ in Garching and are being used in Leeds,[14] whereas the latter are used at the ENS in Paris. The Paris cavities consist of two superconducting mirrors made of optically polished copper onto which a niobium layer is then deposited by cathode sputtering. The lateral dimension of the cavity is approximately 5 cm and its quality factor is on the order of 3×10^8. Also this kind of cavities can be tuned by means of piezo elements.

The atoms used are rubidium atoms, which are prepared in low angular momentum Rydberg states by means of a stepwise laser excitation. At the ENS in Paris, the standard Rydberg states are efficiently and selectively transferred to the so-called circular level in an adiabatic rapid passage process involving static electric and magnetic fields and a radio-frequency electric field. This is a rather complex procedure which makes the Paris experiment unique in its gender!

After interacting with the intracavity field, the Rydberg atoms are detected via field ionization upon exiting the cavity. For Rydberg atoms in the circular state the detection efficiency is up to 80 % with a level assignation error (selectivity) of a few % [60].[15]

[14] We notice that the implementation with closed cavities is also referred to as micromaser.

[15] The author thanks Jean-Michel Raimond and Michel Brune for their detailed explanation of

The dawn of microwave cavity QED can be considered the experimental work of C. Fabre *et al.* on Rydberg atoms and radiation in a resonant cavity [61].

Since that experiment, the quantity of physics phenomena unveiled by microwave cavity QED has been enormous. Here is a short list of the most important achievements: (1) self-induced Rabi oscillations in two-level atoms excited inside a resonant cavity have been observed [62]; (2) a two-photon maser has been realized [63];[16] (3) the sub-Poissonian photon statistics in a micromaser have been observed [64]; (4) the quantum nondemolition measurement of small photon numbers by Rydberg-atom phase-sensitive detection has been performed [65]; (5) quantum jumps of a micromaser field have been measured [66]; (6) the field quantization in a cavity has been directly tested by the observation of quantum Rabi oscillation [67]; (7) Einstein-Podolsky-Rosen pairs of atoms have been generated [68]; (8) a single photon has been measured without destruction [69] and (9) the preparation of pure number states of the radiation field realized [70]; (10) the Wigner function of a one-photon Fock state in a cavity has been measured [71]; (11) a mesoscopic field has been entangled with an atom [72]; (12) the birth and death of a photon in a cavity has been recorded via the measurement of light quantum jumps [73]; (13) the reconstruction of non-classical cavity field states with snapshots of their decoherence has been implemented [74]. Recently, an experimental setup based on two cavities has been realized in Paris. The ongoing experiments will eventually help understanding the delocalization of quantum phenomena over two distinguished objects. This development gives us further confidence on the potential of the two-resonator circuit QED realizations envisioned in this thesis (cf. chapters 5 and 6).

To conclude, the two implementations of cavity QED with natural atoms based on optical or microwave cavities can be considered to be complementary architectures: At optical frequencies the light emitted by the cavity is used to probe the photon-atom interaction, whereas at microwave frequencies this role is played by the atoms. Remarkably, if desired, both the light and atoms emitted by a cavity can be reused for further manipulations.

1.2.2 Cavity QED with "Artificial Atoms"

In this subsection, we briefly introduce the two most prominent groups of "artificial atoms" utilized in cavity QED applications: quantum dots and superconducting qubits. In both cases, after summarizing the basic operation principles we present a selection of the most relevant experimental achievements.

We will keep the discussion on superconducting qubits and circuit QED short given that this is the main topic of the present thesis. An exhaustive treatment of this field of research will be presented in the following chapters. In this brief introduction, we will try to explain the working principle of charge and flux qubits without recurring to the derivation of any Hamiltonian.

the microwave cavity QED setup in occasion of a visit at the ENS in Paris in late 2008.

[16] Related to our work; cf. chapter 8, Sec. 8.3.

Quantum Dots

A quantum dot is defined as a small region of a semiconductor where excitons[17] or electrons[18] are confined in all three spatial dimensions. This scenario resembles one of the prototypical examples studied in quantum mechanics: a particle confined in a three-dimensional box. If the dimensions of the confinement region are comparable to the wavelength of the confined excitons or electrons, the dot is characterized by a discrete energy spectrum, which is similar to the spectrum of natural atoms.[19] Remarkably, the energy levels of a quantum dot can be tuned *in situ* by attaching leads to them and establishing opportune potentials.

There are several ways to confine excitons or electrons in semiconductors, resulting in different methods to produce quantum dots. In general, quantum dots are grown by advanced epitaxial techniques or by depleting a two-dimensional electron gas (2DEG).

Self-assembled quantum dots nucleate spontaneously under suitable conditions during a molecular beam epitaxy (MBE) process, when a material is grown on a substrate to which it is not lattice matched. The resulting strain produces coherently strained islands on top of a so-called two-dimensional "wetting-layer." The islands can subsequently be buried to finally form the quantum dot, the dimensions of which range between 5 and 50 nm. A fundamental application of self-assembled quantum dots is for the realization of single-photon sources. One of the main limitations of this method is represented by the lack of control over the positioning of individual dots.

Individual quantum dots can be created by depleting a 2DEG. The 2DEG, which constitutes a plane where electrons are allowed to move freely, can be realized, for example, in a semiconductor heterostructure such as GaAs/AlGaAs. By combining layers of semiconducting materials, it is possible to create an edge in the band structure of the electrons. As a result, the electrons are localized within this edge and confined in the z-direction of the structure, thus forming a 2DEG. The 2DEG can be depleted by applying a negative voltage to a metal gate fabricated on top of the heterostructure. Due to the Schottky effect, direct tunneling of electrons from the metal gate to the semiconductor heterostructure is not allowed and a Schottky barrier is formed. In addition, due to the Coulomb interaction between the electrons in the 2DEG and those on the metal gates, the electrons in the 2DEG are further confined. This confinement acts now in the $x-y$-direction, depending on the gate geometry on the top of the structure. In this way, a so-called *lateral quantum dot* is realized. Typical dimensions for lateral quantum dots are on the order of a few 100 nm or larger. Such quantum dots are mainly of interest for experiments and applications involving electron (or hole) transport, i.e., an electrical current.

The energy spectrum of a quantum dot can be engineered by controlling the geometrical size, shape, and the strength of the confinement potential defined by the metal gates. In contrast to natural atoms, it is relatively easy to connect quantum

[17] We recall that an exciton is a bound state of an electron and a hole in an insulator or semiconductor, i.e., a Coulomb-correlated electron-hole pair. Excitons are elementary excitations, or quasiparticles, of a solid.

[18] Similar arguments apply to holes.

[19] We find the distinction between natural and "artificial" atoms to be awkward. Everything we find in nature is natural. However, this is the generally accepted classification and we use it here for consistency with the literature.

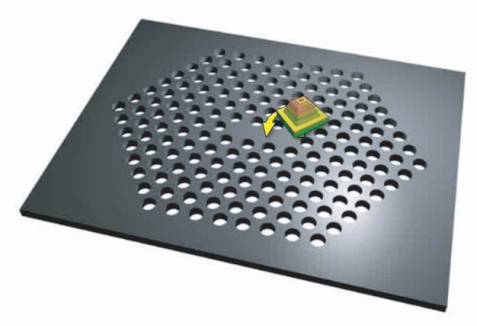

Figure 1.4: Cartoon of a 2D photonic crystal ("L3" resonator) with self-assembled quantum dot in the center (courtesy of Jonathan J. Finley, Michael Kaniber, and Arne Laucht; cf. also Ref. [81]).

dots by tunnel barriers to conducting leads, which allows the application of the techniques of tunneling spectroscopy for their investigation [75, 76].

There are other types of quantum dots such as vertical dots or "dots" created by impurities. In addition, both the charge and spin degree of freedom can be used in manipulating a dot. We remind the interested reader to Refs. [77–80] for an exhaustive discussion on mostly all types of quantum dots.

CAVITY QED WITH QUANTUM DOTS

Self-assembled quantum dots are actively being used in cavity QED applications. The dots are typically fabricated inside 2D photonic crystal membrane cavities, where, depending on the coupling regime, they can either serve as light emitters or be used to investigate the fundamental light-matter interaction as well as the effects of the altered local photonic density of states on their spontaneous emission properties.

Figure 1.4 shows a cartoon of a 2D photonic crystal with self-assembled quantum dot in the center (courtesy of Jonathan J. Finley, Michael Kaniber, and Arne Laucht). By tailoring in a controlled manner the size of a single hole in such a 2D photonic crystal it is possible to disrupt the translational crystal symmetry. This has the effect to create a tiny region where light can be trapped. Such a defect effectively constitutes a nanoscale optical cavity characterized by a volume on the order of a cubic half wavelength. This particular type of cavity is called "L3" resonator since it consists of a line of three missing holes in a line. The wavelengths achievable in L3 resonators are only a few hundred nanometers [81].

Quantum dots in the weak coupling regime. In the weak coupling regime, i.e., when $g < \{\kappa, \gamma\}$, the Purcell effect can be used to enhance the induced emission rate into a cavity mode initially prepared in the vacuum state instead of into other environmental modes.[20] The light is effectively funneled into a privileged direction

[20]Several authors prefer to talk about spontaneous emission into the cavity mode. It is true that the mode is in the vacuum state. It is also true that, according to Einstein's definition of the emission-absorption rates (cf. Ref. [17]), when an atom emits an excitation into the vacuum this should be referred to as a spontaneous emission. However, under suitable conditions, the presence of the cavity effectively guides the emitted light into a privileged direction, a fact which, in our mind, contradicts Einstein's original idea on the concept of spontaneous emission. In fact, a spontaneous emission should be an emission which happens at a not-well-defined time and, more

and, thus, can easily be controlled and manipulated in experiments. In this case, the dot realizes a nanometer-scale single photon source (cf. Refs. [82–85]). Such quantum sources constitute one of the basic hardware elements for the future implementation of quantum telecommunication protocols and quantum cryptography.

The best samples are capable of generating single photons with external quantum efficiencies in excess of approximately 20 % at repetition frequencies higher than 100 MHz.

Quantum dots in the strong coupling regime. In the strong coupling regime, i.e., when $g \gg \max\{\kappa, \gamma\}$, the standard vacuum Rabi dynamics discussed in the case of quantum-optical cavity QED can be realized also with quantum dots in photonic crystal nanocavities. In the case of quantum dots, instead of an atomic state, an exciton (electron-hole pair) is entangled with a photon. This unprecedented scenario allows the study of photon-semiconductor-excitations [86–89]. The typical coupling strengths found in experiments are on the order of a few hundred μeV [86].

Recent developments in the field have led to the observation of photon-exciton entangled states in electrically contacted photonic crystal nanocavities. In this systems, the photon-exciton coupling strength can be electrically turned on and off by tuning the voltage applied to a gate contact [90].

REMARK

A common feature to cavity QED experiments with natural atoms at optical frequencies and with quantum dots is that, in both cases, the quantum nature of the photons emitted by the cavities is tested by means of a Hanbury Brown and Twiss–type experiment. In other words, the stream of emitted photons is first split by an optical beam splitter and, then, the second-order correlation function of the splitter output beams is measured. If at delay time zero the correlation peak vanishes, the emitted photons are single quanta of the electromagnetic field. In fact, it is impossible to record simultaneously two events after splitting due to the quantum nature of the photons [91].

Hanbury Brown and Twiss–type experiments can be realized at microwave frequencies taking advantage of the correlation detection scheme studied in chapters 3 and 4 of this thesis. Hanbury Brown and Twiss–type experiments, which have already been implemented with GHz photons [92], have not been realized in our laboratories yet. To avoid confusion, it is worth stressing that every time we discuss about cross-correlation measurements as one of the seminal results of our work, we refer to *amplitude-amplitude correlation* measurements. This type of measurement is inherently different from a Hanbury Brown and Twiss–type experiment, where *intensity-intensity correlation* measurements are performed.

It is also important to mention that the microwave cross-correlation measurement apparatus to be introduced in chapters 3 and 4 looks similar to the quantum homodyning apparatus employed at optical frequencies to reconstruct the Wigner function of propagating states of light (single photons, squeezed states, and so forth). In optics, quantum homodyning is based on a beam splitter followed by two high efficiency photodetectors. A quantum state of light, e.g., a propagating single photon generated by parametric down-conversion, a, is linearly superposed at the beam splitter with a strong coherent state, e.g., a laser field, B. The two beams at the output of the beam splitter are, thus, the sum and difference of the weak single photon

specifically, in a not-well-defined direction.

and strong coherent state, $a+B$ and $a-B$, respectively. The photodetectors "transform" the amplitudes associated with these two beams into intensities. In other words, they square the incoming amplitudes, giving as a result $I_1 = a^2 + 2aB + B^2$ and $I_2 = a^2 - 2aB + B^2$. The difference between the two intensities at the detectors output finally gives $I_1 - I_2 = 4Ba$. Such an intensity is the product of the amplitude associated with the strong coherent state and that of the weak quantum signal which is intended to be measured. The effect of the coherent state is to "amplify" the weak quantum signal making it easily measurable.[21] This is possible only because the photodetectors practically do not add noise contributions to the single photon and coherent state signals. Repeating a homodyne measurement many times then makes possible to obtain the probability distribution associated with a, which, after opportune mathematical transformations, can be used to reconstruct the Wigner function of the single photon. For a complete review on quantum homodyning we remind the reader to Refs. [91, 93–95].

At microwave frequencies the scenario is quite different due to the technical limitations of microwave amplifiers. The amplifiers add large noise contributions to the signals,[22] making impossible to reproduce exactly the optical experiment. The use of noisy amplifiers allows only the measurement of the first two moments of a given state of the microwave radiation. This is a very restricted subset of the state full-counting statistics, the entire knowledge of which is necessary for full-state tomography [93]. We remind to chapters 3 and 4 for all details about microwave homodyning.

Superconducting Qubits

There exists in nature a special class of materials, such as aluminum or niobium, which, below a certain temperature, become superconducting. This simply means that current can flow through the material without a voltage drop being established at its ends. In simple terms, no dissipation can take place in a superconductor,[23] which, to be qualified as such, must also be perfectly diamagnetic due to the Meißner effect. Below the critical temperature, a superconducting material is characterized by a condensed state made of so-called Cooper-pairs. A Cooper-pair is nothing but two electrons together. The condensed state, which can be described in terms of a single wave function, is separated from the excited states by the superconducting energy gap, Δ_{BSC}.[24] The gap practically *isolates* the condensed states from higher energetic excitations, which are also referred to as quasiparticles. The motivation to utilize superconducting materials for the implementation of "artificial two-level atoms" [called quantum bits (qubits)] originates from the isolation property of the superconducting gap. In fact, when attempting to realize a qubit, the first fundamental requirement is the ability to isolate *one* specific Hilbert space from all other possible Hilbert spaces in the system. In the case of superconducting qubits, the Hilbert space of interest is defined within the superconducting gap!

Let us consider a metallic island, e.g., made of aluminum. Below a critical

[21] Our calculation is purely classical. Similar arguments apply to the full quantum-mechanical case.

[22] The continuous development of ultra-low noise amplifiers will eventually help solving this issue.

[23] At least as far as DC currents are considered.

[24] The subscript "BSC" stands for Bardeen, Cooper, and Schrieffer, i.e., the last names of the three physicists who developed the theory of superconductivity in 1957 [29].

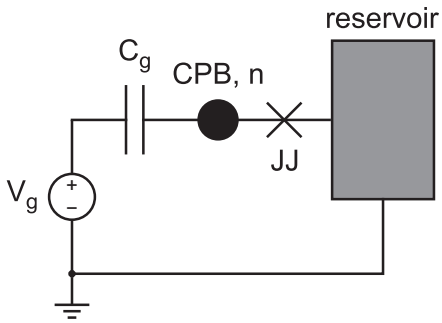

Figure 1.5: The Cooper-pair box: an "artificial two-level atom." CPB: Cooper-pair box (a superconducting island). n: number of excess Cooper pairs on the box. $V_{\rm g}$: gate voltage applied via the gate capacitance $C_{\rm g}$. The CPB is connected to a large superconducting reservoir through a Josephson-tunnel-junction, which makes possible to realize linear superpositions of the two lowest charge states of the box, $n = 0, 1$.

temperature $T_{\rm c} \simeq 1.2\,{\rm K}$ the island resides in the superconducting state.[25] At zero absolute temperature, the superconducting energy gap $\Delta_{\rm BCS}$ for a given superconducting material is related to the material critical temperature $T_{\rm c}$ by the simple relation $\Delta_{\rm BCS}/k_{\rm B}T_{\rm c} \simeq 1.764$ [96]. This relation allows us to express $2\Delta_{\rm BCS}$, which is the experimentally accessible quantity, as an equivalent temperature $T_{\rm BCS} \simeq 2 \times 1.764 T_{\rm c}$ or as an equivalent frequency $f_{\rm BCS} = 2 \times 1.764\, k_{\rm B}T_{\rm c}/h$. In the case of aluminum, $T_{\rm BCS} \simeq 4.234\,{\rm K}$ and $f_{\rm BCS} \simeq 88\,{\rm GHz}$.[26] Here, $k_{\rm B}$ is the Boltzmann constant and h the Planck constant. A gap corresponding to approximately $4.234\,{\rm K}$ constitutes a good isolation from the quasiparticle excitations. Within the condensed state of the aluminum island we now have to choose a suitable Hilbert space to work with. This can easily be realized by noticing that the island behaves as an electrostatic box with total capacitance C_Σ:[27] a Cooper-pair box (cf. Fig. 1.5). The electrostatic energy of the box is given by $E_{\rm C} = e^2/2C_\Sigma$, where e is the electron charge and, in typical applications, $C_\Sigma \simeq 50\,{\rm fF}$. In experiments, the Cooper-pair box is cooled to an operating temperature $T \simeq 50\,{\rm mK}$. If the characteristic energy scales of the system are chosen such that $\Delta_{\rm BCS} \gg E_{\rm C} \gg k_{\rm B}T$, the charge fluctuations on the box are suppressed and the number of Cooper pairs on it can be defined as an integer number n. This represents the Hilbert space we were searching for. By applying an external biasing voltage $V_{\rm g}$ to the box via a capacitive gate $C_{\rm g}$, the electrostatic potential of the box can be modified. This has the effect to induce charge in excess with respect to the neutral background represented by the Cooper pairs in the condensed state. In summary, we have been able to define a Hilbert space, the number of Cooper pairs on a superconducting island, n, and a tuning knob, the external biasing voltage, $V_{\rm g}$. For a special choice of $V_{\rm g}$, the number of excess Cooper pairs on the box can be restricted to 0 or 1. These represent the two states of a super-

[25] We remind that the critical temperature of a given material, $T_{\rm c}$, is defined as the temperature below which the material becomes superconducting.

[26] Remarkably, this simple estimate already gives us a hint that the characteristic transition frequencies of superconducting qubits lie in the microwave range.

[27] The total capacitance is set by the geometric dimensions of the box.

conducting "artificial two-level atom." The states $n = 0, 1$ are still classical states in the sense that no quantum-mechanical superposition of them is possible.[28] How is it possible to create a quantum-mechanical coupling energy between such states? A Josephson tunnel junction is the natural answer to this question. Connecting the Cooper-pair box to a large superconducting reservoir via one or more Josephson junctions allows Cooper pairs to tunnel on and off the box via the junction(s), thus establishing a Josephson coupling energy E_{J} between the Cooper-pair states. The Josephson coupling energy depends on the phase difference ϕ associated with the junction(s) [97]. Figure 1.5 shows a sketch of a voltage biased Cooper-pair box connected to a superconducting reservoir via one Josephson tunnel junction.

Depending on the relationship between the charging energy E_{C} and the Josephson coupling energy E_{J} two scenarios are conceivable. In fact, we remind that charge n and phase ϕ are quantum-mechanical conjugated variables [97]. Hence, if $E_{\mathrm{C}} \gg E_{\mathrm{J}}$, the number of Cooper pairs n on the box is a well-defined quantum variable and the phase difference ϕ on the junction(s) fluctuates. In this case, a so-called *charge qubit* is realized. On the contrary, if $E_{\mathrm{J}} \gg E_{\mathrm{C}}$, the phase difference ϕ on the junction(s) is a well-defined quantum variable and the number of Cooper pairs n on the box fluctuates. In this case, a so-called *flux (or phase) qubit* is realized.[29] In reality, intermediate regimes where $E_{\mathrm{C}} \approx E_{\mathrm{J}}$ are also possible. In that case, both the charge and phase quantum variables must be accounted for when describing the qubit [97–101].

In brief, these are the milestones achieved in the field of superconducting qubits:

1. The quantum coherence of superconducting qubits has been studied spectroscopically [102, 103];

2. Coherent oscillations in charge, phase, and flux qubits have been observed [104–107];

3. Different strategies for a high fidelity readout have been implemented [108–111];

4. Two-qubit gates have been realized [112, 113];

5. Qubits with tunable coupling have been implemented [114–117];

6. Long coherence times have been achieved [118–120].

We remind the reader to the review articles of Refs. [97–101] and to chapters 2, 7, and 8, for a complete introduction to the field of superconducting qubits and their possible applications.

CAVITY QED WITH SUPERCONDUCTING QUBITS: CIRCUIT QED

Superconducting qubits can be strongly coupled to on-chip microwave resonators. The resonators are made by terminating a microstrip or coplanar waveguide transmission line into input and output capacitors. In circuit QED, these capacitors play the role of the mirrors in quantum-optical cavity QED. The typical frequency of

[28] For special values of V_{g} they are eventually degenerate states.

[29] Flux and phase qubits are different types of qubits [97]. We group them together here for simplicity.

operation is on the order of 5 GHz, which corresponds to a resonator length of approximately $10 - 20$ mm. The resonators used in circuit QED applications are quasi one-dimensional structures and are usually made of superconducting materials in order to maximize the cavity internal quality factor. Typical loaded quality factors can reach values of 10^5 at temperatures of approximately 1 K. A detailed study of the resonators used in circuit QED and of their quantization is reported in chapter 2, Sec. 2.1.

In the past decade, we have witnessed a tremendous progress in the realm of circuit QED [97, 121–144]. Different types of superconducting qubits have been strongly coupled to on-chip microwave resonators, which act as quantized cavities. It has been shown that single qubit operations can be realized with very high fidelity [108]. A quantum state has been stored and coherently transferred between two superconducting phase qubits via a microwave resonator [145] and two transmon qubits have been coupled utilizing an on-chip cavity as a quantum bus [146]. Very recently, the Grover search and Deutsch–Jozsa algorithms have been implemented using transmon qubits [147] and the Bell's inequality violated by means of phase and transmon qubits separated by a resonator [148, 149]. Furthermore, microwave single photons have been generated by spontaneous emission [150] and arbitrary quantum states synthesized and characterized via quantum tomography in a system based on a phase qubit [151–153]. In addition, photon number states as well as the Lamb shift have been unveiled exploiting the strong dispersive limit in a transmon-resonator system [154, 155], lasing effects demonstrated using a single Cooper-pair box [156], the nonlinear response of the so-called Jaynes-Cummings (JC) model observed [157, 158], the two-photon driven JC dynamics utilized as a means to probe the symmetry properties of a flux qubit [159], and resonators tuned with a high level of fidelity [160, 161]. Finally, microwave beam splitters have been employed to carry out Hanbury Brown and Twiss experiments [92] and to study the fundamental properties of vacuum fluctuations [162]. These formidable advances show how circuit QED systems are rapidly reaching a level of complexity comparable to that of the already well-established quantum-optical cavity QED [52–58, 70–74, 163–185].

Note added in Fall 2010. Before concluding this short general introduction to circuit QED, it is worth noting that the very first experiment dealing with Josephson tunnel junctions coupled to on-chip cavities dates back to 1989 [186]. We thank J. M. Martinis for bringing such a seminal, almost forgotten, paper to our attention.

1.3 About This Thesis: Two Amplifiers, Two Resonators, and Two Photons

This thesis work is concerned with the development of novel circuit QED implementations, where the *circuit* nature of microwave quantum devices is exploited in order to unveil unprecedented phenomena.

Two distinguished philosophies can be followed while attempting to develop the field of circuit QED. The first doctrine is to open up a textbook on quantum optics and, one by one, try to repeat all experiments already realized in quantum-optical cavity QED. In principle, this is not a faulty approach. In fact, circuit QED has certain advantages compared to traditional cavity QED, such as the possibility to achieve extremely strong coupling strengths between microwave photons and super-

conducting qubits (perhaps even larger than the qubit transition frequency!). In addition, the fact that the qubit resides inside the cavity indefinitely without incurring in the finite transient time issue encountered in optics constitutes an important benefit in experimental implementations. These facts allow the exploration of more exotic regimes of cavity QED not easily reachable in quantum optics (Refs. [153] and [154] are two remarkable examples of nontrivial circuit QED experiments). However, we truly believe that this path will soon have an end with the risk of turning circuit QED into a sterile field. For this reason, we are convinced that different strategies and ideas must be envisioned to create an independent area of research. In particular, we think that the "circuit" part of circuit QED embodies a large potential for new applications, which have not been exploited yet.

Within this framework lies the motivation for our work. As hinted by the title of the thesis, three are the main concepts studied here. Two of them are intimately connected and are presented one after the other in the beginning of the thesis, whereas the third has its own status and is treated at the end. In brief:

(I) Two amplifiers. We have constructed a correlation detection apparatus based on a microwave beam splitter and two amplification channels. Admittedly, in the first stage of this project we were trying to emulate the quantum-optical technique of quantum homodyning. We soon realized that it is not possible to directly export such a technique into the microwave domain. This led us to the development of a full quantum network theory of our correlation measurement setup, with special emphasis on the understanding of the working principles of microwave beam splitters and amplifiers. This part of the project has been our "primary school," where we have learnt, the hard way, the implications of detecting signals in the microwave domain;

(II) Two resonators. The possibility of measuring a pair of quantum microwave signals independently has triggered our attention to the development of a two-resonator circuit QED architecture. In our view, the flexibility in designing on-chip microwave resonators and the simplicity in realizing them must be exploited for coupling together two or more resonators. Indeed, it is easier to couple multiple resonators than multiple superconducting qubits. The latter, even in state-of-the-art experiments, are still largely affected by poor coherence properties. Obviously, qubits must also be involved in our two-resonator architectures in order to provide the necessary nonlinearity to the system, which allows us to explore the fundamental laws of quantum mechanics. Notably, we have shown that two-resonator architectures can be tuned in special regimes where qubit decoherence only minimally affects the manipulation of the system. In addition, two-resonator circuit QED opens up intriguing possibilities in understanding the entanglement characteristic of bipartite systems, which can opportunely be studied by means of our correlation setup. Last but not least, David P. DiVincenzo has recently shown a deep interest in our theoretical study of two-resonator systems and has proposed a fault tolerant architecture for quantum computing having two-resonator cells has the basic hardware components [187];

(III) Two photons. A peculiarity of superconducting qubits is represented by the possibility of tuning them *in situ*, while performing an experiment. This has

allowed us to unveil the upconversion dynamics of a resonator-qubit system, where a qubit of given transition frequency is irradiated with two classical photons of half the qubit transition frequency. The qubit then behaves as a "nonlinear medium," which effectively upconverts the input photons into a single output quantum photon with twice the frequency. We have shown that the possibility to observe this phenomenon is intimately connected to the selection rules of the qubit, which depend on the qubit operation point. We have also been able to show the transition between electric-dipole-type selection rules and a controlled broken symmetry situation for the qubit-resonator system.

These three concepts constitute the bulk of the present thesis, which is meant to be a not so short introduction to the field we like to refer to as "circuit QED^2:" two amplifiers, two resonators, and two photons!

Before enumerating the key results of our work and a few instructions for the further reading of the thesis, we stress that this thesis contains both experimental and theoretical research topics. In a few occasions, as in the case of two amplifiers and two photons, theory and experiments are combined together. In other cases, such as two- and multi-resonators architectures, the research is purely theoretical. For the sake of completeness, we have to make clear that the experimental work on two amplifiers has been carried out by the author, whereas that on two photons by Frank Deppe [159]. Nevertheless, the author has substantially contributed in the development of the theory of two-photon interactions, upconversion dynamics, and controlled symmetry breaking in circuit QED, which is at the basis of the two-photon project.

1.3.1 Seminal Results and Reference Sections

In this thesis, we report on a set of seminal results, which are presented in parallel with a number of reference sections. Our intention is to provide an exhaustive treatment of the basic aspects of circuit QED in connection with our experimental and theoretical findings. The reader only interested in the seminal results can skip the reference sections. Here is a list of topics which we recommend to read:

SEMINAL RESULTS

(i) Theory:

(a) Quantum theory of microwave beam splitters including noise (cf. chapter 3, Sec. 3.1);

(b) Theoretical model for the measurement of the distance from the variance of microwave vacuum fluctuations (cf. chapter 4, Subec. 4.3.2);

(c) Circuit theory of two-resonator circuit QED (cf. chapter 5, Sec. 5.1);

(d) The quantum switch Hamiltonian (cf. chapter 5, Sec. 5.2);

(e) The quantum bus and the leaky cavity: A method to efficiently read out a qubit in two-resonator circuit QED (cf. chapter 6, Sec. 6.1);

(f) Quantum tomography in two-resonator circuit QED (cf. chapter 6, Sec. 6.4);

(g) A two-dimensional cavity grid setup for quantum computation (cf. chapter 7, Secs. 7.1 and 7.6);

(h) Two-photon driven Jaynes-Cummings, selection rules, and controlled symmetry breaking in circuit QED (cf. chapter 8, Secs. 8.3 and 8.4);

(ii) Experiments:

(a) Experimental observation of the distance from the variance of microwave vacuum fluctuations by means of auto-correlation measurements (cf. chapter 4, Subsecs. 4.3.1 and 4.3.2);

(b) Experimental realization of Planck spectroscopy (cf. chapter 4, last part of Subsec. 4.3.1);

(c) Towards the process tomography of microwave beam splitters: cross-correlation and covariance measurements of vacuum fluctuations (cf. chapter 4, Subsec. 4.3.3);

(iii) Technical achievements:

(a) Realization and characterization of a two-channel amplification chain (cf. chapter 3, Sec. 3.2);

(b) Implementation of high-frequency, high-vacuum, cryogenic feedthroughs (cf. chapter 3, Subsec. 3.2.3).

REFERENCE SECTIONS

1. Quantization rules of an LC-resonator circuit (in chapter 2, first part of Subsec. 2.1.3);

2. Quantization of transmission line resonators by means of the phasor picture (in chapter 2, center part of Subsec. 2.1.3);

3. Quantum signals propagating on a transmission line (in chapter 2, last part of Subsec. 2.1.3);

4. From an LC-resonator to a qubit (in chapter 2, Subsec. 2.2.2);

5. Quantum small-signal formalism (in chapter 2, Subsec. 2.3.1);

6. Quantum network theory of amplification (in chapter 3, central part of Subsec. 3.2.2);

7. Quantum theory of mixing (in chapter 3, Subsec. 3.2.5).

1.3.2 Organization of the Thesis

The thesis is organized as follows. In chapter 2, we summarize the main concepts about classical resonant circuits. We then introduce the quantization rules for such circuits and extend those rules to the case of quantum signals propagating on a transmission line. We present the concept of Josephson tunnel junction and its use for the implementation of RF SQUID and three-Josephson-junction SQUID quantum circuits (flux quantum circuits). Under opportune conditions, such circuits can be used to realize superconducting flux qubits. In addition, we study in detail the interaction between flux quantum circuits and quantized microwave fields. We consider both the case of flux quantum circuits as multi-level "artificial atoms" and in the two-level (qubit) approximation.

In chapter 3, we present a full study of three-port and four-port microwave beam splitters, both in the classical and quantum regime. We then describe the two-channel amplification chain, with special emphasis on the quantum-mechanical treatment of amplifiers and mixers. This allows us to follow the quantum signals we intend to measure from the beam splitters to the acquisition electronics and computer aided data postprocessing. Stage by stage, the complexity of the quantum-mechanical formalism describing the quantum signals increases, acquiring more and more contributions the further we go along the detection chain. At the end of the chapter, we summarize the quantum-mechanical expressions for the various quantum signals of interest.

In chapter 4, we review the basic concepts about blackbody radiation and vacuum fluctuations, with emphasis on the derivation of the Planck distribution from Einstein's A and B coefficients. We then present the field of quantum signal theory, focusing on the derivation of the quantum-mechanical mean value and variance of a quantum signal with respect to a given state of the microwave radiation. The case of thermal/vacuum states is studied in detail. The mean value and variance, which are defined as quantum parameters, have to be estimated during an experimental measurement process. This is the next topic of the chapter. In particular, we review the fundamental definitions and properties of auto-correlation and cross-correlation functions, auto-covariance and cross-covariance functions, and variance and covariance for weakly stationary signals. The case of white signals is extensively treated. All these definitions and properties are the basis for our experimental study on the vacuum fluctuations of the microwave radiation field. The measurements of the Planck distribution and the realization of Planck spectroscopy are shown. In addition, the quantum-mechanical characteristics of microwave beam splitters are experimentally studied by means of cross-correlation and covariance measurements.

In chapter 5, we introduce two-resonator circuit QED and develop a suitable formalism to describe it. We show that it is possible to couple two resonators via a largely detuned qubit, which acts as a quantum bus between the two resonators. By tuning the operation point of the qubit, we show that it is possible to realize a superconducting quantum switch between the two resonators. When the switch is on photons can freely move from one resonator to the other, while when the switch is off the two resonators are (theoretically) totally decoupled. The qubit acts as a gate for the photonic excitations in the resonators. We propose several applications for the superconducting quantum switch, ranging from the realization of entanglement between two resonators to the preparation of so-called Schrödinger cat states. Moreover, we study the effect of decoherence on the operation of the

quantum switch and analyze a possible experimental realization.

In chapter 6, we further develop the field of two-resonator circuit QED showing that it is possible to take advantage of the two resonators for efficiently reading out the state of a qubit coupled to both of them. In this implementation of two-resonator circuit QED, one resonator must have a high quality factor and the other one a low quality factor. The high quality factor resonator is defined as quantum bus, whereas the low quality factor one as leaky cavity. The quantum bus allows one to perform cavity QED experiments in the strong coupling regime, while the leaky cavity can be used to independently read out the qubit population via a dispersive measurement. As a possible application, we propose and theoretically analyze a protocol for the generation and measurement of large Schrödinger cat states. In addition, we propose two different methods for the full-state quantum tomography of quantum fields residing in the quantum bus.

In chapter 7, we extend two-resonator circuit QED to the case of a multi-resonator architecture, where the resonators are arranged on a two-dimensional grid (cavity grid). Superconducting qubits can be positioned at the crossing of each pair of resonators, thus allowing to pack a large number of qubits within a small area. The whole grid can easily be realized on the same chip. We show that all basic quantum operations (one- and two-qubit gates) can be performed on such a grid. Taking into account decoherence effects, we demonstrate that, in principle, high-fidelity gates can be realized using state-of-the-art qubits and resonators. In addition, we consider the possibility to utilize the cavity grid for the implementation of a fault-tolerant architecture for quantum computing. The experimental issues related to this architecture are also examined.

In chapter 8, we first present a circuit QED setup based on a flux qubit, where the qubit population is read out by means of a DC SQUID. We then show experimental evidence for a two-photon driven Jaynes-Cummings interaction, which allows us to study the selection rules and symmetry properties of superconducting qubits. Within this framework, we develop a theoretical formalism for the description of the upconversion dynamics at the basis of the two-photon Jaynes-Cummings interaction. In addition, we analyze the role played by spurious fluctuators with respect to selection rules and symmetry breaking and study their influence on the coherent dynamics of a qubit.

Finally, in chapter 9, we summarize our main results and give an outlook on possible future applications of correlation measurements and two-resonator circuit QED. In addition, we outline the crucial milestones on the circuit QED road map which, in our mind, will have to be experimentally proven towards a) quantum computing applications and b) a more complete understanding of the quantum properties of microwave signals and circuits.

In the appendices, we discuss a few technical aspects concerning the measurements of the vacuum fluctuations at microwave frequencies (cf. Appendices A, B, and C) and a possible real implementation of a two-resonator circuit QED architecture (cf. Appendices D and E).

Chapter 2

The Quantum Circuit Toolbox: an Optical Table on a Chip

A circuit QED architecture is composed by one or more on-chip microwave resonators, which act as quantized harmonic oscillators, interacting with one or more nonlinear quantum circuits based on Josephson tunnel junctions. Under opportune conditions, such nonlinear quantum circuits behave as two-level systems and are referred to as superconducting qubits. The qubit-resonator interaction can be used to generate quantum signals, which play an important role in unveiling the basic properties of the quantized microwave field.

Despite the vast body of theoretical work on circuit QED [97, 121–137, 144] and, more in general, on quantum circuits [98, 99, 188–192], a systematic theory which describes in a unified form the various aspects of microwave quantum networks is still missing. Without the presumption of achieving such formidable task, in this chapter an attempt towards a self-consistent treatment of quantum circuits and signals is presented. Indeed, the material to be discussed in the following sections is still partially incomplete and more work is needed to be able to obtain a full theory of quantum networks.[1]

In this chapter, we develop the quantum theory of circuits and signals starting from the stand point of classical microwave engineering. First, after revisiting the basic properties of classical resonators, we give a set of rules for the diagrammatic representation of a quantized lumped-parameter LC-resonator in terms of quantum voltages and currents. The quantum voltage and current are canonically conjugated variables and represent quantized sources associated with the capacitive and inductive part of the resonator, respectively. By inspecting the circuit diagram which represents the LC-resonator, the resonator quantum-mechanical Hamiltonian is readily obtained. The rules for the diagrammatic representation of a quantized LC-resonator can be extended to more sophisticated quantum circuits, thus allowing for the determination of the quantum-mechanical Hamiltonian of advanced circuit QED architectures (as an example, cf. chapter 5, Subsec. 5.1.3). Second, by making use of the phasor representation of voltages and currents, we are able to derive the quantum-mechanical Hamiltonian of any given distributed-parameter resonator without resorting to the oftentimes cumbersome Lagrangian formalism [188]. Third, we extend the concepts of quantum voltage and current of an LC-resonator to the

[1]The author is eager to continue developing the theory of microwave quantum networks in his future research.

case of quantized signals propagating on a transmission line. Such quantum signals constitute the fundamental observables at the basis of the results of chapters 3 and 4. Fourth, we introduce the concept of the Josephson tunnel junction as a nonlinear element for the realization of "artificial atoms." As a propaedeutic example, we show that in the absence of Josephson elements a circuit behaves as a simple harmonic oscillator. Instead, the presence of one or more Josephson junctions within a circuit makes possible the implementation of a superconducting qubit. Fifth, inspired by classical circuit theory we derive the interaction Hamiltonian between different types of "artificial atoms" and quantized resonators by means of the quantum small-signal formalism. In this formalism, quantum voltages or currents are considered to be small AC perturbations about a DC (or quasi-static) biasing point. Finally, we reduce the interaction Hamiltonian to the case of a qubit and demonstrate that the transition matrix elements describing the qubit-resonator coupling can straightforwardly be derived from a transformation (rotation) of the reference frame used to represent the qubit. The quantum circuits presented in this chapter constitute the core of the circuit QED toolbox and, together with the microwave beam splitters, amplifiers, and mixers to be presented in chapter 3, they enable the realization of a complete optical table at microwave frequencies. Remarkably, many of these devices can already be integrated on a single chip.[2]

The chapter is organized as follows. In Sec. 2.1, we introduce the classical and quantum-mechanical theory of microwave resonators. Both the lumped-parameter and distributed-parameter case are considered. Furthermore, the rules for the quantization of the signals propagating on a transmission line are given. In Sec. 2.2, we present the basic concepts about Josephson tunnel junctions, RF SQUIDs, and three-Josephson-junction SQUIDs. We show how to use such devices for the implementation of "artificial atoms" and, eventually, superconducting qubits. In Sec. 2.3, we derive the interaction Hamiltonian between microwave resonators and flux quantum circuits (both RF SQUIDs and three-Josephson-junction SQUIDs) and consider the special case of a superconducting qubit-resonator interaction, where the Hilbert space associated with the flux quantum circuit is truncated to the two lowest states. Finally, in Sec. 2.4, we summarize the main results of this chapter, which will help understanding the more complex quantum circuits to be discussed in the rest of the thesis.

Historical Excursus

Considering the basic nature of the material discussed in this chapter, there is an inevitable overlap with a number of references available in the literature. Those references represent milestones in the fields of microwave engineering, classical and quantum network theory, as well as superconducting qubits. We strongly advise the interested reader to consult such references for a more exhaustive analysis. Given their special relevance, we devote this brief historical excursus to single out those references which we believe have most strongly influenced the development of this thesis.

[2]With the rapid development of parametric amplifiers, microstrip SQUID amplifiers, and different types of quantum-limited amplifiers [193–210], bifurcation amplifiers and shelving techniques [110, 211–221], and proposals for a microwave single photon detector [222–224], all devices necessary for circuit QED experiments will soon be integrated on the same chip (or adjacent chips) and advantageously operated at very low temperatures!

Among such references it is worth mentioning *Linear and Non-Linear Circuits* by L. O. Chua, C. A. Desoer, and E. S. Kuh, McGraw-Hill C., New York, 1987,[3] *Principles of Microwave Circuits* edited by C. G. Montgomery, R. H. Dicke, and E. M. Purcell, IEE Electromagnetic Waves Series 25, Institution of Engineering and Technology, London, 1987, and *Foundations for Microwave Engineering* by R. E. Collin, 2nd ed., Wiley-IEEE Press, New Jersey, 2001. As a historical remark, we notice that many scientists are not aware of the contributions of eminent physicists R. H. Dicke and E. M. Purcell to the field of microwave engineering. Before becoming famous in atomic and laser physics because of the prediction of the so-called collisional narrowing, during the Second World War Dicke worked at the Radiation Laboratory at the Massachusetts Institute of Technology, Cambridge, USA and designed the Dicke radiometer, i.e., a microwave receiver. Purcell also spent the years of the Second World War at the Radiation Laboratory developing microwave radar technology. Soon after the war, he discovered with other colleagues the phenomenon of nuclear magnetic resonance. Because of his discovery, he shared with F. Bloch the Nobel Prize in Physics 1952. Without the fundamental contributions of these authors, the field of microwave engineering would barely have a glimpse of the horizon that has approached in both classical communication and computing technologies and, in recent years, in circuit QED applications. The book edited by Montgomery, Dicke, and Purcell is a monument to the work carried out at the Radiation Laboratory and undoubtedly represents a key reference in microwave engineering.

Regarding the quantization of a harmonic oscillator, we refer to the classic books *Quantum Mechanics - Vol. I* by C. Cohen-Tannoudji, B. Diu, and F. Laloë, Wiley-Interscience, New York, 1977, *Modern Quantum Mechanics*, Revised Edt., by J. J. Sakurai, Addison-Wesley Pub. Comp., Inc., Reading, Mass., 1994, and *The Quantum Vacuum - An Introduction to Quantum Electrodynamics* by P. W. Milonni, Academic Press, Inc., San Diego, 1994. Our approach to quantum network theory has been inspired by the articles *Quantum Limits on Noise in Linear Amplifiers* by C. M. Caves, Phys. Rev. D **26**, 1817 (1982) and *Quantum Network Theory* by B. Yurke and J. S. Denker, Phys. Rev. A **29**, 1419 (1984). Even if strongly influenced by these articles, we have constructed an independent method for the diagrammatic representation of quantum circuits. Our method, which does not rely on the complicated Lagrangian formalism of Ref. [188], is simple to visualize and allows one to obtain straightforwardly useful information about the circuit at hand (cf. Subsec. 2.1.3). Nevertheless, we recommend to read the article by Yurke and Denker, which, besides deriving a rigorous theory of quantum networks, stands at the basis of one of the most important results in quantum optics: The input and output formalism developed by Gardiner and Collett in 1985 [225] and Gardiner, Collett, and Parkins in 1987 [226]. Two other articles which largely influenced the development of this thesis are the classics *Thermal Agitation of Electric Charge in Conductors* by H. Nyquist, Phys. Rev. **32**, 110 (1928) and the lecture of M. H. Devoret reported in Quantum Fluctuations, Lecture Notes of the 1995 Les Houches Summer School, edited by S. Reynaud, E. Giacobino, and J. Zinn-Justin (Elsevier, The Netherlands, 1997), p. 351.

At last, the derivation of the flux quantum circuit Hamiltonian and of its interaction with a quantized resonator follows the line of *Superconducting Persistent-*

[3] A great book, unfortunately out of print.

Current Qubit by T. P. Orlando *et al.*, Phys. Rev. B **60**, 15398 (1999), *Possible Realization of Entanglement, Logical Gates, and Quantum-Information Transfer with Superconducting-Quantum-Interference-Device Qubits in Cavity QED* by C.-P. Yang, S.-I Chu, and S. Han, Phys. Rev. A **67**, 042311 (2003), *Cavity Quantum Electrodynamics for Superconducting Electrical Circuits: An Architecture for Quantum Computation* by A. Blais, R.-S. Huang, A. Wallraff, S. M. Girvin, and R. J. Schoelkopf, Phys. Rev. A **69**, 062320 (2004), and *The Quantum Theory of Light* by R. Loudon, 3rd ed., Oxford Univ. Press Inc., New York, 2000. In particular, the article by Blais *et al.* represents the first work where the circuit nature of cavity QED with superconducting qubits made its appearance. In that article, the use of on-chip microwave resonators is proposed and the resonator quantization derived by means of the Lagrangian density.[4] In addition, an early attempt to develop a quantum small-signal formalism is presented.[5]

2.1 On-Chip Microwave Resonators

In this section, we first summarize the standard textbook introduction to *RLC*-resonators deriving the complex impedance and/or admittance of a series or parallel lumped-parameter resonant circuit (cf. Subsec. 2.1.1). We then present a classical model for distributed-parameter resonators based on transmission lines, discussing both the cases of a short-circuited and open-circuited line. In this context, the concept of mode is introduced by describing the reflection of waves on a semi-infinite transmission line and the origin of the natural frequencies by considering a finite segment of line (cf. Subsec. 2.1.2). Most importantly, we derive the quantization of microwave resonators both in the lumped-parameter and distributed-parameter regime. The fundamental extension to the quantization of signals propagating on a transmission line is also shown (cf. Subsec. 2.1.3).

2.1.1 Lumped-Parameter Resonators

Resonant circuits are of great importance in many branches of physics and engineering, with applications from very low frequencies to optical frequencies. Besides being used in oscillator circuits, tuned amplifiers, frequency filter networks, wavemeters for measuring frequency, etc., they represent a prototypical example of the natural phenomenon of resonance.

Before continuing with our study, it is worth making a remark on the notation to be used in the rest of the thesis. Voltages and currents are associated with plain lowercase characters, e.g., v and i, when representing variables in the time domain. In the frequency domain (phasor picture), they are associated with plain uppercase characters, e.g., V and I. There are a few exceptions. For example, I_{c0} represents the critical current of a Josephson tunnel junction and I_{p} the persistent current circulating in a flux qubit loop. These, typically, are time/frequency independent quantities. Quantum-mechanical voltages and currents are associated with uppercase characters with a hat, e.g., $\hat{V}$ and $\hat{I}$. If it is necessary to specify in which quantum-mechanical picture the operators are represented, a subscript S is used

[4] We will derive it from simple circuit considerations; cf. Subsec. 2.1.3.

[5] We remind to chapter 5, Subsec. 5.1.3 for a thorough analysis of the issues related to the quantum small-signal formalism presented in Ref. [131].

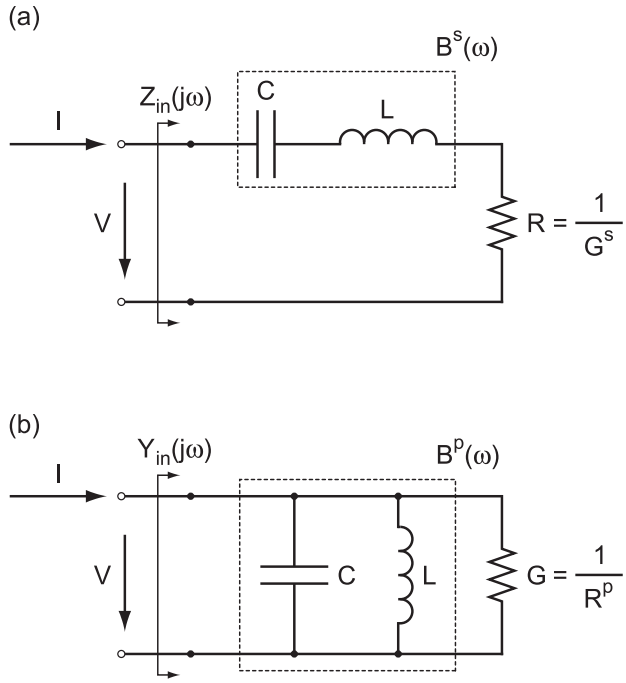

Figure 2.1: Series and parallel RLC-resonators. **(a)** Circuit diagram of a series RLC-resonator. V and I are, respectively, the voltage and current at the circuit input port. $Z_{\rm in}(j\omega)$ is the resonator input impedance. C and L are the series capacitance and inductance associated with the complex part of the input impedance, $B^{\rm s}(\omega)$, which is indicated by a dashed box. $R = 1/G^{\rm s}$ is the resistance representing the internal losses of the resonator. **(b)** Circuit diagram of a parallel RLC-resonator. $Y_{\rm in}(j\omega)$ is the resonator input admittance. C and L are the parallel capacitance and inductance associated with the complex part of the input admittance, $B^{\rm p}(\omega)$, which is indicated by a dashed box. $G = 1/R^{\rm p}$ is the finite conductance representing the internal losses of the resonator.

for the Schrödinger picture, a subscript H for the Heisenberg picture, and, if not indicated differently, a "$\sim$" between the top of the character and the hat for the interaction picture.

We begin considering the two simplest types of lumped-parameter resonators: the series and parallel RLC-resonators [cf. Figs. 2.1(a) and 2.1(b)]. These two networks, which are dual of each other, can easily be studied in the frequency domain. The series network is characterized by a well-defined current I flowing over the entire branch and can be represented by a complex input impedance $Z_{\rm in}(j\omega)$, where $j \equiv \sqrt{-1}$ and ω is a generic angular frequency, $\omega \equiv 2\pi f$ with $f \in [0, +\infty)$. The corresponding parallel network has a well-defined voltage V between the nodes of each branch and can be represented by a complex input admittance $Y_{\rm in}(j\omega)$.

The Series RLC-Resonant Circuit

For the circuit of Fig. 2.1(a), the capacitor C, inductor L, and resistor R are in series and the voltage across C is given by $V_{\rm C} = Z_{\rm C}\, I = I/j\omega C$. The complex impedance $Z_{\rm in}(j\omega)$ can straightforwardly be computed by a circuit inspection,

$$\begin{aligned} Z_{\rm in}(j\omega) &= R + j\omega L + \frac{1}{j\omega C} \\ &= R + j\left(\omega L - \frac{1}{\omega C}\right). \end{aligned} \tag{2.1}$$

From this equation, it is evident that the real part of the impedance is constant with frequency, $\Re\{Z_{\rm in}(j\omega)\} = R$. On the contrary, the imaginary part $B^{\rm s}(\omega) \equiv \Im\{Z_{\rm in}(j\omega)\} = \omega L - 1/\omega C$ varies between $-\infty$ and $+\infty$ as the angular frequency ω varies between 0 and $+\infty$. In particular, $B^{\rm s}(\omega) = 0$ at the special value of the angular frequency

$$\omega_0 \equiv \frac{1}{\sqrt{LC}}\,, \tag{2.2}$$

which is defined as the resonance angular frequency of the circuit. In this case, the input impedance is pure real

$$Z_{\rm in}(j\omega_0) = R\,. \tag{2.3}$$

This has the important consequence that the time-average energies stored in the electric field (i.e., in the capacitor C)

$$\begin{aligned} W_{\rm C} &\equiv \frac{1}{4} C\, V_{\rm C}^*\, V_{\rm C} \\ &= \frac{1}{4\omega^2 C} I^*\, I \end{aligned} \tag{2.4}$$

and in the magnetic field (i.e., in the inductor L)

$$W_{\rm L} \equiv \frac{1}{4} L\, I^*\, I \tag{2.5}$$

must be equal. This property follows from the general expression for the input impedance of any one-port circuit with a suitably defined equivalent terminal current I, as the circuit of Fig. 2.1(a). In this case [227],

$$Z_{\rm in} \equiv \frac{P_{\rm R} + 2j\omega(W_{\rm L} - W_{\rm C})}{I^*\, I/2}\,, \tag{2.6}$$

where

$$P_{\rm R} \equiv \frac{1}{2} R\, I^*\, I \tag{2.7}$$

is the power loss or, equivalently, the energy loss per unit time due to resistor R. We notice that the factor $I^*\, I/2$ in the denominator of Eq. (2.6) serves as a normalization factor and is required in order to make the input impedance $Z_{\rm in}$ independent of the magnitude of the current I at the input of the network. From Eq. (2.6) it appears evident that the input impedance is pure real, $Z_{\rm in} = R$, iff[6] $W_{\rm L} = W_{\rm C}$. This

[6]Throughout this thesis, we adopt the notation used in mathematics, where *if and only if* $\equiv$ "iff."

condition sets the resonance angular frequency of the circuit to be $\omega_0 = 1/\sqrt{LC}$, a result which is consistent with the definition of Eq. (2.2).

In the extreme cases of very low and very high frequency, we obtain the following asymptotic expressions for the input impedance:

$$Z_{\rm in}(j\omega) \approx -j\frac{1}{\omega C} \quad \text{for} \quad 0^+ \leftarrow \omega \ll \omega_0\,, \tag{2.8a}$$

$$Z_{\rm in}(j\omega) \approx j\omega L \quad \text{for} \quad \omega \gg \omega_0\,. \tag{2.8b}$$

The physical meaning of these expressions can easily be understood in terms of open circuits. For $\omega_0 \gg \omega \to 0^+$, the input impedance $Z_{\rm in}$ of the series RLC resonant circuit of Fig. 2.1(a) is very large: The capacitor C tends to be an open circuit. In analogy, for $\omega \gg \omega_0$ the input impedance $Z_{\rm in}$ of the series RLC resonant circuit of Fig. 2.1(a) is still very large: This time the inductor L tends to be an open circuit.

A fundamental parameter specifying the frequency selectivity and the general performance of a resonant circuit is the quality factor Q.[7] The most general definition of Q applicable to all resonant systems is

$$Q \equiv \frac{2\pi\omega(\text{time-average energy stored in system})}{\text{energy loss per cycle in system}}\,, \tag{2.9}$$

where we notice the presence of an extra factor 2π in the numerator, which is needed for consistency with the standard definition of quality factor.[8] For the circuit of Fig. 2.1(a), we already know that on resonance $W_{\rm C} = W_{\rm L}$. In addition, the peak value of electric energy stored in C is $2W_{\rm C}$ and occurs when the energy stored in L is zero, and vice versa. Thus, the time-average energy W stored in the circuit is

$$W = W_{\rm C} + W_{\rm L} = 2W_{\rm C} = 2W_{\rm L} = \frac{1}{2}L\,I^*I\,. \tag{2.10}$$

We also know that the energy loss per unit time in the circuit is $P_{\rm R} = R\,I^*I/2$. Hence, the quality factor for a series RLC-resonator is given by

$$\frac{1}{2\pi}Q^{\rm s} = \frac{\omega_0 L}{R} = \omega_0 G^{\rm s} L = \frac{G^{\rm s}}{\omega_0 C}\,, \tag{2.11}$$

where $G^{\rm s} = 1/R$ is the series conductance of the circuit.[9]

The complex input admittance of the series RLC-resonator is simply the inverse of its input impedance, $Y^{\rm s}_{\rm in} = 1/Z_{\rm in}$. In the vicinity of resonance, we can redefine the angular frequency as $\omega = \omega_0 + \Delta\omega$, where $\Delta\omega$ represents a *small* deviation from the resonance condition. Under these assumptions, we can use the approximation[10]

[7] In optics, oftentimes a different figure of merit is used: the finesse F. The quality factor is related to the finesse as $Q = Ff_0/\Delta f$. Here, $f_0 = \omega_0/2\pi$ and Δf is the free spectral range [228].

[8] It is important to notice that we use the factor of 2π throughout the thesis, in particular in chapter 5, Sec. 5.3 and chapter 8, Sec. 8.3, where we use the quality factor to extract important information about our experiments.

[9] For the series conductance, we use the superscript "s" to distinguish it from the parallel conductance G of the parallel RLC-resonator of Fig. 2.1(b).

[10] The approximation can be obtained by a Taylor expansion to first order of the function $1/x$ in the limit $x \to x_0$ and then applying the substitutions $x_0 \to \omega_0$ and $x \to \Delta\omega$.

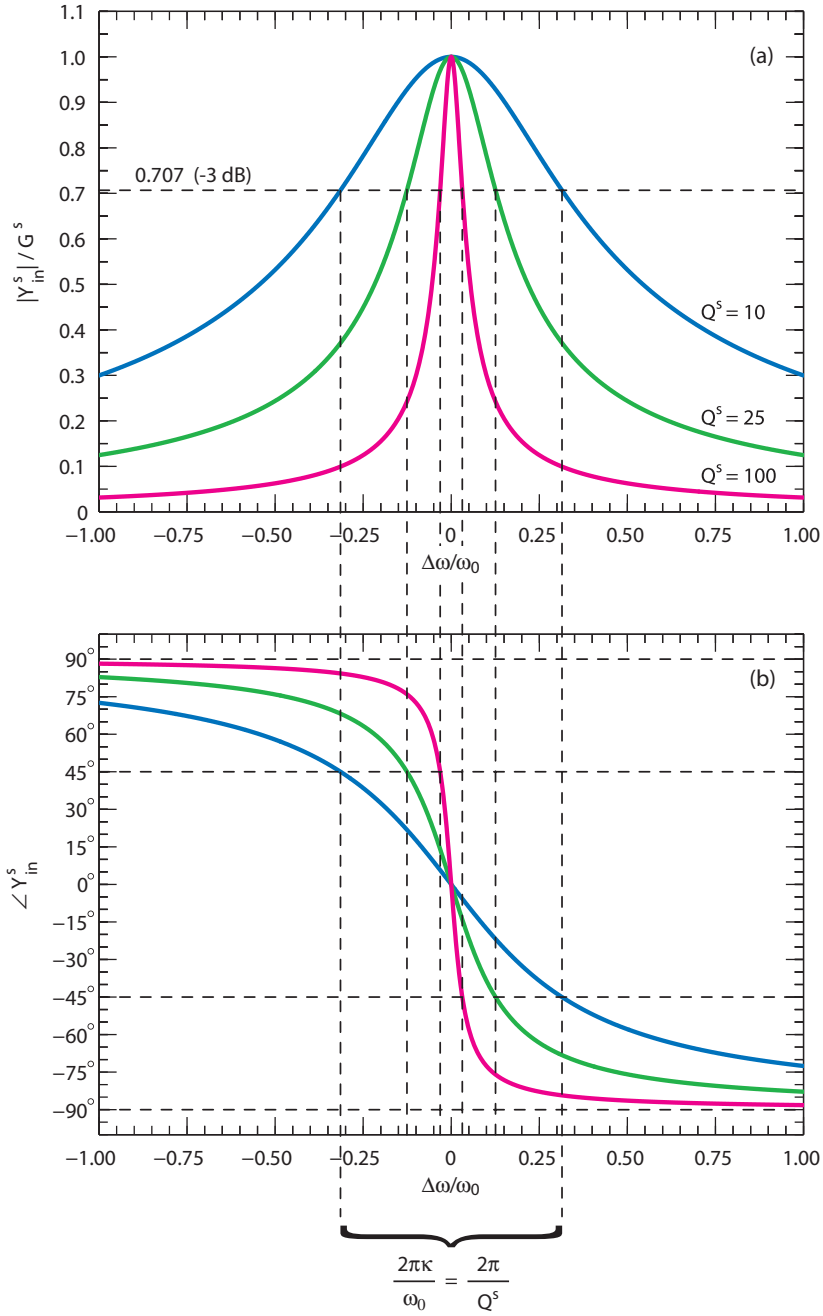

Figure 2.2: Modulus and phase of the complex Lorentzian function associated with $Y^{\rm s}_{\rm in}$ of Eq. (2.13). **(a)** $|Y^{\rm s}_{\rm in}|/G^{\rm s}$ as a function of $\Delta\omega/\omega_0$. The dark blue (dark grey) curve is obtained for $Q^{\rm s} = 10$. The light green (light grey) curve for $Q^{\rm s} = 25$. The magenta (middle grey) curve for $Q^{\rm s} = 100$. The dashed horizontal line indicates a 3 dB loss from the maximum. **(b)** $\angle Y^{\rm s}_{\rm in}$ in degrees as a function of $\Delta\omega/\omega_0$. The color code for the three plotted curves is the same as in **(a)**.

$1/\omega = 1/(\omega_0 + \Delta\omega) \approx (1 - \Delta\omega/\omega_0)/\omega_0$ and rewrite the complex input admittance as

$$\begin{aligned} Y_{\rm in}^{\rm s} &= \left(\frac{1}{G^{\rm s}} + j\omega L + \frac{1}{j\omega C}\right)^{-1} \\ &\approx \left(\frac{1}{G^{\rm s}} + j\omega_0 L + j\Delta\omega L + \frac{1 - \Delta\omega/\omega_0}{j\omega_0 C}\right)^{-1} . \end{aligned} \tag{2.12}$$

Since $j\omega_0 L + 1/j\omega_0 C = 0$ and $LC\omega_0^2 + 1 = 2$, we obtain[11]

$$\begin{aligned} Y_{\rm in}^{\rm s}\left(\frac{\Delta\omega}{\omega_0}\right) &= \frac{G^{\rm s}(\omega_0^2 C)}{\omega_0^2 C + j2G^{\rm s}\,\Delta\omega} \\ &= \frac{G^{\rm s}}{1 + j2\dfrac{Q^{\rm s}}{2\pi}\left(\dfrac{\Delta\omega}{\omega_0}\right)} , \end{aligned} \tag{2.13}$$

which is the general form of a complex Lorentzian function, a typical resonance curve. The modulus of the complex input admittance $Y_{\rm in}^{\rm s}$ is given by

$$|Y_{\rm in}^{\rm s}|\left(\frac{\Delta\omega}{\omega_0}\right) = \frac{G^{\rm s}}{\sqrt{1 + 4\left(\dfrac{Q^{\rm s}}{2\pi}\right)^2\left(\dfrac{\Delta\omega}{\omega_0}\right)^2}} \tag{2.14}$$

and its phase by

$$\angle Y_{\rm in}^{\rm s}\left(\frac{\Delta\omega}{\omega_0}\right) = \arctan\left[-2\frac{Q^{\rm s}}{2\pi}\left(\frac{\Delta\omega}{\omega_0}\right)\right] . \tag{2.15}$$

In Figs. 2.2(a) and 2.2(b) both the normalized modulus $|Y_{\rm in}^{\rm s}|/G^{\rm s}$ and the phase $\angle Y_{\rm in}^{\rm s}$ are plotted as a function of the normalized angular frequency deviation $\Delta\omega/\omega_0$ for three different values of the quality factor, $Q^{\rm s} = 10\,,\ 25\,,$ and 100, respectively. All curves associated with $|Y_{\rm in}^{\rm s}|/G^{\rm s}$ reach a maximum in correspondence of the angular resonance frequency ω_0, which is obtained for a vanishing deviation $\Delta\omega = 0$. When $|Y_{\rm in}^{\rm s}|/G^{\rm s}$ falls 3 dB below its maximum value [i.e., to $\simeq 0.707$ of the maximum; cf. Fig. 2.2(a)], its phase $\angle Y_{\rm in}^{\rm s}$ is $+\pi/4$ rad $(+45^\circ)$ if $\omega < \omega_0$ and $-\pi/4$ rad (-45°) if $\omega > \omega_0$ [cf. dashed vertical lines in Fig. 2.2(b)]. From Eq. (2.12), the corresponding values of $\Delta\omega$ are found to be given by

$$2\frac{Q^{\rm s}}{2\pi}\frac{\Delta\omega}{\omega_0} = \mp 1\,, \tag{2.16}$$

from which it follows that

$$\Delta\omega_{1,2} = \mp\,\omega_0\frac{2\pi}{2Q^{\rm s}}\,. \tag{2.17}$$

It is custom to define the full bandwidth κ (in units Hz) between these two points as

$$\Delta\omega_2 - \Delta\omega_1 \equiv 2\pi\kappa = 2\omega_0\frac{2\pi}{2Q^{\rm s}}\,, \tag{2.18}$$

[11] Henceforth, in the expressions for the input admittance we substitute the "$\approx$" symbol with the "$=$" symbol for simplicity.

which provides an alternative definition of the quality factor $Q^{\rm s}$,

$$Q^{\rm s} \equiv \frac{\omega_0}{\kappa} \equiv \frac{2\pi f_0}{\kappa}\,. \tag{2.19}$$

In summary, the quality factor $Q^{\rm s}$ of a series RLC-resonator can be defined as the fractional bandwidth between the two points where $\angle Y^{\rm s}_{\rm in} = \mp\,\pi/4\,{\rm rad}$ [cf. bottom part of Fig. 2.2(b)]. The definition of Eq. (2.19) is very useful when evaluating the quality factor of a resonator from a set of experimental data. In fact, such a definition is independent from any circuit element, being given only by the observed resonance angular frequency and linewidth in units Hz at $-3\,{\rm dB}$ from the maximum of the resonance curve.

The Parallel RLC-Resonant Circuit

The second example to be considered is that of the circuit of Fig. 2.1(b), where the capacitor C, inductor L, and resistor $R^{\rm p}$ are in parallel and the current on L is given by $I_{\rm L} = Y_{\rm L}V = V/j\omega L$.[12] The complex admittance $Y_{\rm in}(j\omega)$ can again be computed by a circuit inspection

$$\begin{aligned} Y_{\rm in}(j\omega) &= G + \frac{1}{j\omega L} + j\omega C \\ &= G + j\left(\omega C - \frac{1}{\omega L}\right)\,. \end{aligned} \tag{2.20}$$

From this equation it follows that the real part of the admittance is constant with frequency, $\Re\{Y_{\rm in}(j\omega)\} = G$. On the contrary, the imaginary part $B^{\rm p}(\omega) \equiv \Im\{Y_{\rm in}(j\omega)\} = \omega C - 1/\omega L$ varies between $-\infty$ and $+\infty$ as the angular frequency ω varies between 0 and $+\infty$. As for the case of the series circuit, $B^{\rm p}(\omega) = 0$ at the resonance angular frequency ω_0. In this case, the input admittance of the circuit is pure real, $Y_{\rm in}(j\omega_0) = G$. This is possible iff the time-average energies stored in the capacitor C, $W_{\rm C} \equiv C\,V^*V/4$ and in the inductor L, $W_{\rm L} \equiv L\,I^*_{\rm L}I_{\rm L}/4 = V^*V/4\omega^2 L$ are equal, $W_{\rm L} = W_{\rm C}$. The latter condition consistently sets the resonance angular frequency of the circuit to be $\omega_0 = 1/\sqrt{LC}$. In the extreme cases of very low and very high frequency, we obtain the following asymptotic expressions for the input admittance,

$$Y_{\rm in}(j\omega) \approx -j\frac{1}{\omega L} \quad \text{for} \quad 0^+ \leftarrow \omega \ll \omega_0\,, \tag{2.21a}$$

$$Y_{\rm in}(j\omega) \approx j\omega C \quad \text{for} \quad \omega \gg \omega_0\,. \tag{2.21b}$$

This time, the physical meaning of these expressions can be understood in terms of short circuits. For $\omega_0 \gg \omega \to 0^+$, $Y_{\rm in}$ is very large and L tends to be a short circuit. For $\omega \gg \omega_0$, $Y_{\rm in}$ is still very large and C tends to be a short circuit. In the case of a parallel resonant circuit, the time-average energy stored in the circuit is $W = C\,V^*V/2$. From the knowledge of the power loss $P_{\rm R}$ and using Eq. (2.9), the quality factor of the parallel circuit is given by

$$\frac{1}{2\pi}Q^{\rm p} = \frac{\omega_0 C}{G} = \omega_0 R^{\rm p} C = \frac{R^{\rm p}}{\omega_0 L}\,, \tag{2.22}$$

[12] This is the standard example reported in all textbooks. We summarize it here for completeness.

where $R^{\mathrm{p}} = 1/G$ is the parallel resistance of the circuit as opposed to the series conductance G^{s} defined for the series circuit of Fig. 2.1(a). Finally, the complex input impedance of the parallel RLC-resonator can be evaluated following the lines of the calculations which led to Eq. (2.12). We find

$$Z_{\mathrm{in}}^{\mathrm{s}}\left(\frac{\Delta\omega}{\omega_0}\right) \approx \frac{R^{\mathrm{p}}}{1 + j2\dfrac{Q^{\mathrm{p}}}{2\pi}\left(\dfrac{\Delta\omega}{\omega_0}\right)}\,, \tag{2.23}$$

from which it follows that the quality factor Q^{p} of a parallel RLC-resonator can be defined as the fractional bandwidth between the two points where $\angle Z_{\mathrm{in}}^{\mathrm{p}} = \mp\pi/4\,\mathrm{rad}$.

If the resistances R and R^{p} of the circuits of Figs. 2.1(a) and 2.1(b), respectively, represent the losses in the resonant circuit only, the quality factors Q^{s} given by Eq. (2.11) and Q_{p} given by Eq. (2.22) are referred to as *unloaded* or *internal* quality factors. If needed for a clearer notation, they are renamed as $Q_{\mathrm{int}}^{\mathrm{s}}$ and $Q_{\mathrm{int}}^{\mathrm{p}}$. When the resonant circuit is coupled to an external load that can absorb a certain amount of power, this loading effect can be represented as an additional resistor R_{load} in series with R for a series RLC-resonator and in parallel with R^{p} for a parallel RLC-resonator. In this case, the total conductance of the series resonator or resistance of the parallel resonator are smaller and, as a consequence, also the *loaded* quality factors $Q_{\mathrm{load}}^{\mathrm{s}}$ or $Q_{\mathrm{load}}^{\mathrm{p}}$ are smaller,

$$\frac{1}{2\pi}Q_{\mathrm{load}}^{\mathrm{s}} = \frac{1}{(R + R_{\mathrm{load}})\omega_0 C}\,, \tag{2.24a}$$

$$\frac{1}{2\pi}Q_{\mathrm{load}}^{\mathrm{p}} = \frac{R^{\mathrm{p}}R_{\mathrm{load}}}{(R^{\mathrm{p}} + R_{\mathrm{load}})\omega_0 L}\,. \tag{2.24b}$$

The external quality factors $Q_{\mathrm{ext}}^{\mathrm{s}}$ and $Q_{\mathrm{ext}}^{\mathrm{p}}$ are defined as the quality factors the series and parallel resonant circuits would have if they were loss free and only the external loading R_{load} were present,

$$\frac{1}{2\pi}Q_{\mathrm{ext}}^{\mathrm{s}} = \frac{1}{R_{\mathrm{load}}\omega_0 C}\,, \tag{2.25a}$$

$$\frac{1}{2\pi}Q_{\mathrm{ext}}^{\mathrm{p}} = \frac{R_{\mathrm{load}}}{\omega_0 L}\,. \tag{2.25b}$$

Using the definitions of Eqs. (2.11), (2.22), (2.24a), (2.24b), (2.25a), and (2.25b) it is easy to prove that

$$\frac{1}{Q_{\mathrm{load}}^{\mathrm{s}}} = \frac{1}{Q_{\mathrm{ext}}^{\mathrm{s}}} + \frac{1}{Q^{\mathrm{s}}}\,, \tag{2.26a}$$

$$\frac{1}{Q_{\mathrm{load}}^{\mathrm{p}}} = \frac{1}{Q_{\mathrm{ext}}^{\mathrm{p}}} + \frac{1}{Q^{\mathrm{p}}}\,. \tag{2.26b}$$

2.1.2 Distributed-Parameter Resonators

In real applications, microwave resonators in the frequency range from 100 MHz to 10 GHz are usually realized by means of finite segments of transmission lines. These types of resonators are typical examples of distributed-parameter systems as opposed

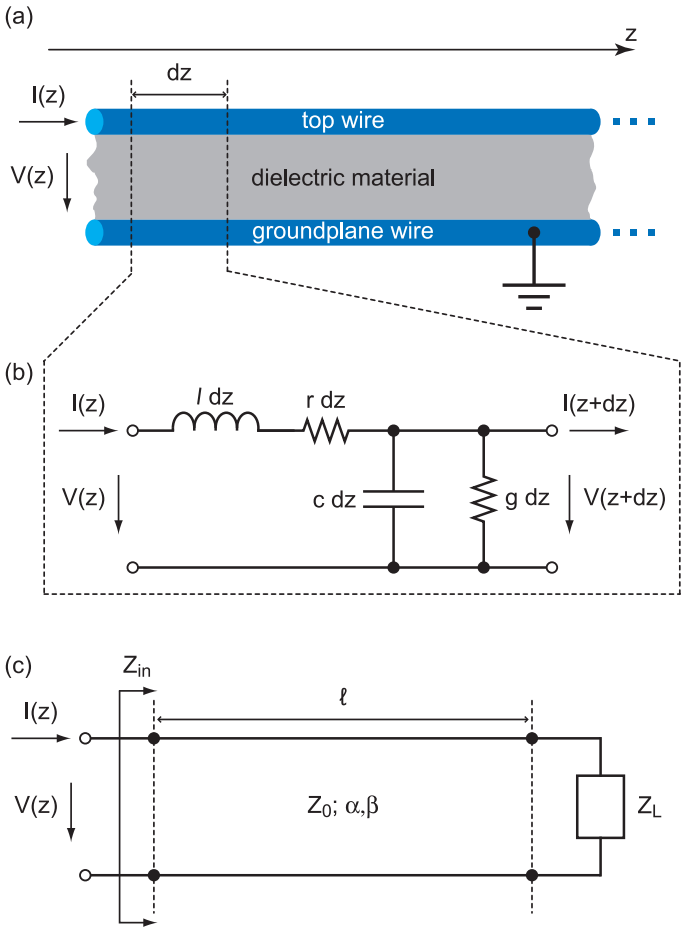

Figure 2.3: Transmission line model and line characteristic parameters. **(a)** A current $I(z)$ flows through the top wire (blue) of an infinite transmission line in the positive z direction. A voltage $V(z)$ drops between the top wire and groundplane wire (blue) via a dielectric material (grey). **(b)** Equivlent circuit model for an infinitesimal segment dz of transmission line. The characteristic parameters of the line are the series inductance $l\,dz$, in series with the resistance $r\,dz$, and the shunting capacitance $c\,dz$, in parallel with the conductance $g\,dz$. The current and voltage at the output of the infinitesimal segment of line are $I(z+dz)$ and $V(z+dz)$ and can be determined by means of differential equations (e.g., cf. Ref. [227]). **(c)** A finite segment ℓ of transmission line terminated on a load impedance Z_{L}. The input impedance of the line, Z_{in}, depends on the line characteristic impedance Z_0, the propagation phase constant β, the attenuation constant α, and the load impedance Z_{L} [cf. Eq. (2.31)].

to the ideal models described in the previous subsection, which are based on lumped elements. The reason to opt for distributed-parameter devices instead of lumped-parameter ones is because the latter are usually characterized by too high losses to be effective at microwave frequencies. Such losses are due to the conductor and/or

dielectric materials as well as large electromagnetic radiation.[13]

A transmission line can be regarded as a quasi one-dimensional (1D) structure composed of two parallel conductors, a top wire and a groundplane wire, separated by a dielectric material [cf. Fig. 2.3(a)]. As shown in Figs. 2.3(b) and 2.3(c), the parameters needed for a complete characterization of a transmission line of length $z = \ell$ are its series inductance l and shunting capacitance c per unit length. Typically, transmission lines are accompanied by (small) losses due to the finite conductivity of the wires and to dielectric losses. All these losses are represented by a resistance per unit length r, which is in series with the inductance l, and a conductance per unit length g, which is in parallel with the capacitance c. Possible radiation losses due to the geometrical configuration of the actual transmission line are assumed to be included in the series resistance r. For the sake of simplicity we consider nondispersive lines [227]. The characteristic impedance of the line is defined as

$$Z_0 \equiv \sqrt{l/c} \tag{2.27}$$

and its propagation phase constant as

$$\beta \equiv \omega/\bar{c}\,, \tag{2.28}$$

where $\bar{c}$ is the velocity of the electromagnetic waves on the line. For a low-loss transmission line it is possible to prove that

$$\beta = \omega\sqrt{lc} \tag{2.29}$$

and that the line attenuation constant is given by

$$\alpha = \frac{1}{2}(rY_0 + gZ_0)\,, \tag{2.30}$$

where $Y_0 \equiv 1/Z_0 = \sqrt{c/l}$ is the characteristic admittance of the transmission line. Hereafter, we consider negligible dielectric losses and, thus, we set $g = 0$. Accordingly, $\alpha = rY_0/2$.

In order to operate a transmission line as a resonator, we must cut it into a finite segment and terminate it at the two edges into suitable circuit elements. In the ideal case, those elements are short or open circuits and determine the boundary conditions the electromagnetic waves have to fulfill in order to be sustained by the line. As a result, the line is characterized by so-called standing waves. Before delving into the details on the form of the standing waves associated with different types of terminations, we analyze the equivalent circuit model for two relevant examples: short-circuited and open-circuited transmission lines.

A fundamental result in the circuit theory of transmission lines, which must be explained before proceeding with our study, is represented by the so-called transformation of impedances. Let us consider again the transmission line of Fig. 2.3. The line is terminated in a load impedance defined as $Z_{\rm L}$ [cf. Fig. 2.3(c)]. Such a load can be a short circuit, $Z_{\rm L} = 0$, an open circuit, $Y_{\rm L} \equiv 1/Z_{\rm L} = 0$, a matched resistor with impedance $Z_{\rm L} = Z_0$, or, more in general, a resistor or any other circuit element

[13] It is worth mentioning that accurate engineering can overcome those issues and state-of-the-art technology might allow for the implementation of high quality factor resonators based on lumped elements.

with unmatched impedance $Z_{\rm L} \neq Z_0$. In the case of a lossy line, the transformation of impedances tells us that the impedance seen at the input of the transmission line is given by [cf. Fig. 2.3(c)]

$$Z_{\rm in} = Z_0 \frac{Z_{\rm L} + Z_0 \tanh(j\beta\ell + \alpha\ell)}{Z_0 + Z_{\rm L} \tanh(j\beta\ell + \alpha\ell)}\,, \tag{2.31}$$

which, as expected, approaches Z_0 for ℓ large since $\tanh x$ approaches 1 for x large and not a pure immaginary quantity.

With this result in hand, we can now straightforwardly analyze the circuit models of short- and open-circuited transmission lines.

Short-Circuited Transmission Lines

If the termination on the righthand side of the transmission line of Fig. 2.3(c) is a short circuit, $Z_{\rm L} = 0$, the input impedance reduces to

$$\begin{aligned} Z_{\rm in} &= Z_0 \tanh(j\beta\ell + \alpha\ell) \\ &= Z_0 \frac{\tanh\alpha\ell + j\tan\beta\ell}{1 + j\tan\beta\ell\,\tanh\alpha\ell}\,. \end{aligned} \tag{2.32}$$

Let $\ell = \lambda_0/2$, where λ_0 is the wavelength at $\omega = 2\pi f = \omega_0 = 2\pi f_0$.[14] For small deviations $\Delta\omega$ around the resonance angular frequency ω_0, we can assume $\omega = \omega_0 + \Delta\omega$. Since at ω_0 we find $\beta\ell = \pi$, we can write $\beta\ell = (\omega/\bar{c})\ell = \pi\omega/\omega_0 = \pi + \pi\Delta\omega/\omega_0$. Given that we are assuming small losses, $\tanh\alpha\ell \approx \alpha\ell$. This condition guarantees that $\alpha\ell \ll 1$. In addition, since $\Delta\omega/\omega_0$ is small, $\tan\beta\ell = \tan(\pi + \pi\Delta\omega/\omega_0) = \tan\pi\Delta\omega/\omega_0 \approx \pi\Delta\omega/\omega_0$. Hence, we obtain

$$\begin{aligned} Z_{\rm in} &= Z_0 \frac{\alpha\ell + j\pi\Delta\omega/\omega_0}{1 + j\alpha\ell\pi\Delta\omega/\omega_0} \\ &\approx Z_0 \left(\alpha\ell + j\pi\frac{\Delta\omega}{\omega_0}\right)\,, \end{aligned} \tag{2.33}$$

where the approximation is valid because the second term in the denominator, $\propto \alpha\,\Delta\omega$, is of second order compared to the two numerator terms, which are proportional to α and $\Delta\omega$, respectively. Reminding that $\beta\ell = \omega_0\sqrt{lc}\;\ell = \pi$, we find that $\pi/\omega_0 = \ell\sqrt{lc}$ and the expression for $Z_{\rm in}$ can be further simplified as

$$\begin{aligned} Z_{\rm in} &= \sqrt{\frac{l}{c}} \left(\frac{\ell}{2} r \sqrt{\frac{c}{l}} + j\Delta\omega\ell\sqrt{lc}\right) \\ &= \frac{1}{2} r\ell + jl\ell\Delta\omega\,. \end{aligned} \tag{2.34}$$

It is of pedagogical interest to compare the result of Eq. (2.34) with the inverse of the input admittance of the series RLC-resonant circuit given by Eq. (2.13), which is valid in the vicinity of resonance. Dividing both numerator and denominator of Eq. (2.13) by $G^{\rm s} = 1/R$ and reminding that $Q^{\rm s}/2\pi = G^{\rm s}/\omega_0 C$, we readily obtain

$$Z^{\rm s}_{\rm in} = R + j2L\Delta\omega\,. \tag{2.35}$$

[14] We remind that, in general, the wavelength $\lambda \equiv \bar{c}/f$.

Comparing the above expression with the impedance of Eq. (2.34), we see that in the vicinity of the frequency for which $\ell = \lambda_0/2$ the short-circuited line behaves as a series resonant circuit with equivalent *total* resistance $R \equiv r\ell/2$ and inductance $L \equiv l\,\ell/2$. The factors 1/2 arise because the current on the short-circuited line is obviously only a half sinusoid. Therefore, the effective circuit parameters R and L are one-half of the total line quantities.

It is remarkable that the quality factor of a short-circuited transmission line resonator can be calculated as if it were the quality factor of a simple series RLC-resonant circuit. Applying the result of Eq. (2.11) to the case of a short-circuited line we find

$$\frac{1}{2\pi}Q^{\mathrm{s}} = \frac{\omega_0 L}{R} = \frac{\omega_0 l}{r} = \frac{\beta}{2\alpha}\,. \tag{2.36}$$

This definition of quality factor can be applied to any transmission line with arbitrary geometrical configuration, as long as one is able to compute the associated propagation phase constant β and attenuation constant α. We refer to Ref. [227] for more details on the specific implementation of transmission line resonators.

Open-Circuited Transmission Lines

If the termination on the righthand side of the transmission line of Fig. 2.3(c) is an open circuit, $Y_{\mathrm{L}} = 1/Z_{\mathrm{L}} = 0$, it can easily be verified that the line is equivalent to a series RLC-resonant circuit in the vicinity of the frequency for which it is a quarter wavelength long, i.e., $\ell = \lambda_0/4$. An analysis similar to the case of the short-circuited line reveals that the input impedance of an open-circuited line is given by

$$\begin{aligned} Z_{\mathrm{in}} &\approx Z_0 \left(\alpha\ell + j\frac{\pi}{2}\frac{\Delta\omega}{\omega_0}\right) \\ &= \frac{1}{2}r\ell + jl\,\ell\Delta\omega\,. \end{aligned} \tag{2.37}$$

As a consequence, all the equivalent circuit parameters can be calculated as in the case of a short-circuited transmission line. We notice that the approximated form for the input impedance of Eq. (2.33) differs from that of Eq. (2.37) by a factor 1/2 ($\pi \to \pi/2$) because the resonator length is now one-half the length in the short-circuit case, $\lambda_0/4$ instead of $\lambda_0/2$.

It is noteworthy to mention that short-circuited transmission lines behave as parallel RLC-resonant circuits in the frequency range where they are close to be one-quarter wavelength long. The same property is true for open-circuited lines that are close to be one-half wavelength long. When a transmission line behaves as an RLC-parallel resonant circuit, it is said to be antiresonant. We do not enter into the details of this matter here and remind to Ref. [227] for further elucidation.

The Reflection of Waves: Modes

The problem of a transmission line terminated at one end, which so far we have analyzed by means of impedance transformations, is analogous to the problem of a string fastened to the bridge of a classical guitar and let loose at the headstock. Mathematically, this boundary condition problem can be formulated by imposing

that the space-time–dependent displacement $i(z,t)$ of the string at the position $z = 0$ must be zero because this end does not move,

$$i(z = 0, t) = 0 \quad \forall t\,. \tag{2.38}$$

If it were not for the bridge where the string is held, the general solution for the string motion would be the sum of two functions. Each of these functions would represent a wave travelling one way through the string and a wave travelling the opposite way, respectively. If we assume that the string carries 1D waves along the z direction with velocity $\bar{c}$, the string motion for the unbound problem would read

$$i(z,t) = f(z - \bar{c}t) + g(z + \bar{c}t)\,. \tag{2.39}$$

Imposing the boundary condition of Eq. (2.38) in the above equation and examining i for any value of t, we obtain the solution $i(t) = f(-\bar{c}t) + g(+\bar{c}t)$. This expression is zero at all times iff $g(+\bar{c}t) = -f(-\bar{c}t)$. Under these conditions, the string motion for the bound problem becomes

$$i(z,t) = f(z - \bar{c}t) - f(-z - \bar{c}t)\,. \tag{2.40}$$

It is easy to check that, $\forall t$, we get $i = 0$ when $z = 0$. In other words, the sum of two waves interferes in order to get a zero displacement of the string in the origin of the z-axis.

For the string motion problem, as for any other problem related to vibrational motion, the standard Ansatz is to consider periodic waves as solutions. Suppose that the wave represented by $f(z - \bar{c}t)$ is a cosine function with amplitude $\tilde{I}_0$ and angular frequency ω. If there are no losses at the bridge of the guitar,[15] the wave reflected back, $-f(-z - \bar{c}t)$, is also a cosine function of the same amplitude and frequency, but travelling in the opposite direction. This situation can most simply be described by employing the complex function notation, i.e., the so-called phasor picture. We start assuming

$$f(z - \bar{c}t) = \tilde{I}_0 \cos(\omega t - \beta z)\,, \tag{2.41}$$

where, once again, $\beta = \omega/\bar{c}$. The amplitude $\tilde{I}_0$ is a positive real number. More generally, we can define the incident wave f^+ as

$$f^+ \equiv f(z - \bar{c}t) \equiv \Re\left\{\tilde{I}_0 e^{j(\omega t - \beta z)}\right\} \tag{2.42}$$

and the associated phasor (or complex phasor amplitude) as

$$F^+ \equiv \tilde{I}_0 e^{-j\beta z}\,. \tag{2.43}$$

In a similar way, we can define the reflected wave f^- as

$$f^- \equiv f(-z - \bar{c}t) \equiv \Re\left\{\tilde{I}_0 e^{j(\omega t + \beta z)}\right\} \tag{2.44}$$

and the associated phasor as

$$F^- \equiv \tilde{I}_0 e^{+j\beta z}\,. \tag{2.45}$$

[15]The bridge behaves as if it were an infinite solid wall, which does not absorb energy.

Remarkably, in the definition of phasor the common time-dependent term, $\exp(j\omega t)$, drops out. Since the angular frequency ω is the same for both incident and reflected waves, the phasors defined by Eqs. (2.43) and (2.45) uniquely represent the associated waves. In experiments, the angular frequency ω is set by means of a so-called local oscillator (LO) signal and, as a consequence, is a known parameter (cf. chapters 3 and 4). In most of the following calculations we will use the phasor picture. When needed, we will insert back the time-dependent terms for explanatory purposes. The phasor picture is a sort of simplified Fourier transform valid for periodic monochromatic functions in the case of no losses.[16]

It can easily be seen that the complex functions of Eqs. (2.42) and (2.44) verify the solution for the string bound problem of Eq. (2.40). Consequently, Eq. (2.40) can be rewritten in the phasor picture as

$$\begin{aligned} I = I(z) &= \tilde{I}_0 \left(e^{-j\beta z} - e^{+j\beta z}\right) \\ &= -2j\tilde{I}_0 \sin(\beta z)\,. \end{aligned} \tag{2.46}$$

I is the complex phasor amplitude associated with $i(z,t)$. The second line of Eq. (2.46) is obtained by applying the Euler definition of sine. In the time domain, the displacement i can finally be written as

$$\begin{aligned} i(z,t) &= \Re\left\{-2j\tilde{I}_0 e^{j\omega t}\sin(\beta z)\right\} \\ &= \Re\left\{-2j\tilde{I}_0(\cos\omega t + j\sin\omega t)\ \sin(\beta z)\right\} \\ &= 2\tilde{I}_0 \sin\beta z \times \sin\omega t \\ &= -\tilde{I}_0 \sin\beta z \times j\left(e^{+j\omega t} - e^{-j\omega t}\right), \end{aligned} \tag{2.47}$$

where the minus sign in front of I_0 represents a global phase. Equation (2.47) is a beautiful example of the power of the Euler representation of sine/cosine functions and, as we will show later, stands at the basis of the quantization of a transmission line resonator.

The solution for the displacement i of Eq. (2.47) reveals two important facts. First, if we observe the string *in time*, the string oscillates at the same angular frequency ω at any fixed point z. In particular, there are some special points where there is no displacement at all, e.g., where $\sin\beta z = 0$. Second, if we observe the string *in space* and take a snapshot of it, the picture is a sine wave at any time t. However, the displacement of this sine wave depends upon the time t. From Eq. (2.47) it also follows that the length corresponding to one period of the sine wave is equal to the wavelength of either of the superimposed waves,

$$\lambda = \frac{2\pi}{\beta}\,. \tag{2.48}$$

The points where there is no motion satisfy the condition $\sin\beta z = 0$, which implies that at these points $\beta z = n\pi$, with $n \in \mathbb{N}$. These points have a peculiar name and are defined as *nodes*. The pattern of motion characteristic of the string problem has the property that at any point the string moves perfectly sinusoidally and that all

[16] With losses, the so-called pseudo-cisoids, a simplified Laplace transform, must be used.

points move at the same frequency (even if some of them move more than others). This special motion is defined as *mode*.

By analogy, we can now think of extending the results obtained for the string problem to the case of electromagnetic waves propagating on a transmission line. The solutions to the problem of a string which is held at one end are formally equivalent to those of a steady-state sinusoidal electromagnetic wave propagating on a transmission line which is open- or short-circuited at one end. Let us begin with the case of an *open-circuited transmission line*. In this case, the displacement acquires the meaning of a current, which has to be zero at the open-circuited end.[17] If the transmission line is loss free, the current on the line is a pure standing wave and can be written as in Eqs. (2.46) and (2.47) in the phasor picture and time domain, respectively. The case of electromagnetic waves, though, is more complex than that of a simple string. To any electromagnetic wave are associated both a current with space-dependent complex phasor amplitude $I(z)$ and a voltage with space-dependent complex phasor amplitude $V(z)$. Assuming steady-state solutions and invoking Kirchhoff's circuit laws in the phasor picture, it is straightforward to prove that for a transmission line the following differential equation holds [227]:

$$\frac{\partial}{\partial z} I(z) = -j\omega c\, V(z)\,. \tag{2.49}$$

Substituting the expression for the current given in Eq. (2.46) into the above equation, bearing in mind that $\beta = \omega\sqrt{lc}$ and $Z_0 = \sqrt{l/c}$, and solving for $V(z)$ we finally obtain

$$\begin{aligned} V(z) &= 2\tilde{I}_0 Z_0 \cos\beta z \\ &= 2\tilde{V}_0 \cos\beta z\,, \end{aligned} \tag{2.50}$$

where $\tilde{V}_0 = Z_0\tilde{I}_0$. V is the complex phasor amplitude associated with $v(z,t)$, which can then be written as

$$\begin{aligned} v(z,t) &= \Re\left\{e^{j\omega t}V(z)\right\} \\ &= \Re\left\{2\tilde{V}_0 e^{j\omega t}\cos(\beta z)\right\} \\ &= \Re\left\{2\tilde{V}_0(\cos\omega t + j\sin\omega t)\,\cos(\beta z)\right\} \\ &= 2\tilde{V}_0\cos\beta z \times \cos\omega t \\ &= \tilde{V}_0\cos\beta z \times (e^{+j\omega t} + e^{-j\omega t})\,. \end{aligned} \tag{2.51}$$

As expected, at time $t = 0$ the voltage reaches a maximum at the node $z = 0$, where $\cos\beta z = 1$. At any other time, it oscillates as a cosine function. The behavior of the current is the dual of the voltage: Where one reaches a maximum the other is at a minimum and vice versa. For the case of an open-circuit termination, the nodal variable, which is zero at the node for all times, is the current.

The case of a *short-circuited transmission line* can be treated as the dual of the open-circuited line. In this case, the displacement acquires the meaning of a voltage, which has to be zero at the short-circuited end. If the transmission line is loss-free,

[17] It is now evident why we have chosen to indicate the displacement of the string as i!

the voltage on the line is a pure standing wave and can be written as in Eqs. (2.46) and (2.47) upon applying the substitutions $I \to V$, $i \to v$, and $\tilde{I}_0 \to \tilde{V}_0$. The current can then be obtained from the following differential equation in the phasor picture [227]:

$$\frac{\partial}{\partial z} V(z) = -j\omega l\, I(z)\,. \tag{2.52}$$

In summary, for a short-circuited transmission line

$$V = V(z) = -2jV_0 \sin(\beta z)\,, \tag{2.53a}$$

$$v(z,t) = -\tilde{V}_0 \sin\beta z \times j(e^{+j\omega t} - e^{-j\omega t})\,, \tag{2.53b}$$

$$I = I(z) = 2\tilde{I}_0 \cos\beta z\,, \tag{2.53c}$$

$$i(z,t) = \tilde{I}_0 \cos\beta z \times (e^{+j\omega t} + e^{-j\omega t})\,. \tag{2.53d}$$

For the case of a short-circuit termination, the nodal variable, which is zero at the node for all times, is the voltage.

The Confinement of Waves: Natural Frequencies

(i) $\lambda/2$ resonators - We now go back to the general problem of a vibrating string. If the string is fastened to both the bridge and headstock of our classical guitar, we have to impose two boundary conditions at, e.g., $z = 0$ and $z = \ell$. Because of these boundary conditions, it is evident that the problem admits periodic solutions. A wave on the string is reflected back and forth at the bridge and headstock in a periodic motion. An interesting question is whether such motion can be sinusoidal. We can imagine to put a sinusoidal periodic wave on the string. If the string is tied at one end, we know that the wave must be as in Eq. (2.47). If it is tied at the other end, it must be the same at the other end too. Hence, the only possibility for a sinusoidal periodic motion to be conceivable is that the sine wave perfectly fits into the string length. In this case, the frequency associated with the sine wave is defined as *natural frequency*. In other words, if the string is started with a sine wave shape that fits in perfectly, then it will continue to keep that perfect shape of a sine wave and will oscillate harmonically at the corresponding natural frequency.

Mathematically, we can formulate the problem as

$$i(z = 0, t) = 0 \quad \forall t\,, \tag{2.54a}$$

$$i(z = \ell, t) = 0 \quad \forall t\,, \tag{2.54b}$$

or, equivalently,

$$I(z = 0) = 0\,, \tag{2.55a}$$

$$I(z = \ell) = 0\,. \tag{2.55b}$$

Since we are only interested in the spatial shape of the sine wave, for simplicity we can use the set of boundary conditions for the phasors, which are independent of time. Notably, Eq. (2.46) fulfills the boundary condition given by Eq. (2.55a) for every value of the propagation phase constant β. In fact, imposing the boundary condition of Eq. (2.55a) for a sine wave is equivalent to solve the half-open

string problem, which led to the solution of Eq. (2.46). Imposing the condition of Eq. (2.55b), instead, adds a new constraint to the problem. The significance of such constraint is that β is no longer arbitrary, as in the case of a half-open string, but fixed by the geometry of the string, i.e., by its length. When the string is tied at both ends the only possibility is that

$$I(z=\ell) = -2j\tilde{I}_0 \sin(\beta\ell) = 0\,. \tag{2.56}$$

In order for a sine to be zero, the angle which is argument of the sine must be an integer multiple of π

$$\beta\ell = m\pi\,, \quad \text{with } m \in \mathbb{N} \tag{2.57}$$

or

$$\beta = \frac{m\pi}{\ell}\,. \tag{2.58}$$

The equation above, which fixes β to the geometry of the string, can be rewritten as

$$\beta = \frac{\omega}{\bar{c}} = \frac{2\pi f}{\bar{c}} = \frac{2\pi}{\lambda} = \frac{m\pi}{\ell}\,, \tag{2.59}$$

where $\lambda \equiv \bar{c}/f$. Finally, we can write

$$\ell = m\frac{\lambda}{2} = m\frac{\bar{c}}{2f}\,. \tag{2.60}$$

Equation (2.60) represents a fundamental result in the theory of confined waves. It tells us that, given a particular wavelength (or frequency), the length of the string must be an integer multiple of half wavelength. We have thus proven that a string tied at two ends can have sinusoidal motion, but only at some special wavelengths (or frequencies). According to Eq. (2.60), there are many different possible wavelengths (or frequencies) for which the boundary conditions of Eqs. (2.55a) and (2.55b) are fulfilled. Each of these wavelengths (or frequencies) corresponds to a mode because, by definition, a mode is a pattern of motion repeating itself sinusoidally. Neglecting the trivial case for $m = 0$, we can define the mode for $m = 1$ as the *fundamental mode* of vibration for the string. In this case, the length of the string is set to be

$$\ell = \frac{\lambda_0}{2}\,, \tag{2.61}$$

where

$$\lambda_0 = \frac{\bar{c}}{f_0}\,, \tag{2.62}$$

and f_0 is the fundamental frequency associated with the string under consideration. The sine wave on the string is then given by the phasor

$$\begin{aligned} I = I(z) &= -2j\tilde{I}_0 \sin\left(\frac{m\pi}{\ell}\right) \\ &= -2j\tilde{I}_0 \sin\left(\frac{m2\pi}{\lambda_0}z\right) \\ &= -2j\tilde{I}_0 \sin\left(2\pi m f_0 \frac{z}{\bar{c}}\right)\,, \end{aligned} \tag{2.63}$$

or, in time domain, by the function

$$\begin{aligned} i(z,t) &= \Re\left\{e^{j2\pi m f_0 t} I(z)\right\} \\ &= -\tilde{I}_0 \sin\left(2\pi m f_0 \frac{z}{\bar{c}}\right) \times j(e^{+j2\pi m f_0 t} - e^{-j2\pi m f_0 t})\,. \end{aligned} \tag{2.64}$$

The *first mode* of vibration for the string is obtained when $m = 2$ and, consequently, $f_1 = 2f_0$. The *second mode* when $m = 3$ and $f_2 = 3f_0$ and so on and so forth. For the m-th mode, the frequency is $f_{m-1} = mf_0$. So, the frequencies associated with the different modes of vibration are integer multiple of the fundamental frequency f_0.[18]

The problem of a string tied at both ends is analogous to that of a finite segment of transmission line with both ends open circuited. At the open circuits the current on the transmission line has to be zero and, thus, it can be written as in Eqs. (2.63) and (2.64) in the phasor picture and time domain, respectively. The corresponding voltage can be derived from Eq. (2.49). In the phasor picture, the voltage reads

$$V(z) = 2\tilde{V}_0 \cos\left(2\pi m f_0 \frac{z}{\bar{c}}\right) \tag{2.65}$$

and, in time domain,

$$v(z,t) = \tilde{V}_0 \cos\left(2\pi m f_0 \frac{z}{\bar{c}}\right) \times (e^{+j2\pi m f_0 t} + e^{-j2\pi m f_0 t})\,. \tag{2.66}$$

As expected, in correspondence of the open circuits the voltage reaches a maximum, thus showing a dual behavior as compared to the current.

Equations (2.63)-(2.66) fully characterize the class of resonators defined as $\lambda/2$ *resonators*, which owes its name to the condition of Eq. (2.60). In summary, for the synthesis of a $\lambda/2$ resonator, given the desired resonance frequency f_0 we first calculate the corresponding wavelength λ_0. We then take a finite segment of transmission line $\lambda_0/2$ long and terminate it into two open circuits. The open-circuit terminations represent the nodes of the resonator. This segment of transmission line can then sustain any current and voltage mode with frequency $f_{m-1} = mf_0$, integer multiple of the fundamental frequency f_0.[19] For $\lambda/2$ resonators the nodal variable is the current. Figures 2.4(a) and 2.4(b) show the first three modes ($m = 1, 2, 3$) for a generic $\lambda/2$ resonator. The modes are obtained from an opportune renormalization of Eqs. (2.65) and (2.63).

(ii) $\lambda/4$ *resonators* - There is another important class of electromagnetic resonators known as $\lambda/4$ *resonators*. Such resonators can be synthesized taking a segment of transmission line and terminating it into an open and a short circuit, respectively. We assume the open to be positioned at $z = 0$ and the short at $z = \ell$. On one hand, the open circuit termination sets the current to zero, as in the case of one node of a $\lambda/2$ resonator. On the other hand, the short circuit sets the voltage to zero. This condition can be expressed as

$$V(z = \ell) = 2\tilde{V}_0 \cos\beta z = 0\,, \tag{2.67}$$

the solution of which is

$$\beta\ell = (2m+1)\frac{\pi}{2}\,, \quad \text{with } m \in \mathbb{N} \tag{2.68}$$

[18] $m > 1$.

[19] Notably, $\forall m$, $\ell = m\lambda/2 = m\bar{c}/2mf_0 = \lambda_0/2$.

or, equivalently,

$$\ell = (2m+1)\frac{\lambda}{4} = (2m+1)\frac{\bar{c}}{4f}\,. \tag{2.69}$$

We can now define the mode for $m = 0$ as the *fundamental mode* for the $\lambda/4$ transmission line resonator. In this case, the length of the string is set to be

$$\ell = \frac{\lambda_0}{4}\,, \tag{2.70}$$

and the voltage and current in the phasor picture and time domain, respectively, are given by

$$\begin{aligned} V = V(z) &= 2\tilde{V}_0 \cos\left[\frac{2(2m+1)\pi}{\lambda_0}\right] \\ &= 2\tilde{V}_0 \cos\left[2\pi(2m+1)f_0\frac{z}{\bar{c}}\right]\,, \end{aligned} \tag{2.71a}$$

$$\begin{aligned} v(z,t) = \tilde{V}_0 &\cos\left[2\pi(2m+1)f_0\frac{z}{\bar{c}}\right] \\ &\times\left[e^{+j2\pi(2m+1)f_0 t} + e^{-j2\pi(2m+1)f_0 t}\right]\,, \end{aligned} \tag{2.71b}$$

$$\begin{aligned} I = I(z) = &-2j\tilde{I}_0 \sin\left[\frac{2(2m+1)\pi}{\lambda_0}\right] \\ &= -2j\tilde{I}_0 \sin\left[2\pi(2m+1)f_0\frac{z}{\bar{c}}\right]\,, \end{aligned} \tag{2.71c}$$

$$\begin{aligned} i(z,t) = -\tilde{I}_0 &\sin\left[2\pi(2m+1)f_0\frac{z}{\bar{c}}\right] \\ &\times j\left[e^{+j2\pi(2m+1)f_0 t} - e^{-j2\pi(2m+1)f_0 t}\right]\,. \end{aligned} \tag{2.71d}$$

The *first mode* of resonance is obtained when $m = 1$ and, consequently, $f_1 = 3f_0$. The *second mode* when $m = 2$ and $f_2 = 5f_0$ and so on and so forth. For the m-th mode, the frequency is $f_m = (2m+1)f_0$. So, the frequencies associated with the different modes are odd integer multiple of the fundamental frequency f_0.[20] The open- and short-circuit terminations represent the nodes of the $\lambda/4$ resonator and the nodal variables are the current in correspondence of the open circuit and the voltage in correspondence of the short. As always, where the voltage reaches a maximum the current is at a minimum and vice versa. Figures 2.4(c) and 2.4(d) show the first three modes ($m = 0, 1, 2$) for a generic $\lambda/4$ resonator. The modes are obtained from an opportune renormalization of Eqs. (2.71a) and (2.71c).

To conclude this subsection, we remind that any generic signal on a transmission line[21] can always be regarded as the superposition of an infinite (or at least a very large) number of modes, combined with opportune amplitudes and phases. Each mode can be described by a very simple sinusoidal wave as those derived for open- and short-circuited transmission line resonators. This is a special case of the general *superposition principle* valid for all linear systems. The possibility to use the superposition principle has important consequences for the quantum theory of signals to be developed below.

[20] $m \geqslant 0$.

[21] Similar to a field in free space.

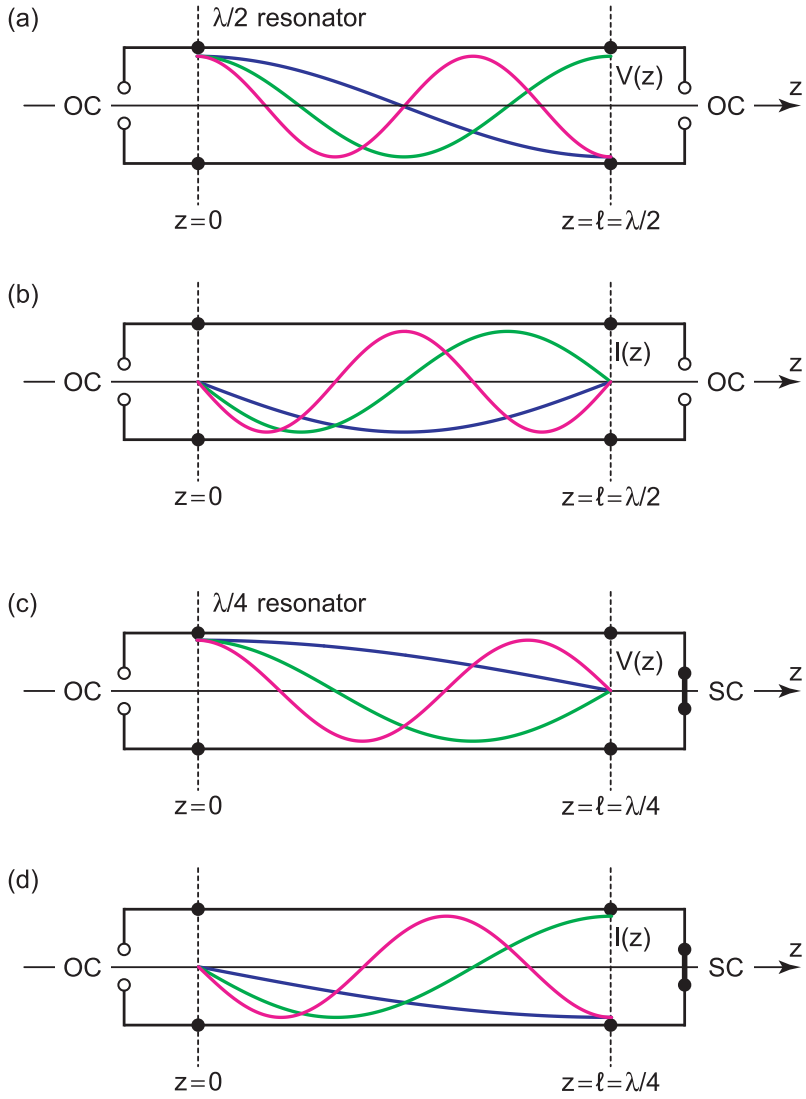

Figure 2.4: Spatial distribution for the voltage V and current I on a $\lambda/2$ resonator [**(a)** and **(b)**] and $\lambda/4$ resonator [**(c)** and **(d)**]. **(a)** Normalized voltage $V(z)/2\tilde{V}_0$ obtained from Eq. (2.65) for $m = 1$, dark blue (dark grey) line, $m = 2$, light green (light grey) line, and $m = 3$, magenta (middle grey) line. The voltage is maximum at each open circuit (OC). **(b)** Normalized current $I(z)/(-2j\,\tilde{I}_0)$ obtained from Eq. (2.63). The color code for the three plotted modes is as in **(a)**. The current is zero at each OC. **(c)** $V(z)/2\tilde{V}_0$ obtained from Eq. (2.71a) for $m = 0$, dark blue (dark grey) line, $m = 1$, light green (light grey) line, and $m = 2$, magenta (middle grey) line. The voltage is maximum at the OC and zero at the short circuit (SC). **(d)** $I(z)/(-2j\,\tilde{I}_0)$ obtained from Eq. (2.71c). The color code for the three plotted modes is as in **(c)**. The current is zero at the OC and maximum at the SC. The modes are plotted until the $z = 0$ and $z = \lambda/2$ or $z = \lambda/4$ planes, which, for clarity, have been separated from the open and short circuit elements.

2.1.3 Quantization of Microwave Resonators and Signals

In Subsecs. 2.1.1 and 2.1.2, the general properties of classical electromagnetic resonators have been studied. The scope of this subsection is to extend those properties to the case of quantum-mechanical resonators. We begin analyzing the simple case of a quantized LC-resonator[22] and show that it behaves as a 1D quantum-mechanical harmonic oscillator. We then generalize the results obtained for an LC-resonator to more complex structures such as quantized transmission line resonators. Finally, we show that any quantum signal of a given frequency propagating on a transmission line, i.e., a monochromatic electromagnetic field, is mathematically equivalent to a 1D quantum-mechanical harmonic oscillator of the same frequency. This result will be very useful for the derivations of chapters 3 and 4.

Lumped-Parameter Quantized Resonators

The classical Hamiltonian, i.e., the total energy, of a lumped-parameter LC-resonator can be written as

$$\begin{aligned} H_{LC} &= \frac{Q^2}{2C} + \frac{\Phi^2}{2L} \\ &= \frac{Q^2}{2C} + \frac{1}{2}\omega^2 C\Phi^2 \,, \end{aligned} \tag{2.72}$$

where Q is the charge associated with capacitor C, Φ the flux associated with inductor L, and $\omega \equiv 1/\sqrt{LC}$ the resonance frequency of the resonator.[23] Substituting the general definitions of charge and flux,

$$Q \equiv Cv \,, \tag{2.73a}$$

$$\Phi \equiv Li \,, \tag{2.73b}$$

where v is the voltage on C and i the current on L, into the Hamiltonian of Eq. (2.72) we readily obtain

$$H_{LC} = \frac{1}{2}Cv^2 + \frac{1}{2}Li^2 \,. \tag{2.74}$$

Depending on the problem, we will use either Eq. (2.72) or Eq. (2.74) for the Hamiltonian of a resonator.

In quantum mechanics, the classical quantities charge and flux are replaced by observables in a Hilbert space, $Q \to \hat{Q}$ and $\Phi \to \hat{\Phi}$. By means of these transformations, the quantum-mechanical version of the Hamiltonian of Eq. (2.72) can be written as

$$\widehat{H}_{LC} = \frac{\hat{Q}^2}{2C} + \frac{1}{2}\omega^2 C\hat{\Phi}^2 \,. \tag{2.75}$$

The observables $\hat{Q}$ and $\hat{\Phi}$ are canonically conjugated and, thus, must satisfy the standard commutation relation

$$[\hat{Q}, \hat{\Phi}] = j\hbar \,. \tag{2.76}$$

[22] We neglect losses for simplicity, $R = 0$.

[23] We remind that lumped-parameter resonators are characterized by one mode only. Hence, the energy of Eq. (2.72) represents the total energy of the resonator.

From this relation it follows that the flux $\hat{\Phi}$ can be interpreted as the *position* operator and the charge $\hat{Q}$ as the corresponding *momentum* operator. It is convenient to replace $\hat{Q}$ and $\hat{\Phi}$ by a pair of dimensionless (non-Hermitian) operators, which are defined as

$$\hat{a} \equiv \frac{1}{\sqrt{2C\hbar\omega}}(\hat{Q} + jC\omega\hat{\Phi}) \tag{2.77}$$

and its adjoint

$$\hat{a}^\dagger \equiv \frac{1}{\sqrt{2C\hbar\omega}}(\hat{Q} - jC\omega\hat{\Phi})\,. \tag{2.78}$$

Consequently, we can rewrite the observables $\hat{Q}$ and $\hat{\Phi}$ as

$$\hat{Q} = \sqrt{\frac{C\hbar\omega}{2}}(\hat{a}^\dagger + \hat{a}) \tag{2.79}$$

and

$$\hat{\Phi} = \sqrt{\frac{\hbar}{2C\omega}}\, j(\hat{a}^\dagger - \hat{a})\,. \tag{2.80}$$

From $[\hat{Q}, \hat{\Phi}] = j\hbar$ it follows that

$$[\hat{a}, \hat{a}^\dagger] = 1\,. \tag{2.81}$$

Equations (2.79) and (2.80) with the aid of Eq. (2.81) allow us to write the Hamiltonian of a quantized LC-resonator in the from

$$\widehat{H}_{LC} = \frac{\hbar\omega}{2}(\hat{a}\hat{a}^\dagger + \hat{a}^\dagger\hat{a}) = \hbar\omega\left(\hat{a}^\dagger\hat{a} + \frac{1}{2}\right)\,, \tag{2.82}$$

which represents a 1D quantum-mechanical harmonic oscillator. The theory of the 1D quantum-mechanical harmonic oscillator is developed equivalently in terms of the Hamiltonian of Eq. (2.75) and the commutation relation of Eq. (2.76) or by the analogous Eqs. (2.82) and (2.81).

From the Hamiltonian of Eq. (2.82) it appears evident that the energy levels of the harmonic oscillator are determined by the eigenvalues of the so-called *number operator* $\hat{N} \equiv \hat{a}^\dagger\hat{a}$. We denote the eigenvalues and (normalized) eigenkets of $\hat{N}$ by n and $|n\rangle$, respectively. Hence,

$$\hat{N}|n\rangle = n|n\rangle\,. \tag{2.83}$$

The scalar product of the vector $\hat{a}|n\rangle$ with itself is given by $\langle n|\hat{N}|n\rangle = \langle n|\hat{a}^\dagger\hat{a}|n\rangle$. It then follows from Eq. (2.83) that $n\langle n|n\rangle = n$, with $n \in \mathbb{N}$. It can also be proven that

$$\hat{a}|n\rangle = \sqrt{n}|n-1\rangle\,, \tag{2.84a}$$

$$\hat{a}^\dagger|n\rangle = \sqrt{n+1}|n+1\rangle\,, \tag{2.84b}$$

and, for consistency, $\hat{a}|0\rangle = 0$. The state $|0\rangle$ is called the vacuum state of the quantum harmonic oscillator. Because of Eqs. (2.84a) and (2.84b) $\hat{a}$ and $\hat{a}^\dagger$ are defined as *lowering (annihilation)* and *raising (creation)* operators, respectively. The annihilation and creation operators are extremely useful in calculations, although

they do not represent observable features of the oscillator. The energy levels of the 1D quantum-mechanical harmonic oscillator are given by

$$E_n = \left(n + \frac{1}{2}\right)\hbar\omega\,, \tag{2.85}$$

with $n = 0, 1, 2, \ldots$. Finally, the wave functions of the oscillator can be expressed in terms of the position operator $\hat{\Phi}$ as

$$\psi_0(\hat{\Phi}) = \left(\frac{C\omega}{\pi\hbar}\right)^{1/4} e^{-\hat{\xi}^2/2}\,, \tag{2.86a}$$

$$\psi_n(\hat{\Phi}) = \frac{j^n}{(2^n n!)}\left(\frac{C\omega}{\pi\hbar}\right)^{1/4}\left(\hat{\xi} - \frac{\partial}{\partial\hat{\xi}}\right)^n e^{-\hat{\xi}^2/2}\,, \tag{2.86b}$$

for the groundstate and excited states, respectively. In the above equations, $\hat{\xi} \equiv \sqrt{C\omega/\hbar}\,\hat{\Phi}$. It is easy to see that the wave functions are the product of $\exp(-\hat{\xi}^2/2)$ and a polynomial of degree n and parity $(-1)^n$ called a Hermite polynomial [229].

We can now apply the general definitions of Eqs. (2.73a) and (2.73b) to the case of the quantum-mechanical observables $\hat{Q}$ and $\hat{\Phi}$, $\hat{Q} \equiv C\hat{V}$ and $\hat{\Phi} \equiv L\hat{I}$. The quantum voltage $\hat{V}$ and current $\hat{I}$ can then be written as

$$\hat{V} = \frac{\hat{Q}}{C} = \sqrt{\frac{\hbar\omega}{2C}}\,(\hat{a}^\dagger + \hat{a}) \tag{2.87}$$

and

$$\hat{I} = \frac{\hat{\Phi}}{L} = \sqrt{\frac{\hbar\omega}{2L}}\,j(\hat{a}^\dagger - \hat{a})\,, \tag{2.88}$$

which are Hermitian operators. It is straightforward to prove that the coefficient in front of Eq. (2.87) has the units of a voltage (volt - V) and the one in front of Eq. (2.88) the units of a current (ampere - A). As for the case of the classical Hamiltonian given by Eq. (2.74), the Hamiltonian of a quantized LC-resonator can be expressed as

$$\begin{aligned}\widehat{H}_{LC} &= \widehat{H}_C + \widehat{H}_L \\ &= \frac{1}{2}C\hat{V}^2 + \frac{1}{2}L\hat{I}^2\,,\end{aligned} \tag{2.89}$$

where $\widehat{H}_C \equiv C\hat{V}^2/2$ is the Hamiltonian associated with capacitor C and $\widehat{H}_L \equiv L\hat{I}^2/2$ the one associated with inductor L. Notably, the following commutation relation holds between quantized voltage and current:

$$[\hat{V}, \hat{I}] = j\hbar\omega^2\,. \tag{2.90}$$

In summary, any quantum-mechanical LC-resonator can be described in terms of two equivalent sets of observables, charge and flux or voltage and current. In standard textbooks, charge and flux (or phase) are usually considered as canonical conjugated variables. For example, in the case of the quantization of a flux quantum circuit this turns out to be the natural choice (e.g., cf. Sec. 2.2). However, in quantum network theory it is oftentimes more practical to utilize voltage and current as

conjugated observables (e.g., cf. chapters 3 and 4). In fact, the voltage drop on a given impedance, from which the power absorbed by the impedance and other useful parameters can be derived, is the quantity usually measured in experiments. Experimentally, we are never able to measure directly a charge or flux (or phase).

It is noteworthy to mention that in theoretical quantum mechanics the dimensionless operators

$$\hat{X} \equiv j\,\frac{\hat{a}^\dagger - \hat{a}}{\sqrt{2}} \tag{2.91}$$

and

$$\hat{Y} \equiv \frac{\hat{a}^\dagger + \hat{a}}{\sqrt{2}} \tag{2.92}$$

are typically used in calculations.[24] In the light of Eqs. (2.87) and (2.88), the meaning of $\hat{X}$ and $\hat{Y}$ becomes evident: They simply represent a dimensionless voltage and current, respectively. The quantities $\hat{X}$ and $\hat{Y}$ are also called *quadrature operators*: The simultaneous knowledge of both of them is a necessary condition for the full characterization of a resonator.

A fundamental difference between classical and quantum-mechanical resonators[25] is that in the quantum case there is a finite energy stored in the oscillator even when the oscillator is in the groundstate $|0\rangle$ (vacuum state). In other words, at zero temperature and without any external driving a quantum-mechanical resonator is characterized by a nonzero energy. It is easy to calculate the total vacuum (also called zero-point) energy associated with a quantized resonator. In order to do so, we can consider the Hamiltonian of Eq. (2.82) and, employing the properties of the annihilation and creation operators [cf. Eqs. (2.84a) and (2.84b)], we can calculate the quantum-mechanical expectation value

$$E_0 = \langle 0|\widehat{H}_{LC}|0\rangle = \frac{\hbar\omega}{2}\,. \tag{2.93}$$

This result is obviously confirmed by the energy spectrum given by Eq. (2.85) for $n = 0$. Similarly, the vacuum (zero-point) energy associated only with the capacitive part (kinetic energy) of $\widehat{H}_{LC}$ is given by

$$\begin{aligned} E_{\mathrm{C0}} &\equiv \frac{1}{2}CV_0^2 \\ &= \langle 0|\widehat{H}_C|0\rangle = \frac{\hbar\omega}{4}\,. \end{aligned} \tag{2.94}$$

Equation (2.94) allows us to calculate the vacuum (zero-point) voltage of capacitor C,

$$V_0 = \sqrt{\frac{\hbar\omega}{2C}}\,. \tag{2.95}$$

The vacuum (zero-point) current I_0 of inductor L can be obtained following an analogous calculation considering only the inductive part (potential energy) of $\widehat{H}_{LC}$.

[24] In the literature, the factor $\sqrt{2}$ in the denominator of the definitions of Eqs. (2.91) and (2.92) is sometimes replaced by a factor 2.

[25] This difference can easily be extended to more complicated circuits.

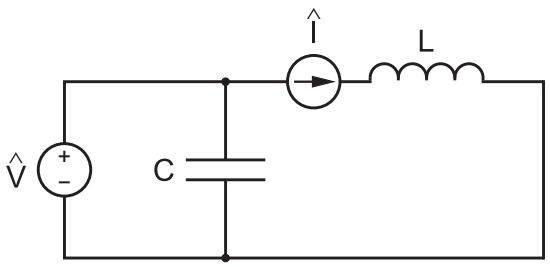

Figure 2.5: Quantum-mechanical circuit associated with an LC-resonator. The quantum voltage source $\hat{V}$ is in parallel with capacitor C and the quantum current source $\hat{I}$ in series with inductor L. Dissipation is not included ($R = 0$).

However, we prefer to derive it from the classical Ohm's impedance law, which can safely be used when dealing with expectation values.[26] We obtain

$$I_0 = \frac{V_0}{Z_0}\,, \tag{2.96}$$

where, as always, $Z_0 = \sqrt{L/C}$. Consequently,

$$I_0 = \sqrt{\frac{C}{L}}\sqrt{\frac{\hbar\omega}{2C}} = \sqrt{\frac{\hbar\omega}{2L}}\,. \tag{2.97}$$

Equations (2.95) and (2.97) show that, on average, the total vacuum energy $\hbar\omega/2$ is equally distributed between the capacitor and inductor composing the LC-resonator.

The Hamiltonian of Eq. (2.89) and the commutation relation of Eq. (2.90) constitute the basis for the construction of the quantum-mechanical circuit associated with an LC-resonator. These are the quantum-circuit construction rules:

(i) The classical capacitor C must be replaced by the parallel combination of a voltage source with quantum voltage

$$\hat{V} = V_0\,(\hat{a}^\dagger + \hat{a}) \tag{2.98}$$

and the capacitor itself. The vacuum voltage is $V_0 = \sqrt{\hbar\omega/2C}$;

(ii) The classical inductor L must be replaced by the series combination of a current source with quantum current

$$\hat{I} = I_0\, j(\hat{a}^\dagger - \hat{a}) \tag{2.99}$$

and the inductor itself. The vacuum current is $I_0 = \sqrt{\hbar\omega/2L}$;

(iii) The presence of both the quantum voltage source and quantum current source is required for the description of an LC-resonator.

[26] We notice that one must be extremely careful when using Ohm's law. Here, for the sake of an example we employ it to derive I_0 because this is an expectation value, i.e., just a number. When dealing with operators and observables Ohm's law is, in general, *not* valid.

Corollary 2.1.1 *The minimum energy stored in an LC-resonator is the quantum-mechanical energy associated with the vacuum state, $\hbar\omega/2$ (also referred to as **quantum noise**). Figure 2.5 shows the quantum-mechanical circuit corresponding to an LC-resonator.*

We remind that we are considering the simple case of a dissipationless resonator, where $R = 0$. The presence of a resistive element is not to be studied here.

Distributed-Parameter Quantized Resonators

We are now in the position to generalize the results obtained for an LC-resonator to the case of quantum-mechanical transmission line resonators. Since transmission lines are distributed-parameter elements, we have to define a capacitance c and inductance l per unit length. The total capacitance and inductance of a transmission line resonator are then given by $C \equiv c\,\ell$ and $L \equiv l\,\ell$, respectively, where ℓ is the resonator length. As shown in Subsec. 2.1.2, ℓ can assume two possible values, $\ell = \lambda_0/2$ or $\ell = \lambda_0/4$, depending on the boundary conditions imposed at the edges of the line (open or short circuits, respectively). We begin assuming that a vacuum voltage $\tilde{V}_0$ and current $\tilde{I}_0$ are distributed over the entire length of the transmission line resonator according to a mode function $\Upsilon(z)$ for the voltage and $\Xi(z)$ for the current. Such mode functions are assumed to be *a priori* unknown. In the Heisenberg picture, the voltage and current on the line can generally be written as

$$\hat{V}_\ell = \tilde{V}_0 \Upsilon(z) \left(\hat{a}^\dagger e^{+j2\pi g(m) f_0 t} + \hat{a} e^{-j2\pi g(m) f_0 t}\right) \tag{2.100}$$

and

$$\hat{I}_\ell = \tilde{I}_0 \Xi(z)\, j \left(\hat{a}^\dagger e^{+j2\pi g(m) f_0 t} - \hat{a} e^{-j2\pi g(m) f_0 t}\right), \tag{2.101}$$

respectively, where $g(m)$ is an *a priori* unknown function of integer m. Comparing the above expressions with the corresponding classical voltage and current of Eqs. (2.66) and (2.64) for $\lambda/2$ resonators, and Eqs. (2.71b) and (2.71d) for $\lambda/4$ resonators, we readily find

$$\Upsilon(z) = \cos\left(2\pi m f_0 \frac{z}{\bar{c}}\right), \tag{2.102a}$$

$$\Xi(z) = -\sin\left(2\pi m f_0 \frac{z}{\bar{c}}\right), \tag{2.102b}$$

$$g(m) = m \tag{2.102c}$$

for $\lambda/2$ resonators (with $m \in \mathbb{N}_0$)[27] and

$$\Upsilon(z) = \cos\left[2\pi(2m+1) f_0 \frac{z}{\bar{c}}\right], \tag{2.103a}$$

$$\Xi(z) = -\sin\left[2\pi(2m+1) f_0 \frac{z}{\bar{c}}\right], \tag{2.103b}$$

$$g(m) = 2m + 1 \tag{2.103c}$$

for $\lambda/4$ resonators (with $m \in \mathbb{N}$). Moreover, the substitutions $e^{-j2\pi g(m) f_0 t} \to \hat{a} e^{-j2\pi g(m) f_0 t}$ and $e^{+j2\pi g(m) f_0 t} \to \hat{a}^\dagger e^{+j2\pi g(m) f_0 t}$ have to be applied to change from

[27] $\mathbb{N}_0$ indicates all integer excluding 0.

the classical to the quantum-mechanical representation. The mode functions $\Upsilon(z)$ and $\Xi(z)$ for the first three modes of a $\lambda/2$ and $\lambda/4$ resonator are respectively shown in Figs. 2.4(a)-2.4(b) and Figs. 2.4(c)-2.4(d).

In the case of $\lambda/2$ resonators and for $m = 1$, the vacuum voltage $\tilde{V}_0$ can be calculated as follows:

$$\begin{aligned}
\frac{\hbar\omega}{2} &= \langle 0| \int_0^{\lambda_0/2} dz \left[\frac{1}{2} c\, \tilde{V}_0^2 \cos^2\left(\frac{2\pi}{\lambda_0} z\right) \times (\hat{a}^\dagger + \hat{a})^2 \right. \\
&\quad \left. - \frac{1}{2} l\, \tilde{I}_0^2 \sin^2\left(\frac{2\pi}{\lambda_0} z\right) \times (\hat{a}^\dagger - \hat{a})^2 \right] |0\rangle \\
&= \int_0^{\lambda_0/2} dz \left(\frac{1}{2} c\, \tilde{V}_0^2 \cos^2 \frac{2\pi}{\lambda_0} z + \frac{1}{2} l\, \tilde{I}_0^2 \sin^2 \frac{2\pi}{\lambda_0} z \right) \\
&= \frac{1}{2} c\, \tilde{V}_0^2 \int_0^{\lambda_0/2} dz \left(\cos^2 \frac{2\pi}{\lambda_0} z + \sin^2 \frac{2\pi}{\lambda_0} z \right) \\
&= \frac{1}{2} C\, \tilde{V}_0^2 \,. \qquad (2.104)
\end{aligned}$$

Since $\cos^2(2\pi z/\lambda_0) + \sin^2(2\pi z/\lambda_0) = 1$, $C \equiv c\lambda_0/2$, and $\tilde{I}_0 = \sqrt{c/l}\, \tilde{V}_0$, we finally obtain

$$\tilde{V}_0 = \sqrt{\frac{\hbar\omega}{C}} = V_0 \sqrt{2} \,. \qquad (2.105)$$

From Ohm's law, $\tilde{I}_0 = \tilde{V}_0/Z_0$, we can then compute the vacuum current, which reads

$$\tilde{I}_0 = \sqrt{\frac{\hbar\omega}{L}} = I_0 \sqrt{2} \,, \qquad (2.106)$$

where $L \equiv l\lambda_0/2$. Equations (2.105) and (2.106) are valid also in the case of $\lambda/4$ resonators for $m = 0$ upon defining $C \equiv c\lambda_0/4$ and $L \equiv l\lambda_0/4$.[28] We notice that the expressions for the vacuum voltage and current are different in the case of lumped-parameter and distributed-parameter resonators.

Quantum Signals Propagating on a Transmission Line

In the last part of this subsection we study the properties of a signal propagating on an infinite transmission line. We consider again a $\lambda/2$ resonator, the Hamiltonian of which can be written as

$$\widehat{H}_{\lambda/2} = \sum_{m=1}^{\infty} \hbar\omega_m \left(\hat{a}_m^\dagger \hat{a}_m + \frac{1}{2} \right) , \qquad (2.107)$$

where $m \in \mathbb{N}$, $\omega_m = m\omega_0 = 2\pi m f_0$, and $\hat{a}_m^\dagger$ and $\hat{a}_m$ are the bosonic creation and annihilation operators for mode m. The resonator is characterized by a discrete

[28] The results of Eqs. (2.105) and (2.106) are very general. In fact, for a generic value of m it is always possible to redefine a new $\lambda/2$ resonator with length $\ell = \lambda_0/2 \equiv \bar{c}/2mf_0$ and then use Eqs. (2.105) and (2.106) to compute the vacuum voltage and current. The same applies to $\lambda/4$ resonators.

infinite spectrum of frequencies. If we now imagine to stretch more and more the resonator on both sides, ℓ becomes larger and larger and the resonance frequency corresponding to the fundamental mode becomes smaller and smaller,

$$f_0 = \frac{\bar{c}}{\lambda_0} = \frac{\bar{c}}{2\ell}\,. \tag{2.108}$$

In the limit of infinite stretching, i.e., when the left end of the resonator, $z = 0$, tends to $-\infty$ and the right end, $z = \ell$, tends to $+\infty$, the fundamental frequency becomes infinitesimally small, $f_0 \to df$. This has the important consequence that all harmonics of the infinitely stretched resonator become infinitesimally close to each other. The resonator, which is now equivalent to an infinite transmission line, is characterized by a continuous infinite spectrum of frequencies. Neglecting the presence of dielectric materials between the conductors, such an infinite transmission line represents a 1D free space[29] where, ideally, signals of any given angular frequency ω are allowed to propagate. Each of these signals can be described mathematically in terms of a single lumped-parameter quantized LC-resonator, which is obviously characterized by a single mode of the same angular frequency ω. Hence, the voltage and current associated with any propagating quantum signal of frequency ω are given by Eqs. (2.87) and (2.88), respectively. We repeat them here as a reference:

$$\hat{V} = \sqrt{\frac{\hbar\omega}{2C}}\,(\hat{a}^\dagger + \hat{a})$$

and

$$\hat{I} = \sqrt{\frac{\hbar\omega}{2L}}\,j(\hat{a}^\dagger - \hat{a})\,.$$

In many applications, for example when computing the power absorbed by a load impedance terminating a transmission line or the quantum-mechanical variance of a signal, it is custom to define the quantum voltage and current per-root-hertz[30] as follows

$$\begin{aligned}\hat{\mathcal{V}} \equiv \frac{\hat{V}}{\sqrt{\omega}} &= \sqrt{\frac{\hbar}{2C}}\,(\hat{a}^\dagger + \hat{a}) \\ &= \sqrt{\frac{\hbar Z_0\omega}{2}}\,(\hat{a}^\dagger + \hat{a}) = \bar{V}_0\,(\hat{a}^\dagger + \hat{a})\end{aligned} \tag{2.109}$$

and

$$\begin{aligned}\hat{\mathcal{I}} \equiv \frac{\hat{I}}{\sqrt{\omega}} &= \sqrt{\frac{\hbar}{2L}}\,j(\hat{a}^\dagger - \hat{a}) \\ &= \sqrt{\frac{\hbar Y_0\omega}{2}}\,j(\hat{a}^\dagger - \hat{a}) = \bar{I}_0\,j(\hat{a}^\dagger - \hat{a})\,,\end{aligned} \tag{2.110}$$

respectively. The vacuum voltage and current per-root-hertz, $\bar{V}_0$ and $\bar{I}_0$, can easily be found noticing that $\omega/C = Z_0\omega^2$, $\omega/L = Y_0\omega^2$, and $Y_0 = 1/Z_0$. Being independent of the total capacitance C and inductance L of the original LC-resonator,

[29] In reality, a quasi-1D free space because of the very small, but finite lateral dimensions characteristic of any real structure.

[30] Strictly speaking, this is an abuse of language because in our definitions we renormalize over $\sqrt{\omega}$, which is an angular frequency with units rad/s and not a natural frequency with units Hz.

the definitions of Eqs. (2.109) and (2.110) are totally general. The only information required are on the characteristic impedance Z_0 of the transmission line and the signal angular frequency ω. Equations (2.109) and (2.110) play a central role in quantum signal theory and will extensively be used in chapters 3 and 4.

Before concluding this section it is worth outlining the main goals of quantum signal theory. One goal is to study signals associated with quantum-mechanical circuits, where the signal energy (frequency) is significantly larger than the environmental thermal energy (temperature). Another goal is to describe the statistical properties, e.g., mean value and variance, of signals generated by quantum-mechanical circuits and then transmitted through classical devices, e.g., amplifiers, in order to be experimentally measured. In this case, the ultimate aim is to fully characterize any given state $|\psi\rangle$ associated with a quantum voltage or current by means of a *tomographic* process. One possibility to achieve full-state tomography is to measure *all* (central) moments of the quantum voltage or current with respect to state $|\psi\rangle$. In real applications, this is oftentimes an extremely hard or even impossible task. However, there is a certain class of states for which the knowledge of the first two central moments, i.e., the quantum-mechanical mean value and variance of the signal, is sufficient to obtain all the necessary information about the state. This is the so-called class of *Gaussian states*. A few remarkable examples of Gaussian states are:

1. the vacuum state (cf. chapter 4), $|\psi\rangle = |0\rangle$;
2. all coherent states, $|\psi\rangle \equiv |\alpha\rangle$;
3. most of the typically encountered thermal states (cf. chapter 4, Subsec. 4.2.2), $|\psi\rangle \equiv |\gamma\rangle$;
4. and a subset of squeezed states [91], $|\psi\rangle \equiv |\chi\rangle$.

In the case of number states $|n\rangle$, the knowledge of the first two moments[31] can sometimes provide valuable information (cf. chapter 4, Subsec. 4.2.1), but it does not constitute a complete characterization of the state.

Since in experiments we usually measure voltages, we hereafter focus on the calculation of the quantum-mechanical mean value and variance associated with a given state $|\psi\rangle$ using the observable of Eq. (2.109) only.

In general, the quantum-mechanical first (central) moment or mean value for the quantum voltage per-root-hertz $\hat{\mathcal{V}}$ with respect to state $|\psi\rangle$ can be written as

$$\begin{aligned} \mu &\equiv \langle \hat{\mathcal{V}} \rangle \\ &= \bar{V}_0 \langle \psi | (\hat{a}^\dagger + \hat{a}) | \psi \rangle \,. \end{aligned} \tag{2.111}$$

The quantum-mechanical second central moment or variance is defined as

$$\begin{aligned} \sigma^2 &\equiv \left(\Delta \hat{\mathcal{V}}\right)^2 \\ &\equiv \langle \hat{\mathcal{V}}^2 \rangle - \langle \hat{\mathcal{V}} \rangle^2 \\ &= \bar{V}_0^2 \langle \psi | (\hat{a}^\dagger + \hat{a})^2 | \psi \rangle - \mu^2 \\ &= \bar{V}_0^2 \langle \psi | [(\hat{a}^\dagger)^2 + 2\hat{a}^\dagger \hat{a} + 1 + (\hat{a})^2] | \psi \rangle - \mu^2 \\ &= \bar{V}_0^2 \left\{ \langle \psi | [(\hat{a}^\dagger)^2 + 2\hat{a}^\dagger \hat{a} + (\hat{a})^2] | \psi \rangle + 1 \right\} - \mu^2 \,, \end{aligned} \tag{2.112}$$

[31] As we will show later (cf. chapter 4, Subsec. 4.2.1), the first moment is, in this case, always zero.

where σ is called the standard deviation of the quantum signal with respect to state $|\psi\rangle$. In order to obtain Eq. (2.112), we have used the commutation relation $[\hat{a}, \hat{a}^\dagger] = 1 \Rightarrow \hat{a}\hat{a}^\dagger = 1 + \hat{a}^\dagger\hat{a}$ for the annihilation and creation operators and the fact that $\langle\psi|\psi\rangle = 1$ for a complete orthonormal set of states. The vacuum contribution $\bar{V}_0$ is always present in the quantum-mechanical expression for the variance of a signal [cf. last line of Eq. (2.112)]. We remind that the mean value μ given by Eq. (2.111) and the variance σ^2 given by Eq. (2.112) are expressed per-root-hertz and per-hertz, respectively.

We will come back to the concepts of quantum-mechanical mean value and variance in chapter 4, Sec. 4.2.

2.2 Flux Quantum Circuits

In this section, we first present the basic concepts on Josephson tunnel junctions (cf. Subsec. 2.2.1). We then show that the introduction of a Josephson element into an *LC*-resonator, which realizes a so-called RF SQUID, generates an anharmonic potential. Under suitable conditions, such potential allows for the implementation of a qubit (cf. Subsec. 2.2.2). We subsequently extend the RF SQUID to the so-called three-Josephson-junction SQUID, which is the type of flux quantum circuit used in our experiments and mostly discussed throughout this thesis (cf. Subsec. 2.2.3). Finally, we reduce the Hamiltonian of the three-Josephson-junction SQUID to a qubit Hamiltonian (two-level approximation) and briefly review the basic qubit formalism.

2.2.1 Josephson Tunnel Junctions

At the basis of all circuit QED architectures with superconducting devices stand the DC and AC Josephson effects [39, 40, 96, 230–232],[32] which describe the quantum-mechanical behavior of Josephson tunnel junctions.

A Josephson tunnel junction is realized by means of two weakly coupled superconducting leads. The weak coupling can be an insulating barrier (S-I-S junction), a normal conducting thin film (S-N-S junction), or a constraint/grain boundary (S-c-S junction) [96]. In superconducting qubit applications S-I-S junctions are typically preferred over other types. In this case, the barrier is an oxide layer (e.g., $\mathrm{Al\,O}_x$) grown between two superconducting electrodes (e.g., made of Al) fabricated by lithography techniques.[33] Figure 2.6(a) shows a simple schematic of an S-I-S junction. A fundamental parameter of a Josephson tunnel junction is the so-called critical current I_{c0}. The critical current is a constant representing the maximum DC supercurrent that the junction can support.

The Josephson effect can be summarized as follows [cf. Fig. 2.6(a)]:

1. *Josephson or weak-link current-phase relation* - When a current bias $I \leqslant I_{\mathrm{c0}}$ is applied to the superconducting electrodes of a Josephson tunnel junction, a DC supercurrent flows between the two electrodes. This current is given by

$$I_{\mathrm{s}} = I_{\mathrm{c0}} \sin \Delta\varphi \,, \tag{2.113}$$

[32] After B. D. Josephson, the Welsh physicist who predicted them in 1962 and 1965, respectively.

[33] There is a very extensive body of work on materials and fabrication techniques of Josephson tunnel junctions for qubit applications [233–237].

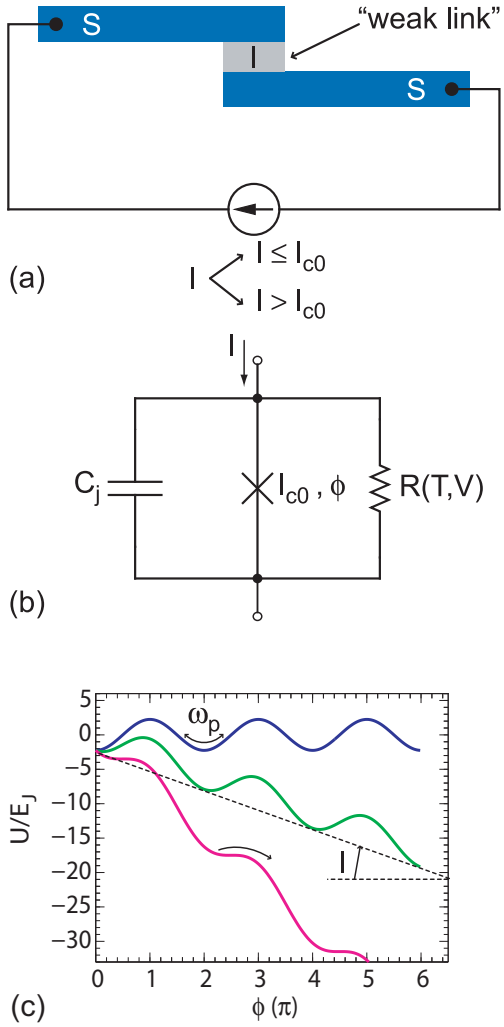

Figure 2.6: The S-I-S Josephson tunnel junction. **(a)** Sketch of a superconductor-insulator-superconductor junction. The grey area between the two superconducting leads (blue) represents the "weak link" characteristic of any Josephson tunnel junction [96]. The external current bias I can either be smaller than the critical current I_{c0}, $I \leqslant I_{c0}$, or exceed it, $I > I_{c0}$. In the first case, we obtain the DC Josephson effect [cf. Eq. (2.113)]. In the second case, we obtain the AC Josephson effect [cf. Eq. (2.114)]. **(b)** The resistively and capacitively shunted junction (RCSJ) model. The resistance R is, in general, a function of the voltage drop across the junction, V, and the junction temperature T (cf. main text for details). **(c)** Normalized tilted washboard potential U/E_J as a function of the gauge-invariant phase ϕ. Dark blue (dark grey) curve: $I = 0$. Magenta (middle grey) curve: $I = I_{c0}$. Light green (light grey) curve: $0 < I < I_{c0}$.

where $\Delta\varphi$ is the "phase difference" across the junction, i.e., the difference in phase factor or, equivalently, argument between the Ginzburg-Landau complex order parameter of the two superconducting electrodes comprising the junction [96].[34] The critical current is an important phenomenological[35] parameter of the device that can be affected by temperature as well as by an applied magnetic field. This parameter also defines the so-called Josephson coupling energy, $E_{\rm J} \equiv (\hbar/2e)I_{\rm c0} = I_{\rm c0}\Phi_0/2\pi$, where the physical constant $\Phi_0 \equiv h/2e$, is the magnetic flux quantum, the inverse of which is the so-called Josephson constant (e is the electron charge).

Equation (2.113) is the mathematical representation of the DC Josephson effect, where a DC supercurrent can flow due to tunneling in the absence of a voltage drop between the two electrodes of the junction;

2. *Superconducting phase evolution equation* - When the current bias applied to the superconducting electrodes of a Josephson tunnel junction exceeds the critical current, $I > I_{\rm c0}$, a finite voltage drop V is established between the two electrodes of the junction and the phase difference $\Delta\varphi$ evolves according to

$$\frac{d}{dt}\Delta\varphi = \frac{2e}{\hbar}V\,. \tag{2.114}$$

This implies that (besides integration constants)

$$\Delta\varphi = \frac{2e}{\hbar}Vt\,, \tag{2.115}$$

which, substituted into Eq. (2.113), finally gives

$$I_{\rm s}(t) = I_{\rm c0}\sin\left(\frac{2e}{\hbar}Vt\right)\,. \tag{2.116}$$

Equation (2.116) is the mathematical representation of the AC Josephson effect, where an AC supercurrent of amplitude $I_{\rm c0}$ and angular frequency $f_{\rm J} = (2e/h)V = \Phi_0^{-1}V$ flows between the two electrodes of the junction.

Using Eq. (2.113) and the fact that

$$V = \frac{\Phi_0}{2\pi}\frac{d}{dt}\Delta\varphi\,,$$

the coupling free energy stored in the junction can be calculated as

$$\begin{aligned} F &= \int dt\, V I_{\rm s} = E_{\rm J}\int \sin(\Delta\varphi)\, d(\Delta\varphi) \\ &= \text{const.} - E_{\rm J}\cos\Delta\varphi\,. \end{aligned} \tag{2.117}$$

This is the electrical work done by a current source in changing the phase across the junction.

[34] In this very brief introduction to the Josephson effect we always refer to the Ginzburg-Landau theory of superconductivity, as in Ref. [96]. Obviously, the BCS theory would give similar, or even more general, results [238].

[35] Its detailed form can be obtained using the Ginzburg-Landau theory.

In all expressions above we have assumed no vector potentials (i.e., zero external magnetic fields), $\mathbf{A} = \mathbf{0}$. If a vector potential is introduced (i.e., an external magnetic field is applied), $\mathbf{A} \neq \mathbf{0}$, we must use the full gauge-invariant definition of gradient (e.g., cf. Ref. [96] for details) and define the gauge-invariant phase

$$\phi \equiv \Delta\varphi - \frac{2\pi}{\Phi_0} \int \mathbf{A} \cdot d\mathbf{s} \,, \tag{2.118}$$

where the integration is from one electrode of the junction to the other. The definition of Eq. (2.118) allows us to rewrite Eq. (2.113) as

$$I_{\rm s} = I_{\rm c0} \sin\phi \,. \tag{2.119}$$

Since in most qubit applications we need to apply DC and/or AC external magnetic fields, Eq. (2.119) is the relation to be used in the rest of this thesis.[36]

For practical purposes, it is useful to describe a Josephson tunnel junction in terms of lumped-circuit elements. The standard accepted model goes under the name of resistively and capacitively shunted junction ($RCSJ$) model [cf. Fig. 2.6(b)].[37] In this model, which accounts for both the DC and AC Josephson effects, the junction is represented by the parallel combination of a capacitor $C_{\rm j}$, a resistor R, and the junction itself (ideal Josephson element). In general, the capacitance $C_{\rm j}$ depends on the detailed geometry of the junction and the material used as insulating layer. The resistance R, which is due to the quasiparticle channel associated with the junction [96], is close to the normal state resistance $R_{\rm n}$ for S-I-S junctions at temperature close to the superconductor critical temperature, $T \lesssim T_{\rm c}$. At lower temperatures, R rises approximately as $R_{\rm n} \exp(\Delta_{\rm BCS}/k_{\rm B}T)$ for a junction voltage $V < V_{\rm g} \equiv 2\Delta_{\rm BCS}/e$, where $\Delta_{\rm BCS}$ is the energy gap of the superconductor and $k_{\rm B}$ the Boltzmann constant. For $V > V_{\rm g}$, $R \approx R_{\rm n}$. For $T = 0$, $R \to \infty$ and the resistor can be substituted by an open circuit. In the case of S-N-S or S-c-S junctions the behavior of R with temperature and voltage can generally be different [96].

By inspection of Fig. 2.6(b), we can equate the bias current I to the total junction current from the three parallel channels (Kirchhoff's current law) obtaining

$$I = I_{\rm c0} \sin\phi + \frac{V}{R} + C_{\rm j} \frac{d}{dt} V \,. \tag{2.120}$$

Substituting Eq. (2.114) for the gauge invariant phase into Eq. (2.120), we find the inhomogeneous ordinary differential equation of second order

$$\frac{d^2}{d\tau^2}\phi + \frac{1}{Q_{\rm j}} \frac{d}{d\tau}\phi + \sin\phi = \frac{I}{I_{\rm c0}} \,, \tag{2.121}$$

where

$$\tau \equiv \omega_{\rm p} t$$

and

$$\omega_{\rm p} \equiv \sqrt{\frac{2eI_{\rm c0}}{\hbar C_{\rm j}}} \tag{2.122}$$

[36] Obviously, $\phi = \Delta\varphi$ for $\mathbf{A} = \mathbf{0}$.

[37] Here, we ignore the possible inductance associated with the junction leads.

is the so-called "plasma frequency" of the junction. In addition, we define the Stewart-McCumber parameter

$$\beta_{\rm c} \equiv \left(\omega_{\rm p} R C_{\rm j}\right)^2 = Q_{\rm j}^2 \,, \tag{2.123}$$

where $Q_{\rm j}$ is the junction quality factor.

In analogy to classical mechanics, Eq. (2.121) can be interpreted as the equation describing the motion of a particle of mass

$$M = \left(\frac{\hbar}{2e}\right)^2 C_{\rm j}$$

moving along the axis given by the gauge invariant phase ϕ in an effective potential

$$\frac{U(\phi)}{E_{\rm J}} = -\cos\phi - \frac{I}{I_{\rm c0}}\phi \tag{2.124}$$

and subjected to a viscous drag force

$$\left(\frac{\hbar}{2e}\right)^2 \frac{1}{R}\frac{d}{dt}\phi \,.$$

The potential of Eq. (2.124) is referred to as tilted washboard potential and is shown in Fig. 2.6(c) for three values of the bias current I. For $R \to \infty$ ($R \to$ OC, i.e., the current on the resistive channel is zero), we can neglect the viscous drag force. In this case, depending on the plasma frequency $\omega_{\rm p}$ and the washboard inclination, which is set by the bias current I, the particle can either be trapped in one well of the potential or run along it [Fig. 2.6(c)].[38]

In qubit applications the operating temperature is usually low enough to justify the substitution of the resistive channel of the $RCSJ$ model with an open circuit. This allows us to neglect the resistor and, thus, to simplify the model significantly (see below).

2.2.2 The RF SQUID

Let us consider the quantum-mechanical LC-resonator of Fig. 2.7(a). The resonator is composed of a capacitor $C_{\rm j}$ and an inductor $L_{\rm F}$ connected in a closed-loop configuration ($L_{\rm F}$ is indeed the geometric self-inductance of such a loop). For pedagogical reasons, we here assume the loop to be in the *normal conducting state*. The reason behind this choice is not to apply the fluxoid quantization valid for superconducting loops, which would complicate the derivation and, possibly, give wrong results. Superconductivity will be switched on as soon as a Josephson element is inserted in the loop (see below). Bearing this assumption in mind, the resonator angular frequency is $\omega_{\rm F} = 1/\sqrt{L_{\rm F} C_{\rm j}}$. The Hamiltonian of such a resonator can be obtained from Eq. (2.72) after the replacements $Q \to \hat{Q}$ and $\Phi \to \hat{\Phi}$,

$$\widehat{H}_{\rm F}^{(I)} = \frac{\hat{Q}^2}{2C_{\rm j}} + \frac{\hat{\Phi}^2}{2L_{\rm F}} \,, \tag{2.125}$$

[38] It is worth mentioning that the particle dynamics strongly depends on the operating temperature. For more details we remind the reader to Ref. [96].

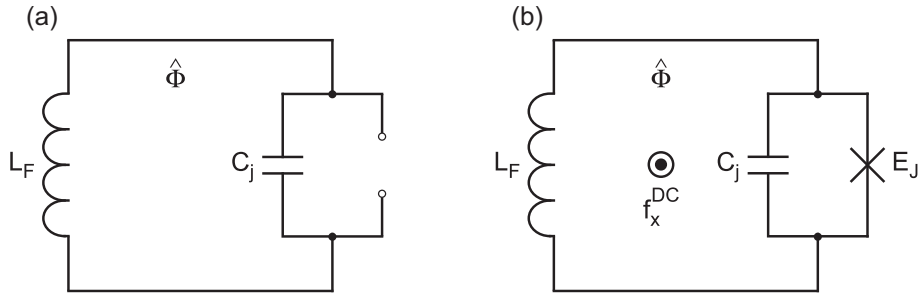

Figure 2.7: From an LC-resonator to an RF SQUID. **(a)** Circuit diagram of a closed-loop LC-resonator in the normal conducting state. The resonator kinetic energy T_F is associated with the capacitor C_j and its potential energy $U_\mathrm{F}^{(\mathrm{I})}$ with the inductor L_F. $\hat{\Phi}$: total flux threading the loop. **(b)** Circuit diagram of an RF SQUID. E_J: Josephson coupling energy depending on $\hat{\Phi}$. In this case, it is crucial to apply the fluxoid quantization for a closed superconducting loop in order to express the RF SQUID Hamiltonian in terms of the total flux $\hat{\Phi}$. The circuit potential energy $U_\mathrm{F}^{(\mathrm{II})}$ depends on E_J and is not parabolic anymore (cf. main text for details). $f_\mathrm{x}^\mathrm{DC} \equiv \Phi_\mathrm{x}^\mathrm{DC}/\Phi_0$ is an external DC (or quasi-static) flux bias, also called frustration.

where $\hat{\Phi}$, which plays the role of position operator, is the total flux threading the loop due to the current flowing on the inductor L_F and $\hat{Q}$, which plays the role of momentum operator, is the charge on the capacitor C_j. As always, the quantized charge $\hat{Q}$ and flux $\hat{\Phi}$ are canonically conjugated variables, $[\hat{Q}, \hat{\Phi}] = j\hbar$. We already mentioned in Subsec. 2.1.3 that in the case of flux quantum circuits it is more convenient to use charge and flux instead of voltage and current as quantization variables.

The Hamiltonian of Eq. (2.125) can be regarded as the sum of a kinetic energy T_F and a potential energy $U_\mathrm{F}^{(I)}$, with

$$T_\mathrm{F} \equiv \frac{\hat{Q}^2}{2C_\mathrm{j}}\,, \tag{2.126a}$$

$$U_\mathrm{F}^{(I)} \equiv \frac{\hat{\Phi}^2}{2L_\mathrm{F}}\,. \tag{2.126b}$$

In Fig. 2.8(a), the potential energy $U_\mathrm{F}^{(I)}$, also called potential landscape, is plotted as a function of $\hat{\Phi}$. The shape of the potential is parabolic, as expected for a simple harmonic oscillator. Figure 2.8(a) also shows the first three energy levels of the oscillator, E_n with $n = 0, 1, 2$. The levels are obviously equally spaced with spacing $\Delta E = \hbar\omega_\mathrm{F}$. The wave functions ψ_n associated with these levels are plotted in Fig. 2.8(b) as a function of $\hat{\Phi}$. Such wave functions can be calculated either analytically using the expressions given in Eqs. (2.86a) and (2.86b) upon replacing C with C_j and ω with ω_F or numerically by diagonalizing the Hamiltonian of Eq. (2.125). The plots reported in Fig. 2.8(b) have been computed numerically. Notably, the first and third wave functions ψ_0 and ψ_2 are even functions of $\hat{\Phi}$, whereas the second wave function ψ_1 is odd. The parity of the wave functions sets the selection rules

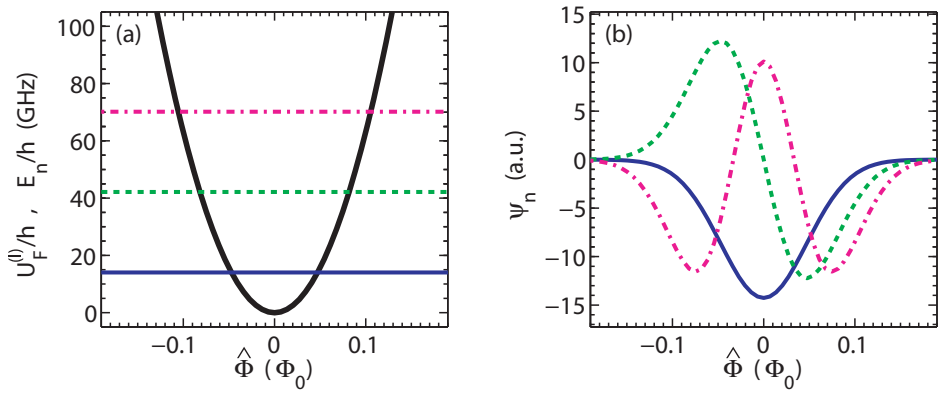

Figure 2.8: Potential landscape, energy levels, and wave functions for an LC-resonator. **(a)** Potential landscape $U_{\rm F}^{(I)}$ as a function of $\hat{\Phi}$ for an LC-resonator (solid black line). The solid dark blue (dark grey) line represents the energy level corresponding to the groundstate, E_0, the dashed light green (light grey) line the energy level E_1, and the dashdot magenta (middle grey) line the energy level E_2. **(b)** Wave functions ψ_n for the three lowest levels of the LC-resonator as a function of $\hat{\Phi}$. The color coding is equivalent to that used for the energy levels in **(a)**. Numerical values used for the plots: $L_{\rm F} = 266\,{\rm pH}$, $C_{\rm j} = 120\,{\rm fF}$, and, thus, $\omega_{\rm F} \simeq 2\pi \times 28.2\,{\rm GHz}$. The latter corresponds to the spacing between two consecutive energy levels, $\Delta E/\hbar = \omega_{\rm F}$. We notice that the minimum energy of the resonator is at $(E_1 - E_0)/2\hbar = \omega_{\rm F}/2 \simeq 2\pi \times 14.1\,{\rm GHz}$. This corresponds to the vacuum energy and constitutes the vertical offset with respect to 0 in **(a)**.

for the oscillator. For example, let us drive the (fundamental) mode $\omega_0 = \omega_{\rm F}$ of the resonator by means of an external classical field (e.g., a sine wave) of frequency ω. In order to drive this mode, the external driving must match the mode frequency, $\omega = \omega_{\rm F}$. The transition between the resonator groundstate ψ_0 (the vacuum state $|0\rangle$) and the first excited state ψ_1 (state $|1\rangle$) is allowed only for a one-photon process, i.e., a process involving one photon of frequency $\omega_{\rm F}$. In this case, the resonator wave function flips from *even* to *odd*. The transition between the groundstate and the second excited state ψ_2 (state $|2\rangle$) is allowed only for a two-photon process, i.e., a process involving two photons of frequency $\omega_{\rm F}$. In this case, the resonator wave function flips from *even* to *odd* and then to *even* again. Similarly, from $|1\rangle$ to $|2\rangle$ only a one-photon process is allowed and the resonator wave function flips from *odd* to *even*. If the resonator were a distributed-parameter resonator, similar rules would apply for higher modes, $\omega_m = m\omega_{\rm F}$ with $m \in \mathbb{N}$ and $m \geqslant 2$. Remarkably, because of selection rules we are not allowed to drive any mode m of the resonator from $|0\rangle$ to $|2\rangle$ by means of a one-photon process with two times the mode frequency! Such process would correspond to drive the $|0\rangle - |1\rangle$ transition of the $2m + 1$ resonator mode.[39]

If we now insert an ideal Josephson tunnel junction[40] in parallel to the capacitor $C_{\rm j}$, we can regard the parallel combination between the capacitor and the junction

[39]The selection rules outlined here are valid only under the assumption of perfect linearity.
[40]Here, "ideal" means that the resistive channel of the junction is negligibly small.

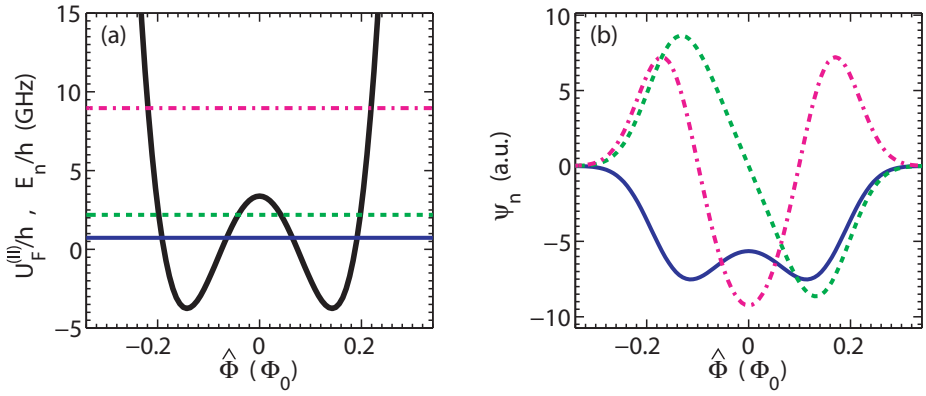

Figure 2.9: Potential landscape, energy levels, and wave functions for an RF SQUID. **(a)** Potential landscape $U_{\rm F}^{(II)}$ as a function of $\hat{\Phi}$ for an RF SQUID biased at $\Phi_{\rm x}^{\rm DC} = \Phi_0/2$ (solid black line). The solid dark blue (dark grey) line represents the energy level corresponding to the groundstate, E_0, the dashed light green (light grey) line the energy level E_1, and the dashdot magenta (middle grey) line the energy level E_2. **(b)** Wave functions ψ_n for the three lowest levels of the RF SQUID as a function of $\hat{\Phi}$. The color coding is equivalent to that used for the energy levels in **(a)**. Numerical values used for the plots: $I_{\rm c0} = 1.35\,\mu$A corresponding to $E_{\rm J} \simeq 670.5\,$GHz. The values for all the other parameters are the same as those used in Fig. 2.8. Also, $(E_1 - E_0)/h \simeq 1.46\,$GHz, $(E_2 - E_0)/h \simeq 8.23\,$GHz, and $(E_2 - E_1)/h \simeq 6.77\,$GHz. In this case, the vertical offset with respect to 0 in **(a)** is given by $(E_1 - E_0)/2\hbar \simeq 2\pi \times 730\,$MHz.

itself as a simplified version of the *RCSJ* model described in Subsec. 2.2.1. If, in addition, we make the circuit loop superconducting and thread such a loop with an external DC (or quasi-static) flux bias $\Phi_{\rm x}^{\rm DC} \equiv f_{\rm x}^{\rm DC}\,\Phi_0$, the so-obtained circuit is referred to as RF SQUID [96, 232, 239, 240]. The dimensionless quantity $f_{\rm x}^{\rm DC}$ is called magnetic frustration and is oftentimes used instead of $\Phi_{\rm x}^{\rm DC}$. The Hamiltonian of the RF SQUID is obtained by adding the energy contribution associated with the Josephson junction to the Hamiltonian of Eq. (2.125) and imposing fluxoid quantization[41] around the superconducting loop [239]. This gives

$$\widehat{H}_{\rm F}^{(II)} = \frac{\hat{Q}^2}{2C_{\rm j}} + \frac{(\hat{\Phi} - \Phi_{\rm x}^{\rm DC})^2}{2L_{\rm F}} - E_{\rm J}\cos\left(2\pi\frac{\hat{\Phi}}{\Phi_0}\right)\,, \tag{2.127}$$

where all global energy offsets have been neglected. In Eq. (2.127), $C_{\rm j}$ assumes now the role of junction capacitance, $E_{\rm J} = I_{\rm c0}\Phi_0/2\pi$ is the Josephson coupling energy, and $I_{\rm c0}$ the junction critical current. Notably, it is possible to write the Josephson contribution $-E_{\rm J}\cos(2\pi\hat{\Phi}/\Phi_0)$ in this form because of fluxoid quantization. Fluxoid quantization allows us to express the Josephson energy as a function of the total flux threading the loop, $\hat{\Phi}$, which, in this case, is equivalent to the phase difference across the Josephson junction (the reader can check pages 72 and 73 of Ref. [239]).

[41] Indeed, in this case simply flux quantization [232]. In the rest of the thesis, we keep using the nomenclature "fluxoid quantization" for generality.

In this case, the potential energy becomes

$$U_{\rm F}^{(II)} \equiv \frac{(\hat{\Phi}-\Phi_{\rm x}^{\rm DC})^2}{2L_{\rm F}} - E_{\rm J}\cos\left(2\pi\frac{\hat{\Phi}}{\Phi_0}\right). \tag{2.128}$$

Figure 2.9(a) shows a plot of $U_{\rm F}^{(II)}$ as a function of $\hat{\Phi}$ for an external DC flux bias $\Phi_{\rm x}^{\rm DC} = \Phi_0/2$. For this choice of $\Phi_{\rm x}^{\rm DC}$, $U_{\rm F}^{(II)}$ is symmetric and the RF SQUID is said to be biased at the *degeneracy point*. We notice that the potential $U_{\rm F}^{(II)}$ is not a parabolic potential. Instead, it is characterized by a double-well shape, which indicates that the Hamiltonian of Eq. (2.127) associated with an RF SQUID is inherently different from a simple harmonic oscillator. Figure 2.9(a) also shows the first three energy levels for the RF SQUID, E_n with $n = 0, 1, 2$, which are manifestly not equally spaced as in the case of the harmonic oscillator. The introduction of the Josephson junction adds a nonlinearity to the circuit, which is now characterized by an anharmonic potential. In particular, the third energy level E_2 is very far away from the first two. This has the important consequence that the first two levels can be used to implement a qubit. In reality, besides the experiments of Ref. [240], the RF SQUID has rarely been used for qubit applications due to a number of technical issues. Here, we use it as an example to show the similarities and differences between harmonic (without Josephson elements) and anharmonic (with Josephson elements) oscillators. The wave functions ψ_n associated with the first three energy levels of an RF SQUID are plotted in Fig. 2.9(b) as a function of $\hat{\Phi}$ and for $\Phi_{\rm x}^{\rm DC} = \Phi_0/2$. Such wave functions have to be calculated numerically by diagonalizing the Hamiltonian of Eq. (2.127). It is worth mentioning that the wave functions maintain the parity properties characteristic of the harmonic oscillator, at least at the special point $\Phi_{\rm x}^{\rm DC} = \Phi_0/2$ (degeneracy point). A comprehensive study of the selection rules associated with flux quantum circuits is reported in chapter 8, Subsec. 8.4.2.

In summary, the RF SQUID is an interesting circuit characterized by an anharmonic potential [cf. Eq.(2.128)]. When setting $I_{\rm c0} = 0$, which corresponds to substituting the ideal Josephson tunnel junction of the RF SQUID with an open circuit [cf. Fig. 2.7(a)], switching off superconductivity, and neglecting the external DC flux bias $\Phi_{\rm x}^{\rm DC}$, the RF SQUID reduces to a simple harmonic oscillator [cf. Eq. (2.125)]. This clearly shows the importance of Josephson elements in superconducting circuit QED architectures. In the next subsection, we present a more complex flux quantum circuit based on three (or even more) Josephson junctions.

2.2.3 The Three-Josephson-Junction SQUID

The example of the RF SQUID shows that the presence of both the Josephson tunnel junction with energy $E_{\rm J}$ and equivalent inductance $L_{\rm j} \equiv \Phi_0/2\pi I_{\rm c0}$ and the self-inductance of the circuit loop $L_{\rm F}$ play a role in the shaping of the circuit potential.

Defining the parameter $\Lambda \equiv L_{\rm j}/L_{\rm F}$, we can divide all quantum circuits based on Josephson elements into two major categories. Circuits of the *first type* are characterized by a $\Lambda \ll 1$. In this case, the flux induced by the circulating currents in the circuit loop is important. Such circulating currents, which correspond to quantized states in the circuit, can have opposite signs. Under opportune conditions, these special current states can be used to implement qubits. Hereafter, we refer

to the circulating currents in a circuit loop as "persistent currents." Circuits of the *second type* are characterized by a $\Lambda \gg 1$ so that the induced flux in the circuit loop is unimportant. For circuits of the second type, two energy scales determine the quantum-mechanical behavior of the circuit: the Josephson coupling energy, $E_{\rm J} = I_{\rm c0}\Phi_0/2\pi$, and the Coulomb energy for single charges, $E_{\rm c} \equiv e^2/2C_{\rm j}$. The energies can be determined by the phases of the Cooper-pair wave function of the nodes of the circuit (also defined as islands) and the number of excess Cooper pairs on each node (island) [189]. Phase and number are quantum-mechanical conjugated variables and correspond to charge and flux in the Hamiltonian of a quantized harmonic oscillator [e.g., cf. Eq. (2.125)]. In the "phase" limit, $E_{\rm J} \gg E_{\rm c}$, the phase is a well-defined quantum-mechanical variable and the charge fluctuates. In the "charge" limit, $E_{\rm c} \gg E_{\rm J}$, the charges on the nodes are well defined and the phase fluctuates. When $E_{\rm J} \approx E_{\rm c}$, the eigenstates of the circuit must be considered as quantum-mechanical superpositions of either charge states or phase states. Such superposition states are important in designing qubits.

Quantum circuits of the first and second type have both advantages and disadvantages for the implementation of superconducting qubits. Traditionally, circuits of the second type were considered to be good with respect to flux noise because of the very small dimensions due to a small loop inductance. However, these circuits are largely affected by background charge noise (e.g., charge qubits [97–101, 241]) or substrate impurities (e.g., phase qubits [97–101, 242]). Additionally, this type of circuits was considered hard to be read out. Circuits of the first type were considered to be bad with respect to flux noise because of the large loop inductance, but only marginally affected by background charge noise and substrate noise. In addition, these circuits should in principle be easy to be read out. Over the years, the frontier between circuits of the first and second type has become more and more undefined. Nowadays, there is vast variety of quantum circuits for quantum computing purposes that combine one or the other aspect of the two categories defined above [101, 120, 243, 244].

For example, the RF SQUID was thought to be a bad choice for qubit implementations because of the very large $L_{\rm F}$, which, in that case, is a necessary condition to obtain a double-well potential [cf. Fig. 2.9(a)]. For this very reason the three-Josephson-junction SQUID was introduced by J. E. Mooij and T. P. Orlando in 1999 [189, 245]. Such a circuit makes possible to obtain a double-well potential even for a very small circuit loop inductance, $L_{\rm F} \to 0$. In this sense, the three-Josephson-junction SQUID combines the advantages of the first and second type of quantum circuits: It is characterized by quantum states associated with μA persistent currents, which are minimally affected by charge and substrate noise and can easily be read out; it is small and, thus, less susceptible to flux noise. However, a decade after the Mooij-Orlando proposal, decoherence in superconducting circuits appears not to be due to the physical dimensions of the circuit [246], but to a combination of several different mechanisms the origin of which is still largely unknown [118–120, 234–236, 241, 242, 246–262]. As all the other types of superconducting qubits, also the three-Josephson-junction SQUID suffers in large measure from decoherence issues [118, 119, 261, 262]. Nevertheless, its performances are among the best available and that is the reason why we have chosen it for our experimental investigations.[42]

[42]In fact, many important groups pursue the three(or four)-Josephson-junction SQUID path

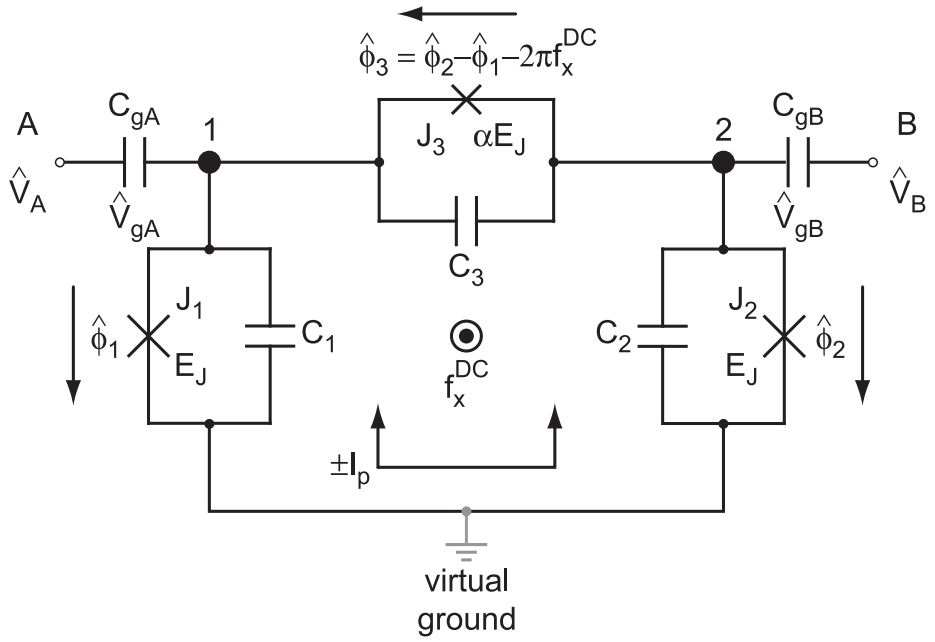

Figure 2.10: Circuit diagram of a three-Josephson-junction SQUID. A superconducting loop is interrupted by three Josephson tunnel junctions, J_i with $i = \{1, 2, 3\}$. Each junction, marked by a cross ($\times$), is the parallel combination of an ideal Josephson junction and a capacitor C_i. Two of the three junctions are equal, whereas the third is α-times larger than the other two. Hence, two junctions are characterized by the energy $E_J = I_{c0}\Phi_0/2\pi$ and the third by $\alpha E_J = \alpha I_{c0}\Phi_0/2\pi$. A gauge-invariant phase $\hat{\phi}_i$ is associated with each junction i. Due to fluxoid quantization, $\hat{\phi}_3 = \hat{\phi}_2 - \hat{\phi}_1 - 2\pi f_x^{DC}$. f_x^{DC} is an external DC (or quasi-static) flux bias. The nodes 1 and 2 represent a pair of superconducting islands connected to the external voltage sources $\hat{V}_A$ and $\hat{V}_B$ via the capacitors C_{gA} and C_{gB}. These capacitors sustain the voltages $\hat{V}_{gA}$ and $\hat{V}_{gB}$, respectively. The counterclockwise and clockwise persistent currents $\pm I_p$ circulate around the loop. These currents are associated with the qubit states $|+\rangle$ and $|-\rangle$ (cf. main text). The circuit virtual ground is indicated [189].

The circuit diagram of the three-Josephson-junction SQUID is represented in Fig. 2.10. In the first part of the following derivation we do not make use of operator hats, as indicated in the figure. We will use the hats when promoting the classical variables to quantum variables. In the figure(s), we always use hats given that, in the end, the entire system under analysis is quantized. The three-Josephson-junction SQUID circuit, which is an extension of the RF SQUID, is made by a superconducting loop interrupted by three Josephson tunnel junctions, J_i with $i = \{1, 2, 3\}$. Each junction is marked by a cross ($\times$) and is modeled as the parallel combination of an ideal Josephson junction and a capacitor C_i. This is as in the

for quantum computing implementations with superconducting devices. For example, the NEC and NTT groups in Japan, MIT, UC Berkeley, and University of Syracuse, USA, TU Delft, The Netherlands, University of Karlsruhe and IPHT-Jena, Germany.

RCSJ model, but with the parallel resistive channel neglected due to the typically very low operating temperature of the device. We notice that two of the three junctions are equal, whereas the third is α-times larger than the other two.[43] The parameter α depends on the geometry of the junctions and is set during fabrication. Consequently, two junctions have Josephson coupling energy $E_{\rm J} = I_{\rm c0}\Phi_0/2\pi$ and the third $\alpha E_{\rm J} = \alpha I_{\rm c0}\Phi_0/2\pi$. A gauge-invariant phase ϕ_i is associated with each junction i. In addition, $C_1 = C_2 = C$ and $C_3 = \alpha C$.

We first focus only on the classical potential energy $U_{\rm F}$ of the circuit. For the calculation of $U_{\rm F}$ the self-inductance of the loop is considered to be negligible, $\Lambda \gg 1$, so that the total flux threading the loop is the external DC flux bias $\Phi_{\rm x}^{\rm DC} = f_{\rm x}^{\rm DC}\,\Phi_0$. In this case, fluxoid quantization around the superconducting loop containing the junctions gives $\phi_1 - \phi_2 + \phi_3 = -2\pi f_{\rm x}^{\rm DC}$. The Josephson energy due to each junction is $E_{{\rm J}i}(1-\cos\phi_i)$, where, in our case, $E_{\rm J1} = E_{\rm J2} = E_{\rm J}$ and $E_{\rm J3} = \alpha E_{\rm J}$. The total Josephson energy (equivalent to the potential energy) is then $U_{\rm F} = \sum_{i=1}^{3} E_{{\rm J}i}(1-\cos\phi_i)$. Imposing the fluxoid quantization condition, we readily obtain

$$\begin{aligned} U_{\rm F} &= E_{\rm J}(1-\cos\phi_1) + E_{\rm J}(1-\cos\phi_2) + \alpha E_{\rm J}(1-\cos\phi_3) \\ &= E_{\rm J}[2+\alpha-\cos\phi_1-\cos\phi_2-\alpha-\cos(2\pi f_{\rm x}^{\rm DC}+\phi_1-\phi_2)]\,, \end{aligned} \tag{2.129}$$

where $(2+\alpha)E_{\rm J}$ is a global energy offset. The important feature of this potential energy is that it is a function of two independent phases. For a range of external DC bias $f_{\rm x}^{\rm DC}$, these two phases, ϕ_1 and ϕ_2, permit two stable configurations, which correspond to DC currents circulating in opposite directions (persistent currents). These two states of opposite current can be used as the two states of a qubit. We will give more details on the physical origin of the DC persistent current states towards the end of this subsection.

Before deriving the entire classical Hamiltonian of the three-Josephson-junction SQUID, it is worth plotting the potential $U_{\rm F}$ as a function of the independent phase drops on the circuit. This potential can be best visualized in a rotated coordinate frame obtained by choosing as coordinates the sum and difference of the gauge-invariant phases ϕ_1 and ϕ_2,

$$\phi_{\rm p} \equiv \frac{\phi_1+\phi_2}{2}\,, \tag{2.130a}$$

$$\phi_{\rm m} \equiv \frac{\phi_1-\phi_2}{2}\,. \tag{2.130b}$$

In the rotated frame the potential energy reads

$$U_{\rm F}(\phi_{\rm p},\phi_{\rm m}) = E_{\rm J}[2+\alpha-2\cos\phi_{\rm p}\cos\phi_{\rm m}-\alpha\cos(2\pi f_{\rm x}^{\rm DC}+2\phi_{\rm m})]\,. \tag{2.131}$$

Manifestly, this is a 2D periodic function with period $f_{\rm x}^{\rm DC} = 1$ and is symmetric about $f_{\rm x}^{\rm DC} = 0.5$. Figure 2.11(a) shows a portion of $U_{\rm F}(\phi_{\rm p},\phi_{\rm m})$ defined over a single unit cell of the periodic potential for $f_{\rm x}^{\rm DC} = 0.5$. Cutting the potential landscape along $\phi_{\rm p} = 0$ results in the magenta line indicated in the plot. Such a slice, defined as $U_{\rm m}(\phi_{\rm m}) \equiv U_{\rm F}(\phi_{\rm p}=0,\phi_{\rm m})$, is reported in Fig. 2.11(b) for clarity. Remarkably, $U_{\rm m}$ is very similar to the potential of an RF SQUID [cf. Fig. 2.9(a)]. We also notice

[43] In order to avoid confusion, it is useful to mention that usually $\alpha < 1$ and, thus, being α-times larger actually means that the third junction is smaller than the other two [189].

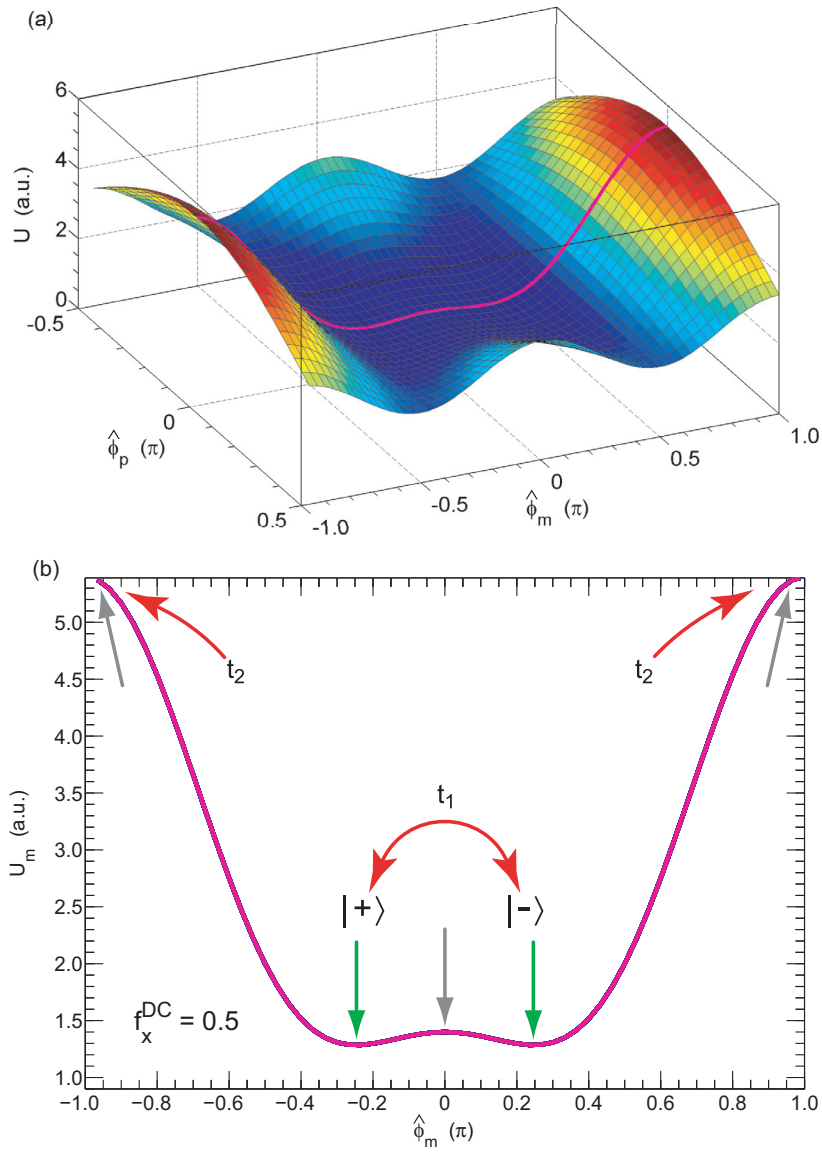

Figure 2.11: Potential landscape of a three-Josephson-junction SQUID for a single unit cell centered around $\hat{\phi}_{\rm p} = \hat{\phi}_{\rm m} = 0$ and $f_{\rm x}^{\rm DC} = 0.5$ [189]. **(a)** Color-code plot of the 2D potential landscape $U_{\rm F}(\hat{\phi}_{\rm p}, \hat{\phi}_{\rm m})$. Magenta (middle grey) line: slice of the potential landscape along $\hat{\phi}_{\rm p} = 0$. **(b)** Plot of the double-well potential $U_{\rm m}(\hat{\phi}_{\rm m}) \equiv U_{\rm F}(\hat{\phi}_{\rm p} = 0, \hat{\phi}_{\rm m})$ obtained from cutting the 2D potential in **(a)**. The qubits states $|+\rangle$ and $|-\rangle$ are confined at the bottom of the left and right wells of $U_{\rm m}(\hat{\phi}_{\rm m})$, respectively. The red arrows indicate the interwell barriers. The grey arrows indicate the three potential maxima at $\phi_{\rm m} = -\pi, 0, +\pi$. The green arrows indicate the two degenerate potential minima at $\phi_{\rm m} = \mp \arccos(1/2\alpha)$, with $\alpha > 1/2$.

that the *intrawell* barrier[44] between the two states at the bottom of the double-well, $|+\rangle$ and $|-\rangle$, is much lower than the *interwell* barrier indicated in Fig. 2.11(b) by the arrows pointing towards the neighboring lattice cells (red arrows). The phase particle associated with the circuit tends to be confined at the bottom of the shallow double-well without escaping to neighboring lattice cells. The states $|+\rangle$ and $|-\rangle$ or a linear superposition of them are the metastable states used in our qubit experiments (cf. chapter 8).

Figure 2.12(a) shows the plot of a single unit cell of $U_{\rm F}(\phi_{\rm p}, \phi_{\rm m})$ for $f_{\rm x}^{\rm DC} = 0.468$. The potential landscape is now highly asymmetric and cutting it along $\phi_{\rm p} = 0$ results in the magenta line reported in Fig. 2.12(b). Controlling the external DC bias $f_{\rm x}^{\rm DC}$ allows one to play with the symmetry properties of the circuit potential and constitutes an important knob for qubit operations.

We now consider the classical kinetic energy $T_{\rm F}$ associated with the circuit. This energy corresponds to the electrostatic energy stored in all the circuit capacitors C_j with $j = \{1, 2, 3, {\rm gA}, {\rm gB}\}$. Since the external biasing voltages at ports A and B are $V_{\rm A}$ and $V_{\rm B}$, respectively, (cf. Fig. 2.10) and each capacitor C_j has a voltage across it of V_j, the kinetic energy can be written as

$$T_{\rm F} = \frac{1}{2}\sum_j C_j V_j^2 - Q_{\rm gA} V_{\rm A} - Q_{\rm gB} V_{\rm B}\,, \tag{2.132}$$

where $Q_{\rm gA} \equiv C_{\rm gA} V_{\rm gA}$ and $Q_{\rm gB} \equiv C_{\rm gB} V_{\rm gB}$. The last two terms in Eq. (2.132) subtract the work done by the voltage sources to give the available electric free energy [263]. The voltage across each Josephson tunnel junction, i, is given by the usual Josephson voltage-phase relation

$$V_i = \frac{\Phi_0}{2\pi}\frac{\partial}{\partial t}\,\phi_i\,. \tag{2.133}$$

The ground point in the circuit of Fig. 2.10 labels the zero of potential and is a virtual ground.

From the inspection of the left and right branches of the circuit of Fig. 2.10 and applying Kirchhoff's voltage law [264], we find that the voltages across the gate capacitors gA and gB are

$$V_{\rm gA} = V_{\rm A} - V_1\,, \tag{2.134a}$$

$$V_{\rm gB} = V_{\rm B} - V_2\,, \tag{2.134b}$$

respectively. The convention on the voltage signs are as follows: The external source voltages $V_{\rm A}$ and $V_{\rm B}$ drop from ports A and B to the virtual ground; the voltages V_1 and V_2 drop from nodes 1 and 2 to the virtual ground, respectively, and the voltages $V_{\rm gA}$ and $V_{\rm gB}$ drop from ports A and B to nodes 1 and 2, respectively. Defining the vector of independent gauge-invariant phases as

$$\vec{\phi} \equiv \begin{bmatrix} \phi_1 \\ \phi_2 \end{bmatrix}\,, \tag{2.135}$$

the capacitance matrix of the circuit as

$$\mathbf{C}_{\rm F} = C \begin{bmatrix} 1+\alpha+\gamma_{\rm g} & -\alpha \\ -\alpha & 1+\alpha+\gamma_{\rm g} \end{bmatrix}\,, \tag{2.136}$$

[44] This barrier depends on the choice of the parameter α [189].

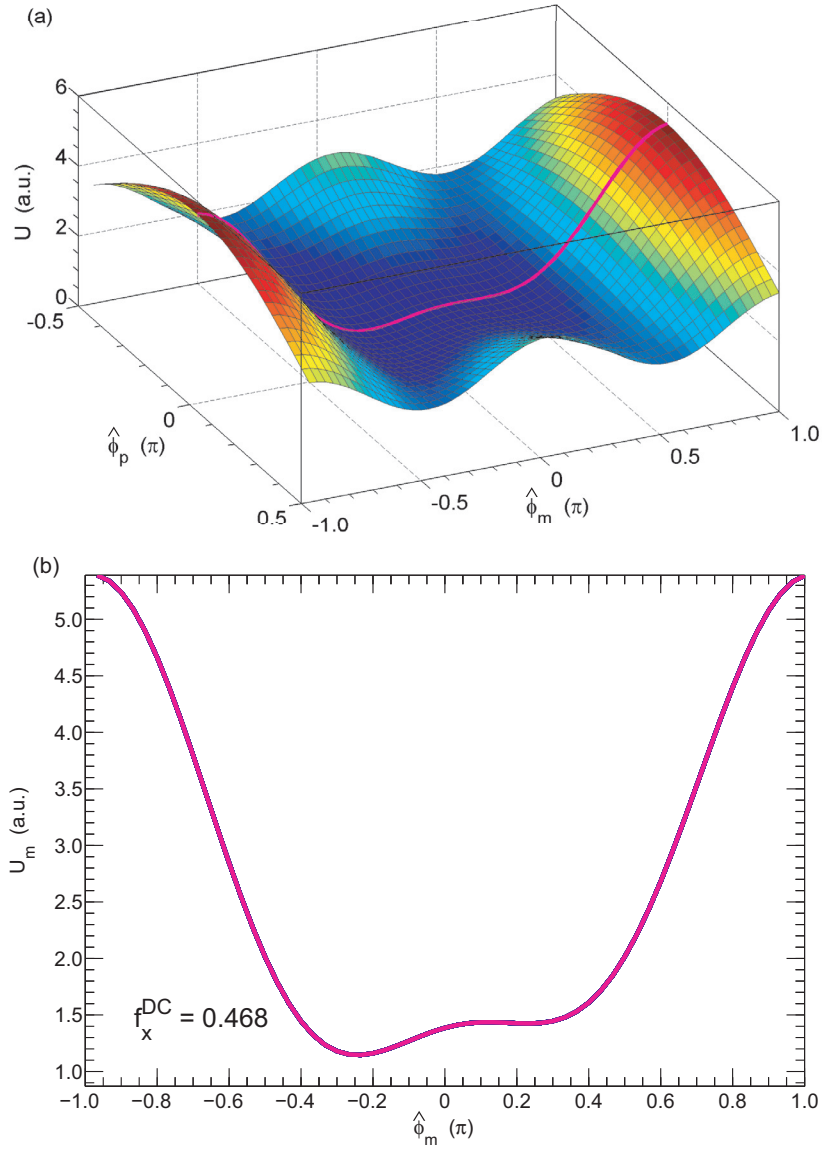

Figure 2.12: Potential landscape of a three-Josephson-junction SQUID for a single unit cell centered around $\hat{\phi}_{\rm p} = \hat{\phi}_{\rm m} = 0$ and $f_{\rm x}^{\rm DC} = 0.468$. Due to this bias condition the potential is highly asymmetric. **(a)** Color-code plot of the 2D potential landscape $U_{\rm F}(\hat{\phi}_{\rm p}, \hat{\phi}_{\rm m})$. Magenta (middle grey) line: slice of the potential landscape along $\hat{\phi}_{\rm p} = 0$. **(b)** Plot of the double-well potential $U_{\rm m}(\hat{\phi}_{\rm m}) \equiv U_{\rm F}(\hat{\phi}_{\rm p} = 0, \hat{\phi}_{\rm m})$ obtained from cutting the 2D potential in **(a)**.

and neglecting the constant term

$$-\frac{1}{2}\vec{V}^T\mathbf{C}_{\mathrm{g}}\vec{V}\,,$$

where the source voltage vector

$$\vec{V} \equiv \begin{bmatrix} V_{\mathrm{A}} \\ V_{\mathrm{B}} \end{bmatrix} \tag{2.137}$$

and the gate capacitance matrix

$$\mathbf{C}_{\mathrm{g}} = \gamma_{\mathrm{g}} C \begin{bmatrix} 1 & 0 \\ 0 & 1 \end{bmatrix}\,, \tag{2.138}$$

we can finally express the circuit kinetic energy in terms of the time derivatives of the phases as

$$T_{\mathrm{F}} = \frac{1}{2}\left(\frac{\Phi_0}{2\pi}\right)^2 \left(\frac{\partial}{\partial t}\vec{\phi}\right)^T \mathbf{C}_{\mathrm{F}} \frac{\partial}{\partial t}\vec{\phi}\,. \tag{2.139}$$

In all above definitions and equations we have assumed $C_{\mathrm{gA}} = C_{\mathrm{gB}} = \gamma_{\mathrm{g}} C$, where γ_{g} is a parameter that accounts for both the external gate capacitances and, eventually, parasitic capacitances to ground. Such parameter is usually extremely small compared to all other characteristic parameters of the circuit, $\gamma_{\mathrm{g}} \simeq 0.01$ [189]. This is an important fact because it signifies that the three-Josephson-junction SQUID is only weakly coupled to background charge fluctuations and, thus, is almost insensitive to charge noise.

The classical equations of motion can then be found from the Lagrangian $\mathcal{L}_{\mathrm{F}} = T_{\mathrm{F}} - U_{\mathrm{F}}$, the canonical momenta for the three junctions being $P_i = \partial\mathcal{L}_{\mathrm{F}}/\partial\phi_i$. We can now transform the Lagrangian by shifting it as

$$\mathcal{L}_{\mathrm{F}} = T_{\mathrm{F}} - U_{\mathrm{F}} - \left(\frac{\Phi_0}{2\pi}\right)\left(\frac{\partial}{\partial t}\vec{\phi}\right)^T \mathbf{C}_{\mathrm{g}}\vec{V}\,. \tag{2.140}$$

For the transformed Lagrangian the canonical momenta are then given by the vector

$$\vec{P} = \left(\frac{\Phi_0}{2\pi}\right)^2 \mathbf{C}_{\mathrm{F}}\frac{\partial}{\partial t}\vec{\phi} - \left(\frac{\Phi_0}{2\pi}\right)\mathbf{C}_{\mathrm{g}}\vec{V}\,. \tag{2.141}$$

These momenta are directly proportional to the charges on the islands at nodes 1 and 2 of Fig. 2.10,

$$\vec{Q} = \frac{2\pi}{\Phi_0}\vec{P}\,. \tag{2.142}$$

This relation tells us that we have reduced the three-Josephson-junction SQUID to a *two-port equivalent circuit* characterized by two independent variables (i.e., *two degrees of freedom*). These are the gauge-invariant phases ϕ_1 and ϕ_2, the first derivatives of which, according to Eq. (2.142), are proportional to the charges Q_1 and Q_2 on the islands 1 and 2 of Fig. 2.10. In the case of the RF SQUID, instead, we were dealing with a *one-port equivalent circuit* characterized by one independent variable (i.e., *one degree of freedom*). This was the total flux Φ threading the RF SQUID loop or, equivalently, its canonically conjugated variable, the charge Q.

For the three-Josephson-junction SQUID, the kinetic energy part of the classical Hamiltonian can readily be written as

$$T_{\rm F} = \vec{Q}_{\rm tot}^{T} \frac{1}{2\mathbf{C}_{\rm F}} \vec{Q}_{\rm tot} \,, \tag{2.143}$$

where the total charge of the two-port circuit is given by the sum of the charges $\vec{Q}$ and induced charges $\vec{Q}_{\rm g} \equiv \mathbf{C}_{\rm g}\vec{V}$ on the islands 1 and 2,

$$\begin{aligned} \vec{Q}_{\rm tot} &\equiv \vec{Q} + \vec{Q}_{\rm g} \\ &= \frac{2\pi}{\Phi_0}\left(\vec{P} + \frac{\Phi_0}{2\pi}\mathbf{C}_{\rm g}\vec{V}\right) . \end{aligned} \tag{2.144}$$

The kinetic energy of Eq. (2.143) is just the electrostatic energy of the two-port circuit (e.g., cf. Ref. [265] and references therein). To conclude the treatment of the classical circuit we remind that the characteristic electric energy of the circuit is the so-called charging energy, $E_{\rm c} = e^2/2C$. Finally, the classical Hamiltonian of the three-Josephson-junction SQUID can be expressed as

$$H_{\rm F} = \frac{1}{2}\left(\vec{P} + \frac{\Phi_0}{2\pi}\vec{Q}_{\rm g}\right)^{T} \frac{1}{\vec{M}_{\rm F}} \left(\vec{P} + \frac{\Phi_0}{2\pi}\vec{Q}_{\rm g}\right) + U\big(\vec{\phi}\big) \,, \tag{2.145}$$

where the anisotropic effective mass $\vec{M}_{\rm F}$ is defined as[45]

$$\vec{M}_{\rm F} \equiv \frac{\Phi_0}{2\pi}\mathbf{C}_{\rm F}\frac{\Phi_0}{2\pi} \,. \tag{2.146}$$

The Hamiltonian of Eq. (2.145) can also be derived following a more formal approach based on the usual definition $H_{\rm F} = \sum_i P_i(\partial\phi_i/\partial t) - \mathcal{L}$.

The transition to the quantum-mechanical circuit is realized considering the classically conjugated variables in the Hamiltonian of Eq. (2.145) as quantum-mechanical operators. This means that the independent gauge-invariant phases become position operators, $\phi_i \rightarrow \hat{\phi}_i$, and the classical charges ($\vec{Q} \propto \vec{P}$) become momenta operators,[46] $P_i \rightarrow \hat{P}_i = -j\hbar\partial/\partial\hat{\phi}_i$. The wave functions can then be considered as $|\Psi\rangle = \Psi_n(\hat{\phi}_1, \hat{\phi}_2)$, where n indicates the n-th energy level of the quantum-mechanical circuit.

Without loosing generality, we can transform out of the problem the induced charges on the islands. We thus obtain a new Hamiltonian that we use as the quantum-mechanical Hamiltonian of the three-Josephson-junction SQUID,

$$\begin{aligned} \widehat{H}_{\rm F} = &\frac{1}{2}\vec{\hat{P}}^{T}\,\vec{M}_{\rm F}^{-1}\,\vec{\hat{P}} \\ &+ E_{\rm J}[2 + \alpha - \cos\hat{\phi}_1 - \cos\hat{\phi}_2 - \alpha\cos(2\pi f_{\rm x}^{\rm DC} + \hat{\phi}_1 - \hat{\phi}_2)] \,. \end{aligned} \tag{2.147}$$

The energy levels and wave functions for the Hamiltonian of Eq. (2.147) are obtained numerically by rewriting $\widehat{H}_{\rm F}$ in the charge basis or, equivalently, by expanding the wave functions in terms of states of constant phase [189].[47]

[45] For visualization reasons, we split the $(\Phi_0/2\pi)^2$ contribution between the left and right side of the mass.

[46] Equivalently, $\vec{\phi} \rightarrow \vec{\hat{\phi}}$ and $\vec{P} \rightarrow \vec{\hat{P}} = -j\hbar\partial/\partial\vec{\hat{\phi}}$.

[47] We have double checked all our numerical calculations by comparing the results obtained both in charge and phase basis without finding any discrepancy.

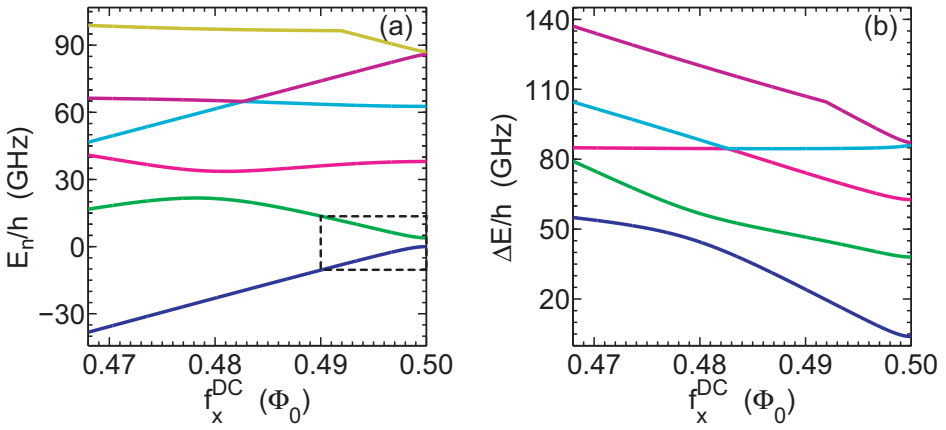

Figure 2.13: Energy levels for the six lowest states of a three-Josephson junction SQUID plotted as a function of $f_{\mathrm{x}}^{\mathrm{DC}} \in [0.468, 0.5]$. Since the energy levels are symmetric with respect to the $f_{\mathrm{x}}^{\mathrm{DC}}$-axis, the plots stop at the qubit degeneracy point $f_{\mathrm{x}}^{\mathrm{DC}} = 0.5$. **(a)** Energy band diagram. E_n is the energy of each level of the three-Josephson junction SQUID, with $n = 0, 1, 2, 3, 4, 5$. Dark blue (dark grey) line: energy level E_0 for the groundstate $|\mathrm{g}\rangle$. Light green (light grey) line: energy level E_1 for the first excited state $|\mathrm{e}\rangle$. Magenta (middle grey) line: energy level E_2 for the second excited state (auxiliary state) $|\mathrm{a}\rangle$, and so forth. The dashed black box indicates the frustration region where the two-level (qubit) approximation can be applied (cf. main text). **(b)** Difference between the energy E_n for the first five excited states and E_0, $\Delta E \equiv E_n - E_0$, with $n = 1, 2, 3, 4, 5$.

In the charge basis, the numerical calculations are done in the coordinate system of the gauge-invariant phases $(\hat{\phi}_1, \hat{\phi}_2)$. The resulting energy band diagram for the six lowest states of the circuit is plotted as a function of $f_{\mathrm{x}}^{\mathrm{DC}}$ in Fig. 2.13(a). The frustration ranges between $f_{\mathrm{x}}^{\mathrm{DC}} = 0.468$ and the degeneracy point $f_{\mathrm{x}}^{\mathrm{DC}} = 0.5$. Notably, the band diagram is symmetric with respect to the axis set by $f_{\mathrm{x}}^{\mathrm{DC}} = 0.5$.[48] The energy E_0 corresponding to the groundstate $|\mathrm{g}\rangle$ is represented by the dark blue (dark grey) line and the energy E_1 of the first excited state $|\mathrm{e}\rangle$ by the light green (light grey) line. The magenta (middle grey) line represents the energy E_2 of the second excited state $|\mathrm{a}\rangle$ (also referred to as auxiliary state; cf. chapter 7, Sec. 7.4). Figure 2.13(b) shows the difference between the energy E_n of the first five excited states and the energy of the groundstate E_0, $\Delta E \equiv E_n - E_0$ with $n = 1, 2, 3, 4, 5$.

In the phase basis, we prefer to rotate the coordinate system of the gauge-invariant phases into a new frame which diagonalizes the capacitance matrix $\mathbf{C}_{\mathrm{F}}$. Such rotated frame can easily be obtained employing the quantum-mechanical version of the transformations of Eqs. (2.130a) and (2.130b), where we substitute ϕ_{p} with $\hat{\phi}_{\mathrm{p}}$ and ϕ_{m} with $\hat{\phi}_{\mathrm{m}}$. In the rotated frame the total circuit Hamiltonian then

[48] This is the reason why we only plot it up to 0.5.

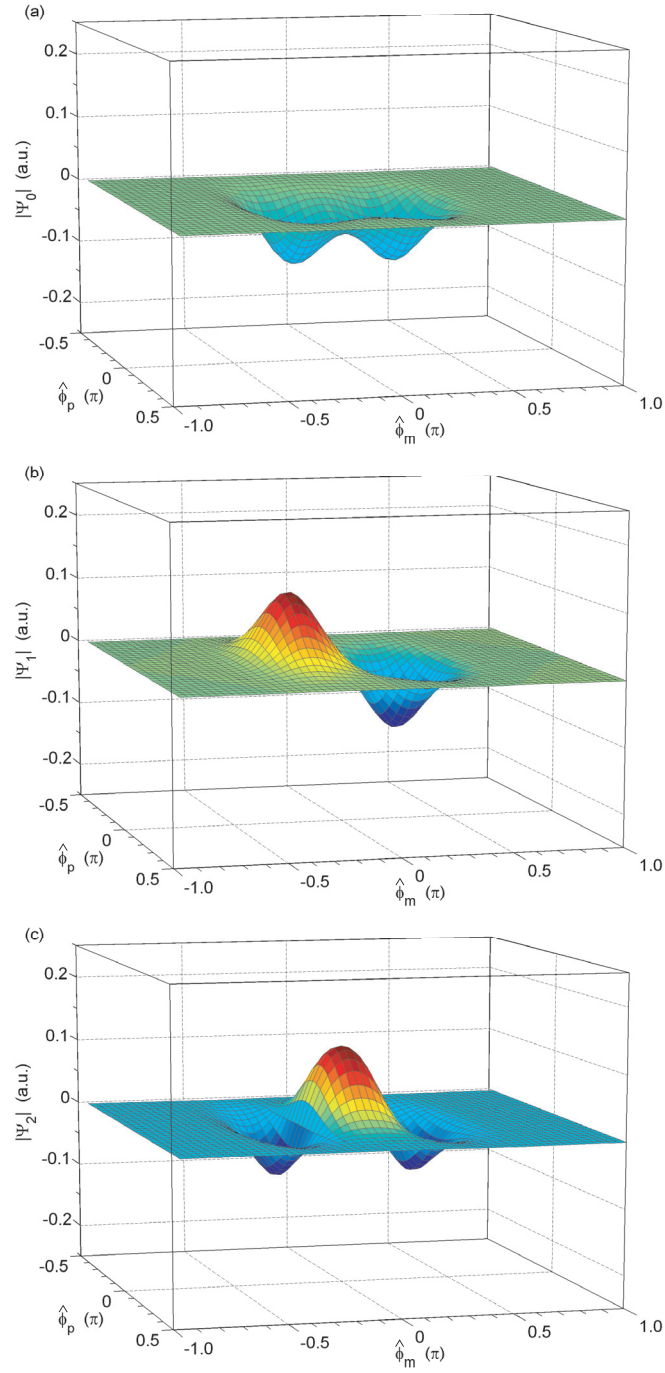

Figure 2.14: Wave function amplitudes for a three-Josephson-junction SQUID as a function of $\hat{\phi}_{\rm p}$ and $\hat{\phi}_{\rm m}$ and for $f_{\rm x}^{\rm DC} = 0.5$. **(a)** $|\Psi_0|$: ground-state $|{\rm g}\rangle$. **(b)** $|\Psi_1|$: first excited state $|{\rm e}\rangle$. **(c)** $|\Psi_2|$: second excited state (auxiliary state) $|{\rm a}\rangle$.

reads

$$\widehat{H}_{\mathrm{F}} = \frac{1}{2}\frac{\hat{P}_{\mathrm{p}}^2}{M_{\mathrm{p}}} + \frac{1}{2}\frac{\hat{P}_{\mathrm{m}}^2}{M_{\mathrm{m}}} + E_{\mathrm{J}}[2 + \alpha - 2\cos\hat{\phi}_{\mathrm{p}}\cos\hat{\phi}_{\mathrm{m}} - \alpha\cos(2\pi f_{\mathrm{x}}^{\mathrm{DC}} + 2\hat{\phi}_{\mathrm{m}})]\,, \tag{2.148}$$

where

$$\hat{P}_{\mathrm{p}} \equiv -j\hbar\frac{\partial}{\partial\hat{\phi}_{\mathrm{p}}}\,, \tag{2.149a}$$

$$\hat{P}_{\mathrm{m}} \equiv -j\hbar\frac{\partial}{\partial\hat{\phi}_{\mathrm{m}}} \tag{2.149b}$$

and

$$M_{\mathrm{p}} \equiv \left(\frac{\Phi_0}{2\pi}\right)^2 2C\left(1+\gamma_{\mathrm{g}}\right)\,, \tag{2.150a}$$

$$M_{\mathrm{m}} \equiv \left(\frac{\Phi_0}{2\pi}\right)^2 2C\left(1+2\alpha+\gamma_{\mathrm{g}}\right)\,. \tag{2.150b}$$

Figure 2.14 shows the wave functions Ψ_n for the three lowest states $|\mathrm{g}\rangle$, $|\mathrm{e}\rangle$, and $|\mathrm{a}\rangle$ of the three-Josephson-junction SQUID as a function of $\hat{\phi}_{\mathrm{p}}$ and $\hat{\phi}_{\mathrm{m}}$ and for $f_{\mathrm{x}}^{\mathrm{DC}} = 0.5$. As expected, the parity properties of these wave functions are analogous to those found in the case of the RF SQUID: Ψ_0 is even [cf. Fig. 2.14(a)], Ψ_1 is odd [cf. Fig. 2.14(b)], and Ψ_2 is again even [cf. Fig. 2.14(c)]. In particular, we notice that the first two wave functions are strongly localized in correspondence to the two wells of the 2D potential of Fig. 2.11(a), two bumps down or one bump up and one down, respectively. This is different for the third wave function, which, instead, is delocalized above the shallow barrier of the potential landscape (three bumps). The wave functions of higher states become more and more delocalized. This peculiarity of the wave functions, together with the fact that $E_1 - E_0 \ll E_2 - E_0$ in the vicinity of the degeneracy point,[49] [cf. Fig. 2.13(b)] gives a hint that the two lowest states of the quantum circuit, $|\mathrm{g}\rangle$ and $|\mathrm{e}\rangle$, can be used to implement a qubit.

Two-Level (Qubit) Approximation

We will encounter again the Hamiltonian of Eq. (2.148) in chapter 8, where $\widehat{H}_{\mathrm{F}}$ represents the free energy term in the interaction between a three-Josephson-junction SQUID (a flux quantum circuit) and an external classical and/or quantized electromagnetic field. In that chapter (as in Sec. 2.3) such Hamiltonian is defined as $\widehat{H}_{\mathrm{F}}^0$, where the superscript "0" indicates that we are dealing with the free energy term of the interaction. We will not use this superscript in this section. The numerical diagonalization of $\widehat{H}_{\mathrm{F}}$ described above allows us to calculate the energy eigenvalues $E_n \equiv \hbar\Omega_n$, with $n = \mathrm{g}, \mathrm{e}, \mathrm{a}, \ldots$ of the circuit and the corresponding eigenstates $\{|n\rangle\} = \{|\mathrm{g}\rangle, |\mathrm{e}\rangle, |\mathrm{a}\rangle, \ldots\}$. Applying the closure theorem

$$\sum_n |n\rangle\langle n| = \mathbf{I}\,, \tag{2.151}$$

[49] Consequently, also $E_1 - E_0 \ll E_2 - E_1$.

($\mathbf{I}$ is the $n \times n$ identity matrix) twice, the flux quantum circuit Hamiltonian can be expressed in the energy eigenbasis as

$$\widehat{H}_{\mathrm{F}} = \sum_n \hbar\Omega_n \left|n\right\rangle \left\langle n\right| . \tag{2.152}$$

As pointed out earlier, in the vicinity of the degeneracy point $f_{\mathrm{x}}^{\mathrm{DC}} = 0.5$ [cf. dashed black box in Fig. 2.13(a)] we can restrict ourselves to the two lowest states of the flux quantum circuit, $|\mathrm{g}\rangle$ and $|\mathrm{e}\rangle$, and neglect all higher states. In this case, the circuit Hamiltonian can be approximated as

$$\begin{aligned}\widehat{H}_{\mathrm{F}} &\approx \widehat{H}_{\mathrm{Q}} = \widehat{H}_{\mathrm{ge}} \\ &= \hbar\frac{\Omega_{\mathrm{ge}}}{2}\left(|\mathrm{e}\rangle\langle\mathrm{e}| - |\mathrm{g}\rangle\langle\mathrm{g}|\right) = \hbar\frac{\Omega_{\mathrm{Q}}}{2}\hat{\sigma}_z ,\end{aligned} \tag{2.153}$$

where $\Omega_{\mathrm{Q}} = \Omega_{\mathrm{ge}} \equiv \Omega_{\mathrm{e}} - \Omega_{\mathrm{g}}$, i.e., the zero of energy is taken at the middle level between the groundstate $|\mathrm{g}\rangle$ and excited state $|\mathrm{e}\rangle$, and $|\mathrm{e}\rangle\langle\mathrm{e}| - |\mathrm{g}\rangle\langle\mathrm{g}| = \hat{\sigma}_z$ is the usual Pauli operator for a spin-1/2 system in the energy eigenbasis.[50] The Hamiltonian of Eq. (2.153) represents the Hamiltonian of a flux two-level system or qubit expressed in its energy eigenbasis.

To attach a more physical meaning to the qubit Hamiltonian $\widehat{H}_{\mathrm{Q}}$, we now attempt to derive it in the coordinate system of the so-called diabatic basis $|+\rangle$ and $|-\rangle$ [cf. Fig. 2.11(b)]. What is the physical meaning of the states $|+\rangle$ and $|-\rangle$? In the beginning of this subsection, we already mentioned that these states represent the counterclockwise and clockwise DC persistent currents circulating in the flux quantum circuit loop, but we did not explain their origin. Let us consider again the 2D potential landscape of Fig. 2.11(a) obtained at the degeneracy point, $\Phi_{\mathrm{x}}^{\mathrm{DC}} = \Phi_0/2$. We first remind that the potential assumes the shape of a double-well iff $\alpha > 1/2$ ($\alpha = 1/2$ is called the critical value of the potential) [189]. In this case, cutting the 2D potential along $\hat{\phi}_{\mathrm{p}} = 0$ results in the 1D potential U_{m} of Fig. 2.11(b). Since this potential is a periodic function of $\hat{\phi}_{\mathrm{m}}$, we only plot one unit cell, namely the one centered around the value $\hat{\phi}_{\mathrm{m}} = 0$. We are now interested in computing the classical[51] stable solutions of the function

$$U_{\mathrm{m}}\left(\phi_{\mathrm{m}}, \Phi_{\mathrm{x}}^{\mathrm{DC}} = \frac{\Phi_0}{2}\right) = E_{\mathrm{J}}[2 + \alpha - 2\cos\phi_{\mathrm{m}} - \alpha\cos(\pi + 2\phi_{\mathrm{m}})] . \tag{2.154}$$

This is equivalent in finding the minima of $U_{\mathrm{m}}(\phi_{\mathrm{m}}, \Phi_{\mathrm{x}}^{\mathrm{DC}} = \Phi_0/2)$,

$$\frac{\partial}{\partial\phi_{\mathrm{m}}}U_{\mathrm{m}}\left(\phi_{\mathrm{m}}, \Phi_{\mathrm{x}}^{\mathrm{DC}} = \frac{\Phi_0}{2}\right) = \sin\phi_{\mathrm{m}}(1 - 2\alpha\cos\phi_{\mathrm{m}}) = 0 . \tag{2.155}$$

The first set of solutions,

$$\phi_{\mathrm{m}} = k\pi \tag{2.156}$$

with $k \in \mathbb{Z}$, obviously corresponds to unstable solutions (maxima), as shown in Fig. 2.11(b). In the figure, the grey arrows indicate the three maxima present within the first unit cell, $\phi_{\mathrm{m}} = -\pi, 0, +\pi$. The second set of solutions,

$$\phi_{\mathrm{m}} = \mp\arccos\frac{1}{2\alpha} + 2k\pi , \tag{2.157}$$

[50] We remind that it is always possible to add a global energy offset to the Hamiltonian of a quantum circuit, which gives freedom when choosing the zero of energy.

[51] This is why, again, we will not use the operator hats in this part of the derivation.

corresponds instead to stable solutions (minima), as shown in Fig. 2.11(b). The green arrows indicate the two degenerate minima present within the first unit cell, $\phi_{\rm m} = \mp \arccos(1/2\alpha)$. As expected, all solutions are symmetric with respect to the point $\phi_{\rm m} = 0$.[52] Hereafter, we define the two stable solutions corresponding to the degenerate minima in the first unit cell as $\mp\phi_{\rm m}^{*} \equiv \mp \arccos(1/2\alpha)$.

The next step of our derivation is to expand in a Taylor series up to first order the potential $U_{\rm m}$ in the vicinity of the degeneracy point, $\Phi_{\rm x}^{\rm DC} \to \Phi_0/2$, and at the potential energy minima $\mp\phi_{\rm m}^{*}$. Readily,

$$U_{\rm m}\left(\phi_{\rm m} = \phi_{\rm m}^{*}, \Phi_{\rm x}^{\rm DC}\right) \approx U_{\rm m}\left(\phi_{\rm m}^{*}, \Phi_{\rm x}^{\rm DC}\right)\Big|_{\Phi_{\rm x}^{\rm DC}=\frac{\Phi_0}{2}} + \frac{\partial}{\partial \Phi_{\rm x}^{\rm DC}} U_{\rm m}\left(\phi_{\rm m}^{*}, \Phi_{\rm x}^{\rm DC}\right)\Big|_{\Phi_{\rm x}^{\rm DC}=\frac{\Phi_0}{2}} \delta\Phi_{\rm x}^{\rm DC}\,, \qquad (2.158)$$

where $\delta\Phi_{\rm x}^{\rm DC} \equiv \Phi_{\rm x}^{\rm DC} - \Phi_0/2$.[53] This expansion allows us to accurately describe the circuit for a narrow DC bias window around the degeneracy point (linear approximation). We have thus found the DC bias dependence of the flux qubit Hamiltonian. Since the zero-order term of the expansion of Eq. (2.158) vanishes, we are able to define the so-called *energy bias* as

$$\begin{aligned}\hbar\epsilon\left(\Phi_{\rm x}^{\rm DC}\right) &\equiv 2\left|\left(\frac{\partial}{\partial \Phi_{\rm x}^{\rm DC}} U_{\rm m}\left(\phi_{\rm m}^{*}, \Phi_{\rm x}^{\rm DC}\right)\Big|_{\Phi_{\rm x}^{\rm DC}=\frac{\Phi_0}{2}} \delta\Phi_{\rm x}^{\rm DC}\right)\right| \\ &= 2|I_{\rm p}|\delta\Phi_{\rm x}^{\rm DC}\,, \end{aligned} \qquad (2.159)$$

where the DC persistent current $I_{\rm p}$ is given by[54]

$$I_{\rm p} = \pm\, I_{\rm c0}\sqrt{1 - \frac{1}{(2\alpha)^2}}\,. \qquad (2.160)$$

The sign of $I_{\rm p}$ depends on the choice of the potential minimum. When choosing $-\phi_{\rm m}^{*}$ as a solution, the persistent current is positive (it circulates counterclockwise in the loop) and corresponds to state $|+\rangle$. For $+\phi_{\rm m}^{*}$, the persistent current is negative (it circulates clockwise in the loop) and corresponds to state $|-\rangle$. It is now clear the physical meaning of the two states $|+\rangle$ and $|-\rangle$. They simply represent the classical states (classical DC currents) of the flux quantum circuit within the two-level approximation, i.e., the classical states of a qubit! Bearing this in mind, we can write the first part of the flux qubit Hamiltonian in the diabatic basis $|+\rangle$ and $|-\rangle$ as

$$\widehat{\widehat{H}}_z = \frac{1}{2}\hbar\,\epsilon\left(\Phi_{\rm x}^{\rm DC}\right)\hat{\hat{\sigma}}_z\,, \qquad (2.161)$$

where $\hat{\hat{\sigma}}_z$ is the usual Pauli operator for a spin-1/2 system in the diabatic basis. The Hamiltonian $\widehat{\widehat{H}}_z$ vanishes right at the flux degeneracy point $\Phi_{\rm x}^{\rm DC} = \Phi_0/2$, whereas far away from this point it can fully be described by the classical states $|+\rangle$ and $|-\rangle$.

[52] It is an easy exercise to show that for $\alpha \leqslant 1/2$ the potential $U_{\rm m}(\phi_{\rm m}, \Phi_{\rm x}^{\rm DC} = \Phi_0/2)$ admits only one set of solutions (minimum) at $\phi_{\rm m} = 2k\pi$. This minimum bifurcates into two degenerate minima only for $\alpha > 1/2$.

[53] In general, $\delta\Phi_{\rm x}^{\rm DC} \equiv \Phi_{\rm x}^{\rm DC} - \Phi_{(k)}$, where $\Phi_{(k)} \equiv (2k+1)\,\Phi_0/2$, with $k \in \mathbb{Z}$.

[54] We remind that the derivative of an energy with respect to a flux has the units of a current.

These states are well localized at the bottom of each of the two wells of the potential of Fig. 2.11(b), where they are separated by the energy barrier in the center of $U_{\rm m}$.

What is the role played by the energy barrier? We start again considering the case $\Phi_{\rm x}^{\rm DC} = \Phi_0/2$. In this case, the barrier gives rise to a tunneling matrix element t_1 between the two classical states $|+\rangle$ and $|-\rangle$, which otherwise would be degenerate. An estimate of t_1 can be obtained by the JWKB semiclassical approximation.[55] For this we must calculate the action S_1 between the two minima at $\mp\phi_{\rm m}^*$ (here, we always assume $\phi_{\rm p} = 0$) and then use

$$t_1 \approx \frac{\hbar\omega_{\rm att}}{2\pi} e^{-S_1/\hbar}\,, \tag{2.162}$$

where $\omega_{\rm att}$ is the attempt frequency of escape in one of the wells of the 2D potential of Fig. 2.11(a). Since we are only interested in evaluating the action between the minima $\mp\phi_{\rm m}^*$ of the potential $U_{\rm m}$ of Fig. 2.11(b), we can safely assume $\omega_{\rm att} = \omega_{\rm m}$. In order to compute $\omega_{\rm m}$ we have to make a simple model of each side of the double-well potential $U_{\rm m}$. Near the minimum at $+\phi_{\rm m}^*$ the potential is equivalent to an anisotropic 2D harmonic oscillator. Hence, the flux quantum circuit Hamiltonian in the vicinity of the minimum is approximately (with $\vec{Q}_{\rm g} = \vec{0}$)

$$\begin{aligned} H_{\rm F} \approx & \frac{P_{\rm p}^2}{2M_{\rm p}} + \frac{1}{2} M_{\rm p}\omega_{\rm p}^2\,\phi_{\rm p}^2 \\ & + \frac{P_{\rm m}^2}{2M_{\rm m}} + \frac{1}{2} M_{\rm m}\omega_{\rm m}^2\,(\phi_{\rm m} - \phi_{\rm m}^*)^2 \\ & + U_0\,, \end{aligned} \tag{2.163}$$

where

$$\frac{\hbar\omega_{\rm p}}{E_{\rm J}} \equiv \sqrt{\frac{4}{\alpha(1+\gamma)(E_{\rm J}/E_{\rm c})}}\,, \tag{2.164a}$$

$$\frac{\hbar\omega_{\rm m}}{E_{\rm J}} \equiv \sqrt{\frac{4(4\alpha^2-1)}{\alpha(1+2\alpha+\gamma)(E_{\rm J}/E_{\rm c})}}\,, \tag{2.164b}$$

and $U_0 \equiv 2 - 1/2\alpha = U_{\rm min}$ is the potential energy at the minimum (similar results are obtained for the other minimum at $-\phi_{\rm m}^*$).

In general, the action from point $\vec{\phi}_a$ to point $\vec{\phi}_b$ is

$$S_{ab} = \int_{\vec{\phi}_a}^{\vec{\phi}_b} |d\phi_q| \sqrt{2M_{qq}(E-U)}\,. \tag{2.165}$$

Here, $\vec{q}$ is a unit vector along the path of integration, $d\phi_q$ the differential path length, and $M_{qq} \equiv \vec{q}^{\,T}\,\mathbf{M}\,\vec{q}$ is the component of the mass tensor along the path direction. In Eq. (2.165), we can approximate the energy difference $E-U$ as the deviation in the potential energy ΔU from the minima along the path.

[55] Usually, this approximation is referred to as WKB approximation. However, H. Jeffreys had used it before Wentzel, Kramers, and Brillouin [266].

We are now able to estimate t_1. The path of integration is taken from $-\phi^*_{\rm m}$ to $+\phi^*_{\rm m}$ along the direction $\vec{q} = \vec{u}_{\rm m}$,[56] so that $M_{qq} = M_m$ for this path. The potential energy at the minima is $U_{\rm min}$. The difference in the potential energy from the minima at $-\phi^*_{\rm m}$ along this path can be written as $\Delta U_1 = E_{\rm J}[2\alpha(\cos\phi_{\rm m} - 1/2\alpha)^2]$. The action along this path is then [189]

$$\begin{aligned} S_1 &= \int_{-\phi^*_{\rm m}}^{+\phi^*_{\rm m}} d\phi_{\rm m}\, \sqrt{4M_{\rm m}\alpha E_{\rm J}} \left(\cos\phi_{\rm m} - \frac{1}{2\alpha}\right) \\ &= \hbar\sqrt{4\alpha(1+2\alpha+\gamma)(E_{\rm J}/E_{\rm c})} \left(\sin\phi^*_{\rm m} - \frac{1}{2\alpha}\phi^*_{\rm m}\right) , \end{aligned} \tag{2.166}$$

which finally allows us to obtain the intracell tunneling matrix element t_1. It is also possible to estimate the energy dispersion t_2, which is responsible for intercell tunneling [cf. Fig. 2.11(b)]. The derivation is analogous to that used to estimate t_1. Without delving into the details of such derivation [189], we just mention that for a suitable choice of parameters (e.g., that of Fig. 2.11) we find $t_2 \ll t_1$. Hence, the tunneling from unit cell to unit cell, t_2, can safely be neglected, whereas $t_1 \neq 0$ also at the qubit degeneracy point. We notice that the estimate based on Eq. (2.162) is not entirely correct. In particular, the prefactor in front of the exponential function is incomplete. We remind to Ref. [267] for more details on this subtle issue and on the proper use of the JWKB approximation. Nevertheless, this little inconsistency does not affect in any manner the results of this chapter.

So far, we have estimated the tunneling matrix elements in the case $\Phi_{\rm x}^{\rm DC} = \Phi_0/2$. As $\Phi_{\rm x}^{\rm DC}$ is changed from $\Phi_{\rm x}^{\rm DC} = \Phi_0/2$, the potential $U_{\rm m}$ is modified such that one well becomes higher than the other. In this case, the barrier height also changes and the new tunneling matrix element is given by $t_{\rm Q} = t_1 + \delta t_1$ where t_1 is the intracell tunneling matrix element obtained from Eqs. (2.162) and (2.166) at the degeneracy point and δt_1 is the change in the intracell tunneling matrix element due to new biasing point. For a narrow DC bias window around the degeneracy point (linear approximation), it is possible to give an analytical estimate of δt_1 (e.g., cf. Appendix B in Ref. [189]). Under these conditions, we can define the *energy gap* of the qubit as $\hbar\delta_{\rm Q} \equiv t_{\rm Q}$ and we can write the second part of the flux qubit Hamiltonian in the diabatic basis $|+\rangle$ and $|-\rangle$ as

$$\widehat{\widehat{H}}_x = \frac{1}{2}\hbar\delta_{\rm Q}\hat{\hat{\sigma}}_x\,, \tag{2.167}$$

where $\hat{\hat{\sigma}}_x$ is the usual Pauli operator for a spin-1/2 system in the diabatic basis.

The total Hamiltonian of the flux qubit in the diabatic basis $|+\rangle$ and $|-\rangle$ can finally be written as

$$\begin{aligned} \widehat{\widehat{H}}_{\rm Q} &= \widehat{\widehat{H}}_z + \widehat{\widehat{H}}_x \\ &= \frac{1}{2}\hbar\left[\epsilon\left(\Phi_{\rm x}^{\rm DC}\right)\hat{\hat{\sigma}}_z + \delta_{\rm Q}\hat{\hat{\sigma}}_x\right] . \end{aligned} \tag{2.168}$$

This result is extremely important because it reveals that in the diabatic basis any external field, in this simple case the external DC flux bias $\Phi_{\rm x}^{\rm DC}$, couples to the qubit only via the $\hat{\hat{\sigma}}_z$ part of the Hamiltonian. More in general if the external fields

[56] Here, $\vec{u}_{\rm m}$ represents the unit vector along the $\phi_{\rm m}$ direction.

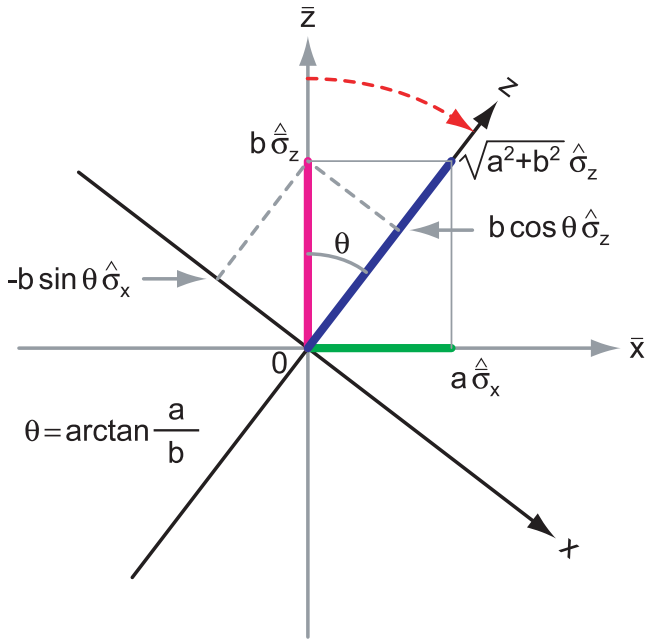

Figure 2.15: Rotation from the qubit diabatic basis to the energy eigenbasis frame. $0\bar{x}\bar{z}$: frame associated with the qubit diabatic basis $|+\rangle$ and $|-\rangle$. $a\,\hat{\bar{\sigma}}_x$ and $b\,\hat{\bar{\sigma}}_z$: generic components of a qubit in the diabatic basis. The interaction with external fields happens via the $\hat{\bar{\sigma}}_z$ term only (cf. Sec. 2.3). After a rotation by an angle $\theta = \arctan(a/b)$ from $0\bar{x}\bar{z}$ to $0xz$ (red broken arrow), the qubit Hamiltonian is in diagonal form, $\sqrt{a^2+b^2}\,\hat{\sigma}_z$. In the new frame, the component $b\,\hat{\bar{\sigma}}_z$ is decomposed into two components, $-b\sin\theta\,\hat{\sigma}_x$ and $b\cos\theta\,\hat{\sigma}_z$. These two components play a crucial role in the qubit-resonator interaction explained in Subsec. 2.3.3.

were RF classical and/or quantized fields, they would also couple to the qubit via a $\hat{\bar{\sigma}}_z$-type interaction. We will come back to this topic in the next section.

Before studying the interaction between flux quantum circuits and quantized fields, we analyze the mathematical transformation which brings us from the diabatic basis to the energy eigenbasis and vice versa. This transformation, for example, allows us to move from the Hamiltonian of Eq. (2.168), $\widehat{\bar{H}}_{\rm Q}$, to the Hamiltonian of Eq. (2.153), $\widehat{H}_{\rm Q}$. By means of this transformation, we are able to compute analytically the qubit energy $\Omega_{\rm Q}$ and other relevant qubit parameters. There are two equivalent approaches to describe such transformation: a geometric approach and an analytic one. Being both methods formally correct, we prefer starting with that based on geometric considerations because it is more intuitive and easy to visualize.

Figure 2.15 shows the reference frame $0\bar{x}\bar{z}$ associated with the qubit diabatic basis $|+\rangle$ and $|-\rangle$. In the figure, the two quantities a and b are used instead of $\hbar\delta_{\rm Q}$ and $\hbar\epsilon(\Phi_{\rm x}^{\rm DC})$, respectively. This is to keep the figure general and to be able to utilize it again when interpreting the qubit-resonator interaction Hamiltonian (cf. Sec. 2.3). In the $0\bar{x}\bar{z}$ frame, the qubit Hamiltonian of Eq. (2.168) can be written as the scalar

product

$$\widehat{\widehat{H}}_{\mathrm{Q}} = \frac{1}{2}\hbar\vec{\Omega}\cdot\vec{\hat{\sigma}}\,, \tag{2.169}$$

where $\vec{\Omega} \equiv \left[\delta_{\mathrm{Q}}, 0, \epsilon\left(\Phi_{\mathrm{x}}^{\mathrm{DC}}\right)\right]$ and $\vec{\hat{\sigma}} \equiv (\hat{\sigma}_x, \hat{\sigma}_y, \hat{\sigma}_z)$. The angle between vector $\vec{\Omega}$ and the $\bar{z}$-axis is then

$$\theta = \arctan\frac{\delta_{\mathrm{Q}}}{\epsilon\left(\Phi_{\mathrm{x}}^{\mathrm{DC}}\right)} \tag{2.170}$$

and, consequently,

$$\cos\theta = \frac{\epsilon\left(\Phi_{\mathrm{x}}^{\mathrm{DC}}\right)}{\|\vec{\Omega}\|} \tag{2.171}$$

and

$$\sin\theta = \frac{\delta_{\mathrm{Q}}}{\|\vec{\Omega}\|}\,. \tag{2.172}$$

Here, $\|\vec{\Omega}\| = \sqrt{\delta_{\mathrm{Q}}^2 + \epsilon^2\left(\Phi_{\mathrm{x}}^{\mathrm{DC}}\right)}$.

As indicated in Fig. 2.15, a clockwise rotation by the angle θ brings us into the new reference frame $0xz$. In this frame, the qubit Hamiltonian is diagonal and can be written as

$$\widehat{H}_{\mathrm{Q}} = \hbar\frac{\|\vec{\Omega}\|}{2}\hat{\sigma}_z\,. \tag{2.173}$$

By comparing the Hamiltonian of Eq. (2.173) with the one of Eq. (2.153), we find

$$\|\vec{\Omega}\| = \Omega_{\mathrm{Q}} = \sqrt{\delta_{\mathrm{Q}}^2 + \epsilon^2\left(\Phi_{\mathrm{x}}^{\mathrm{DC}}\right)}\,. \tag{2.174}$$

Thus, the frame $0xz$ is the natural frame associated with the qubit energy eigenbasis $|\mathrm{g}\rangle$ and $|\mathrm{e}\rangle$.

The rotation which transforms the frame $0\bar{x}\bar{z}$ into $0xz$ can more formally be defined by means of the unitary rotation operator

$$\widehat{\mathcal{D}}(\theta) \equiv \exp\left(-\frac{j\hat{\sigma}_y\theta}{2}\right)\,, \tag{2.175}$$

which rotates the frame about the y-axis. We remind that rotations in the so-called two-component (Pauli) formalism are defined by the operator

$$\exp\left(-\frac{j\vec{\hat{\sigma}}\cdot\vec{u}\,\varphi}{2}\right) = \begin{bmatrix} \cos\dfrac{\varphi}{2} - ju_z\sin\dfrac{\varphi}{2} & (-ju_x - u_y)\sin\dfrac{\varphi}{2} \\ (-ju_x + u_y)\sin\dfrac{\varphi}{2} & \cos\dfrac{\varphi}{2} + ju_z\sin\dfrac{\varphi}{2} \end{bmatrix}\,, \tag{2.176}$$

where $\vec{u} \equiv (u_x, u_y, u_z)$. By comparing Eq. (2.175) with Eq. (2.176) and assuming $\hat{\sigma}_y = \vec{\hat{\sigma}}\cdot(u_x = 0, u_y = 1, u_z = 0)$, we can straightforwardly rewrite the unitary rotation operator $\widehat{\mathcal{D}}(\theta)$ in a more convenient matrix form,

$$\widehat{\mathcal{D}}(\theta) = \begin{bmatrix} \cos\dfrac{\theta}{2} & -\sin\dfrac{\theta}{2} \\ \sin\dfrac{\theta}{2} & \cos\dfrac{\theta}{2} \end{bmatrix}\,. \tag{2.177}$$

It is now an easy exercise to prove that the unitary transformation

$$\begin{aligned}\widehat{\mathcal{D}}^{\dagger}(\theta)\ \widehat{\bar{H}}_{\mathrm{Q}}\ \widehat{\mathcal{D}}(\theta) &= \widehat{\mathcal{D}}^{\dagger}\ \frac{1}{2}\hbar\epsilon\left(\Phi_{\mathrm{x}}^{\mathrm{DC}}\right)\hat{\bar{\sigma}}_{z}\ \widehat{\mathcal{D}} + \widehat{\mathcal{D}}^{\dagger}\ \frac{1}{2}\hbar\delta_{\mathrm{Q}}\hat{\bar{\sigma}}_{x}\ \widehat{\mathcal{D}} \\ &= \widehat{H}_{\mathrm{Q}}\,. \end{aligned} \tag{2.178}$$

[*Hint:* One has to work with the matrices corresponding to the operators $\widehat{\mathcal{D}}^{\dagger}$, $\widehat{\mathcal{D}}$, $\hat{\sigma}_z$, and $\hat{\sigma}_x$ (equivalently, $\hat{\bar{\sigma}}_z$ and $\hat{\bar{\sigma}}_x$) and extensively use the double-angle trigonometric identities $\cos^2(\theta/2) - \sin^2(\theta/2) = \cos\theta$ and $2\sin(\theta/2)\cos(\theta/2) = \sin\theta$. At the end, the definitions given by Eqs. (2.171), (2.172), and (2.174) must be applied].

Before concluding this subsection, it is worth mentioning that several authors have investigated both theoretically and experimentally different variants of the three-Josephson-junction SQUID. Two remarkable examples are represented by the four-Josephson-junction SQUID (e.g., cf. Refs. [118, 119, 268]) and the large loop three-Josephson-junction SQUID (e.g., cf. Ref. [269]). The first example exploits the symmetries of a flux quantum circuit based on four Josephson tunnel junctions to protect the qubit from unwanted coupling to the noisy environment. In such environment, in fact, unintended junctions due to the standard fabrication process can spoil the qubit quantum coherence. The second example takes advantage of a large circuit loop with nonnegligible inductive energy, $\Lambda \ll 1$, to achieve very strong coupling to external fields. Strong coupling is a desirable condition for both fast qubit control and other quantum computing protocols based on circuit QED architectures. The basic physics of all those devices is analogous to that described here.

2.3 Interaction between Resonators and Flux Quantum Circuits

We have now in hand all the necessary formalism to adequately describe quantum circuits and signals. We can thus attempt to study the circuit-signal quantum-mechanical interaction, which stands at the basis of all circuit QED applications.

In this section, we first introduce the so-called quantum small-signal formalism in the linear regime. This formalism allows us to derive the interaction Hamiltonian between a quantized RF SQUID and a quantized electromagnetic field (cf. Subsec. 2.3.1). Following a similar path, we then derive the interaction Hamiltonian for the case of a quantized three-Josephson-junction SQUID (cf. Subsec. 2.3.2). Finally, we consider the case of a qubit-signal interaction and briefly revise the most relevant properties of the so-called Jaynes-Cummings Hamiltonian (cf. Subsec. 2.3.3).

In Sec. 2.2, we have shown that flux quantum circuits can be controlled by means of an external DC (or quasi-static) flux bias

$$\Phi_{\mathrm{x}}^{\mathrm{DC}} \equiv f_{\mathrm{x}}^{\mathrm{DC}}\,\Phi_0\,. \tag{2.179}$$

Such flux bias inherently represents an interaction between the quantum circuit and an external current source,

$$\Phi_{\mathrm{x}}^{\mathrm{DC}} = M_{\mathrm{FX}} i_{\mathrm{x}}^{\mathrm{DC}}\,, \tag{2.180}$$

where M_{FX} represents the mutual inductance between the flux quantum circuit and the biasing network and $i_{\mathrm{x}}^{\mathrm{DC}}$ a DC biasing current. Nothing prevents us from

generalizing this interaction to the case of AC signals, where we can define

$$\Phi_{\mathrm{x}} \equiv \Phi_{\mathrm{x}}^{\mathrm{DC}} + \Phi_{\mathrm{x}}^{\mathrm{AC}} \,. \tag{2.181}$$

Here,

$$\Phi_{\mathrm{x}}^{\mathrm{AC}} = M_{\mathrm{FX}} i_{\mathrm{x}}^{\mathrm{AC}} \,, \tag{2.182}$$

where $i_{\mathrm{x}}^{\mathrm{AC}}$ is a generic AC current flowing in the external network. Within this framework, flux quantum circuits behave very much as standard electronic devices. A DC current bias i^{DC} allows one to polarize the circuit, i.e., to choose the desired operation point. Once the polarization point is set, a *small* fluctuating signal $\delta\, i$ (an AC signal) can be applied to the circuit and the *circuit response* to it can be studied. In electronics this method is referred to as small-signal analysis. We can heuristically transfer it to the case of quantum circuits bearing in mind two important caveats. First, the AC signal must be small enough not to give rise to nonlinear effects. We shall consider the case of large, but still not exceedingly large, AC signals in chapter 8, Subsec. 8.4.2 (small-signal formalism in the nonlinear regime). Second, we always have to remember that we are dealing with circuits, which are oftentimes characterized by complex topologies. The Hamiltonians of the flux quantum circuits derived in the previous section do not fully account for the circuit topology. As we shall show in chapter 5, Subsec. 5.1.3, this can give origin to spurious terms in the interaction Hamiltonian. These terms are only artifacts without any physical meaning. We will underline the critical steps where such artifacts can pop up throughout the following derivations.

Keeping those caveats in mind, we can quantize the AC flux of Eq. (2.182) promoting it to its corresponding quantum-mechanical operator,

$$\hat{\Phi}_{\mathrm{x}}^{\mathrm{AC}} = M_{\mathrm{FX}} \hat{I}_{\mathrm{x}}^{\mathrm{AC}} \,, \tag{2.183}$$

where, in general, $\hat{I}_{\mathrm{x}}^{\mathrm{AC}}$ can represent the quantum current of a propagating wave on an infinite transmission line, the standing wave on a transmission line resonator, or, more simply, the quantum current of a lumped-parameter LC-resonator.

In the case of a simple LC-resonator $\hat{I}_{\mathrm{x}}^{\mathrm{AC}} \to \hat{I}$, where $\hat{I} = I_0\, j(\hat{a}^\dagger - \hat{a})$ and the vacuum current I_0 is given by Eq. (2.97). Also, in the case of a resonator we redefine the mutual inductance between the flux quantum circuit and the resonator as M_{FR}, $M_{\mathrm{FX}} \to M_{\mathrm{FR}}$. Therefore,

$$\hat{\Phi}_{\mathrm{x}}^{\mathrm{AC}} = M_{\mathrm{FR}} I_0\, j(\hat{a}^\dagger - \hat{a}) \,. \tag{2.184}$$

In the case of a transmission line resonator, $\hat{\Phi}_{\mathrm{x}}^{\mathrm{AC}}$ depends on the resonator mode function and, thus, on the specific position of the flux quantum circuit on the line. In general, for a $\lambda/2$ resonator we have to substitute I_0 with $\tilde{I}_0\, \Xi(z)$, where $\tilde{I}_0$ is given by Eq. (2.106) and $\Xi(z)$ by Eq. (2.102b). Similarly, for a $\lambda/4$ resonator we have to apply the same substitution as for a $\lambda/2$ resonator, but with the mode function $\Xi(z)$ given by Eq. (2.103b) this time.

For an infinite transmission line we have to use multi-mode annihilation and creation operators, as defined in chapter 8, Subsec. 8.4.2, Eq. (8.18). We will not further discuss this case in the present section, where we mostly focus on the interaction with a simple LC resonator.

The fundamental equation at the basis of the quantum small-signal formalism can finally be expressed as

$$\hat{\Phi}_{\mathrm{x}} = \Phi_{\mathrm{x}}^{\mathrm{DC}} + \hat{\Phi}_{\mathrm{x}}^{\mathrm{AC}} \,. \tag{2.185}$$

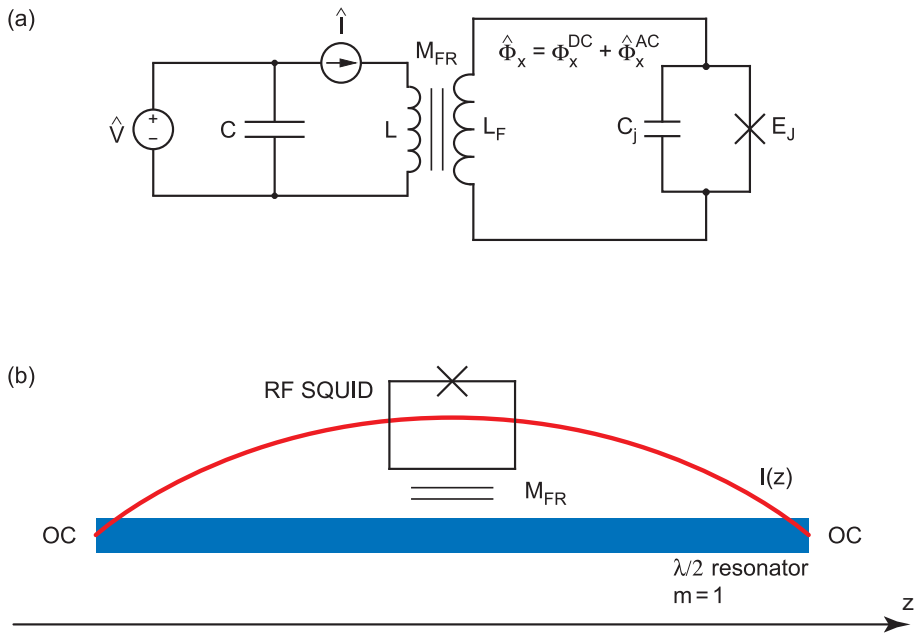

Figure 2.16: Interaction between a resonator and an RF SQUID. **(a)** A lumped-parameter LC-resonator interacting with an RF SQUID via the mutual inductance M_{FR}. The resonator is constructed according to the rules given in Subsec. 2.1.3. The RF SQUID is as described in Subsec. 2.2.2, but with the external flux through the loop, $\hat{\Phi}_{\mathrm{x}}$, now given by the sum of a DC (or quasi-static) bias $\Phi_{\mathrm{x}}^{\mathrm{DC}}$ and an AC quantum excitation $\hat{\Phi}_{\mathrm{x}}^{\mathrm{AC}}$, $\hat{\Phi}_{\mathrm{x}} = \Phi_{\mathrm{x}}^{\mathrm{DC}} + \hat{\Phi}_{\mathrm{x}}^{\mathrm{AC}}$. **(b)** The first spatial mode, $m = 1$, of a $\lambda/2$ resonator interacting with an RF SQUID. The geometric contribution to the interaction is due to the mutual inductance M_{FR}. The RF SQUID is positioned at the maximum of the current mode function $I(z)$ to optimize the coupling strength. The resonator is open-circuited (OC) at both edges.

2.3.1 The Interaction Hamiltonian for the RF SQUID

Figure 2.16(a) shows the circuit diagram of an RF SQUID interacting with a lumped-parameter LC-resonator. The resonator circuit is constructed according to the rules given in Subsec. 2.1.3. In order to derive the interaction Hamiltonian $\widehat{H}_{\mathrm{I}}$ associated with this circuit, we employ the quantum small-signal formalism.

We first write the generic Hamiltonian of an RF SQUID quantum circuit as

$$\widehat{H}_{\mathrm{F}} = \frac{\hat{Q}^2}{2C_{\mathrm{j}}} + \frac{(\hat{\Phi} - \hat{\Phi}_{\mathrm{x}})^2}{2L_{\mathrm{F}}} - E_{\mathrm{J}} \cos\left(2\pi \frac{\hat{\Phi}}{\Phi_0}\right) . \tag{2.186}$$

We then split it up into the sum of two components, $\widehat{H}_{\mathrm{A}} + \widehat{H}_{\mathrm{B}}$, where

$$\widehat{H}_{\mathrm{A}} = \frac{\hat{Q}^2}{2C_{\mathrm{j}}} - E_{\mathrm{J}} \cos\left(2\pi \frac{\hat{\Phi}}{\Phi_0}\right) , \tag{2.187a}$$

$$\widehat{H}_{\mathrm{B}} = \frac{(\hat{\Phi} - \hat{\Phi}_{\mathrm{x}})^2}{2L_{\mathrm{F}}} . \tag{2.187b}$$

Among these two Hamiltonians, $\widehat{H}_{\mathrm{A}}$ is independent from any external classical or quantum signal, whereas $\widehat{H}_{\mathrm{B}}$ explicitly depends on $\hat{\Phi}_{\mathrm{x}}$. Inserting the general expression for $\hat{\Phi}_{\mathrm{x}}$ given by Eq. (2.185) into $\widehat{H}_{\mathrm{B}}$, we obtain

$$\begin{aligned} \widehat{H}_{\mathrm{B}} &= \frac{[(\hat{\Phi} - \Phi_{\mathrm{x}}^{\mathrm{DC}}) + \hat{\Phi}_{\mathrm{x}}^{\mathrm{AC}}]^2}{2L_{\mathrm{F}}} \\ &= \frac{(\hat{\Phi} - \Phi_{\mathrm{x}}^{\mathrm{DC}})^2}{2L_{\mathrm{F}}} + \frac{(\hat{\Phi} - \Phi_{\mathrm{x}}^{\mathrm{DC}})\hat{\Phi}_{\mathrm{x}}^{\mathrm{AC}}}{L_{\mathrm{F}}} + \frac{(\hat{\Phi}_{\mathrm{x}}^{\mathrm{AC}})^2}{2L_{\mathrm{F}}} . \end{aligned} \tag{2.188}$$

The last term of this Hamiltonian, $(\hat{\Phi}_{\mathrm{x}}^{\mathrm{AC}})^2/2L_{\mathrm{F}}$, is one example of the artifacts due to circuit topology and has to be neglected.[57]

We can now isolate the term of Eq. (2.188) interacting only with the DC (or quasi-static) flux bias,

$$\widehat{H}_{\mathrm{Z}} = \frac{(\hat{\Phi} - \Phi_{\mathrm{x}}^{\mathrm{DC}})^2}{2L_{\mathrm{F}}} . \tag{2.189}$$

This Hamiltonian together with $\widehat{H}_{\mathrm{A}}$ allows us to define the free energy term of the RF SQUID Hamiltonian, $\widehat{H}_{\mathrm{F}}^0 \equiv \widehat{H}_{\mathrm{A}} + \widehat{H}_{\mathrm{Z}}$, which resumes the Hamiltonian of Eq. (2.127). Diagonalizing $\widehat{H}_{\mathrm{F}}^0$ gives the RF SQUID energy eigenstates $\{|n\rangle\} = \{|\mathrm{g}\rangle, |\mathrm{e}\rangle, |\mathrm{a}\rangle, \ldots\rangle\}$ and the corresponding eigenvalues $\hbar\Omega_n$, with $n = \mathrm{g}, \mathrm{e}, \mathrm{a}, \ldots$. Finally, applying the closure theorem ($\sum_n |n\rangle\langle n| = \mathbf{I}$, where $\mathbf{I}$ is the $n \times n$ identity matrix) twice, the RF SQUID free energy Hamiltonian can be expressed in the energy eigenbasis as $\widehat{H}_{\mathrm{F}}^0 = \sum_n \hbar\Omega_n |n\rangle\langle n|$.

We now focus on the remaining term in the Hamiltonian of Eq. (2.188) besides $\widehat{H}_{\mathrm{Z}}$. That term defines the interaction Hamiltonian between the RF SQUID and the LC-resonator. Using the expression of Eq. (2.184) for $\hat{\Phi}_{\mathrm{x}}^{\mathrm{AC}}$, the interaction Hamiltonian reads

$$\widehat{H}_{\mathrm{I}} = \frac{(\hat{\Phi} - \Phi_{\mathrm{x}}^{\mathrm{DC}})\, M_{\mathrm{FR}} I_0\, j(\hat{a}^\dagger - \hat{a})}{L_{\mathrm{F}}} . \tag{2.190}$$

This Hamiltonian can be rewritten invoking again the closure theorem for the energy eigenstates of $\widehat{H}_{\mathrm{F}}^0$ twice, obtaining

$$\widehat{H}_{\mathrm{I}} = \frac{M_{\mathrm{FR}} I_0}{L_{\mathrm{F}}} \sum_{m,n} |m\rangle\langle m|(\hat{\Phi} - \Phi_{\mathrm{x}}^{\mathrm{DC}})|n\rangle\langle n|\, j(\hat{a}^\dagger - \hat{a}) , \tag{2.191}$$

where $m, n = \mathrm{g}, \mathrm{e}, \mathrm{a}, \ldots$. The total Hamiltonian of the RF SQUID coupled to the LC-resonator is thus $\widehat{H}_{\mathrm{T}} = \widehat{H}_{\mathrm{F}}^0 + \widehat{H}_{\mathrm{I}} + \widehat{H}_{\mathrm{LC}}$, where $\widehat{H}_{\mathrm{LC}}$ is given by Eq. (2.82).

[57] More details in chapter 5, Subsec. 5.1.3.

The coupling coefficients between the RF SQUID and the LC-resonator can finally be evaluated by inspecting the Hamiltonian of Eq. (2.191). Expressing the coefficients as angular frequencies, we obtain

$$g_{mn}\left(\Phi_{\mathrm{x}}^{\mathrm{DC}}\right) \equiv \frac{1}{\hbar}\frac{M_{\mathrm{FR}}I_0}{L_{\mathrm{F}}}\langle m|(\hat{\Phi}-\Phi_{\mathrm{x}}^{\mathrm{DC}})|n\rangle \tag{2.192}$$

and

$$\widehat{H}_{\mathrm{I}} = \hbar\sum_{m,n} g_{mn}|m\rangle\langle n|\, j(\hat{a}^{\dagger}-\hat{a})\,. \tag{2.193}$$

This is the interaction Hamiltonian associated with the circuit of Fig. 2.16(a). Figure 2.16(b) shows the interaction between an RF SQUID and a $\lambda/2$ resonator. In this case, the quantity I_0 of Eq. (2.192) must be substituted with $\tilde{I}_0\,\Xi(z)$, where $\tilde{I}_0$ is given by Eq. (2.106) and $\Xi(z)$ by Eq. (2.102b). The mutual inductance M_{FR} maintains the same meaning as for the simple LC-resonator case.

2.3.2 The Interaction Hamiltonian for the Three-Josephson-Junction SQUID

In the case of a three-Josephson junction SQUID, the quantum small-signal analysis can be carried out more easily in terms of frustrations. First, we define the classical total frustration

$$f_{\mathrm{x}} \equiv f_{\mathrm{x}}^{\mathrm{DC}} + \delta f_{\mathrm{x}} \tag{2.194}$$

and, then, we substitute δf_{x} with $\hat{f}_{\mathrm{x}}^{\mathrm{AC}} \equiv \hat{\Phi}_{\mathrm{x}}^{\mathrm{AC}}/\Phi_0$. The quantity δf_{x} plays the role of a small perturbation (usually an oscillating field).

In this manner, we can write the general Hamiltonian of a three-Josephson junctions SQUID as

$$\begin{aligned}\widehat{H}_{\mathrm{F}} = \frac{1}{2}\frac{\hat{P}_{\mathrm{p}}^2}{M_{\mathrm{p}}} + \frac{1}{2}\frac{\hat{P}_{\mathrm{m}}^2}{M_{\mathrm{m}}} + E_{\mathrm{J}}[2+\alpha-2\cos\hat{\phi}_{\mathrm{p}}\cos\hat{\phi}_{\mathrm{m}} \\ -\alpha\cos(2\pi f_{\mathrm{x}}+2\hat{\phi}_{\mathrm{m}})]\,,\end{aligned} \tag{2.195}$$

where $\hat{P}_{\mathrm{p}}$, $\hat{P}_{\mathrm{m}}$, M_{p}, and M_{m} are defined in Eqs. (2.149a), (2.149b), (2.150a), and (2.150b), respectively.

Following a similar calculation as for the RF SQUID, we split up the Hamiltonian $\widehat{H}_{\mathrm{F}}$ of Eq. (2.195) into the two Hamiltonians

$$\widehat{H}_{\mathrm{A}} = \frac{1}{2}\frac{\hat{P}_{\mathrm{p}}^2}{M_{\mathrm{p}}} + \frac{1}{2}\frac{\hat{P}_{\mathrm{m}}^2}{M_{\mathrm{m}}} + E_{\mathrm{J}}(2+\alpha-2\cos\hat{\phi}_{\mathrm{p}}\cos\hat{\phi}_{\mathrm{m}})\,, \tag{2.196a}$$

$$\widehat{H}_{\mathrm{B}} = -\alpha E_{\mathrm{J}}\cos(2\pi f_{\mathrm{x}}+2\hat{\phi}_{\mathrm{m}})\,. \tag{2.196b}$$

Inserting the expression for f_{x} given by Eq. (2.194) into $\widehat{H}_{\mathrm{B}}$, we obtain

$$\begin{aligned}\widehat{H}_{\mathrm{B}} &= -\alpha E_{\mathrm{J}}\cos[(2\pi f_{\mathrm{x}}^{\mathrm{DC}}+2\hat{\phi}_{\mathrm{m}})+2\pi\delta f_{\mathrm{x}}] \\ &= -\alpha E_{\mathrm{J}}[\cos(2\pi f_{\mathrm{x}}^{\mathrm{DC}}+2\hat{\phi}_{\mathrm{m}})\cos(2\pi\delta f_{\mathrm{x}}) \\ &\quad -\sin(2\pi f_{\mathrm{x}}^{\mathrm{DC}}+2\hat{\phi}_{\mathrm{m}})\sin(2\pi\delta f_{\mathrm{x}})]\,.\end{aligned} \tag{2.197}$$

In the spirit of the quantum small-signal analysis, we now expand in a Maclaurin series up to first order with respect to the perturbation δf_{x} the Hamiltonian $\widehat{H}_{\mathrm{B}}$ of Eq. (2.197). This allows us to write $\widehat{H}_{\mathrm{B}} = \widehat{H}_{\mathrm{Z}} + \widehat{H}_{\mathrm{I}}$, where

$$\widehat{H}_{\mathrm{Z}} = -\alpha E_{\mathrm{J}} \cos(2\pi f_{\mathrm{x}}^{\mathrm{DC}} + 2\hat{\phi}_{\mathrm{m}}) \tag{2.198}$$

and

$$\widehat{H}_{\mathrm{I}} = 2\pi\alpha E_{\mathrm{J}} \sin(2\pi f_{\mathrm{x}}^{\mathrm{DC}} + 2\hat{\phi}_{\mathrm{m}}) \times \delta f_{\mathrm{x}} \,. \tag{2.199}$$

The free energy term of the three-Josephson-junction SQUID Hamiltonian is given by $\widehat{H}_{\mathrm{F}}^{0} = \widehat{H}_{\mathrm{A}} + \widehat{H}_{\mathrm{Z}}$, which resumes the Hamiltonian of Eq. (2.148). Hence, we can write $\widehat{H}_{\mathrm{F}}^{0}$ in the energy eigenbasis $\{|n\rangle\} = \{|\mathrm{g}\rangle, |\mathrm{e}\rangle, |\mathrm{a}\rangle, \ldots\}$ as in Eq. (2.152).

Substituting δf_{x} with $\hat{f}_{\mathrm{x}}^{\mathrm{AC}}$ and using the expression of Eq. (2.184) for $\hat{\Phi}_{\mathrm{x}}^{\mathrm{AC}}$, the interaction Hamiltonian $\widehat{H}_{\mathrm{I}}$ becomes

$$\widehat{H}_{\mathrm{I}} = \alpha M_{\mathrm{FR}} I_{\mathrm{c0}} I_0 \sin(2\pi f_{\mathrm{x}}^{\mathrm{DC}} + 2\hat{\phi}_{\mathrm{m}}) \otimes j(\hat{a}^{\dagger} - \hat{a}) \,. \tag{2.200}$$

Invoking the closure theorem for the energy eigenstates of $\widehat{H}_{\mathrm{F}}^{0}$ twice, we obtain

$$\widehat{H}_{\mathrm{I}} = \alpha M_{\mathrm{FR}} I_{\mathrm{c0}} I_0 \sum_{m,n} |m\rangle\langle m| \sin(2\pi f_{\mathrm{x}}^{\mathrm{DC}} + 2\hat{\phi}_{\mathrm{m}}) |n\rangle\langle n| \otimes j(\hat{a}^{\dagger} - \hat{a}) \,, \tag{2.201}$$

where, again, $m, n = \mathrm{g}, \mathrm{e}, \mathrm{a}, \ldots$. The total Hamiltonian of the three-Josephson-junction SQUID coupled to the LC-resonator is thus $\widehat{H}_{\mathrm{T}} = \widehat{H}_{\mathrm{F}}^{0} + \widehat{H}_{\mathrm{I}} + \widehat{H}_{\mathrm{LC}}$, in a similar way as for the RF SQUID case.

In the three-Josephson-junction SQUID case, the coupling coefficients expressed as angular frequencies are defined as

$$g_{mn}(f_{\mathrm{x}}^{\mathrm{DC}}) \equiv \frac{\alpha M_{\mathrm{FR}} I_{\mathrm{c0}} I_0}{\hbar} \langle m| \sin(2\pi f_{\mathrm{x}}^{\mathrm{DC}} + 2\hat{\phi}_{\mathrm{m}}) |n\rangle \,. \tag{2.202}$$

This definition allows us to write $\widehat{H}_{\mathrm{I}}$ for the three-Josephson-junction SQUID as in Eq. (2.193).

2.3.3 The Qubit-Signal Interaction Hamiltonian

The interaction Hamiltonian of Eq. (2.193), which depends on the specific set of energy eigenstates $\{|n\rangle\}$, is formally equivalent for both the quantized RF SQUID and the three-Josephson-junction SQUID coupled to a quantized LC-resonator. We can thus write the total Hamiltonian of any flux quantum circuit as[58]

$$\begin{aligned} \widehat{H}_{\mathrm{T}} &= \widehat{H}_{\mathrm{F}}^{0} + \widehat{H}_{\mathrm{I}} + \widehat{H}_{\mathrm{LC}} \\ &= \sum_{n} \hbar\Omega_n \, |n\rangle \, \langle n| \\ &\quad + \hbar \sum_{m,n} g_{mn} |m\rangle\langle n| \, j(\hat{a}^{\dagger} - \hat{a}) \\ &\quad + \hbar\omega \left(\hat{a}^{\dagger}\hat{a} + \frac{1}{2} \right) , \end{aligned} \tag{2.203}$$

[58] Neglecting the interaction with the environment.

where the coupling coefficients g_{mn} are defined in Eqs. (2.192) and (2.202) for the RF SQUID and the three-Josephson-junction SQUID, respectively.

In the vicinity of the degeneracy point, $f_{\rm x}^{\rm DC} = 0.5$, we can restrict ourselves to the subset $\{|{\rm g}\rangle, |{\rm e}\rangle\}$ of the energy eigenstates $\{|n\rangle\}$ and neglect all higher states. In this case, the approximated total Hamiltonian of the circuit becomes

$$\begin{aligned}\widehat{H}_{\rm T} \approx\ & \hbar(\Omega_{\rm g}\,|{\rm g}\rangle\langle{\rm g}| + \Omega_{\rm e}\,|{\rm e}\rangle\langle{\rm e}|) \\ & + \hbar(g_{\rm gg}\,|{\rm g}\rangle\langle{\rm g}| + g_{\rm ge}\,|{\rm g}\rangle\langle{\rm e}| \\ & + g_{\rm eg}\,|{\rm e}\rangle\langle{\rm g}| + g_{\rm ee}\,|{\rm e}\rangle\langle{\rm e}|)\, j(\hat{a}^\dagger - \hat{a}) \\ & + \hbar\omega\left(\hat{a}^\dagger\hat{a} + \frac{1}{2}\right). \end{aligned} \tag{2.204}$$

This Hamiltonian can be simplified after the following assumptions:

(i) - We take the zero of energy at the middle level between the groundstate $|{\rm g}\rangle$ and excited state $|{\rm e}\rangle$ and define $\Omega_{\rm ge} \equiv \Omega_{\rm e} - \Omega_{\rm g}$;

(ii) - Because of the opposite parity of the wave functions associated with the states $|{\rm g}\rangle$ and $|{\rm e}\rangle$ [cf. Fig. 2.9(b) for the RF SQUID and Figs. 2.14(a) and 2.14(b) for the three-Josephson-junction SQUID], we assume $g_{\rm gg} = -\,g_{\rm ee}$;

(iii) - We assume the transition matrix elements to be equal, $g_{\rm ge} = g_{\rm eg}$.

Under these assumptions, we obtain

$$\begin{aligned}\widehat{H}_{\rm T} \approx\ & \hbar\frac{\Omega_{\rm ge}}{2}(|{\rm e}\rangle\langle{\rm e}| - |{\rm g}\rangle\langle{\rm g}|) \\ & + \hbar[g_{\rm ee}(|{\rm e}\rangle\langle{\rm e}| - |{\rm g}\rangle\langle{\rm g}|) + g_{\rm ge}(|{\rm g}\rangle\langle{\rm e}| + |{\rm e}\rangle\langle{\rm g}|)]\, j(\hat{a}^\dagger - \hat{a}) \\ & + \hbar\omega\left(\hat{a}^\dagger\hat{a} + \frac{1}{2}\right). \end{aligned} \tag{2.205}$$

Using the standard definitions $|{\rm g}\rangle \equiv [0,1]^T$ and $|{\rm e}\rangle \equiv [1,0]^T$, it is easy to prove that $|{\rm e}\rangle\langle{\rm e}| - |{\rm g}\rangle\langle{\rm g}| = \hat{\sigma}_z$ and $|{\rm g}\rangle\langle{\rm e}| + |{\rm e}\rangle\langle{\rm g}| = \hat{\sigma}_x$. Hence,

$$\begin{aligned}\widehat{H}_{\rm T} \approx\ & \hbar\frac{\Omega_{\rm ge}}{2}\hat{\sigma}_z \\ & + \hbar g_{\rm ee}\hat{\sigma}_z\, j(\hat{a}^\dagger - \hat{a}) + \hbar g_{\rm ge}\hat{\sigma}_x\, j(\hat{a}^\dagger - \hat{a}) \\ & + \hbar\omega\left(\hat{a}^\dagger\hat{a} + \frac{1}{2}\right), \end{aligned} \tag{2.206}$$

which represents the total Hamiltonian of a flux[59] qubit coupled to a quantum signal in the qubit energy eigenbasis.

To attach a more physical meaning to the Hamiltonian $\widehat{H}_{\rm T}$ of Eq. (2.206), we can attempt to derive it starting from the coordinate system of the qubit diabatic basis $|+\rangle$ and $|-\rangle$.

In Subsec. 2.2.3, we already noticed that in the qubit diabatic basis any external field couples to the qubit via a $\hat{\bar{\sigma}}_z$-type interaction. Employing the quantum small-signal formalism developed here, we can write the general Hamiltonian of a flux

[59]Indeed, such a Hamiltonian is valid for other types of superconducting qubits (e.g., charge qubits [131]).

qubit in the diabatic basis as

$$\widehat{\widehat{H}}_{\rm Q} = \frac{1}{2}\hbar[\epsilon(\hat{\Phi}_{\rm x})\hat{\bar{\sigma}}_z + \delta_{\rm Q}\hat{\bar{\sigma}}_x]\,. \tag{2.207}$$

Given that $\hbar\epsilon$, as defined in Eq. (2.159), is a linear function of the external DC flux bias $\Phi_{\rm x}^{\rm DC}$, we can straightforwardly generalize it to the case of a quantized AC flux as

$$\begin{aligned}\hbar\epsilon(\hat{\Phi}_{\rm x}) &= 2|I_{\rm p}|\left(\Phi_{\rm x}^{\rm DC} - \frac{\Phi_0}{2} + \hat{\Phi}_{\rm x}^{\rm AC}\right)\\ &= \hbar\epsilon\left(\Phi_{\rm x}^{\rm DC}\right) + 2|I_{\rm p}|\hat{\Phi}_{\rm x}^{\rm AC}\,,\end{aligned} \tag{2.208}$$

where $I_{\rm p}$ is given by Eq. (2.160).

Inserting the general expression for $\hbar\epsilon$ given by Eq. (2.208) into the Hamiltonian of Eq. (2.207), using the expression of Eq. (2.184) for $\hat{\Phi}_{\rm x}^{\rm AC}$, and changing $M_{\rm FR}$ with $M_{\rm QR}$, we can write $\widehat{\widehat{H}}_{\rm Q} = \widehat{\widehat{H}}_{\rm A} + \widehat{\widehat{H}}_{\rm B}$, where

$$\widehat{\widehat{H}}_{\rm A} = \frac{1}{2}\hbar\left[\epsilon\left(\Phi_{\rm x}^{\rm DC}\right)\hat{\bar{\sigma}}_z + \delta_{\rm Q}\hat{\bar{\sigma}}_x\right]\,, \tag{2.209a}$$

$$\widehat{\widehat{H}}_{\rm B} = M_{\rm QR}|I_{\rm p}|I_0\hat{\bar{\sigma}}_z\, j(\hat{a}^\dagger - \hat{a})\,. \tag{2.209b}$$

Notably, the Hamiltonian $\widehat{\widehat{H}}_{\rm A}$ resembles the flux qubit Hamiltonian of Eq. (2.168) valid for DC excitations.

The total Hamiltonian of a qubit coupled to a quantized signal in the qubit diabatic basis is then

$$\begin{aligned}\widehat{\widehat{H}}_{\rm T} = &\frac{1}{2}\hbar\left[\epsilon\left(\Phi_{\rm x}^{\rm DC}\right)\hat{\bar{\sigma}}_z + \delta_{\rm Q}\hat{\bar{\sigma}}_x\right]\\ &+ \hbar g_{\rm QR}\hat{\bar{\sigma}}_z\, j(\hat{a}^\dagger - \hat{a})\\ &+ \hbar\omega\left(\hat{a}^\dagger\hat{a} + \frac{1}{2}\right)\,,\end{aligned} \tag{2.210}$$

where the qubit-resonator coupling coefficient is defined as

$$g_{\rm QR} \equiv \frac{1}{\hbar}M_{\rm QR}|I_{\rm p}|I_0\,. \tag{2.211}$$

The total Hamiltonian $\widehat{\widehat{H}}_{\rm T}$ of Eq. (2.210) can be rotated into the energy eigenbasis either by inspection of Fig. 2.15 or by performing the unitary transformation $\widehat{\mathcal{D}}^\dagger(\theta)\ \widehat{\widehat{H}}_{\rm T}\ \widehat{\mathcal{D}}(\theta)$. In this way we obtain

$$\begin{aligned}\widehat{H}_{\rm T} &= \widehat{\mathcal{D}}^\dagger(\theta)\ \widehat{\widehat{H}}_{\rm T}\ \widehat{\mathcal{D}}(\theta)\\ &= \hbar\frac{\Omega_{\rm Q}}{2}\hat{\sigma}_z\\ &\quad + \hbar g_{\rm QR}\cos\theta\,\hat{\sigma}_z\, j(\hat{a}^\dagger - \hat{a}) - \hbar g_{\rm QR}\sin\theta\,\hat{\sigma}_x\, j(\hat{a}^\dagger - \hat{a})\\ &\quad + \hbar\omega\left(\hat{a}^\dagger\hat{a} + \frac{1}{2}\right)\,,\end{aligned} \tag{2.212}$$

which allows us to map back the unknown coefficients of the Hamiltonian of Eq. (2.206). We finally find,

$$\Omega_{\rm ge} = \Omega_{\rm Q} = \sqrt{\delta_{\rm Q} + \epsilon^2 \left(\Phi_{\rm x}^{\rm DC}\right)}\,, \tag{2.213a}$$

$$g_{\rm ee} = g_{\rm QR} \cos\theta\,, \tag{2.213b}$$

$$g_{\rm ge} = -g_{\rm QR} \sin\theta\,. \tag{2.213c}$$

Circuit QED and the Jaynes-Cummings Approximation

The Hamiltonian $\widehat{H}_{\rm T}$ of Eq. (2.212) and its dynamics[60] are the starting point for a large subset of circuit QED applications (not only with flux qubits). It is useful to represent this Hamiltonian in an interaction picture with respect to both qubit and resonator,

$$\hat{a}^\dagger \rightarrow \hat{a}^\dagger\, e^{+j\omega t}\,, \tag{2.214a}$$

$$\hat{a} \rightarrow \hat{a}\, e^{-j\omega t}\,, \tag{2.214b}$$

$$\hat{\sigma}^\mp \rightarrow \hat{\sigma}^\mp\, e^{\mp j\Omega_{\rm Q} t}\,, \tag{2.214c}$$

where $\hat{\sigma}_x = \hat{\sigma}^+ + \hat{\sigma}^-$, $\hat{\sigma}_z = \hat{\sigma}^+\hat{\sigma}^- - \hat{\sigma}^-\hat{\sigma}^+$, and $\hat{\sigma}^+$ and $\hat{\sigma}^-$ are the lowering and raising operators between the qubit energy groundstate $|{\rm g}\rangle$ and excited state $|{\rm e}\rangle$, respectively. In this picture, only the time-dependent interaction terms of $\widehat{H}_{\rm T}$ explicitly appear,

$$\begin{aligned}\widehat{\widetilde{H}}_{\rm T} = {} & \hbar g_{\rm QR} \cos\theta\, \hat{\sigma}_z\, j\left(\hat{a}^\dagger e^{+j\omega t} - \hat{a} e^{-j\omega t}\right) \\ & - \hbar g_{\rm QR} \sin\theta\, \left(\hat{\sigma}^+ e^{+j\Omega_{\rm Q} t} + \hat{\sigma}^- e^{-j\Omega_{\rm Q} t}\right) \\ & \otimes\; j\left(\hat{a}^\dagger e^{+j\omega t} - \hat{a} e^{-j\omega t}\right)\,. \end{aligned} \tag{2.215}$$

This Hamiltonian assumes a particularly simple form when $|\omega| \gg |g_{\rm QR}|$ and $|\Omega_{\rm Q} + \omega| \gg |g_{\rm QR}|$. Under these assumptions and defining the qubit-resonator detuning as $\Delta \equiv \Omega_{\rm Q} - \omega$, we are allowed to apply the so-called rotating wave approximation (RWA),[61] which yields

$$\widehat{\widetilde{H}}_{\rm T} \approx \hbar j \tilde{g}_{\rm QR} \left(\hat{\sigma}^+ \hat{a} e^{+j\Delta t} - \hat{\sigma}^- \hat{a}^\dagger e^{-j\Delta t}\right)\,, \tag{2.216}$$

where $\tilde{g}_{\rm QR} \equiv g_{\rm QR} \sin\theta$.

[60] Studied here in the absence of dissipation. In fact, dissipation constitutes a vast topic of research on its own and will not be discussed in details in this chapter.

[61] Interestingly, it has recently been proposed the realization of an ultra-strong coupling regime of circuit QED [270], where the RWA breaks down. Indeed, such extreme regime of circuit QED, which is not going to be treated in this thesis, seems to be experimentally feasible [271]. *Note added in Fall 2010: A variety of theoretical proposals [272–276] and some very preliminary experiments [277, 278] on the ultra-strong coupling regime of circuit QED has flourished in the past few months. Even if interesting from a purely academical point of view, such a regime will not be useful in applications in the immediate future, in particular in quantum computing. A very large coupling is counter-productive since it requires extremely fast gate operations, which must rely on correspondingly fast electronics, as well as the technical difficulty of effectively switching off the coupling at the end of a gate operation.*

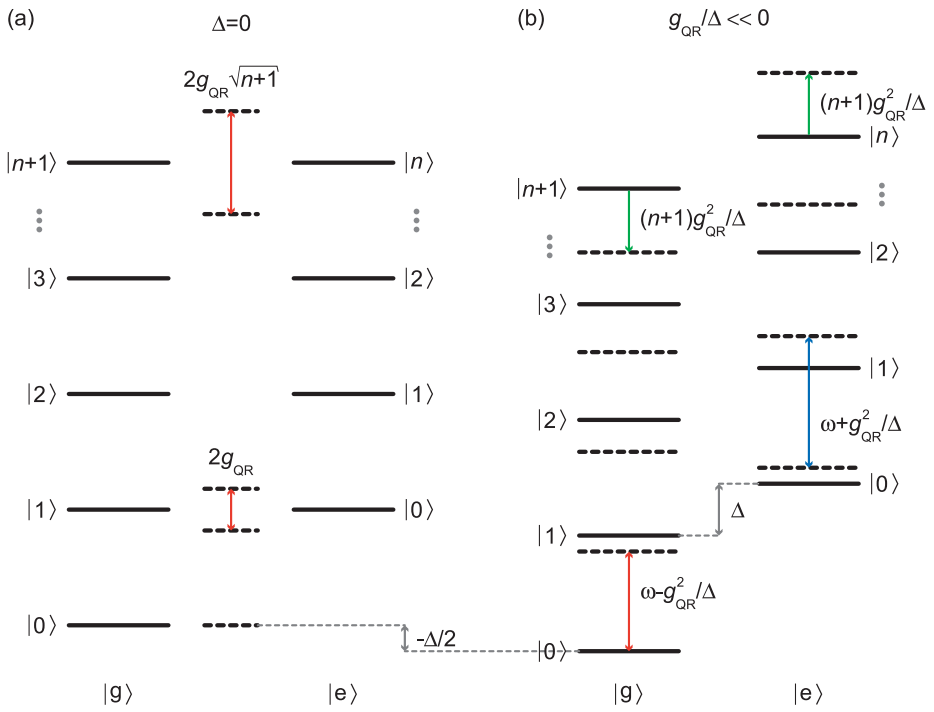

Figure 2.17: The Jaynes-Cummings energy diagram. All quantities are expressed as angular frequencies. **(a)** The resonant regime, $\Delta = 0$. Solid black lines: unperturbed energy levels obtained for $g_{\rm QR} = 0$. Dashed black lines: perturbed energy levels obtained for a finite $g_{\rm QR}$ and associated with the dressed states of Eqs. (2.217a) and (2.217b). The red double arrows indicated the energy separation between the various doublets of the resonant JC ladder. Such an energy scales with $\sqrt{n+1}$ and is smallest for the single excitation states, $|{\rm g}, 1\rangle$ and $|{\rm e}, 0\rangle$, where, according to our convention, $n = 0$. **(b)** The dispersive regime, $g_{\rm QR}/\Delta \ll 1$. Solid black lines: unperturbed energy levels obtained for $g_{\rm QR} = 0$. Dashed black lines: perturbed energy levels obtained for a finite $g_{\rm QR}$ under the dispersive assumption (cf. main text). The global energy offset $-\Delta/2$ is a convention. The red double arrow indicates the "perturbed" $|{\rm g}, 1\rangle$-$|{\rm g}, 0\rangle$ ($|-, 0\rangle$-$|{\rm g}, 0\rangle$) energy separation, which is reduced by a quantity $g_{\rm QR}^2/\Delta$ with respect to the unperturbed case. The blue double arrow indicate the "perturbed" $|{\rm e}, 1\rangle$-$|{\rm e}, 0\rangle$ ($|+, 1\rangle$-$|+, 0\rangle$) energy separation, which is augmented by a quantity $g_{\rm QR}^2/\Delta$ with respect to the unperturbed case. The green single arrows indicate energy level shifts due to higher photonic excitations, scaling linearly with $n+1$. The grey double arrows indicate the various detunings.

At the qubit degeneracy point, where $\cos\theta = 0$, $\sin\theta = 1$ and, thus, $\tilde{g}_{\rm QR} = g_{\rm QR}$, the Hamiltonian of Eq. (2.216) is typically referred to as *Jaynes-Cummings Hamiltonian*. In absence of dissipation processes, the exact diagonalization of $\widehat{\widetilde{H}}_{\rm T}$

yields the groundstate $|\mathrm{g},0\rangle$ and the excited eigenstates (dressed states) [131, 279]

$$\overline{|-,n\rangle} = -\sin\varphi_n\,|\mathrm{e},n\rangle + \cos\varphi_n\,|\mathrm{g},n+1\rangle\ , \tag{2.217a}$$

$$\overline{|+,n\rangle} = \cos\varphi_n\,|\mathrm{e},n\rangle + \sin\varphi_n\,|\mathrm{g},n+1\rangle\ . \tag{2.217b}$$

The corresponding eigenenergies are

$$E_{\mathrm{g},0} = -\hbar\frac{\Delta}{2} \tag{2.218}$$

and

$$E_{\overline{\mp},n} = (n+1)\hbar\omega \mp \hbar\frac{\sqrt{4g_{\mathrm{QR}}^2(n+1)+\Delta^2}}{2}\,, \tag{2.219}$$

respectively.

In the expressions above,

$$\varphi_n \equiv \frac{1}{2}\arctan\left(\frac{2g_{\mathrm{QR}}\sqrt{n+1}}{\Delta}\right)\,. \tag{2.220}$$

Usually, the Jaynes-Cummings (JC) Hamiltonian is accompanied by two types of dissipation processes: qubit decoherence (i.e., energy relaxation and dephasing) and resonator energy relaxation.[62] The first process is governed by a rate γ_{Q}, which depends on the relaxation and dephasing rates characteristic of the specific qubit. The second process directly depends on the loaded quality factor of the resonator and is governed by a rate κ_{R}.[63]

There are two fundamental regimes of the Jaynes-Cummings dynamics. The *resonant regime*, where $\Delta = 0$, and the *dispersive regime*, where $g_{\mathrm{QR}}/\Delta \ll 1$.

(i) $\Delta = 0$.

In this case, the degeneracy of the pair of states with $n+1$ quanta is lifted by $2g_{\mathrm{QR}}\sqrt{n+1}$ due to the qubit-field interaction [131, 279]. In the manifold with a single excitation, Eqs. (2.217a) and (2.217b) reduce to the maximally entangled qubit-field states $\overline{|\mp,0\rangle} = (|\mathrm{g},1\rangle \mp |\mathrm{e},0\rangle)/\sqrt{2}$. An initial state with one photon and the qubit in the groundstate, $|\mathrm{g},1\rangle$, flops into a state with an excited qubit and zero photons, $|\mathrm{e},0\rangle$, and back again at the vacuum Rabi angular frequency g_{QR}/π. Because of such dynamics, states $|\mathrm{g},1\rangle$ and $|\mathrm{e},0\rangle$ are called *bright states* of the JC interaction. In contrast, state $|\mathrm{g},0\rangle$ is referred to as a *dark state* because when the system resides in such a state the JC evolution is frozen [279].

Since the excitation is half atom and half photon, the decay rate of state $\overline{|\mp,0\rangle}$ is given by the average value

$$\Gamma_{\overline{\mp},0} = \frac{\gamma_{\mathrm{Q}}+\kappa_{\mathrm{R}}}{2}\,. \tag{2.221}$$

Strong coupling is achieved when $g \gg \max\{\gamma_{\mathrm{Q}},\kappa_{\mathrm{R}}\}$;

[62] Resonator dephasing has also been studied [252, 280–283] and observed [141, 151], but can be considered to be negligible as compared to energy relaxation [284].

[63] It is worth mentioning that in quantum-optical implementations of cavity QED there is one more relevant rate, that is the inverse dwell time of an atom inside a cavity, $1/t_{\mathrm{dwell}}$ [174]. This rate is oftentimes a major obstacle in experiments and substantial technical efforts must be made to overcome this important issue [53–56, 163, 175–178].

(ii) $g_{\rm QR}/\Delta \ll 1$.

In this case, for $\varphi_n \to 0$ we obtain $\cos\varphi_n \approx 1$ and $\sin\varphi_n \approx \varphi_n = g_{\rm QR}/\Delta$. The eigenstates of the one excitation manifold take then the form [131, 279]

$$\overline{|-,0\rangle} \approx -\frac{g_{\rm QR}}{\Delta}\,|{\rm e},0\rangle + |{\rm g},1\rangle\ , \tag{2.222a}$$

$$\overline{|+,0\rangle} \approx |{\rm e},0\rangle + \frac{g_{\rm QR}}{\Delta}\,|{\rm g},1\rangle\ . \tag{2.222b}$$

The corresponding decay rates can easily be estimated associating with the "quton" (a state more qubit then photon), $|{\rm e},0\rangle$, the decay rate $\gamma_{\rm Q}$ and with the "phobit" (a state more photon then qubit), $|{\rm g},1\rangle$, the decay rate $\kappa_{\rm R}$ and then computing the probability amplitudes. Here, we have adopted the quton-phobit nomenclature introduced by D. I. Schuster [285]. We find

$$\Gamma_{\overline{-,0}} \approx \left(\frac{g_{\rm QR}}{\Delta}\right)^2 \gamma_{\rm Q} + \kappa_{\rm R}\,, \tag{2.223a}$$

$$\Gamma_{\overline{+,0}} \approx \gamma_{\rm Q} + \left(\frac{g_{\rm QR}}{\Delta}\right)^2 \kappa_{\rm R}\,. \tag{2.223b}$$

Figure 2.17 shows the energy diagram for the dressed states associated with the JC Hamiltonian of Eq. (2.216). Figure 2.17(a) refers to the resonant regime, where $\Delta = 0$, while Fig. 2.17(b) refers to the dispersive regime, where $g_{\rm QR}/\Delta \ll 1$. In the figure, the energy associated with state $|{\rm g},0\rangle$ and the entire ladder of energy states appear to be detuned by a global offset $-\Delta/2$ in the dispersive regime as compared to the resonant regime [cf. Eq. (2.218)]. This means that the zero of energy is chosen differently in the resonant and dispersive regime. Such a convention does not affect the calculations, since only energy differences are of physical interest. All quantities reported in Fig. 2.17 can easily be calculated by means of Eqs. (2.218) and (2.219). In particular, the unperturbed energy levels (solid black lines) are obtained when switching off the qubit-resonator interaction, $g_{\rm QR} = 0$. The perturbed energy levels in the resonant regime [dashed black lines in Fig. 2.17(a)] are simply obtained by setting $\Delta = 0$ in Eqs. (2.218) and (2.219).

To gain further insight into the more complex dispersive regime of the JC dynamics, we can define the two Hermitian conjugated superoperators

$$\hat{\Xi}^\dagger \equiv j g_{\rm QR}\hat{\sigma}^+\hat{a}\,, \tag{2.224a}$$

$$\hat{\Xi} \equiv -j g_{\rm QR}\hat{\sigma}^-\hat{a}^\dagger\,. \tag{2.224b}$$

Under dispesive conditions, it is possible to show that the Dyson series for the evolution operator associated with the time-dependent Hamiltonian of Eq. (2.216) can be rewritten in the exponential form

$$\widehat{U} = \exp\left(-\frac{j\,\widehat{\widehat{H}}_{\rm eff}\,t}{\hbar}\right), \tag{2.225}$$

where the effective Hamiltonian $\widehat{\widehat{H}}_{\rm eff}$ is given by

$$\widehat{\widehat{H}}_{\rm eff} = \hbar\frac{[\hat{\Xi}^\dagger,\hat{\Xi}]}{\Delta}\,. \tag{2.226}$$

The commutator $[\hat{\Xi}^\dagger, \hat{\Xi}]$ can be expanded as

$$[\hat{\Xi}^\dagger, \hat{\Xi}] = g_{\rm QR}^2 \left(\hat{\sigma}^+ \hat{\sigma}^- \hat{a} \hat{a}^\dagger - \hat{\sigma}^- \hat{\sigma}^+ \hat{a}^\dagger \hat{a} \right) . \tag{2.227}$$

Applying the commutation relation for bosonic operators of Eq. (2.81), remembering that $\hat{\sigma}^+ \hat{\sigma}^- = (\hat{\sigma}_z + \mathbf{I}_2)/2$, where $\mathbf{I}_2$ is the 2×2 identity matrix, and neglecting all terms proportional to $\mathbf{I}_2$ we finally obtain the effective Hamiltonian

$$\widehat{\widetilde{H}}_{\rm eff} = \hbar \frac{g_{\rm QR}^2}{\Delta} \hat{\sigma}_z \left(\hat{a}^\dagger \hat{a} + \frac{1}{2} \right) . \tag{2.228}$$

The term proportional to the number operator $\hat{a}^\dagger \hat{a}$ represents the so-called AC-Stark or -Zeeman shift of the qubit levels [also called dynamic shift; cf. Fig. 2.17(b)]. The AC-Stark shift refers to the case of charge qubits (electric coupling) and the AC-Zeeman shift to the case of flux qubits (magnetic coupling). The offset $\hbar g_{\rm QR}^2/2\Delta$ is the qubit Lamb shift due to vacuum fluctuations. In the literature, the result of Eq. (2.228) is usually found by means of the Schrieffer-Wolff unitary transformation followed by Taylor expansion to second order in the coupling coefficient (standard second-order perturbation theory; e.g., cf. Ref. [131]). If not otherwise stated, we prefer to use the approach outlined above because it is more convenient from the calculation point of view.

The AC-Stark or -Zeeman shift for states $|-,0\rangle$-$|{\rm g},0\rangle$ (associated with the qubit groundstate $|{\rm g}\rangle$ and due to a single photonic excitation) can also be found by expanding the energy difference $E_{\overline{-,0}} - E_{\rm g,0}$ [cf. Eqs. (2.218) and (2.219) and Fig. 2.17(b)] in a Maclaurin series up to first order,

$$\begin{aligned} E_{\overline{-,0}} - E_{\rm g,0} &= \hbar\omega - \hbar \frac{\sqrt{4g_{\rm QR}^2 + \Delta^2}}{2} + \hbar \frac{\Delta}{2} \\ &= \hbar\omega - \hbar \frac{\Delta}{2} \sqrt{1 + \left(2 \frac{g_{\rm QR}}{\Delta} \right)^2} + \hbar \frac{\Delta}{2} \\ &\approx \hbar\omega - \hbar \frac{\Delta}{2} \left[1 + \frac{1}{2} \left(2 \frac{g_{\rm QR}}{\Delta} \right)^2 \right] + \hbar \frac{\Delta}{2} \\ &= \hbar \left(\omega - \frac{g_{\rm QR}^2}{\Delta} \right) , \end{aligned} \tag{2.229}$$

where we have used the property $\sqrt{1+x} \approx 1 + x/2$ for $x \to 0$ and the substitution $x = (2g_{\rm QR}/\Delta)^2$. In the case of states $|+,1\rangle$-$|+,0\rangle$ (associated with the qubit excited state $|{\rm e}\rangle$ and due to a single photonic excitation), the result of an expansion similar to that of Eq. (2.229) gives $\hbar(\omega + g_{\rm QR}^2/\Delta)$. These results can be generalized to the case of states with higher photonic excitations $\overline{|\mp, n\rangle}$, where the state dynamic shift scales linearly with the number of photons in the resonator, $(n+1)\, g_{\rm QR}^2/\Delta$ [cf. Fig. 2.17(b)].

2.4 Summary and Conclusions

In summary, the main facts about circuit QED which we should bear in mind as a guide for the rest of the thesis are:

1. The concept of quality factor expressed by Eq. (2.19);
2. The concept of impedance transformation of Eq. (2.31);
3. The set of Eqs. (2.63)- (2.66), which fully characterize the class of $\lambda/2$ resonators and the set of Eqs. (2.71a)-(2.71d), which fully characterize the class of $\lambda/4$ resonators;
4. The fundamental set of rules for the construction of a quantum-mechanical LC-resonator, Eqs. (2.98) and (2.99) and the corresponding Fig. 2.5;
5. Equations (2.100) and (2.101) for the synthesis of quantum-mechanical transmission line resonators;
6. Equations (2.109) and (2.110) for the description of generic quantum signals propagating on a transmission line;
7. The expressions for the quantum-mechanical mean value and variance of a given quantum signal, Eqs. (2.111) and (2.112);
8. The RCSJ model of Fig. 2.16(b);
9. The Hamiltonians of Eqs. (2.127) and (2.148) representing the quantum-mechanical RF SQUID and three-Josephson-junction SQUID, respectively;
10. The qubit Hamiltonian in the diabatic basis of Eq. (2.168) and the rotation sketched in Fig. 2.15;
11. The expression at the basis of the quantum small-signal formalism, Eq. (2.185);
12. The interaction Hamiltonian for a flux quantum circuit of Eq. (2.193);
13. The total Hamiltonian for a qubit-resonator system given by Eq. (2.212), which leads to the JC Hamiltonian.

In conclusion, in this chapter we have realized a complete classification of the basic quantum circuits needed in circuit QED applications through the development of a consistent quantum theory of networks.

Chapter 3

Correlation Homodyne Detection at Microwave Frequencies: Experimental Setup

Circuit QED experiments are technically demanding due to the necessity of operating sensitive devices based on micro- or nano-structures at high (microwave) frequencies, very low temperatures (a few tens of mK), very low noise, and high vacuum environments. In addition, the challenge of dealing with ultra-weak signals characterized by powers on the order of a few aWplaces circuit QED at the cutting edge of state-of-the-art microwave technology.

Starting from the mid 80's, there have been a succession of milestone experiments showing that the tasks required for the ultimate implementation of circuit QED experiments with signals at the quantum-level were feasible. The experimental test of the quantum behavior of the phase difference across a Josephson tunnel junction has opened the avenue to microwave spectroscopy of Josephson circuits [286]. Within the same work, it has been shown that the reduction of noise disturbance brought about by room-temperature electronics is a fundamental condition for the observation of quantum effects in micro-circuits. Another important step forward in quantum electronics has been achieved with the implementation of the Josephson parametric amplifier [193], which has largely contributed to the development of ultra-weak signal detection. The invention of the radio-frequency single-electron transistor [287] and microstrip SQUID amplifier [288] has boosted the search for quantum-limited detectors. This search has witnessed further progress with the development of the Josephson bifurcation amplifier [110, 211–220] and continues growing in the realms of circuit QED and nanomechanics [194–210].

A common feature to all these achievements is the accurate design of the experimental setup. Therein lies the bias for the development of a correlation homodyne apparatus at microwave frequencies, which constitutes the experimental bulk of this thesis. Our correlation homodyne scheme extends standard circuit QED setups based on a single detection chain to the richer domain of a double detection chain. The theoretical analysis and technical specifications of the basic equipment required for the implementation of such an apparatus constitute the main topic of this chapter.

The chapter is organized as follows. In Sec. 3.1, we present two types of microwave beam splitters based on a three- and four-port network, respectively. These

are the Wilkinson power divider and the 180° hybrid ring. In particular, we develop a full classical and quantum theory of the noise properties for the Wilkinson power divider. In Sec. 3.2, we describe the key devices used in our detection chain and show the measurement of a relevant set of their parameters. The key devices are: the cryogenic circulators, the RF HEMT (cryogenic) amplifiers, the cold feedthroughs, the RF multioctave band amplifiers, the mixers, and the IF FET amplifiers. Section 3.3 is a short "bridge" between the end of this chapter and the beginning of the following one, where the detection chain analyzed here is used to investigate the properties of vacuum fluctuations at microwave frequencies.

The material discussed in this chapter is entirely unpublished.[1] The author has developed the noise theory of microwave beam splitters presented within the chapter and has extensively contributed to the design of the experimental setup, which is based on his original idea triggered by discussions with Enrique Solano [289]. In addition, the author has largely participated in the hardware realization of the setup (development of the beam splitters, cabling, cold feedthroughs, cryogenic, and room temperature electronics). This was completed with the help of Edwin P. Menzel, who largely contributed to the measurement software, Miguel Á. Araque Caballero, and Achim Marx. Frank Deppe has also assisted with fruitfull discussions and technical support with cryogenics and software. Several other students have contributed to the realization of the setup (cf. Preface). All data shown in this chapter were taken and retrieved by the author, except for the room temperature amplifiers data and their corresponding 1 dB compression point measurements. These were taken by Miguel Á. Araque Caballero with the help of Edwin P. Menzel and were independently retrieved by the author. The author acknowledges a discussion with J. M. Martinis and D. Sank, who helped proving the four-port scattering matrix of the Wikinson power divider.

3.1 Microwave Beam Splitters

In chapter 2, we have introduced the basic quantum devices required for circuit QED experiments. However, in order to realize a complete optical table on a chip an additional class of devices is needed: the microwave beam splitters.

The flexibility in patterning complex structures on a chip by lithography techniques allows for the design of a variety of microwave beam splitters.[2] Here, we consider a subset of microwave beam splitters: the Wilkinson power divider, a three-port network (cf. Subsec. 3.1.1), and the 180° hybrid ring, a four-port network (cf. Subsec. 3.1.2). In the case of the Wilkinson power divider we develop a detailed classical and quantum noise model.

The standard mathematical representation of microwave beam splitters and the study of their noise properties is based on the concept of scattering matrix. We will extensively use the scattering matrix formalism throughout this chapter. We recommend the reader not acquainted with this concept to consult Refs. [227, 264, 290] for a basic introduction. Here, we only remind that any signal s (voltage or current) entering into a device is designated as *incident signal* and indicated by the

[1] *Note added in Fall 2010: A few elements of the experimental setup have now been shown in Ref. [162].*

[2] In this chapter, we only consider quasi 1D structures. The entire class of 3D waveguide beam splitters is thus not treated here [227].

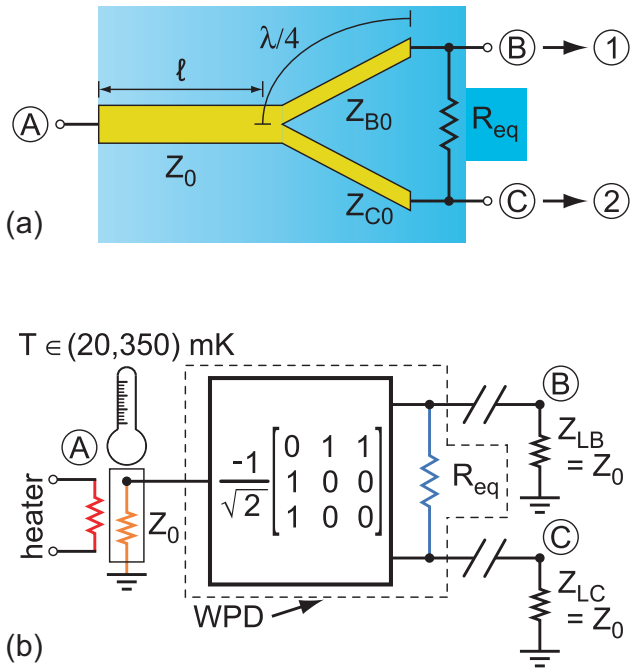

Figure 3.1: Basic Wilkinson power divider (referred to as WPD in the figure). **(a)** A: input port. B and C: output ports. The signals at ports B and C are fed into channels 1 and 2 of the detection chain, respectively (cf. bottom part of Fig. 3.10). An input transmission line with indefinite length ℓ and characteristic impedance Z_0 is connected in parallel with two output $\lambda/4$ lines with characteristic impedances Z_{B0} and Z_{C0}, respectively. Ports B and C are connected with a resistance R_{eq}. **(b)** In the experiments, port A is terminated into a purely real (resistive) impedance Z_0, which constitutes the primary noise source and is associated with the noise voltage u_{n} (cf. main text). The temperature of the primary noise source is controlled by means of a heater and continuously monitored with a RuO thermometer. The temperature typically varies between 20 and 350 mK. The dashed box delimits the Wilkinson power divider including the resistance R_{eq}. The scattering matrix for a Wilkinson power divider operated at its center frequency is indicated [cf. Eq. (3.7)]. After being connected to other devices (assumed to be impedance matched and schematically indicated by slashes in the figure), the output ports B and C are finally terminated into two load impedances $Z_{\mathrm{LB}} = Z_{\mathrm{LC}} = Z_0$. Cf. also the left part of Fig. 3.16 for more details.

symbol s^+. In contrast, any signal exiting from a device is designated as *reflected or scattered signal* and indicated by the symbol s^-.

3.1.1 The Wilkinson Power Divider

Wilkinson three-port splitters belong to the class of three-port junctions (also known as T-junctions)[3] referred to as power dividers. This nomenclature, owing its origin to historical reasons and engineering applications, is rather unfortunate because it seems to imply that Wilkinson three-port splitters act only on the power of an incoming signal. In reality, they act *only* on the amplitude and phase of any given input signal. By extension, the power expressed in decibel (dB) at one output of the splitter can be computed and found to be (nominally) 3 dB lower than at the input. Bearing this caveat in mind, we hereafter adopt the nomenclature used in all standard books and refer to Wilkinson three-port splitters as Wilkinson power dividers. Oftentimes, Wilkinson power dividers are utilized backwards, in which case they are called Wilkinson power combiners.

Since any given T-junction is made of three ports ($N = 3$), it is completely characterized by a scattering matrix of the third order, $\mathbf{S}_{\mathrm{T}} = [S_{pq}]$ with $p, q = \mathrm{A}, \mathrm{B}, \mathrm{C}$. For a T-junction to be well-defined six of the S_{pq} elements have to be independent (i.e., $2 \times N$) [290]. A T-junction is said to be *reciprocal* when, $\forall p, q$, its scattering matrix $\mathbf{S}_{\mathrm{T}}$ is symmetrical about the leading diagonal, i.e., $S_{pq} = S_{qp}$. This has the important consequence that interchanging the input and output ports of the junction does not change its transmission properties. The T-junctions used to implement power dividers are reciprocal.

Theorem 3.1.1 *Fundamental theorem for a lossless reciprocal T-junction: It is impossible to match all three ports of the T-junction simultaneously.*

Proof The proof of this theorem follows straightforwardly from the *unitary* character of the scattering matrix of a lossless T-junction,

$$\mathbf{S}_{\mathrm{T}}^{*}\mathbf{S}_{\mathrm{T}} = \mathbf{I}_3\,, \tag{3.1}$$

where $\mathbf{I}_3$ is the 3×3 identity matrix. Notably, the unitary property expressed by Eq. (3.1) is valid for any generic *lossless* N-junction. A T-junction is said to be completely matched if the input impedance of any port is unity when matched loads are connected to the other two ports. If we start with the assumption that all three ports of a T-junction are matched, then, $\forall p$, all diagonal elements of its scattering matrix must be equal to zero, $S_{pp} = 0$. In this case,

$$\mathbf{S}_{\mathrm{T}} = \begin{bmatrix} 0 & S_{\mathrm{AB}} & S_{\mathrm{AC}} \\ S_{\mathrm{AB}} & 0 & S_{\mathrm{BC}} \\ S_{\mathrm{AC}} & S_{\mathrm{BC}} & 0 \end{bmatrix}\,, \tag{3.2}$$

where the reciprocity property has been already used. Since $\mathbf{S}_{\mathrm{T}}$ is unitary, the off-diagonal elements of $\mathbf{S}_{\mathrm{T}}^{*}\mathbf{S}_{\mathrm{T}}$ must be zero. This means that the sum of the products

[3]This does not mean that such devices are based on Josephson tunnel junctions. There are no Josephson junctions embedded in any of the beam splitters described in this chapter. However, N-junction is the commonly used name for multi-port microwave devices characterized by N ports [290].

of the complex conjugate elements in any row of $\mathbf{S}_{\mathrm{T}}$ with the elements in another row is zero. For example, from the (A,B) element of $\mathbf{S}_{\mathrm{T}}^{*}\mathbf{S}_{\mathrm{T}}$,

$$S_{\mathrm{AC}}^{*}\, S_{\mathrm{BC}} = 0\,, \tag{3.3}$$

it follows that either S_{AC} or S_{BC} must be zero,[4]

$$S_{\mathrm{AC}} = 0 \;\vee\; S_{\mathrm{BC}} = 0\,. \tag{3.4}$$

If this condition were true, it would mean that not all diagonal elements of $\mathbf{S}_{\mathrm{T}}^{*}\mathbf{S}_{\mathrm{T}}$ are unity. For example, if $S_{\mathrm{AC}} = 0$, $S_{\mathrm{AB}}^{*}S_{\mathrm{AB}} = 1$ for the (A,A) element of $\mathbf{S}_{\mathrm{T}}^{*}\mathbf{S}_{\mathrm{T}}$ to be unity. Consequently, $S_{\mathrm{BC}}^{*}S_{\mathrm{BC}} = 0$ for the (B,B) element of $\mathbf{S}_{\mathrm{T}}^{*}\mathbf{S}_{\mathrm{T}}$ to be unity. This finally leads to the absurd conclusion that the (C,C) element of $\mathbf{S}_{\mathrm{T}}^{*}\mathbf{S}_{\mathrm{T}}$, given by $S_{\mathrm{AC}}^{*}S_{\mathrm{AC}} + S_{\mathrm{BC}}^{*}S_{\mathrm{BC}}$, must be zero. Being this finding against the unitary property of all lossless T-junctions, we can safely state that the diagonal elements of $\mathbf{S}_{\mathrm{T}}$ must not all vanish, thus proving the theorem. Q.D.E.

More in general, one can prove that *two* of the transmission coefficients S_{AB}, S_{BC}, and S_{AC} must simultaneously vanish in order to realize a completely matched T-junction [227]. This allows us to attach a more physical meaning to the theorem, which simply means that a fully matched T-junction would not function as a T-junction. It can also be seen, by the use of similar arguments, that any two of the diagonal elements of $\mathbf{S}_{\mathrm{T}}^{*}$ can vanish iff the third port of the T-junction is completely decoupled from the junction itself [290].

In the light of the just proven theorem, we can conclude that it is possible to construct a lossless power divider (or splitter) simply taking a lossless transmission line and dividing it into two output lines at some desired point. The price to be paid for such a simple design is twofold: First, the output ports cannot be matched if the input port is matched; second, there is no isolation between the two output ports [227]. Isolation is an important condition so that a reflected signal at one output port does not couple into the other output port, and vice versa.

E. Wilkinson has developed an N-junction power divider that allows to *equally* split the input signal among the output ports, where all N ports are impedance *matched*, and the output ports are *isolated* [291]. In these terms, the Wilkinson power divider seems to represent the ideal beam splitter. The secret feature of the Wilkinson power divider, e.g., for $N = 3$, is the use of a resistor connected between the two output ports. The presence of a resistive element has the nontrivial consequence to enable full matching and isolation. In this case, the three-port scattering matrix (as we like to define it: the *reduced* scattering matrix) of such a splitter can be shown to be a *nonunitary* matrix. This nonunitary reduced three-port scattering matrix is the matrix typically used to represent Wilkinson power dividers operated in the classical regime. It is worth mentioning that the resistor adds no resistive loss to the power split, so an ideal Wilkinson divider is 100% efficient [227]. Consequently, the reason behind the seemingly nonunitary scattering matrix of a Wilkinson power divider cannot be attributed to losses in the resistor, as oftentimes incorrectly believed. As we shall show below, a more correct representation of the Wilkinson power divider, particularly useful in the quantum regime, can be obtained

[4]Here, $\vee$ represents a *vel*, i.e., an inclusive OR.

when considering the resistor as the termination of a fourth port of the divider. Under this assumption, the *complete* scattering matrix of the Wilkinson power divider is a four-port unitary matrix.

A number of different versions and configurations of the Wilkinson power divider has been developed over the years. In particular, the two-way multisection broadband design created by S. B. Cohn is among the most popular classes of Wilkinson power dividers and is used in a variety of practical implementations [292]. Because of its large bandwidth, this type of splitter is also the one utilized in most of our experiments.

In order to avoid unnecessary complications, we prefer to consider the basic Wilkinson power divider here instead of the more involved Cohn's design. In fact, we can assume the Wilkinson and Cohn power dividers to be formally equivalent, being only their characteristic operational bandwidths significantly different.

The basic Wilkinson power divider is illustrated in Fig. 3.1(a). It consists of two quarter-wave transmission line sections with characteristic impedances Z_{B0} and Z_{C0} connected in parallel with an input transmission line, which has a characteristic impedance Z_0 and undefined length ℓ. All transmission lines are assumed to be lossless. In typical applications, $Z_0 = 50\,\Omega$. In addition, a resistor with equivalent resistance R_{eq} is connected between ports B and C and the output ports are assumed to be terminated in suitable load impedances Z_{LB} and Z_{LC}, respectively [cf. Fig. 3.1(b)]. After a tedious calculation (cf. Ref. [227] for a detailed derivation), we can express all impedances in terms of R_{eq} as

$$Z_{\mathrm{B0}} = K\sqrt{R_{\mathrm{eq}} Z_0}\,, \tag{3.5a}$$

$$Z_{\mathrm{C0}} = \frac{1}{K}\sqrt{R_{\mathrm{eq}} Z_0}\,, \tag{3.5b}$$

$$Z_{\mathrm{LB}} = \frac{K^2 R_{\mathrm{eq}}}{K^2+1}\,, \tag{3.5c}$$

$$Z_{\mathrm{LC}} = \frac{R_{\mathrm{eq}}}{K^2+1}\,, \tag{3.5d}$$

where K is the splitting factor (cf. Ref. [227]). If we do not require port A to be matched at all frequencies, the value of the resistance R_{eq} can be chosen arbitrarily. For example, a 3 dB power divider is obtained by choosing $K^2 = 1$. In this case, if we specify the load impedances to be matched, $Z_{\mathrm{LB}} = Z_{\mathrm{LC}} = Z_0$, from Eq. (3.5c) it follows that $R_{\mathrm{eq}} = 2Z_0$. From Eq. (3.5a) we then find that $Z_{\mathrm{B0}} = Z_{\mathrm{C0}} = \sqrt{2}Z_0$. These values allow for the synthesis of a basic Wilkinson power divider, whose full functionality is guaranteed only in the close vicinity of the center frequency f_0 set by the quarter-wave transmission line sections. Because of such quarter-wave sections, the so obtained power divider is a narrow-band device. Many tricks can be applied in order to extend the operational frequency range and make the power divider broader, but we will not delve into such engineering details here (e.g., the interested reader can cf. Refs. [227, 292]).

Right at the center frequency f_0, the reduced three-port scattering matrix $\widetilde{\mathbf{S}}_{\mathrm{WPD}}$ of the Wilkinson power divider of Fig. 3.1(a) can be derived by means of the so-called even/odd mode analysis. The calculation is very cumbersome (the reader can go through it step by step following the excellent tutorial by J. Stiles, cf. Ref. [293]).

Here, we limit ourselves to give only the final result,

$$\widetilde{\widetilde{\mathbf{S}}}_{\mathrm{WPD}} = -\frac{j}{\sqrt{2}}\begin{bmatrix} 0 & 1 & 1 \\ 1 & 0 & 0 \\ 1 & 0 & 0 \end{bmatrix}. \tag{3.6}$$

Notably, this scattering matrix is nonunitary, $\widetilde{\widetilde{\mathbf{S}}}^{*}_{\mathrm{WPD}}\widetilde{\widetilde{\mathbf{S}}}_{\mathrm{WPD}} \neq \mathbf{I}_3$. Even if so, this is the matrix presented in standard microwave textbooks (e.g., cf. Ref. [227]). In order to recover a unitary scattering matrix, in the next subsection we will introduce a complete model of the Wilkinson power divider, where the resistor R_{eq} constitutes the termination of a fourth *internal* port of the divider. This model has important consequences on the noise properties of the Wilkinson power divider and, thus, for the experiments to be discussed in chapter 4.

Additionally, it is important to mention that, while developing the noise analysis of the basic Wilkinson power divider, we will deal only with *real* input and output voltages and/or currents, instead of complex phasors. This assumption guarantees that, when promoting the classical voltages and currents to the corresponding quantum-mechanical operators, such operators are always *Hermitian*. In order to fulfill the Hermitian condition, we will thus multiply the scattering matrix of Eq. (3.6) by a global phase $-j = \exp(-\pi/2)$, which, as such, does not affect the general validity of our derivations. Notably, global phases do not play any active role when considering the correlation measurements to be shown in the next chapter. Hence, the matrix to be used will be

$$\widetilde{\mathbf{S}}_{\mathrm{WPD}} = -\frac{1}{\sqrt{2}}\begin{bmatrix} 0 & 1 & 1 \\ 1 & 0 & 0 \\ 1 & 0 & 0 \end{bmatrix}. \tag{3.7}$$

The Wilkinson Power Divider Noise Model

In standard room-temperature applications, the scattering matrix given by Eq. (3.7) is sufficient to characterize the properties of a Wilkinson power divider. However, the experiments to be described in chapter 4 have been performed at very low temperatures. The main aim of those experiments is to study the cross-over from thermal states to vacuum states at microwave frequencies in a range between approximately 4.5 and 7.5 GHz and to characterize the quantum-mechanical properties of microwave beam splitters. In that framework, we will be able to show that the matrix of Eq. (3.7) does not suffice to represent a quantum-mechanical Wilkinson power divider.

In this subsection, we will develop the bulk of the quantum theory of the Wilkinson power divider based on a thorough noise analysis. Although the analysis developed here is for a basic Wilkinson power divider, a version of the two-way multisection broadband divider of Cohn's class is used in the actual experiments. The Cohn-type power divider is preferred over the simple Wilkinson power divider because of its wide operational frequency range.

Before delving into the noise theory of the Wilkinson power divider, we start describing the wiring and a few other technical properties of the device used in the

Table 3.1: MITEQ-USA two-way power divider model PD2-2000/18000-30S: nominal specifications [294]. The insertion loss is defined in terms of the scattering parameters as $10\log[|S_{\mathrm{BA}}|^2/(1-|S_{\mathrm{AA}}|^2)]$. The isolation is $10\log|S_{\mathrm{BC}}|$. The voltage standing-wave ratio (VSWR) is a measure of the amount of reflections at a given port. VSWR = 1 means no reflections (a perfect match). VSWR = 1.5 means $\simeq 14\,\mathrm{dB}$ return loss, i.e., 20 % of the signal (voltage) or 4 % of the power reflected back. VSWR = ∞ means total reflection (a short or open circuit).

frequency range (GHz)	insertion loss (dB, Max.)	isolation (dB, Typ.)	input VSWR (-)	output VSWR (-)
$2-18$	0.8	16	1.5 : 1	1.5 : 1

experiments. This is important to understand the environment in which the divider is operated. We opted for a commercial device the fabrication and packaging of which was realized by MITEQ-USA. The nominal specifications of the device are reported in Table 3.1.

As shown in Fig. 3.1(b) and in the left part of Fig. 3.16, the first steps of our experiments are:

1. The input port A of the power divider is terminated into a purely real matched load impedance Z_0.[5] Such a termination is a broadband[6] $50\,\Omega$ resistor produced by HUBER+SUHNER [295] with SMA precision connector. Since the termination is not specified for very low temperature (a few tens of mK) applications, during our experiments we always monitor the DC resistance of an identical termination, which is cooled to the same temperature of the power divider input termination. In this way, we assure that the termination does not become superconducting. The input termination Z_0 represents the noise source under investigation;

2. The power divider is heat sunk to the mixing chamber stage of a homemade dilution refrigerator. The dilution refrigerator used in our experiments has been developed entirely at the Walther-Meissner-Institut by K. Uhlig, A. Marx, C. Probst, and S. Höß. The mixing chamber stage can reach a base temperature $T = T_{\mathrm{b}} \lesssim 20\,\mathrm{mK}$. The power divider is screwed to a tempered-silver plate (cf. left part in Fig. 3.16) directly attached to the mixing chamber (not shown);

3. The input termination Z_0 is clamped by means of a gold-plated OFHC[7]-copper holder. A resistive heater [cf. red resistor in Fig. 3.1(b)] is then attached to the holder by means of a silver strap. The heater, an SMD 0402 component ($1.0\times0.5\,\mathrm{mm}$) of $1\,\mathrm{k}\Omega$, allows us to accurately control the temperature of the

[5] In this case, some authors redefine $Z_0 = R_0$. In this thesis, for the sake of generality, we prefer to keep on using the impedance notation Z_0.

[6] At least at room temperature.

[7] Oxygen-free high-conductive.

termination, i.e., the temperature of our noise source. Typically, we vary the termination temperature in a range comprised between approximately 20 and 350 mK;

4. The temperature of the Z_0 termination is measured by means of a RuO thermometer directly screwed to the termination clamp (cf. Fig. 3.16). The design and precise calibration of the thermometer were performed by K. Neumaier. We notice that the effective electronic temperature of the resistor cannot directly be accessed. In fact, within calibration errors, we can only measure the temperature T of the termination clamp. At low temperatures [$T \in (20, 50)$ mK], the termination electronic temperature $\widetilde{T}$, i.e., the real temperature of the resistor, is usually approximately equal to the measured temperature, $\widetilde{T} \approx T$. At high temperatures [$T \in (150, 350)$ mK], the heating stabilization time in our experiments is not long enough to let the system reach a complete thermodynamical equilibrium (cf. chapter 4). We can thus assume, in this case, that the termination electronic temperature $\widetilde{T}$ is slightly lower than the measured temperature, $\widetilde{T} \lesssim T$. In general, we can model the resistor electronic temperature as

$$\widetilde{T} = T - \eta(T - T^{\min}) \,, \tag{3.8}$$

where η accounts for a temperature gradient between the resistor clamp and the resistor itself and $T^{\min}$ is the minimum measured temperature, $T^{\min} \equiv \min\{T\}$. In the light of the discussion which brought to the model of Eq. (3.8) and assuming a reasonable upper bound for η of 10%, we expect $0 < \eta < 0.1$. It is also possible to compute a mean temperature difference between clamp and resistor as

$$\begin{aligned} \overline{\Delta T} &= -\frac{1}{T^{\max} - T^{\min}} \int_{T^{\min}}^{T^{\max}} dT\, \eta(T - T^{\min}) \\ &= -\frac{\eta}{2}(T^{\max} - T^{\min}) \,, \end{aligned} \tag{3.9}$$

where $T^{\max}$ is the maximum measured temperature, $T^{\max} \equiv \max\{T\}$. We expect the quantity $\overline{\Delta T}$, which also accounts for possible slight calibration errors, to be small (a few mK) and generally negative (cf. chapter 4 for the experimental results);

5. Finally, Fig. 3.1(b) shows that the output ports B and C of the power divider are connected to two transmission lines. Those lines can contain a number of microwave devices such as circulators, amplifiers, mixers, and so forth (slashes) and are ultimately terminated in the matched load impedances Z_{LB} and Z_{LC}, respectively. If all devices between the divider output ports and the load impedances are matched, we can disregard the presence of such devices for the moment and analyze the circuit as if it were directly terminated into Z_{LB} and Z_{LC}.[8] For convenience, the standard scattering matrix of the Wilkinson power divider [Eq. (3.7)] is reported again in Fig. 3.1(b), where the dashed black box indicates the boundaries of the divider, including resistor R_{eq}.

[8] In reality, of course, the signals will change according to the gain of the amplifiers and the global attenuation of the lines, both disregarded here.

Following the steps enumerated above, the Z_0 termination is employed as a noise source generating a thermal state $|\gamma\rangle$ and, when the temperature T is low enough, the vacuum state $|0\rangle$.[9] Trivially speaking, the signal generated at the power divider input port is split by the divider and, after being transmitted through the output matched transmission lines, is measured as a voltage on the load impedances $Z_{\rm LB}$ and $Z_{\rm LC}$. The topology of the entire circuit of Fig. 3.1(b) is equivalent to that of a tripolar double bipole. As a consequence, the circuit can be represented diagrammatically as in Figure 3.3, where $v_{\rm B}$ and $v_{\rm C}$ constitute the voltages to be measured. We now attempt to rigorously derive those voltages in terms of all other circuit parameters. In order to achieve this goal, we proceed according to the fundamental principles of classical network theory and theory of electronic circuits [227, 264, 296]. The procedure is visualized in Figs. 3.2, 3.3, 3.4, and 3.5.
These are the main steps:

(i) First, we derive the equivalent circuit model of a noisy resistor, both in the classical and quantum regime. In general, any given resistor $r_{\rm n}$ [cf. Fig. 3.2(a)] at absolute temperature T exhibits voltage (current) fluctuations $v_{\rm n}$ ($i_{\rm n}$) due to thermal Johnson-Nyquist noise. This is the electronic noise generated by the thermal agitation of the charge carriers (usually the electrons) inside an electrical conductor at equilibrium, which happens regardless of any applied voltage. Thermal noise is approximately white, meaning that the power spectral density is nearly uniform throughout the frequency spectrum. Additionally, the amplitude of the signal has very nearly a Gaussian probability density function.

Classical regime. In the white-noise frequency limit, the effective or root mean square (RMS) thermal noise voltage and current associated with resistor $r_{\rm n}$ over a frequency bandwidth $\mathrm{BW} = f_2 - f_1$ can be obtained analyzing the circuits of Figs. 3.2(b), 3.2(c), and 3.2(d). Following the basic arguments described in the seminal work by H. Nyquist [297], we first terminate the noisy resistor $r_{\rm n}$ into a load impedance $Z_{\rm L}$ [cf. Fig. 3.2(b)]. We then substitute the noisy resistor $r_{\rm n}$ by a Thévenin equivalent circuit given by an ideal noiseless resistor r in series with a noise voltage source $v_{\rm n}$. We assume the load impedance $Z_{\rm L}$ to be matched to resistor r, $Z_{\rm L} = r$, and the entire circuit to be in thermodynamic equilibrium at temperature T [cf. Fig. 3.2(c)]. In this case, the current flowing on the loaded circuit can easily be evaluated noting that the voltage $v_{\rm n}$ is equally divided between r and $Z_{\rm L}$,

$$i_{\rm L} = v_{\rm n}/2r\,. \tag{3.10}$$

A similar result suffices in the inverted scenario, where the noisy resistor plays the role of load impedance and viceversa. In the direct scenario, there is a power flow from the left to the right side of the circuit and, obviously, an opposite flow happens in the inverted scenario. The two flows must be equal due to the thermodynamic equilibrium condition [297]. In real applications, the load impedance $Z_{\rm L}$ is the input impedance of a detector which absorbs the power generated by the noisy resistor and, thus, allows one to measure the resistor noise. In order to consider only one of the two simultaneous flows, we can invoke the transformation of impedances of Eq. (2.31) and break the circuit

[9] These states are obviously multi-mode states of the microwave field.

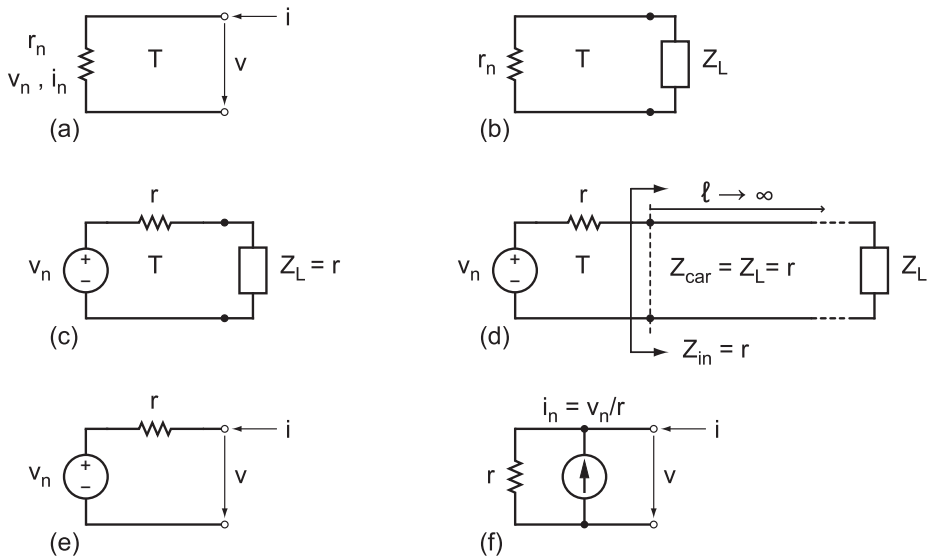

Figure 3.2: The classical and quantum Nyquist theorems. **(a)** Circuit diagram for a noisy resistor $r_{\rm n}$ with input port voltage v and current i in thermodynamic equilibrium at temperature T. $v_{\rm n}$ and $i_{\rm n}$): voltage and current fluctuations due to thermal Johnson-Nyquist noise. **(b)** The noisy resistor $r_{\rm n}$ is terminated into a load impedance $Z_{\rm L}$. **(c)** The noisy resistor is substituted by its Thévenin equivalent circuit characterized by the series of a noise voltage source $v_{\rm n}$ and an ideal resistor r, and the load impedance is assumed to be matched, $Z_{\rm L} = r$. **(d)** A semi-infinite transmission line of characteristic impedance $Z_{\rm car} = Z_{\rm L} = r$ is inserted right after r. Since the length of such a line $\ell \to \infty$, according to Eq. (2.31) the line input impedance $Z_{\rm in} = r$ and, thus, $v_{\rm n}$ is equally divided between r and $Z_{\rm in}$. **(e)** Thévenin equivalent circuit for a noisy resistor given by an ideal noiseless resistor r in series with a noise voltage source $v_{\rm n,RMS} \to v_{\rm n}$ (cf. main text). **(f)** Norton equivalent circuit for a noisy resistor given by an ideal noiseless resistor r in parallel with a noise current source $i_{\rm n,RMS} \to i_{\rm n} = v_{\rm n}/r$.

inserting right after the ideal resistor r a semi-infinite[10] transmission line with characteristic impedance $Z_{\rm car}$ matched to the load impedance, $Z_{\rm car} = Z_{\rm L} = r$ [cf. Fig. 3.2(d)]. The semi-infinite transmission line sustains a continuous of electromagnetic modes each, according to the equipartition law, characterized by an average energy $k_{\rm B}T$. Within the bandwidth BW, the power associated with the line modes is consequently given by $k_{\rm B}T\,{\rm BW}$. This power has to be equal to the power associated with the noisy resistor, $\overline{i_{\rm L}^2}\,r$, where the current has been first squared and then averaged over time.[11] Imposing the two powers

[10]Semi-infinite because we know the starting point of the line. The line is still infinitely long, thus sustaining a continuous of modes (cf. chapter 2, Subsec. 2.1.2).

[11]In the case of signals which are ergodic for the average, the time average can be substituted by the mean value [298–302], $\overline{i_{\rm L}^2}\,r \to \langle i_{\rm L}^2 \rangle\, r$.

to be equal and using the result of Eq. (3.10), we find

$$\frac{\overline{v_{\rm n}^2}}{4r^2}\, r = k_{\rm B} T\, {\rm BW}\,, \tag{3.11}$$

from which we can finally obtain the RMS noise voltage and current

$$v_{\rm n,RMS} \equiv \sqrt{\overline{v_{\rm n}^2}} = \sqrt{4 k_{\rm B} T\, r\, {\rm BW}} \quad ({\rm V})\,, \tag{3.12a}$$

$$i_{\rm n,RMS} \equiv \sqrt{\overline{i_{\rm n}^2}} = \sqrt{\frac{4 k_{\rm B} T\, {\rm BW}}{r}} \quad ({\rm A})\,. \tag{3.12b}$$

The bandwidth depends on the details of the measurement apparatus and it is typically taken to be a so-called "boxcar," i.e., a rectangle, with upper and lower frequency cutoff f_1 and f_2. If the system under consideration does not have a boxcar frequency response, then an equivalent noise bandwidth is defined as the boxcar with a) the same amplitude as the peak amplitude of the frequency response magnitude squared and b) the same integrated area as the actual system frequency response magnitude squared. To simplify the notation, we will hereafter indicate the RMS noise voltage and current simply as $v_{\rm n}$ and $i_{\rm n}$, $v_{\rm n,RMS} \to v_{\rm n}$ and $i_{\rm n,RMS} \to i_{\rm n}$, respectively, even if in the beginning of the above derivation the symbols $v_{\rm n}$ and $i_{\rm n}$ originally referred to time-dependent fluctuations instead of RMS values.

Hence, a noisy resistor can be modeled as a noise voltage source with RMS voltage $v_{\rm n}$ given by Eq.(3.12a) in series with an ideal noiseless resistor r. This is the fundamental Thévenin (voltage controlled) model of a noisy resistor [cf. Fig. 3.2(e)]. By means of the inverse first Ohm's law,

$$i_{\rm n} = \frac{v_{\rm n}}{r}\,,$$

we can then obtain the fundamental Norton (current controlled) model of a noisy resistor [cf. Fig. 3.2(f)].

Quantum regime. The main departure between the classical and quantum version of the Nyquist result of Eq. (3.11) is due to the fundamental quantum-mechanical requirement that the minimum energy associated with any electromagnetic mode of angular frequency ω be the vacuum energy $\hbar\omega/2$. We can therefore conjecture that, in the limit of a circuit in the vacuum regime, $k_{\rm B} T \to \hbar\omega/2$. In this case, Eq. (3.11) becomes

$$\frac{V_{\rm n0}^2}{4r^2}\, r = \frac{\hbar\omega}{2}\, {\rm BW}\,, \tag{3.13}$$

where $V_{\rm n0}$ represents the vacuum voltage of a quantum-mechanical resistor with a given resistance r. Normalizing such a voltage over $\sqrt{\rm BW}$ and assuming $r = Z_0$, we thus obtain the vacuum voltage per-root-hertz of a standard resistive load Z_0,

$$\bar{V}_{\rm n0} \equiv \sqrt{2\hbar Z_0 \omega} = 2\, \bar{V}_0\,. \tag{3.14}$$

Remarkably, we find that the vacuum voltage of a noisy resistor is *two times as large as* the vacuum voltage of a capacitor associated with a transmission

line [cf. Eq. (2.109)]. A similar result applies to the vacuum current of a noisy resistor.

A more rigorous analysis of the quantum-mechanical noisy resistor can be carried out by substituting the classical noise voltage $v_{\rm n}$ of Fig. 3.2(c) by the corresponding quantum-mechanical operator $\hat{V}_{\rm n}$,

$$v_{\rm n} \to \hat{V}_{\rm n} \equiv \bar{V}_{\rm n0}\,(\hat{a}^\dagger + \hat{a})\,, \tag{3.15}$$

where $\hat{a}^\dagger$ and $\hat{a}$ are the bosonic creation and annihilation operators associated with the internal modes of the resistor. We want to prove that the vacuum noise voltage $\bar{V}_{\rm n0}$ is as heuristically found in Eq. (3.14).

Assuming a purely real load impedance[12] $Z_{\rm L} = Z_0$ and assuming $r = Z_0$, we can easily derive the quantum current flowing on the loaded circuit,

$$\begin{aligned}\hat{I}_{\rm L} &= \frac{\hat{V}_{\rm n}}{2Z_0} \\ &= \frac{\bar{V}_{\rm n0}}{2Z_0}\,(\hat{a}^\dagger + \hat{a})\,.\end{aligned} \tag{3.16}$$

In addition, we consider one single-mode of the semi-infinite transmission line of Fig. 3.2(d) to be characterized by the creation and annihilation bosonic operators $\hat{b}^\dagger$ and $\hat{b}$. In the case of the vacuum and thermal white Gaussian noise considered here, the extension to multi-mode operators is straightforward, since the noise frequency distribution is uniform over the bandwidth BW. As a consequence, we can derive all expressions per-root-hertz or per-hertz and simply multiply the final result by $\sqrt{\rm BW}$ or BW in order to obtain the desired multi-mode expressions. Under these conditions, we can write the quantum voltage associated with the transmission line as $\hat{V} = \bar{V}_0\,(\hat{b}^\dagger + \hat{b})$.[13]

Assuming the entire circuit of Fig. 3.2(d) to be prepared in the vacuum state $|0\rangle$ (i.e., $T \to 0^+$) and imposing the power generated by resistor r ($= Z_0$) to be equal to the power on the transmission line, we finally obtain

$$\begin{aligned}\langle \hat{I}_{\rm L}^2 \rangle_0\, Z_0 = \langle 0|\hat{I}_{\rm L}^2|0\rangle\, Z_0 &= \frac{\bar{V}_{\rm n0}^2}{4Z_0^2}\,\langle 0|(\hat{a}^\dagger + \hat{a})^2|0\rangle\, Z_0 \\ &= \frac{\langle \hat{V}^2 \rangle_0}{Z_0} = \frac{\bar{V}_0^2}{Z_0}\,\langle 0|(\hat{b}^\dagger + \hat{b})^2|0\rangle\,,\end{aligned} \tag{3.17}$$

from which it follows again the result of Eq. (3.14).

Armed with the classical and quantum-mechanical models of a noisy resistor, we can proceed with our network analysis;

(ii) Second, we notice that besides the load impedances $Z_{\rm LB}$ and $Z_{\rm LC}$, which are typically at a very different temperature stage as compared to the Wilkinson

[12] If $Z_{\rm L}$ were complex, the phasor picture of quantum mechanics should be used. Due to its difficulty, the phasor picture will be studied by the author in a later paper.

[13] For simplicity, hereafter we will use the notation $\hat{V}$ instead of $\hat{\mathcal{V}}$ for the quantum voltage on a transmission line, which, we remind the reader, is defined per-root-hertz.

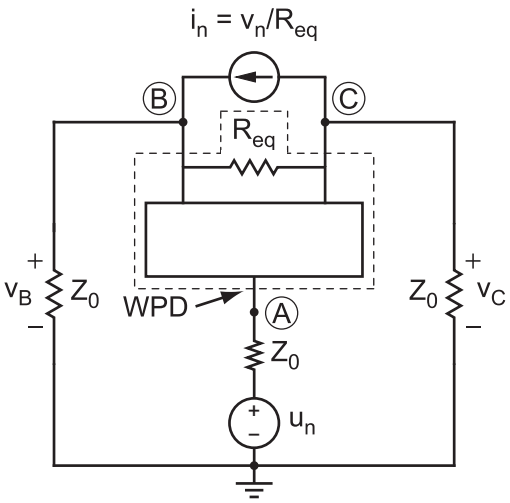

Figure 3.3: Circuit representation of a Wilkinson power divider (WPD; indicated by a dashed box) including noise sources. The noisy resistive impedance Z_0 at the input port A is substituted by a Thévenin equivalent circuit, where u_n represents the noise voltage of the primary noise source (cf. main text). The noisy resistor R_eq between ports B and C is substituted by a Norton equivalent circuit, where $i_\mathrm{n} = v_\mathrm{n}/R_\mathrm{eq}$ represents the noise current of the secondary noise source (cf. main text). The voltage drops v_B and v_C constitute the output voltages of the WPD.

power divider, the circuit of Fig. 3.1(b) contains *two independent* noise sources. These are the *primary noise source* associated with the input port termination Z_0, which we originally intended to characterize, and the *secondary noise source* associated with the equivalent resistor R_eq between ports B and C, which is part of the basic Wilkinson power divider. Both these noise sources contribute to the final voltage signals v_B and v_C to be measured over the load impedances Z_LB and Z_LC, respectively.

As shown in Fig. 3.3, we substitute the noisy input port termination Z_0 with the Thévenin equivalent circuit of Fig. 3.2(e) and the noisy resistor R_eq with the Norton circuit of Fig. 3.2(f). For clarity of notation, the noise source at port A is now indicated as u_n and the one between ports A and B as $i_\mathrm{n} = v_\mathrm{n}/R_\mathrm{eq}$.

It is worth pointing out already at this stage that the noise voltage source at input port A does not modify the axial symmetry of the circuit and, thus, contributes to the voltages v_B and v_C in the same amount, both in amplitude and sign. However, the noise current source between ports B and C does modify the axial symmetry of the circuit and, thus, contributes to the voltages v_B and v_C with the same amount in amplitude, but *opposite* sign. This antisymmetry conjecture will be proven in the next steps of our derivation;

(iii) Third, the circuit of Fig. 3.3 can be analyzed invoking the superposition principle of network theory [264], where the total output voltages at ports B and

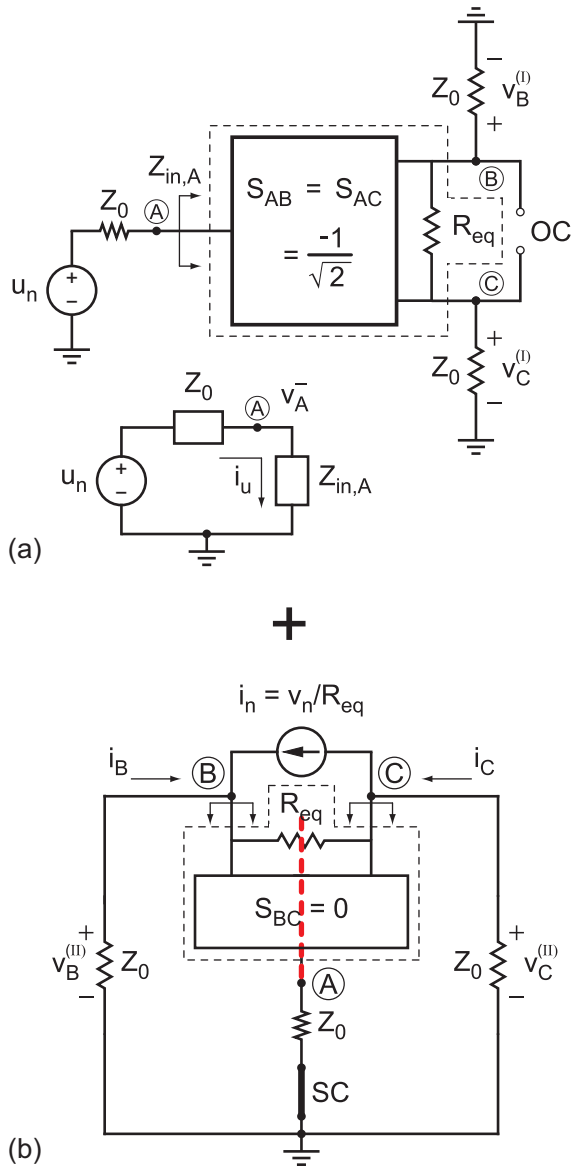

Figure 3.4: Superposition principle for the Wilkinson power divider. **(a)** The source i_n is switched off, $i_n \rightarrow$ OC. At the input port A we see an impedance $Z_{in,A}$ to ground. The series circuit below the main circuit of **(a)** shows that the noise voltage u_n is divided between the termination Z_0 and the input impedance $Z_{in,A}$, on which a current i_u flows. At port A the voltage is defined as v_A^-. At ports B and C we find the two partial output voltages $v_B^{(I)}$ and $v_C^{(I)}$ due to u_n only. **(b)** The source u_n is switched off, $u_n \rightarrow$ SC. Since $S_{BC} = 0$, the divider input impedances at ports B and C are independent (dashed red line). The partial output voltages $v_B^{(II)}$ and $v_C^{(II)}$ are due to v_n only. The final result is obtained summing the partial voltages found in **(a)** and **(b)**.

C, $v_{\rm B}$ and $v_{\rm C}$, can be decomposed in the sum of the independent contributions $v_{\rm B}^{\rm (I)}$ and $v_{\rm C}^{\rm (I)}$, due to the noise voltage source $u_{\rm n}$, and $v_{\rm B}^{\rm (II)}$ and $v_{\rm C}^{\rm (II)}$, due to the noise voltage source $v_{\rm n}$, $v_{\rm B} = v_{\rm B}^{\rm (I)} + v_{\rm B}^{\rm (II)}$ and $v_{\rm C} = v_{\rm C}^{\rm (I)} + v_{\rm C}^{\rm (II)}$. Following this approach, the main steps are:

(I) The noise current source $i_{\rm n}$ is replaced by an open circuit and only the effect of the noise voltage source $u_{\rm n}$ is considered [cf. Fig. 3.4(a)].
Defining the input impedance between port A and ground as $Z_{\rm in,A}$, the circuit is reduced to the simple series circuit sketched on the left-bottom part of Fig. 3.4(a). From Kirchhoff's voltage law it follows that

$$-u_{\rm n} - Z_0\, i_{\rm u} - Z_{\rm in,A}\, i_{\rm u} = 0\,, \tag{3.18}$$

where $i_{\rm u}$ is the current flowing in the circuit. In Eq. (3.18), we adopt the standard sign convention for the voltages on Z_0 and $Z_{\rm in,A}$, i.e., we assume them dropping in the opposite direction of the current flow. The sign of $u_{\rm n}$ is set by the Thévenin model for the noisy resistor. In this way, we find

$$i_{\rm u} = -\frac{1}{Z_0 + Z_{\rm in,A}} u_{\rm n}$$

and, from first Ohms's law,

$$v_{\rm A}^{-} = -\frac{Z_{\rm in,A}}{Z_0 + Z_{\rm in,A}} u_{\rm n}\,, \tag{3.19}$$

which resembles the usual result for a voltage divider [296]. The minus sign in the expression for $v_{\rm A}^{-}$ indicates that the physical voltage drops between point A and ground [it is the opposite of the conventional sign assumed in Eq. (3.18)]. Thus, $v_{\rm A}^{+} = -v_{\rm A}^{-}$ is the incident voltage at the input port A of the Wilkinson power divider.
At this point, we need to make use of some of the elements of the reduced three-port scattering matrix $\widetilde{\mathbf{S}}_{\rm WPD}$ of the Wilkinson power divider [cf. Eq. (3.7)]. Considering the scattering parameter between port A and port B or C, $S_{\rm AB} = S_{\rm AC} = -1/\sqrt{2}$, we can calculate the reflected voltages at ports B and C and obtain the partial voltages $v_{\rm B}^{\rm (I)}$ and $v_{\rm C}^{\rm (I)}$ as

$$\begin{aligned} v_{\rm B}^{-} = v_{\rm C}^{-} &= v_{\rm B}^{\rm (I)} = v_{\rm C}^{\rm (I)} \\ &= -\frac{1}{\sqrt{2}} v_{\rm A}^{+} = -\frac{Z_{\rm in,A}}{\sqrt{2}(Z_0 + Z_{\rm in,A})} u_{\rm n}\,. \end{aligned} \tag{3.20}$$

Under matching conditions $Z_{\rm in,A} = Z_0$ and, thus,

$$v_{\rm B}^{\rm (I)} = v_{\rm C}^{\rm (I)} = -\frac{1}{2\sqrt{2}}\, u_{\rm n}\,. \tag{3.21}$$

This result quantifies the amount of voltage associated with the primary noise source that we are expected to measure at the output. The factor $-1/\sqrt{2}$ is due to the Wilkinson divider, whereas the factor $1/2$ owns its origin to the voltage division at the input. The latter, which can

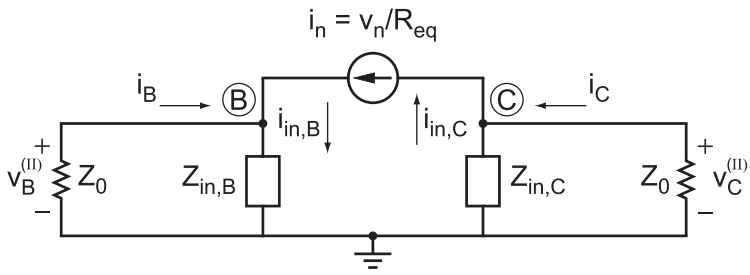

Figure 3.5: Noise contribution of the Wilkinson power divider internal resistance. The noise current $i_{\rm n}$ is divided between the input impedance $Z_{\rm in,B}$ ($Z_{\rm in,C}$) of the power divider at port B (C) and a load impedance Z_0. $i_{\rm in,B}$ ($i_{\rm in,C}$): current flowing on $Z_{\rm in,B}$ ($Z_{\rm in,C}$).

easily be missed at first glance, is due to the *internal resistance* of our noise source, which in this case is simply Z_0. Remarkably, this is exactly what happens in any commercial signal generator. The generator is characterized by some internal resistance $R_{\rm g}$ which absorbs part of the signal generated by the internal oscillator. The output power specified on the machine is referred to the machine output plane and already accounts for internal losses. In our case, we have to be careful to include such losses in the calculations without doing the trivial mistake of assuming $v_{\rm B}^{\rm (I)} = v_{\rm C}^{\rm (I)} = u_{\rm n}/\sqrt{2}$;[14]

(II) The noise voltage source $u_{\rm n}$ is replaced by a short circuit and only the effect of the noise current source $i_{\rm n}$ is considered [cf. Fig. 3.4(b)].

In Fig. 3.4(b), the dashed black box indicates, as always, the power divider. Since for a Wilkinson divider the scattering parameter between ports B and C is zero, $S_{\rm BC} = 0$, no current is allowed to flow between these two ports. As a consequence, we can consider the impedances seen at the input of ports B and C of the diver as independent circuit elements [cf. dashed red line in Fig. 3.4(b)]. The circuit of Fig. 3.4(b) can therefore be reduced to that of Fig. 3.5.

Following the usual sign conventions, we can apply Kirchhoff's voltage law to the left and right loops of the circuit of Fig. 3.5,

$$v_{\rm B}^{\rm (II)} + v_{\rm in,B} = Z_0\, i_{\rm B} + Z_{\rm in,B}\, i_{\rm in,B} = 0\,, \tag{3.22a}$$

$$v_{\rm C}^{\rm (II)} - v_{\rm in,C} = Z_0\, i_{\rm C} - Z_{\rm in,C}\, i_{\rm in,C} = 0\,. \tag{3.22b}$$

Under matching conditions, $Z_{\rm in,B} = Z_{\rm in,C} = Z_0$, from Eq. (3.22a) it follows that

$$i_{\rm in,B} = -\, i_{\rm B} \tag{3.23}$$

and from Eq. (3.22b) that

$$i_{\rm in,C} = i_{\rm C}\,. \tag{3.24}$$

[14] A resistor is not only a noise source, but also a circuit element on which a voltage drop is established.

Applying Kirchhoff's current law to nodes B and C of the circuit of Fig. 3.5,

$$i_{\mathrm{B}} - i_{\mathrm{in,B}} + i_{\mathrm{n}} = 0\,, \tag{3.25a}$$

$$i_{\mathrm{C}} + i_{\mathrm{in,C}} - i_{\mathrm{n}} = 0\,, \tag{3.25b}$$

and using the results of Eqs. (3.23) and (3.24), we obtain

$$i_{\mathrm{B}} = -\frac{1}{2}\,i_{\mathrm{n}}\,, \tag{3.26a}$$

$$i_{\mathrm{C}} = \frac{1}{2}\,i_{\mathrm{n}}\,. \tag{3.26b}$$

In Eqs. (3.25a) and (3.25b), we adopted the standard sign convention for currents, i.e., we assumed them to be positive when entering a node and negative when exiting it (cf. Fig. 3.5).

Finally, the partial voltages $v_{\mathrm{B}}^{(\mathrm{II})}$ and $v_{\mathrm{C}}^{(\mathrm{II})}$ can straightforwardly be calculated from Eqs. (3.26a) and (3.26b) as

$$v_{\mathrm{B}}^{(\mathrm{II})} = -\,v_{\mathrm{C}}^{(\mathrm{II})} = -\,\frac{Z_0}{2} i_{\mathrm{n}} = -\,\frac{Z_0}{2R_{\mathrm{eq}}}\,v_{\mathrm{n}}\,. \tag{3.27}$$

For a basic Wilkinson power divider $R_{\mathrm{eq}} = 2Z_0$ and, thus,

$$v_{\mathrm{B}}^{(\mathrm{II})} = -\,v_{\mathrm{C}}^{(\mathrm{II})} = -\,\frac{1}{4}\,v_{\mathrm{n}}\,. \tag{3.28}$$

This result, which has been carefully checked also with spice simulations (data not shown), quantifies the amount of voltage associated with the secondary noise source that we are expected to measure at the output of the divider. The minus sign is in accordance with our conjecture about the breaking of the axial symmetry of the power divider by the secondary noise source.

Instead of a Norton representation we could have used a Thévenin representation for the noise source v_{n}, in the same manner as we have done for u_{n}. However, because of symmetry reasons[15] it is then hard to make use of the scattering matrix elements of the Wilkinson power divider. The use of $\widetilde{\mathbf{S}}_{\mathrm{WPD}}$, readily possible only within the Norton representation of the noisy resistor associated with R_{eq}, significantly simplifies the analysis of the circuit.

In summary, applying the superposition principle finally gives the total results

$$\begin{aligned} v_{\mathrm{B}} &= v_{\mathrm{B}}^{(\mathrm{I})} + v_{\mathrm{B}}^{(\mathrm{II})} \\ &= -\frac{Z_{\mathrm{in,A}}}{\sqrt{2}(Z_0 + Z_{\mathrm{in,A}})}\,u_{\mathrm{n}} - \frac{Z_0}{2R_{\mathrm{eq}}}\,v_{\mathrm{n}}\,, \end{aligned} \tag{3.29a}$$

$$\begin{aligned} v_{\mathrm{C}} &= v_{\mathrm{C}}^{(\mathrm{I})} + v_{\mathrm{C}}^{(\mathrm{II})} \\ &= -\frac{Z_{\mathrm{in,A}}}{\sqrt{2}(Z_0 + Z_{\mathrm{in,A}})}\,u_{\mathrm{n}} + \frac{Z_0}{2R_{\mathrm{eq}}}\,v_{\mathrm{n}}\,, \end{aligned} \tag{3.29b}$$

[15] The broken axial symmetry of the power divider.

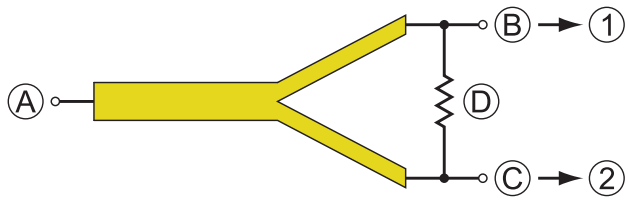

Figure 3.6: The Wilkinson power divider as a four-port beam splitter. In order to obtain the complete scattering matrix of a Wilkinson divider given by Eq. (3.34), a fourth port D must be considered. Since such a port is always terminated in a resistive element, we refer to it as *internal* port of the divider. The other three ports A, B, and C are defined as in Fig. 3.1.

which are valid for any generic power divider, including Cohn's design. In the case of a basic Wilkinson power divider, these equations become

$$v_{\mathrm{B}} = -\frac{1}{2\sqrt{2}} u_{\mathrm{n}} - \frac{1}{4} v_{\mathrm{n}} \,, \tag{3.30a}$$

$$v_{\mathrm{C}} = -\frac{1}{2\sqrt{2}} u_{\mathrm{n}} + \frac{1}{4} v_{\mathrm{n}} \,. \tag{3.30b}$$

By means of the general representation of a quantum-mechanical resistor given by Eqs. (3.14) and (3.15), it is straightforward to quantize Eqs. (3.30a) and (3.30b).

First, we assume single-mode signals with angular frequency $\omega = \omega_0 = 2\pi f_0$. Since Eq. (3.15) is defined per-root-hertz, the single-mode assumption is the most suitable approach for the quantization of Eqs. (3.30a) and (3.30b). In the usual scenario of thermal white Gaussian noise, the necessary extension to the multi-mode case can easily be performed at any point of the calculation by multiplying voltages or currents times $\sqrt{\mathrm{BW}}$ and powers times BW.

Second, we note that the secondary noise source *does not* represent a standard resistive load. In fact, in the case of a basic Wilkinson power divider the internal resistance $r = R_{\mathrm{eq}} = 2Z_0$ is two times as large as the resistance of a standard load, e.g., the primary noise source. This has the fundamental consequence that the vacuum voltage of the secondary noise source is $\sqrt{2}$ larger than that of the primary source,

$$\bar{V}'_{\mathrm{n0}} \equiv \sqrt{2\hbar R_{\mathrm{eq}} \omega} = \sqrt{2\hbar (2Z_0)\omega} = \sqrt{2}\, \bar{V}_{\mathrm{n0}} = 2\sqrt{2}\, \bar{V}_0 \,. \tag{3.31}$$

Third, using the expressions of Eqs. (3.14) and (3.31) for the vacuum voltage of a standard (Z_0) and nonstandard ($2Z_0$) resistor, respectively, we can promote the noise voltage of the primary noise source, u_{n}, and secondary noise source, v_{n}, to the corresponding quantum-mechanical operators as

$$\begin{aligned} u_{\mathrm{n}} \to \hat{U}_{\mathrm{n}} &= \bar{V}_{\mathrm{n0}} \, (\hat{a}^\dagger + \hat{a}) \\ &= 2\, \bar{V}_0 \, (\hat{a}^\dagger + \hat{a}) = 2\, \hat{V}_{\mathrm{A}} \,, \end{aligned} \tag{3.32a}$$

$$\begin{aligned} v_{\mathrm{n}} \to \hat{V}_{\mathrm{n}} &= \bar{V}'_{\mathrm{n0}} \, (\hat{d}^\dagger + \hat{d}) \\ &= 2\sqrt{2}\, \bar{V}_0 \, (\hat{d}^\dagger + \hat{d}) = 2\sqrt{2}\, \hat{V}_{\mathrm{D}} \,, \end{aligned} \tag{3.32b}$$

where $\hat{V}_{\rm A} \equiv \bar{V}_0\,(\hat{a}^\dagger + \hat{a})$ and $\hat{V}_{\rm D} \equiv \bar{V}_0\,(\hat{d}^\dagger + \hat{d})$ represent the quantum voltages incident at the input port A and at a newly defined port D (cf. Fig. 3.6) of the power divider, respectively, and $\hat{a}^\dagger$, $\hat{a}$, $\hat{d}^\dagger$, and $\hat{d}$ are usual bosonic creation and annihilation operators. Since port D is always terminated into resistance $R_{\rm eq}$, we refer to such a port as the *internal* port of the divider.

Fourth, we promote $v_{\rm B}$ and $v_{\rm C}$ to their corresponding quantum-mechanical operators by substituting Eqs. (3.32a) and (3.32b) into Eqs. (3.30a) and (3.30b),

$$\begin{aligned} v_{\rm B} \to \hat{V}_{\rm B} &= -\frac{1}{2\sqrt{2}} 2\,\hat{V}_{\rm A} - \frac{1}{4} 2\sqrt{2}\,\hat{V}_{\rm D} \\ &= -\frac{1}{\sqrt{2}}\,\hat{V}_{\rm A} - \frac{1}{\sqrt{2}}\,\hat{V}_{\rm D}\,, \end{aligned} \tag{3.33a}$$

$$\begin{aligned} v_{\rm C} \to \hat{V}_{\rm C} &= -\frac{1}{2\sqrt{2}} 2\,\hat{V}_{\rm A} + \frac{1}{4} 2\sqrt{2}\,\hat{V}_{\rm D} \\ &= -\frac{1}{\sqrt{2}}\,\hat{V}_{\rm A} + \frac{1}{\sqrt{2}}\,\hat{V}_{\rm D}\,. \end{aligned} \tag{3.33b}$$

The knowledge of the input-output relations of Eqs. (3.33a) and (3.33b) allows us to extend the reduced three-port scattering matrix $\widetilde{\mathbf{S}}_{\rm WPD}$ of Eq. (3.7) to the complete four-port scattering matrix

$$\mathbf{S}_{\rm WPD} = -\frac{1}{\sqrt{2}} \begin{bmatrix} 0 & 1 & 1 & 0 \\ 1 & 0 & 0 & 1 \\ 1 & 0 & 0 & -1 \\ 0 & 1 & -1 & 0 \end{bmatrix}. \tag{3.34}$$

In order to obtain this matrix, the inverse relations for the voltages at the input ports A and D as a function of the voltages at the output ports B and C, obtained by inverting Eqs. (3.33a) and (3.33b), have been used. It can easily be shown that, differently from the matrix of Eq. (3.7), the complete scattering matrix of Eq. (3.34) is unitary, $\mathbf{S}^*_{\rm WPD}\mathbf{S}_{\rm WPD} = \mathbf{I}_4$, where $\mathbf{I}_4$ is the 4×4 identity matrix.

It is worth mentioning that the scattering matrix of Eq. (3.34) is equally applicable to *both* quantum voltages $\hat{V}_{\rm A}$, $\hat{V}_{\rm D}$, $\hat{V}_{\rm B} \equiv \bar{V}_0\,(\hat{b}^\dagger + \hat{b})$, and $\hat{V}_{\rm C} \equiv \bar{V}_0\,(\hat{c}^\dagger + \hat{c})$ *and* currents $\hat{I}_{\rm A} \equiv j\bar{I}_0\,(\hat{a}^\dagger - \hat{a})$, $\hat{I}_{\rm D} \equiv j\bar{I}_0\,(\hat{d}^\dagger - \hat{d})$, $\hat{I}_{\rm B} \equiv j\bar{I}_0\,(\hat{b}^\dagger - \hat{b})$, and $\hat{I}_{\rm C} \equiv j\bar{I}_0\,(\hat{c}^\dagger - \hat{c})$. Here, $\hat{b}^\dagger$, $\hat{b}$, $\hat{c}^\dagger$, and $\hat{c}$ are the bosonic creation and annihilation operators for the output ports B and C, respectively.

As already mentioned, in the experiments to be shown in the next chapter we do not use a basic Wilkinson power divider. We use, instead, the more complex Cohn-type power divider, where the noise properties of the resistive network at the divider output ports [292] can be hard to analyze with simple circuit theory. However, for the self-consistency of the complete four-port scattering matrix of any divider, a matrix analogous to that of Eq. (3.34) is expected also for the Cohn design. In addition, we would like to stress that the choice of naming the input ports as A and D was dictated by our historical introduction of the Wilkinson power divider, where only three ports are defined: port A as the input and ports B and C as the outputs. In the case of the hybrid ring, to be discussed next, the input ports are defined as A and C and the output ports as B and D.

Before concluding our analysis of the basic Wilkinson power divider, we want to show the relevance of the unitary character of the scattering matrix of Eq. (3.34).

Let us assume that the reduced matrix of Eq. (3.7) were the complete matrix representing a Wilkinson divider, even in the quantum-mechanical regime. In that case, the quantum voltages at the divider output ports would read

$$\hat{V}_{\rm B} = -\frac{1}{\sqrt{2}}\,\hat{V}_{\rm A}\,, \tag{3.35a}$$

$$\hat{V}_{\rm C} = -\frac{1}{\sqrt{2}}\,\hat{V}_{\rm A}\,. \tag{3.35b}$$

The first test is to check whether the quantum-mechanical power at the input port of the divider is equal to the total power delivered to the output ports. This can readily be confirmed assuming the divider to be prepared in the vacuum state $|0\rangle$. In this case, using the relations of Eqs. (3.35a) and (3.35b), we find

$$\begin{aligned}\frac{\langle 0|\hat{V}_{\rm A}^2|0\rangle}{Z_0} &= \frac{\langle 0|\hat{V}_{\rm B}^2|0\rangle}{Z_0} + \frac{\langle 0|\hat{V}_{\rm C}^2|0\rangle}{Z_0} \\ &= \frac{\bar{V}_0^2}{Z_0}\,. \end{aligned} \tag{3.36}$$

In addition to power conservation, the quantum voltages and currents at the input and output ports of the divider must obey the fundamental commutation relations $[\hat{V}_{\rm A},\hat{I}_{\rm A}] = [\hat{V}_{\rm B},\hat{I}_{\rm B}] = [\hat{V}_{\rm C},\hat{I}_{\rm C}]$ and $[\hat{V}_{\rm B},\hat{I}_{\rm C}] = [\hat{I}_{\rm B},\hat{V}_{\rm C}] = 0$. However, if we use the relations of Eqs. (3.35a) and (3.35b), we find the inconsistent results $[\hat{V}_{\rm B},\hat{I}_{\rm B}] = [\hat{V}_{\rm C},\hat{I}_{\rm C}] = j\,\hbar\omega/2 \neq [\hat{V}_{\rm A},\hat{I}_{\rm A}] = j\,\hbar\omega$ and $[\hat{V}_{\rm B},\hat{I}_{\rm C}] = [\hat{I}_{\rm B},\hat{V}_{\rm C}] = j\,\hbar\omega/2 \neq 0$.

Such a fundamental inconsistency suggests that, in the quantum regime, the input-output relations given by Eqs. (3.35a) and (3.35b), and, thus, the reduced scattering matrix of Eq. (3.7), are necessarily incomplete. It can readily be verified, instead, that making use of the relations of Eqs. (3.33a) and (3.33b) allows us to obtain the consistent results $[\hat{V}_{\rm A},\hat{I}_{\rm A}] = [\hat{V}_{\rm D},\hat{I}_{\rm D}] = j\,\hbar\omega = [\hat{V}_{\rm B},\hat{I}_{\rm B}] = [\hat{V}_{\rm C},\hat{I}_{\rm C}] = [\hat{V}_{\rm A},\hat{I}_{\rm A}]/2 + [\hat{V}_{\rm D},\hat{I}_{\rm D}]/2 = j\,\hbar\omega$ and $[\hat{V}_{\rm B},\hat{I}_{\rm C}] = [\hat{I}_{\rm B},\hat{V}_{\rm C}] = 0$, as required by basic quantum-electrodynamics [303].

Finally, we notice that the quantum voltages of Eqs. (3.33a) and (3.33b) represent the noise voltages at the input of the detection chain of Fig. 3.10. To establish a general notation, we will rename such quantum voltages as $\hat{V}_{\rm B} \to \hat{V}_1$ and $\hat{V}_{\rm C} \to \hat{V}_2$, as shown in the bottom part of Fig. 3.10. We will make extensive use of Eqs. (3.33a) and (3.33b) in chapter 4 in order to explain our experimental results.

3.1.2 The 180° Hybrid Ring

The 180° hybrid ring is a four-port splitter belonging to the class of four-port junctions referred to as directional couplers.

Since any given directional coupler is made of four ports ($N = 4$), it is completely characterized by a scattering matrix of the fourth order, $\mathbf{S}_{\rm dir} = [S_{pq}]$ with $p, q =$ A, B, C, and D [cf. Fig. 3.7(a)]. For a directional coupler to be well-defined eight of the S_{pq} elements have to be independent (i.e., $2 \times N$) [290]. Directional couplers are reciprocal junctions.

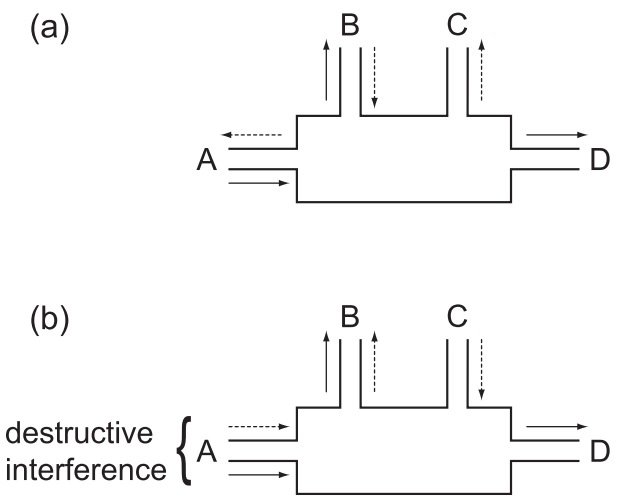

Figure 3.7: Sketch of a generic four-port junction also referred to as directional coupler. **(a)** A wave incident at port A is reflected by ports B and D (solid arrows). Similarly, a wave incident at port B is reflected by ports A and C (broken arrows). Ports A and C are isolated as well as ports B and D. **(b)** Sketch used to prove Theorem 3.1.2. In order to prove the theorem, the waves indicated by broken arrows in **(a)** have to be reversed in time and the two waves incident at port A must be made to cancel each other by destructive interference.

Definition A directional coupler is defined as a four-port junction such that, with all lines terminated in their characteristic impedances, ports A and B are matched and there is no coupling between A and C and B and D. Figure 3.7(a) is a diagrammatic representation of a directional coupler.

A wave incident at port A is reflected (leaves) by ports B and D. A wave incident at port B is reflected (leaves) by ports C and A. There are several theorems valid for directional couplers.

Theorem 3.1.2 *All four ports of a directional coupler are matched.*

Proof The waves indicated by broken arrows in Figure 3.7(b) can be reversed in time and combined with the waves indicated by solid arrows. If the amplitudes and phases of the two waves relative to each other are properly adjusted, the two waves incident at port A can be made to cancel each other (destructive interference). Consequently, we are only left with a wave incident at port C and reflected at ports B and D. Hence, a wave incident on the junction at port C is transmitted to ports B and D without any reflection and port C is matched. Similarly, port D is also matched. This, together with the definition of directional coupler, implies that all directional couplers are completely matched. Q.D.E.

The high level of symmetry characteristic of a directional coupler is at the basis of Theorem 3.1.2. In contrast, we remind that the matching properties for three-port junctions are much poorer: It is impossible for any T-junction to have all three ports matched.

Another theorem of importance applicable to directional couplers is the following:

Theorem 3.1.3 *Any given four-port junction such that two noncoupling ports are matched is a directional coupler.*

We leave the proof to the reader as an exercise.[16]

The scattering matrix of a generic directional coupler is of the form

$$\mathbf{S}_{\mathrm{dir}} = \begin{bmatrix} 0 & S_{\mathrm{AB}} & 0 & S_{\mathrm{AD}} \\ S_{\mathrm{BA}} & 0 & S_{\mathrm{BC}} & 0 \\ 0 & S_{\mathrm{CB}} & 0 & S_{\mathrm{CD}} \\ S_{\mathrm{DA}} & 0 & S_{\mathrm{DC}} & 0 \end{bmatrix} . \tag{3.37}$$

The vanishing diagonal elements show that the junction is completely matched. The remainder of the zero elements indicate that ports A and C as well as ports B and D are decoupled from each other. We are left with eight elements, which, in principle are necessary for representing a four-port junction. However, such elements are not entirely independent due to the reciprocity and unitary of S_{dir},

$$S_{pq} = S_{qp} \quad \forall p, q \,, \tag{3.38a}$$

$$|S_{\mathrm{AB}}|^2 + |S_{\mathrm{AD}}|^2 = 1 \tag{3.38b}$$

and

$$S^*_{\mathrm{BA}} S_{\mathrm{BC}} + S^*_{\mathrm{DA}} S_{\mathrm{DC}} = 0 \,, \tag{3.39a}$$

$$S^*_{\mathrm{AB}} S_{\mathrm{AD}} + S^*_{\mathrm{CB}} S_{\mathrm{CD}} = 0 \,. \tag{3.39b}$$

From these conditions it follows that

$$|S_{\mathrm{AB}}| = |S_{\mathrm{CD}}| \,, \tag{3.40a}$$

$$|S_{\mathrm{AD}}| = |S_{\mathrm{BC}}| \,, \tag{3.40b}$$

which mean that the coupling from port A to port B is equal to that from port C to port D and, similarly, the coupling from port A to port D is equal to that from port B to port C.

By properly choosing the location of the reference planes, it is also possible to eliminate the arbitrariness in the phases of the various scattering elements. For example, the location of the terminal plane at port B can be chosen in such a way that S_{AB} is real and positive, the location of the plane at port D such that S_{AD} is positive imaginary, and the location of the plane at port C such that S_{CD} is positive real. From Eqs. (3.40a) and (3.40b) it follows that $S_{\mathrm{AB}} = S_{\mathrm{CD}} = \alpha \in \mathbb{R}^+$. From Eqs. (3.38a), (3.39a), and (3.39b) it follows that $\alpha S_{\mathrm{BC}} + S^*_{\mathrm{DA}} \alpha = 0$ and, if $\alpha \neq 0$, $S_{\mathrm{BC}} = S_{\mathrm{DA}} = j\beta$ with $\beta \in \mathbb{R}^+$. In addition, from Eq. (3.38b) it follows that $\alpha^2 + \beta^2 = 1$.

[16]The unmotivated reader can also find the proof in Ref. [290] at the bottom of page 300.

Under all these assumptions, the scattering matrix of Eq. (3.37) reduces to

$$\mathbf{S}_{\text{dir}} = \begin{bmatrix} 0 & \alpha & 0 & j\beta \\ \alpha & 0 & j\beta & 0 \\ 0 & j\beta & 0 & \alpha \\ j\beta & 0 & j\beta & 0 \end{bmatrix}, \tag{3.41}$$

which is regarded as the standard form for the scattering matrix of a directional coupler.

Before proceeding with our study, it is worth stating one more fundamental theorem for directional couplers (cf. Ref. [290] for the proof).

Theorem 3.1.4 *Any completely matched four-port junction is a directional coupler.*

We now turn our attention to a subclass of directional couplers designed, at least in some specified bandwidth, for 3 dB coupling. Directional couplers with 3 dB coupling are also referred to as hybrid junctions and are widely used in microwave technology and telecommunication networks [227]. It is needless to mention that there are innumerous configurations for hybrid junctions. For the sake of an example, we here focus only on the so-called "rat-race" hybrid ring. Figure 3.8 gives justice to such a name. The figure schematically represents a microstrip 180° junction. To gain insight into the operating principles of the device, consider a wave incident at port A. This wave splits equally into two waves travelling around the ring circuit in opposite directions. The two waves arrive in phase at ports B and D and out of phase at port C. As a consequence, ports A and C are decoupled. In a similar way, ports B and D are decoupled because the two paths connecting these ports differ in length by $\lambda/2$. In brief, the rat-race hybrid ring is based on interference effects between the various waves travelling around the ring.

A quantitative analysis of the rat-race hybrid ring can be found in Ref. [227]. Here, we limit ourselves to summarize the main steps of such a derivation, with the hope to be of some guidance to the reader interested in the rigorous proof. First, we assume each input transmission line to have a characteristic impedance Z_0 and the central ring a characteristic impedance Z_1. The electrical length of the ring between ports A and B, B and C, and C and D is defined as θ_1. Thus, the electrical length between ports A and D is $\theta_2 = 3\theta_1$. We then split up the circuit into two subcircuits, which are symmetric with respect to the plane $a-a$ (cf. Fig. 3.8). We can thus study only one-half of the structure in terms of scattering matrices for a simpler two-port junction, the junction associated with ports A and B. By symmetry arguments we can extend those results and construct the entire four-port scattering matrix of the hybrid. Invoking the superposition principle, we can find solutions when plane $a-a$ is open circuited [solutions indicated as (I)] and when plane $a-a$ is short circuited

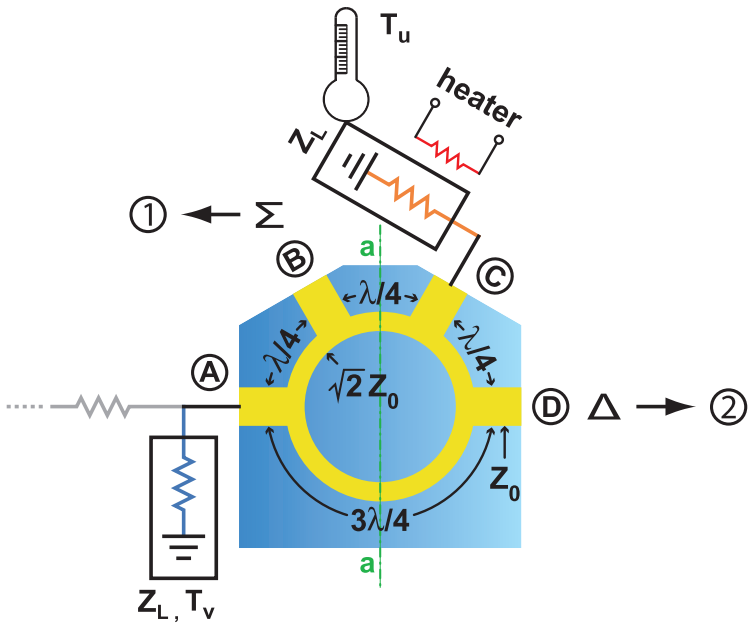

Figure 3.8: A microstrip 180° hybrid ring (rat-race). Port C is terminated into the resistive impedance Z_{L}, which is maintained at temperature T_{u}. Similar to the case of the Wilkinson power divider, this impedance constitutes the primary noise source and is associated with the noise voltage u_{n}. The temperature T_{u} is controlled by means of a heater and monitored with a thermometer. Port A is terminated into another resistive impedance Z_{L}, which is maintained at temperature T_{v}. This impedance constitutes the secondary noise source and is associated with the noise voltage v_{n}. The output signals are obtained at ports B and D. Due to the properties of the hybrid junction (cf. main text), at port B (Σ) the sum of the input signals at ports A and B is obtained, while at port D (Δ) the difference of the input signals is obtained. The signals at ports B and D are then fed into channels 1 and 2 of the detection chain, respectively (cf. bottom part of Fig. 3.10). Cf. also the right part of Fig. 3.16 for more details. We stress that, as shown in the right part of Fig. 3.16, in reality port A is connected to the series of two attenuators (symbolized by the grey resistor on the left of port A). These attenuators are then connected to a coaxial cable, which can be used to send probing signals to the splitter. In all experiments discussed in this thesis, such probing signals were never applied and, thus, the two attenuators can be regarded as a $50\,\Omega$ impedance load to ground. In fact, we remind that microwave coaxial attenuators are characterized by a resistive path to ground.

[solutions indicated as (II)]. Hence, we obtain

$$\begin{bmatrix} V_{\mathrm{A}}^{-} \\ V_{\mathrm{B}}^{-} \end{bmatrix} = \frac{1}{2} \begin{bmatrix} S_{\mathrm{AA}}^{(\mathrm{I})} + S_{\mathrm{AA}}^{(\mathrm{II})} & S_{\mathrm{AB}}^{(\mathrm{I})} + S_{\mathrm{AB}}^{(\mathrm{II})} \\ S_{\mathrm{BA}}^{(\mathrm{I})} + S_{\mathrm{BA}}^{(\mathrm{II})} & S_{\mathrm{BB}}^{(\mathrm{I})} + S_{\mathrm{BB}}^{(\mathrm{II})} \end{bmatrix} \begin{bmatrix} V_{\mathrm{A}}^{+} \\ V_{\mathrm{B}}^{+} \end{bmatrix} , \tag{3.42a}$$

$$\begin{bmatrix} V_{\mathrm{D}}^{-} \\ V_{\mathrm{C}}^{-} \end{bmatrix} = \frac{1}{2} \begin{bmatrix} S_{\mathrm{AA}}^{(\mathrm{I})} - S_{\mathrm{AA}}^{(\mathrm{II})} & S_{\mathrm{AB}}^{(\mathrm{I})} - S_{\mathrm{AB}}^{(\mathrm{II})} \\ S_{\mathrm{BA}}^{(\mathrm{I})} - S_{\mathrm{BA}}^{(\mathrm{II})} & S_{\mathrm{BB}}^{(\mathrm{I})} - S_{\mathrm{BB}}^{(\mathrm{II})} \end{bmatrix} \begin{bmatrix} V_{\mathrm{A}}^{+} \\ V_{\mathrm{B}}^{+} \end{bmatrix} , \tag{3.42b}$$

where V_{A}^{+} and V_{B}^{+} are incident waves at ports A and B, respectively, and V_{A}^{-}, V_{B}^{-}, V_{D}^{-}, and V_{C}^{-} are reflected waves at ports A, B, D, and C, respectively. From Eqs. (3.42a) and (3.42b) we can then identify the eight four-port parameters necessary to characterize the hybrid junction,

$$\begin{aligned} S_{\mathrm{AA}} &= \frac{1}{2}\left(S_{\mathrm{AA}}^{(\mathrm{I})} + S_{\mathrm{AA}}^{(\mathrm{II})}\right) & S_{\mathrm{AB}} &= \frac{1}{2}\left(S_{\mathrm{AB}}^{(\mathrm{I})} + S_{\mathrm{AB}}^{(\mathrm{II})}\right) \\ S_{\mathrm{BA}} &= \frac{1}{2}\left(S_{\mathrm{BA}}^{(\mathrm{I})} + S_{\mathrm{BA}}^{(\mathrm{II})}\right) & S_{\mathrm{BB}} &= \frac{1}{2}\left(S_{\mathrm{BB}}^{(\mathrm{I})} + S_{\mathrm{BB}}^{(\mathrm{II})}\right) \\ S_{\mathrm{CA}} &= \frac{1}{2}\left(S_{\mathrm{BA}}^{(\mathrm{I})} - S_{\mathrm{BA}}^{(\mathrm{II})}\right) & S_{\mathrm{CB}} &= \frac{1}{2}\left(S_{\mathrm{BB}}^{(\mathrm{I})} - S_{\mathrm{BB}}^{(\mathrm{II})}\right) \\ S_{\mathrm{DA}} &= \frac{1}{2}\left(S_{\mathrm{AA}}^{(\mathrm{I})} - S_{\mathrm{AA}}^{(\mathrm{II})}\right) & S_{\mathrm{DB}} &= \frac{1}{2}\left(S_{\mathrm{AB}}^{(\mathrm{I})} - S_{\mathrm{AB}}^{(\mathrm{II})}\right) . \end{aligned}$$

From symmetry arguments, we find $S_{\mathrm{DD}} = S_{\mathrm{AA}}$, $S_{\mathrm{CC}} = S_{\mathrm{BB}}$, and $S_{\mathrm{CD}} = S_{\mathrm{BA}}$ and, from reciprocity, we find all the five remaining elements. Simple circuit considerations and some algebra (cf. Ref. [227]) finally allows us to obtain the physical relations

$$S_{\mathrm{AA}}^{(\mathrm{I})} = \frac{1}{\Delta_{\mathrm{HR}}}\left[Y_0^2 - Y_1^2 + \varrho_1\varrho_2 - Y_1\left(\varrho_1 + \varrho_2\right)\cot\theta_1 + jY_0\left(\varrho_2 - \varrho_1\right)\right] , \tag{3.43a}$$

$$S_{\mathrm{AB}}^{(\mathrm{I})} = S_{\mathrm{BA}}^{(\mathrm{I})} = -\frac{2jY_0Y_1\csc\theta_1}{\Delta_{\mathrm{HR}}} , \tag{3.43b}$$

$$S_{\mathrm{BB}}^{(\mathrm{I})} = S_{\mathrm{AA}}^{(\mathrm{I})} - \frac{2jY_0\left(\varrho_2 - \varrho_1\right)}{\Delta_{\mathrm{HR}}} , \tag{3.43c}$$

where

$$\begin{aligned} \Delta_{\mathrm{HR}} = {} & Y_0^2 - \varrho_1\varrho_2 + Y_1\left(\varrho_1 + \varrho_2\right)\cot\theta_1 + Y_1^2 \\ & + jY_0\left(\varrho_1 + \varrho_2 - 2Y_1\cot\theta_1\right) , \end{aligned} \tag{3.44}$$

$\varrho_1 = Y_1\tan(3\theta_1/2)$, $\varrho_2 = Y_1\tan(\theta_1/2)$, $Y_0 = 1/Z_0$, and $Y_1 = 1/Z_1$. The short-circuit two-port scattering matrix parameters are obtained by replacing ϱ_1 by $\varrho_3 = -Y_1\cot(3\theta_1/2)$ and ϱ_2 by $\varrho_4 = -Y_1\cot(\theta_1/2)$. From the above set of equations it is possible to construct the entire 4×4 scattering matrix of the hybrid ring. We remind that the electrical length θ_1 is related to the normalized frequency f/f_0 as $f/f_0 = 2\theta_1/\pi$, where f_0 is the center frequency of operation of the device. Consequently, the center frequency is obtained for $\theta_1 = \pi/2$.

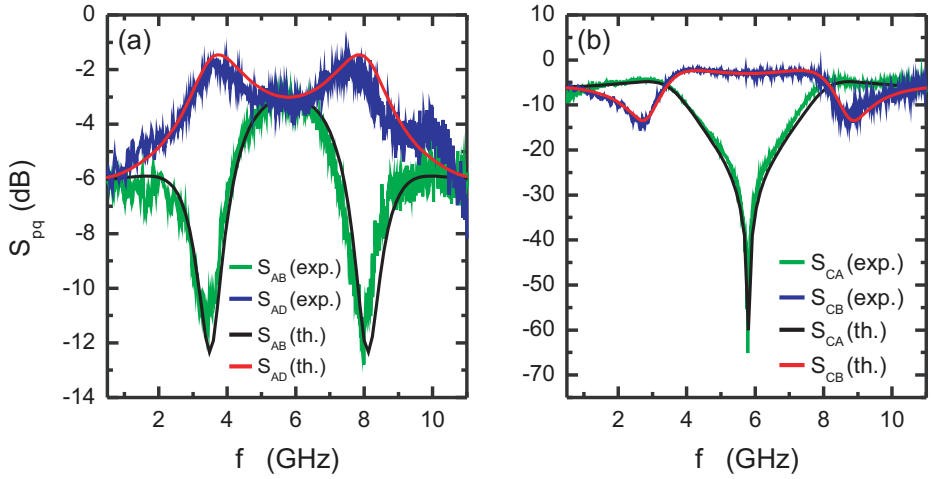

Figure 3.9: Scattering parameters for the 180° hybrid ring (rat race) manufactured by MITEQ-Estonia. **(a)** Light green (light grey) line: coupling parameter between ports A and B, S_{AB}, with ports C and D terminated. Dark blue (dark grey) line: coupling parameter between ports A and D, S_{AD}, with ports B and C terminated. The black and red lines are theoretical calculations for the scattering parameters S_{AB} and S_{AD}, respectively, obtained from the model of Eqs. (3.42a)-(3.44). **(b)** Light green (light grey) line: isolation parameter between ports C and A, S_{CA}, with ports B and D terminated. Dark blue (dark grey) line: coupling parameter between ports C and B, S_{CB}, with ports A and D terminated. The black and red lines are theoretical calculations for S_{CA} and S_{CB}, respectively, obtained from the model of Eqs. (3.42a)-(3.44). The hybrid center frequency is at approximately 5.85 GHz.

Figure 3.9 shows the measurement of a set of relevant scattering matrix parameters S_{pq} for the commercial rat-race hybrid ring used in some of our experiments. The device was developed by T. Neemela at MITEQ-Estonia under the direct supervision of the author. The input lines and internal ring are microstrip lines made of 15 µm thick copper covered with a film of gold and patterned over an alumina substrate. The substrate is glued to a Kovar[17] package. Kovar allows for a better thermal compatibility between package and substrate, which otherwise is likely to break after a few thermal cycles at very low temperatures. The measurements were performed using a vector network analyzer (VNA). The sample was fixed inside the vacuum chamber of a testing dipstick equipped with microwave cables.[18] The dipstick was then cooled to about 4.2 K in liquid helium and the sample thermalized by means of exchange helium gas. All cables were accurately calibrated out. The frequency range was chosen to extend from 1 to 11 GHz. Since it is possible to measure only the transmission between two ports at the time (at least with our VNA), all ports not under test have to be terminated into matched loads. Thus, for the measurement of each scattering parameter shown in Fig. 3.9 it was necessary to make a new cool down. When using a dipstick, the measurement of the reflection

[17]Kovar is a trademark of Carpenter Technology Corporation and is a nickel-cobalt ferrous alloy.
[18]The dipstick has been designed and realized by the author.

parameters is more complex than simple transmission measurements because of the difficulty in calibrating out the long input cables. For this reason we were not able to measure the reflection coefficients of our hybrid ring at low temperatures. However, we measured them at room temperature (data not shown). These measurements show reflection parameters with amplitudes on the order of approximately $-20\,\mathrm{dB}$ or better for all four ports of the hybrid, indicating excellent matching conditions.

The light green (light grey) line in Figure 3.9(a) corresponds to the measured coupling parameter between ports A and B, S_{AB}, with ports C and D terminated. The dark blue (dark grey) line corresponds to the measured coupling parameter between ports A and D, S_{AD}, with ports B and C terminated. The black and red lines are theoretical calculations for the scattering parameters S_{AB} and S_{AD}, respectively, obtained from the model given by Eqs. (3.42a)-(3.44).

The light green (light grey) line in Figure 3.9(b) corresponds to the measured isolation parameter between ports C and A, S_{CA}, with ports B and D terminated. The dark blue (dark grey) line corresponds to the measured coupling parameter between ports C and B, S_{CB}, with ports A and D terminated. Again, the black and red lines are theoretical calculations for S_{CA} and S_{CB}, respectively, obtained from the model developed above. Remarkably, all measured coupling parameters are very close to $-3\,\mathrm{dB}$ in the vicinity of the hybrid center frequency, which was designed to be $f_0 = 5.85\,\mathrm{GHz}$. Close to f_0 the isolation parameters S_{CA} is higher than $50\,\mathrm{dB}$, indicating superb isolation conditions.

Right at the center frequency f_0 (or, equivalently, for $\theta_1 = \pi/2$), the scattering matrix of the hybrid ring becomes

$$\mathbf{S}_{\mathrm{dir}} = -j\frac{1}{\sqrt{2}}\begin{bmatrix} 0 & 1 & 0 & -1 \\ 1 & 0 & 1 & 0 \\ 0 & 1 & 0 & 1 \\ -1 & 0 & 1 & 0 \end{bmatrix}, \tag{3.45}$$

which is the standard form for the scattering matrix of a $3\,\mathrm{dB}$ 180° rat-race hybrid ring. In this case, $Z_1 = \sqrt{2}\,Z_0$ in order for all ports to be matched [227]. As for the case of the scattering matrix of the Wilkinson power divider, we will multiply all the elements of the matrix of Eq. (3.45) by a global phase $-j$. This will allow us to work with Hermitian operators when quantizing the hybrid ring.

In the experiments to be presented in chapter 4, the hybrid ring is screwed to a tempered-silver plate (cf. right part of Fig. 3.16), in a similar manner as for the power divider. Port C is terminated into a load impedance Z_0 acting as the primary noise source of the experiment. The temperature of the termination is controlled and measured by means of a resistive heater and a thermometer, respectively. Port A is connected to a cascade of two $20\,\mathrm{dB}$ Aeroflex attenuators in series to an input line used in some experiments to feed in signals into the hybrid ring. In the experiments discussed in this thesis, however, the input line was not used. Nevertheless, the presence of the attenuators creates a resistive path to ground with resistance equivalent to Z_0. Such resistive path acts as a secondary noise source in a similar fashion as for the power divider.

Let u_{n} and v_{n} be the noise voltages of the primary (port C) and secondary (port

A) noise sources. Assuming all ports of the hybrid ring to be matched and using the Thévenin model of a noisy resistor, the noise voltages at the output ports B and D can easily be found keeping in mind that the incident voltages v_{A}^{+} and v_{C}^{+} are given by the voltage divisions

$$v_{\mathrm{A}}^{+} = \frac{1}{2} v_{\mathrm{n}} \,, \tag{3.46a}$$

$$v_{\mathrm{C}}^{+} = \frac{1}{2} u_{\mathrm{n}} \,. \tag{3.46b}$$

From the standard scattering matrix of Eq. (3.45), opportunely multiplied by a global phase $-j$, we obtain the reflected voltages at ports B and D as

$$v_{\mathrm{B}}^{-} = -\frac{1}{\sqrt{2}} \left(v_{\mathrm{A}}^{+} + v_{\mathrm{C}}^{+} \right) \,, \tag{3.47a}$$

$$v_{\mathrm{D}}^{-} = \frac{1}{\sqrt{2}} \left(v_{\mathrm{A}}^{+} - v_{\mathrm{C}}^{+} \right) \,. \tag{3.47b}$$

Finally, from Eqs. (3.46a) and (3.46b) it follows that

$$v_{\mathrm{B}}^{-} = v_{\mathrm{B}} = \, -\frac{1}{2\sqrt{2}} \left(v_{\mathrm{n}} + u_{\mathrm{n}} \right) \,, \tag{3.48a}$$

$$v_{\mathrm{D}}^{-} = v_{\mathrm{D}} = \frac{1}{2\sqrt{2}} \left(v_{\mathrm{n}} - u_{\mathrm{n}} \right) \,. \tag{3.48b}$$

Following a path similar to that used to obtain the quantum-mechanical relations of Eqs. (3.33a) and (3.33b), we can promote v_{B} and v_{D} to their corresponding quantum-mechanical operators obtaining

$$\begin{aligned} v_{\mathrm{B}} \rightarrow \hat{V}_{\mathrm{B}} &= -\frac{1}{2\sqrt{2}} \bar{V}_{\mathrm{n0}} \left(\hat{a}^{\dagger} + \hat{a} \right) - \frac{1}{2\sqrt{2}} \bar{V}_{\mathrm{n0}} (\hat{c}^{\dagger} + \hat{c}) \\ &= -\frac{1}{\sqrt{2}} \hat{V}_{\mathrm{A}} - \frac{1}{\sqrt{2}} \hat{V}_{\mathrm{C}} \,, \end{aligned} \tag{3.49a}$$

$$\begin{aligned} v_{\mathrm{D}} \rightarrow \hat{V}_{\mathrm{D}} &= \frac{1}{2\sqrt{2}} \bar{V}_{\mathrm{n0}} \left(\hat{a}^{\dagger} + \hat{a} \right) - \frac{1}{2\sqrt{2}} \bar{V}_{\mathrm{n0}} \left(\hat{c}^{\dagger} + \hat{c} \right) \\ &= \frac{1}{\sqrt{2}} \hat{V}_{\mathrm{A}} - \frac{1}{\sqrt{2}} \hat{V}_{\mathrm{C}} \,, \end{aligned} \tag{3.49b}$$

where $\hat{a}^{\dagger}$, $\hat{a}$, $\hat{c}^{\dagger}$, and $\hat{c}$ are bosonic creation and annihilation operators for the input ports A and C of the ring, respectively, and $\hat{b}^{\dagger}$, $\hat{b}$, $\hat{d}^{\dagger}$, and $\hat{d}$ for the output ports B and D. The voltages of Eqs. (3.49a) and (3.49b) are the signals at the input of the detection chain implemented in our experiments (cf. next section). For simplicity, we will rename them as $\hat{V}_{\mathrm{B}} \rightarrow \hat{V}_1$ and $\hat{V}_{\mathrm{D}} \rightarrow \hat{V}_2$ (cf. Fig. 3.10).

3.2 The Detection Chain

We now take the perspective of the noise voltages at the output ports B and C of the Wilkinson power divider or at the output ports B and D of the 180° hybrid ring

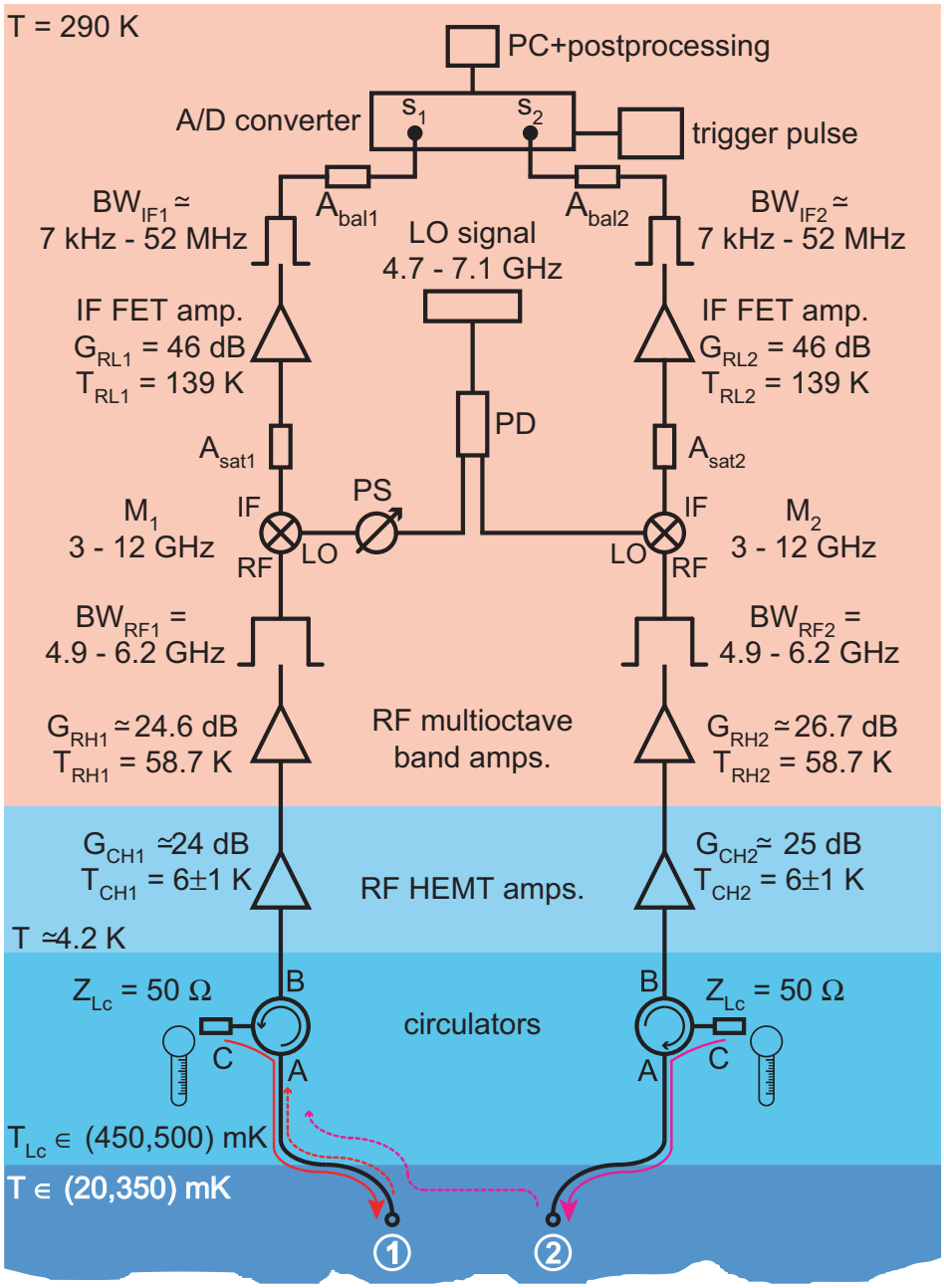

Figure 3.10: The entire setup for cross-correlation homodyne detection. The two channels of the detection chain are indicated as 1 and 2 and are connected directly to the output ports of the microwave beam splitters [ports B and C for the Wilkinson power divider (cf. Fig. 3.1) and ports B and D for the 180° hybrid ring (cf. Fig. 3.8)]. Bottom part. Solid red arrow: noise due to circulator on channel 1; broken red arrow: circulator noise reflected by the splitter into channel 1. Solid magenta arrow: noise due to circulator on channel 2; broken magenta arrow: circulator noise transmitted via the splitter from channel 1 to channel 2. (cf. main text). All relevant temperature stages of the detection chain are indicated together with the characteristic parameters of all devices.

and follow them along our detection chain. Since we have to deal with two output voltages originating from the splitters, the detection chain has to be composed by two channels (cf. Fig. 3.10). As indicated in Figs. 3.1(a) and 3.8, the output ports of the power divider and hybrid are both renamed as ports 1 and 2 in order to use a homogeneous notation along the detection chain. As indicated at the bottom of Fig. 3.10, these two ports constitute the starting point of each channel of the detection chain.

3.2.1 The Cryogenic Circulators

The first stage in each channel of the detection chain is represented by a cryogenic circulator (cf. Fig. 3.10 and bottom part of Fig. 3.17). As indicated by the circular arrows inside the circulator symbol in Fig. 3.10, the characteristic property of a circulator is that a wave incident at port A is coupled into port B only and a wave incident at port B into port C only: The circulator is manifestly an example of a nonreciprocal network. This property is obtained by adding a ferrite material to a T-junction, which otherwise has similar properties as the ideal three-port power divider studied in the beginning of Sec. 3.1.1. For any circulator, the following theorem can be proven [304]:

Theorem 3.2.1 *Any lossless, matched, nonreciprocal T-junction is a perfect three-port circulator.*

Proof As always, the proof follows from the basic properties of the scattering matrix. A perfectly matched T-junction has a scattering matrix of the form

$$\mathbf{S}_{\mathrm{circ}} = \begin{bmatrix} 0 & S_{\mathrm{AB}} & S_{\mathrm{AC}} \\ S_{\mathrm{BA}} & 0 & S_{\mathrm{BC}} \\ S_{\mathrm{CA}} & S_{\mathrm{CB}} & 0 \end{bmatrix} . \tag{3.50}$$

In the case of a nonreciprocal junction the scattering matrix is no longer symmetrical with respect to the leading diagonal, i.e., $S_{pq} \neq S_{qp}$. Nevertheless, if the junction is lossless the scattering matrix must still be unitary and Eq. (3.1) holds. The unitary condition requires that

$$S^*_{\mathrm{AB}} S_{\mathrm{AB}} + S^*_{\mathrm{AC}} S_{\mathrm{AC}} = 1 \,, \tag{3.51a}$$

$$S^*_{\mathrm{BA}} S_{\mathrm{BA}} + S^*_{\mathrm{BC}} S_{\mathrm{BC}} = 1 \,, \tag{3.51b}$$

$$S^*_{\mathrm{CA}} S_{\mathrm{CA}} + S^*_{\mathrm{CB}} S_{\mathrm{CB}} = 1 \tag{3.51c}$$

and that

$$S^*_{\mathrm{AC}} S_{\mathrm{BC}} = S^*_{\mathrm{AB}} S_{\mathrm{CB}} = S^*_{\mathrm{BA}} S_{\mathrm{CA}} = 0 \,. \tag{3.52}$$

If $S_{\mathrm{BA}} \neq 0$, from Eq. (3.52) it follows that $S_{\mathrm{CA}} = 0$. From Eq. (3.51c), it follows that $|S_{\mathrm{CB}}| = 1$. Thus, from Eq. (3.52) it follows that $S_{\mathrm{AB}} = 0$, from Eq. (3.51a) that $|S_{\mathrm{AC}}| = 1$, and from Eq. (3.52) again that $S_{\mathrm{BC}} = 0$. Equation (3.51b) then implies that $|S_{\mathrm{BA}}| = 1$ and

$$|S_{\mathrm{BA}}| = |S_{\mathrm{CB}}| = |S_{\mathrm{AC}}| = 1 \,, \tag{3.53a}$$

$$S_{\mathrm{AB}} = S_{\mathrm{BC}} = S_{\mathrm{CA}} = 0 \,. \tag{3.53b}$$

Table 3.2: PAMTECH cryogenic circulator model CTH1392KS2: nominal specifications [305]. Cf. Table 3.1 for the definition of insertion loss, isolation, and VSWR.

frequency range (GHz)	insertion loss (dB, Typ.)	isolation [dB, Min. (Typ.)]	input VSWR (Typ.)	temperature range (K)
$4-8$	0.4	18 (20)	$1.22:1$	$0.01-77$

The above parameters obviously fulfill the requirements for a perfect circulator. Q.D.E.

If we choose properly all terminal planes at ports A, B, and C such that $S_{\mathrm{BA}} = S_{\mathrm{CB}} = S_{\mathrm{AC}} = 1$ (zero phases), the resulting circulator scattering matrix is given by

$$\mathbf{S}_{\mathrm{circ}} = \begin{bmatrix} 0 & 0 & 1 \\ 1 & 0 & 0 \\ 0 & 1 & 0 \end{bmatrix} , \tag{3.54}$$

which is regarded as the standard form for the scattering matrix of a circulator.

Real circluators are realized by placing an axially magnetized ferrite post in the center of a waveguide or stripline symmetrical junction (a special type of T-junction also called Y-junction) [227]. Suitable tuning elements are placed at the three ports in order to achieve best matching. The circulators used in our experiments were

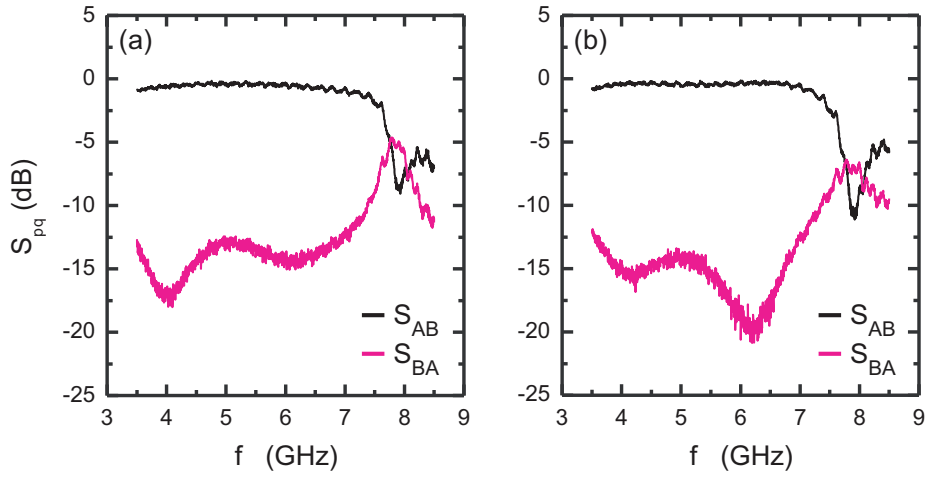

Figure 3.11: Relevant scattering parameters for the PAMTECH cryogenic circulators measured between 3.5 and 8.5 GHz. **(a)** Circulator of channel 1. Black line: coupling parameter S_{AB}. Magenta (middle grey) line: isolation parameter S_{BA}. **(b)** As in **(a)** for the circulator of channel 2.

manufactured by Passive Microwave Technology Inc. (PAMTECH). We refer to Table 3.2 for the nominal specifications. As shown in Fig. 3.10 and in the bottom part of Fig. 3.17, port C of the circulators is terminated into a load impedance $Z_{\rm Lc}(= Z_0)$, which is then heat sunk to the still stage of our dilution refrigerator. The still temperature is nominally held at $T \simeq 500\,\mathrm{mK}$. Owing to such low operation temperature, the circulators have to meet special requirements and must be designed for cryogenic applications. In addition, due to the magnetized ferrite material they must be enclosed inside tick cryoperm shields (cf. bottom part of Fig. 3.17). These shields protect our experiment from DC magnetic fields. For the experiments discussed in this thesis, the presence of DC magnetic fields in the proximity of the noise sources does not constitute a major issue and, in principle, the bulky shields could have been avoided. However, for future experiments based on flux qubits the shields will become important in order to suppress possible disturbance to the quasi-static operation of the qubit. Figures 3.11(a) and 3.11(b) show the measured scattering parameters $S_{\rm AB}$ (coupling, black lines) and $S_{\rm BA}$ [isolation, magenta (middle grey) lines] for the circulators of channel 1 and 2, respectively, employed in our experiments. Notably, the circulators are characterized by a fairly broad bandwidth extending from approximately 3.5 to 7.5 GHz around the center frequency, which was designed to be at $f_0 = 5.85\,\mathrm{GHz}$ (our measurements are close to the specified nominal values reported in Table 3.2). Being the coupling parameter never worse than approximately $-1\,\mathrm{dB}$, the intrinsic losses of the circulators are very small and, for all practical purposes, do not limit the device performance. The measurements were made at room temperature with a VNA. Calibration was performed.

As indicated in Fig. 3.10, the temperature $T_{\rm Lc}$ of the terminations $Z_{\rm Lc}$ at port C of each circulator varies between approximately 450 and 500 mK during the experiment. This phenomenon is due to the heating of the primary noise source at the splitter input, which is thermalized at the mixing chamber of the dilution refrigerator. Varying the temperature of the mixing chamber results in a temperature-dependent heat flow between the mixing chamber and still stage of the refrigerator. While heating the mixing chamber to 350 mK (cf. first temperature stage at the very bottom of Fig. 3.10), the still temperature decreases to approximately 450 mK. When letting cool the mixing chamber to base temperature, the still temperature stabilizes back to the nominal value of 500 mK. We refer to Appendix A for more details on the dependence of the still temperature as a function of the mixing chamber (primary noise source) temperature. As we will show in Appendix A, the still (circulators) temperature drop is measurable, but does not substantially affect our experimental results. Moreover, since the still temperature is monitored at all times, we can accurately account for the effect of the circulators when retrieving the data.

Nevertheless, it is important to understand the exact role played by the circulators in terms of noise added to the signals to be measured. We remind that the two quantum voltages at the output of the Wilkinson power divider or 180° hybrid ring are defined as $\hat{V}_1$ and $\hat{V}_2$, respectively. To keep a general notation, we refer to such voltages as $\hat{V}_k$, where $k = \{1, 2\}$ indicates one of the two channels of the detection chain. The quantum voltage $\hat{V}_k$ constitutes the input voltage of one of the cryogenic circulators. Due to its finite temperature, according to Eq. (3.12a) the circulator inevitably generates a quantum noise voltage

$$\hat{E}_{ck} = \bar{V}_0(\hat{\zeta}_k^\dagger + \hat{\zeta}_k)\,, \tag{3.55}$$

where $\hat{\zeta}_k^\dagger$ and $\hat{\zeta}_k$ are bosonic creation and annihilation operators. Consequently, at the circulator output we must add an effective noise contribution to the input voltage $\hat{V}_k$, obtaining

$$\hat{V}_{ck} = \hat{V}_k + \delta_{ck}\hat{E}_{ck}\,. \tag{3.56}$$

In Eq. (3.56), the coefficient δ_{ck} represents an attenuation constant which accounts for the effective contribution of the circulator noise. The meaning of the coefficient δ_{ck} can be understood following the path of the quantum noise voltage generated by the termination $Z_{\rm Lc}$ at port C of the circulator through the detection chain (red/magenta solid/broken arrows in the bottom part of Fig. 3.10). Let us focus on the case of a Wilkinson power divider. The noise generated in port C, e.g., of the circulator on channel 1 is directed to the output port B of the Wilkinson power divider [solid red arrow in Fig. 3.10; cf. also Fig. 3.1(a) for the port notation used for the divider]. Part of the noise signal is absorbed by the divider and part is reflected back towards port A of the circulator (broken red arrow in Fig. 3.10). The amount of reflected signal can be estimated from the output VSWR of the divider given in Table 3.1. An output VSWR of 1.5 : 1 corresponds to approximately 20 % reflection [306]. The portion of signal absorbed by the Wilkinson power divider is partially transmitted to port C of the divider. This is due to the finite isolation between ports B and C. Looking up Table 3.1 again, we find that the nominal isolation between ports B and C is typically 16 dB. This means that approximately 16 % of the absorbed signal is transmitted to port C. Since the power divider is a symmetric device, a similar noise contribution originating from the circulator on channel 2 (solid magenta arrow in Fig. 3.10) is transmitted from port C to port B of the divider (broken magenta arrow in Fig. 3.10). Hence, the effective quantum noise voltage added by one circulator is given by the sum of the reflected noise on one channel and the noise transmitted from the other channel (sum of broken red and magenta arrows in Fig. 3.10). In first approximation, this amounts to 36 % of the total noise of Eq. (3.55) which is generated by one circulator. Thus, in the experiments we have to assume a coefficient $\delta_{ck} \simeq 0.36$. Similar arguments apply to the case of the 180° hybrid ring, where the coefficient $\delta_{ck} \simeq 0.06$ because of smaller output reflections (typically −25 dB) and better isolation between the output ports (typically −50 dB).

3.2.2 The RF HEMT Cryogenic Amplifiers

The second stage of the detection chain is represented by a pair of RF HEMT cryogenic amplifiers, one for each channel (cf. Fig. 3.10 and center-top part of Fig. 3.17).

The cryogenic amplifiers are the first active device in the detection chain and, thus, their performance is critical for the success of the experiment. In fact, it is because of these amplifiers that we are able to measure the ultra-small quantum signals generated within the coldest region of the cryostat. In contrast to the case of the passive devices analyzed so far in this chapter (beam splitters and circulators), obtaining a detailed quantum model for the process of amplification is a very hard task. Instead of delving into the details of the basic constituents of a cryogenic amplifier, we prefer to attack the problem of amplification from the perspective of quantum network theory. Following the general quantization rules introduced in chapter 2, we start with the classical network modeling an amplifier and then promote it to its corresponding quantum network. Given an input signal, the prop-

erties of such a quantum network allow us to find a) the signal at the output of the amplifier and b) the amount of noise added by the amplifier to the signal. In particular, assuming that the amplifier noise owns its origin to the internal resistive channels of the amplifier, we are able to quantify the minimum noise which must be added by the amplifier to the input signal at zero operating temperature (case of ideal amplifier). This result is a special case of the fundamental theorem for linear phase-preserving amplifiers derived in Ref. [307].

Classification of Quantum-Mechanical Amplifiers

Before describing the classical network model of an amplifier and its quantum version, it is worth summarizing the basic classification and nomenclature for quantum amplifiers. To achieve this task, we follow the seminal work by C. M. Caves [307].

Definition An amplifier is a device that takes an input signal and produces an output signal by allowing the input signal to interact with the internal degrees of freedom of the amplifier.

The input and output signals are assumed to be quantized coordinates of the collective motion of an Avogadro number of electrons. Such motion produces charges and magnetic fluxes which can be represented directly as bosonic modes [188].

The internal degrees of freedom of the amplifier can be bosonic or fermionic modes or a complex admixture of them.

An amplifier can be thought as a collection of interacting modes: The external modes associated with the input and output signals and the internal modes associated with the amplifier internal degrees of freedom, each of them characterized by an angular frequency ω_p, with $p \in \mathbb{R}$. Hereafter, we only consider one single mode with frequency ω_0 (single-mode signal assumption).[19] The single-mode assumption reflects reality if both the input modes and amplifier modes are narrow-band signals. In this case, the input and output signals are nearly sinusoidal oscillations with bandwidth $\mathrm{BW} = \Delta f = f_2 - f_1 = \Delta\omega/2\pi$, where $\Delta\omega = \omega_2 - \omega_1 \ll \omega_0$ is a narrow angular frequency span centered around $\omega_0 = 2\pi f_0$. Information about the signals is carried by slow variations of the signal complex amplitude on a time scale $\tau \approx 1/\Delta f$, i.e., by phase or amplitude modulations. We describe the input modes with single-mode bosonic annihilation and creation operators $\hat{a}$ and $\hat{a}^\dagger$ and the output modes with $\hat{\tilde{a}}$ and $\hat{\tilde{a}}^\dagger$, respectively. The usual commutation relations for single-mode bosonic operators hold, $[\hat{a}, \hat{a}^\dagger] = [\hat{\tilde{a}}, \hat{\tilde{a}}^\dagger] = 1$. In general, the output modes are function of the input modes as

$$\hat{\tilde{a}} = \mathcal{T}(\hat{a}, \hat{a}^\dagger)\,, \tag{3.57a}$$

$$\hat{\tilde{a}}^\dagger = \mathcal{T}^\dagger(\hat{a}, \hat{a}^\dagger)\,, \tag{3.57b}$$

where $\mathcal{T}$ is the amplifier transfer function. Equations (3.57a) and (3.57b) must satisfy appropriate commutation and anticommutation relations (cf. Ref. [307]). In addition, the operating state of the amplifier must be specified in order to have a complete picture of the amplification process. The amplifier operating state is assumed to be independent of the input modes. Formally, this corresponds to assume

[19] If necessary, the generalization to multi-mode signals can readily be carried out at any step of the derivation of the amplifier model [307].

that the initial density matrix of the entire system is the product of the density matrix associated with the input modes and the density matrix associated with the operating state of the amplifier,

$$\hat{\rho}_{\rm tot} = \hat{\rho}_{\rm in} \otimes \hat{\rho}_{\rm op} \,. \tag{3.58}$$

We now specialize Eqs. (3.57a) and (3.57b) to the relevant case of *linear amplifiers*.

Definition A linear amplifier is an amplifier that relates the input and output modes through purely linear relations. The signal information is carried by the complex amplitude of the input and output modes (and not by the number of quanta, i.e., energy or intensity of the signals).

As a consequence, we can simplify Eq. (3.57a) as

$$\hat{\tilde{a}} = \hat{\mathcal{L}}\hat{a} + \hat{\mathcal{M}}\hat{a}^\dagger + \hat{\xi} \,. \tag{3.59}$$

A similar results is found when linearizing Eq. (3.57b).

The operator $\hat{\xi}$ accounts for the additive noise of the amplifier. This noise is independent of the input signal level and is solely due to the amplifier internal modes (resistive channels). Typically,

$$\langle \hat{\xi} \rangle_{\rm op} = 0 \,, \tag{3.60}$$

where the subscript "op" indicates that the mean value is computed for the amplifier prepared in the operating state. A similar result as in Eq. (3.60) also holds for the Hermitian noise operator $\hat{\xi}^\dagger$, i.e., $\langle \hat{\xi}^\dagger \rangle_{\rm op} = 0$.

The operators $\hat{\mathcal{L}}$ and $\hat{\mathcal{M}}$ are clearly related to the amplifier gain. In particular, neglecting any gain fluctuation we can define the amplifier gain as

$$L \equiv \langle \hat{\mathcal{L}} \rangle_{\rm op} \,, \tag{3.61a}$$

$$M \equiv \langle \hat{\mathcal{M}} \rangle_{\rm op} \,. \tag{3.61b}$$

Substituting Eqs. (3.61a) and (3.61b) into Eq. (3.59), we finally obtain the standard input-output relation for a linear amplifier,

$$\hat{\tilde{a}} = L\hat{a} + M\hat{a}^\dagger + \hat{\xi} \,. \tag{3.62}$$

All our ignorance about the internal modes of the amplifier in the operating state is hidden in the operator $\hat{\xi}$ and in the constants L and M.

In order to make a suitable classification of linear amplifiers, it is crucial to revise the notion of phase-insensitive noise.

Definition A state whose noise is randomly distributed in phase space is said to be phase-insensitive. More formally, a state with phase-insensitive noise is such that

$$\langle \hat{a}^2 \rangle - \langle \hat{a} \rangle^2 = 0 \,. \tag{3.63}$$

The reader should be aware that $\langle \hat{a}^2 \rangle$ is not the variance of a signal, it is only a part of it. However, it is an important part. For example, for a squeezed state this part of the variance defines the variance phase-dependence, which also means that squeezed states are not phase-insensitive states [91]! Coherent states and thermal-equilibrium states are instead phase-insensitive [cf. Ref. [307], p. 1822, right after Eq. (3.13)]. In particular, for a thermal-equilibrium state (hereafter referred to simply as thermal state) it can be shown that [307],

$$\langle \hat{a}^2 \rangle = \langle \hat{a} \rangle^2 = 0 \,, \tag{3.64}$$

which embodies the twofold property of a thermal state: phase-insensitive and with vanishing mean value (i.e., $\langle \hat{a} \rangle = \langle \hat{a}^\dagger \rangle = 0$). We will use the fundamental condition of Eq. (3.64) in chapter 4. To appreciate the relevance of Eq. (3.64) it is worth mentioning that many authors believe that, when computing the variance of a thermal state, the terms $\hat{a}^2$ [and $(\hat{a}^\dagger)^2$] are cancelled because of a RWA. They think the filter used in the experiments acts as a physical RWA, which erases the phase information carried by the signal. In the light of the condition expressed by Eq. (3.64) it is now clear that this is not the case and the reason why for a thermal state such terms vanish is because of the phase-insensitive property. Of course, if instead of the variance of the signal it is its power to be measured, then the RWA argument holds. Variance measurements and power measurements are inherently different even if the units typically used are the same in both cases (W). These two types of measurement give the same result iff the state being monitored is phase-insensitive! It is unfortunate that many do not appreciate the beauty of this statement.[20] We will come back to variance measurements in the next chapter.

All linear amplifiers can be reduced to two fundamental classes. The class of *phase-preserving* amplifiers and the class of *phase-sensitive* amplifiers. In the literature, phase-preserving amplifiers are oftentimes defined as phase-insensitive amplifiers [307]. Then, among phase-insensitive amplifiers the subclasses of phase-preserving and phase-conjugating amplifiers are defined. Since it is hardly conceivable to realize a phase-conjugating amplifier (and rather useless), we prefer to call all phase-insensitive amplifiers as phase-preserving (indeed, in contemporary literature this is most common notation; e.g., cf. Ref. [309]).

Definition A linear amplifier is said to be phase-preserving when, given an input signal with phase-insensitive noise, the output in both terms of signal and noise shows no phase preference. A phase shift of the input signal corresponds to an equivalent phase shift of the output. This can be formalized in the two following conditions:

1. The expression for $\langle \hat{\hat{a}} \rangle$ is invariant under arbitrary phase transformations of the input signal of the kind

$$\hat{a} \rightarrow \hat{\hat{a}} = \hat{a}\, e^{-j\varphi} \,; \tag{3.65}$$

[20] The author admits that it took a while for himself to understand such subtle, but nevertheless crucial differences. The reader can try to solve the following exercise. Calculate the variance of a squeezed state and compare it to the power measured by means of a square-law detector. *Hint:* Check Ref. [308] for a definition of classical square law detector and extend it to the quantum case by means of our procedure for the quantization of a classical network. Then compute the mathematical variance of the quantum signal. Check Ref. [91] for a simple definition of squeezed state.

2. If the input signal has phase-insensitive noise, the output signal also has phase-insensitive noise,
$$\langle \hat{a}^2 \rangle = \langle \hat{a} \rangle^2 \quad \Rightarrow \quad \langle \hat{\hat{a}}^2 \rangle = \langle \hat{\hat{a}} \rangle^2 \,. \tag{3.66}$$

The first condition means that a phase shift of the input signal produces the same phase shift of the output signal (phase-preservation).[21] The second condition means that the amplifier adds noise which is randomly distributed in phase space [cf. the definition of Eq. (3.63)].

Definition A linear amplifier that fails to meet both conditions 1. and 2. is defined as phase-sensitive amplifier.

We can now work out the constraints due to the conditions for a linear phase-preserving amplifier. Condition 1. implies that

$$M = 0 \tag{3.67}$$

and condition 2. that
$$\langle \hat{\xi}^2 \rangle_{\rm op} = 0 \,. \tag{3.68}$$

Equation (3.68) also holds for the Hermitian noise operator $\hat{\xi}^\dagger$, i.e., $\langle (\hat{\xi}^\dagger)^2 \rangle_{\rm op} = 0$. We remind that Eqs. (3.67) and (3.68) are constraints for both the standard input-output relation of Eq. (3.62) and the amplifier operating state.[22] From Eq. (3.67) it follows that the power gain for a phase-preserving amplifier is given by $G = g^2$, where $g = L$ is called the signal gain.

Quantum Network Theory of Amplification

In hand now are all necessary tools to study the amplification process from the point of view of quantum network theory. We assume linear phase-preserving amplifiers, which are the ones used in our experiments. Figure 3.12(a) shows the network model associated with one such amplifier. It is sufficient to define the amplifier signal noise and gain in order to obtain a minimal model consistent with quantum mechanics [307]. The amplifier is represented as a two-port network comprising both noise and gain, a so-called noisy two-port network. The input signal is assumed to be either $\hat{V}_{\rm c1}$ or $\hat{V}_{\rm c2}$, i.e., one of the output signals of the Wilkinson power divider [cf. Eqs. (3.33a) and (3.33b)] or hybrid ring [cf. Eqs. (3.49a) and (3.49b)] with the addition of the temperature-dependent noise introduced by the cryogenic circulators. As already pointed out in Subsec. 3.2.1, the circulators have no other practical effect on the signals at the output of the splitters than adding this (tiny) noise [cf. Eqs. (3.56)]. As always, in the figure and calculations we refer to the generic quantum voltage $\hat{V}_{ck}$, with $k = \{1, 2\}$.

In analyzing the noise produced at the output of a linear two-port network due to the internal noise sources, we can replace all such sources by a series noise voltage generator,
$$\hat{E}_{{\rm n}k} = \bar{V}_0(\hat{\xi}_k^\dagger + \hat{\xi}_k) \,, \tag{3.69}$$

[21] We recall that $\langle \hat{\xi} \rangle_{\rm op} = 0$, cf. Eq. (3.60).

[22] It can happen that a phase-sensitive amplifier, prepared in some initial operating state, can then be prepared in a new state which makes it phase-preserving.

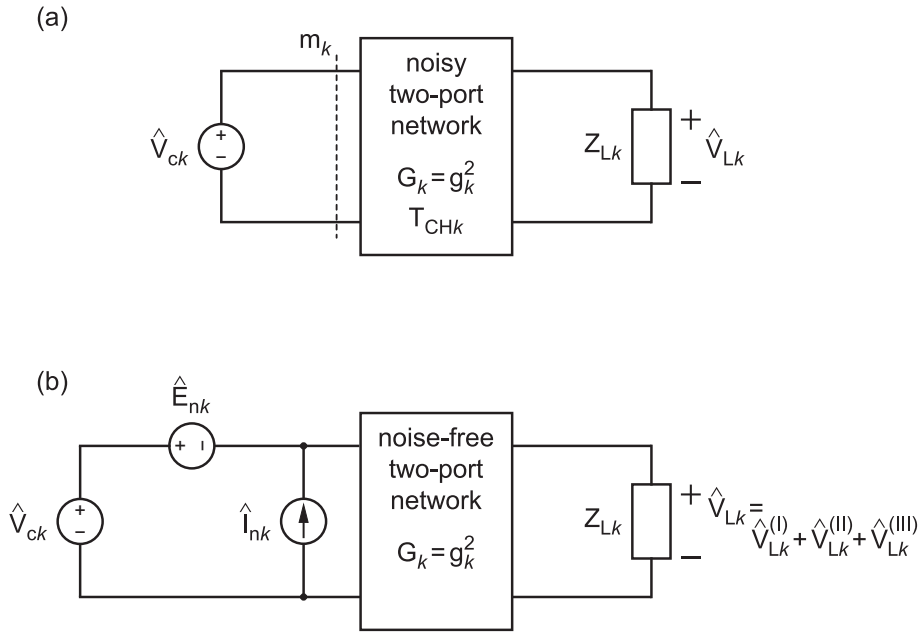

Figure 3.12: Circuit models for the quantum network theory of amplification. **(a)** Noisy two-port network with input voltage source, $\hat{V}_{ck}$, and output load impedance, $Z_{\mathrm{L}k}$. **(b)** Equivalent input noise voltage source, $\hat{E}_{\mathrm{n}k}$, and noise current source, $\hat{I}_{\mathrm{n}k}$, for the noisy two-port network of **(a)**. Applying the superposition principle to the circuit model of **(b)** allows us to obtain the output voltage on the load impedance, $\hat{V}_{\mathrm{L}k}$ (cf. main text for the full derivation).

and a shunt noise current generator,

$$\hat{I}_{\mathrm{n}k} = \bar{I}_0\, j(\hat{\xi}_k^{\dagger} - \hat{\xi}_k)\,, \tag{3.70}$$

at the input, as shown in Fig. 3.12(b). In Eqs. (3.69) and (3.70), $\hat{\xi}_k^{\dagger}$ and $\hat{\xi}_k$ are the bosonic creation and annihilation operators associated with the noise for the cryogenic amplifier of the first or second amplification chain, $\bar{V}_0 = \sqrt{\hbar Z_0 \omega_0/2}$ is calculated at the center angular frequency ω_0, and $\bar{I}_0 = \bar{V}_0/Z_0$. Two equivalent noise sources are required at the input because if the input is short-circuited, the source $\hat{I}_{\mathrm{n}k}$ does not produce any output noise. However, the noisy two-port network does have a noise output under short circuit conditions at the input, hence the need for $\hat{E}_{\mathrm{n}k}$ to be included in the network. Similar arguments hold for the case of open circuit conditions at the input with the role of $\hat{I}_{\mathrm{n}k}$ and $\hat{E}_{\mathrm{n}k}$ interchanged [227]. If Γ_k is the reflection coefficient of the two-port network, it is custom to define the impedance mismatch $m_k \equiv 1 - |\Gamma_k|^2$. In real amplifiers the impedance mismatch can be of relevance and can have important consequences in the quantitative derivation of the model. For simplicity, we hereafter assume $m_k = 1$ (perfect matching conditions) and remind the interested reader to Ref. [227] for a complete analysis of the noise properties of classical amplifiers including impedance mismatch.

The output signal including noise on the load impedance $Z_{\mathrm{L}k}$ (cf. Fig. 3.12) can be obtained invoking the superposition principle for linear networks. This corresponds

to consider one source (voltage or current) at the time and switch off all other sources by substituting them with short circuits (for voltage sources) or open circuits (for current sources). First, we replace $\hat{E}_{\mathrm{n}k}$ with a short circuit (SC) and $\hat{I}_{\mathrm{n}k}$ with an open circuit (OC),

$$\hat{E}_{\mathrm{n}k} \quad \rightarrow \quad \mathrm{SC}\,, \tag{3.71a}$$

$$\hat{I}_{\mathrm{n}k} \quad \rightarrow \quad \mathrm{OC}\,. \tag{3.71b}$$

In this way, the input contribution to the output voltage on the load impedance $Z_{\mathrm{L}k}$ is only given by the quantum signal $\hat{V}_{\mathrm{c}k}$,

$$\hat{V}_{\mathrm{L}k}^{(\mathrm{I})} = g_k \hat{V}_{\mathrm{c}k}\,, \tag{3.72}$$

where g_k is the signal gain for either one of the two cryogenic amplifiers. Second, we replace $\hat{V}_{\mathrm{c}k}$ with a short circuit and $\hat{I}_{\mathrm{n}k}$ with an open,

$$\hat{V}_{\mathrm{c}k} \quad \rightarrow \quad \mathrm{SC}\,, \tag{3.73a}$$

$$\hat{I}_{\mathrm{n}k} \quad \rightarrow \quad \mathrm{OC}\,. \tag{3.73b}$$

In this way, the input contribution to the output voltage on $Z_{\mathrm{L}k}$ is only given by the quantum noise voltage $\hat{E}_{\mathrm{n}k}$ of the amplifier,

$$\hat{V}_{\mathrm{L}k}^{(\mathrm{II})} = g_k \hat{E}_{\mathrm{n}k}\,. \tag{3.74}$$

Third, we replace both $\hat{E}_{\mathrm{n}k}$ and $\hat{V}_{\mathrm{c}k}$ with short circuits,

$$\hat{E}_{\mathrm{n}k} \quad \rightarrow \quad \mathrm{SC}\,, \tag{3.75a}$$

$$\hat{V}_{\mathrm{c}k} \quad \rightarrow \quad \mathrm{SC}\,. \tag{3.75b}$$

In this special case, the input of the amplifier is under short circuit conditions and, thus, the input voltage is zero. As a consequence, the output voltage on $Z_{\mathrm{L}k}$ after amplification is also zero,

$$\hat{V}_{\mathrm{L}k}^{(\mathrm{III})} = 0\,. \tag{3.76}$$

Superimposing the solutions of Eqs. (3.72), (3.74), and (3.76) finally allows us to obtain the total voltage on the load impedance $Z_{\mathrm{L}k}$,

$$\begin{aligned} \hat{V}_{\mathrm{L}k} &= \hat{V}_{\mathrm{L}k}^{(\mathrm{I})} + \hat{V}_{\mathrm{L}k}^{(\mathrm{II})} + \hat{V}_{\mathrm{L}k}^{(\mathrm{III})} \\ &= g_k(\hat{V}_{\mathrm{c}k} + \hat{E}_{\mathrm{n}k})\,. \end{aligned} \tag{3.77}$$

Throughout the rest of this thesis, we prefer to use Eq. (3.77) rather than Eq. (3.62) as the basic input-output relation for a linear phase-preserving amplifier.

It is now an easy exercise to calculate the generic variance of the output signal given by Eq. (3.77) normalized over the load impedance Z_0 for the amplifier in a given operating state. Using Eq. (3.77) and defining the power gain for either one of the two cryogenic amplifiers as $G_{\mathrm{CH}k} \equiv g_k^2$ (cf. Fig. 3.10), the normalized variance is given by

$$\begin{aligned} \frac{1}{Z_0}(\Delta\hat{V}_{\mathrm{L}k})^2 &\equiv \frac{1}{Z_0}\big(\langle\hat{V}_{\mathrm{L}k}^2\rangle_{\mathrm{op}} - \langle\hat{V}_{\mathrm{L}k}\rangle_{\mathrm{op}}^2\big) \\ &= \frac{G_{\mathrm{CH}k}}{Z_0}\big[\langle\hat{V}_{\mathrm{c}k}^2\rangle_{\mathrm{op}} + 2\langle\hat{V}_{\mathrm{c}k}\rangle_{\mathrm{op}}\langle\hat{E}_{\mathrm{n}k}\rangle_{\mathrm{op}} + \langle\hat{E}_{\mathrm{n}k}^2\rangle_{\mathrm{op}} \\ &\quad - \langle\hat{V}_{\mathrm{c}k}\rangle_{\mathrm{op}}^2 - 2\langle\hat{V}_{\mathrm{c}k}\rangle_{\mathrm{op}}\langle\hat{E}_{\mathrm{n}k}\rangle_{\mathrm{op}} - \langle\hat{E}_{\mathrm{n}k}\rangle_{\mathrm{op}}^2\big]\,. \end{aligned} \tag{3.78}$$

It has been possible to obtain Eq. (3.78) by assuming signals $\hat{V}_{ck}$ and $\hat{E}_{nk}$ to be completely uncorrelated (this is a good assumption since they are generated by independent sources, i.e., the two amplifiers). Only in this case we are allowed to write $2\langle\hat{V}_{ck}\hat{E}_{nk}\rangle_{op} = 2\langle\hat{V}_{ck}\rangle_{op}\langle\hat{E}_{nk}\rangle_{op}$. In addition, because of the definition of Eq. (3.69) and the condition of Eq. (3.60), $\langle\hat{E}_{nk}\rangle^2_{op} = \langle(\hat{\xi}^\dagger_k + \hat{\xi}_k)\rangle^2_{op} = 0$. Using again the definition of Eq. (3.69) and defining the variance of signal $\hat{V}_{ck}$ as $(\Delta\hat{V}_{ck})^2 \equiv \langle\hat{V}^2_{ck}\rangle_{op} - \langle\hat{V}_{ck}\rangle^2_{op}$ we then obtain

$$\begin{aligned}\frac{1}{Z_0}(\Delta\hat{V}_{Lk})^2 &= G_{CHk}\left[\frac{(\Delta\hat{V}_{ck})^2}{Z_0} + \frac{\bar{V}_0^2}{Z_0}\langle(\hat{\xi}^\dagger_k)^2 + \hat{\xi}^\dagger_k\hat{\xi}_k + \hat{\xi}_k\hat{\xi}^\dagger_k + (\hat{\xi}_k)^2\rangle_{op}\right] \\ &= G_{CHk}\left[\frac{(\Delta\hat{V}_{ck})^2}{Z_0}\right. \\ &\quad \left. + \hbar\omega_0\langle\hat{\xi}^\dagger_k\hat{\xi}_k\rangle_{op} + \frac{\hbar\omega_0}{2}\right], \end{aligned} \tag{3.79}$$

where we have used the phase-insensitive noise condition of Eq. (3.68) and the commutation relation for the noise bosonic operators, $[\hat{\xi}_k, \hat{\xi}^\dagger_k] = 1$.

The equivalent noise temperature of the amplifier is defined as

$$T_{CHk} \equiv \frac{1}{k_B}\left(\hbar\omega_0\langle\hat{\xi}^\dagger_k\hat{\xi}_k\rangle_{op} + \frac{\hbar\omega_0}{2}\right). \tag{3.80}$$

Together with the power gain, the noise temperature is the commonly used figure of merit to characterize the quality of an amplifier. From Eq. (3.80) it is evident that the noise temperature is defined for one single internal mode of the amplifier with frequency ω_0. That is, it represents the equivalent amount of noise (expressed in number of quanta) added by the amplifier to a single-mode input signal. If we are interested in the noise power added by the amplifier for a bandwidth Δf, this is simply given by

$$P_{CHk} = k_B T_{CHk}\,\Delta f\,. \tag{3.81}$$

Given that the amplifier noise is generated by its internal resistive channels, we can assume that $\langle\hat{\xi}^\dagger_k\hat{\xi}_k\rangle_{op}$ follows a Bose-Einstein distribution,

$$\langle\hat{\xi}^\dagger_k\hat{\xi}_k\rangle_{op} = \frac{1}{e^{\hbar\omega_0/k_B T_{opk}} - 1}\,, \tag{3.82}$$

where T_{opk} is the amplifier operating temperature.[23] This assumption is not valid in general. In fact, the noise of an amplifier can be more complex than the simple white Gaussian noise associated with a resistor in thermal equilibrium at a given temperature. However, since we are interested in the amplifier behavior for a narrow frequency bandwidth around the center frequency f_0 and, in our experiments, we do not access higher moments than the second central moment (the variance), for our purposes Eq. (3.82) can be considered to be a good model.

Equations (3.80) and (3.82) have important consequences on the limiting performance of the amplifier. If the amplifier were prepared in an operating state close

[23] Equation (3.82) holds only for a narrow-bandwidth amplifier.

to zero absolute temperature, $T \to 0^+$, its noise temperature would approach the minimum possible value allowed by quantum mechanics,

$$T_{\mathrm{CH}k} \to \frac{\hbar\omega_0}{2} = T_{\mathrm{CH}k}^{\min}\,. \tag{3.83}$$

This is due to the fact that the Bose-Einstein distribution of Eq. (3.82) vanishes at very low temperatures. Equation (3.83) represents one form of the *fundamental theorem for phase-preserving linear amplifiers* [307], which states that one such amplifier must add a minimum noise equivalent to the vacuum fluctuations associated with its mode of operation. A more formal statement of this theorem can be found in Ref. [307].

It is worth mentioning that the network model of an amplifier developed so far is oversimplified. For example, the value for the internal resistance ($R_{\mathrm{e}k}$) associated with the amplifier noise voltage and of the internal conductance ($G_{\mathrm{i}k}$) associated with the amplifier noise current do not explicitly appear in Eqs. (3.79) and (3.80). The simple model behind these equations seems to imply that the noise properties of the amplifier only depend on the amplifier operating temperature $T_{\mathrm{op}k}$. In particular, in the limit of high temperature, $T_{\mathrm{op}k} \gg \hbar\omega_0/2k_{\mathrm{B}}$, Eq. (3.82) becomes asymptotically close to $k_{\mathrm{B}}T_{\mathrm{op}k}$ and the amplifier noise temperature saturates to temperature $T_{\mathrm{op}k}$, $T_{\mathrm{CH}k} \approx T_{\mathrm{op}k}$. This is only partially correct. In fact, in a more realistic model (e.g., cf. Ref. [227]) the internal resistance and conductance of the amplifier enter in the form of dimensionless quantities renormalized over the resistance of the input source. This means that the design of a low noise amplifier can be optimized playing with at least two parameters: the amplifier operating temperature and its internal resistance (conductance).[24] Nevertheless, the fundamental limit given by Eq. (3.83) holds even if $R_{\mathrm{e}k} \to 0$ ($G_{\mathrm{i}k} \to 0$) and $T_{\mathrm{op}k} \to 0^+$ simultaneously.

We now turn our attention to a more technical analysis of the specifications and characteristic parameters of the HEMT cryogenic amplifiers employed in our experiments.

As indicated in Fig. 3.10, the cryogenic amplifiers are thermalized at a constant operating temperature of approximately 4.2 K inside the vacuum chamber of the dilution refrigerator (cf. center-top part of Fig. 3.17). The operating temperature can be assumed to be constant since it is set by the helium bath of the cryostat, which acts as a large heat reservoir. At this temperature, the noise temperature for both amplifiers is nominally $T_{\mathrm{CH1}} = T_{\mathrm{CH2}} = 6 \pm 1\,\mathrm{K}$.[25] These nominal values were measured at the Onsala Space Observatory and GARD group at Chalmers University of Technology, Gothenburg, Sweden,[26] where the cryogenic amplifiers were also manufactured. The amplifiers are based on two-stage high electron-mobility transistors (HEMTs) [310, 311], which allow for the operation at low temperatures (where regular semiconductor transistors do not work) and for very low noise performances. The HEMTs used in our amplifiers are based on gallium-arsenide technology and are engineered to dissipate power on the order of 15 mW (nominal value). Low power dissipation is a highly desirable property for cryogenic amplifiers to be used

[24] For this very reason it is possible to design room temperature amplifiers with noise temperatures of less than 60 K, which is much lower than room temperature (here assumed to be 290 K).

[25] In chapter 4, we will show more accurate noise temperature measurements.

[26] The noise temperature measurements were actually performed at 12 K, but nothing should prevent us from assuming similar values at 4.2 K, where the noise temperature should be even lower.

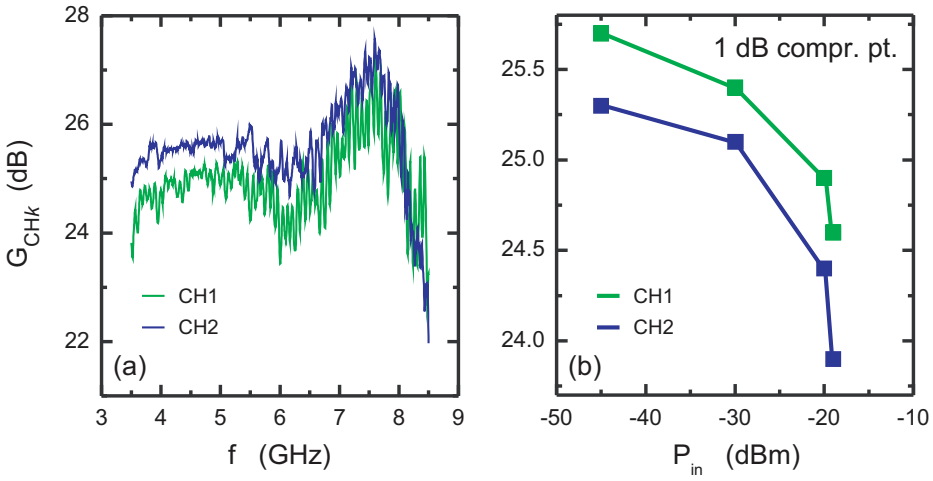

Figure 3.13: The RF HEMT cryogenic amplifiers. **(a)** Light green (light grey) line: power gain for the cryogenic amplifier of channel 1, G_{CH1}. Dark blue (dark grey) line: power gain for the cryogenic amplifier of channel 2, G_{CH2}. **(b)** Power dependence of the gain for the two cryogenic amplifiers. The light green (light grey) squares refer to the amplifier of channel 1 and the dark blue (dark grey) squares to that of channel 2. The light green (light grey) horizontal line indicates the 1 dB compression point for the amplifier of channel 1 and the dark blue (dark grey) horizontal line the 1 dB compression point for the amplifier of channel 2.

in dilution refrigerators. Even if at 4.2 K the available cooling power is fairly large (practically unlimited as long as one refills helium), it is not a wise idea to thermalize a device with very large power consumption in the vacuum chamber of a dilution refrigerator, if for not better reason because of possible instabilities in the refrigerator operation or heat leaks to nearby stages.

In our case, the two-stage transistors have to be biased with two drain voltages, two gate voltages, and a ground reference for a total of five DC bias lines for each amplifier (the expert reader may notice the CINCH connectors providing the DC bias lines in the center-top part of Fig. 3.17). The optimal value used in the experiments for the drain voltage of each stage of each amplifier is $v_{\mathrm{d}} \simeq 1.5\,\mathrm{V}$ and for the drain current $i_{\mathrm{d}} \simeq 5\,\mathrm{mA}$. From these values we can also estimate the power consumption for the two stages, $P_{\mathrm{diss}} = 2v_{\mathrm{d}}i_{\mathrm{d}} \simeq 15\,\mathrm{mW}$, which is consistent with the nominal value given by the manufacturer.

Figure 3.13(a) shows a measurement of the power gain for both cryogenic amplifiers employed in our experiments at the optimal bias points. The gain is pretty flat ($\mp \sim 3\,\mathrm{dB}$) over a bandwidth extending from approximately 4 to 8 GHz. At the frequency of interest, $f_0 = 5.85\,\mathrm{GHz}$, we find the power gains $\widetilde{G}_{\mathrm{CH1}} = 10^{G_{\mathrm{CH1}}/10} \simeq 24\,\mathrm{dB}$ and $\widetilde{G}_{\mathrm{CH2}} = 10^{G_{\mathrm{CH2}}/10} \simeq 25\,\mathrm{dB}$. The measurement of the power gain of an amplifier can easily be performed by means of a VNA, which allows us to measure the direct transmission parameter S_{21} of the amplifiers. After an opportune network calibration, S_{21} corresponds to the desired amplifier power gain. Network calibration is a nontrivial task at low temperatures. In order to obtain the curves of Fig. 3.13(a),

we have to make a first cool down where the cryogenic amplifiers are replaced by a through connector and the entire network response is measured and stored for calibration. Only then the amplifiers are placed back into the network instead of the through connectors and, in a second cool down, the amplifier power gain is measured. This cumbersome procedure allows us to clean the measurement from the unwanted transmission response of all cables and other necessary microwave components. It is important to mention that our original plan was to thermalize the cryogenic amplifiers at the 1 K-pot stage of the refrigerator aiming at slightly better amplifier noise temperatures. The measurements of Fig. 3.13(a) are indeed performed under these conditions. However, during those measurements we pretty soon figured out that the available cooling power of the 1 K-pot was insufficient to both thermalize the amplifiers and properly operate the dilution refrigerator [312]. As a consequence, the amplifiers were thermalized at 4.2 K in all subsequent experiments.

Another important figure of merit of an amplifier is the so-called 1 dB compression point. The 1 dB compression point is determined by the power level at which the amplifier power gain decreases by 1 dB with respect to the optimal value. Experimentally, the 1 dB compression point can be obtained by monitoring the amplifier gain as a function of the amplifier input power. For sufficiently low power levels the gain is flat and maximum. When the power is increased above some threshold, the amplifier starts being saturated. In other words, the elongation of the sinusoidal excitation (proportional to the power) at the amplifier input around the DC biasing point becomes large enough to excite a nonlinear response. Because of such response the gain curve looses its flatness and the gain decreases. This is an example that all assumptions on linear amplifiers are valid only for a very restricted range of parameters. Outside this range, the internal degrees of freedom of the amplifier are not independent of the input signal level anymore and all our models fail. Figure 3.13(b) shows a rough estimate of the 1 dB compression point for our cryogenic amplifiers at $f_0 = 5.85\,\mathrm{GHz}$. Saturation happens at approximately $-20\,\mathrm{dB}$. Notably, this signal is extremely large as compared to the signals we intend to measure (on the order of $-140\,\mathrm{dBm}$ or less!) and, thus, the cryogenic amplifiers will hardly be saturated in the experiments. We remind to Ref. [312] for a more profound discussion on amplifier compression and on the technical limitations of the measurements shown in Fig. 3.13(b).

3.2.3 The Cold Feedthroughs

Before entering the third stage of the detection chain, the signals have to pass from the vacuum chamber of the dilution refrigerator to the helium bath and, finally, to the room temperature microwave equipment.

The interface between the high vacuum and ^{4}He stage is implemented by means of a pair of cold feedthroughs, as shown in the bottom part of Fig. 3.18. Such devices represent a crucial link between the actual dilution stage of the refrigerator and the external world and cost a great deal of work to the author to be designed and developed. We can summarize the technical challenges behind the realization of the cold feedthroughs saying that the feedthroughs have to be operated at 4.2 K, they must be highly hermetic to avoid any leak to the cryostat vacuum chamber, they have to sustain high frequency signals up to 40 GHz, and, last but not least, they should not break after each cool down (i.e., they have to be robust with respect

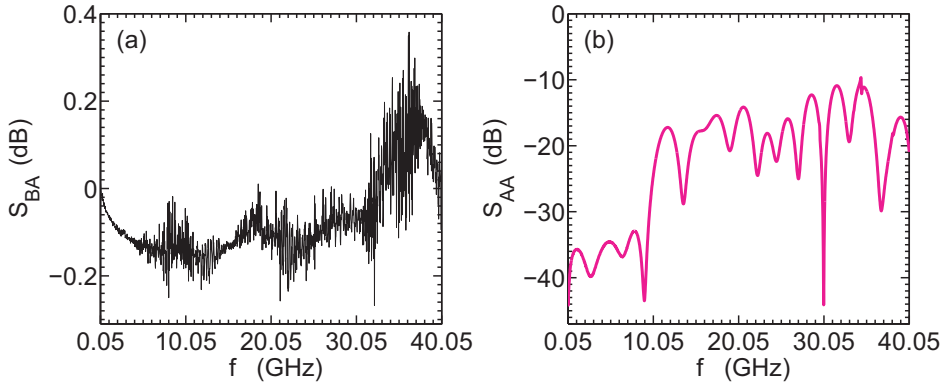

Figure 3.14: Transmission and reflection characteristics for the cold hermetic microwave feedthroughs developed at the Walther-Meissner-Institut by the author. **(a)** Measurement of the direct transmission parameter S_{BA} from 50 MHz to 40.05 GHz. The tiny "gain" above approximately 30 GHz is due to a slight miscalibration of the VNA. **(b)** Measurement of the reflection parameter S_{AA} from 50 MHz to 40.05 GHz.

to heavy duty thermal cycling).

After a fairly large set of trial-and-error steps, the cold feedthroughs were successfully implemented. The basic recipe for their manufacturing is as follows:

1. Design an OFHC-copper housing as sketched and shown in the bottom-right part of Fig. 3.18. The housing serves to accommodate a so-called glass bead. This is the key ingredient for the feedthrough to work. The beads used are V100 glass support beads produced by the ANRITSU Company, Japan. The beads are specified for a temperature range between 55 and 300°C, but, as it turns out, they work very well down to 4.2 K. The bead sleeve and center conductor are made of Kovar and are gold plated. The bead itself is corning 7070 glass. The model V100 is used to mate with so-called V sparkplug launcher male/female connectors (V102M/F) [313]. The V connector is a Wiltron/ANRITSU Corporation connector, developed in 1989. This connector uses a 1.85 mm geometry and is mode-free up to 65 GHz;

2. The glass bead is soldered inside the inner hole of the housing. This is the critical step for the final product to be hermetic. The solder has to flow all around the bead. The soldering has to be done on a hot plate with the aid of extra soldering irons. A stainless-steel soldering fixture has to be mounted into the top and bottom threads of the housing. These threads will then be used for the actual sparkplug connectors. The fixture avoids solder to flow into the threads eventually damaging them. A reasonable amount of Castolin eutectic has to be used to perform proper hot soft soldering of the bead to the housing;

3. After cooling and cleaning with acetone and isopropyl alcohol, two sparkplug connectors are screwed into the top and bottom threads of the housing. The threads have to be made using the ANRITSU drill and tap set, model 01 − 304 [313] (or equivalent tools), which allows one to make a flat surface at

the bottom of the thread (instead of the standard conical shape, which would prevent from a good galvanic electrical contact between the sparkplugs and glass bead; cf. the bottom-right part of Fig. 3.18). Loctite 243 can be applied to the sparkplug connector's therads to improve the connector stability;

4. Finally, the sparkplug connector must be torqued by means of the appropriate ANRITSU torquing kit model $01-105$A.

Once the feedthrough is manufactured, it has to be first tested for DC shorts against ground. Then, the transmission and reflection parameters have to be measured. If the device works properly at room temperature, the cold testing begins. In our case, the testing was performed using a dipstick equipped with microwave cables. The feedthrough was placed on the top part of the vacuum chamber of the dipstick with the input and output sparkplug connectors connected to two standard stainless-steel UT085 coaxial cables. After cooling the dipstick in a large vessel filled with liquid helium, the first basic check is against leaks between the vacuum chamber of the dipstick and the helium bath. This is realized by means of a leak detector set for ^{4}He-mass detection, which allows for the continuous monitoring of the feedthrough hermeticity while the feedthrough is cold. The typical leak rate detected for all our feedthroughs was on the order of $5.0 \times 10^{-8}\,\mathrm{mbar\,L\,s^{-1}}$ or better. This procedure was repeated for at least ten times for each feedthrough. If the feedthrough passed all 4.2 K tests, it was then remeasured both in DC and high frequency as a check. Figures 3.14(a) and 3.14(b) show a measurement of the direct transmission parameter S_{BA} (black line) and of the reflection parameter S_{AA} [magenta (middle grey) line] for a feedthrough after ten cooling cycles between room temperature and 4 K. The feedthrough performances are excellent from 50 MHz to 40.05 GHz (the upper limit of our VNA). We notice that the transmission parameter S_{BA} shows a tiny "gain" above approximately 30 GHz. This is obviously a small calibration artifact[27] due to the very low value of the transmission being measured. We have been using glass-bead feedthroughs in several stages of our dilution refrigerator for more than two years now and they have proven to be very reliable both electrically and mechanically. The cryostat has been cooled several times (on the order of 15), sometimes for more than $3-4$ consecutive months, without ever having a leak due to the feedthroughs.[28]

Room temperature feedthroughs can also be used. However, cold feedthroughs have a double advantage allowing the use of the helium bath to cool microwave devices (e.g., dissipative amplifiers which cannot be cooled in the cryostat vacuum chamber) and precool all microwave cables more efficiently. In addition, the technology developed here can be used in different applications such as packaging of microwave devices for low-temperature high-vacuum applications.

Before proceeding to the next stage of detection, it is noteworthy to mention that in the vacuum chamber of the cryostat almost all coaxial cables are either UT085 or UT047 cables with niobium inner conductor and cupro-nickel outer conductor. A few cables have a stainless-steel inner and outer conductor. The inner conductor of the niobium cables becomes superconducting below a critical temperature of approximately 9.3 K. These special cables are used to minimize losses and heat

[27] The feedthroughs are passive devices.

[28] We have heard from other groups using 3.5 mm feedthroughs that they suffer from feedthrough-related leaks every $7-8$ cool downs [314].

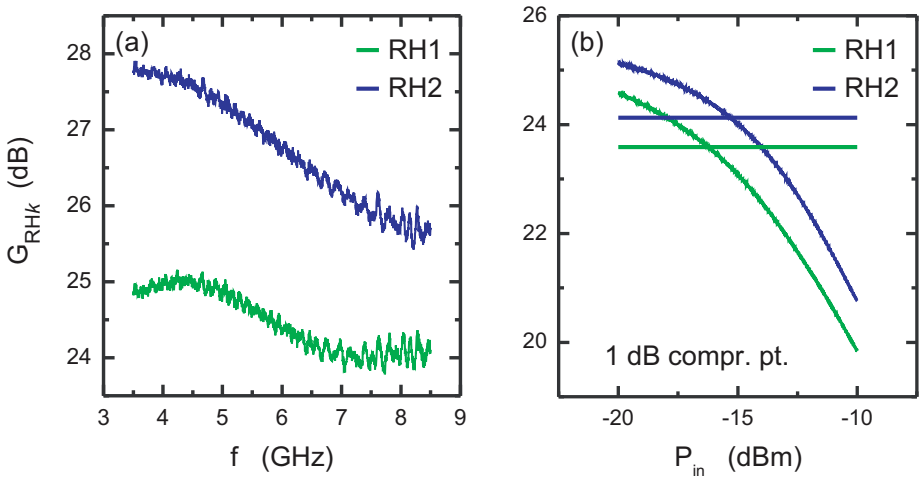

Figure 3.15: The RF multioctave band amplifiers - JS2. **(a)** Light green (light grey) line: power gain for the JS2 amplifier of channel 1, G_{RH1}. Dark blue (dark grey) line: power gain for the JS2 amplifier of channel 2, G_{RH2}. **(b)** Power dependence of the gain for the two JS2 amplifiers. The light green (light grey) data points refer to the amplifier of channel 1 and the dark blue (dark grey) data points to that of channel 2. The light green (light grey) horizontal line indicates the 1 dB compression point for the JS2 of channel 1 and the dark blue (dark grey) horizontal line the 1 dB compression point for the JS2 of channel 2.

conduction between different stages of the cryostat and are particularly important before the cryogenic amplifiers, where avoiding signal losses is critical.

3.2.4 The RF Multioctave Band Amplifiers

After the cold feedthroughs, the signals reach room temperature via a set of approximately 1.2 m-long UT085 cables. These cables were manufactured by KEYCOM Characteristic Technologies and were specified for low temperature, less heat conduction, and less insertion loss applications [315]. The inner conductor is made of silver plated beryllium copper (plate thickness of 2.5 μm) and the outer conductor of stainless-steel SUS304 with a copper clad of 5 μm.[29]

The signals then reach the third stage of the detection chain, which comprises a pair of RF multioctave band amplifiers (one per channel; cf. Figs. 3.10 and the top part of Fig. 3.18). In the design of an amplification chain care must be taken that the limiting amplifier in terms of added noise is the first amplifier of the chain. As explained in Subsec. 3.2.2, a linear amplifier[30] is completely characterized by

[29]Probably due to the copper clad, we had many problems with those cables related to thermal cycling. Even if we accurately precooled the cables first in liquid nitrogen and then in liquid helium for at least ten times before usage and we bent them in order to diminish stresses and dielectric (teflon in this case) sliding, the inner conductor of the cables always moved considerably after each cool down (on the order of 1 mm). We recently became aware that KEYCOM has slightly changed the production of such cables [315].

[30]Well before the 1 dB compression point.

its power gain, noise temperature, and impedance mismatch. In our case, $G_{\mathrm{CH}k}$ is the power gain, $T_{\mathrm{CH}k}$ the noise temperature, and $m_{\mathrm{CH}k}$ the impedance mismatch of either one of the two cryogenic amplifiers. Similarly, $G_{\mathrm{RH}k}$ is the power gain, $T_{\mathrm{RH}k}$ the noise temperature, and $m_{\mathrm{RH}k}$ the impedance mismatch of either one of the two RF multioctave band amplifiers. Assuming perfect matching conditions for all amplifiers, i.e., $m_{\mathrm{CH}k} = m_{\mathrm{RH}k} = 1$, it can be shown that the total noise (in terms of noise temperature) added by the cascade of cryogenic and RF multioctave band amplifiers at the mixers input (cf. Fig. 3.10) is given by Friis' equation [227],

$$T_{\mathrm{M}k} = T_{\mathrm{CH}k} + \frac{T_{\mathrm{RH}k}}{G_{\mathrm{CH}k}} \,. \tag{3.84}$$

According to Friis' equation, the noise added by the next amplification stage is diminished by the power gain of the previous stage. In other words, it is desirable to design the amplification chain such that the first amplifier has high gain and low noise temperature and the second amplifier low noise temperature. Under these conditions, the noise contribution from the second amplifier may be neglected.

The RF multioctave band amplifiers used in our experiments are JS2 amplifiers manufactured by MITEQ-USA. Figure 3.15(a) shows a measurement of the power gain for both JS2 amplifiers. At the frequency of interest, $f_0 = 5.85\,\mathrm{GHz}$, we find $G_{\mathrm{RH1}} \simeq 24.6\,\mathrm{dB}$ and $G_{\mathrm{RH2}} \simeq 26.7\,\mathrm{dB}$. The nominal noise temperature for the JS2 amplifiers is $T_{\mathrm{RH}k} = 58.7\,\mathrm{K}$. Given these numbers, we can now estimate the noise added by the JS2 amplifiers to the chains. By means of Eq. (3.84) we obtain $\Delta T_{\mathrm{M1}} \equiv T_{\mathrm{M1}} - T_{\mathrm{CH1}} \simeq 0.23\,\mathrm{K}$ for the first channel of the detection chain and $\Delta T_{\mathrm{M2}} \equiv T_{\mathrm{M2}} - T_{\mathrm{CH2}} \simeq 0.19\,\mathrm{K}$ for the second channel. Notably, $\Delta T_{\mathrm{M1}} \simeq \Delta T_{\mathrm{M2}} \ll T_{\mathrm{CH}k} = 6 \pm 1\,\mathrm{K}$. Hence, the noise added by the JS2 amplifiers is negligible and the cryogenic amplifiers are the limiting amplifiers of the chain (at least until the mixers).

Figure 3.15(b) shows the measurement of the 1 dB compression point for the JS2 amplifiers at $f_0 = 5.85\,\mathrm{GHz}$. Saturation happens at approximately $-15\,\mathrm{dB}$. This signal is still fairly large compared to the signals at the output of the cryogenic amplifiers (on the order of $-115\,\mathrm{dBm}$ or less) and, thus, the JS2 amplifiers will hardly be saturated in the experiments.

In summary, the only effect of the JS2 amplifiers on the quantum voltage at the output of either one of the cryogenic amplifiers, $\hat{V}_{\mathrm{CH}k}$, is to increase its amplitude by the signal gain $g_{\mathrm{RH}k} = \sqrt{G_{\mathrm{RH}k}}$. At the output of either one of the JS2 amplifiers the quantum voltage then become

$$\hat{V}_{\mathrm{RH}k} = g_{\mathrm{RH}k} \hat{V}_{\mathrm{CH}k} \,. \tag{3.85}$$

3.2.5 The Mixers

After the JS2 amplifiers, the signals of Eq. (3.85) are filtered by means of a pair of Mini-Circuits bandpass filters, VBFZ5500+. We remind that the signals we intend to measure are generated by cold resistors and, thus, can be assumed to be white Gaussian noise. The power associated with such signals is thus proportional to the measurement bandwidth $\Delta f = \Delta\omega/2\pi$,

$$P_{\mathrm{RH}k} = \frac{\langle \hat{V}^2_{\mathrm{RH}k} \rangle}{Z_0} \Delta f \,. \tag{3.86}$$

If the measurement bandwidth Δf is too large, the active devices following the JS2 amplifiers in the detection chain (i.e., mixers and IF amplifiers; cf. Fig. 3.10) can easily be saturated because of a too large input power. The bandpass filters, selecting a narrow bandwidth Δf, are one possible remedy to this issue.

The filtered signals, which we keep on calling $\hat{V}_{\mathrm{RH}k}$ for simplicity, then reach the fourth stage of the detection chain. This stage comprises a pair of mixers M_k (one per channel; cf. Fig. 3.10). Mixers are three-port active microwave devices typically based on a combination of Schottky barrier diodes [227, 308]. The three ports of a mixer are referred to as radio frequency (RF), local oscillator (LO), and intermediate frequency (IF) ports, respectively (cf. Fig. 3.10). The quantum voltage $\hat{V}_{\mathrm{RH}k}$ is fed into one of the RF ports, while the corresponding LO port is fed with a reference sinusoidal signal generated by a microwave source (cf. Fig. 3.10). The analysis of the operation principle of a classical mixer is rather complex and we will not delve into details here. We remind the reader to Refs. [227, 308] for a complete introduction to the topic.

A poor man's approach to mixing in the quantum regime can readily be carried out knowing that the signal at the mixer output is proportional to the product of the input signals (RF and LO). The proportionality factor is given by a function of the amplitude of the RF signal and, in general, depends on the amplitude of the LO signal. Under suitable conditions this function can be linerized, thus simplifying the analysis substantially. We start assuming the RF and LO signals to be given by the expressions

$$\hat{V}^{\mathrm{S}}_{\mathrm{RF}} = \bar{V}_{\mathrm{RF0}}(\hat{a}^{\dagger}_{\mathrm{RF}} + \hat{a}_{\mathrm{RF}})\,, \tag{3.87a}$$

$$\hat{V}^{\mathrm{S}}_{\mathrm{LO}} = \bar{V}_{\mathrm{LO0}}(\hat{a}^{\dagger}_{\mathrm{LO}} + \hat{a}_{\mathrm{LO}})\,, \tag{3.87b}$$

where $\hat{a}^{\dagger}_{\mathrm{RF}}$, $\hat{a}_{\mathrm{RF}}$, $\hat{a}^{\dagger}_{\mathrm{LO}}$, and $\hat{a}_{\mathrm{LO}}$ are the bosonic creation and annihilation operators in the Schrödinger picture for the RF and LO signals, respectively, and $\bar{V}_{\mathrm{RF0}} \equiv \sqrt{\hbar Z_0 \omega_{\mathrm{RF}}/2}$ and $\bar{V}_{\mathrm{LO0}} \equiv \sqrt{\hbar Z_0 \omega_{\mathrm{LO}}/2}$ are the RF and LO vacuum voltages per-root-hertz. The RF and LO signals are characterized by the angular frequencies ω_{RF} and ω_{LO}, respectively, which, in general, are different. In order to gain insight into the mixer operation, it is convenient to represent the RF and LO signals of Eqs. (3.87a) and (3.87b) in the Heisenberg picture and, consequently, make explicit the operator's time dependence. We obtain

$$\hat{V}^{\mathrm{H}}_{\mathrm{RF}} = \bar{V}_{\mathrm{RF0}}(\hat{a}^{\dagger}_{\mathrm{RF}} e^{+j\omega_{\mathrm{RF}}t} + \hat{a}_{\mathrm{RF}} e^{-j\omega_{\mathrm{RF}}t})\,, \tag{3.88a}$$

$$\hat{V}^{\mathrm{H}}_{\mathrm{LO}} = \bar{V}_{\mathrm{LO0}}(\hat{a}^{\dagger}_{\mathrm{LO}} e^{+j\omega_{\mathrm{LO}}t} + \hat{a}_{\mathrm{LO}} e^{-j\omega_{\mathrm{LO}}t})\,. \tag{3.88b}$$

Omitting the indexes indicating the specific picture (S or H), the signal at the output of an ideal mixer is given by

$$\begin{aligned}\hat{V}_{\mathrm{IF}} = f(\bar{V}_{\mathrm{RF0}})[&\hat{a}^{\dagger}_{\mathrm{RF}}\hat{a}^{\dagger}_{\mathrm{LO}} e^{+j(\omega_{\mathrm{RF}}+\omega_{\mathrm{LO}})t} \\ &+ \hat{a}^{\dagger}_{\mathrm{RF}}\hat{a}_{\mathrm{LO}} e^{+j(\omega_{\mathrm{RF}}-\omega_{\mathrm{LO}})t} + \hat{a}_{\mathrm{RF}}\hat{a}^{\dagger}_{\mathrm{LO}} e^{-j(\omega_{\mathrm{RF}}-\omega_{\mathrm{LO}})t} \\ &+ \hat{a}_{\mathrm{RF}}\hat{a}_{\mathrm{LO}} e^{-j(\omega_{\mathrm{RF}}+\omega_{\mathrm{LO}})t}]\,.\end{aligned} \tag{3.89}$$

Under the realistic assumption $\omega_{\mathrm{RF}} \approx \omega_{\mathrm{LO}}$, which allows us to make a RWA approximation, assuming a linear mixer response, $f(\bar{V}_{\mathrm{RF0}}) \approx \tilde{\delta}_{\mathrm{M}}$ (we do not work out the

explicit dependence of $\tilde{\delta}_{\rm M}$ on the LO amplitude [227]), and defining the intermediate frequency $\omega_{\rm IF} \equiv \omega_{\rm RF} - \omega_{\rm LO}$ we then obtain the IF signal

$$\hat{V}_{\rm IF} \approx \tilde{\delta}_{\rm M} \bar{V}_{\rm RF0} (\hat{a}^{\dagger}_{\rm RF} \hat{a}_{\rm LO} e^{+j\omega_{\rm IF} t} + \hat{a}_{\rm RF} \hat{a}^{\dagger}_{\rm LO} e^{-j\omega_{\rm IF} t}) \,, \tag{3.90}$$

which is regarded as the standard quantum-mechanical input-output relation for a mixer operated in the linear regime. This result constitutes also the central equation of any microwave receiver. The definition of $\omega_{\rm IF}$ justifies the origin of the nomenclature chosen for the output port of a mixer. The IF signal is in fact characterized by an angular frequency which is the difference between the angular frequencies of the RF and LO signals. Since the RF and LO frequencies are usually similar [cf. assumption before Eq. (3.90)], the intermediate angular frequency is usually low, $\omega_{\rm IF} \ll \min\{\omega_{\rm RF}, \omega_{\rm LO}\}$. The mixer is said to *down convert* the input RF signal. In particular, when

$$\omega_{\rm RF} = \omega_{\rm LO} \quad \Rightarrow \quad \omega_{\rm IF} = 0 \,, \tag{3.91}$$

the overall microwave receiver comprising circulators, all amplifiers, filters, phase-shifter(s), and mixers (cf. Fig. 3.10) is referred to as *homodyne detector* (from ancient Greek: *homo*=equal and *dynamis*=force). When

$$\omega_{\rm RF} \neq \omega_{\rm LO} \quad \Rightarrow \quad \omega_{\rm IF} \neq 0 \,, \tag{3.92}$$

the overall microwave receiver is referred to as *heterodyne detector* (from ancient Greek: *hetero*=different and *dynamis*=force).

In the case of homodyne detection, since $\omega_{\rm IF} = 0$ we can set

$$\omega_{\rm RF} = \omega_{\rm LO} = \omega_0 \,. \tag{3.93}$$

This is a critical condition because it states that in a homodyne detector the frequency of the signal to be measured is set by the reference frequency provided by the LO signal. Hence, frequency is typically not a degree of freedom in experiments based on mixing schemes. This will have dramatic consequences in the experiments to be discussed in chapter 4. After Eq. (3.93), we can rewrite the vacuum voltage associated with the RF signal simply as $\bar{V}_{\rm RF0} = \bar{V}_0$. The expression for the IF signal (in the Heisenberg picture) reduces to[31]

$$\hat{V}_{\rm IF} = \tilde{\delta}_{\rm M} \bar{V}_0 (\hat{a}^{\dagger}_{\rm RF} \hat{a}_{\rm LO} + \hat{a}_{\rm RF} \hat{a}^{\dagger}_{\rm LO}) \,. \tag{3.94}$$

The LO signal is usually a sinusoidal excitation generated by a microwave source, as shown in Fig. 3.10. Quantum mechanically, such excitation is represented by a coherent state [32, 91], $|\alpha_{\rm LO}\rangle$, with complex amplitude

$$\alpha_{\rm LO} = |\alpha_{\rm LO}| e^{j\varphi_{\rm LO}} \,, \tag{3.95}$$

where the real amplitude $|\alpha_{\rm LO}|$ is a dimensionless quantity defined in units of the vacuum voltage $\bar{V}_0$. The phase $\varphi_{\rm LO}$ can be adjusted by means of a phase shifter (cf. Fig. 3.10). Depending on the specific experimental requirements, the LO phase can either play a role as a tuning knob, in which case must be considered in the calculations, or it is irrelevant, in which case can safely be set to zero. In the next

[31] Hereafter, we use "=" instead of "≈" for the expressions of all IF signals.

chapter, we will show two distinguished experiments where both these scenarios apply.

We are now in the position to calculate a partial mean value of the result of Eq. (3.94) with respect to the LO operators only. Using the basic properties of the coherent state,

$$\hat{a}_{\rm LO}|\alpha_{\rm LO}\rangle = \alpha_{\rm LO}|\alpha_{\rm LO}\rangle \quad \text{and} \quad \langle\alpha_{\rm LO}|\hat{a}^{\dagger}_{\rm LO} = \langle\alpha_{\rm LO}|\alpha^{*}_{\rm LO}\,,$$

the partial mean value is given by

$$\begin{aligned}\hat{V}_{\rm IF} &= \tilde{\delta}_{\rm M}\bar{V}_0\langle\alpha_{\rm LO}|(\hat{a}^{\dagger}_{\rm RF}\hat{a}_{\rm LO} + \hat{a}_{\rm RF}\hat{a}^{\dagger}_{\rm LO})|\alpha_{\rm LO}\rangle \\ &= \tilde{\delta}_{\rm M}\bar{V}_0(\alpha_{\rm LO}\hat{a}^{\dagger}_{\rm RF} + \alpha^{*}_{\rm LO}\hat{a}_{\rm RF}) \\ &= \delta_{\rm M}\bar{V}_0(\hat{a}^{\dagger}_{\rm RF}e^{+j\varphi_{\rm LO}} + \hat{a}_{\rm RF}e^{-j\varphi_{\rm LO}})\,, \end{aligned} \tag{3.96}$$

where $\delta_{\rm M} \equiv \tilde{\delta}_{\rm M}|\alpha_{\rm LO}|$.

Results similar to those obtained for homodyne detection can be found for heterodyne detection, where the major difference is represented by the finite intermediate frequency. In this case, the LO phase $\varphi_{\rm LO}$ loses its meaning due to continuous rotation of the IF operators.[32]

It is an easy exercise to specialize the general result of Eq. (3.96) to our quantum voltage, $\hat{V}_{{\rm RH}k}$.

For the case of a Wilkinson power divider:

1. The voltage at the input of mixer $\rm M_1$ is given by

$$\begin{aligned}\hat{V}_{\rm RH1} = g_{\rm RH1}\,g_{\rm CH1}\bar{V}_0\Bigg\{\Bigg[&-\frac{1}{\sqrt{2}}(\hat{a}^{\dagger}+\hat{a}) - \frac{1}{\sqrt{2}}(\hat{b}^{\dagger}+\hat{b})\Bigg] \\ &+ \delta_{\rm c1}(\hat{\zeta}^{\dagger}_1+\hat{\zeta}_1) + (\hat{\xi}^{\dagger}_1+\hat{\xi}_1)\Bigg\}. \end{aligned} \tag{3.97}$$

   Thus, at the mixer output we obtain

$$\begin{aligned}\hat{V}_{\rm M1} = \delta_{\rm M1}\,g_{\rm RH1}\,g_{\rm CH1}\bar{V}_0\Bigg\{\Bigg[&-\frac{1}{\sqrt{2}}(\hat{a}^{\dagger}e^{+j\varphi_{\rm LO}}+\hat{a}e^{-j\varphi_{\rm LO}}) - \frac{1}{\sqrt{2}}(\hat{b}^{\dagger}e^{+j\varphi_{\rm LO}}+\hat{b}e^{-j\varphi_{\rm LO}})\Bigg] \\ &+ \delta_{\rm c1}(\hat{\zeta}^{\dagger}_1e^{+j\varphi_{\rm LO}}+\hat{\zeta}_1e^{-j\varphi_{\rm LO}}) + (\hat{\xi}^{\dagger}_1e^{+j\varphi_{\rm LO}}+\hat{\xi}_1e^{-j\varphi_{\rm LO}})\Bigg\}; \end{aligned} \tag{3.98}$$

2. The voltage at the input of mixer $\rm M_2$ is given by

$$\begin{aligned}\hat{V}_{\rm RH2} = g_{\rm RH2}\,g_{\rm CH2}\bar{V}_0\Bigg\{\Bigg[&-\frac{1}{\sqrt{2}}(\hat{a}^{\dagger}+\hat{a}) + \frac{1}{\sqrt{2}}(\hat{b}^{\dagger}+\hat{b})\Bigg] \\ &+ \delta_{\rm c2}(\hat{\zeta}^{\dagger}_2+\hat{\zeta}_2) + (\hat{\xi}^{\dagger}_2+\hat{\xi}_2)\Bigg\}. \end{aligned} \tag{3.99}$$

[32] If phase-sensitive heterodyne detection has to be performed, the technical remedy to the phase arbitrariness is to trigger on the IF signal. In this case, the LO phase reacquires its meaning.

Thus, at the mixer output we obtain

$$\hat{V}_{\mathrm{M2}} = \delta_{\mathrm{M2}}\, g_{\mathrm{RH2}}\, g_{\mathrm{CH2}} \bar{V}_0 \Bigg\{ \Bigg[-\frac{1}{\sqrt{2}}(\hat{a}^\dagger e^{+j\varphi_{\mathrm{LO}}} + \hat{a} e^{-j\varphi_{\mathrm{LO}}}) + \frac{1}{\sqrt{2}}(\hat{b}^\dagger e^{+j\varphi_{\mathrm{LO}}} + \hat{b} e^{-j\varphi_{\mathrm{LO}}}) \Bigg]$$
$$+ \delta_{\mathrm{c2}}(\hat{\zeta}_2^\dagger e^{+j\varphi_{\mathrm{LO}}} + \hat{\zeta}_2 e^{-j\varphi_{\mathrm{LO}}}) + (\hat{\xi}_2^\dagger e^{+j\varphi_{\mathrm{LO}}} + \hat{\xi}_2 e^{-j\varphi_{\mathrm{LO}}}) \Bigg\}. \tag{3.100}$$

For the case of a 180° hybrid ring:

1. The voltage at the input of mixer M_1 is given by

$$\hat{V}_{\mathrm{RH1}} = g_{\mathrm{RH1}}\, g_{\mathrm{CH1}} \bar{V}_0 \Bigg\{ \Bigg[-\frac{1}{\sqrt{2}}(\hat{a}^\dagger + \hat{a}) - \frac{1}{\sqrt{2}}(\hat{b}^\dagger + \hat{b}) \Bigg]$$
$$+ \delta_{\mathrm{c1}}(\hat{\zeta}_1^\dagger + \hat{\zeta}_1) + (\hat{\xi}_1^\dagger + \hat{\xi}_1) \Bigg\}. \tag{3.101}$$

Thus, at the mixer output we obtain

$$\hat{V}_{\mathrm{M1}} = \delta_{\mathrm{M1}}\, g_{\mathrm{RH1}}\, g_{\mathrm{CH1}} \bar{V}_0 \Bigg\{ \Bigg[-\frac{1}{\sqrt{2}}(\hat{a}^\dagger e^{+j\varphi_{\mathrm{LO}}} + \hat{a} e^{-j\varphi_{\mathrm{LO}}}) - \frac{1}{\sqrt{2}}(\hat{b}^\dagger e^{+j\varphi_{\mathrm{LO}}} + \hat{b} e^{-j\varphi_{\mathrm{LO}}}) \Bigg]$$
$$+ \delta_{\mathrm{c1}}(\hat{\zeta}_1^\dagger e^{+j\varphi_{\mathrm{LO}}} + \hat{\zeta}_1 e^{-j\varphi_{\mathrm{LO}}}) + (\hat{\xi}_1^\dagger e^{+j\varphi_{\mathrm{LO}}} + \hat{\xi}_1 e^{-j\varphi_{\mathrm{LO}}}) \Bigg\}; \tag{3.102}$$

2. The voltage at the input of mixer M_2 is given by

$$\hat{V}_{\mathrm{RH2}} = g_{\mathrm{RH2}}\, g_{\mathrm{CH2}} \bar{V}_0 \Bigg\{ \Bigg[\frac{1}{\sqrt{2}}(\hat{a}^\dagger + \hat{a}) - \frac{1}{\sqrt{2}}(\hat{b}^\dagger + \hat{b}) \Bigg]$$
$$+ \delta_{\mathrm{c2}}(\hat{\zeta}_2^\dagger + \hat{\zeta}_2) + (\hat{\xi}_2^\dagger + \hat{\xi}_2) \Bigg\}. \tag{3.103}$$

Thus, at the mixer output we obtain

$$\hat{V}_{\mathrm{M2}} = \delta_{\mathrm{M2}}\, g_{\mathrm{RH2}}\, g_{\mathrm{CH2}} \bar{V}_0 \Bigg\{ \Bigg[\frac{1}{\sqrt{2}}(\hat{a}^\dagger e^{+j\varphi_{\mathrm{LO}}} + \hat{a} e^{-j\varphi_{\mathrm{LO}}}) - \frac{1}{\sqrt{2}}(\hat{b}^\dagger e^{+j\varphi_{\mathrm{LO}}} + \hat{b} e^{-j\varphi_{\mathrm{LO}}}) \Bigg]$$
$$+ \delta_{\mathrm{c2}}(\hat{\zeta}_2^\dagger e^{+j\varphi_{\mathrm{LO}}} + \hat{\zeta}_2 e^{-j\varphi_{\mathrm{LO}}}) + (\hat{\xi}_2^\dagger e^{+j\varphi_{\mathrm{LO}}} + \hat{\xi}_2 e^{-j\varphi_{\mathrm{LO}}}) \Bigg\}. \tag{3.104}$$

The mixers used in our experiments were manufactured by Marki Microwave, Inc., model M3 − 0312. The RF and LO ports of such mixers can accept signals in a frequency range between 3 and 12 GHz. The IF port can deliver signals in a frequency range from DC to 4 GHz. The typical conversion loss, LO-RF isolation, and LO-IF isolation are 5.5, 34, and 25 dB, respectively. The 1 dB compression point for the RF port is at +5 dBm and the two-tone third-order intercept point

at +15 dBm. The latter qualifies the linearity of the mixer: Keeping the RF power below +15 dBm avoids signal distortion. However, the condition on the mixer saturation at the RF port is more stringent in this case. The LO port must be driven with a power comprised between +7 and +10 dBm (low diode option, L). Such power is required to saturate the mixer LO port and, thus, to operate the mixer in the linear regime [227].

When performing homodyne measurements the IF signal is obviously a DC signal. However, for heterodyne measurements given the RF frequency $f_{\mathrm{RF}} = \omega_{\mathrm{RF}}/2\pi$, we always choose the LO frequency $f_{\mathrm{LO}} = \omega_{\mathrm{LO}}/2\pi$ such that the IF frequency $f_{\mathrm{IF}} = \omega_{\mathrm{IF}}/2\pi = 10\,\mathrm{MHz}$. This choice is important when measuring coherent signals because it is equal to the frequency of the signal used to phase lock the microwave sources and data timing generator (e.g., cf. Ref. [312] for more details). When measuring noise of some specified bandwidth $\mathrm{BW} = \Delta\omega/2\pi$, one special angular frequency, i.e., the center frequency $f_0 = \omega_0/2\pi$, participate in a pure homodyne measurement. All other frequencies comprised within the noise bandwidth participate in heterodyne measurements. To simplify the calculations, we will usually consider only the special noise component at angular frequency ω_0. However, the presence of all other noise components contributes to the final result. To conclude, it is worth mentioning that, in our experiments, the effective noise bandwidth is $\mathrm{BW}_{\mathrm{eff}} = 2\mathrm{BW} = \Delta\omega/\pi$ due to the presence of the noise image frequencies. This type of measurement is called double sideband (DSB) mixing [312, 316].

3.2.6 The IF FET Amplifiers and the Rest of the Detection Chain

If necessary, the signals at the mixers' output [cf. Eqs. (3.98), (3.100), (3.102), and (3.104)] are fed into a pair of Aeroflex attenuators, A_{sat1} and A_{sat2} (cf. Fig. 3.10). These attenuators are used to decrease the signal level (and thus its power) in order not to saturate the following IF amplifiers. The value of the attenuators A_{sat1} and A_{sat2} depends on the specific experiment and usually ranges between 0 and 30 dB.

The IF amplifiers are FET-based amplifiers manufactured by the NF Corp., Japan, model SA-421F5. The typical bandwidth of such amplifiers extends from 16 Hz to 40 MHz, the nominal power gain is $G_{\mathrm{RL}k} = 46\,\mathrm{dB}$, and the nominal noise temperature $T_{\mathrm{RL}k} = 139\,\mathrm{K}$. The input impedance is $1\,\mathrm{M}\Omega$, which is not an issue for IF signals. For such low frequency signals, the input impedance of the amplifiers need not be $50\,\Omega$-matched. The only effect of the IF amplifiers on the input quantum voltage $\hat{V}_{\mathrm{M}k}$ is thus to increase the signal level by the signal gain $g_{\mathrm{RL}k} = \sqrt{G_{\mathrm{RL}k}}$, obtaining the output quantum voltage $\hat{V}_{\mathrm{RL}k} = g_{\mathrm{RL}k}\hat{V}_{\mathrm{M}k}$.

After the IF amplifiers, the signals are filtered again this time by means of a combination of Mini-Circuits low-pass filters, SLP−21.4+, and Aeroflex inner only DC-blocks, 8535. The resulting bandwidth is then $\mathrm{BW}_{\mathrm{IF}k} \simeq (7\,\mathrm{kHz}, 52\,\mathrm{MHz})$. To keep the notation simple, the contribution of all attenuators, the attenuation due to coaxial cables and connectors, and any mismatching effect due to filters and DC-blocks is considered to be included in the overall gain of each channel of the detection chain.

Before reaching an A/D converter, the signals can be further attenuated in order to balance the two channels of the detection chain, which, in reality, are never characterized by the same exact parameters. In the experiments to be discussed

in chapter 4, the values of the balancing attenuators are fixed to $A_{\mathrm{bal1}} = 0\,\mathrm{dB}$ and $A_{\mathrm{bal2}} = 3\,\mathrm{dB}$.

An Acqiris A/D acquisition card with sampling rate $f_{\mathrm{sampling}} = 420\,\mathrm{MS\,s^{-1}}$ and 12-bit nominal resolution is finally used to obtain one realization s_k of the quantum voltage $\hat{V}_{\mathrm{RL}k}$. Each realization is collected into a PC and the data postprocessed as explained in chapter 4, Sec. 4.3. The acquisition card is triggered by means of a triggering pulse generated by a Tektronix DTG 5334 data timing generator (cf. Fig. 3.10). The triggering signals have a maximum peak-to-peak amplitude of $3.5\,\mathrm{V_{pp}}$ and a rise/fall-time of approximately 340 ps. The pulses are 1 µs long, which is on the order of the experimental measurement time Δt_{m}.

3.3 From the Experimental Setup to The Results

The natural continuation of the material treated in this chapter is represented by the postprocessing stage of the experimental data acquired by means of the two-channel detection chain. The data postprocessing is realized on a personal computer (PC; cf. top part of Fig. 3.10), where the raw data are averaged in order to obtain relevant statistical quantities such as the mean value and variance of the signals to be measured.

The postprocessing stage is a key step in our experiments and, thus, deserves to be treated in an independent chapter. The next chapter represents a thorough analysis of the methods used to extract relevant information from our data and contains the bulk of our experimental findings.

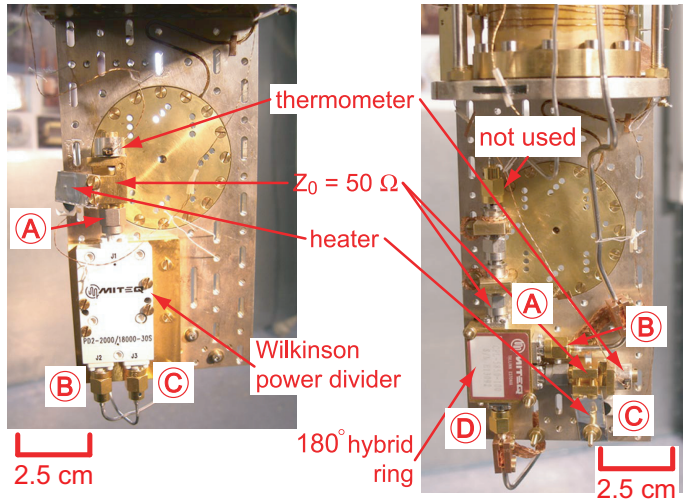

Figure 3.16: Pictures of the two types of microwave beam splitter employed in our experiments. Left side: Wilkinson power divider mounted on a tempered-silver plate. The spacer between the back side of the divider and the plate is a gold-plated OFHC-copper plate of a few millimeters thickness. Right side: 180° hybrid ring mounted directly on the tempered-silver plate. In both sides, the scale is indicated for a better comparison between the dimensions of the various devices.

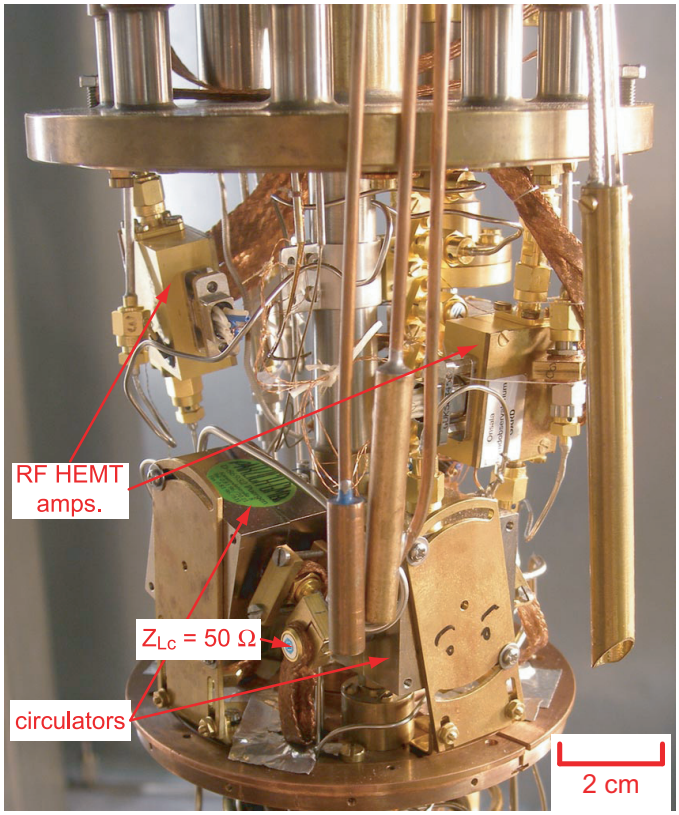

Figure 3.17: Picture of cryogenic circulators and amplifiers. The circulators are located on the bottom part. The tick cryoperm shields are visible. The RF HEMT amplifiers are located just below the flange which separates the cryostat vacuum chamber from the helium bath. The scale is indicated.

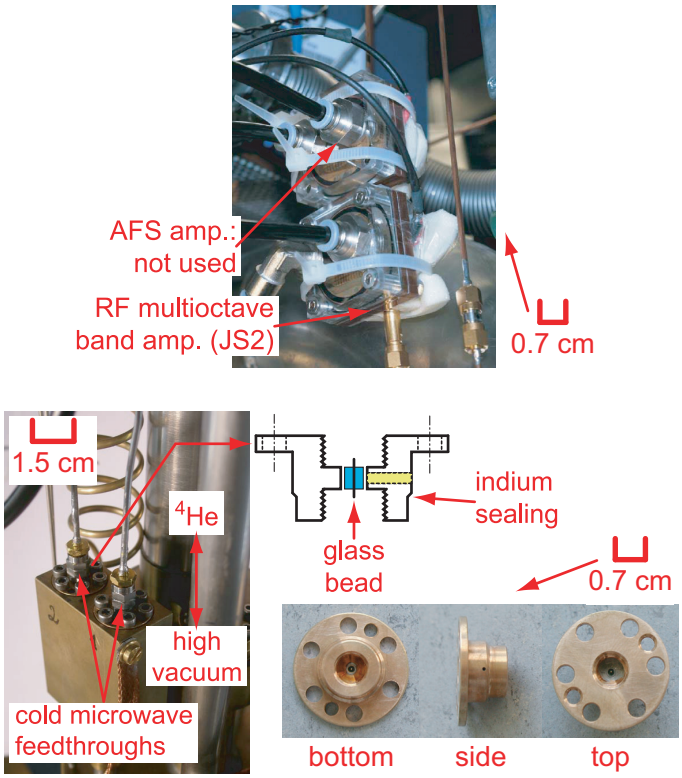

Figure 3.18: The cold feedthroughs and room temperature microwave amplifiers. Bottom left: the cold feedthroughs mounted on a box immersed in liquid helium during the experiments. Bottom right: cold feedthrough technical drawing. The glass bead (light blue) and the position where the indium sealing is applied are indicated. The cavity channel used to apply the solder is shown in yellow. The bottom, side, and top view of one feedthrough without V sparkplug launcher connectors are shown. It is possible to see the glass bead soldered inside the feedthrough. The side view also shows the cavity channel used for soldering. Top: the JS2 amplifier of channel 1 of the detection chain. The picture refers to a setup configuration slightly different from the one used in the experiments described in this thesis. The AFS amplifiers were never used to obtain the experimental results reported in this thesis. The scale is indicated in all pictures for a better comparison.

Chapter 4

Correlation Homodyne Detection at Microwave Frequencies: Experimental Results

The field of superconducting quantum circuits has recently witnessed a series of rapid developments, which were almost unpredictable only a few years ago. The most striking advances have been possible thanks to the accurate engineering of the electromagnetic environment where superconducting qubits are embedded. The use of on-chip resonant cavities as environment has made possible the first experimental implementation of a cavity QED system [174, 180, 185] using microcircuits coupled to microwave signals [139], which has given rise to the rich field of circuit QED. Ever since, circuit QED has become the new standard in the community working on superconducting qubits and has already pushed the envelope of experimental research to a high level of complexity [101, 144]. On one hand, the biggest strength of circuit QED compared to its cavity QED quantum-optical counterpart is offered by the flexibility of engineering microwave devices: qubits, acting as "artificial atoms," and resonators, acting as on-chip cavities. The latter, in particular, are easy to fabricate and can be coupled to the qubits very strongly. On the other hand, the biggest weakness of circuit QED is represented by the measurement resources available for quantum signals at microwave frequencies, which are by far less advanced than those available on an optical table. For instance, the standard microwave homodyne detection employed in circuit QED experiments is very inefficient compared to measurements performed with an optical photodetector. This fact has two important consequences: Both the high-fidelity single-shot readout of the qubit state and the detection of a propagating microwave single photon cannot be realized in circuit QED yet.[1]

The qubit readout and microwave photodetection issues are intimately interconnected since they are both limited by the low efficiency of microwave amplifiers, which are typically used as detectors in circuit QED experiments. Nonlinear mea-

[1]We notice that, in circuit QED as well as in quantum-optical cavity QED, either the state of the qubit or the field emitted by the resonator can be used to infer information about the coupled system. In this chapter, we focus on studying a set of relevant properties of the field only. We remind that, though, there are particular circuit QED architectures where the qubit can directly be read out with very high fidelity [151]. This can be used to perform full-state quantum tomography of intracavity fields [153, 284]. *Note added in Fall 2010: Very recently a significant improvement on circuit QED readout has been realized [111].*

surements based on "bifurcation amplifiers"[2] [110, 211–220] or mesoscopic shelving [221] are being used or proposed to overcome the readout issue. The direct detection of propagating microwave photons at the level of a single quantum appears to be a more challenging task. Two distinguished paths can be pursued to achieve this goal. The first is to improve on the performances of linear microwave amplifiers. These can either be phase-sensitive [194–201] or phase-preserving [203–206, 208, 209] amplifiers. The advantage of phase-preserving amplifiers is the possibility to measure both signal quadrature operators, $\hat{X}$ and $\hat{Y}$ (i.e., both quantum voltage and current), simultaneously, without a preferred direction in phase space (cf. chapter 2, Subsec. 2.1.3 and Refs. [307, 309, 317] for a definition of quadrature operators). The drawback is that this type of amplifier cannot beat the standard quantum limit (cf. Refs. [307, 309, 317]). Phase-sensitive amplifiers can beat this limit at the expense that only one quadrature at the time can be measured [307, 309, 317]. The second path is to develop true single photon detectors at microwave frequencies [222–224].[3] The development of ultra low-noise amplifiers and microwave single photon detectors will enable the direct transfer to circuit QED of a large set of exquisite techniques belonging to the realm of quantum optics. Among those, it is worth mentioning balanced homodyne detection [91, 93] and Hanbury Brown and Twiss (HBT) interferometry [91]. Even if we truly believe that these paths will have to be followed to reach a deeper knowledge on circuit QED systems, we are convinced that it is important to understand how much information can be obtained on microwave quantum signals by using standard noisy amplifiers, as those described in chapter 3, Subsec. 3.2.2.

In this chapter, we develop a cross-correlation homodyne detection scheme based on a microwave beam splitter and two amplification channels with noisy amplifiers. Our scheme resembles the setup employed in HBT correlation measurements [91] and quantum-optical balanced homodyne detection [93]. In optics, the latter represents the most accurate method for the full-state tomography of a propagating quantum field [94, 95, 320, 321]. This was the main reason behind our choice to setting up a cross-correlation homodyne detector. However, our experimental findings reveal that at microwave frequencies cross-correlation homodyne detection only allows for a *partial* reconstruction of the state associated with a quantum signal. The impossibility for a full-state tomography is due to the noise added by the microwave amplifiers. Because of this noise, extensive ensemble averages are required in order to reach a reasonable signal-to-noise ratio (SNR), which allows the measurement of a subset of the statistical moments of ultra-weak quantum signals. In particular, our results show that by means of cross-correlation homodyne detection it is possible to measure with high fidelity only the first two central moments, i.e., the mean value and variance, of a given quantum signal.[4] It is well-known that the knowledge of the mean value and variance of a quantum signal is a sufficient condition for the full characterization of all Gaussian states [93]. This is a rich class of states which

[2]The author finds this definition inappropriate considering that the bifurcation readout is more a threshold-latching mechanism rather than an amplification process.

[3]For *microwave* single photon detector we intend a photodetector at frequencies *below* 10 GHz. In fact, there already exist single photon detectors in the range of 500 GHz [318, 319], which, for us, is already in the THz regime.

[4]Theoretically, it is possible to measure higher moments, but the higher the moment, the more extensive the ensemble average needed to resolve it. In other words, cross-correlation homodyne detection is a rather inefficient method to obtain the full-counting statistics of a quantum signal.

includes thermal/vacuum states, coherent states, and squeezed states. In this thesis, we will mainly focus on the characterization of thermal/vacuum states.

If the high-fidelity measurement of the first two moments of a microwave quantum signal were the only achievement reached by means of cross-correlation homodyne detection, we could safely state that such scheme is not worth the efforts. In fact, similar results can be obtained using the standard microwave homodyne detection based on a single amplification chain (e.g., cf. [150, 193, 198]). However, the splitting of a quantum signal via microwave beam splitters allows us to explore a set of phenomena which would otherwise be inaccessible. We will show that employing cross-correlation homodyne detection we have been able to a) fully characterize the thermal/vacuum fluctuations at microwave frequencies for a wide range of frequencies as compared to the experimental measurement bandwidth and b) confirm experimentally the theoretical models for the microwave beam splitters described in chapter 3, Sec. 3.1. The latter constitutes an unprecedented result, which paves the way to the tomographic characterization of quantum devices [322] at microwave frequencies.

In addition, it is worth pointing out that cross-correlation homodyne detection can be used to realize HBT interferometry[5] at microwave frequencies [92] and can serve as an entanglement detector in two- or multi-resonator architectures (cf. chapters 5 and 7 and Refs. [136, 137]).

The chapter is organized as follows. In Sec. 4.1, we revise the basic concepts of thermal/vacuum states with special emphasis on the derivation of the Planck distribution via Einstein's A and B coefficients. In Sec. 4.2, we give an overview of quantum signal theory and derive the expressions for the mean value and variance of any given quantum signal. In general, the mean value and variance belong to the larger set of the quantum parameters of a signal. In the rest of the section, we specialize such quantum parameters to the case of number states and thermal/vacuum states. In Sec. 4.3, we link the abstract concepts of quantum-mechanical mean value and variance to real statistical measurements based on a large set of realizations of a quantum signal associated with a given state. Such statistical measurements represent an estimation of the theoretical quantum parameters. In particular, we study the concepts of auto-correlation function, from which it is possible to obtain the auto-covariance function and, thus, estimate the variance of a quantum signal. We then generalize these results to the case of cross-correlation and cross-covariance functions, which allow us to estimate the covariance of a quantum signal. We apply experimentally all these concepts to the case of thermal/vacuum microwave states. Within this framework, we develop a complete theoretical model which makes possible to extract valuable information on vacuum fluctuations at microwave frequencies from the knowledge of the variance and covariance of the vacuum state. Finally, in Sec. 4.4 we summarize our results and give a brief outlook on future applications of cross-correlation homodyne detection.

The material discussed in this chapter is entirely unpublished.[6] The main contributions of the author are on the development of the theoretical idea at the basis

[5] The reader should be aware that all cross-correlation measurements presented in this thesis refer to the correlation of the *amplitude* of two signals and not of their intensity. Intensity correlation is an exquisite feature of HBT interferometry.

[6] *Note added in Fall 2010: At the time of the final submission of this thesis, part of this chapter was published in Physical Review Letters [162]. The technical calibration of the setup was also independently published [323].*

of the experiments and of the model utilized to fit the data. Experiments and data analysis were entirely performed by the author. The data were partially taken together with Edwin P. Menzel, while performing a simultaneous experiment based on the same setup. With Edwin P. Menzel the author shared innumerous nights by the side of the cryostat. Achim Marx, Frank Deppe, and Enrique Solano contributed with fruitful discussions. The author would like to thank the very helpful criticism on the interpretation of the Planck spectroscopy measurements brought by the Quantronics group - Saclay, in particular by D. Esteve, D. Vion, C. Urbina, and P. Bertet. In addition, we acknowledge discussions with P. J. Leek.

4.1 Introduction

The routine experiment in circuit QED is either based on the measurement of propagating microwave classical signals, which encode information on a qubit-resonator quantum system (e.g., cf. Ref. [139]), or on the low-frequency measurement of a qubit, which encodes information on intra-resonator microwave quantum states (e.g., cf. Refs. [138, 141, 145, 151]). The measurement of propagating nonclassical signals in the microwave range is only recently attracting the attention of the community. Inspired by the pioneering work by B. Yurke and collaborators [188, 193, 324], the use of Josephson tunnel junctions for the implementation of parametric amplifiers is gaining increasing interest [194–201]. Parametric amplification naturally leads to the possibility of squeezing microwave vacuum fluctuations [193, 198] as well as enabling the phase-sensitive measurement of propagating microwave quantum signals [194–201]. The possibility of measuring propagating fields is also at the basis of the work on the microstrip SQUID amplifier [203–206] and Josephson parametric converter [208, 209], and of recent photon-detection proposals [222–224]. In addition, the importance of studying such fields has been stressed by the seminal theoretical [325, 326] and experimental [92] works on the quantum statistics of GHz photons emitted by conductors.

A common feature to all the experiments mentioned above is the necessity to prepare the system under analysis in the vacuum state $|0\rangle$. The vacuum state is the simplest quantum state available in nature and its properties play a fundamental role in many aspects of the quantization of the radiation field [327]. Given its importance, we decided to use the vacuum state as a benchmark test for our cross-correlation homodyne detection scheme. In our experiments, the vacuum state is generated by means of cold resistors. The quantum voltage associated with it is then split via a microwave beam splitter, the output voltages of which propagate on two different transmission lines. After being amplified by means of noisy amplifiers, one realization of each quantum voltage is finally recorded by an acquisition card. Before delving into the details of the measurement of microwave vacuum fluctuations, it is worthwhile reviewing a few relevant examples involving the vacuum. This will help us to better appreciate the importance of vacuum fluctuations in QED.

The first example to show the importance of the vacuum is certainly represented by the concept of spontaneous emission. The theory on the absorption and emission of radiation was developed by A. Einstein in its 1917 paper "Zur Quantentheorie der Strahlung" [17]. This paper is cram full with gems of rare beauty, among which the derivation of the so-called A and B coefficients. In summary, Einstein assumes N_1 and N_2 numbers of two-level atoms with energy levels E_1 (groundstate) and E_2

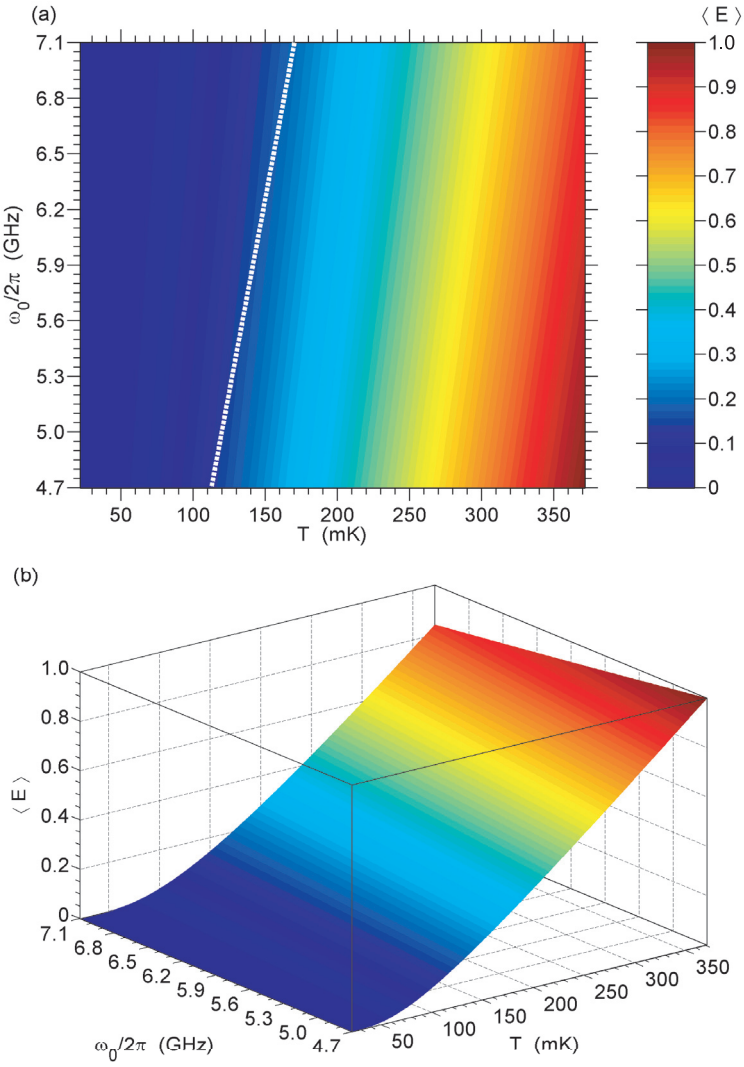

Figure 4.1: The Planck spectrum (also referred to as Planck distribution). **(a)** Color-code plot (top view) of the Planck spectrum given by Eq. (4.13) as a function of both temperature, T, and angular frequency, ω_0. As it will appear clear later in the chapter, the angular frequency is set by the angular frequency of the LO signal applied to a microwave mixer, $\omega_0 = \omega_{\rm LO}$. **(b)** Color-code plot (3D view) of the Planck spectrum. In Subsec. 4.3.2, we will show a set of experimental results corresponding to the theory plotted in the present figure.

(excited state), respectively, with $E_2 > E_1$. Using a more contemporary jargon, we would say N_1 and N_2 number of qubits. The rate at which N_1 changes due to the absorption of radiation, which causes an atom to make an upward transition from the level E_1 to the level E_2, is assumed to be proportional to N_1 and to the spectral

density $\rho(\omega_0)$ at the atom transition angular frequency $\omega_0 \equiv (E_2 - E_1)/\hbar$,

$$\frac{d}{dt}(N_1)_{\rm abs} = -B_{12}N_1\,\rho(\omega_0)\,, \tag{4.1}$$

where B_{12} is the absorption rate constant. Einstein then proposes two kinds of emission processes by which the atom can decay from the excited state to the groundstate. The first is *spontaneous* emission

$$\frac{d}{dt}(N_1)_{\rm spont} = A_{21}N_2 \tag{4.2}$$

and the second is *stimulated* emission

$$\frac{d}{dt}(N_1)_{\rm stim} = B_{21}N_2\,\rho(\omega_0)\,, \tag{4.3}$$

where A_{21} and B_{21} are the associated rate constants. As it appears from Eq. (4.2), spontaneous emission occurs in the absence of any radiation: The environment in which the two-level atom is embedded is the vacuum. Imposing now the equilibrium condition

$$\frac{d}{dt}(N_1)_{\rm abs} + \frac{d}{dt}(N_1)_{\rm spont} + \frac{d}{dt}(N_1)_{\rm stim} = 0 \tag{4.4}$$

and since $N_1/N_2 = \exp(\hbar\omega_0/k_{\rm B}T)$ in thermal equilibrium, we obtain

$$\rho(\omega_0) = \frac{A_{21}/B_{21}}{(B_{12}/B_{21})e^{\hbar\omega_0/k_{\rm B}T} - 1}\,. \tag{4.5}$$

At very high temperatures, $\rho(\omega_0)$ becomes so large that spontaneous emission can be considered negligible compared to stimulated emission. This means that $B_{21} = B_{12}$ and Eq. (4.5) can be rewritten as

$$\rho(\omega_0) = \frac{A_{21}/B_{21}}{e^{\hbar\omega_0/k_{\rm B}T} - 1}\,. \tag{4.6}$$

In the limit $k_{\rm B}T \gg \hbar\omega_0$, this equation reduces to approximately $(A_{21}/B_{21})k_{\rm B}T/\hbar\omega_0$ and the classical Rayleigh-Jeans law is applicable. Invoking this law, we obtain

$$\frac{A_{21}}{B_{21}} = \frac{\hbar\omega_0^3}{\pi^2c^3} \tag{4.7}$$

(c is the velocity of light in vacuum) and, finally,

$$\rho(\omega_0) = \frac{\hbar\omega_0^3/\pi^2c^3}{e^{\hbar\omega_0/k_{\rm B}T} - 1}\,, \tag{4.8}$$

which represents the Planck spectrum for $\rho(\omega_0)$. Einstein's work has two major consequences. First, it introduces the concept of stimulated emission, without which the Wien distribution instead of the Planck distribution would have been found [327]. Second, it shows for the first time that atomic radiation is characterized by spontaneous emission. This is a nonclassical process, where there is nothing to tell us *when* the atom undergoes a transition from the excited state to the groundstate [327].

We now try to give an argument on the relationship between vacuum and stimulated emission based on the assumption that there is a vacuum electromagnetic field

characterized by a spectral energy density $\rho_0(\omega_0) = (\hbar\omega_0^3)/2\pi^2c^3$. This assumption can be explained in modern QED, but it was not entirely clear when the A and B coefficients were derived. In the light of Einstein's derivation, we can ask the question whether an excited atom can be subjected to stimulated emission under the action of the vacuum field *only*. If this process exists, then the rate at which an atom in the excited state is stimulated by the vacuum field to drop to the groundstate should be

$$\frac{d}{dt}(N_2)^{(0)}_{\rm stim} = -B_{21}\,\rho_0(\omega_0)N_2 = -B_{21}\left(\frac{\hbar\omega_0^3}{2\pi^2c^3}\right)N_2\,. \tag{4.9}$$

Using Eq. (4.7), we have

$$\begin{aligned}\frac{d}{dt}(N_2)^{(0)}_{\rm stim} &= -B_{21}\frac{A_{21}}{2B_{21}}N_2 = -\frac{1}{2}A_{21}N_2 \\ &= \frac{1}{2}\frac{d}{dt}(N_2)_{\rm spont}\,.\end{aligned} \tag{4.10}$$

This equation shows that we can *almost* interpret spontaneous emission as stimulated emission due to the vacuum field, but only half the correct A coefficient for spontaneous emission is obtained. Consequently, the associated rate due to vacuum fluctuations is $R_{\rm VF} = A_{21}/2$. This point, which has important consequences also for the experiments to be discussed in the next sections, is not widely appreciated and oftentimes spontaneous emission is considered to be *entirely* induced by the vacuum field. Equation (4.10) suggests that spontaneous emission *is* related to vacuum radiation, but is not simply emission induced by this radiation. It can be shown that the missing one-half comes from the radiation reaction field [327],[7] which induces transitions at a rate $R_{\rm RR} = A_{21}/2$. Hence, the Einstein A coefficient for spontaneous emission is correctly given by

$$A_{21} = R_{\rm VF} + R_{\rm RR}\,. \tag{4.11}$$

A noteworthy fact is that for a two-level atom in the groundstate the effects of the vacuum and radiation reaction field cancel each other and the corresponding "spontaneous absorption" rate is zero, $A_{12} = R_{\rm VF} - R_{\rm RR} = 0$.

From the standpoint of modern QED, the Planck spectrum of Eq. (4.8) is incomplete. As we will show in Subsec. 4.2.2, a simple calculation based on the commutation relations valid for bosonic field operators reveals that the correct Planck spectrum should be

$$\tilde{\rho}(\omega_0) = \frac{\hbar\omega_0^3/\pi^2c^3}{e^{\hbar\omega_0/k_{\rm B}T}-1} + \frac{\hbar\omega_0^3}{2\pi^2c^3} \tag{4.12}$$

or, in terms of average energy of the atoms,

$$\langle E\rangle = \frac{\hbar\omega_0}{e^{\hbar\omega_0/k_{\rm B}T}-1} + \frac{1}{2}\hbar\omega_0\,. \tag{4.13}$$

To summarize, the Planck spectrum of Eq. (4.8) as derived by Planck and obtained from Einstein's A and B coefficients contains information about the vacuum

[7] We remind that the radiation reaction field is the field generated by a charged particle (in vacuum) acting on the particle itself.

fluctuations, which are responsible for half the spontaneous emission rate. However, it does not include the offset due to the vacuum fluctuations arising from the canonical quantization of the electromagnetic field, i.e., from the bosonic commutation relations. Such offset is included in our more mature version of the Planck distribution as shown by the second term of Eqs. (4.12) and (4.13).[8] Thus, the Planck distribution as expressed by Eq. (4.13) encodes information on the vacuum fluctuations two times: One time because of one half of the spontaneous emission coefficient and another time because of the bosonic commutation relations.

At microwave frequencies, the vacuum state can be reached by cooling the environment to sufficiently low temperatures. For example, the energy corresponding to an angular frequency $\omega_0 = 2\pi \times 10\,\mathrm{GHz}$ is $\hbar\omega_0 \simeq 6.626 \times 10^{-24}\,\mathrm{J}$ and its equivalent temperature $T = \hbar\omega_0/k_\mathrm{B} \simeq 480\,\mathrm{mK}$, where k_B is the Boltzmann constant. In this case, the energy associated with the vacuum fluctuations is $E_0 = \hbar\omega_0/2 \simeq 3.313 \times 10^{-24}\,\mathrm{J}$, which corresponds to a temperature $T_\mathrm{cr} \simeq 240\,\mathrm{mK}$. When cooling below such a temperature, the contribution arising from the thermal radiation is negligible and the vacuum fluctuations of the electromagnetic field become appreciable. In our experiments, we study the most simple source of thermal radiation: a resistor (cf. chapter 3, Sec. 3.1). We gradually cool down the resistor from temperatures higher than T_cr to a minimum temperature of approximately 20 mK. While cooling, we measure the variance of the signal emitted by the resistor and, simultaneously, record its temperature. In this manner, we are able to measure the Planck spectrum in an angular frequency window centered around ω_0 as a function of temperature [cf. Eq. (4.8)]. As discussed in detail in Subsec. 4.3.2, from such measurement we obtain indirect information on the one-half part of the spontaneous emission coefficient which accounts for the vacuum fluctuations. This represents an indirect observation of the variance of the vacuum fluctuations emitted (propagating) at angular frequency ω_0. Furthermore, we can measure the Planck spectrum in angular frequency windows centered around different values of ω_0. This type of experiment is one of the building elements for the implementation of so-called "Planck spectroscopy," which may be employed to characterize the thermal properties of various microwave devices, including nanomechanical resonators (cf. chapter 9). Figures 4.1(a) and 4.1(b) show a color-code plot (top and 3D view) of the Planck spectrum given by Eq. (4.13) as a function of both temperature and frequency. The parameters used to obtain such plots are extracted from our experiments in order to allow for a better comparison between the theory and the experimental results to be presented later in this chapter.

It is worth mentioning that if we were able to measure the offset associated with the vacuum fluctuations due to the commutation relations, we could then realize a direct observation of the variance of the vacuum fluctuations. As we show in Subsec. 4.3.3, there are however fundamental limitations preventing such measurement.

Another fundamental incarnation of the vacuum fluctuations in QED is represented by the Lamb shift. According to the Schrödinger and Dirac equations, atomic states with equal principal quantum number n and equal total angular momentum quantum number j, such as the $2s_{1/2}$ and $2p_{1/2}$ states of hydrogen atoms, are degenerate. However, in 1947 W. E. Lamb Jr. and R. C. Retherford

[8] It is worth mentioning that the offset due to the vacuum fluctuations made its first appearance in Planck's "second theory." However, the path followed by Planck to derive it was incorrect and the vacuum field contribution dropped out Planck's final expression for the spectral energy density.

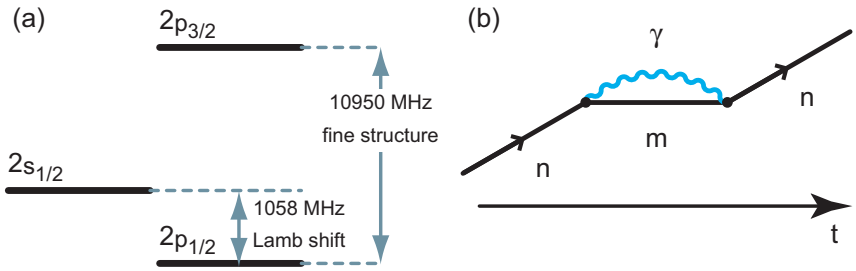

Figure 4.2: The Lamb shift in atomic physics. **(a)** Energy level diagram for the $n = 2$ states of the hydrogen atom. The Lamb shift is approximately 1058 MHz. Both the Lamb shift and fine structure splitting are in the microwave range. **(b)** Feynman diagram representing the Lamb shift in terms of emission and absorption of virtual photons, which are indicated as γ. The arrow marked by t indicates the direction of increasing time. More details are given in the main text.

made an experiment showing that these two states actually differ by approximately 1.06 GHz [cf. Fig. 4.2(a)]. Interestingly, the experiment was also realized employing microwave technology, which had greatly advanced during World War II. The Lamb shift can be interpreted as the result of emission into and re-absorption from the vacuum of virtual photons. This simple explanation, however, is not accompanied by a correspondingly simple theory. In summary, the Lamb shift is the energy (or equivalently frequency) shift of a state $|n\rangle\,|0\rangle$, in which the atom is in stationary level n and the field in the vacuum state with no photons. Such shift is due to the emission process $|n\rangle\,|0\rangle \rightarrow |m\rangle\,|1\rangle$ followed by the absorption process $|m\rangle\,|1\rangle \rightarrow |n\rangle\,|0\rangle$ [cf. Fig. 4.2(b)]. Altogether, this is a virtual process which brings the system back to the original state $|n\rangle\,|0\rangle$ via the intermediate state $|m\rangle\,|1\rangle$. The intermediate state corresponds to the atom in level m and the field populated with a single-photon excitation. A simple-minded approach to explain the Lamb shift via second-order perturbation theory would lead to the uncomfortable conclusion that the shift is infinite, where experiments show that it has to be small [327]. The solution to this conundrum was given in 1947 by H. A. Bethe, who proposed the mass renormalization approach in order to obtain the correct results for the Lamb shift [19]. According to P. A. M. Dirac, the "Bethe log," so-called because it reduces a linear infinite divergence to a logarithmic one and, eventually, to a finite result, deeply changed the character of modern physics.

The last example we would like to report in this brief summary of vacuum-related phenomena goes under the name of Casimir effect. If we consider the vacuum fluctuations of a three-dimensional infinite volume, these fluctuations are characterized by a continuous energy spectrum with infinite energy. We can imagine to "engineer" this scenario by placing a cavity (a resonator) within the three-dimensional volume just defined. The cavity confines a finite volume and the intracavity vacuum field is now characterized by a discrete energy spectrum. However, the vacuum field energy is still infinite since we have to sum over all infinite modes. The presence of the cavity, though, significantly modifies the environment. This is now separated into two distinguished regions, one with a continuous energy distribution of levels and

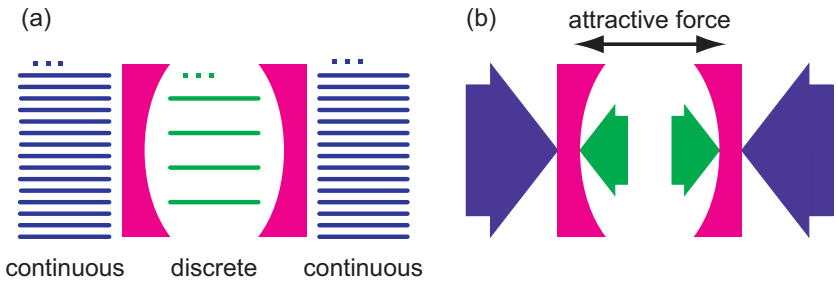

Figure 4.3: The Casimir effect. **(a)** A cavity [magenta (middle grey)], made of two uncharged and perfectly conducting plates (in Casimir's original model the plates were parallel [327]), separates the environment into two distinguished regions. The region outside of the cavity is characterized by a continuous energy spectrum [dark blue (dark grey) lines], whereas the one inside the cavity by a discrete spectrum [light green (light grey) lines]. **(b)** The vacuum field outside of the cavity "pushes" the two plates towards each other [dark blue (dark grey) arrow], whereas the field inside the cavity "repulses" them [light green (light grey) arrow]. The final effect is an attractive force [327].

the other with a discrete one [cf. Fig. 4.3(a)]. In simple words, there are "more" possible levels outside than inside the cavity. The idea is that the virtual photons of the vacuum field carry linear momentum $\hbar\mathbf{k}/2$ (where $\mathbf{k}$ represents a wavevector). Then, vacuum virtual photons reflected on the outside of the cavity plates push the plates together, whereas reflections on the inside repulses them. Since there are "more" possible levels outside the cavity than inside, the global effect results in an attraction of the two plates [cf. Fig. 4.2(b) for a simplified sketch representing this phenomenon and Ref. [327] for a rigorous proof].

All these examples show that playing with the vacuum is similar to playing with the subtraction of infinite expressions characterized by a different order of infinity. This makes possible the observation of vacuum-field-related effects, which are a profound test of the validity of QED.

4.2 Quantum Signal Theory

After presenting the general concepts of quantum signal theory, this section is devoted to the calculation of the first two quantum-mechanical central moments (mean value and variance) associated with quantum voltages with respect to number states (cf. Subsec. 4.2.1) and thermal/vacuum states (cf. Subsec. 4.2.2). In particular, we show that the quantum-mechanical variance (even after opportune normalizations) of a given quantum signal is generally different from the power associated with that signal. Finally, as a special application of the results obtained for thermal/vacuum states, we calculate the mean value and variance for the quantum voltages associated with the key devices of the two channels of the detection chain described in chapter 3. The quantum-mechanical mean value and variance are an important subset of the so-called signal quantum parameters.

In chapter 3, Subsecs. 3.2.5 and 3.2.6, we have derived the quantum-mechanical

expression for the quantum voltages to be measured in our experiments,

$$\hat{V}_{\mathrm{RL}k} = g_{\mathrm{RL}k}\hat{V}_{\mathrm{M}k}\,, \tag{4.14}$$

where $g_{\mathrm{RL}k}$ is the signal gain of the last amplification stage (i.e., the gain of the IF FET amplfiers) and $\hat{V}_{\mathrm{M}k}$ are the signals at the mixers' output, which are given by Eqs. (3.98) and (3.100) for the case of the Wilkinson power divider and by Eqs. (3.102) and (3.104) for the case of the 180° hybrid ring. Henceforth, where not further specified, both the Wilkinson power divider and 180° hybrid ring will simply be referred to as microwave beam splitters.

Given the quantum voltages (in general, quantum signals) $\hat{V}_{\mathrm{RL}k}$ of Eq. (4.14) and the state $|\psi\rangle$ at the input ports of either one of the two microwave beam splitters, we are able to predict exactly all quantum-mechanical parameters of interest. Such parameters are based on the concept of the *quantum-mechanical mean value*. The quantum-mechanical mean value with respect to state $|\psi\rangle$ can be of the bare voltages $\hat{V}_{\mathrm{RL}k}$,

$$\mu_{\mathrm{RL}k} \equiv \langle\hat{V}_{\mathrm{RL}k}\rangle_\psi \equiv \langle\psi|\hat{V}_{\mathrm{RL}k}|\psi\rangle \tag{4.15}$$

or any well-defined function $f(\hat{V}_{\mathrm{RL}k})$,

$$\langle f(\hat{V}_{\mathrm{RL}k})\rangle_\psi\,. \tag{4.16}$$

Of particular relevance is the case when $f(\hat{V}_{\mathrm{RL}k}) = \hat{V}^r_{\mathrm{RL}k}$, with $r \in \mathbb{N}_0$. For $r = 1$ we simply obtain Eq. (4.15), whereas for $r = 2$ we get the quantum-mechanical second moment of signal $\hat{V}_{\mathrm{RL}k}$ with respect to state $|\psi\rangle$,

$$\langle\hat{V}^2_{\mathrm{RL}k}\rangle_\psi \equiv \langle\psi|\hat{V}^2_{\mathrm{RL}k}|\psi\rangle\,. \tag{4.17}$$

The second moment can opportunely be skewed by the mean value squared in order to obtain the quantum-mechanical variance of the signal,

$$\sigma^2_{\mathrm{RL}k} \equiv \left(\Delta\hat{V}_{\mathrm{RL}k}\right)^2 \equiv \langle\psi|\hat{V}^2_{\mathrm{RL}k}|\psi\rangle - \mu^2_{\mathrm{RL}k}\,, \tag{4.18}$$

which is also referred to as second central moment. The formalism at the basis of these exact predictions is here defined *quantum signal theory*.

Equations (4.15) and (4.16) are very simple expressions for obtaining quantum-mechanical mean values, but they are not of general validity. In practice, in fact, they are only useful for so-called *pure states*. Pure states are those which can be represented by a linear combination of a complete orthonormal set of eigenstates $\{|p\rangle\}$ (ket states),

$$|\psi\rangle = \sum_p c_p|p\rangle\,, \tag{4.19}$$

where c_p is a generic complex coefficient and N_p is the dimensionality of the ket space. An example is in order. The quantum signal (voltage or current) sustained by an infinite or semi-infinite transmission line is spanned by the complete orthonormal set of photon number states

$$\{|n_m\rangle\}\,, \tag{4.20}$$

with $n_m = 0, 1, 2, \ldots$ (i.e., $n \in \mathbb{N}$) for each mode m of the line.[9] In this case, the most general pure state associated with a quantum signal on the line is given by

$$|\psi\rangle_{\text{line}} = \sum_{n_m} c(n_m)|n_m\rangle \,. \tag{4.21}$$

Such a state, in its full generality, is rarely encountered in real applications. However, there are several states in which the superposition is restricted to the number states of a single mode of the line. Examples of such states are single-mode squeezed states, coherent states, simple superposition of single-mode number states, and single-mode number states (including the vacuum state). Later (cf. Subsec. 4.2.1), we will use the case of number states as an example for the calculation of some relevant quantum-mechanical parameters. A fundamental feature common to superposition states is that the contribution of each basis state, $|n_m\rangle$, has a specified amplitude and a well-defined phase, which is relative to the overall phase angle of the complete superposition. This property is embodied in the complex coefficient $c(n_m)$.

In general, Eq. (4.19) allows us to define the so-called *pure ensemble* as a collection of physical systems such that every member is characterized by the same state $|\psi\rangle$. If we perform a measurement on a pure ensemble of an observable $\hat{\mathcal{O}}$, which is spanned by a set of eigenstates $|p\rangle$, the quantum-mechanical mean value is defined as

$$\begin{aligned} \langle\hat{\mathcal{O}}\rangle_\psi &\equiv \langle\psi|\hat{\mathcal{O}}|\psi\rangle \\ &= \sum_p p\,|\langle p|\psi\rangle|^2 \,, \end{aligned} \tag{4.22}$$

where p is a measured value and $|\langle p|\psi\rangle|^2$ is the probability for obtaining p. Equation (4.22) represents the general form of Eq. (4.15).

In contrast, we define the so-called *mixed ensemble* as a collection where each fraction of the members with a relative population w_i is characterized by state $|\psi^{(i)}\rangle$. A mixed ensemble is, thus, a mixture of pure ensembles. The fractional populations have a classical statistical origin. Hence, they are constrained to fulfill the standard normalization condition

$$\sum_i w_i = 1 \,, \tag{4.23}$$

but the number of terms in the sum need not coincide with the dimensionality N_p of the ket space (it can be smaller or larger). In addition, the set of states $\{|\psi^{(i)}\rangle\}$ needs not be an orthogonal set. If we perform a measurement on a mixed ensemble of the observable $\hat{\mathcal{O}}$, the quantum-mechanical mean value is now defined as

$$\begin{aligned} \langle\hat{\mathcal{O}}\rangle &\equiv \sum_i w_i \langle\psi^{(i)}|\hat{\mathcal{O}}|\psi^{(i)}\rangle \\ &= \sum_i \sum_p w_i\,|\langle p|\psi^{(i)}\rangle|^2\, p \,, \end{aligned} \tag{4.24}$$

[9] In the special case of a transmission line resonator, $m = 1, 2, 3, \ldots$ (i.e., $m \in \mathbb{N}_0$). In this case, m is related to the propagation phase constant β; cf. chapter 2, Subsec. 2.1.2.

where $|\langle p|\psi^{(i)}\rangle|^2$ is the quantum-mechanical probability for state $|\psi^{(i)}\rangle$ to be found in an eigenstate $|p\rangle$ of $\hat{\mathcal{O}}$ and w_i is the probability factor for finding a state $|\psi^{(i)}\rangle$ in the ensemble. Applying twice the closure theorem of quantum mechanics (e.g., cf. Ref. [266]) then motivates the definition of a density operator $\hat{\rho}$,

$$\hat{\rho} \equiv \sum_i |\psi^{(i)}\rangle\langle\psi^{(i)}| \,. \tag{4.25}$$

The density operator $\hat{\rho}$ is the standard form to represent a *mixed state*. An example is in order. The quantum signal (voltage or current) associated with a resistor in thermodynamical equilibrium with its environment cannot be represented by a pure state of the form of Eq. (4.21). For a resistor, all that can be specified is a set of probabilities $P(n_m^{(i)})$ that the signal is found in a range of states $|n_m^{(i)}\rangle$, each corresponding to one of a complete orthonormal set of photon number states such as in Eq. (4.20). The quantum signal of a resistor is manifestly a multi-mode signal and the use of the multi-mode set of number states $\{|n_m^{(i)}\rangle\}$ is appropriate. The most general mixed state associated with such a quantum signal is given by

$$\hat{\rho}_{\rm res} = \sum_{n_m^{(i)}} P(n_m^{(i)})|n_m^{(i)}\rangle\langle n_m^{(i)}| \,. \tag{4.26}$$

As for the case of the pure state of Eq. (4.21), the mixed state of Eq. (4.26) in its full complexity is rarely used in calculations.[10] Typically, all considerations are restricted to the number states of one single mode among all infinite modes associated with the resistor. Within this framework (cf. Subsec. 4.2.2), we will later work out some relevant quantum-mechanical parameters of quantum signals associated with resistors. In strict contrast to pure states, a fundamental feature of mixed states is that the contribution of each basis state, $|n_m\rangle$, does not have a well-defined phase with respect to the complete state. This is due to the statistical origin of the complete state.

Finally, an extremely powerful relation for density operators allows us to obtain the quantum-mechanical mean value of an observable $\hat{\mathcal{O}}$ as

$$\langle\hat{\mathcal{O}}\rangle \equiv {\rm Tr}\,\{\hat{\rho}\,\hat{\mathcal{O}}\}\,, \tag{4.27}$$

where the trace "Tr" of an operator is the invariant sum of its diagonal matrix elements for *any* complete orthonormal set of eigenstates (i.e., we can use the most convenient set for each specific case!). The relation of Eq. (4.27) can be used for both mixed and pure states. Thus, the quantum-mechanical mean value for the quantum voltages to be measured, $\hat{V}_{{\rm RL}k}$, can be rewritten as

$$\langle\hat{V}_{{\rm RL}k}\rangle \equiv {\rm Tr}\{\hat{\rho}\,\hat{V}_{{\rm RL}k}\} \tag{4.28}$$

and, for $f(\hat{V}_{{\rm RL}k})$, as

$$\langle f(\hat{V}_{{\rm RL}k})\rangle \equiv {\rm Tr}\{\hat{\rho}\,f(\hat{V}_{{\rm RL}k})\}\,. \tag{4.29}$$

We will make extensive use of these relations in particular in the case of thermal states.

[10] Even if, this time, the general form of Eq. (4.26) is closer to reality than any approximation we are going to use.

4.2.1 Number States

The photon number states constitute a paradigmatic example in the quantum theory of light. In contrast of being among the hardest to be generated and characterized experimentally, number states are the easiest to be comprehended on theoretical basis. Because of their simple properties, number states are the natural starting point in the quantum theory of signals. Number states are pure states and, hence, the density operator formalism needs not be used to study them.[11]

As shown by Eq. (4.21), number states form a complete orthonormal set of states for any quantum signal (voltage or current) on a transmission line. Number states are also the standard basis for the single-mode quantum-mechanical harmonic oscillator and for the Planck distribution. Hereafter, we consider single-mode number states only. Dropping the mode subscript m from the multi-mode states of Eq. (4.21), a complete orthonormal set of single-mode number states is then

$$\{|n\rangle\}\,, \tag{4.30}$$

with $n \in \mathbb{N}$. Such a set of states has already been introduced in chapter 2, Subsec. 2.1.3. Under single-mode assumptions, the pure state associated with a quantum signal on a transmission line assumes the form

$$|\psi\rangle_{\text{line}} = \sum_n c(n)|n\rangle\,. \tag{4.31}$$

We start reminding a few fundamental properties of single-mode number states:[12]

$$\hat{a}|n\rangle = \sqrt{n}|n-1\rangle\,, \tag{4.32a}$$

$$\hat{a}|0\rangle = 0\,, \tag{4.32b}$$

$$\hat{a}^\dagger|n\rangle = \sqrt{n+1}|n+1\rangle\,. \tag{4.32c}$$

In addition,

$$(\hat{a})^2|n\rangle = \hat{a}(\hat{a}|n\rangle) = \sqrt{n(n-1)}|n-2\rangle\,, \tag{4.33a}$$

$$\hat{a}^\dagger\hat{a}|n\rangle = \hat{a}^\dagger(\hat{a}|n\rangle) = n|n\rangle\,, \tag{4.33b}$$

$$(\hat{a}^\dagger)^2|n\rangle = \hat{a}^\dagger(\hat{a}^\dagger|n\rangle) = \sqrt{(n+1)(n+2)}|n+2\rangle \tag{4.33c}$$

and, since $\{|n\rangle\}$ represents a complete orthonormal set of kets,

$$\langle n''|n'\rangle = \delta_{n'',n'}\ , \tag{4.34}$$

where $|n'\rangle, |n''\rangle \in \{|n\rangle\}$.

Using the properties of Eqs. (4.32a), (4.32c), and (4.34), it is straightforward to invoke Eq. (2.111) and calculate the quantum-mechanical mean value per-root-hertz

[11] Even if nothing would prevent us from using it.

[12] Notably, the properties given here for the generic ket $|n\rangle$ can directly be applied to the corresponding bra $\langle n|$.

for a generic quantum voltage $\hat{V} = \bar{V}_0\,(\hat{a}^\dagger + \hat{a})$ with respect to a number state $|n\rangle$ as

$$\begin{aligned}\mu_n &\equiv \langle \hat{V} \rangle_n \\ &= \bar{V}_0 \langle n|(\hat{a}^\dagger + \hat{a})|n\rangle \\ &= \bar{V}_0(\sqrt{n+1}\langle n+1|n\rangle + \sqrt{n}\langle n|n-1\rangle) = 0\,, \end{aligned} \tag{4.35}$$

$\forall n \in \mathbb{N}$.

Using the properties of Eqs. (4.33a), (4.33c), (4.33b), and (4.34) and the result for the mean value of Eq. (4.35), we can invoke Eq. (2.112) and calculate the quantum-mechanical variance per-hertz normalized over the load impedance Z_0 as

$$\begin{aligned}\bar{\sigma}_n^2 &\equiv \frac{\sigma_n^2}{Z_0} \equiv \frac{1}{Z_0}(\Delta\hat{V})_n^2 \\ &= \frac{\bar{V}_0^2}{Z_0}\left\{\langle n|[(\hat{a}^\dagger)^2 + 2\hat{a}^\dagger\hat{a} + (\hat{a})^2]|n\rangle + 1\right\} - \mu_n^2 \\ &= 2\frac{\bar{V}_0^2}{Z_0}\left(n + \frac{1}{2}\right) = \hbar\omega\left(n + \frac{1}{2}\right)\,, \end{aligned} \tag{4.36}$$

$\forall n \in \mathbb{N}$. As expected, for the vacuum state $|0\rangle$ the normalized variance is equal to the energy of the total vacuum fluctuations of the signal, $\hbar\omega/2$. For higher number states $|n\rangle$, with $n > 1$, the normalized variance scales with the number of photons and is augmented by $\hbar\omega$ for each extra photon.

4.2.2 Thermal/Vacuum States

In contrast to number states, thermal states are usually easy to generate experimentally. All we need to create a thermal state is a resistor in thermodynamical equilibrium with a heat reservoir at a specified temperature T. For temperatures $T \ll T_{\rm cr}$ (cf. Sec. 4.1), a thermal state effectively becomes a vacuum state. As described in Sec. 4.1, thermal states have been studied since the dawn of quantum mechanics and have always played a central role in the theory of quantum fields. The Planck distribution of Eq. (4.13) is one example of their relevance. A distinct feature of thermal states typically encountered in experiments is in that they belong to the special class of Gaussian states (cf. chapter 2, Subsec. 2.1.3.) As a consequence, they can be completely characterized by means of the first two quantum-mechanical (central) moments. Thermal states, which represent the basic ingredient of our experiments, are a prototypical example of mixed states and, hence, the density operator formalism is necessary to study them. Given their simplicity, such states are an ideal playground to get acquainted with the concept of statistical mixture. Due to their statistical nature, thermal states cannot carry coherent information and are characterized by a totally uncertain phase.

As shown by Eq. (4.26), thermal states are associated with multi-mode signals and are specified by the probability distribution $P(n_m^{(i)})$ to find the quantum signal (voltage or current) of a resistor in a number state $|n_m^{(i)}\rangle$. The general form of Eq. (4.26) can be substantially simplified by considering only one single resistor mode with angular frequency ω_0. In this case, we can model the resistor as if it were a single-mode LC-resonator with angular frequency ω_0 maintained in thermodynamical equilibrium at temperature T. As demanded by intuition, the resonator

is then populated with a thermal state. Employing the set given by Eq. (4.30) as a complete orthonormal set for describing a single-mode thermal state, the density operator for such a state assumes the form

$$\hat{\rho}_{\rm th} = \sum_n P_{\rm th}(n)|n\rangle\langle n|\,, \tag{4.37}$$

where $P_{\rm th}(n)$ is the probability distribution for a single mode.

We remind a few fundamental properties of single-mode thermal states. In Sec. (4.1), we have proven by means of Einstein's A and B coefficients[13] that for atoms with transition angular frequency ω_0 in thermodynamical equilibrium at temperature T the mean (average) energy is given by Eq. (4.13). This result can be directly extended to the mean energy $\langle E_n\rangle$ of a single-mode LC-resonator with angular frequency $\omega = \omega_0$ at temperature T. From Eq. (2.85), the mean energy associated with such a resonator can be written as

$$\langle E_n\rangle_{\rm th} = \hbar\omega_0\left(\langle n\rangle_{\rm th} + \frac{1}{2}\right)\,, \tag{4.38}$$

where $\langle n\rangle_{\rm th}$ is the thermal population of the resonator in terms of mean number of photons. Comparing Eqs. (4.38) and (4.13), we then obtain

$$\langle n\rangle_{\rm th} = \frac{1}{e^{\hbar\omega_0/k_{\rm B}T} - 1}\,, \tag{4.39}$$

which, according to our model, represents the mean number of thermal photons populating a single mode of a resistor. Using the shorthand notation

$$\varepsilon \equiv e^{-\hbar\omega_0/k_{\rm B}T} \tag{4.40}$$

and recalling the sum of a geometric series $\sum_n^\infty \varepsilon^n = 1/(1-\varepsilon)$, we readily find

$$\begin{aligned}\langle n\rangle_{\rm th} &= \frac{1}{\varepsilon^{-1}-1} = \frac{\varepsilon}{1-\varepsilon}\\ &= (1-\varepsilon)\varepsilon\frac{\partial}{\partial\varepsilon}\left(\sum_n^\infty \varepsilon^n\right) = (1-\varepsilon)\sum_n^\infty n\varepsilon^n\,.\end{aligned} \tag{4.41}$$

Dropping the "∞" from all sums for simplicity, from the general definition of mean value

$$\langle n\rangle = \sum_n nP(n) \tag{4.42}$$

it finally follows that for single-mode thermal states

$$\begin{aligned}P_{\rm th}(n) &= (1-\varepsilon)\varepsilon^n\\ &= (1-e^{-\hbar\omega_0/k_{\rm B}T})e^{-n\hbar\omega_0/k_{\rm B}T}\,.\end{aligned} \tag{4.43}$$

With Eqs. (4.37) and (4.43) in hand, we can write the density operator representing a single-mode thermal state as

$$\hat{\rho}_{\rm th} = (1-e^{-\hbar\omega_0/k_{\rm B}T})\sum_n e^{-n\hbar\omega_0/k_{\rm B}T}|n\rangle\langle n|\,, \tag{4.44}$$

[13]Induced absorption, induced emission, and spontaneous emission.

which is characterized by only diagonal number-state matrix elements. It now appears evident that the number states are the natural basis for the density operator of Eq. (4.44) because the thermal distribution gives information only on the probabilities of finding a system in its various energy eigenstates, which are equivalent to the states $|n\rangle$.

From the general relation of Eq. (4.27), the mean number of thermal photons in the resistor is given by

$$\langle n\rangle_{\rm th} = {\rm Tr}\left\{\hat{\rho}_{\rm th}\,\hat{N}\right\}, \tag{4.45}$$

where $\hat{N} = \hat{a}^\dagger\hat{a}$ is the number operator. It is then an easy exercise to rewrite the density operator of Eq. (4.44) as

$$\hat{\rho}_{\rm th} = \sum_n \frac{\langle n\rangle_{\rm th}^n}{(1+\langle n\rangle_{\rm th})^{1+n}}|n\rangle\langle n|\,. \tag{4.46}$$

The results of Eqs. (4.44) and (4.46) can readily be generalized to multi-mode states from the definition of grand probability distribution (e.g., cf. Ref. [91]).

The quantum-mechanical mean value per-root-hertz for a generic quantum voltage $\hat{V}$ with respect to a thermal state with density operator $\hat{\rho}_{\rm th}$ given by Eq. (4.37) can be calculated by means of Eq. (4.27). Applying the closure theorem of quantum mechanics for a generic complete orthonormal set $\{|m\rangle\}$,[14] $\sum_m |m\rangle\langle m| = \mathbf{I}$,[15] using the definition of matrix trace, and recalling that $\mu_n = 0$ [cf. Eq. (4.35)], we find

$$\begin{aligned}
\mu_{\rm th} &\equiv \langle\hat{V}\rangle_{\rm th} \\
&= {\rm Tr}\left\{\hat{\rho}_{\rm th}\,\hat{V}\right\} \\
&= {\rm Tr}\Big\{\sum_n P_{\rm th}(n)|n\rangle\langle n|\hat{V}\Big\} = {\rm Tr}\Big\{\sum_{m,n} P_{\rm th}(n)|n\rangle\langle n|\hat{V}|m\rangle\langle m|\Big\} \\
&= \sum_n P_{\rm th}(n)\langle n|\hat{V}|n\rangle = \sum_n P_{\rm th}(n)\,\mu_n = 0\,.
\end{aligned} \tag{4.47}$$

Similarly, the quantum-mechanical variance per-hertz normalized over the load impedance Z_0 can be calculated recalling the results of Eqs. (4.36) and (4.47), the general definition of Eq. (4.42) for the case of Eq. (4.39), and the condition $\sum_n P_{\rm th}(n) = 1$. We find

$$\begin{aligned}
\bar{\sigma}_{\rm th}^2 &\equiv \frac{\sigma_{\rm th}^2}{Z_0} \equiv \frac{1}{Z_0}(\Delta\hat{V})_{\rm th}^2 \equiv \frac{1}{Z_0}(\langle\hat{V}^2\rangle_{\rm th} - \langle\hat{V}\rangle_{\rm th}^2) \\
&= \frac{1}{Z_0}{\rm Tr}\left\{\hat{\rho}_{\rm th}\,\hat{V}^2\right\} - \frac{\mu_{\rm th}^2}{Z_0} = \frac{1}{Z_0}{\rm Tr}\Big\{\sum_{m,n} P_{\rm th}(n)|n\rangle\langle n|\hat{V}^2|m\rangle\langle m|\Big\} \\
&= \frac{1}{Z_0}\sum_n P_{\rm th}(n)\langle n|\hat{V}^2|n\rangle = \sum_n P_{\rm th}(n)\frac{\sigma_n^2}{Z_0} \\
&= \hbar\omega_0\left(\frac{1}{e^{\hbar\omega_0/k_{\rm B}T}-1}+\frac{1}{2}\right) = \frac{\hbar\omega_0}{2}\coth\frac{\hbar\omega_0}{2k_{\rm B}T}\,.
\end{aligned} \tag{4.48}$$

[14] Here, m must not be confused with the index for the mode number. When applying the closure theorem we use always m and n for consistency with most books.

[15] As always, $\mathbf{I}$ represents an identity matrix with dimensionality given by the dimensionality of $\{|m\rangle\}$.

As expected, the normalized variance per-hertz is equal to the mean energy given by the Planck distribution including vacuum [cf. Eq. (4.13)]. If we intend to calculate the normalized variance in units W, we must multiply the result of Eq. (4.48) by the measurement bandwidth Δf in units Hz.

Remarkably, the first two quantum-mechanical moments for thermal states are equal to those for number states, but with n replaced by $\langle n \rangle_{\text{th}}$.

Only in the special case of thermal states, the normalized variance in units W is equivalent to the power associated with a quantum signal (e.g., voltage) on a resistor of real impedance (resistance) Z_0. The power Π_{Z_0} absorbed by the resistor can be calculated quantum-mechanically: *(i)* assuming that the power is measured by means of a power meter or square law detector. In this case, all rapidly rotating terms of the kind $(\hat{a}^\dagger)^2$ and $(\hat{a})^2$ are filtered out by the internal network of the power meter or square law detector. This is the experimental version of a theoretical RWA; *(ii)* recalling the property for number states given by Eq. (4.33b); *(iii)* the general definition of Eq. (4.42) for the case of Eq. (4.39); *(iv)* that $\sum_n P_{\text{th}}(n) = 1$ because of the standard normalization condition for probability distributions. In this way we obtain

$$\begin{aligned}
\Pi_{Z_0} &= \frac{\langle \hat{V}^2 \rangle_{\text{th}}}{Z_0} \Delta f \\
&= \frac{\bar{V}_0^2}{Z_0} \langle [(\hat{a}^\dagger)^2 + 2\hat{a}^\dagger \hat{a} + 1 + (\hat{a})^2] \rangle_{\text{th}} \Delta f \\
&\approx \frac{\hbar \omega_0}{2} \text{Tr} \left\{ \hat{\rho}_{\text{th}} \left(2\hat{a}^\dagger \hat{a} + 1 \right) \right\} \Delta f \\
&= \hbar \omega_0 \Big\{ \sum_n P_{\text{th}}(n) \langle n | \left(\hat{a}^\dagger \hat{a} + \frac{1}{2} \right) | n \rangle \Big\} \Delta f \\
&= \hbar \omega_0 \Big[\sum_n n P_{\text{th}}(n) + \frac{1}{2} \sum_n P_{\text{th}}(n) \Big] \Delta f \\
&= \hbar \omega_0 \left(\langle n \rangle_{\text{th}} + \frac{1}{2} \right) \Delta f = \Delta f \frac{\hbar \omega_0}{2} \coth \frac{\hbar \omega_0}{2 k_{\text{B}} T} \, . \qquad (4.49)
\end{aligned}$$

Notably, the result of Eq. (4.49) is only an *approximated* solution because of the RWA. For thermal states, due to all assumptions explained above and due to the vanishing mean value $\mu_{\text{th}} = 0$, the results for the power absorbed by the resistor and for the normalized variance in units W coincide, $\Pi_{Z_0} = \Delta f \, \bar{\sigma}_{\text{th}}^2$. If, however, we were to measure a single-mode squeezed state, the two results would be different. The variance would be the only quantity able to account for the squeezed state nontrivial phase dependence, which is encoded in the square terms $(\hat{a}^\dagger)^2$ and $(\hat{a})^2$ (cf. Ref. [91], bottom of p. 203 for a definition of squeezed states). A power meter or square law detector alone is insufficient to fully characterize a squeezed state directly! Even if we have measured thermal states only, in all the experiments presented in this chapter we never used power meters or square law detectors to estimate quantum signal parameters. As explained in Sec. 4.3, we always resorted to signal post-processing in order to estimate the quantum-mechanical variance as given by Eq. (4.48). This allows us to obtain less distorted estimations compared to mere power measurements, which only give approximated results. Our approach will

be indispensable when extending the measurements from thermal/vacuum states to squeezed states or more complex Gaussian states.

The Quantum Voltages $\hat{V}_{\mathrm{RL}k}$ and the Detection-Chain States

In Subsec. (4.2.2), we obtained the general relations for the quantum-mechanical mean value per-root-hertz and variance normalized over the load impedance Z_0 in the case of a generic quantum voltage $\hat{V}$ with respect to a generic thermal state with density operator $\hat{\rho}_{\mathrm{th}}$. We now specialize these results to the relevant case of the quantum voltages $\hat{V}_{\mathrm{RL}k}$ given by Eq. (4.14) with respect to the various states of the detection chain used in our experiments (cf. chapter 3 for a thorough description of the chain). We remind that $k = 1, 2$.

In summary, we can write the quantum voltages $\hat{V}_{\mathrm{RL}k}$ as

$$\hat{V}_{\mathrm{RL}k} = g_{\mathrm{RL}k}\delta_{\mathrm{M}k}g_{\mathrm{RH}k}g_{\mathrm{CH}k} \times (\hat{V}_{k,\varphi} + \delta_{\mathrm{c}k}\hat{E}_{\mathrm{c}k,\varphi} + \hat{E}_{\mathrm{n}k,\varphi}) , \tag{4.50}$$

where the subscript "φ" indicates the phase picked by the signals during mixing (cf. chapter 3, Subsec. 3.2.5).

In general, the detailed structure of the first term in Eq. (4.50), $\hat{V}_{k,\varphi}$, depends on which output port of which microwave beam splitter we are considering. The terms in the square brackets of Eqs. (3.98), (3.100), (3.102), and (3.104) show the exact form for $\hat{V}_{k,\varphi}$ in the case of the two output ports of a Wilkinson power divider and 180° hybrid ring, respectively, in units of $\bar{V}_0$. As explained in Sec. 3.1, the output signals of the microwave beam splitters, and, consequently, the quantum voltages $\hat{V}_{k,\varphi}$, depend on the interplay between a primary and secondary noise source at the beam splitter input. As it will appear clear by the end of this chapter, the experiments to be presented in Subsec. 4.3.3 are highly sensitive to the different contributions arising from the primary and secondary noise sources. In contrast, the experiments to be presented in Subsecs. 4.3.1 and 4.3.2 do not allow us to discern between the two noise sources, which, in that case, can be considered to constitute one *single effective noise source*. Such effective noise source can be described by a single set of bosonic creation and annihilation superoperators, $\hat{\Xi}^{\dagger}$ and $\hat{\Xi}$. The main physical assumption behind the definition of the superoperators $\hat{\Xi}^{\dagger}$ and $\hat{\Xi}$ is that the primary and secondary noise sources are characterized by exactly the *same absolute temperature*.[16] Under the assumption of a single effective noise source, the quantum voltage at the output port of either one of the microwave beam splitters is given by

$$\hat{V}_{k,\varphi} = \bar{V}_0(\hat{\Xi}^{\dagger}e^{+j\varphi_{\mathrm{LO}}} + \hat{\Xi}e^{-j\varphi_{\mathrm{LO}}}) , \tag{4.51}$$

where φ_{LO} is the phase induced by the LO signal. Such a phase is irrelevant for the experiments of Subsecs. 4.3.1 and 4.3.2 and we show it here only for the sake of completeness. The state associated with the single effective noise source is a thermal state with density operator

$$\hat{\rho}_{\mathrm{eff}} = \sum_n \frac{\langle n\rangle_{\mathrm{eff}}^n}{(1+\langle n\rangle_{\mathrm{eff}})^{1+n}} |n\rangle\langle n| , \tag{4.52}$$

where

$$\langle n\rangle_{\mathrm{eff}} = \frac{1}{e^{\hbar\omega_0/k_{\mathrm{B}}T} - 1} . \tag{4.53}$$

[16] In Subsec. 4.3.3, we will show that this assumption does not hold in general.

In first approximation, the temperature T of the effective noise source is assumed to be the temperature of the clamp of the primary noise source Z_0 (cf. description of the noise model for a Wilkinson power divider in chapter 3, Subsec. 3.1.1). This temperature typically varies between approximately 20 and 350 mK (cf. bottom part of Fig. 3.10).

Recalling the results for the first two quantum-mechanical central moments of a thermal state given by Eqs. (4.47) and (4.48), we readily find

$$\begin{aligned}\mu_k &\equiv \langle \hat{V}_{k,\varphi} \rangle_{\text{eff}} \\ &= \text{Tr}\left\{\hat{\rho}_{\text{eff}}\, \hat{V}_{k,\varphi}\right\} = 0\end{aligned} \tag{4.54}$$

and

$$\begin{aligned}\bar{\sigma}_k^2 \equiv \frac{\sigma_k^2}{Z_0} &\equiv \frac{1}{Z_0}(\Delta \hat{V}_{k,\varphi})_{\text{eff}}^2 \\ &= \frac{1}{Z_0}\text{Tr}\left\{\hat{\rho}_{\text{eff}}\, \hat{V}_{k,\varphi}^2\right\} - \frac{\mu_k^2}{Z_0} = \frac{\hbar\omega_0}{2}\coth\frac{\hbar\omega_0}{2k_{\text{B}}T}\,.\end{aligned} \tag{4.55}$$

Equation (4.55) reveals that, in the low temperature limit, $T \ll \hbar\omega_0/2k_{\text{B}}$, the quantum-mechanical variance of a thermal state approaches the variance of the vacuum state at angular frequency ω_0, $\bar{\sigma}_k^2 \approx \hbar\omega_0/2$.

As shown in chapter 3, Subsec. 3.2.1, the quantum voltage $\hat{E}_{ck,\varphi}$ owns its origin to the two cryogenic circulators [cf. the argument which led to Eq. (3.55)]. At the output of either one of the two circulators and including the LO phase for generality, such a voltage is given by

$$\delta_{ck}\hat{E}_{ck,\varphi} = \delta_{ck}\bar{V}_0(\hat{\zeta}_k^{\dagger}e^{+j\varphi_{\text{LO}}} + \hat{\zeta}_k e^{-j\varphi_{\text{LO}}})\,. \tag{4.56}$$

The state associated with the quantum noise voltage $\hat{E}_{ck,\varphi}$ it is a thermal state characterized by the density operator

$$\hat{\rho}_{ck} = \sum_n P_{ck}(n)|n\rangle\langle n|\,, \tag{4.57}$$

where P_{ck} is the probability distribution for a single mode of the circulator noise, which depends on the exact temperature T_{Lc} of the Z_{Lc} termination at port C of the circulator (cf. Fig. 3.10).

As already pointed out in chapter 3, Subsec. 3.2.1, the temperature T_{Lc} depends on the heat flow between the mixing chamber and still stage of the cryostat. In general, the function describing this flow is unknown and, thus, is the exact form of P_{ck}. Here, we assume state $\hat{\rho}_{ck}$ such that

$$\begin{aligned}\mu_{ck} &\equiv \langle \hat{E}_{ck,\varphi} \rangle_{ck} \\ &= \text{Tr}\left\{\hat{\rho}_{ck}\, \hat{E}_{ck,\varphi}\right\} = 0\end{aligned} \tag{4.58}$$

and

$$\begin{aligned}\bar{\sigma}_{ck}^2 \equiv \frac{\sigma_{ck}^2}{Z_0} &\equiv \frac{1}{Z_0}(\Delta \hat{E}_{ck,\varphi})_{ck}^2 \\ &= \frac{1}{Z_0}\text{Tr}\left\{\hat{\rho}_{ck}\, \hat{E}_{ck,\varphi}^2\right\} - \frac{\mu_{ck}^2}{Z_0} = \varsigma(T_{\text{Lc}})\,,\end{aligned} \tag{4.59}$$

where $\varsigma(T_{\mathrm{Lc}})$ is an unknown function of T_{Lc} expressed in units J. In Appendix A, we will derive $\varsigma(T_{\mathrm{Lc}})$ phenomenologically from our experiments. In addition, we will show that it is possible to accurately account for it when retrieving the data.

The noise properties of phase-preserving linear amplifiers have already been described in chapter 3, Subsec. 3.2.2, while developing the quantum network theory of amplification. Within that context, Eq. (3.69) represented the formal expression for the quantum noise voltage associated with an amplifier. Such an expression can straightforwardly be extended in order to include the LO phase due to mixing, therefore obtaining the quantum noise voltages

$$\hat{E}_{\mathrm{n}k,\varphi} \equiv \bar{V}_0(\hat{\xi}_k^{\dagger} e^{+j\varphi_{\mathrm{LO}}} + \hat{\xi}_k e^{-j\varphi_{\mathrm{LO}}})\,. \tag{4.60}$$

It is worth stressing that these voltages represent the *noise referred to the input* of either one of the two cryogenic amplifiers and, thus, need to be multiplied by the amplifier signal gain $g_{\mathrm{CH}k}$ (and all other amplifiers/mixers gains/attenuations), as Eq. (4.50) correctly shows. The state associated with such voltages is the so-called operating state of the amplifier (cf. chapter 3, Subsec. 3.2.2), which is characterized by the density operator $\hat{\rho}_{\mathrm{op}k}$. The general structure of $\hat{\rho}_{\mathrm{op}k}$ depends on the internal modes of the amplifier (its internal degrees of freedom) and can be rather complicated.[17] However, for a stable operating temperature $T_{\mathrm{op}k}$ (in our case $T_{\mathrm{op}k} \simeq 4.2\,\mathrm{K}$; cf. Fig. 3.10) and under the reasonable assumption that the mean value

$$\mu_{\mathrm{op}k} = \mathrm{Tr}\,\{\hat{\rho}_{\mathrm{op}k}\,\hat{E}_{\mathrm{n}k,\varphi}\} = 0\,, \tag{4.61}$$

the definition of Eq. (3.80) allows us to write

$$\begin{aligned}\bar{\sigma}^2_{\mathrm{op}k} &\equiv \frac{\sigma^2_{\mathrm{op}k}}{Z_0} \equiv \frac{1}{Z_0}(\Delta\hat{E}_{\mathrm{n}k,\varphi})^2_{\mathrm{op}k} \\ &= \frac{1}{Z_0}\mathrm{Tr}\,\{\hat{\rho}_{\mathrm{op}k}\,\hat{E}_{\mathrm{n}k,\varphi}\} - \frac{\mu^2_{\mathrm{op}k}}{Z_0} = k_{\mathrm{B}}T_{\mathrm{CH}k}\,,\end{aligned} \tag{4.62}$$

where $T_{\mathrm{CH}k}$ is a well-defined constant temperature referred to as the amplifier noise temperature. We recall that the noise model developed in chapter 3, Subsec. 3.2.2 is an oversimplified model. In fact, in the high temperature limit $T_{\mathrm{op}k} \gg \hbar\omega_0/2k_{\mathrm{B}}$, which is certainly valid for microwave signals of approximately 5 GHz, Eq. (3.82) reduces to $\approx k_{\mathrm{B}}T_{\mathrm{op}k}/\hbar\omega_0$. From Eq. (3.80), it then follows that $T_{\mathrm{CH}k} \approx T_{\mathrm{op}k}$. For real amplifiers, it is not generally true that the amplifier noise temperature equals the amplifier operating temperature. The reader should bear this important caveat in mind when reading through this chapter (cf. also the opportune explanations given in chapter 3, Subsec. 3.2.2, Quantum Network Theory of Amplification).

Defining the total attenuation due to cables, connectors, and other device losses of either one of the two channels of the detection chain as $\delta_{\mathrm{att}k}$, the power gain of the channel is given by

$$G_k \equiv g_k^2 \equiv (g_{\mathrm{RL}k}\delta_{\mathrm{M}k}g_{\mathrm{RH}k}g_{\mathrm{CH}k}\delta_{\mathrm{att}k})^2\,. \tag{4.63}$$

In addition, recalling that the effective measurement bandwidth is given by

$$\mathrm{BW}_k = 2\min\{\mathrm{BW}_{\mathrm{IF}k}, \mathrm{BW}_{\mathrm{RF}k}\} = 2\mathrm{BW}_{\mathrm{IF}k} \tag{4.64}$$

[17] We remind that the noise of an amplifier is, in general, a frequency dependent non-Gaussian noise.

and using the results of Eqs. (4.54), (4.55), (4.58), (4.59), (4.61), and (4.62), finally allows us to write the basic theoretical model for determining the quantum-mechanical variance (normalized over the load impedance Z_0) in units W associated with the quantum voltage $\hat{V}_{\mathrm{RL}k}$ with respect to the thermal states of the beam splitters and circulators, and the operating state of the amplifiers. We obtain

$$\begin{aligned}\tilde{\sigma}_k^2 &\equiv \mathrm{BW}_k\,\bar{\sigma}_k^2 \equiv \frac{\mathrm{BW}_k}{Z_0}\sigma_k^2 \\ &= G_k \mathrm{BW}_k \frac{1}{Z_0}(\mathrm{Tr}\,\{\hat{\rho}_{\mathrm{eff}}\,\hat{V}_{k,\varphi}^2\} + \mathrm{Tr}\,\{\hat{\rho}_{ck}\,\hat{E}_{ck,\varphi}\} + \mathrm{Tr}\,\{\hat{\rho}_{\mathrm{op}k}\,\hat{E}_{\mathrm{n}k,\varphi}\}) \\ &= G_k \mathrm{BW}_k \left[\frac{\hbar\omega_0}{2}\coth\frac{\hbar\omega_0}{2k_{\mathrm{B}}T} + \varsigma(T_{\mathrm{Lc}}) + k_{\mathrm{B}}T_{\mathrm{CH}k}\right]. \end{aligned} \tag{4.65}$$

It is needless to say that the quantum-mechanical mean value associated with the quantum voltages $\hat{V}_{\mathrm{RL}k}$ vanishes because of Eqs. (4.54), (4.58), and (4.61).

Equation (4.65) clearly shows that the LO phase is totally irrelevant when computing the variance of thermal states. For this reason, we will hereafter drop the unnecessary subscript "φ."

4.3 Quantum Parameter Estimation

After presenting the main idea at the basis of quantum parameter estimation, in this section we introduce the experimental method used to measure the classical auto-correlation function for a set of realizations $\{s_k\}_i$ (with $i \in \mathbb{N}$) of the quantum voltage $\hat{V}_{\mathrm{RL}k}$ with respect to the thermal/vacuum states associated with the different stages of our detection chain (cf. Subsec. 4.3.1). Afterwards, we show how to obtain from the auto-correlation function the classical auto-covariance function and, then, the variance associated with the set of realizations $\{s_k\}_i$ for a temperature range comprised between approximately 20 and 350 mK. The classical variance represents an estimation of the quantum-mechanical variance given by Eq. (4.65), which has thoroughly been discussed in the previous section. Based on Eq. (4.65), we then introduce a fitting model for the temperature dependence of the variance, enabling, for the first time to our knowledge, the high fidelity observation of the "distance" between the experimental measurement and theoretical value of vacuum fluctuations at microwave frequencies. Furthermore, we present the frequency dependence of the variance for a frequency range comprised between approximately 4.7 and 7.1 GHz. Our data and fits constitute a clear demonstration that we are able to characterize the microwave vacuum state for a broad range of parameters. In addition, the fits allow us to thoroughly characterize the experimental setup by extracting the total gain and noise temperature as a function of frequency for both channels of the detection chain (cf. Subsec. 4.3.2). Finally, we take advantage of our two-channel detection chain to obtain an estimation of the cross-correlation function of the signals at the output ports of the microwave beam splitters. In this manner, we have access to the cross-covariance function and, thus, to the covariance of such signals. The most relevant features of our correlation measurements are: a) the almost total cancellation of the noise contribution added by the cryogenic amplifiers; b) the possibility of controlling the sign of the cross-correlation function by means of a phase shifter; c) the cancellation of the thermal/vacuum noise associated with the

primary and secondary noise sources (cf. Subsec. 4.3.3). The latter represents an unprecedented result, which helps unveiling the quantum-mechanical behavior of microwave beam splitters.

In Appendix A, we discuss the role played by the temperature-dependent noise contribution due to the cryogenic circulators. In Appendix B, we show that a simple polynomial fit leads to ambiguity in the interpretation of our experiments. Finally, in Appendix C, we present an alternative method for the analysis of the temperature-frequency dependence of the auto-covariance (Planck spectroscopy) data shown in Subsec. 4.3.2.

Brief Review of Quantum Parameter Estimation

Calculating the exact form of the quantum-mechanical mean value and variance or, more in general, of a quantum parameter for a given signal is a deterministic process, which follows from the fundamental laws of quantum mechanics. Because of its deterministic nature, such a process suffers from the impossibility of giving us a measurable - classical - quantity. Quantum parameters are representations of the noumenological reality residing behind the phenomenological reality we intend to grasp with our experimental - classical - hands [328]. Thus, all the results of Sec. 4.2 do not correspond to real measurements. Even further, such results cannot be measured, but they can only be estimated. By what means we can perform such estimations is our next quest.

The estimation of quantum parameters is realized through the experimental process of measurement. Let us focus on the case of random signals, e.g., thermal states (vacuum states in the limit of very low temperatures):

1. At the top of either one the two channels of the detection chain (cf. Fig. 3.10), after all circulators, amplifiers, attenuators, mixers, and filters, the quantum voltage $\hat{V}_{\mathrm{RL}k}$ is recorded by means of an A/D acquisition card. The signal s_k recorded by the card is a classical realization of the quantum voltage, $\hat{V}_{\mathrm{RL}k} \to s_k$. Each realization s_k corresponds to one single measurement and is characterized by a random time dependence. The duration of one time-trace $s_k(t)$ is set by the measurement time Δt_{m}, i.e., by the time window during which the acquisition card is "open."

   Reminder: Every time we refer to a classical realization (signal), we remove the "$\wedge$," which is reserved only to quantum-mechanical operators;

2. We are allowed to repeat the measurement of point 1. a number N_{c} of times.[18] In this manner, we obtain a set of realizations indicated as $\{s_k\}_i$, with $i = 1, 2, \ldots, N_{\mathrm{c}}$. For random signals, the elements of this set are generally different one from another. Employing the experimental jargon, such elements are referred to as cycles, which explains the subscript "c" in N_{c};

3. There are now two possible scenarios. The short and long measurement time limits:

   (a) In the limit of *short measurement time*, the quantum parameters (mean value and variance) associated with the voltage $\hat{V}_{\mathrm{RL}k}$ cannot be estimated

[18] In the experiments, N_{c} ranges between a few hundreds and a few millions, up to 100 million.

from a single time-trace, $s_k(t)$. In this case, we need to collect a sufficiently large number N_c of realizations in order to obtain unambiguous information about the moments of $\hat{V}_{\mathrm{RL}k}$.
The quantum-mechanical mean value given by Eq. (4.15) can then be estimated resorting to the *classical ensemble average*

$$\begin{aligned}\mu_{\mathrm{RL}k} &= \langle\psi|\hat{V}_{\mathrm{RL}k}|\psi\rangle \\ &\approx \frac{1}{N_\mathrm{c}}\sum_{i=1}^{N_\mathrm{c}}\{s_k\}_i \equiv \langle s_k\rangle\,. \end{aligned} \tag{4.66}$$

Oftentimes, the quantity $\langle s_k\rangle$ is also defined as m_k. It is well-known from any basic course in statistics that the larger the number of realizations, N_c, the more accurate the estimation given by Eq. (4.66) [298]. Trivially, in the limit $N_\mathrm{c}\to\infty$ we would expect to obtain a perfect parameter estimation.[19]
More in general, the quantum-mechanical mean value for any well-defined function $f(\hat{V}_{\mathrm{RL}k})$ can be estimated as

$$\langle\psi|f(\hat{V}_{\mathrm{RL}k})|\psi\rangle \approx \frac{1}{N_\mathrm{c}}\sum_{i=1}^{N_\mathrm{c}} f(\{s_k\}_i) \equiv \langle f(s_k)\rangle\,. \tag{4.67}$$

When $f(\hat{V}_{\mathrm{RL}k}) = \hat{V}^2_{\mathrm{RL}k}$, the quantum-mechanical variance given by Eq. (4.18) can be estimated by means of a classical ensemble average as

$$\begin{aligned}\sigma^2_{\mathrm{RL}k} &= \langle\psi|\hat{V}^2_{\mathrm{RL}k}|\psi\rangle - \mu^2_{\mathrm{RL}k} \\ &\approx \frac{1}{N_\mathrm{c}}\sum_{i=1}^{N_\mathrm{c}}(\{s_k\}_i)^2 - \Big(\frac{1}{N_\mathrm{c}}\sum_{i=1}^{N_\mathrm{c}}\{s_k\}_i\Big)^2 \equiv \langle s_k^2\rangle - \langle s_k\rangle^2\,; \end{aligned} \tag{4.68}$$

(b) In the limit of *long measurement time*, one single time-trace $s_k(t)$ may be sufficient to estimate the quantum parameters of $\hat{V}_{\mathrm{RL}k}$.
In this case, assuming time-traces with a continuous time dependence, the quantum-mechanical mean value given by Eq. (4.15) can be estimated resorting to the *classical time average*

$$\begin{aligned}\mu_{\mathrm{RL}k} &= \langle\psi|\hat{V}_{\mathrm{RL}k}|\psi\rangle \\ &\approx \frac{1}{\Delta t_\mathrm{m}}\int_{-\Delta t_\mathrm{m}/2}^{+\Delta t_\mathrm{m}/2} dt\, s_k(t) \equiv \overline{s_k}\,. \end{aligned} \tag{4.69}$$

The quantum-mechanical mean value for $f(\hat{V}_{\mathrm{RL}k})$ can be estimated as

$$\langle\psi|f(\hat{V}_{\mathrm{RL}k})|\psi\rangle \approx \frac{1}{\Delta t_\mathrm{m}}\int_{-\Delta t_\mathrm{m}/2}^{+\Delta t_\mathrm{m}/2} dt\, f[s_k(t)] \equiv \overline{f(s_k)}\,. \tag{4.70}$$

[19]Indeed, that of parameter estimation is a vast chapter in the theory of statistics. It is possible to define parameter estimators with higher or lower level of distortion and a large set of tests to verify estimation accuracy. We remind to Refs. [298, 301] for a more complete treatment of this topic.

Finally, when $f(\hat{V}_{\mathrm{RL}k}) = \hat{V}^2_{\mathrm{RL}k}$, the quantum-mechanical variance given by Eq. (4.18) can be estimated as

$$\begin{aligned}\sigma^2_{\mathrm{RL}k} &= \langle\psi|\hat{V}^2_{\mathrm{RL}k}|\psi\rangle - \mu^2_{\mathrm{RL}k} \\ &\approx \frac{1}{\Delta t_{\mathrm{m}}}\int_{-\Delta t_{\mathrm{m}}/2}^{+\Delta t_{\mathrm{m}}/2} dt\, s_k^2(t) \equiv \overline{s_k^2} - \overline{s_k}^2\,. \end{aligned} \tag{4.71}$$

If the classical realizations s_k are ergodic with respect to the first moment, then $\overline{s_k} = \langle s_k\rangle = m_k$. Similarly, if they are ergodic with respect to the second moment, then also $\overline{s_k^2} = \langle s_k^2\rangle$. These properties can be very useful when performing experiments, making possible to switch between ensemble and time average depending on the specific experimental needs. For an introduction to the complex topic of ergodic processes we remind the reader to Refs. [300–302].

In the experimental reality, the time traces $s_k(t)$ recorded by the acquisition card are not a continuous function of time. The acquisition card samples each time trace at a given sampling rate f_{sampling} (cf. chapter 3, Subsec. 3.2.6), transforming the trace into a discrete function of time

$$s_k(t) \to s_k[\,j\,]\,, \tag{4.72}$$

where $j = 1, 2, \ldots, N_{\mathrm{s}}$ and $N_{\mathrm{s}} \equiv \Delta t_{\mathrm{m}}\, f_{\mathrm{sampling}}$ is the number of samples within one single trace. Under these more realistic assumptions, the quantum-mechanical mean value and variance are estimated as

$$\mu_{\mathrm{RL}k} \approx \frac{1}{N_{\mathrm{s}}}\sum_{j=1}^{N_{\mathrm{s}}} s_k[\,j\,]\,, \tag{4.73a}$$

$$\sigma^2_{\mathrm{RL}k} \approx \frac{1}{N_{\mathrm{s}}}\sum_{j=1}^{N_{\mathrm{s}}} s_k^2[\,j\,] - \Big(\frac{1}{N_{\mathrm{s}}}\sum_{j=1}^{N_{\mathrm{s}}} s_k[\,j\,]\Big)^2\,. \tag{4.73b}$$

Hereafter, we will give all relevant expressions in terms of realizations with both a continuous and a discrete time dependence. We find the continuous case to be helpful from a pedagogical point of view, whereas the fully discretized case reflects more closely the experimental reality.

All estimations enumerated above take place in the so-called post-processing stage of the experiment (cf. very top part of Fig. 3.10) and are carried out with the aid of a PC.

4.3.1 Estimation of The Auto-Correlation Function

In our brief introduction to quantum parameter estimation we have made a sharp distinction between short and long measurement time. The question we want to address now is on the possibility to make full use of the twofold nature of a given set of realizations $\{s_k(t)\}_i$ (or $\{s_k[\,j\,]\}_i$ in the fully discretized case). Such set encodes information in both the number of cycles N_{c} and measurement time Δt_{m} (or number of samples N_{s}). The ensemble average takes only advantage of the large number

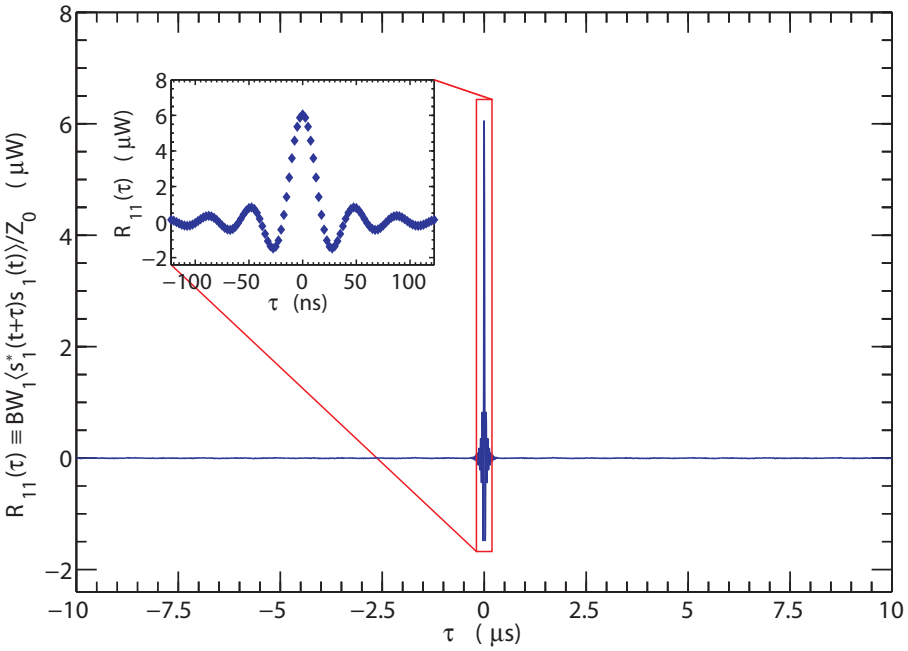

Figure 4.4: Auto-correlation function $R_{11}(\tau)$ for a vacuum state obtained by cooling to 30 mK a Wilkinson power divider with a resistive load at the input port. At first glance, the auto-correlation function reminds of a delta Dirac centered in the origin of the time axis. The zoom-in shown in the inset reveals that the function is actually a cardinal sine [cf. Eq. (4.82)], which owns its origin to the finite measurement bandwidth BW_1.

of cycles in the set, while the time average only of the long time duration (or, equivalently, large number of samples) of one single trace. One way to combine these two opposite approaches is to define a third limit, where the number of realizations is large enough to obtain an accurate global ensemble average and, simultaneously, each realization is long enough (or with a large enough number of samples) for the time correlation of one trace with itself to be well defined. We refer to this limit as the *intermediate measurement time* limit. In this regime, all information about the signals to be measured is encoded in the so-called auto-correlation function.

Before giving the expression utilized in the experiments for the estimation of the auto-correlation function, we recall a few basic definitions valid for random signals [300, 301]:[20]

1. Given a continuous random signal $x(t)$, we define the auto-correlation function $R_{xx}(t_1, t_2)$ as the mean value of the product of two samples of the signal at the two times t_1 and t_2, respectively,

$$R_{xx}(t_1, t_2) \equiv \langle x^*(t_1)\, x(t_2) \rangle = \int_{-\infty}^{+\infty} \int_{-\infty}^{+\infty} da\, db\; a^* b\, f_{x_{t1}, x_{t2}}(a, b)\,, \tag{4.74}$$

[20]The extension to deterministic signals is straightforward.

where the function $f_{x_{t1},x_{t2}}(a,b)$ is the joint probability density of the two random variables $x(t_1) \equiv x_{t1}$ and $x(t_2) \equiv x_{t2}$;

2. Given a discrete random signal $x[n]$, we define the auto-correlation function $R_{xx}[n_1,n_2]$ as the mean value of the product of two samples of the signal at the two discrete times n_1 and n_2, respectively,

$$\begin{aligned} R_{xx}[n_1,n_2] &\equiv \langle x^*[n_1]\, x[n_2]\rangle \\ &= \int_{-\infty}^{+\infty}\int_{-\infty}^{+\infty} da\, db\; a^* b\, f_{x_{n1},x_{n2}}(a,b)\,, \end{aligned} \tag{4.75}$$

where the function $f_{x_{n1},x_{n2}}(a,b)$ is the joint probability density of the two random variables $x[n_1] = x_{n1}$ and $x[n_2] = x_{n2}$.

The majority of continuous and discrete signals encountered in reality have the characteristic to be a function of *only one independent variable*. These signals belong to the class of so-called *stationary signals*. There are two types of stationary signals:

(a) *strictly stationary signals* are those signals for which all statistical properties are independent of time;

(b) *weakly stationary signals* are those signals for which the mean value is independent of time, $\langle x(t)\rangle \equiv \mu_x(t) = \mu_x\,,\ \forall t$ (continuous signals) and $\langle x[n]\rangle \equiv \mu_x[n] = \mu_x\,,\ \forall n$ (discrete signals), and the auto-correlation function depends only on the time lag $\tau = t_1 - t_2$ for continuous signals and $\ell = n_1 - n_2$ for discrete ones, $R_{xx}(t_1,t_2) = R_{xx}(\tau)$ or $R_{xx}[n_1,n_2] = R_{xx}[\ell]$.

Weakly stationary signals are the most common ones.

The auto-correlation function for a continuous or discrete random signal can be rewritten as a function of the time lag τ or ℓ as

$$R_{xx}(t_2,\tau) \equiv \langle x^*(t_2+\tau)\, x(t_2)\rangle\,, \tag{4.76a}$$

$$R_{xx}[n_2,\ell] \equiv \langle x^*[n_2+\ell]\, x[n_2]\rangle\,, \tag{4.76b}$$

or, substituting $t_2 \to t$ and $n_2 \to n$, more simply as

$$R_{xx}(t,\tau) \equiv \langle x^*(t+\tau)\, x(t)\rangle\,, \tag{4.77a}$$

$$R_{xx}[n,\ell] \equiv \langle x^*[n+\ell]\, x[n]\rangle\,. \tag{4.77b}$$

Equation (4.77b) clearly shows the dependence of the auto-correlation function from the first sample n of the signal and the interval ℓ between the first and second sample which are involved in the calculation. If the signal x is weakly stationary, the auto-correlation function depends only on the time lag τ or ℓ and, thus, is given by

$$R_{xx}(\tau) \equiv \langle x^*(t+\tau)\, x(t)\rangle\,, \tag{4.78a}$$

$$R_{xx}[\ell] \equiv \langle x^*[n+\ell]\, x[n]\rangle\,. \tag{4.78b}$$

Since the signal s_k measured in our experiments is weakly stationary, our next task is to find a suitable estimation for the auto-correlation functions of Eqs. (4.78a) and (4.78b) in the case $x = s_k$.

There are several methods to estimate the auto-correlation function of a weakly stationary signal. In the case of signal s_k, the most general way is to perform a double averaging, which involves both the number of cycles N_c and the measurement time Δt_m (or number of samples N_s) in two different steps. In a first step, the average of the i-th cycle $\{s_k(t)\}_i \equiv s_k^{(i)}(t)$ or $\{s_k[\,j\,]\}_i \equiv s_k^{(i)}[\,j\,]$ is carried out with respect to the measurement time Δt_m or number of samples N_s of that cycle, as follows

$$\mathcal{R}_{kk}^{(i)}(\tau) \equiv \frac{1}{\Delta t_\mathrm{m}} \int_{-\Delta t_\mathrm{m}/2}^{+\Delta t_\mathrm{m}/2} dt\, s_k^{(i)}(t+\tau) s_k^{(i)}(t)\,, \tag{4.79a}$$

$$\mathcal{R}_{kk}^{(i)}[\ell] \equiv \frac{1}{N_\mathrm{s}} \sum_{j=1}^{N_\mathrm{s}} s_k^{(i)}[\,j+\ell\,] s_k^{(i)}[\,j\,]\,. \tag{4.79b}$$

The above equations are referred to as *biased estimations* due to the normalization over the number of samples N_s. A particularly relevant feature of this class of estimations is that their Fourier transform is directly related to the true spectral density of the signal and, consequently, does not present unphysical negative values. For instance, if we were to use an unbiased estimation, the Fourier transform would present negative values! We remind the reader to Ref. [301] for more details on biased and unbiased estimations. It is noteworthy to mention that Eqs. (4.79a) and (4.79b) on their own do not constitute an accurate estimation for the auto-correlation function of signal $s_k^{(i)}$, as one might be tempted to assume. In fact, if only one single realization of the signal is available, as often happens in classical telecommunications, it can be shown that Eqs. (4.79a) and (4.79b) are an inconsistent estimation for the auto-correlation function [301]. In that case, special techniques must be used in order to obtain more accurate results [301]. In our case, however, a large number of realizations N_c is available. We can thus perform a second averaging step, where the average of $\mathcal{R}_{kk}^{(i)}(\tau)$ or $\mathcal{R}_{kk}^{(i)}[\ell]$ is carried out with respect to the number of cycles N_c. We obtain

$$\begin{aligned} R_{kk}(\tau) &\approx \frac{1}{N_\mathrm{c}} \sum_{i=1}^{N_\mathrm{c}} \mathcal{R}_{kk}^{(i)}(\tau) \\ &= \frac{1}{N_\mathrm{c}} \sum_{i=1}^{N_\mathrm{c}} \frac{1}{\Delta t_\mathrm{m}} \int_{-\Delta t_\mathrm{m}/2}^{+\Delta t_\mathrm{m}/2} dt\, s_k^{(i)}(t+\tau)\, s_k^{(i)}(t)\,, \end{aligned} \tag{4.80a}$$

$$\begin{aligned} R_{kk}[\ell] &\approx \frac{1}{N_\mathrm{c}} \sum_{i=1}^{N_\mathrm{c}} \mathcal{R}_{kk}^{(i)}[\ell] \\ &= \frac{1}{N_\mathrm{c}} \sum_{i=1}^{N_\mathrm{c}} \frac{1}{N_\mathrm{s}} \sum_{j=1}^{N_\mathrm{s}} s_k^{(i)}[\,j+\ell\,]\, s_k^{(i)}[\,j\,]\,. \end{aligned} \tag{4.80b}$$

Differently from Eqs. (4.79a) and (4.79b), the estimations for the auto-correlation function of signal s_k given by Eqs. (4.80a) and (4.80b) are among the most accurate estimations available. It is worth reminding that, in this case, the level of accuracy, i.e., the variance of the estimation, depends almost entirely on the number of cycles N_c. The number of samples N_s only contributes to improving the quality of the

central part of the auto-correlation function. Once again, we remind the reader to Ref. [301] for a more elaborate analysis.

The estimation of Eq. (4.80b) is the one employed in our experiments. Hereafter, in order to avoid too many indexes in the equations and cumbersome definitions, we will refer to an auto-correlation function or its estimation as the same entity. For simplicity, we also prefer to discuss the case of continuous signals instead of the more realistic case of discrete signals. In addition, since signal s_k has units V/Hz,[21] we will scale the auto-correlation function by the bandwidth BW_k and normalize it by the load impedance Z_0 in order to obtain units W, $R_{kk}(\tau) \equiv \mathrm{BW}_k \langle s_k^*(t+\tau)\, s_k(t)\rangle / Z_0$.

Figure 4.4 shows the auto-correlation function $R_{11}(\tau)$ of signal s_1, when a Wilkinson power divider is used as the microwave beam splitter. The data refer to an experiment performed at a stable temperature $T \simeq 30\,\mathrm{mK}$. Similar results are obtained for signal s_2 (data not shown). We stress one more time that, in the experiments, we measure an approximation of $R_{kk}(\tau)$ or $R_{kk}[\ell]$ [cf. Eqs. (4.80a) and (4.80b), respectively].

Since signal s_k is the sum of the noise contributions due to the single effective noise source described by Eq. (4.51), the cryogenic circulators, and the cryogenic amplifier of one of the two channels of the detection chain, the auto-correlation function is given by [301]

$$R_{kk}(\tau) = \frac{\mathrm{BW}_k}{Z_0}[\varepsilon_k\, \delta(\tau) + \mu_k^2]\,, \tag{4.81}$$

where $\delta(\tau)$ represents a dimensionless delta Dirac centered in the origin of the time axis and the quantity ε_k has units V^2/Hz.[22] In general, all weakly stationary signals characterized by an auto-correlation function similar to that of Eq. (4.81) are defined as *white signals*. Equation (4.81) is an idealized function valid in principle only for signals with an infinite bandwidth BW_k. It is easy to show that the power associated with such signals, i.e., the integral of the signal spectral density, is infinity [301]! This result, due to the infinite bandwidth, does not carry any physical meaning.

In reality, however, the measurement bandwidth is always limited. For example, in our experiments the *nominal measurement bandwidth* BW_k is set by Eq. (4.64). In this case, the signal is said to be white over the finite bandwidth BW_k and the auto-correlation function of Eq. (4.81) becomes [301]

$$R_{kk}(\tau) = \frac{\mathrm{BW}_k}{Z_0}\left(\varepsilon_k \frac{\sin \pi \mathrm{BW}_k\, \tau}{\pi \mathrm{BW}_k\, \tau} + \mu_k^2\right). \tag{4.82}$$

This function is a translated cardinal sine[23] with argument $\mathrm{BW}_k\, \tau$. The inset of Fig. 4.4 clearly shows an experimental curve resembling a cardinal sine. In order to give a more quantitative analysis of the experimental data, we use the simple model of Eq. (4.82) to fit the curve in the inset of Fig. 4.4. Figures 4.5(a) and 4.5(b) show such a fitting for signals s_1 and s_2, where ε_k and BW_k $(k = 1, 2)$ are used as free fitting parameters. It is worth fitting both signals in order to extract the

[21] This comes from our self-consistent definition of the quantum voltage $\hat{V}_{\mathrm{RL}k}$ and we keep it also for the measured signal s_k given that in all the formalism developed so far we have always assumed $\hat{V}_{\mathrm{RL}k} \to s_k$. In reality, the signals recorded by the acquisition card have units V.

[22] We already know from Subsec. 4.2.2 that $\mu_k = 0$. We continue keeping it in all auto-correlation functions for consistency.

[23] We recall that a cardinal sine (sinc) is defined as $(\sin \pi x)/\pi x$.

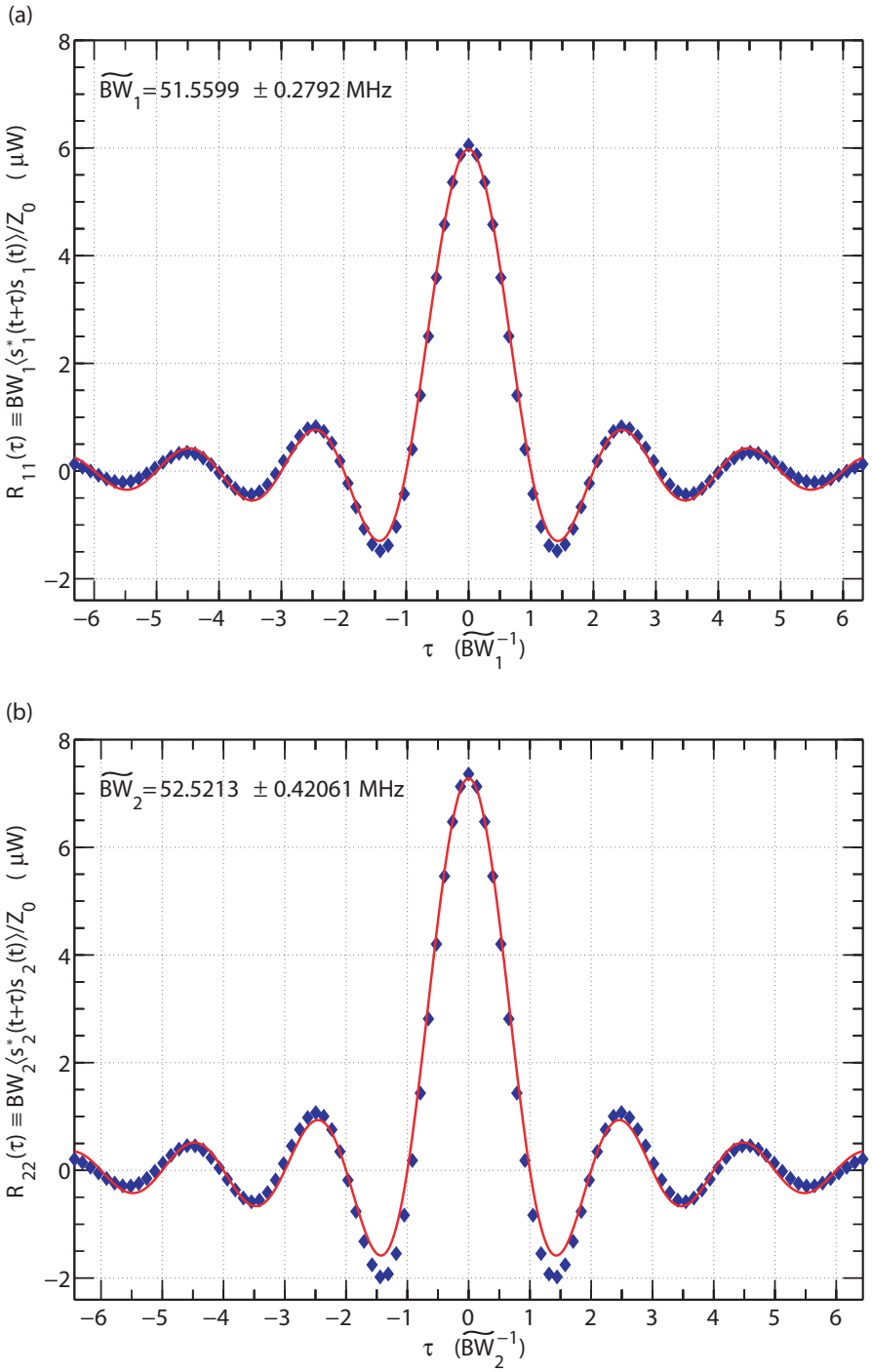

Figure 4.5: Auto-correlation functions $R_{kk}(\tau)$ for channels 1 and 2. The measurements refer to the same state as in Fig. 4.4. **(a)** Full blue diamonds: experimental data. Red line: fit obtained from the model of Eq. (4.82) with ε_1 and BW_1 as free fitting parameters. **(b)** As in **(a)** for channel 2.

experimental measurement bandwidth $\widetilde{\mathrm{BW}}_k$ for both channels of the detection chain. As indicated in the figures, we find $\widetilde{\mathrm{BW}}_1 \simeq 51.56\,\mathrm{MHz}$ and $\widetilde{\mathrm{BW}}_2 \simeq 52.52\,\mathrm{MHz}$. The fitting is practically perfect for both channels and reveals that the cardinal sine (auto-correlation function) intercepts the x-axis, which, in the figures, is given in units of inverse experimental bandwidth, at exact integer multiples of $\widetilde{\mathrm{BW}}_k^{-1}$. Notably, the experimental bandwidth is approximately twice as large as the nominal bandwidth of the filter/DC block combination at the output port of each mixer, $\widetilde{\mathrm{BW}}_k \simeq 52\,\mathrm{MHz} \simeq 2\mathrm{BW}_{\mathrm{IF}k}$, where $\mathrm{BW}_{\mathrm{IF}k} = 7\,\mathrm{kHz} - 24.5\,\mathrm{MHz}$ (cf. Fig. 3.10). This effect is due to DSB mixing.

Remarkably, in our definitions of white signals we did not make any assumption on the probability density of the random signals themselves. In the case of signal s_k, all information about the signal probability density (or distribution) is encoded in the density operators of the states associated with the quantum voltage $\hat{V}_{\mathrm{RL}k}$, as explained in Subsec. 4.2.2.

4.3.2 Auto-Covariance Function and Variance

The auto-correlation function presented in the previous section can opportunely be skewed in order to obtain the so-called auto-covariance function for a random signal. The various definitions of auto-covariance follow directly from the corresponding definitions of auto-correlation:

1. Given a continuous random signal $x(t)$, we define the auto-covariance function $C_{xx}(t_1, t_2)$ as

$$\begin{aligned} C_{xx}(t_1, t_2) &\equiv \langle [x(t_1) - \mu_x(t_1)]^* \, [x(t_2) - \mu_x(t_2)] \rangle \\ &= R_{xx}(t_1, t_2) - \mu_x(t_1)\, \mu_x(t_2)\,, \end{aligned} \tag{4.83}$$

   where $\mu_x(t)$ is the mean value of the signal $x(t)$ at time t;

2. If the signal x is weakly stationary, the auto-covariance function depends only on the time lag τ and, thus, reduces to

$$C_{xx}(\tau) \equiv R_{xx}(\tau) - \mu_x^2\,. \tag{4.84}$$

A fundamental property of the auto-covariance function given by Eq. (4.83) is obtained when $t_1 = t_2 = t$. In this case, the auto-covariance reduces to the time-dependent variance of the random signal,

$$\begin{aligned} C_{xx}(t, t) &= \langle [x(t) - \mu_x(t)]^* \, [x(t) - \mu_x(t)] \rangle \\ &= \langle x^2(t) \rangle - \mu_x^2(t) = \tilde{\sigma}_x^2(t)\,. \end{aligned} \tag{4.85}$$

In the case of weakly stationary signals, the variance is obtained setting the delay time $\tau = 0$ and is just a number,

$$C_{xx}(\tau = 0) \equiv R_{xx}(\tau = 0) - \mu_x^2 = \tilde{\sigma}_x^2\,. \tag{4.86}$$

In the special case of signal s_k, which is white over a bandwidth BW_k, the auto-covariance is given by the cardinal sine function

$$C_{kk}(\tau) = \frac{\mathrm{BW}_k}{Z_0} \varepsilon_k \frac{\sin \pi \mathrm{BW}_k\, \tau}{\pi \mathrm{BW}_k\, \tau}\,. \tag{4.87}$$

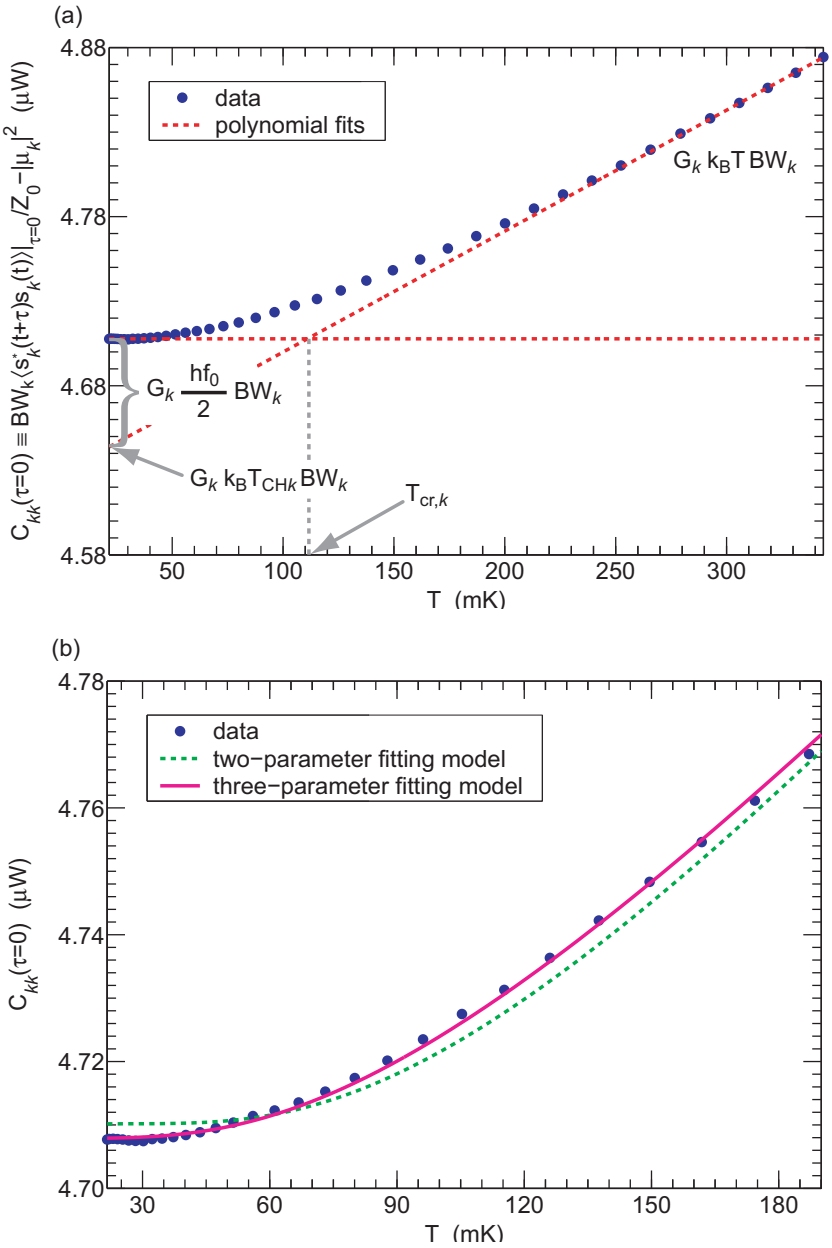

Figure 4.6: Planck distribution for a thermal/vacuum state at $\omega_{\mathrm{LO}} = 2\pi \times 5.3\,\mathrm{GHz}$ centered around a measurement bandwidth $\mathrm{BW}_k = 52\,\mathrm{MHz}$. **(a)** Full blue circles: experimental data estimating the temperature dependence of the quantum-mechanical variance of Eq. (4.90), $C_{kk}(\tau = 0) = \tilde{\sigma}_k^2(T)$. Dashed red lines: curves obtained using the polynomial fitting model from which $f_0 = \omega_0/2\pi$ and, equivalently, $T_{\mathrm{cr},k}$ are estimated. **(b)** Full blue circles: same experimental data as in **(a)**. Dashed light green (light grey) line: fitted curve obtained from the two-parameter fitting model [cf. Eq. (4.90)]. Magenta (middle grey) line: fitted curve obtained from the three-parameter fitting model [cf. Eq. (4.98)]. The magenta line fits the data almost perfectly.

At delay time $\tau = 0$ the cardinal sine is unity and Eq. (4.87) becomes equivalent to the variance of signal s_k,

$$\tilde{\sigma}_k^2 = \frac{\mathrm{BW}_k}{Z_0}\varepsilon_k \,. \tag{4.88}$$

The result of Eq. (4.88) must be the same as that of Eq. (4.65). Hence, mapping back Eq. (4.88) into Eq. (4.65), we readily find that $\varepsilon_k = \sigma_k^2$. On one hand, Eq. (4.88) accounts for the general statistical properties of one realization s_k of the quantum voltage $\hat{V}_{\mathrm{RL}k}$, i.e., it accounts for the fact that the signal is white over a finite bandwidth BW_k. On the other hand, Eq. (4.65) accounts for the detailed statistical properties of the quantum states associated with the quantum voltage $\hat{V}_{\mathrm{RL}k}$, i.e., it accounts for the probability density (or distribution) of such states.

Since for signal s_k the mean value $\mu_k = 0$ (cf. Subsec. 4.2.2), the auto-correlation function given by Eq. (4.82) is equivalent to the auto-covariance function of Eq. (4.87),

$$R_{kk}(\tau) = C_{kk}(\tau) \,. \tag{4.89}$$

This result, in conjunction with the possibility of mapping Eq. (4.88) into Eq. (4.65) and vice versa, embodies the soul of our experiments. That is, if we are able to obtain an accurate estimation for the auto-correlation function of signal s_k by means of Eq. (4.80a) [or Eq. (4.80b)], then setting the delay time $\tau = 0$ (or $\ell = 0$) allows us to measure the quantum-mechanical variance for the quantum voltage $\hat{V}_{\mathrm{RL}k}$ with respect to the various quantum states of the two channels of the detection chain.

Figure 4.6(a) shows the measurement, i.e., a quantum-parameter estimation, of the quantum-mechanical variance given by Eq. (4.65) as a function of temperature T. As for the case of the auto-correlation data of Fig. 4.4, also in this case a Wilkinson power divider is employed as microwave beam splitter. The experimental results of Fig. 4.6(a) are obtained first estimating the auto-correlation function of signal s_k by means of Eq. (4.80b) for many different values of the temperature and, then, extracting the data points associated with delay time $\ell = 0$. In other words, we first measure a set of cardinal sine functions as in Fig. 4.4 for an increasing monotonous set of temperatures and, then, plot only the points corresponding to the peak of each cardinal sine. The final curve evidently reminds of a Plank distribution with a large vertical offset. The origins of such an offset will soon be explained.

A first inspection of the data of Fig. 4.6(a) shows that at high temperatures the variance is characterized by a linear dependence with T, while at low temperatures it becomes flat. The polynomial (linear) fit indicated by the dashed red lines in the figure help visualizing such a behavior. What is the origin of the plateau at low temperatures? In the answer to this question lies the quantum-mechanics of our problem. In order to gain insight into the physics underlying our data, we recall the theoretical model for the variance of the quantum voltage $\hat{V}_{\mathrm{RL}k}$ found in Subsec. 4.2.2, Eq. (4.65):

$$\tilde{\sigma}_k^2(T) \approx G_k \,\mathrm{BW}_k \left[\frac{\hbar\omega_0}{2}\coth\frac{\hbar\omega_0}{2k_{\mathrm{B}}T} + k_{\mathrm{B}}T_{\mathrm{CH}k}\right] . \tag{4.90}$$

The expression for the variance in Eq. (4.90) differs from that in Eq. (4.65) because the noise associated with the circulators has been neglected for simplicity.[24] We

[24]This is also the reason for the "≈" sign instead of the "=" sign in Eq. (4.90).

remind the reader to Appendix A for more details on the treatment of the circulators noise in the analysis of the experimental data.

The asymptotic response of Eq. (4.90) in the *high temperature limit* is given by

$$\lim_{T\to+\infty} \tilde{\sigma}_k^2(T) \approx G_k \,\mathrm{BW}_k \, k_\mathrm{B}(T + T_{\mathrm{CH}k}) \,. \tag{4.91}$$

In this limit, the variance $\tilde{\sigma}_k^2$ is the sum of two contributions: The variance of the thermal state associated with the single effective noise source at the output of the power divider [cf. Eqs. (4.51) and (4.52)], which is a linear function of T, and the variance of the noise due to one of the cryogenic amplifiers, which is a constant offset. On one hand, the slope of Eq. (4.91) is proportional to the power gain G_k and bandwidth BW_k. The latter is set by the narrowest filter in the detection chain and, as shown in Subsec. 4.3.1, can be extracted from the fit based on the model of Eq. (4.82). On the other hand, the y-intercept of Eq. (4.91) is proportional to the amplifier noise temperature $T_{\mathrm{CH}k}$. Thus, the simple first-order polynomial fit indicated by the oblique dashed red line in Fig. 4.6(a) allows us to estimate both power gain and amplifier noise temperature.

The asymptotic response of Eq. (4.90) in the *low temperature limit* is given by

$$\lim_{T\to 0^+} \tilde{\sigma}_k^2(T) \approx G_k \,\mathrm{BW}_k \left(\frac{\hbar\omega_0}{2} + k_\mathrm{B} T_{\mathrm{CH}k} \right) . \tag{4.92}$$

In this limit, the variance $\tilde{\sigma}_k^2$ is also the sum of two contributions: The variance of the vacuum state associated with the noise source at the power divider output and, again, the variance of the noise due to one of the cryogenic amplifiers. Notably, both these contributions are constant offsets. This fact has a very important consequence. It shows that the vacuum and amplifier contribution to the total variance are *degenerate*, in the sense that the sum of two offsets is still an offset. This means that the auto-correlation experiments discussed here are insensitive to the fundamental offset which is due to the vacuum fluctuations and which is a direct consequence of the commutation relations for bosonic signal operators. In summary, we are not allowed to perform a *direct* measurement of the variance of the vacuum fluctuations, at least with phase-preserving amplifiers.

Nevertheless, the intercept point between Eqs. (4.91) and (4.92) on the horizontal axis,

$$T_{\mathrm{cr},k} = \frac{\hbar\omega_0}{2k_\mathrm{B}} \,, \tag{4.93}$$

which is referred to as cross-over temperature, is also related to the energy of the vacuum fluctuations of the noise at the power divider output. Below the cross-over temperature, the system can safely be assumed to be in the vacuum state. We notice that the cross-over temperature encodes exactly the same amount of information as the difference between the y-intercepts of Eqs. (4.91) and (4.92) [cf. Fig. 4.6(a)]. Assuming no knowledge on the angular frequency ω_0, we might be tempted to use the zero- and first-order polynomial fits indicated by the horizontal and oblique dashed red lines in Fig. 4.6(a), respectively, in order to estimate the experimental cross-over temperature and, thus, the variance associated with the vacuum fluctuations. Such an estimate would represent an *indirect* measurement of the variance of the vacuum fluctuations. It is worth recalling here that the Planck spectrum of Eq. (4.8) can be derived via Einstein's A and B coefficients without knowing the bosonic

commutation relations (cf. Sec. 4.1). Since one half of the spontaneous emission coefficient is due to the vacuum fluctuations, the Planck distribution embodies the vacuum regardless of any vertical offset (cf. Sec. 4.1). The presence of the vacuum manifests itself in the plateau of the Planck distribution: Observing such a plateau constitutes an indirect measurement of the vacuum fluctuations.

The fundamental relation of Eq. (3.93), which stands at the basis of our model, reminds us that we indeed posses a full knowledge of ω_0, being this the angular frequency of the LO signal. As a consequence, if from the polynomial fits of Fig. 4.6(a) we obtain an estimate for ω_0 which is not equal to the LO angular frequency, the result does not contain any physical meaning. Under more realistic assumptions, the fitted ω_0 should be equal to $\omega_{\rm LO}$ within the measurement bandwidth BW_k. In this case, if the fitted ω_0 differs from $\omega_{\rm LO}$ for more than the measurement bandwidth, then, again, the result does not have any physical meaning.

The experimental data[25] of Fig. 4.6(a) refer to a LO angular frequency $\omega_{\rm LO} = 2\pi \times 5.3\,\mathrm{GHz}$. Assuming a measurement bandwidth $\mathrm{BW}_k = 52\,\mathrm{MHz}$,[26] the polynomial fit indicated by the dashed red lines give a gain $G_k \simeq 89.64\,\mathrm{dB}$ and a noise temperature $T_{\mathrm{CH}k} \simeq 7.03\,\mathrm{K}$. In this case, the fitted cross-over temperature is $T_{\mathrm{cr},k} \simeq 108.9\,\mathrm{mK}$, which corresponds to an angular frequency $\omega_0 \simeq 2\pi \times 2.27\,\mathrm{GHz}$. The angular frequency ω_0 obtained from the fit differs from $\omega_{\rm LO}$ by more than $2\pi \times 3\,\mathrm{GHz}$, which is larger than the measurement bandwidth by orders of magnitude! Similar results are reproducible throughout all our experiments.

What is the reason for such a conceptual catastrophe? The most plausible answer is that it is incorrect attempting to fit the angular frequency ω_0, which, within the (narrow) measurement bandwidth, must be equal to $\omega_{\rm LO}$. But if we assume perfect knowledge of ω_0, we also assume perfect knowledge of the variance of the vacuum fluctuations. If this were the whole truth, given our data we would not be allowed to tell anything about the variance of the vacuum fluctuations, the knowledge of which is assumed *a priori* among the hypothesis of our model [cf. Eq. (3.93)]. However, from the derivation of Eq. (4.8) via Einstein's A and B coefficients (cf. Sec. 4.1), we know that the Planck spectrum embodies the vacuum fluctuations.[27] The presence of the vacuum fluctuations manifests itself in the plateau observed in the experiments. We thus reach a dilemma: Either we accept the fact that only a qualitative observation of the vacuum fluctuations via the measurement of the plateau of the Planck distribution is conceivable or we try to follow a different path in order to extract quantitative information about the vacuum. The latter is the option to be pursued in the following.

One possibility to restore physical meaning to our results and carry out a quantitative analysis of the data is to further develop the theoretical model at the basis of our experiments. As already discussed in chapter 3, Subsec. 3.1.1, the measured temperature T does not reflect the effective temperature of the resistive termination utilized as a noise source. In fact, such an effective temperature is more correctly

[25]These data refer to channel 1, i.e., $k = 1$. For the sake of generality, we keep on using the generic index k.

[26]This bandwidth is slightly different from the experimental measurement bandwidth of each of the two detection channels (cf. last part of Subsec. 4.3.1). However, this does not affect the present discussion and, assuming a single approximated value, it helps here maintaining the discussion more general.

[27]Regardless of any vertical offset.

given by Eq. (3.8),

$$\widetilde{T} = T - \eta(T - T^{\min}) \,,$$

from which it is possible to obtain the mean temperature difference between clamp and resistor given by Eq. (3.9),

$$\overline{\Delta T} = -\frac{\eta}{2}(T^{\max} - T^{\min}) \,.$$

Substituting T with the effective temperature $\widetilde{T}$, $T \to \widetilde{T}$, we can rewrite the asymptotic behavior of Eq. (4.90) in the high temperature limit as

$$\lim_{\widetilde{T}\to+\infty} \tilde{\sigma}_k^2(\widetilde{T}) \approx G_k \, \mathrm{BW}_k \, k_{\mathrm{B}}(\widetilde{T} + T_{\mathrm{CH}k}) \,. \tag{4.94}$$

The intercept between Eq. (4.94) and the $\widetilde{T}$-independent Eq. (4.92) is now found to be

$$\widetilde{T}_{\mathrm{cr},k} = \frac{\hbar\omega_0}{2k_{\mathrm{B}}} = T_{\mathrm{cr},k} - \eta(T_{\mathrm{cr},k} - T^{\min}) \,, \tag{4.95}$$

or, equivalently,

$$T_{\mathrm{cr},k} = \frac{1}{1-\eta}\frac{\hbar\omega_0}{2k_{\mathrm{B}}} - \frac{\eta}{1-\eta}T^{\min} \,. \tag{4.96}$$

According to Eq. (4.96), the parameter η quantifies the deviation (i.e., the *distance*) between the *measured cross-over temperature* $T_{\mathrm{cr},k}$ and the *theoretical cross-over temperature* $\widetilde{T}_{\mathrm{cr},k}$. Obtaining the more physical quantity $\overline{\Delta T}$ from Eq. (3.9) and assuming $0 \leqslant |\overline{\Delta T}| < \widetilde{T}_{\mathrm{cr},k}$, which is typically the case in our experiments, it allows us to define the measurement fidelity of the variance of the quantum fluctuations as

$$\mathcal{F} \equiv 1 - \frac{|\overline{\Delta T}|}{\widetilde{T}_{\mathrm{cr},k}} \,. \tag{4.97}$$

In this sense, the quantity $|\overline{\Delta T}|$ tells us how close we can observe the vacuum in the experiments. Together with the power gain G_k and noise temperature $T_{\mathrm{CH}k}$, η, from which the mean temperature difference $\overline{\Delta T}$ can be estimated, constitutes a free fitting parameter of the model. As explained in chapter 3, Subsec. 3.1.1, we would expect, in general, $\overline{\Delta T}$ to be a negative quantity. As we will show next, this is almost always true in our experiments, with the exception of a few cases, where $\overline{\Delta T} < 0$. This could be due to unknown systematic errors in the experiment and, thus, further experiments would be needed to shed light on such an issue. Such negative values impose us to use of the absolute value of $\overline{\Delta T}$ when defining the fidelity of Eq. (4.97).

We now have in hand an advanced theoretical model based on *three fitting parameters* that allows us to gain quantitative information on the measurement of the vacuum fluctuations. This model may be applied to the polynomial fits shown in Fig. 4.6(a) and the distance in temperature from the vacuum fluctuations may be estimated. However, there is an important issue related to this type of fit, i.e., that the number of experimental data points used to obtain the fitted curves is totally arbitrary. We can choose to use 5 data points or 500 data points in order to get the oblique dashed red line of Fig. 4.6(a), resulting in two different sets of values for the fitted parameters. This leads to an unacceptable level of ambiguity in the

interpretation of the experiments, which suggests that a simple polynomial fit is unsuitable for a proper quantitative analysis of the data (cf. Appendix B for more details on the ambiguity of the polynomial fit).

Since the combined high/low temperature asymptotic behavior of Eq. (4.90) constitutes an inaccurate fitting procedure, we can go one step back and utilize Eq. (4.90), rather than its asymptotic functions, as fitting model. Figure 4.6(b) shows the same experimental data of Fig. 4.6(a) with two overlaid fitted curves. The dashed light green (light grey) line is obtained using Eq. (4.90) as fitting model with the power gain G_k and noise temperature $T_{\mathrm{CH}k}$ as the only free fitting parameters (*two-parameter fitting model*). The resulting curve approaches the data, but the fitting is far from being perfect. We notice, in fact, a pronounced gap between data and fitted curve: The basic model of Eq. (4.90) is not confirmed by the experiments. On the contrary, the magenta (middle grey) line fits the experimental data almost perfectly. Such a curve is obtained applying our effective temperature model to Eq. (4.90) and using

$$\tilde{\sigma}_k^2(T) \approx G_k \,\mathrm{BW}_k \left\{ \frac{\hbar\omega_0}{2} \coth \frac{\hbar\omega_0}{2k_{\mathrm{B}}[T - \eta(T - T^{\min})]} + k_{\mathrm{B}} T_{\mathrm{CH}k} \right\} \tag{4.98}$$

as fitting function, with G_k, $T_{\mathrm{CH}k}$, and η as free fitting parameters (*three-parameter fitting model*). In this case, from the fitting we find $G_k \simeq 89.62 \pm 0.05\,\mathrm{dB}$, $T_{\mathrm{CH}k} \simeq 7.04 \pm 0.08\,\mathrm{K}$,[28] and $\eta \simeq -0.0081 \pm 0.0130$. Since $T^{\max} \simeq 360.28\,\mathrm{mK}$ and $T^{\min} \simeq 21.70\,\mathrm{mK}$, we obtain $\overline{\Delta T} \simeq 1.37 \pm 2.20\,\mathrm{mK}$. The latter corresponds to a fidelity in the measurement of the variance of the vacuum fluctuations, $\mathcal{F} \simeq 98.92 + 0.42 - 1.73\,\%$. It is remarkable that even for such a high fidelity, i.e., small $|\overline{\Delta T}|$, the difference between the two- and three-parameter fits is so dramatic [cf. Fig. 4.6(b)]. If $|\overline{\Delta T}| \simeq 0$, the dashed light green and magenta lines would overlap and fit almost perfectly the data. As a consequence, we would posses an almost perfect knowledge of the variance of the vacuum fluctuations. Only in that case the basic model of Eq. (4.90) would be confirmed by the data. To summarize, the crucial result of our three-parameter fitting model is that we are able to perform an indirect measurement of the distance from the theoretical (ideal) variance of the vacuum fluctuations at microwave frequencies with an experimental fidelity very close to 99 %. Our experimental findings together with the theoretical interpretation and modeling constitute an unprecedented result, which helps understanding the basis of the quantization of microwave signals. This is an important step for the further development of the research field of circuit QED.

Planck Spectroscopy

In order to consolidate the validity of our three-parameter fitting model and gain further insight into the fundamental concept of vacuum fluctuations, we can now try to extend the experimental parameter space at hand by adding an extra dimension. While sweeping the temperature of the noise source (resistive termination), we can simultaneously vary the LO angular frequency ω_{LO} over a large range. Figures 4.7(a) and 4.7(c) show the results of a set of experiments where the variance associated with

[28] Notably, these results are very similar to those obtained from the simple polynomial fitting. In fact, within the given confidence bounds, power gain and noise temperature are practically insensitive to different fitting models.

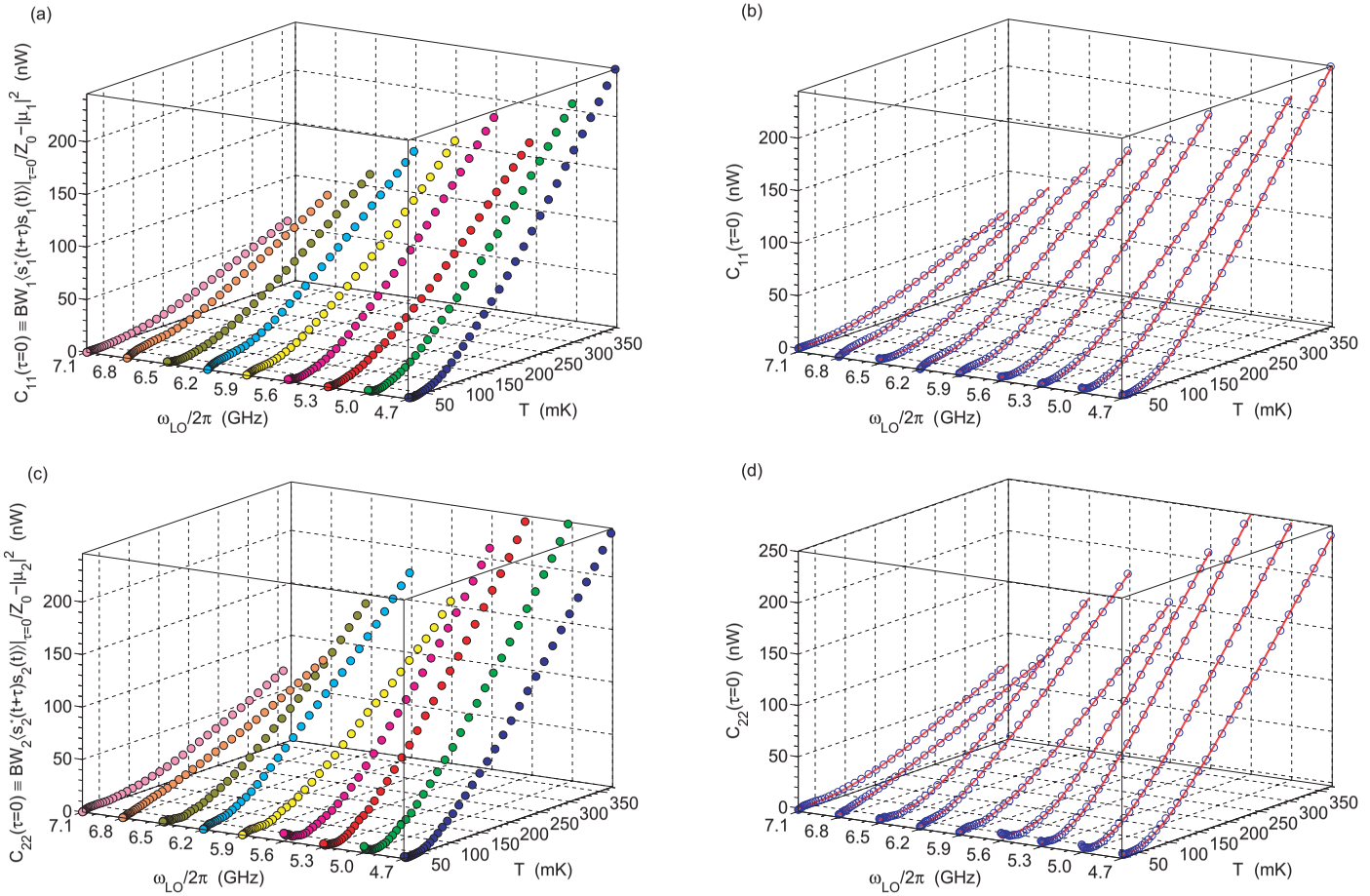

Figure 4.7: Planck spectroscopy: raw data and fitting. **(a)** Experimental data associated with 9 Planck distributions measured at 9 different $\omega_{\rm LO}$ for channel 1. Each face color for a set of full circles represents a different angular frequency. **(b)** Open dark blue circles: same experimental data as in **(a)**. Red lines: fitted curves obtained from the three-parameter fitting model [cf. Eq. (4.98)]. **(c)** As in **(a)** for channel 2. **(d)** as in **(b)** for channel 2. The experimental data are the result of a moving average (cf. main text for details).

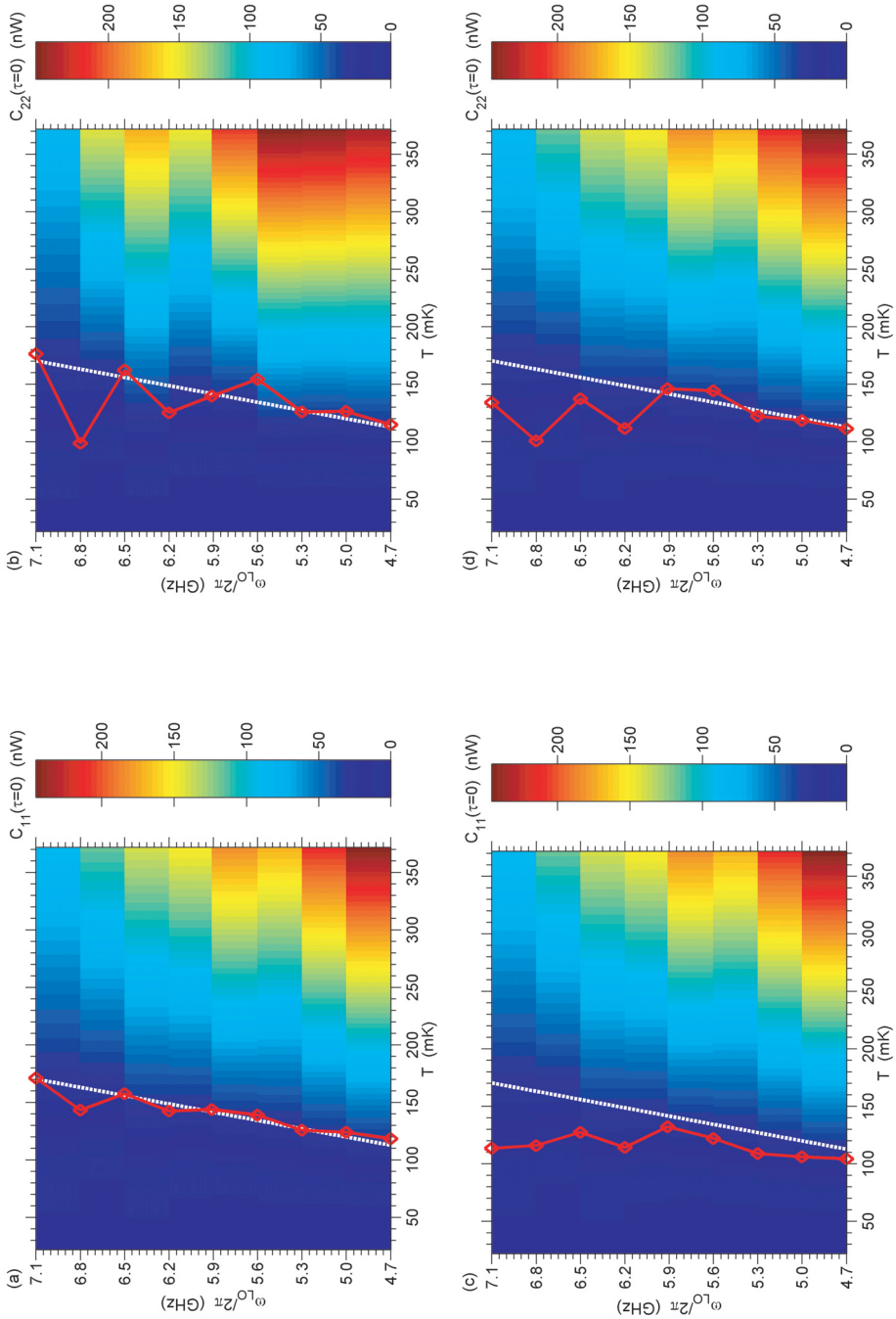

Figure 4.8: Planck spectroscopy: theory vs. fitting. **(a)** 2D color-code plot of the fitted Planck distributions in Fig. 4.7(b). Dashed white line: theoretical cross-over temperature. Open brown-red diamonds connected by a brown-red line: cross-over temperatures obtained from the three-parameter fitting model. **(b)** As in **(a)** for channel 2. **(c)** As in **(a)** with the open brown-red diamonds connected by a brown-red line now representing the cross-over temperatures obtained from the polynomial fitting model. **(d)** As in **(c)** for channel 2.

thermal/vacuum states for both channels of the detection chain is measured at 9 different values of the LO angular frequency, from $\omega_{\rm LO}^{(1)}/2\pi = 4.7\,{\rm GHz}$ to $\omega_{\rm LO}^{(9)}/2\pi = 7.1\,{\rm GHz}$ with a spacing (frequency resolution) $f_{\rm r} = 300\,{\rm MHz}$ (in general, $\omega_{\rm LO}^{(h)} = \omega_{\rm LO}^{(h)} + 2\pi(h-1)f_{\rm r}$ with $h = 1, 2, ..., 9$). In the figures, each face color associated with a set of full circles represents a different LO frequency. For each LO frequency, the temperature-dependent Planck distribution is obtained via a so-called downsweep measurement.

A downsweep is realized by first heating the noise source (resistive termination) to 800 mK and let it stabilize at this temperature for 30 min. At the end of the stabilization time, the resistive termination is let cool to the cryostat base temperature. Since the cooling power of the cryostat depends on the temperature of the mixing chamber (also heated up during the stabilization time), in the temperature range comprised between 800 and 400 mK the temperature of the resistor drops rapidly due to a high cooling power and the quality of the data is low. For this reason, all data points above approximately 350 mK are not plotted in the figures and are disregarded from the analysis. Below 350 mK, the resistor cools very slowly due to a lower cooling power. As a consequence, the data quality drastically improves because of the possibility to perform more averaging. In fact, we remind that the data plotted in the figures are obtained by means of the estimation given by Eq. (4.80b), the accuracy of which depends on the number of averaged cycles (signal realizations). Since the temperature, even if slowly below 350 mK, is continuously dropping, the estimation of the variance refers to all signal realizations (cycles) contained within the temperature range $T \mp \overline{\delta T}/2$, where $\overline{\delta T}$ is the average temperature drop corresponding to a fixed cooling time $\delta t_{\rm cooling}$.[29] The more cycles are recorded within the average temperature drop $\overline{\delta T}$, the more accurate is the estimation of the signal variance $\langle \tilde{\sigma}_k^2(T) \rangle_T$, where the subscript "$T$" indicates that in a downsweep the variance is the average of the variance of each realization in the temperature range $T \mp \overline{\delta T}/2$. To maintain the notation simple, in all figures and following derivations we will indicate $\langle \tilde{\sigma}_k^2(T) \rangle_T$ simply as $\tilde{\sigma}_k^2(T)$.

To minimize statistical errors, each trace displayed in Figs. 4.7(a) and 4.7(c) is obtained by averaging 4 distinct traces for the same LO frequency,[30] but measured at different times. The fact that the distinct traces are measured at different times results in an inhomogeneity between their corresponding temperatures. In other words, the same range of variance is obtained at different temperatures for any of the 4 distinct traces. Hence, special care must be taken when averaging the 4 distinct traces together. In the case of Figs. 4.7(a) and 4.7(c), the displayed traces are obtained in two steps: First, the moving average for the p-th trace of each one of the 4 distinct traces associated with the h-th LO frequency is computed and, second, the so-obtained new 4 traces are averaged together. In this way, the temperature inhomogeneity between the 4 distinct traces is largely reduced and their global average is much more accurate. More formally, given the trace $\{x_i^{(h)}\}_p$, where $i \in [0, N_i]$ and $N_i \in \mathbb{N}$ is the number of temperature points contained in the trace,[31] the forward moving average (also called sliding or smoothing average with lag) of

[29] Given that the Planck distribution is a continuous monotonic function, we assume $\overline{\delta T}/2 > 0$. Also, $\overline{\delta T}$ must not be confused with the distance from the vacuum, $\overline{\Delta T}$.

[30] Typical value. The number of distinct averaged traces can slightly vary.

[31] It is important to stress that in a downsweep the vector containing the temperature points is ordered from high to low temperatures.

such a trace is the new trace $\{y_j^{(h)}\}_p$, where each element is given by

$$y_j^{(h)} \equiv \frac{1}{N_{\text{lag}}} \sum_{i=j}^{j-(N_{\text{lag}}-1)} x_i^{(h)} \,. \tag{4.99}$$

Here, N_{lag} represents the number of points used when averaging in the forward direction (also called lag) and j is contained in the range $[0, N_j]$, where $N_j \equiv N_i - (N_{\text{lag}} - 1)$. We have chosen to perform a moving average with lag because the temperature drop during a downsweep is highly anisotropic, being the forward direction, from high to low temperatures, the privileged direction. The moving average with lag inevitably results in a slight loss of information. In fact, as shown by Eq. (4.99) the last $(N_{\text{lag}} - 1)$ points must be neglected. In our experiments, these points correspond to very low temperatures. Usually, we let the system cool for enough long time to have a redundancy of points at very low temperatures. As a consequence, the loss of points due to the moving average is not an issue. If we had realized a moving average with lead (i.e., in the backward direction), the loss of points would have happened at high temperatures. Due to the more rapid temperature drop at high temperatures, the number of points in this region is not as dense as at low temperatures and the loss of information would have been a severe problem. Assuming the same number of points N_i (and, thus, N_j) for all traces, each displayed trace is finally obtained as

$$\{y_j^{(h)}\} = \frac{1}{4} \sum_{p=1}^{4} \{y_j^{(h)}\}_p \,. \tag{4.100}$$

The generalization to more that 4 distinct traces is straightforward. In Appendix C, we show a different averaging method, which, instead of being based on a moving average, uses a bin average to obtain the final traces displayed in the plots.

The experimental results of Figs. 4.7(a) and 4.7(c) constitute the paradigmatic example of a new measurement technique which we define as *Planck spectroscopy*. Given a test device, in this case the resistive termination acting as a noise source, by means of Planck spectroscopy we obtain information on the variance of the states associated with such a device. In the case of the thermal and vacuum states generated by a resistor, which are Gaussian states, Planck spectroscopy is equivalent to a complete tomographic measurement of the states. In fact, we recall that the knowledge of the mean value (in this case zero) and variance of any Gaussian state fully characterizes the state (cf. chapter 2, Subsec. 2.1.3). Planck spectroscopy can almost directly be implemented to characterize more complex devices such as on-chip resonators or parametric amplifiers (cf. Sec. 4.4), thus making it an appealing tool in the realm of quantum microwave engineering.

In order to extract quantitative information from the data of Figs. 4.7(a) and 4.7(c), we resort again to our three-parameter fitting model. In Figs. 4.7(b) and 4.7(d), the data points are represented by open dark blue circles. The red lines overlaid to the data are fitted curves obtained from the three-parameter fitting model. The fitting is of high quality for all traces and allows us to extract for each channel k of the detection chain the distance $\overline{\Delta T_k}$ in units K between the fitted and theoretical cross-over temperature as a function of the LO angular frequency ω_{LO}. It is important to stress that, in general, the distance $\overline{\Delta T}$ should be independent

of which channel of the detection chain is considered. In fact, such a temperature difference refers to effective noise sources which are located before the splitter. However, as we will show later, each channel of the detection chain is characterized by a different total power gain and a different noise temperature. Because of this unbalance and considering that the number of averages used for the signals from both channels is equal, the results for $\overline{\Delta T}$ associated with the two channels are slightly different. This is the reason why we here define two temperature differences, $\overline{\Delta T_1}$ and $\overline{\Delta T_2}$ (or, more in general, $\overline{\Delta T_k}$). Figures 4.8(a) and 4.8(b) show the fitted Planck distributions of Figs. 4.7(b) and 4.7(d) in a 2D color-code plot. The theoretical and fitted cross-over temperatures as a function of the LO frequency are overlaid to the curves associated with the 9 Planck distributions for a more clear visualization of the frequency dependence of the vacuum fluctuations. The function corresponding to the theoretical cross-over temperature is represented by a dashed white line and is obtained from Eq. (4.93) imposing $\omega_0 = \omega_{\rm LO}$. The data points associated with the fitted cross-over temperatures are indicated by open brown-red diamonds connected by a brown-red line. These points are obtained from the three-parameter fitting model, i.e., by extracting the fitting parameter η from Eq. (4.98) and, then, computing the corresponding cross-over temperature from Eq. (4.96). The agreement between the theory and the results from the three-parameter fitting model is superb for the entire parameter space.

Figures 4.8(c) and 4.8(d) show the same fitted Planck distributions shown in Figs. 4.8(a) and 4.8(b), with the difference that the fitted cross-over temperatures overlaid to the Planck distributions are now estimated from the simple polynomial fitting model instead of the three-parameter fitting model. As before, the theoretical cross-over temperature is represented by a dashed white line and the fitted cross-over temperatures by open brown-red diamonds connected by a brown-red line. The latter are obtained finding the intercept between the two asymptotic curves in the limits of low and high temperature for the Planck distributions [e.g., cf. the horizontal and oblique dashed red lines in Fig. 4.6(a)] at each LO frequency. In this case, there is a substantial discrepancy between theory and fittings. As already mentioned above, in Appendix B we show that this is not the only major issue related to the polynomial fit, which, thus, is unsuitable for a quantitative analysis of our data.

Yet another possibility to visualize the cross-over between thermal and vacuum states can be obtained by computing the second derivative of the Planck distribution with respect to temperature. This is equivalent to calculate the rate of change with temperature of the specific heat at constant volume C_V associated with a given noise source,

$$\mathcal{C}(T) \equiv \frac{\partial}{\partial T} C_V = \frac{\partial}{\partial T} \left(\frac{\partial}{\partial T} \langle E \rangle \right)_V , \tag{4.101}$$

where the mean energy $\langle E \rangle$ is given by Eq. (4.13). Figures 4.9(a) and 4.9(b) show a color-code plot (top and 3D view) of Eq. (4.101). The parameters used to obtain such plots are extracted from our experiments in order to allow for a better comparison between theory and experimental results. The plots indicate that the second derivative defines a new cross-over temperature between thermal and vacuum states in correspondence of the maximum curvature of the Planck distribution,

$$T_{{\rm cr},k}^{({\rm II})} = \max\{\mathcal{C}(T)\} , \tag{4.102}$$

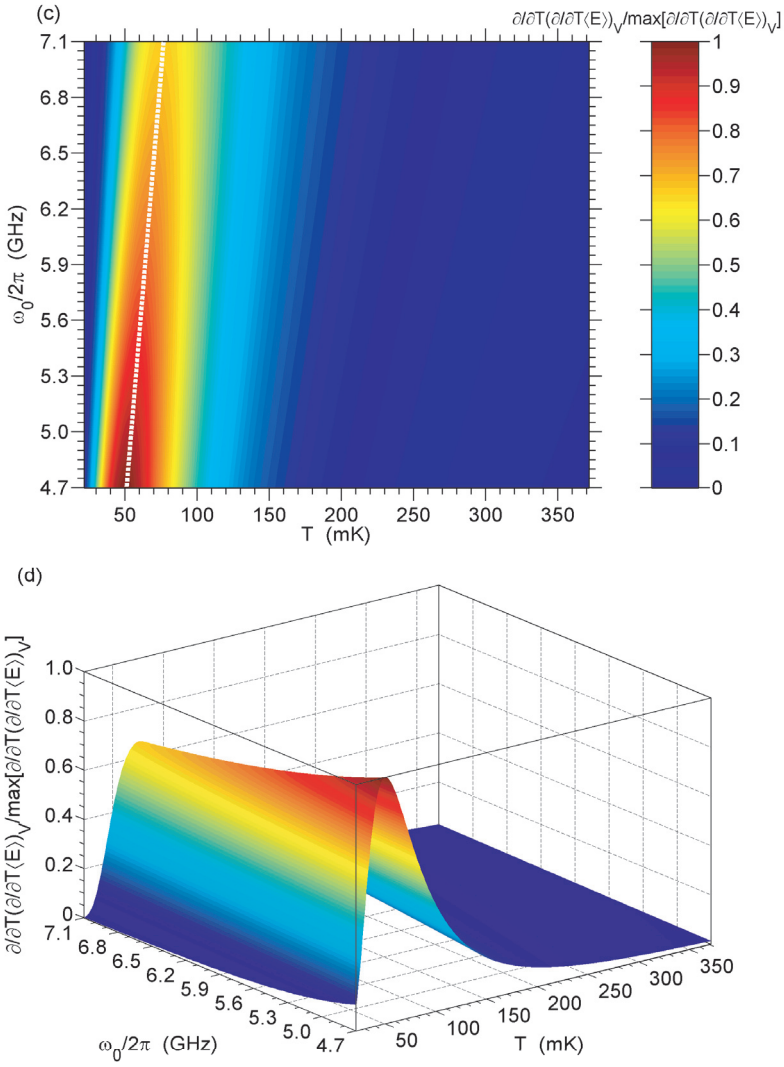

Figure 4.9: Color-code plots of the second derivative of the Planck distribution with respect to temperature as a function of $\omega_{\rm LO} = \omega_0$ [cf. Eqs. (4.101) and (4.13)]. The parameters used to plot the figures are extracted from our experiments. **(a)** Top view of $\partial/\partial T(\partial/\partial T\langle E\rangle)_V$ normalized over $\max[\partial/\partial T(\partial/\partial T\langle E\rangle)_V]$. Dashed white line: Second derivative maximum showing the frequency dependence of the vacuum fluctuations. **(b)** 3D view of the plot in **(a)**.

which is obtained finding the solution to $(\partial/\partial T)\mathcal{C}(T) = 0$. In the figures, the cross-over temperature $T^{(\mathrm{II})}_{\mathrm{cr},k}$ has been calculated numerically[32] and is represented by the dashed white line in Fig. 4.9(a), which corresponds to the sharp ridge shown in the 3D plot of Fig. 4.9(b). The nature of such a cross-over is closely related to the angular frequency ω_0 of the signal being measured, in a similar manner as for the cross-over temperature defined by Eq. (4.93). However, the cross-over condition expressed by Eq. (4.102) is more strict and, according to this definition, the vacuum is now "reached" at lower temperatures. The difference between the theoretical cross-over temperature defined by the plain Planck distribution [Eq. (4.93)] and the one defined by the second derivative of the Planck distribution [Eq. (4.102)] can easily be seen by comparing the dashed white lines in Figs. 4.1(a) and 4.9(a).

In our experiments the noise source is represented by the resistive termination, the volume of which can safely be assumed to be constant. The contraction/expansion due to the cooling/heating cycles between 350 and 20 mK is in fact negligible. In this case, we can apply the definition of Eq. (4.101) to the variance given by Eq. (4.65) and obtain

$$\begin{aligned}\mathcal{C}_k(T) &= \frac{\partial^2}{\partial T^2}\,\tilde{\sigma}_k^2(T) \\ &= G_k\,\mathrm{BW}_k\,\hbar\omega_0 \frac{\partial^2}{\partial T^2}\,\frac{e^{2z}+1}{e^{2z}-1} \\ &= 2G_k \frac{\mathrm{BW}_k\,\hbar\omega_0}{T^2}\,\frac{z}{\sinh^2 z}\,(z\coth z - 1)\,, \end{aligned} \tag{4.103}$$

where $z \equiv \hbar\omega_0/2k_{\mathrm{B}}T$. Unfortunately, computing the second derivative expressed by Eq. (4.103) from the raw data reported in Figs. 4.7(a) and 4.7(c) is a challenging task. In fact, it is an easy exercise in numerical analysis to prove that any small random (statistical) error in the data prevents from obtaining a meaningful second derivative. Interpolation is not helpful either because any interpolating function utilized to *emulate* the data will result in second derivatives other than the searched one.[33] The most suitable functions emulating the raw data are represented by the fitted curves reported in Figs. 4.7(b) and 4.7(d), which are obtained from the three-parameter fitting model. Figures 4.10(a) and 4.10(b) show the second derivative with respect to temperature of such fitted curves. The theoretical cross-over temperature defined by Eq. (4.102) as well as the maxima of the second derivatives of the fitting functions associated with each LO frequency are reported on top of the so-obtained 2D color-code plot. As always, the theory is represented by the dashed white lines, whereas the maxima extrapolated from the data by open dark blue diamonds connected by a dark blue line. Also in this case the agreement between theory and experiment is excellent (due to technical reasons, we always find that the results for channel 1 are better than for channel 2). Figures 4.10(c) and 4.10(d) show a 3D plot of the second derivatives, where the sharp ridge clearly indicates the cross-over region.

A close inspection of Figs. 4.7 and 4.8 indicates that the data suffer from an irregular frequency-dependent structure, which has nothing to do with the intrinsic frequency dependence of the Planck distribution. It is enough to consider the pattern formed by the highest temperature points of each displayed trace for both

[32] The analytical calculations are trivial, but cumbersome and are not reported in this thesis.

[33] The author has tried a large variety of interpolation functions and methods without success.

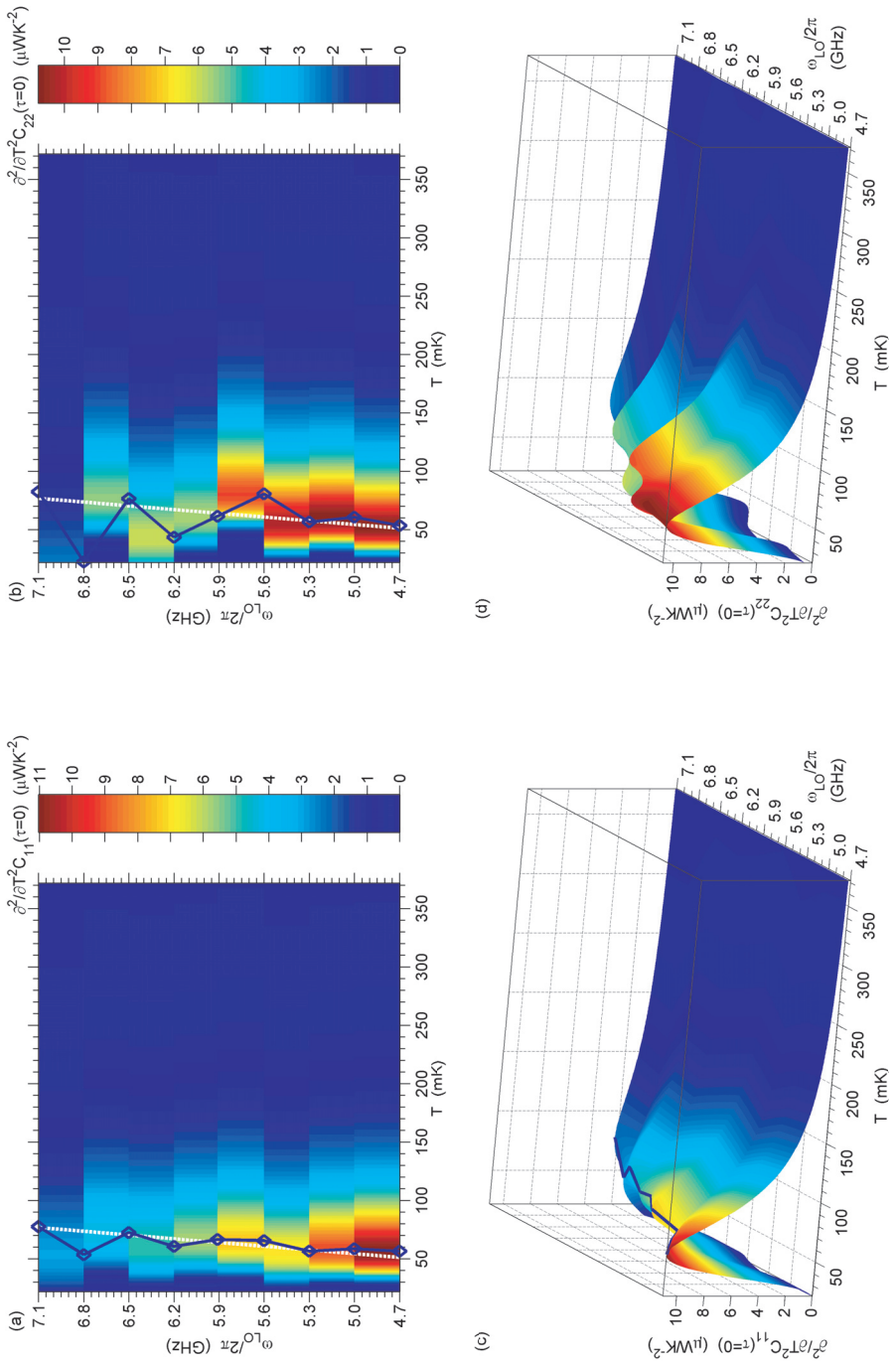

Figure 4.10: Color-code plots of the second derivative of the Planck spectroscopy data with respect to temperature for channels 1 and 2. **(a)** Top view of $\partial^2\tilde{\sigma}_1^2(T)/\partial T^2 = \partial^2 C_{11}(\tau = 0)/\partial T^2$. Dashed white line: theoretical calculation of the second derivative maximum. Open dark blue diamonds connected by dark blue line: maxima of the second derivative extrapolated from the data. **(b)** As in **(a)** for channel 2. **(c)** 3D view of the plot in **(a)**. The dark blue line indicates the ridge corresponding to the second derivative maxima. **(d)** As in **(c)** for channel 2. Due to a lower quality of the data, the ridge is not indicated.

channels to realize the presence of such a structure. This is due to the dependence on the LO angular frequency of the total gain of each channel of the detection chain, $G_k = G_k(\omega_{\rm LO})$. The frequency-dependent gain can accurately be estimated by means of the three-parameter fitting model. The results are shown in Figs. 4.11(a) and 4.11(b). We notice that there is an increasing drop in the gain at higher LO frequencies mostly owing to the RF bandpass filters located before the mixers, which are characterized by a nominal high-frequency cutoff at approximately 6.2 GHz (cf. Fig. 3.10). The insets of Figs. 4.11(a) and 4.11(b) show the total gain as a function of frequency estimated by means of the simple polynomial fitting model. The results are very similar to those obtained from the three-parameter model, showing that the gain is insensitive to the specific fitting procedure.

Each trace in Figs. 4.7 and 4.8 has opportunely been shifted in the y-direction by an offset power equivalent to the noise temperature of the cryogenic amplifiers at the specific LO frequency of that trace. This allows for a better and more direct comparison between the different displayed traces.[34] This manipulation of the data is legitimate, but we must always bear it in mind. In fact, as for the case of the total gain, also the noise temperature of the cryogenic amplifiers is characterized by a pronounced angular frequency dependence, $T_{{\rm CH}k} = T_{{\rm CH}k}(\omega_{\rm LO})$. Such a dependence is clearly shown in Figs. 4.11(c) and 4.11(d), where the noise temperatures estimated from the three-parameter fitting model are reported for all LO frequencies (full dark blue squares). Figure 4.11(c) refers to the cryogenic amplifier of channel 1 and Figure 4.11(d) to the cryogenic amplifier of channel 2. The insets of Figs. 4.11(c) and 4.11(d) show the noise temperatures estimated by means of the simple polynomial fitting model (full light green squares). As for the total gain, also the noise temperature is practically insensitive to the employed fitting procedure. The results of Figs. 4.11(c) and 4.11(d) are very important because they reveal that the noise generated by the cryogenic amplifiers is not white noise.[35]

To summarize the main findings of Planck spectroscopy, in Figs. 4.12(a) and 4.12(b) we give an overview of the cross-over temperatures estimated from the three-parameter fitting model for channels 1 and 2, respectively. In these figures, the dark blue diamonds represent the measured cross-over temperatures as a function of the LO frequency. The solid red lines are obtained by means of a linear fit to the data, while the dashed red lines represent the theory. As it appears, the experimental results for channel 1 are of higher quality than for channel 2, revealing an unbalance between the two channels. Such an unbalance probably owns its origin to the misbehavior or not optimal biasing of one of the active devices, e.g., an amplifier or mixer.[36] In addition, we notice that the slope of the curves obtained from the linear fits (solid red lines) is shallower than the slope of the theoretical curves (dashed red lines) and that theory and curves obtained from the linear fits intercept each other in the frequency range comprised between 5.3 and 5.9 GHz. This indicates that at low frequencies we overestimate the cross-over temperature, whereas we underestimate it at high frequencies. A possible frequency dependence of the distance $\overline{\Delta T_k}$ between

[34] Indeed, the displayed traces could have also been normalized over the frequency-dependent gain. However, there is no large improvement in the appearance of the data to justify such a normalization.

[35] This fact does not particularly surprise the author, but it seems to impress a number of theorists working on circuit QED due to the potential extension of these results to so-called *process tomography* [322].

[36] Just a speculation. To be confirmed experimentally.

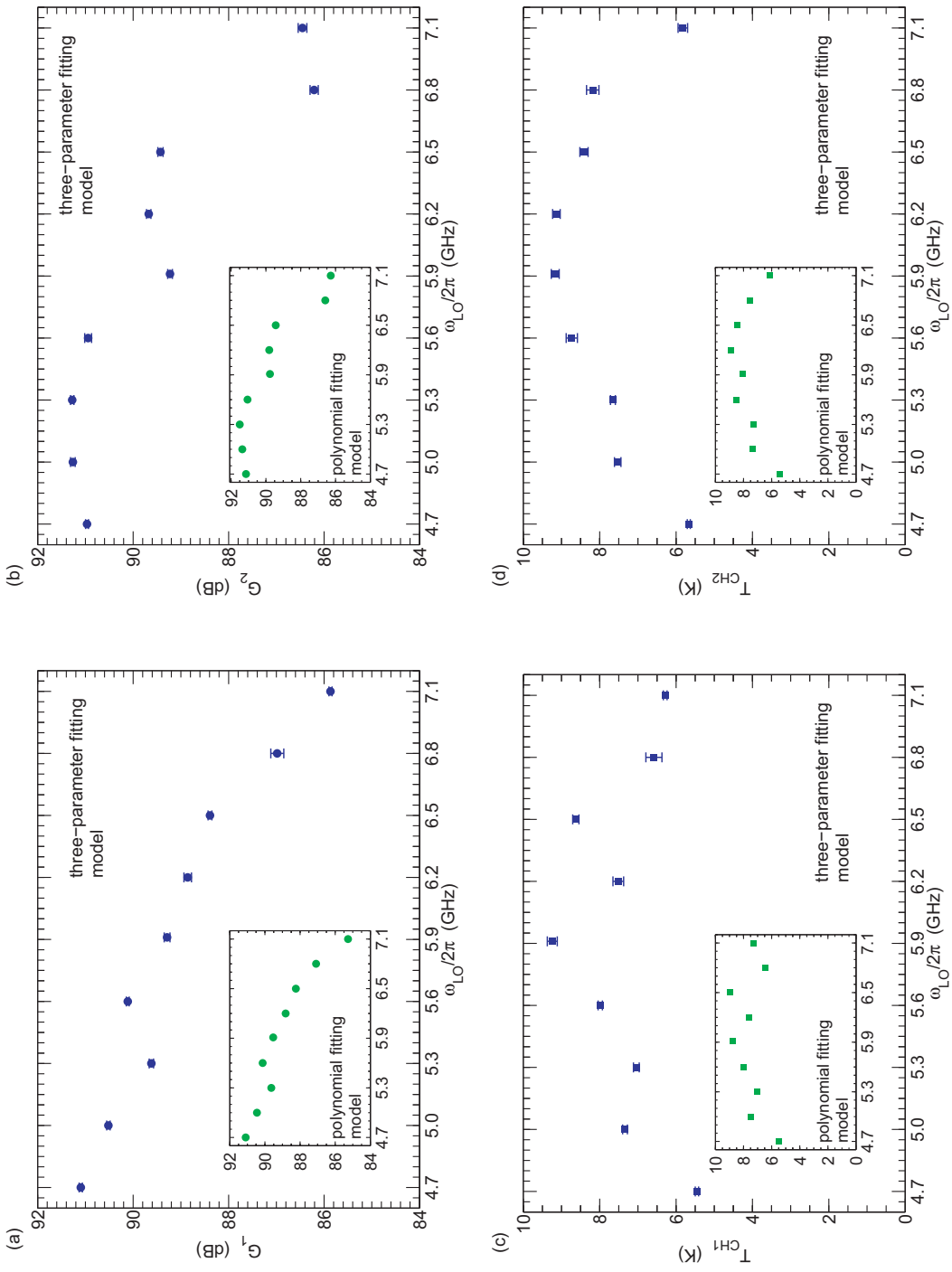

Figure 4.11: **(a)** Power gain G_1 obtained from the three-parameter and, in the inset, from the polynomial fitting model. **(b)** As in **(a)** for G_2. **(c)** Noise temperature T_{CH1} obtained from the three-parameter and, in the inset, from the polynomial fitting model. **(d)** As in **(c)** for T_{CH2}.

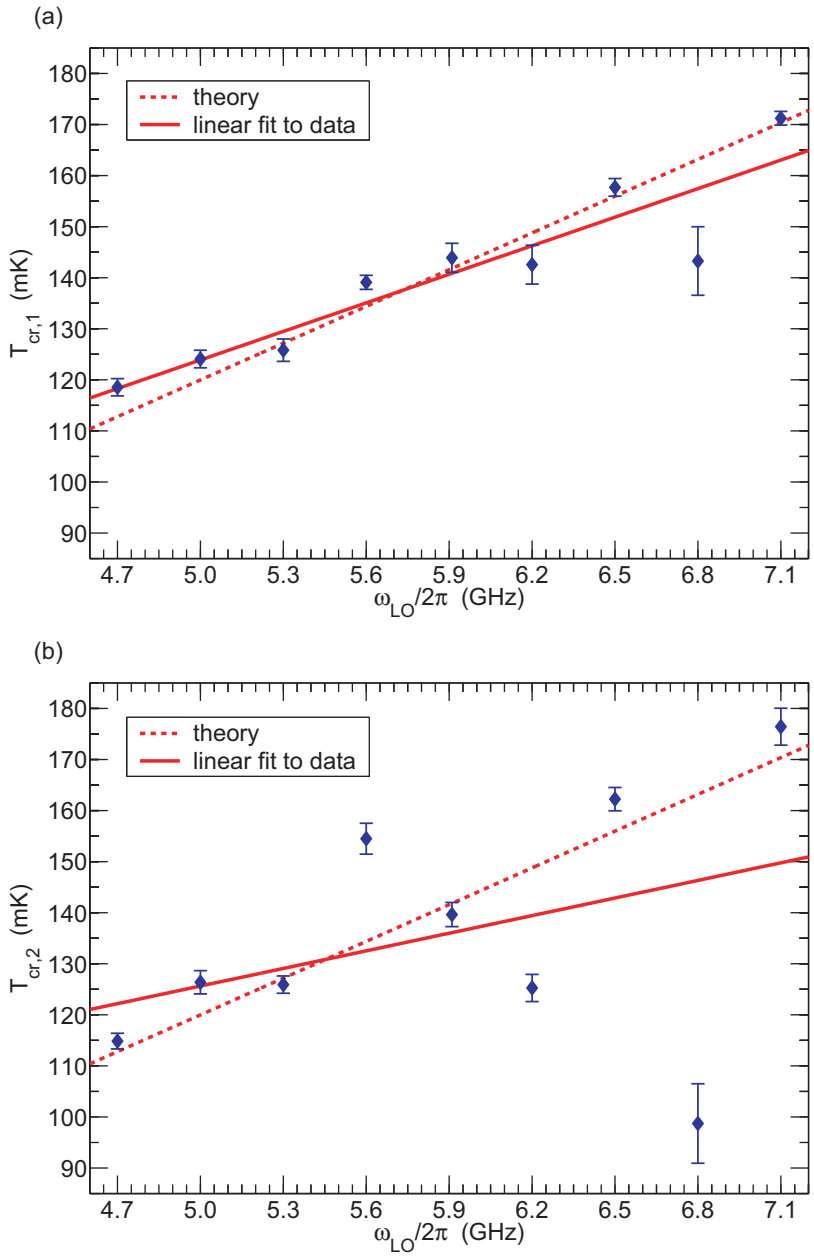

Figure 4.12: Summary of the cross-over temperatures estimated from the three-parameter fitting model [cf. Eq. (4.98)] for channels 1 and 2 as a function of the LO angular frequency $\omega_{\rm LO}$. Dark blue diamonds: data points for the cross-over temperatures obtained from Eq. (4.96) using the channel-dependent η_k (here, $\eta \to \eta_k$) fitted from Eq. (4.98). The confidence bounds are indicated. Solid red lines: linear fits to data. Dashed red lines: frequency dependence of the theoretical cross-over temperature associated with the vacuum. **(a)** Results for channel 1. **(b)** Results for channel 2.

the theoretical and measured cross-over temperature can arise from the frequency dependence of the total gain G_k and noise temperature $T_{\mathrm{CH}k}$ analyzed above. In fact, for the same number of averages the estimation of $\overline{\Delta T_k}$ converges *slightly* faster if the gain is higher and/or the noise temperature lower. Nevertheless, since there is no other evident reason for a frequency dependence of $\overline{\Delta T_k}$, such dependence should not be too pronounced. To make sure that the spread in the estimations of $\overline{\Delta T_k}$ found in the experiments [cf. Figs. 4.12(a) and 4.12(b)] is attributable solely to statistical errors, we performed the following experiment (data not shown). While measuring one downsweep, the LO frequency was varied between three different values at short time intervals. In this way, we almost simultaneously obtained three Planck distributions for the three LO frequencies. Under these conditions, the estimated distance $\overline{\Delta T_k}$ should not show any major frequency dependence. Indeed, this expectation has been confirmed by the experiment.[37] Finally, we notice that the estimated mean temperature difference $\overline{\Delta T_k}$ for both detection channels are negative, as it should be according to our model (cf. 3, Subsec. 3.1.1, The Wilkinson Power Divider Noise Model), in 61 % of the cases [cf. Figs. 4.12(a) and 4.12(b)]. In addition, the corresponding values of $|\eta|$ are typically very small, on the order of a few percent.[38]

4.3.3 Cross-Correlation Function, Cross-Covariance Function, and Covariance

In this subsection, we follow a deductive approach to explain a set of measured data. We start describing the experimental results from a purely qualitative perspective and then attempt to find the correct theoretical picture which explains them in quantitative terms.

Let us begin recalling a few basic definitions valid for continuous random signals. The extension to discrete signals is straightforward.

1. Given two distinct continuous random signals $x(t)$ and $y(t)$, we define the cross-correlation function $R_{xy}(t_1, t_2)$ as the mean value of the product of one sample of the first signal at time t_1 and one sample of the second signal at time t_2, respectively,
$$R_{xy}(t_1, t_2) \equiv \langle x^*(t_1)\, y(t_2) \rangle \,; \tag{4.104}$$

2. Given the signals $x(t)$ and $y(t)$, we define the cross-covariance function $C_{xy}(t_1, t_2)$ as
$$\begin{aligned} C_{xy}(t_1, t_2) &\equiv \langle [x(t_1) - \mu_x(t_1)]^* \, [y(t_2) - \mu_y(t_2)] \rangle \\ &= R_{xy}(t_1, t_2) - \mu_x(t_1)\, \mu_y(t_2) \,, \end{aligned} \tag{4.105}$$
where $\mu_x(t)$ and $\mu_y(t)$ are the time-dependent mean values of signals $x(t)$ and $y(t)$, respectively;

[37] We only found very little frequency dependence correlated to the frequency dependence of the gain and noise temperature.

[38] As suggested by D. Vion, it would also be interesting to make a multi-branch fit, where a single value of η for all Planck distributions in a Planck spectroscopy can be obtained. Ideally, this value should be positive, close to a few percent, and equal for both detection channels. This approach will be the object of future investigations.

3. When $t_1 = t_2 = t$, the cross-covariance function of Eq. (4.105) reduces to the time-dependent covariance of the random signal,

$$\begin{aligned} C_{xy}(t,t) &= \langle [x(t) - \mu_x(t)]^* \, [y(t) - \mu_y(t)] \rangle \\ &= \langle x(t)\, y(t) \rangle - \mu_x(t)\, \mu_y(t) = \tilde{\sigma}_{xy}(t)\,. \end{aligned} \tag{4.106}$$

If the cross-correlation function and, thus, the cross-covariance function of two random signals $x(t_1)$ and $y(t_2)$ depends only on the time lag $\tau = t_1 - t_2$ and the signals mean values are time-independent, the two signals are said to be *jointly stationary*. In this case,

4. the cross-correlation function is given by

$$R_{xy}(\tau) = \langle x^*(t+\tau)\, y(t) \rangle\,, \tag{4.107}$$

5. the cross-covariance function by

$$C_{xy}(\tau) = R_{xy}(\tau) - \mu_x\, \mu_y\,, \tag{4.108}$$

6. and the covariance, which is found for $\tau = 0$, reduces to just a number

$$C_{xy}(\tau = 0) = R_{xy}(\tau = 0) - \mu_x\, \mu_y = \tilde{\sigma}_{xy}\,; \tag{4.109}$$

7. It is well-known from the theory of probability that two random variables are *independent* if their joint probability density is given by the product of the probability density of each variable. Recalling the general definition of Eq. (4.74), when two samples x_{t1} and x_{t2} of a random signal x are independent, the density $f_{x_{t1},x_{t2}}(a,b) = f_{x_{t1}}(a) \times f_{x_{t2}}(b)$ and the auto-correlation function of the random signal is equal to the product of its mean values at times t_1 and t_2, $\mu_x(t_1) \times \mu_y(t_2)$,

$$\begin{aligned} R_{xx}(t_1,t_2) &\equiv \langle x^*(t_1)\, x(t_2) \rangle \\ &= \int_{-\infty}^{+\infty} \int_{-\infty}^{+\infty} da\, db\; a^* b\, f_{x_{t1}}(a)\, f_{x_{t2}}(b) \\ &= \int_{-\infty}^{+\infty} da\, a^*\, f_{x_{t1}}(a) \int_{-\infty}^{+\infty} db\, b\, f_{x_{t2}}(b) \\ &= \langle x^*(t_1) \rangle \, \langle x(t_2) \rangle = \mu_x(t_1)\, \mu_x(t_2)\,. \end{aligned} \tag{4.110}$$

Similarly, the cross-correlation function of independent random signals is given by

$$R_{xy}(t_1,t_2) \equiv \langle x^*(t_1) \rangle \, \langle y(t_2) \rangle = \mu_x(t_1)\, \mu_x(t_2)\,; \tag{4.111}$$

8. A direct consequence of Eqs. (4.110) and (4.111) and of the definitions given by Eqs. (4.83) and (4.105) is that the auto- and cross-covariance functions associated with independent random signals both vanish, $C_{xx}(t_1,t_2) = C_{xy}(t_1,t_2) = 0$. It is worth reminding that this is only a necessary condition for the independence of two random signals. In general, if the auto- and cross-covariance of two random signals are zero, the two signals are said to be *uncorrelated*,

which does not mean they are independent. The class of independent random signals is characterized by the property that if two samples x_{t1} and x_{t2} are independent, also their functions $g[x_{t1}]$ and $g[x_{t2}]$ are independent. That is, if $C_{xy}(t_1, t_2) = 0$, also $C_{g[xy]}(t_1, t_2) = 0$. This is not valid in the case of uncorrelated signals [301].

Taking advantage of our two-channel detection chain, we can measure the cross-correlation function associated with the realizations s_1 and s_2 of the quantum voltages $\hat{V}_{\mathrm{RL1}}$ and $\hat{V}_{\mathrm{RL2}}$, respectively. In order to understand what is new in the measurement of the cross-correlation function in comparison to the case of the auto-correlation function treated in Subsec. 4.3.1, we can start with the following example. We know that the realizations s_k correspond to white noise over the bandwidths BW_k. Let us consider only one monochromatic component of such a noise at frequency ω_0. Referring to Fig. 3.10, we set the phase induced by the LO signal on channel 2 to zero and that induced on channel 1 to ϕ_{LO}. This can easily be realized by means of the phase shifter indicated in the figure. At the output of the mixers we then obtain

$$\tilde{s}_1 \propto \sqrt{\varepsilon_1}\,\cos(\omega_0 t + \delta\phi)\,|\alpha_{\mathrm{LO}}|\,\cos(\omega_{\mathrm{LO}} t + \varphi_{\mathrm{LO}})\,, \tag{4.112a}$$

$$\tilde{s}_2 \propto \sqrt{\varepsilon_2}\,\cos(\omega_0 t)\,|\alpha_{\mathrm{LO}}|\,\cos(\omega_{\mathrm{LO}} t)\,, \tag{4.112b}$$

where $\sqrt{\varepsilon_1}$ and $\sqrt{\varepsilon_2}$ represent random amplitudes (e.g., with Gaussian distribution) with units $\mathrm{V}/\sqrt{\mathrm{Hz}}$, $\delta\phi$ a fixed relative phase between signals $\tilde{s}_1$ and $\tilde{s}_2$ due to a possible phase unbalance between channels 1 and 2, $|\alpha_{\mathrm{LO}}|$ the amplitude of the LO signal (in reality we know that this quantities factors out from the final expression for the mixing; cf. Subsec. 3.2.5), and ω_{LO} the LO angular frequency. In the case of homodyne detection, $\omega_{\mathrm{LO}} = \omega_0$, we can perform a RWA and rewrite Eqs. (4.112a) and (4.112b) as

$$\tilde{s}_1 \propto \frac{1}{2}\sqrt{\varepsilon_1}|\alpha_{\mathrm{LO}}|\,\cos(\delta\phi - \varphi_{\mathrm{LO}})\,, \tag{4.113a}$$

$$\tilde{s}_2 \propto \frac{1}{2}\sqrt{\varepsilon_2}|\alpha_{\mathrm{LO}}|\,. \tag{4.113b}$$

Thus, the cross-product of signals s_1 and s_2 can be written as

$$c_{12} = \tilde{s}_1 \times \tilde{s}_2 \propto \frac{1}{4}\sqrt{\varepsilon_1}\sqrt{\varepsilon_2}|\alpha_{\mathrm{LO}}|^2\,\cos(\delta\phi - \varphi_{\mathrm{LO}})\,. \tag{4.114}$$

Under the realistic assumptions that $\mathrm{BW}_1 \approx \mathrm{BW}_2 = \mathrm{BW}$ and that the signals s_1 and s_2 are jointly stationary, the result of Eq. (4.114) can straightforwardly be extended to all frequency components of the white noise within the bandwidth BW. In this case, applying the definition of Eq. (4.107) allows us to find the cross-correlation and cross-covariance functions R_{12} and C_{12} as [300, 301],

$$\begin{aligned} R_{12}(\tau) &= C_{12}(\tau) \\ &\equiv \frac{\mathrm{BW}}{Z_0}\langle s_1^*(t+\tau)\, s_2(t)\rangle \\ &= \frac{\mathrm{BW}}{Z_0}\,\varepsilon_{12}\frac{\sin\pi\mathrm{BW}\tau}{\pi\mathrm{BW}\tau}\,\cos(\delta\phi - \varphi_{\mathrm{LO}})\,, \end{aligned} \tag{4.115}$$

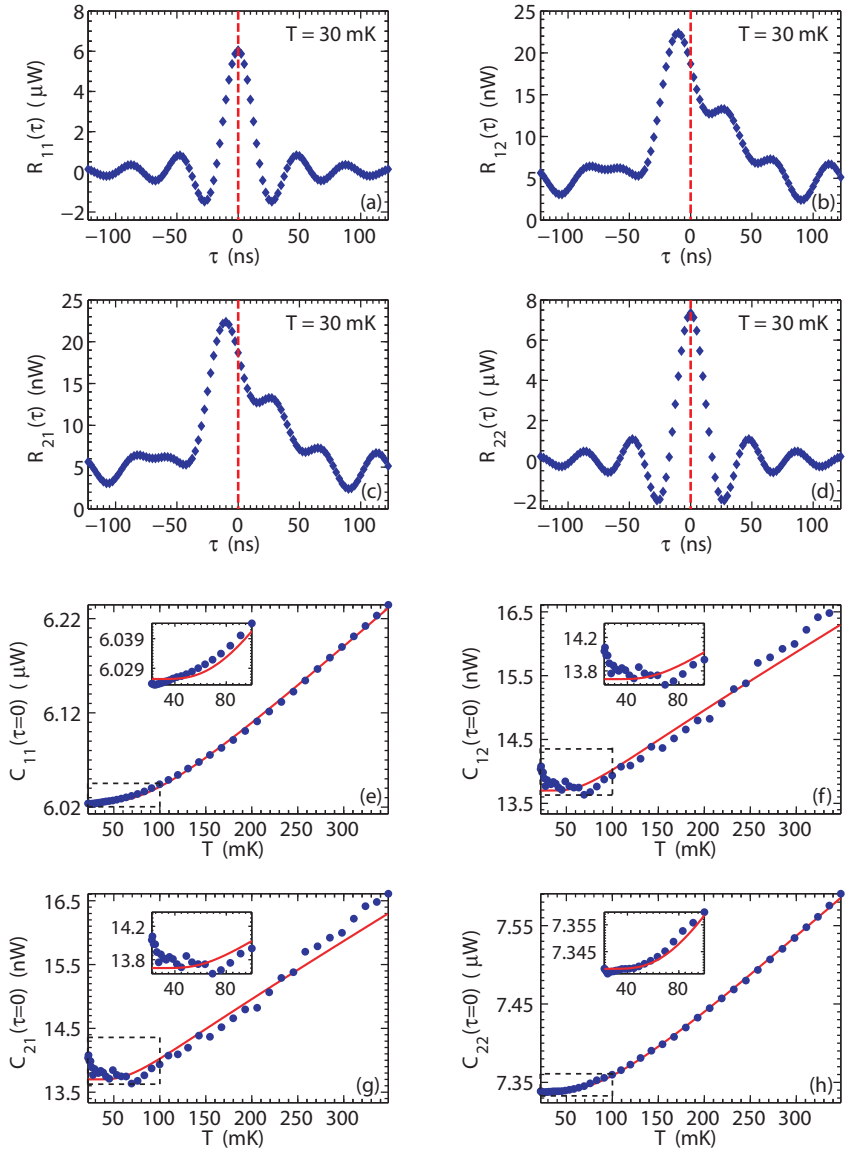

Figure 4.13: Full correlation and covariance matrices for a Wilkinson power divider for a thermal/vacuum state at $\omega_{\rm LO} = \omega_0 = 2\pi \times 5.0\,{\rm GHz}$. From Figs. 4.11(a) and 4.11(b), $G_1 \approx 90.5\,{\rm dB}$, $G_2 \approx 91.3\,{\rm dB}$, and $G_{12} \approx 90.9\,{\rm dB}$ [cf. Eq. (4.124)]. **(a)** Auto-correlation function $R_{11}(\tau)$. **(b)** Cross-correlation function $R_{12}(\tau)$ at $\varphi_{\rm LO} = 0$. **(c)** Cross-correlation function $R_{21}(\tau) = R_{12}(\tau)$. **(d)** Auto-correlation function $R_{22}(\tau)$. **(e)** Temperature dependence of the auto-covariance function at delay time zero, $C_{11}(\tau = 0) = \tilde{\sigma}_1^2(T)$ (variance). **(f)** Temperature dependence of the cross-covariance function at delay time zero, $C_{12}(\tau = 0) = \tilde{\sigma}_{12}(T)$ (covariance). **(g)** Covariance $\tilde{\sigma}_{21}(T) = \tilde{\sigma}_{12}(T)$. **(h)** Variance $C_{22}(\tau = 0) = \tilde{\sigma}_2^2(T)$. Blue circles: data points. Red line: fitted curves. Insets: zoom-in into the thermal-to-vacuum state cross-over region.

where $\varepsilon_{12} \equiv \langle \sqrt{\varepsilon_1}\sqrt{\varepsilon_2} \rangle = \sigma_{12}$. The cross-correlation and cross-covariance functions R_{21} and C_{21} are obtained from Eq. (4.115) by swapping the indexes 1 and 2. Equation (4.115) reveals that the sign of the cross-correlation (cross-covariance) function can be tuned by means of the phase induced by the LO signal and can also be negative. Setting for simplicity $\delta\phi = 0$ (perfect phase matching between the two channels of the detection chain), the absolute value of the cross-correlation (cross-covariance) function reaches its maximum when $\cos\varphi_{\mathrm{LO}} = \mp 1$, i.e., for $\varphi_{\mathrm{LO}} = n\pi$ with $n \in \mathbb{N}$.

Figures 4.13(b) and 4.13(c) show a set of experimental data corresponding to the measurement (i.e., estimation) of the cross-correlation functions $R_{12}(\tau)$ and $R_{21}(\tau)$ for the states generated by the primary and secondary noise source at the input of a Wilkinson power divider (cf. Subsec. 3.1.1) cooled to a stable temperature of 30 mK. We notice that, in our experiments, the cross-correlation function is independent of the order of the indexes, $R_{12} = R_{21}$, and the two curves of Figs. 4.13(b) and 4.13(c) are exactly the same. The experiment refers to a measurement bandwidth BW $\simeq$ 52 MHz centered at an angular frequency $\omega_0 = 2\pi \times 5.0$ GHz. The displayed curves remind of a cardinal sine, even if the data quality is visibly worse than for the case of the auto-correlation functions $R_{11}(\tau)$ and $R_{22}(\tau)$ plotted in Figs. 4.13(a) and 4.13(d), where the cardinal sine is practically perfect. The reason behind such a behavior will become clear towards the end of this subsection. For the curves in Figs. 4.13(b) and 4.13(c), the phase of the LO signal is opportunely chosen in order to maximize the cross-correlation function. This is achieved by realizing a large set of measurements, each of them at a different φ_{LO} (data not shown), until the peak value of the cross-correlation function reaches a positive maximum.[39] The positive sign is chosen only for convenience. Nothing would prevent us from opting for a negative sign, as long as the modulus of the peak value of the cross-correlation function stays maximum. An inspection of Figs. 4.13(b) and 4.13(c) reveals that the peak value reached by the cross-correlation function is on the order of a few tens of nW, while the peak values for the auto-correlation functions are of several μW. The discrepancy between the experimental data for the auto-correlation and cross-correlation functions becomes more evident by repeating the cross-correlation measurements at many different temperatures and, then, extracting those values corresponding to a time lag $\tau = 0$. This procedure allows us to obtain the temperature dependence of the covariance associated with signals s_1 and s_2. The dashed red lines in Figs. 4.13(b) and 4.13(c) indicate how to perform such a measurement for a temperature $T = 30$ mK. For a temperature range comprised between approximately 350 and 20 mK, the temperature-dependent covariance functions $C_{12}(\tau = 0) = \tilde{\sigma}_{12}$ and $C_{21}(\tau = 0) = \tilde{\sigma}_{21}$ are reported in Figs. 4.13(f) and 4.13(g). As for the case of the cross-correlation function, also the covariances are independent of the order of the indexes, $C_{12} = C_{21}$, and, thus, the two curves of Figs. 4.13(f) and 4.13(g) are exactly the same. Such curves, which seem to resemble a Planck distribution, are characterized by a large data scattering in comparison to the curves associated with the variance, which are plotted in Figs. 4.13(e) and 4.13(h). Since the amount of averaging for all curves in Fig. 4.13 is the same, the large data scattering indicates that the signal associated with the covariance must be much weaker than the sig-

[39] The LO phase is a knob which allows us to correlate or decorrelate the signals associated with the two noise sources. Due to the technical difficulties in finding the exact maximum of the cross-correlation function and, thus, the optimum value of the LO phase, the data presented here could be slightly decorrelated. This does not constitute a major issue for our analysis.

nal associated with the variance. This conclusion is confirmed by comparing the span between the minimum and maximum value for the covariance C_{12} to the same span for the variance $C_{11}(\tau = 0) = \tilde{\sigma}_1^2$ and/or $C_{22}(\tau = 0) = \tilde{\sigma}_2^2$. The span for the covariance is approximately $70 - 90$ times smaller than the one for the variance [compare Fig. 4.13(f) to Figs. 4.13(e) and 4.13(h)]. In addition, a comparison between Figs. 4.13(e) and 4.13(h), and Figs. 4.13(f) and 4.13(g) reveals that the large vertical offset due to the noise added by the cryogenic amplifiers is reduced almost to zero in the cross-correlation measurements.

A quantitative analysis of the different features characterizing auto- and cross-correlation functions can be carried out recalling the noise model developed for the Wilkinson power divider in Subsec. 3.1.1. According to that noise model, we must take into account two noise sources at the input of the beam splitter, the primary and secondary noise source. While in the analysis of the auto-correlation measurements the two noise sources can be assumed to constitute a single effective noise source, for the cross-correlation data this hypothesis does not hold anymore. This is best understood by calculating the covariance $\tilde{\sigma}_{12}$ for the quantum voltages $\hat{V}_{\mathrm{RL1}}$ and $\hat{V}_{\mathrm{RL2}}$ associated with the states of the two channels of the detection chain. Neglecting the noise contribution due to the cryogenic circulators (cf. Appendix A), the quantum voltages at the input of the acquisition card are given by

$$\hat{V}_{\mathrm{RL1}} = g_{\mathrm{RL1}}\delta_{\mathrm{M1}}\, g_{\mathrm{RH1}}\, g_{\mathrm{CH1}} \times (\hat{V}_{1,\varphi} + \hat{E}_{\mathrm{n1},\varphi})\,, \tag{4.116a}$$

$$\hat{V}_{\mathrm{RL2}} = g_{\mathrm{RL2}}\delta_{\mathrm{M2}}\, g_{\mathrm{RH2}}\, g_{\mathrm{CH2}} \times (\hat{V}_{2} + \hat{E}_{\mathrm{n2}})\,, \tag{4.116b}$$

where

$$\hat{V}_{1,\varphi} \equiv -\frac{1}{\sqrt{2}}\,\hat{V}_{\mathrm{A},\varphi} - \frac{1}{\sqrt{2}}\,\hat{V}_{\mathrm{D},\varphi}\,, \tag{4.117a}$$

$$\hat{V}_{2} \equiv -\frac{1}{\sqrt{2}}\,\hat{V}_{\mathrm{A}} + \frac{1}{\sqrt{2}}\,\hat{V}_{\mathrm{D}} \tag{4.117b}$$

and

$$\hat{V}_{\mathrm{A},\varphi} \equiv \bar{V}_0(\hat{a}^\dagger e^{+j\varphi_{\mathrm{LO}}} + \hat{a}e^{-j\varphi_{\mathrm{LO}}})\,, \tag{4.118a}$$

$$\hat{V}_{\mathrm{D},\varphi} \equiv \bar{V}_0(\hat{d}^\dagger e^{+j\varphi_{\mathrm{LO}}} + \hat{d}e^{-j\varphi_{\mathrm{LO}}})\,, \tag{4.118b}$$

$$\hat{V}_{\mathrm{A}} \equiv \bar{V}_0(\hat{a}^\dagger + \hat{a})\,, \tag{4.118c}$$

$$\hat{V}_{\mathrm{D}} \equiv \bar{V}_0(\hat{d}^\dagger + \hat{d})\,, \tag{4.118d}$$

$$\hat{E}_{\mathrm{n1},\varphi} = \bar{V}_0(\hat{\xi}_1^\dagger e^{+j\varphi_{\mathrm{LO}}} + \hat{\xi}_1 e^{-j\varphi_{\mathrm{LO}}})\,, \tag{4.118e}$$

$$\hat{E}_{\mathrm{n2}} = \bar{V}_0(\hat{\xi}_2^\dagger + \hat{\xi}_2)\,. \tag{4.118f}$$

The quantum voltages $\hat{V}_{\mathrm{A},\varphi}$ and $\hat{V}_{\mathrm{A}}$ represent the primary noise source with and without the phase induced by the LO signal, respectively. In analogy, $\hat{V}_{\mathrm{D},\varphi}$ and $\hat{V}_{\mathrm{D}}$ represent the quantum voltages of the secondary noise source with and without LO phase. The states associated with such voltages are given by the density operators

[cf. Eq. (4.52)]

$$\hat{\rho}_{\mathrm{A}} = \sum_n \frac{\langle n\rangle_{\mathrm{A}}^n}{(1+\langle n\rangle_{\mathrm{A}})^{1+n}} |n\rangle\langle n| \,, \tag{4.119a}$$

$$\hat{\rho}_{\mathrm{D}} = \sum_n \frac{\langle n\rangle_{\mathrm{D}}^n}{(1+\langle n\rangle_{\mathrm{D}})^{1+n}} |n\rangle\langle n| \,, \tag{4.119b}$$

with

$$\langle n\rangle_{\mathrm{A}} \equiv \frac{1}{e^{\hbar\omega_0/k_{\mathrm{B}}T_{\mathrm{A}}}-1} \,, \tag{4.120a}$$

$$\langle n\rangle_{\mathrm{D}} \equiv \frac{1}{e^{\hbar\omega_0/k_{\mathrm{B}}T_{\mathrm{D}}}-1} \,. \tag{4.120b}$$

The temperatures of the primary and secondary noise sources, T_{A} and T_{D}, respectively, are typically similar, but in general *not equal*. Recalling that our measurement method is based on downsweeps, the temperature difference $T_{\mathrm{A}} - T_{\mathrm{D}}$ is expected to be larger at high temperatures due to a short stabilization time which does not allow the system to reach a thermodynamical equilibrium (cf. Subsec. 4.3.2), with $T_{\mathrm{D}} \lesssim T_{\mathrm{A}}$. At very low temperatures, instead, we expect $T_{\mathrm{D}} \approx T_{\mathrm{A}}$ because of the very slow cooling process. Hence, we can model the relationship between the temperatures T_{D} and T_{A} as

$$T_{\mathrm{D}} = T_{\mathrm{A}} - \gamma_{\mathrm{AD}}(T_{\mathrm{A}} - T^{\min}) \,, \tag{4.121}$$

where γ_{AD} accounts for a temperature gradient between the two noise sources and $T^{\min}$ is the minimum measured temperature, $T^{\min} \equiv \min\{T\}$. Remembering the definition of effective temperature given by Eq. (3.8) and remembering that, when fitting the auto-correlation data, for each detection channel we find two slightly different values of the parameter η, η_1 and η_2, respectively, we can define a new effective temperature $\widetilde{T}_{\mathrm{A}}^*$ as

$$\widetilde{T}_{\mathrm{A}}^* = T_{\mathrm{A}} - \eta^*(T_{\mathrm{A}} - T^{\min}) \,, \tag{4.122}$$

where $\eta^* = (\eta_1 + \eta_2)/2$. We finally obtain the relationship

$$T_{\mathrm{D}} = \widetilde{T}_{\mathrm{A}}^* - \gamma_{\mathrm{AB}}(\widetilde{T}_{\mathrm{A}}^* - T^{\min}) \,. \tag{4.123}$$

From Eqs. (4.122) and (4.123) it appears evident that when $T_{\mathrm{A}} \to T^{\min}$ (i.e., at very low temperatures), $T_{\mathrm{D}} \approx T_{\mathrm{A}}$, as expected.

Defining the total power cogain of the detection chain as

$$\begin{aligned} G_{12} &\equiv g_{\mathrm{RL1}}\, \delta_{\mathrm{M1}}\, g_{\mathrm{RH1}}\, g_{\mathrm{CH1}}\, \delta_{\mathrm{att1}}\, g_{\mathrm{RL2}}\, \delta_{\mathrm{M2}}\, g_{\mathrm{RH2}}\, g_{\mathrm{CH2}}\, \delta_{\mathrm{att2}} \\ &= \sqrt{G_1}\,\sqrt{G_2} \,, \end{aligned} \tag{4.124}$$

the covariance $\tilde{\sigma}_{12}$ can be written as

$$\begin{aligned} \tilde{\sigma}_{12} &\equiv \mathrm{BW}\,\bar{\sigma}_{12} \equiv \frac{\mathrm{BW}}{Z_0}\sigma_{12} \\ &= G_{12}\,\mathrm{BW}\frac{1}{Z_0}\langle \hat{V}_{\mathrm{RL1}}\,\hat{V}_{\mathrm{RL2}}\rangle \\ &= G_{12}\,\mathrm{BW}\frac{1}{Z_0}\left(\langle \hat{V}_{1,\varphi}\,\hat{V}_2\rangle + \langle \hat{V}_{1,\varphi}\,\hat{E}_{\mathrm{n2}}\rangle + \langle \hat{E}_{\mathrm{n1},\varphi}\,\hat{V}_2\rangle + \langle \hat{E}_{\mathrm{n1},\varphi}\,\hat{E}_{\mathrm{n2}}\rangle\right) . \end{aligned} \tag{4.125}$$

It is reasonable to assume independence between signals $\hat{V}_{1,\varphi}$ and $\hat{E}_{\mathrm{n2}}$ as well as between signals $\hat{E}_{\mathrm{n1},\varphi}$ and $\hat{V}_2$ given that such signals are associated with completely different stages of the detection chain and with totally independent devices. Under this assumption and reminding that the mean value for the quantum voltages associated with the states of the cryogenic amplifiers are zero [e.g., cf. Eq. (4.61)],

$$\langle \hat{V}_{1,\varphi}\, \hat{E}_{\mathrm{n2}} \rangle = \langle \hat{V}_{1,\varphi} \rangle \, \langle \hat{E}_{\mathrm{n2}} \rangle = 0 \,, \tag{4.126a}$$

$$\langle \hat{E}_{\mathrm{n1},\varphi}\, \hat{V}_2 \rangle = \langle \hat{E}_{\mathrm{n1},\varphi} \rangle \, \langle \hat{V}_2 \rangle = 0 \,. \tag{4.126b}$$

In addition, since the cryogenic amplifiers are two distinct devices, we can also assume the quantum voltages associated with them to be independent signals,[40] thus

$$\langle \hat{E}_{\mathrm{n1},\varphi}\, \hat{E}_{\mathrm{n2}} \rangle = \langle \hat{E}_{\mathrm{n1},\varphi} \rangle \, \langle \hat{E}_{\mathrm{n2}} \rangle = 0 \,. \tag{4.127}$$

Under these conditions, setting $\varphi_{\mathrm{LO}} = n\pi$ to maximize the absolute value of the covariance,[41] and invoking the definitions of Eqs. (4.118a), (4.118b), (4.118c), (4.118d), (4.119a), (4.119b), (4.120a), (4.120b), (4.122), and (4.123) the expression for the covariance reduces to

$$\begin{aligned}
\tilde{\sigma}_{12} &= G_{12}\,\mathrm{BW}\frac{1}{Z_0}\langle \hat{V}_{1,\varphi}\, \hat{V}_2 \rangle \\
&= (-1)^n G_{12}\,\mathrm{BW}\frac{1}{Z_0}\frac{1}{2}(\langle \hat{V}_{\mathrm{A}}^2 \rangle - \langle \hat{V}_{\mathrm{D}}^2 \rangle) \\
&= (-1)^n G_{12}\,\mathrm{BW}\frac{1}{Z_0}\frac{1}{2}(\mathrm{Tr}\,\{\hat{\rho}_{\mathrm{A}}\, \hat{V}_{\mathrm{A}}^2\} - \mathrm{Tr}\,\{\hat{\rho}_{\mathrm{D}}\, \hat{V}_{\mathrm{D}}^2\}) \\
&= (-1)^n G_{12}\,\mathrm{BW}\,\frac{1}{2}\hbar\omega_0 \left(\frac{1}{e^{\hbar\omega_0/k_{\mathrm{B}}T_{\mathrm{A}}} - 1} - \frac{1}{e^{\hbar\omega_0/k_{\mathrm{B}}T_{\mathrm{D}}} - 1} \right) \\
&= (-1)^n G_{12}\mathrm{BW}\,\frac{\hbar\omega_0}{4}\Bigg\{ \coth\frac{\hbar\omega_0}{2k_{\mathrm{B}}\widetilde{T}_{\mathrm{A}}^*} \\
&\qquad - \coth\frac{\hbar\omega_0}{2k_{\mathrm{B}}[\widetilde{T}_{\mathrm{A}}^* - \gamma_{\mathrm{AD}}(\widetilde{T}_{\mathrm{A}}^* - T^{\mathrm{min}})]} \Bigg\} .
\end{aligned} \tag{4.128}$$

For $\varphi_{\mathrm{LO}} = 0$, obtained for example for $n = 0$, the contribution of the secondary noise source is smaller than the contribution of the primary noise source and the covariance is maximum in modulus and positive in sign,[42]

$$\tilde{\sigma}_{12} = G_{12}\,\mathrm{BW}\,\frac{\hbar\omega_0}{4}\left\{ \coth\frac{\hbar\omega_0}{2k_{\mathrm{B}}\widetilde{T}_{\mathrm{A}}^*} - \coth\frac{\hbar\omega_0}{2k_{\mathrm{B}}[\widetilde{T}_{\mathrm{A}}^* - \gamma_{\mathrm{AD}}(\widetilde{T}_{\mathrm{A}}^* - T^{\mathrm{min}})]} \right\} . \tag{4.129}$$

[40] In reality, there could be some tiny level of correlation between the noise generated by the cryogenic amplifiers, which share part of the biasing electronics.

[41] A more specific choice of the angle will be done in the light of the final expression of the covariance.

[42] We recall here that the noise model of Subsec. 3.1.1 is valid only for a basic Wilkinson power divider. In our experiments, the equivalent resistance R_{eq} is more complicated than the one assumed in such a simplified model. However, the quality of the data, even if generally very high, does not permit us to appreciate the subtleties of a possibly more refined model as, e.g., that of Ref. [292].

The red curves overlaid to the data of Figs. 4.13(e), 4.13(f), 4.13(g), and 4.13(h) are fits obtained using Eqs. (4.98) and (4.129) as theoretical models for the variance and covariance, respectively. From the fitting of the variance data we find the power gains G_1 and G_2 as well as the temperature gradients η_1 and η_2. The power cogain is then given by Eq. (4.124) and does not constitute a free fitting parameter in the model of Eq. (4.129). In analogy, the quantity $\eta^* = (\eta_1 + \eta_2)/2$ is also set to a fixed value and cannot be used as a free fitting parameter in Eq. (4.129). The temperature T_A is a measured quantity and, thus, both the temperature $\widetilde{T}_\mathrm{A}^*$ of Eq. (4.122) and $T^\mathrm{min} = \min\{T\}$ are fixed quantities. As a consequence, the only available free fitting parameter in Eq. (4.129) is represented by the temperature gradient between the two noise sources, γ_AD. Remarkably, the covariance data and the corresponding fits obtained applying the theoretical model of Eq. (4.129) with γ_AD as the only fitting parameter[43] are in very good agreement, confirming the validity of our noise model for the Wilkinson power divider (cf. Subsec. 3.1.1). From the fitting of the data shown in Figs. 4.13(f) and 4.13(g) we find the dimensionless coefficient $\gamma_\mathrm{AD} \simeq 0.01$. This is a reasonable value because it means that the temperatures T_A and T_D are only slightly different, as expected. We have thus demonstrated that the Wilkinson power divider, a seemingly three-port classical device, quantum-mechanically behaves as a four-port beam splitter.

According to Eq. (4.129), the covariance $\tilde{\sigma}_{12}$ for the case of a Wilkinson power divider and for $\varphi_\mathrm{LO} = 0$ is given by the *difference* between the variance of the primary noise source and the variance of the secondary noise source. The vacuum offset due to each one of the two noise sources cancels out completely. To summarize our findings, the variance is proportional to

$$\langle(-\hat{V}_\mathrm{A} - \hat{V}_\mathrm{D})^2\rangle = \hat{V}_\mathrm{A}^2 + \hat{V}_\mathrm{D}^2$$

for channel 1 and to

$$\langle(-\hat{V}_\mathrm{A} + \hat{V}_\mathrm{D})^2\rangle = \hat{V}_\mathrm{A}^2 + \hat{V}_\mathrm{D}^2$$

for channel 2.[44] The covariance is proportional to

$$\langle(-\hat{V}_\mathrm{A} - \hat{V}_\mathrm{D}) \times (-\hat{V}_\mathrm{A} + \hat{V}_\mathrm{D})\rangle = \hat{V}_\mathrm{A}^2 - \hat{V}_\mathrm{D}^2\,.$$

In the light of these results it is now evident that the signal associated with the covariance, which is given by the difference of the variance of the two noise sources, has to be much weaker than the signal associated with the variance, which is given by the sum of the variance of the two noise sources. This explains the difference in data quality between the auto- and cross-correlation functions as well as between the temperature-dependent variance and covariance functions. It also explains the factor of approximately $70 - 90$ between the spans associated with variance and covariance and, partially, the reduction in the peak value of the cross-correlation function as compared to the auto-correlation function. Such reduction also depends on the cancellation of the covariance of the noise added by the cryogenic amplifiers, as expressed by Eq. (4.127). Because of the latter, the vertical offset for the covariance

[43] In reality, we also used a fitting parameter to obtain the small vertical offset observed in the covariance measurements. Since the fitted value is very small and we cannot attribute a secure physical meaning to it (see below), we disregarded it from the present discussion.

[44] We can neglect the phase induced by the LO for the variance because it drops from the final expression.

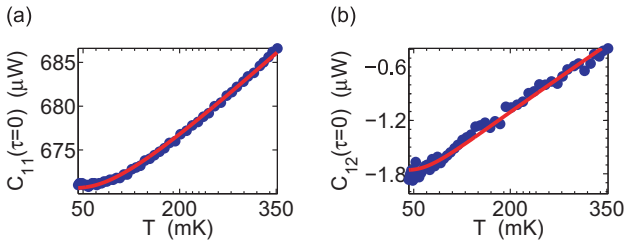

Figure 4.14: Temperature dependence of the variance and covariance for a 180° hybrid ring for a thermal/vacuum state at $\omega_{\rm LO} = \omega_0 = 2\pi \times 5.85\,{\rm GHz}$. **(a)** Variance $C_{11}(\tau = 0) = \tilde{\sigma}_1^2(T)$. Full blue circles: data. Red curve: fit obtained from the model of Eq. (4.98). **(b)** Covariance $C_{12}(\tau = 0) = \tilde{\sigma}_{12}(T)$. Full blue circles: data. Red curve: fit obtained from the model of Eq. (4.129). The different power scale compared to Figs. 4.13(e) and 4.13(f) results from a different amplifier configuration.

goes almost to zero. The tiny vertical offset found in the covariance measurements of Figs. 4.13(f) and 4.13(g) might be due to amplifiers' gain drift and/or other uncontrolled temperature trends.

Very similar results as in Figs. 4.13(e) and 4.13(f) have been found when employing a 180° hybrid ring as microwave beam splitter, as shown in Fig. 4.14. In a similar fashion as for the Wilkinson power divider, also for the hybrid ring the phase of the LO signal, $\varphi_{\rm LO}$, has been adjusted to obtain a maximum positive value of the covariance data [cf. full blue circles in Fig. 4.14(b)]. Under this condition, and reminding that the input-output relations for the 180° hybrid ring are formally equivalent to those of the Wilkinson power divider [compare Eqs. (3.49a) and (3.49b) to Eqs. (3.33a) and (3.33b)], we can use again the models of Eqs. (4.98) and (4.129) to fit the experimental data. This allows us to obtain the red curves shown in Figs. 4.14(a) and 4.14(b).

The reason why most of the experiments where performed using a power divider instead of a hybrid ring is because the first is broader in frequency and, thus, it makes possible to measure a wider Planck spectroscopy.

Finally, in Fig. 4.15(a), the variance C_{11} and the covariance C_{12} are plotted together on the same scale for both x- and y-axis. This helps visualizing the large difference in vertical offset between the two curves. The y-intercept for the variance is found to be at approximately 6800 mK. The covariance is then plotted alone in Fig. 4.15(b), in order to more clearly show the intercept with the y-axis. In this case, the y-intercept is found to be at approximately 15 mK. This result is the experimental proof of the validity of Eq. (4.127), i.e., the noisy signals added by the two cryogenic amplifiers are uncorrelated.[45] The tiny offset of 15 mK shown in Fig. 4.15(b), owns its origin to the inevitable finite number of averages performed to obtain the results and to possible drifts in the gain of the amplifiers or other unwanted experimental offsets. Nevertheless, an offset of 15 mK can be assumed to be negligible for all practical purposes.

[45] With the experimental data at hand, we cannot prove the independence of such signals.

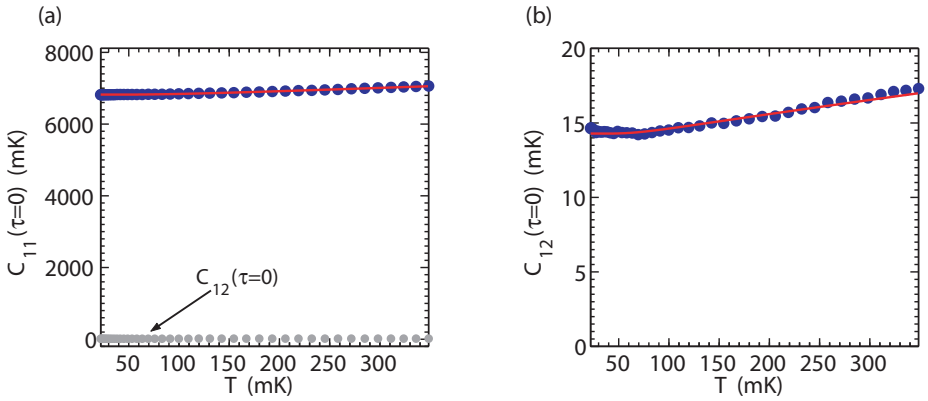

Figure 4.15: Comparison between variance $\tilde{\sigma}_1^2 = C_{11}(\tau = 0)$ and covariance $\tilde{\sigma}_{12} = C_{12}(\tau = 0)$. **(a)** Blue circles: data points associated with the temperature dependence of the variance. Red line: fitted curve obtained from the three-parameter fitting model [cf. Eq. (4.98)]. Grey circles: data points associated with the temperature dependence of the covariance. For the covariance the vertical offset due to the noise of the amplifiers is practically suppressed. **(b)** Blue circles: data points associated with the temperature dependence of the covariance. Red line: fitted curve obtained from Eq. (4.129) using γ_{AD} and the vertical offset given by the residual noise of the system as only free fitting parameters.

4.4 Summary and Outlook

In summary, the main results presented in this chapter are:

1. We have understood that the Planck distribution as derived by Planck, that is without the knowledge of the commutation relations for bosonic fields, inherently encodes information about the vacuum fluctuations of the electromagnetic field.

   By deriving the Planck distribution from Einstein's A and B coefficients, we have been able to show that the vacuum manifests itself in the Planck distribution as one half of the spontaneous emission coefficient.

   We have then shown that the correct Planck distribution obtained by properly quantizing the electromagnetic field has to be shifted by an offset quantity, which is also due to the vacuum fluctuations. The same vacuum appears in the Planck distribution "two times." This means that even if we are not able to resolve experimentally the tiny offset associated with the vacuum fluctuations due to unwanted offsets (e.g., the noise power of the amplifiers and/or offsets due to the drift of the amplifiers bias point), we should still be able to extract information about the vacuum state because of the spontaneous emission contribution to the Planck distribution;

2. We have measured the Planck distribution by means of an autocorrelation technique and developed a fitting model which has allowed us to quantify the distance from the variance associated with the vacuum fluctuations. In

other words, we have been able to show how close we can observe the variance of the vacuum state. This is a beautiful example of a two times indirect measurement: First, it is impossible to directly measure the vacuum state or the energy (or power) associated with it. This would correspond to extract energy from an infinite reservoir, thus realizing a sort of perpetual motion of the first kind. Only a set of properties of the vacuum state, e.g., its variance, can be accessed experimentally. Second, we have found that by means of autocorrelation measurements it is impossible to even measure directly the variance of the vacuum state. Only an indirect measurement of the variance is allowed. Remarkably, this indirect variance measurement contains useful information about the vacuum state, consistently with our conjecture of point 1.;

3. We have realized a so-called Planck spectroscopy measurement, that is, we have been able to measure the distance from the variance of the vacuum state for a wide range of parameters (temperature and frequency). The frequency span accessed in our experiments allows us to monitor the raising of the vacuum level with the center frequency of the noise bandwidth being measured;

4. We have performed a cross-correlation measurement which has helped us to understand the operation principle of microwave beam splitters at the quantum level. In particular, we have shown that the beam splitters used in our experiments behave always as an equivalent four-port junction, even if at first glance they appear to be three-port junctions. The experimental results confirm our theoretical models, which were derived in the beginning of the previous chapter. This is an important result which sheds new light on quantum microwave devices and paves the way towards microwave device quantum process tomography.

Concerning future applications of correlation homodyne detection, at least two possibilities stand out:

1. The amplitude-amplitude measurements presented in this thesis can straightforwardly be extended to intensity-intensity (power-power) correlations, which will allow the implementation of HBT interferometry. This represents an indispensable tool in the future development of circuit QED;

2. Correlation measurements can be used to probe the quantum properties of two-resonator circuit QED architectures. The next two chapters will introduce and analyze in detail the field of two-resonator circuit QED. Eventually, a combination of the experimental techniques developed in this and the previous chapter with the schemes proposed in the next chapters will make possible to open up a new avenue of research in circuit QED.

Chapter 5

Two-Resonator Circuit QED: a Superconducting Quantum Switch

A striking feature of circuit QED is the possibility to make use of more than one resonator by employing simple fabrication techniques. Multi-resonator architectures can be implemented more easily than multi-cavity architectures in quantum-optical cavity QED. In the latter case, in fact, the cavity dimensions represent a major constraint to the scalability of the system. We thus believe that investigating multi-resonator devices constitutes an important step in circuit QED, which can ultimately allow us to unveil novel physical phenomena absent in the quantum-optical domain.

In this chapter, we introduce a systematic formalism for two-resonator circuit QED, where two on-chip microwave resonators with high quality factor are simultaneously coupled to one superconducting qubit. Within this framework, we demonstrate that the qubit can function as a quantum switch between the two resonators, which are assumed to be originally independent. In this three-circuit network, the qubit mediates a *geometric second-order circuit interaction* between the otherwise decoupled resonators. In the dispersive regime, it also gives rise to a *dynamic second-order perturbative interaction*. The geometric and dynamic coupling strengths can be tuned to be equal, thus permitting to switch on and off the interaction between the two resonators via a qubit population inversion or a shifting of the qubit operation point. We also show that our quantum switch represents a flexible architecture for the manipulation and generation of nonclassical microwave field states as well as the creation of controlled multipartite entanglement in circuit QED. In addition, we clarify the role played by the geometric interaction, which constitutes a fundamental property characteristic of superconducting quantum circuits without counterpart in quantum-optical systems. We develop a detailed theory of the geometric second-order coupling by means of circuit transformations for superconducting charge and flux qubits. Furthermore, we show the robustness of the quantum switch operation with respect to decoherence mechanisms. Finally, we propose a realistic design for a two-resonator circuit QED setup based on a flux qubit and estimate all the related parameters. In this manner, we show that this setup can be used to implement a superconducting quantum switch with available technology.

Before delving into the details of the theory of two-resonator circuit QED, it is worth giving a brief overview on related works or works that could eventually benefit

from it. In circuit QED, several other scenarios have been envisioned where a qubit interacts with different bosonic modes, e.g., those of an adjacent nanomechanical resonator or similar. It has been proposed to implement quantum transducers [329] as well as Jahn-Teller models and Kerr nonlinearities [330], to generate nontrivial nonclassical states of the microwave radiation [331, 332], to create entanglement via Landau-Zener sweeps [333], and to carry out high fidelity measurements of microwave quantum fields [332, 334]. Moreover, multi-resonator setups might serve to probe quantum walks [335] and to study the scattering process of single microwave photons [336]. All these proposals, however, do not develop a systematic theory of a realistic architecture based on two on-chip microwave resonators and do not take into account the fundamental geometric second-order coupling between them. Also, our quantum switch is inherently different from the quantum switches investigated in atomic systems [337]. First, we consider a qubit simultaneously coupled to two resonators, which are not positioned one after the other in a cascade configuration as in Ref. [337]. Second, our switch behaves as a tunable quantum coupler between the two resonators. Last, atomic systems naturally lack a geometric first- and second-order coupling. Furthermore, it is important to stress that the dynamic interaction studied here cannot be cast within the framework of the quantum reactance theory (capacitance or inductance, depending on the specific implementation) [218, 338–344]. The main hypothesis for a quantum reactance to be defined is a resonator characterized by a resonance frequency extremely different from the transition frequency of the qubit. Typically, the resonator frequency is considered to be very small (practically zero) compared to the qubit one. Such a scenario is undesirable for the purposes of this work, where a truly quantized high-frequency cavity initialized in the vacuum state has to be used. Also, to our knowledge, the quantum reactance works mentioned above do not directly exploit a geometric coupling between two resonators to compensate a dynamic one, being their main focus the tunable coupling of qubits. Nevertheless, we believe that a circuit theory approach [98, 99, 188, 190–192, 264] to two-resonator circuit QED, which we pursue throughout this manuscript, allows for a deep comprehension of the matter discussed here. Finally, we point out that the geometric first-order coupling between two resonators can be reduced or erased by simple engineering, whereas the second-order coupling due to the presence of a qubit circuit is a fundamental issue. As we show later, whenever the coupling between qubit and resonators is wanted to be large, an appreciable geometric second-order coupling inevitably appears, especially for resonators perfectly isolated in first order. The only circumstances where the geometric coupling between the two resonators can be safely neglected is under resonant conditions. In that case, the vacuum Rabi coupling between the qubit and each resonator is typically much larger than any geometric coupling. In summary, the lesson to be learnt when studying two-resonator circuit QED setups is that quantum circuits behave differently from natural atoms and we must be extremely careful when making analogies and/or approximations.

The chapter is organized as follows. In Sec. 5.2, we develop a systematic formalism for two-resonator circuit QED employing second-order circuit theory and, focusing on the dispersive regime, we are able to derive the effective Hamiltonian of a quantum switch. In Sec. 5.3, we discuss the main limitations to the quantum switch operation due to decoherence processes of qubit and cavities. In Sec. 5.4, we propose a realistic implementation of a two-resonator circuit QED architecture, which is suitable for the realization of a superconducting quantum switch. Finally,

in Sec. 5.5, we summarize our main results, draw our conclusions, and give a brief outlook.

The material discussed in this chapter is a revised version of article number 5 on the *List of Publications* and is published in *Physical Review B* - Ref. [136]. The author is the main contributor to the development of the concept of two-resonator circuit QED. The possible application as a quantum switch originated from discussions with Frank Deppe, who also largely contributed in the treatment of decoherence. Enrique Solano has always participated in the discussion and has triggered the attention of the author towards the possibility to use "transverse modes!" On the night between the 13th[1] and 14th April 2005, the author turned such modes into two resonators... In addition, Enrique Solano has contributed to the development of multipartite entanglement using the quantum switch. The author acknowledges many fruitful discussions with M. J. Storcz, H. Christ, and F. K. Wilhelm.

5.1 Analysis of a Three-Circuit Network

In the following, we theoretically study a three-circuit network where a superconducting charge or flux qubit [97–100] interacts with two on-chip microwave cavities, a two-resonator circuit QED setup (cf. Fig. 5.1 for a generic sketch and Fig. 5.12 for a realistic implementation). In the absence of the qubit, the resonators are assumed to have negligible or small geometric first-order (direct) crosstalk. This scenario is similar to that of quantum optics, where an atom can interact with two orthogonal cavity modes [345]. However, there are some crucial differences. The nature of the three-circuit system considered here requires to account for a *geometric second-order circuit interaction* between the two resonators. This gives rise to coupling terms in the interaction Hamiltonian, which are formally equivalent to those describing a beam splitter. This interaction is mediated by the circuit part of the qubit and does not depend on the qubit state. It is noteworthy to mention that this coupling does not exist in the two-mode JC model studied in quantum optics, where atoms do not sustain any geometric interaction. This means that introducing a second resonator causes a departure from the neat analogy between cavity and one-resonator circuit QED [97, 121–144]. In the dispersive regime, where the transition frequency of the qubit is largely detuned from that of the cavities, also other beam-splitter-type interaction terms between the two resonators appear. Their existence is known in quantum optics [346] and results from a *dynamic second-order perturbative interaction*, which depends on the state of the qubit. The sign of this interaction can be changed by an inversion of the qubit population or by shifting the qubit operation point. The latter mechanism can also be used to change the interaction strength. Notably, for a suitable set of parameters, the geometric and dynamic second-order coupling coefficients can be made exactly equal by choosing a proper qubit-resonator detuning. In this case, the interaction between the two cavities can be switched on and off, thereby enabling the implementation of a *discrete quantum switch* as well as a *tunable coupler*.

In order to fully understand a two-resonator circuit QED system, we take the perspective of classical circuit theory [264] and extend it to the quantum regime to derive the Hamiltonian of a quantized three-circuit network. In general, the latter

[1] Author's birthday.

is composed of two on-chip microwave resonators and a superconducting qubit. Our approach is similar to that of Refs. [98, 99, 188, 190–192]. In addition, we account for second-order circuit elements linking different parts of the network, which is considered to be closed and nondissipative. Here, closed means that we assume no energy flow between the network under analysis and other possible adjacent networks. These could be additional circuitry used to access the three-circuit network from outside and where excitations could possibly decay. Nondissipative means that we consider capacitive and inductive circuit elements only, more in general, reactive elements. We neglect resistors, which could represent dissipation processes of qubit and resonators. In summary, the network of our model is altogether a conservative system. The detailed role of decoherence mechanisms is studied later in Sec. 5.3.

The first step of our derivation is to demonstrate a geometric second-order coupling between the circuit elements of a simple *three-node network*. This means that we assume the various circuit elements to be concentrated in three confined regions of space (nodes). Any topologically complex *three-circuit network* can be reduced to such a three-node network, where each node is fully characterized by its capacitance matrix $\mathbf{C}$ and/or inductance matrix $\mathbf{M}$. The topology of the different circuits (e.g., two microstrip or coplanar waveguide resonators coupled to a superconducting qubit) is thus absorbed in the definition of $\mathbf{C}$ and $\mathbf{M}$, simplifying the analysis significantly. The system Hamiltonian can then be straightforwardly obtained. In fact, the classical energy of a conservative network can be expressed as $E = (\vec{V}^T \mathbf{C}\, \vec{V} + \vec{I}^T \mathbf{M}\, \vec{I})/2$, where the vectors $\vec{V}$ and $\vec{I}$ represent the voltages and currents on the various capacitors and inductors [264]. The usual quantization of voltages and currents [131] (cf. chapter 2, Subsec. 2.1.3) and the addition of the qubit Hamiltonian allows us to obtain the fully quantized Hamiltonian of the three-node network (cf. Subsec. 5.1.1). Special attention is then reserved to compute contributions to the matrices $\mathbf{C}$ and $\mathbf{M}$ up to second order. These are consequently redefined as $\mathbf{C^{(2)}}$ and $\mathbf{M^{(2)}}$, respectively (cf. Subsec. 5.1.2). Corrections of third or higher order to the capacitance and inductance matrices are discussed in Appendix D, where we show that they are not relevant for this work.

We finally consider two examples of possible implementations of two-resonator circuit QED (cf. Subsec. 5.1.3). These examples account for two superconducting resonators coupled to a charge quantum circuit (e.g., a Cooper-pair box or a transmon) or a flux quantum circuit (e.g., an RF SQUID or a three-Josephson-junction SQUID). Before moving to a two-level approximation, the Hamiltonians of these devices can be used to deduce the geometric second-order circuit interaction between the two resonators. This result is better understood considering the lumped-element equivalent circuits of the entire systems. In this way, also the conceptual step from a three-circuit to a three-node network is clarified and the role played by the topology of the different circuits becomes more evident. We show that special care must be taken when quantizing the interaction Hamiltonian between charge or flux quantum circuits and microwave fields by the simple promotion of an AC classical field to a quantum one. Interestingly, comparing the standard Hamiltonian of charge and flux quantum circuits coupled to quantized fields with *ab initio* models based on lumped-element equivalent circuits, we prove that the latter are better suited to describe circuit QED systems.

5.1.1 The Hamiltonian of a Generic Three-Node Network

The system to be studied is sketched in Figs. 5.1(a) and 5.1(b), where the microwave resonators are represented by symbolic mirrors. A more realistic setup is discussed in Sec. 5.4 and is drawn in Fig. 5.12(a). A and B represent the two cavities and Q a superconducting qubit, making altogether a three-node network. The coupling channels between the three nodes are assumed to be capacitive and/or inductive. We also hypothesize the first-order interaction between A and B to be weak and that between A or B and Q to be strong by design. In other words, the first-order capacitance and inductance matrices are $\mathbf{C} = C_{kl}$ and $\mathbf{M} = M_{kl}$, with $k, l \in \{\mathrm{A}, \mathrm{B}, \mathrm{Q}\}$, where $C_{kl} = C_{lk}$ and $M_{kl} = M_{lk}$ because of symmetry reasons. In addition, we assume $C_{\mathrm{AB}} \equiv c \ll C_{kl\neq\mathrm{AB}}$ and $M_{\mathrm{AB}} \equiv m \ll M_{kl\neq\mathrm{AB}}$. The elements c and m represent a first-order crosstalk between A and B, which can be either spurious or engineered and, here, is considered to be small. In Sec. 5.4, we delve into a more detailed analysis of the geometric first-order coupling between two microstrip resonators. Restricting the cavities to a single relevant mode, the total Hamiltonian of the system is given by

$$\widehat{H}_{\mathrm{T}} = \frac{1}{2}\vec{\hat{V}}^{T}\,\mathbf{C}^{(\mathbf{n})}\,\vec{\hat{V}} + \frac{1}{2}\vec{\hat{I}}^{T}\,\mathbf{M}^{(\mathbf{n})}\,\vec{\hat{I}} + \frac{1}{2}G\left(E_{\mathrm{c}}, E_{\mathrm{J}}\right)\hat{\tilde{\sigma}}_{x}\,, \tag{5.1}$$

where $\mathbf{C}^{(\mathbf{n})}$ and $\mathbf{M}^{(\mathbf{n})}$ are the renormalized capacitance and inductance matrices up to the n-th order, with $\mathbf{C}^{(\mathbf{1})} \equiv \mathbf{C}$ and $\mathbf{M}^{(\mathbf{1})} \equiv \mathbf{M}$. Also, $\vec{\hat{V}} \equiv [\hat{V}_{\mathrm{A}}, \hat{V}_{\mathrm{B}}, \hat{V}_{\mathrm{Q}}]^{T}$ and $\vec{\hat{I}} \equiv [\hat{I}_{\mathrm{A}}, \hat{I}_{\mathrm{B}}, \hat{I}_{\mathrm{Q}}]^{T}$. In general, G is a function of the charging energy E_{c} and/or coupling energy E_{J} of the Josephson tunnel junctions in the qubit. For instance, $G = E_{\mathrm{J}}$ for a charge qubit and $G \propto \sqrt{E_{\mathrm{c}}E_{\mathrm{J}}}\exp(-\mu\sqrt{E_{\mathrm{c}}/E_{\mathrm{J}}})$ for a flux qubit ($\mu \equiv$ const). Furthermore, $\hat{V}_{\mathrm{A}} \equiv v_{\mathrm{DC}} + v_{\mathrm{A0}}(\hat{a}^{\dagger} + \hat{a})$, $\hat{V}_{\mathrm{B}} \equiv v_{\mathrm{B0}}(\hat{b}^{\dagger} + \hat{b})$, $\hat{V}_{\mathrm{Q}} \equiv v_{\mathrm{Q}}\hat{\tilde{\sigma}}_{z}$, $\hat{I}_{\mathrm{A}} \equiv i_{\mathrm{DC}} + i_{\mathrm{A0}}\,j(\hat{a}^{\dagger} - \hat{a})$, $\hat{I}_{\mathrm{B}} \equiv i_{\mathrm{B0}}\,j(\hat{b}^{\dagger} - \hat{b})$, and $\hat{I}_{\mathrm{Q}} \equiv i_{\mathrm{Q}}\hat{\tilde{\sigma}}_{z}$. In these expressions, $\hat{\tilde{\sigma}}_{x}$ and $\hat{\tilde{\sigma}}_{z}$ are the usual Pauli operators for a spin-1/2 system in the diabatic basis, which consists of the eigenstates $|-\rangle$ and $|+\rangle$ of $C_{\mathrm{AQ}}v_{\mathrm{DC}}v_{\mathrm{Q}}\hat{\tilde{\sigma}}_{z}$ (charge case) or $M_{\mathrm{AQ}}i_{\mathrm{DC}}i_{\mathrm{Q}}\hat{\tilde{\sigma}}_{z}$ (flux case). Additionally, $\hat{a}^{\dagger}$, $\hat{b}^{\dagger}$, $\hat{a}$, and $\hat{b}$ are bosonic creation and annihilation operators for the fields of cavities A and B, respectively, and $j \equiv \sqrt{-1}$. The DC voltage v_{DC} and current i_{DC} account for the quasi-static polarization of the qubit and can be applied through any suitable bias circuit. For definiteness, we have chosen here cavity A to perform this function. This is the standard approach followed by the charge qubit circuit QED community [139]. However, for flux qubits the current i_{DC} is more easily applied via an external coil [141, 159, 262, 347]. In the latter case, we impose $i_{\mathrm{DC}} = 0$ and add to the Hamiltonian of Eq. (5.1) the term $(\Phi_{\mathrm{x}}^{\mathrm{DC}} - \Phi_0/2)\hat{I}_{\mathrm{Q}}$, where $\Phi_{\mathrm{x}}^{\mathrm{DC}}$ is an externally applied flux bias and $\Phi_0 \equiv h/2e = 2.07 \times 10^{-15}$ Wb is the flux quantum. The results of our derivation are not affected by this particular choice. The vacuum (zero point) fluctuations of the voltage and current of each resonator are given by $v_{\mathrm{A0}} \equiv \sqrt{\hbar\omega_{\mathrm{A}}/2C_{\mathrm{AA}}}$, $v_{\mathrm{B0}} \equiv \sqrt{\hbar\omega_{\mathrm{B}}/2C_{\mathrm{BB}}}$, $i_{\mathrm{A0}} \equiv \sqrt{\hbar\omega_{\mathrm{A}}/2M_{\mathrm{AA}}}$, and $i_{\mathrm{B0}} \equiv \sqrt{\hbar\omega_{\mathrm{B}}/2M_{\mathrm{BB}}}$, respectively.[2] Here, ω_{A} and ω_{B} are the transition angular frequencies of the two cavities. Finally, v_{Q} and i_{Q} represent the voltage of the superconducting island(s) and the current through the loop of the qubit circuit.

[2] In this subsection, we make use of a lumped-parameter model. Hence, the factor of 2 in the denominator of the square roots representing the vacuum voltages and currents is necessary (cf. chapter 2, Subsec. 2.1.3).

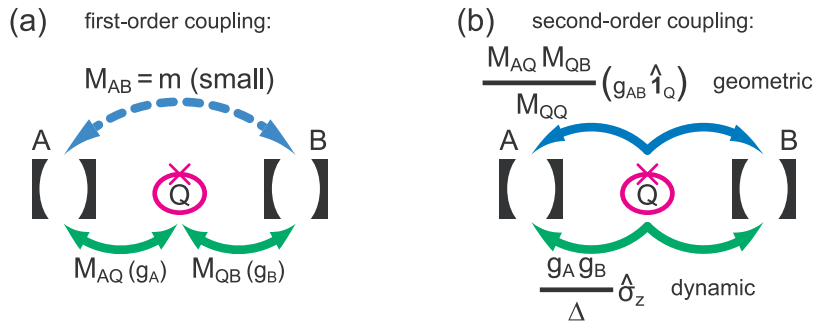

Figure 5.1: Sketch of the system under analysis. All constants are defined in the main text. Only inductive couplings are considered. **(a)** Schematic representation of the first-order coupling Hamiltonian of our three-node network. Two cavities (resonators) A and B interact with a generic superconducting qubit Q. A and B can have a weak geometric first-order coupling $M_{\rm AB} = m$ [broken blue (dark grey) arrow], as in the Hamiltonian $\widehat{H}^{(1)}_{\rm AB}$ of Eq. (5.2). The two solid green (light grey) arrows represent a two-mode Jaynes-Cummings dynamics with coupling coefficients $g_{\rm A} \propto M_{\rm AQ}$ and $g_{\rm B} \propto M_{\rm QB}$, respectively. **(b)** Visualization of the effective second-order coupling Hamiltonian $\widehat{H}_{\rm eff}$ of Eq. (5.14). The solid blue (dark grey) arrows show the second-order *geometric* coupling channel mediated by a virtual excitation of the circuit associated with Q, as in the Hamiltonian $\widehat{H}^{(2)}_{\rm AB}$ of Eq. (5.3). This channel is characterized by a constant $g_{\rm AB} \propto M_{\rm AQ}M_{\rm QB}/M_{\rm QQ}$ (the small contribution from m is neglected) and is qubit-state independent. The solid green (light grey) arrows show the second-order *dynamic* channel mediated by a virtual excitation of the qubit Q. This channel is characterized by a constant $g_{\rm A}g_{\rm B}/\Delta$ and is qubit-state dependent.

Depending on the specific qubit implementation, either $v_{\rm Q}$ or $i_{\rm Q}$ dominates, thus defining the charge and flux regimes.

5.1.2 The Capacitance and Inductance Matrices up to Second Order

The matrices $\mathbf{C^{(n)}}$ and $\mathbf{M^{(n)}}$ account for corrections up to the n-th order interaction process between the elements of the network. In fact, in order to write the exact Hamiltonian of the circuit, all possible electromagnetic paths connecting its nodes must be considered. A consequence of this approach to circuit theory is that the direct coupling

$$\widehat{H}^{(1)}_{\rm AB} = \hat{V}_{\rm A}\, c\, \hat{V}_{\rm B} + \hat{I}_{\rm A}\, m\, \hat{I}_{\rm B} \tag{5.2}$$

between resonators A and B [cf. Fig. 5.1(a)], here assumed to be small, is not the only interaction mechanism to be considered. In fact, an indirect coupling mediated by the circuit associated with the qubit Q has also to be included in the Hamiltonian. The dominating term for the A-Q-B excitation pathway can be derived from its

second-order electromagnetic energy [cf. Fig. 5.1(b)], which gives

$$\begin{aligned}\widehat{H}^{(2)}_{\mathrm{AB}} = \widehat{H}^{(1)}_{\mathrm{AB}} \\ &+ \hat{V}_{\mathrm{A}}\, C_{\mathrm{AQ}} \frac{1}{C_{\mathrm{QQ}}} C_{\mathrm{QB}}\, \hat{V}_{\mathrm{B}} \\ &+ \hat{I}_{\mathrm{A}}\, M_{\mathrm{AQ}} \frac{1}{M_{\mathrm{QQ}}} M_{\mathrm{QB}}\, \hat{I}_{\mathrm{B}}\,. \end{aligned} \tag{5.3}$$

Note that the inverse path (B-Q-A) is already included in this equation. In our work, we assume $0 \lesssim c \lesssim C_{\mathrm{AQ}}C_{\mathrm{QB}}/C_{\mathrm{QQ}}$ and $0 \lesssim m \lesssim M_{\mathrm{AQ}}M_{\mathrm{QB}}/M_{\mathrm{QQ}}$ (cf. Sec. 5.4). When $c, m \simeq 0$, the direct coupling between A and B is negligible, i.e., the contribution of $\widehat{H}^{(1)}_{\mathrm{AB}}$ can be omitted. On the other hand, when $c > 0$ and/or $m > 0$, both first- and second-order circuit theory contributions are relevant. In this case, c and m can represent a spurious or an engineered crosstalk. The latter can deliberately be exploited to increase the strength of the geometric second-order coupling. However, c and m should be small enough to leave the mode structure and quality factors of A and B unaffected.

From the knowledge of $\widehat{H}^{(2)}_{\mathrm{AB}}$, the capacitance matrix up to second order is readily obtained

$$\mathbf{C}^{(2)} = \begin{bmatrix} C_{\mathrm{AA}} & c + \dfrac{C_{\mathrm{AQ}}C_{\mathrm{QB}}}{C_{\mathrm{QQ}}} & C_{\mathrm{AQ}} \\ c + \dfrac{C_{\mathrm{BQ}}C_{\mathrm{QA}}}{C_{\mathrm{QQ}}} & C_{\mathrm{BB}} & C_{\mathrm{BQ}} \\ C_{\mathrm{QA}} & C_{\mathrm{QB}} & C_{\mathrm{QQ}} \end{bmatrix}. \tag{5.4}$$

The second-order corrections to the self-capacitances, i.e., the diagonal elements C_{kk} are absorbed in their definitions [3] (cf. Subsec. 5.1.3). In analogy, the corrected inductance matrix $\mathbf{M^{(2)}}$ is found substituting C_{kl} with M_{kl} and c with m in matrix (5.4) yielding

$$\mathbf{M}^{(2)} = \begin{bmatrix} M_{\mathrm{AA}} & m + \dfrac{M_{\mathrm{AQ}}M_{\mathrm{QB}}}{M_{\mathrm{QQ}}} & M_{\mathrm{AQ}} \\ m + \dfrac{M_{\mathrm{BQ}}M_{\mathrm{QA}}}{M_{\mathrm{QQ}}} & M_{\mathrm{BB}} & M_{\mathrm{BQ}} \\ M_{\mathrm{QA}} & M_{\mathrm{QB}} & M_{\mathrm{QQ}} \end{bmatrix}. \tag{5.5}$$

Again, second-order corrections to the self-inductances are absorbed in the definition of M_{kk}. The matrices $\mathbf{C^{(2)}}$ and $\mathbf{M^{(2)}}$ constitute the *first main result* of this chapter. They show that, if a large qubit-resonator coupling (i.e., a vacuum Rabi coupling $\propto C_{\mathrm{AQ}}$, C_{QB} for charge quantum circuits and $\propto M_{\mathrm{AQ}}$, M_{QB} for flux quantum circuits) is present, as in most circuit QED implementations [144], a relevant geometric second-order coupling ($\propto C_{\mathrm{AQ}}C_{\mathrm{QB}}/C_{\mathrm{QQ}}$ or $\propto M_{\mathrm{AQ}}M_{\mathrm{QB}}/M_{\mathrm{QQ}}$ for charge

[3] In Refs. [137, 331], we have studied charge qubits in multi-resonator systems. In that case, we have performed numerical simulations to study the geometric first-order capacitance between two resonators [in a configuration similar to that of Fig. 5.2(c)]. We have found a scattering matrix element $S_{\mathrm{ab}} \simeq -50\,\mathrm{dB}$ at approximately 4 GHz, which gives $C_{\mathrm{AB}} = c = 3 \times 10^{-3}\, C_{\mathrm{BB}}$. Assuming $C_{\mathrm{AQ}} \approx C_{\mathrm{QB}}$, we can easily compare c to the second-order cross-capacitance between A and B and obtain $c/\left(C^2_{\mathrm{AQ}}/C_{\mathrm{QQ}}\right) \simeq 0.9$. For these calculations, we use $C_{\mathrm{BB}} \simeq 2.2\,\mathrm{pF}$, $C_{\mathrm{AQ}} \simeq 22\,\mathrm{fF}$, and $C_{\mathrm{QQ}} \simeq 67\,\mathrm{fF}$ from Ref. [146]. In particular, we find $c \simeq 7\,\mathrm{fF}$ and $C_{\mathrm{AQ}}C_{\mathrm{QB}}/C_{\mathrm{QQ}} \simeq 7.5\,\mathrm{fF}$. In this case, an example of third-order cross-capacitance is $C_{\mathrm{AQ}}C_{\mathrm{QB}}C_{\mathrm{BQ}}/C_{\mathrm{QQ}}C_{\mathrm{BB}} \simeq 76\,\mathrm{aF}$.

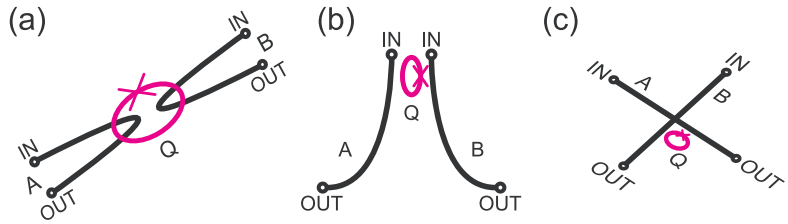

Figure 5.2: Three generic sketches of a possible setup. **(a)** A flux qubit (Q) sits at the current antinode of, e.g., the first mode of two $\lambda/2$ resonators (solid black lines, only inner conductor shown). The open circles at the "IN" and "OUT" ports denote the position of the coupling capacitors to be used in real implementations [e.g., cf. Sec. 5.4 and Fig. 5.12(a)]. **(b)** A charge qubit (Q) sits at the voltage antinode of, e.g., the first mode of two $\lambda/2$ resonators. **(c)** A charge or flux qubit sits at the voltage (e.g., second mode, λ resonators) or current (e.g., first mode, $\lambda/2$ resonators) antinode of two orthogonal resonators [137].

and flux quantum circuits, respectively) has to be expected. This coupling becomes relevant in the dispersive regime [131, 140, 154, 155], where a dynamic second-order coupling, whose magnitude can be comparable to that of the geometric one, is also present (cf. Subsec. 5.2.1). We study in more detail the relationship between m and $M_{\mathrm{AQ}}M_{\mathrm{QB}}/M_{\mathrm{QQ}}$ in Sec. 5.4. There, we show that for a realistic design engineered for a flux qubit, which is our experimental expertise [159, 262] (cf. chapters 2 and 8), the geometric second-order interaction dominates over the first-order one.

Figures 5.2(a)-(c) show three generic sketches, where the coupling of two on-chip resonators to one superconducting qubit is illustrated. In particular, the sketch drawn in Fig. 5.2(a) is suitable when a flux qubit is intended to be utilized. In this case, the qubit is positioned at the current antinode of the first mode (cf. chapter 2, Secs. 2.1 and 2.3) of two $\lambda/2$ resonators. Moreover, this design clearly allows for engineering a strong coupling between the qubit and each resonator, while reducing the geometric first-order coupling between resonators A and B. This is due to the fact that the two cavities are close to each other only in the restricted region where the qubit is located and then develop abruptly towards opposite directions. The sketch in Fig. 5.2(b), instead, is more suitable for charge qubit applications. The qubit can easily be fabricated near a voltage antinode [131, 139]. Similar arguments as in the previous case apply for the qubit-resonator couplings and the geometric first-order coupling between A and B. Finally, the sketch of Fig. 5.2(c) relies on an orthogonal-cavity design, which can be used for both charge and flux qubits. The main properties of such a setup have already been presented in Refs. [137, 331] where orthogonal cavities have been exploited for different purposes. In conclusion, we want to stress that based on the general sketches of Figs. 5.2(a)-(c), a large variety of specific experimental implementations can be envisioned.

5.1.3 The Role of Circuit Topology: Two Examples

All results of Subsecs. 5.1.1 and 5.1.2 are general and do not rely *a priori* on the knowledge of the three-circuit network topology. Here, we explain with the aid of two easy examples how to obtain a reduced three-node network starting from a

three-circuit one. The examples are based on the coupling of two superconducting coplanar waveguide or microstrip resonators to a single Cooper-pair box [131, 139] (or a transmon [120, 243, 244]) or to an RF SQUID (or a three Josephson-tunnel-junction SQUID) [125, 134, 289, 347] (cf. chapter 2, Subsecs. 2.2.2 and 2.2.3).

The first example is the case of a single Cooper-pair box (a charge quantum circuit), which is formally equivalent to the more appealing case of the transmon. As we have shown in chapter 1, a single Cooper-pair box [131, 139] is made of a superconducting island connected to a large reservoir via two Josephson tunnel junctions with Josephson energy $E_{\rm J}$ and capacitance $C_{\rm J}$. The box is capacitevely coupled to two resonators A and B by the gate capacitors $C_{\rm ga}$ and $C_{\rm gb}$, respectively. In the charge basis, the Hamiltonian of a single Cooper-pair box can be written as [131]

$$\begin{aligned}\widehat{H}_{\rm c} &= 4E_{\rm c}\sum_n (\hat{n}-n_{\rm g})^2\,|n\rangle\langle n| \\ &\quad -\frac{E_{\rm J}}{2}\sum_n \left(|n\rangle\langle n+1| + |n+1\rangle\langle n|\right), \end{aligned} \tag{5.6}$$

where $E_{\rm c}=e^2/2C_\Sigma$ is the box electrostatic energy (e is the electron charge), $C_\Sigma = C_{\rm ga}+2C_{\rm J}+C_{\rm gb}$ is its total capacitance,[4] $\langle n|\,\hat{n}\,|n\rangle$ represents the number of excess Cooper pairs on the island, and $n_{\rm g}$ is the global dimensionless gate charge applied to it. The latter is the sum of a DC signal $n_{\rm g}^{\rm DC}$ (here, considered to be applied through cavity A) and a high-frequency excitation $\delta n_{\rm g}$ applied through cavities A and/or B, $n_{\rm g}\equiv n_{\rm g}^{\rm DC}+\delta n_{\rm g}$. In particular, $\delta n_{\rm g}$ can represent the quantized electric fields (equivalent to the voltages) of the two cavities acting as quantum harmonic oscillators. Restricting ourselves to the two lowest charge states $n=0,1$, we can rewrite the Hamiltonian of Eq. (5.6) as

$$\begin{aligned}\widehat{H}_{\rm c} &= 2E_{\rm c}\left(1-2n_{\rm g}+2n_{\rm g}^2+\hat{\tilde{\sigma}}_z-2n_{\rm g}\hat{\tilde{\sigma}}_z\right)-\frac{E_{\rm J}}{2}\hat{\tilde{\sigma}}_x \\ &= 2E_{\rm c}\left(1-2n_{\rm g}^{\rm DC}\right)\hat{\tilde{\sigma}}_z-\frac{E_{\rm J}}{2}\hat{\tilde{\sigma}}_x \\ &\quad -4E_{\rm c}\delta n_{\rm g}\left(1-2n_{\rm g}^{\rm DC}-\delta n_{\rm g}+\hat{\tilde{\sigma}}_z\right). \end{aligned} \tag{5.7}$$

The second line of the above equation forms the standard charge qubit, which can be controlled by the quasi-static bias $n_{\rm g}^{\rm DC}\equiv C_{\rm ga}v_{\rm DC}/2e$. The third line contains four high-frequency interaction terms. Among those, two of them are particularly interesting.[5] These are $4E_{\rm c}\delta n_{\rm g}^2$ and $-4E_{\rm c}\delta n_{\rm g}\hat{\tilde{\sigma}}_z$. We now quantize the high-frequency excitations $\delta n_{\rm g}\to\delta\hat{n}_{\rm g}\equiv C_{\rm ga}v_{\rm A0}(\hat{a}^\dagger+\hat{a})/2e + C_{\rm gb}v_{\rm B0}(\hat{b}^\dagger+\hat{b})/2e$, using the fact that they are the quantized voltages of the two resonators. We subsequently perform a

[4] In the definition of self-capacitance, we neglect the capacitance of the island itself because it is small compared to the other capacitances, $C_{\rm isl}\ll\min\{C_{\rm ga},2C_{\rm J},C_{\rm gb}\}$.

[5] The remaining two interaction terms, when quantizing the AC excitations, result in a displacement-type of operator [131], which act on the two resonators coordinates. These operators reduce to zero right at the charge degeneracy point (i.e., for $n_{\rm g}^{\rm DC}=1/2$). In general, these terms are small and can thus be neglected [131].

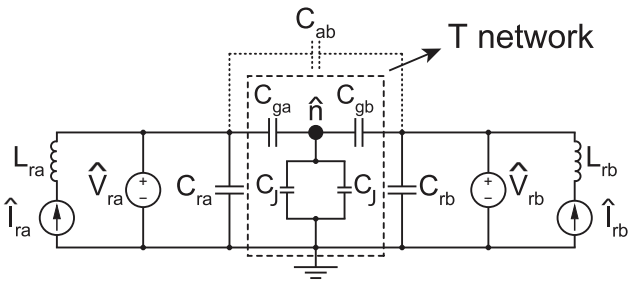

Figure 5.3: Equivalent circuit diagram for an implementation of two-resonator circuit QED based on a charge qubit (cf. Subsec. 5.1.3 for details). $\hat{V}_{\rm ra}$ and $\hat{V}_{\rm rb}$: quantized voltage sources associated with resonators A and B in parallel to the self-capacitances $C_{\rm ra}$ and $C_{\rm rb}$ of the resonators. $\hat{I}_{\rm ra}$ and $\hat{I}_{\rm rb}$: quantized current sources associated with resonators A and B in series to the self-inductances $L_{\rm ra}$ and $L_{\rm rb}$ of the resonators. The number of excess Cooper pairs on the charge qubit island (big dot) is $\langle n|\,\hat{n}\,|n\rangle$. $C_{\rm J}$: capacitance of each of the two Josephson tunnel junctions connecting the island to ground. $C_{\rm ga}$ and $C_{\rm gb}$: coupling capacitances between the qubit and the two resonators. $C_{\rm ab}$: first-order cross-capacitance between A and B (typically small, dotted line). The dashed box marks a T-network composed of $C_{\rm ga}$, $2C_{\rm J}$, and $C_{\rm gb}$.

rotating-wave approximation (RWA) and, finally, write the interaction Hamiltonian

$$\begin{aligned}\widehat{H}_{\rm c}^{\rm int} &= \hbar G_{\rm AB}(\hat{a}^\dagger+\hat{a})(\hat{b}^\dagger+\hat{b})\\ &\quad-\hbar G_{\rm A}\hat{\tilde{\sigma}}_z(\hat{a}^\dagger+\hat{a})-\hbar G_{\rm B}\hat{\tilde{\sigma}}_z(\hat{b}^\dagger+\hat{b})\\ &\quad+\hbar\widetilde{\omega}_{\rm A}\hat{a}^\dagger\hat{a}+\hbar\widetilde{\omega}_{\rm B}\hat{b}^\dagger\hat{b}\,,\end{aligned}\tag{5.8}$$

where all constant energy offsets, e.g., the Lamb shifts, have been neglected. Remarkably, in the first line of Eq. (5.8) we identify a geometric resonator-resonator interaction term with second-order coupling coefficient $G_{\rm AB}\equiv v_{\rm A0}v_{\rm B0}C_{\rm ga}C_{\rm gb}/C_\Sigma\hbar$. Furthermore, the two terms in the second line of Eq. (5.8) represent the expected first-order interactions between qubit and resonators, which are characterized by the coupling coefficients $G_{\rm A}\equiv e(C_{\rm ga}/C_\Sigma)v_{\rm A0}/\hbar$ and $G_{\rm B}\equiv e(C_{\rm gb}/C_\Sigma)v_{\rm B0}/\hbar$, respectively. In the third line, the two small renormalizations $\widetilde{\omega}_{\rm A}\equiv(C_{\rm ga}v_{\rm A0})^2/C_\Sigma\hbar$ and $\widetilde{\omega}_{\rm B}\equiv(C_{\rm gb}v_{\rm B0})^2/C_\Sigma\hbar$ of the resonator angular frequencies are artifacts due to the simple model behind the Hamiltonian of Eq. (5.6). A more advanced model based on a realistic circuit topology yields similar renormalization terms, which, however, are governed by different topology-dependent constants. Among the possible ways to find the correct constants, we choose the circuit transformations of Figs. 5.3, 5.4, and 5.5. This approach also allows us to better understand the geometric second-order interaction term.

In Fig. 5.3, the two cavities are represented as LC-resonators with total capacitances and inductances $C_{\rm ra}$, $C_{\rm rb}$, $L_{\rm ra}$, and $L_{\rm rb}$, respectively. The quantized voltages and currents of the two resonators are $\hat{V}_{\rm ra}\equiv v_{\rm A0}(\hat{a}^\dagger+\hat{a})$, $\hat{V}_{\rm rb}\equiv v_{\rm B0}(\hat{b}^\dagger+\hat{b})$, $\hat{I}_{\rm ra}\equiv i_{\rm A0}\,j(\hat{a}^\dagger-\hat{a})$, and $\hat{I}_{\rm rb}\equiv i_{\rm B0}\,j(\hat{b}^\dagger-\hat{b})$, respectively. Also, $C_{\rm ab}$ accounts for a first-order cross-capacitance between resonators A and B, which, for simplicity, is neglected in Eqs. (5.7) and (5.8). In addition, here we are only interested in the

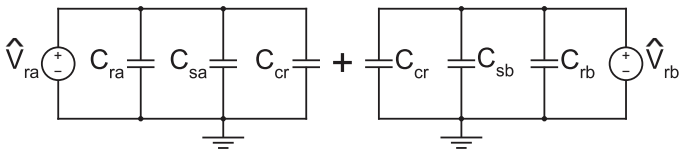

Figure 5.4: The circuit of Fig. 5.3 expressed as the sum of two topologically less complex circuits. $C_{\rm cr} \equiv C_{\rm ga}C_{\rm gb}/C_\Sigma$: second-order cross-capacitance. $C_{\rm sa} \equiv 2C_{\rm J}C_{\rm ga}/C_\Sigma$ and $C_{\rm sb} \equiv 2C_{\rm J}C_{\rm gb}/C_\Sigma$: resonator shift capacitances. $C_{\rm ab}$ is neglected for simplicity.

geometric properties of the charge quantum circuit. The dynamic properties of this circuit are studied following a more canonical approach within a two-level approximation in Sec. 5.2. The dynamic properties are governed by the two Josephson tunnel junctions and by the number of excess Cooper pairs on the island, $\langle n|\,\hat{n}\,|n\rangle$. To simplify our derivations, we can then assume $\hat{n} = 0$ and consider only the capacitance $C_{\rm J}$ of the two Josephson tunnel junctions, but not their Josephson energy.

We now derive in three steps the geometric part of the interaction Hamiltonian by means of circuit theory. The procedure is visualized in Figs. 5.3, 5.4, and 5.5. The steps are:

(i) First, we assume that the circuit associated to the charge qubit is positioned at a voltage antinode [131] of both resonators. Consequently, we can replace the two current sources of Fig. 5.3 with open circuits, $\hat{I}_{\rm ra} = \hat{I}_{\rm rb} = 0$. Thus, we can eliminate both $L_{\rm ra}$ and $L_{\rm rb}$ from the circuit diagram because they are in series to open circuits;

(ii) Second, we apply the superposition principle of circuit theory [264]. One at the time, we replace each of the two voltage sources with short circuits, $\hat{V}_{\rm ra} = 0$ or $\hat{V}_{\rm rb} = 0$. This allows us to split up the circuit of Fig. 5.3 into the two subcircuits of Fig. 5.4, which are topologically less complex. As a consequence, in the respective subcircuits, $C_{\rm rb}$ or $C_{\rm ra}$ can be substituted by short circuits and all other capacitors opportunely rearranged. In this way, for the case of cavity A, we find the small shift capacitance $C_{\rm sa} \equiv 2C_{\rm J}C_{\rm ga}/C_\Sigma$, which gives the correct angular frequency renormalization of the resonator, $\widetilde{\omega}_{\rm A}^{\rm corr} \equiv 2C_{\rm J}C_{\rm ga}v_{\rm A0}^2/C_\Sigma\hbar$.

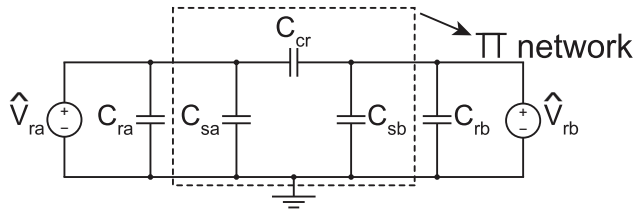

Figure 5.5: The circuits of Fig. 5.4 rearranged as a single Π-network (dashed box). The latter is equivalent to the T-network of Fig. 5.3. The magnitudes of $C_{\rm ra}$ and $C_{\rm rb}$ are increased by the presence of the shift capacitances $C_{\rm sa}$ and $C_{\rm sb}$.

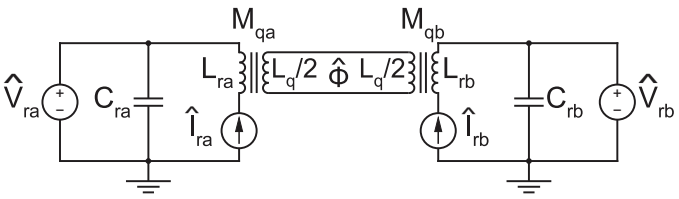

Figure 5.6: Equivalent circuit diagram for an implementation of two-resonator circuit QED based on a flux qubit (cf. Subsec. 5.1.3 for details). The two resonators A and B are inductively coupled via $M_{\rm qa}$ and $M_{\rm qb}$ to a flux qubit with total self-inductance $L_{\rm q} = L_{\rm q}/2 + L_{\rm q}/2$ and flux operator $\hat{\Phi}$. The first-order mutual inductance m between the two resonators is neglected to simplify the notation.

Remarkably, we also find the second-order cross-capacitance $C_{\rm cr} \equiv C_{\rm ga}C_{\rm gb}/C_{\Sigma}$, corresponding to the geometric second-order coupling between the resonators. This coincides with our result obtained in Eq. (5.3) of Subsec. 5.1.2 and is consistent with the simple model of Eqs. (5.6)-(5.8). We notice that $C_{\rm cr}$ deviates from the simple series of the two gate capacitances $C_{\rm ga}$ and $C_{\rm gb}$ because of the presence of $C_{\rm J}$ in C_{Σ}. For the case of cavity B, $C_{\rm sb} \equiv 2C_{\rm J}C_{\rm gb}/C_{\Sigma}$ and $\widetilde{\omega}_{\rm B}^{\rm corr} \equiv 2C_{\rm J}C_{\rm gb}v_{\rm B0}^2/C_{\Sigma}\hbar$ can be derived in an analogous manner. In Subsec. 5.1.2, the two renormalization constants as well as $C_{\rm J}$ are absorbed in the definitions of $C_{\rm AA}$, $C_{\rm BB}$, and $C_{\rm QQ}$, respectively;

(iii) Third, we notice that the cross-capacitance $C_{\rm cr}$, which is responsible for the geometric second-order interaction between A and B, is subjected to both quantum voltages $\hat{V}_{\rm ra}$ and $\hat{V}_{\rm rb}$. Hence, we can finally draw the circuit diagram of Fig. 5.5. Indeed, we could have identified the T-network of Fig. 5.3 (indicated by a dashed box) and transformed it into the equivalent Π-network of Fig. 5.5 (also indicated by a dashed box) in one single step [264], obtaining the same results. We prefer to explicitly show the steps of Fig. 5.4 for pedagogical reasons.

The second example is based on an RF SQUID. We choose the RF SQUID here for pure pedagogical reasons. In fact, our treatment could be extended to the more common case of three-Josephson-junction SQUID [189]. The Hamiltonian of an RF SQUID [97, 98, 125, 289] (cf. chapter 2, Subsec. 2.2.2) can be expressed as

$$\widehat{H}_{\rm f} = \frac{\hat{Q}^2}{2C_{\rm J}} + \frac{(\hat{\Phi} - \Phi_{\rm x})^2}{2L_{\rm q}} - E_{\rm J}\cos\left(2\pi\frac{\hat{\Phi}}{\Phi_0}\right), \tag{5.9}$$

where $\hat{Q}$ is the operator for the charge accumulated on the capacitor $C_{\rm J}$ associated with the Josephson tunnel junction. The flux operator $\hat{\Phi}$ is the conjugated variable of $\hat{Q}$, i.e., $[\hat{\Phi}, \hat{Q}] = j\hbar$. In analogy to the dimensionless gate charge $n_{\rm g}$ of the previous example, the flux bias $\Phi_{\rm x} \equiv \Phi_{\rm x}^{\rm DC} + \delta\Phi_{\rm x}$ consists of a DC and an AC component.

The self-inductance of the superconducting loop is defined as $L_{\rm q}$. When the RF SQUID is coupled to two quantized resonators, we can quantize the high-frequency excitations performing the transformations $\delta\Phi_{\rm x} \rightarrow \delta\hat{\Phi}_{\rm x} \equiv M_{\rm qa}i_{\rm A0}\,j(\hat{a}^{\dagger} -$

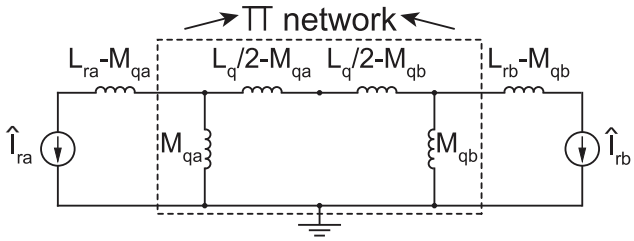

Figure 5.7: The disconnected circuit of Fig. 5.6 is transformed into a connected circuit [264]. Again, we can identify a Π-network (dashed box).

$\hat{a}) + M_{\rm qb} i_{\rm B0}\, j(\hat{b}^\dagger - \hat{b})$. Here, $M_{\rm qa}$ and $M_{\rm qb}$ are the mutual inductances between the loop and each resonator. We can then assume $\hat{\Phi} = 0$, perform a two-level approximation and a RWA, and finally obtain the same interaction Hamiltonian as in Eq. (5.8). However, in this case the coefficients are redefined as $\widetilde{\omega}_{\rm A} \equiv (M_{\rm qa} i_{\rm A0})^2 / L_{\rm q}\hbar$, $\widetilde{\omega}_{\rm B} \equiv (M_{\rm qb} i_{\rm B0})^2 / L_{\rm q}\hbar$, and $G_{\rm AB} \equiv i_{\rm A0} i_{\rm B0} M_{\rm qa} M_{\rm qb} / L_{\rm q}\hbar$. The term with coupling coefficient $G_{\rm AB}$ constitutes the geometric second-order interaction between A and B. As it appears clear from the discussion below, once again the renormalization terms $\widetilde{\omega}_{\rm A}$ and $\widetilde{\omega}_{\rm B}$ do not catch the circuit topology properly. This issue can be clarified analyzing the circuit diagram drawn in Fig. 5.6, where all the geometric elements for this example are shown. The geometric first-order mutual inductance m between the two resonators is neglected to simplify the notation. Again, the Josephson tunnel junctions responsible for the dynamic behavior are not included.

We now study the geometric part of the interaction Hamiltonian between the RF SQUID and the two resonators following a similar path as for the case of the single Cooper-pair box (cf. Figs. 5.6, 5.7, and 5.8). The four main transformation steps are:

(i) First, we assume the circuit corresponding to the flux qubit to be positioned at a current antinode. Thus, in Fig. 5.7, we replace all voltage sources and capacitors of Fig. 5.6 with short circuits. The self-inductance of the qubit loop is split up into two $L_{\rm q}/2$ inductances to facilitate the following transformation steps;

(ii) Second, a well-known theorem of circuit theory [264] allows us to transform

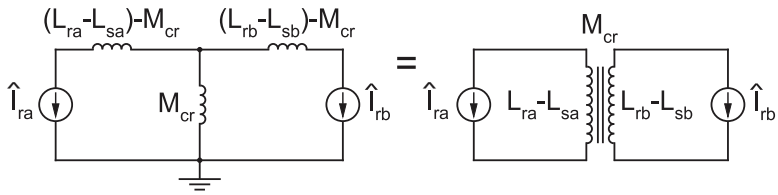

Figure 5.8: Left side: T-network obtained from the Π-network of Fig. 5.7. We identify the second-order mutual inductance $M_{\rm cr} \equiv M_{\rm qa} M_{\rm qb} / L_{\rm q}$ and the shift inductances $L_{\rm sa} \equiv M_{\rm qa}^2 / L_{\rm q}$ and $L_{\rm sb} \equiv M_{\rm qb}^2 / L_{\rm q}$. Right side: The connected circuit on the left side is transformed into a disconnected circuit [264].

the three disconnected circuits of Fig. 5.6 into the connected circuit of Fig. 5.7. Here, the region indicated by the dashed box evidently forms a Π-network;

(iii) Third, a Π-to-T-network transformation [264] results in the circuit on the left side of Fig. 5.8;

(iv) Fourth, applying the inverse theorem of that used in step (ii) finally allows us to draw the equivalent circuit on the right side of Fig. 5.8. Here, $M_{\mathrm{cr}} \equiv M_{\mathrm{qa}} M_{\mathrm{qb}} / L_{\mathrm{q}}$ represents the second-order mutual inductance between resonators A and B, corresponding to the geometric second-order coupling between them. Remarkably, this coincides with our result obtained in Eq. (5.3) of Subsec. 5.1.2 and is consistent with the simple model of Eq. (5.9).

However, in this model the small shift inductances $L_{\mathrm{sa}} \equiv M_{\mathrm{qa}}^2 / L_{\mathrm{q}}$ and $L_{\mathrm{sb}} \equiv M_{\mathrm{qb}}^2 / L_{\mathrm{q}}$ (here defined to be strictly positive) acquire the wrong sign. Our circuit approach reveals that the correct renormalization constants of the resonators angular frequency are $\widetilde{\omega}_{\mathrm{A}} = -L_{\mathrm{sa}} i_{\mathrm{A0}}^2 / \hbar$ and $\widetilde{\omega}_{\mathrm{B}} = -L_{\mathrm{sb}} i_{\mathrm{B0}}^2 / \hbar$. This result is also confirmed by our numerical simulations (cf. Sec. 5.4 and Table 5.1). In Subsec. 5.1.2, these renormalization constants are absorbed in the definitions of M_{AA} and M_{BB}.

5.2 Derivation of the Quantum Switch Hamiltonian

In this section, we analyze the Hamiltonian of a three-node quantum network as found in Subsec. 5.1.2. In particular, we focus on the relevant case of large qubit-resonator detuning, i.e., the dispersive regime of two-resonator circuit QED. Under this assumption, we are able to derive an effective Hamiltonian describing a quantum switch between two resonators. We compare the analytical results to those of extensive simulations (cf. Subsec. 5.2.1). We also propose a protocol for the quantum switch operation stressing two possible variants. One is based on a qubit population inversion and the other on an adiabatic shift pulse with the qubit in the energy groundstate (cf. Subsec. 5.2.2). Finally, we give a few examples of advanced applications of the quantum switch and, more in general, of dispersive two-resonator circuit QED (cf. Subsec. 5.2.3).

5.2.1 Balancing the Geometric and Dynamic Coupling

We now give the total Hamiltonian of the three-node quantum network of Figs. 5.1(a) and 5.1(b). In order to avoid unnecessarily cumbersome calculations, we restrict ourselves to purely inductive interactions up to geometric second-order corrections. In this framework, the most suitable quantum circuit to be used is a flux qubit. Hereafter, all specific parameters and corresponding simulations refer to this particular case. Nevertheless, the formalism which we develop remains general and can be extended to purely capacitive interactions (charge qubits) straightforwardly.

The flux qubit is assumed to be positioned at a current antinode. As a consequence, the vacuum fluctuations i_{A0} and i_{B0} have maximum values $i_{\mathrm{A0}}^{\mathrm{max}}$ and $i_{\mathrm{B0}}^{\mathrm{max}}$ at the qubit position and we can impose $v_{\mathrm{A0}} = v_{\mathrm{B0}} = 0$. Also, in the standard operation of a flux qubit no DC voltages are applied, i.e., $v_{\mathrm{DC}} = 0$, and the quasi-static

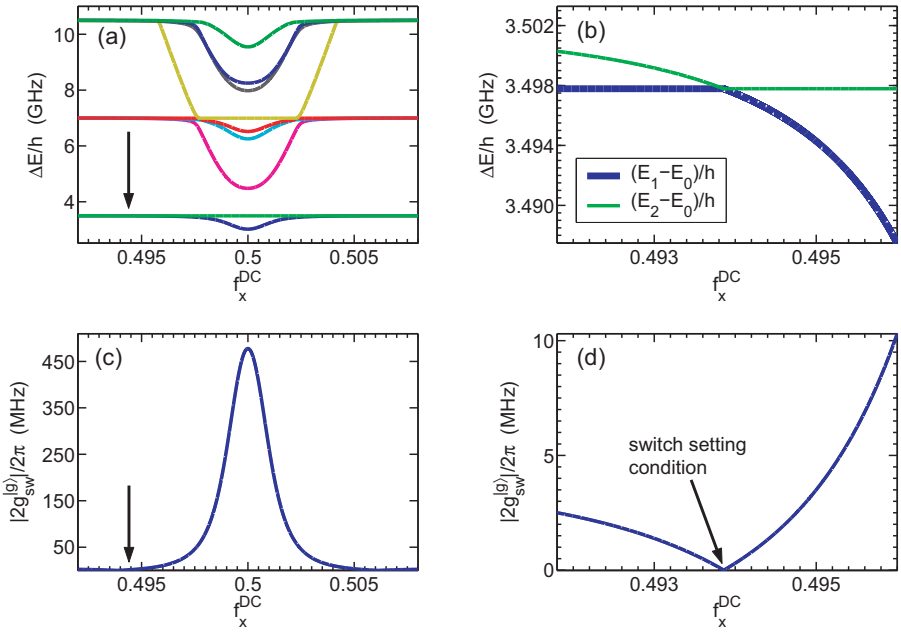

Figure 5.9: Simulation of the Hamiltonian of Eq. (5.10) in the dispersive regime (cf. Subsec. 5.2.1 for a detailed description of the system parameters). **(a)** The differences between the first nine excited energy levels of the quantum switch Hamiltonian and the groundstate energy level, ΔE, as a function of the frustration $f_{\rm x}^{\rm DC} \equiv \Phi_{\rm x}^{\rm DC}/\Phi_0$. The two lowest lines [blue (dark grey) and green (light grey), respectively] are associated with resonators A and B. The dispersive action of the qubit, which modifies the shape of the resonator lines, is clearly noticeable in the vicinity of the qubit degeneracy point. In this region, the third energy difference [hyperbolic shape, magenta (middle grey) line] represents the modified transition frequency of the qubit. **(b)** Close-up of the area indicated by the black arrow in **(a)**. Here, the two modified resonator lines [thick blue (dark grey) and thin green (light grey), respectively] cross each other. **(c)** Quantum switch coupling coefficient $|2g_{\rm sw}^{|{\rm g}\rangle}|$ extrapolated from the energy spectrum of **(a)** plotted versus $f_{\rm x}^{\rm DC}$. **(d)** Close-up of the area indicated by the black arrow of **(c)**. The switch setting condition $|2g_{\rm sw}^{|{\rm g}\rangle}| = 0$ is reached at $f_{\rm x}^{\rm DC} \simeq 0.4938$.

flux bias is usually controlled by an external coil and not by the cavities (cf. Subsec. 5.1.1). Again, we impose $i_{\rm DC} = 0$ and add to the Hamiltonian of Eq. (5.1) the term $(\Phi_{\rm x}^{\rm DC} - \Phi_0/2)\hat{I}_{\rm Q}$. Under all these assumptions and substituting $\mathbf{M}^{(n)}$ of Eq. (5.1) by $\mathbf{M}^{(2)}$ of matrix (5.5), we readily obtain

$$\begin{aligned}\widehat{H}' = &\frac{1}{2}\hbar\epsilon\hat{\tilde{\sigma}}_z + \frac{1}{2}\hbar\delta_{\rm Q}\hat{\tilde{\sigma}}_x + \hbar\omega_{\rm A}\hat{a}^\dagger\hat{a} + \hbar\omega_{\rm B}\hat{b}^\dagger\hat{b} \\ &+ \hbar g_{\rm A}\hat{\tilde{\sigma}}_z(\hat{a}^\dagger + \hat{a}) + \hbar g_{\rm B}\hat{\tilde{\sigma}}_z(\hat{b}^\dagger + \hat{b}) \\ &+ \hbar g_{\rm AB}(\hat{a}^\dagger + \hat{a})(\hat{b}^\dagger + \hat{b})\,. \end{aligned} \tag{5.10}$$

Here, all global energy offsets have been neglected and we have included both first- and second-order circuit theory contributions. In Eq. (5.10), $\hbar\epsilon \equiv 2i_{\rm Q}(\Phi_{\rm x}^{\rm DC} -$

$\Phi_0/2$) is the qubit energy bias, $\delta_{\rm Q} \equiv \delta_{\rm Q}(E_{\rm c}, E_{\rm J})$ is the qubit gap [97, 189], $\omega_{\rm A} \equiv 1/\sqrt{M_{\rm AA}C_{\rm AA}}$ and $\omega_{\rm B} \equiv 1/\sqrt{M_{\rm BB}C_{\rm BB}}$ are the angular frequencies of resonators A and B, respectively, $g_{\rm A} \equiv i_{\rm Q} i_{\rm A0} M_{\rm AQ}/\hbar$ and $g_{\rm B} \equiv i_{\rm Q} i_{\rm B0} M_{\rm BQ}/\hbar$ are the qubit-resonator coupling coefficients, and, finally, the second-order coupling coefficient $g_{\rm AB} \equiv i_{\rm A0} i_{\rm B0} \left(m + M_{\rm AQ}M_{\rm QB}/M_{\rm QQ}\right)/\hbar$. In general, $g_{\rm A}$ and $g_{\rm B}$ can be different due to parameter spread during the sample fabrication. Later, we show that the architecture proposed here is robust with respect to such imperfections. We now rotate the system Hamiltonian of Eq. (5.10) into the qubit energy eigenbasis $\{|{\rm g}\rangle, |{\rm e}\rangle\}$ obtaining

$$\begin{aligned}\widehat{H} = {} & \hbar\frac{\Omega_{\rm Q}}{2}\hat{\sigma}_z + \hbar\omega_{\rm A}\hat{a}^\dagger\hat{a} + \hbar\omega_{\rm B}\hat{b}^\dagger\hat{b} \\ & + \hbar g_{\rm A}\cos\theta\,\hat{\sigma}_z(\hat{a}^\dagger + \hat{a}) + \hbar g_{\rm B}\cos\theta\,\hat{\sigma}_z(\hat{b}^\dagger + \hat{b}) \\ & - \hbar g_{\rm A}\sin\theta\,\hat{\sigma}_x(\hat{a}^\dagger + \hat{a}) - \hbar g_{\rm B}\sin\theta\,\hat{\sigma}_x(\hat{b}^\dagger + \hat{b}) \\ & + \hbar g_{\rm AB}(\hat{a}^\dagger + \hat{a})(\hat{b}^\dagger + \hat{b})\,. \end{aligned} \tag{5.11}$$

Here, $\Omega_{\rm Q} = \sqrt{\epsilon^2 + \delta_{\rm Q}^2}$ is the $\Phi_{\rm x}^{\rm DC}$-dependent transition frequency of the qubit and $\theta = \arctan\left(\delta_{\rm Q}/\epsilon\right)$ is the usual mixing angle. In the Hamiltonian of Eq. (5.11) and in all the following Hamiltonians expressed in the qubit energy eigenbasis, we use the redefined Pauli operators $\hat{\sigma}_x$ and $\hat{\sigma}_z$, where $\hat{\sigma}_x = \hat{\sigma}^+ + \hat{\sigma}^-$, $\hat{\sigma}_z = \hat{\sigma}^+\hat{\sigma}^- - \hat{\sigma}^-\hat{\sigma}^+$, and $\hat{\sigma}^+$ and $\hat{\sigma}^-$ are the lowering and raising operators between the qubit energy groundstate $|{\rm g}\rangle$ and excited state $|{\rm e}\rangle$, respectively. Expressing $\widehat{H}$ in an interaction picture with respect to the qubit and both resonators, $\hat{a}^\dagger \to \hat{a}^\dagger \exp(+j\omega_{\rm A}t)$, $\hat{a} \to \hat{a}\exp(-j\omega_{\rm A}t)$, $\hat{b}^\dagger \to \hat{b}^\dagger \exp(+j\omega_{\rm B}t)$, $\hat{b} \to \hat{b}\exp(-j\omega_{\rm B}t)$, and $\hat{\sigma}^\mp \to \hat{\sigma}^\mp \exp\left(\mp j\Omega_{\rm Q}t\right)$, assuming $\omega_{\rm A} = \omega_{\rm B} \equiv \omega \equiv 2\pi f$, and performing a RWA yields

$$\begin{aligned}\widehat{\widetilde{H}} = {} & \hbar\sin\theta[\hat{\sigma}^-(g_{\rm A}\hat{a}^\dagger + g_{\rm B}\hat{b}^\dagger)e^{-j\Delta t} + \hat{\sigma}^+(g_{\rm A}\hat{a} + g_{\rm B}\hat{b})e^{+j\Delta t}] \\ & + \hbar g_{\rm AB}(\hat{a}^\dagger\hat{b} + \hat{a}\hat{b}^\dagger)\,. \end{aligned} \tag{5.12}$$

Here, $\Delta \equiv \Omega_{\rm Q} - \omega$ is the qubit-resonator detuning. The first two terms of Eq. (5.12) represent a standard two-mode JC dynamics [345, 348]. The last term, instead, constitutes a beam-splitter-type interaction specific to two-resonator circuit QED. This interaction is not present in the quantum optical version [345, 348]. The coupling coefficient $g_{\rm AB}$ is typically much smaller than $g_{\rm A}$ and $g_{\rm B}$ (see below). However, in the dispersive regime ($|\Delta| \gg \max\{g_{\rm A}, g_{\rm B}, g_{\rm AB}\}$), $g_{\rm AB}$ becomes comparable to all other dispersive coupling strengths. To gain further insight into this matter, we can define two superoperators $\hat{\Xi}^\dagger \equiv \hat{\sigma}^+(g_{\rm A}\hat{a} + g_{\rm B}\hat{b})$ and $\hat{\Xi} \equiv \hat{\sigma}^-(g_{\rm A}\hat{a}^\dagger + g_{\rm B}\hat{b}^\dagger)$. It can be shown that the Dyson series for the evolution operator associated with the time-dependent Hamiltonian of Eq. (5.12) can be rewritten in the exponential form $\widehat{U} = \exp(-j\widehat{\widetilde{H}}_{\rm eff}t/\hbar)$, where $\widehat{\widetilde{H}}_{\rm eff} = \hbar[\hat{\Xi}^\dagger, \hat{\Xi}]/\Delta + \hbar g_{\rm AB}(\hat{a}^\dagger\hat{b} + \hat{a}\hat{b}^\dagger)$. Thus

$$\begin{aligned}\widehat{\widetilde{H}}_{\rm eff} = {} & \hbar\frac{(g_{\rm A}\sin\theta)^2}{\Delta}\hat{\sigma}_z\left(\hat{a}^\dagger\hat{a} + \frac{1}{2}\right) \\ & + \hbar\frac{(g_{\rm B}\sin\theta)^2}{\Delta}\hat{\sigma}_z\left(\hat{b}^\dagger\hat{b} + \frac{1}{2}\right) \\ & + \hbar\left(\frac{g_{\rm A}g_{\rm B}\sin^2\theta}{\Delta}\hat{\sigma}_z + g_{\rm AB}\right)(\hat{a}^\dagger\hat{b} + \hat{a}\hat{b}^\dagger)\,. \end{aligned} \tag{5.13}$$

In this Hamiltonian, the first two terms represent dynamic (AC-Zeeman) shifts (AC-Stark shifts in the case of charge qubits) of the transition angular frequency of resonators A and B, respectively. If $g_{\mathrm{A}} = g_{\mathrm{B}} \equiv g$ and we only use eigenstates of $\hat{\sigma}_z$, the first two terms of Eq. (5.13) equally renormalize ω_{A} and ω_{B}, respectively. The Hamiltonian of Eq. (5.13) can be further simplified through an additional unitary transformation described by $\widehat{U}_0 = \exp(j\widehat{H}_0 t/\hbar)$, where $\widehat{H}_0 \equiv \hbar(g_{\mathrm{A}}^2 \sin^2\theta/\Delta)\hat{\sigma}_z(\hat{a}^\dagger\hat{a} + 1/2) + \hbar(g_{\mathrm{B}}^2 \sin^2\theta/\Delta)\hat{\sigma}_z(\hat{b}^\dagger\hat{b} + 1/2)$. When $g_{\mathrm{A}} = g_{\mathrm{B}} \equiv g$, this transformation yields the final effective Hamiltonian

$$\widehat{H}_{\mathrm{eff}} = \hbar\left(\frac{g^2 \sin^2\theta}{\Delta}\hat{\sigma}_z + g_{\mathrm{AB}}\right)(\hat{a}^\dagger\hat{b} + \hat{a}\hat{b}^\dagger)\,, \tag{5.14}$$

which constitutes the *second main result* of this chapter. This Hamiltonian is the key ingredient for the implementation of a quantum switch between the two resonators. In fact, it clearly represents a tunable interaction between A and B characterized by an effective coupling coefficient

$$g_{\mathrm{sw}}^{|\mathrm{g}\rangle} \equiv g_{\mathrm{AB}} - \frac{g^2 \sin^2\theta}{\Delta}\,, \tag{5.15a}$$

$$g_{\mathrm{sw}}^{|\mathrm{e}\rangle} \equiv g_{\mathrm{AB}} + \frac{g^2 \sin^2\theta}{\Delta}\,, \tag{5.15b}$$

for $|\mathrm{g}\rangle$ and $|\mathrm{e}\rangle$, respectively. The switching of such an interaction triggers, or prevents, the exchange of quantum information between A and B. On one hand, the first part of this interaction is a purely geometric coupling, which is constant and qubit-state independent. On the other hand, the second part is a dynamic coupling, which depends on the state of the qubit. The *switch setting condition*

$$\frac{g^2 \sin^2\theta}{|\Delta|} = |g_{\mathrm{AB}}| \tag{5.16}$$

can easily be fulfilled varying Δ, changing $\sin\theta$, or inducing AC-Zeeman or -Stark shifts [146] (cf. chapter 6, Subsec. 6.3.1). This task can also be accomplished modifying the qubit transition frequency Ω_{Q} via a suitable quasi-static magnetic field in connection with a special qubit design [139, 349] (cf. chapter 6, Subsec. 6.3.1). This allows one to keep the qubit at the degeneracy point. Here, we focus on the first option, i.e., finding a suitable qubit bias for which the detuning Δ fulfills the relation of Eq. (5.16). For a flux qubit, this can be realized polarizing the qubit by means of an external flux.

To better understand the switch setting condition, we numerically diagonalize the entire system Hamiltonian of Eq. (5.10), without performing any approximation. The results are presented in Fig. 5.9, which shows the energy spectrum of the quantum switch Hamiltonian and the effective coupling coefficient $|2g_{\mathrm{sw}}^{|\mathrm{g}\rangle}|$ for a flux qubit with $i_{\mathrm{Q}} = 370\,\mathrm{nA}$, $\delta_{\mathrm{Q}}/2\pi = 4\,\mathrm{GHz}$, $f = 3.5\,\mathrm{GHz}$, $g/2\pi = 472\,\mathrm{MHz}$, and $g_{\mathrm{AB}}/2\pi = 2.2\,\mathrm{MHz}$. The parameters for the flux qubit are chosen from our previous experimental works [159, 262], whereas the three coupling coefficients are the result of detailed simulations (cf. Sec. 5.4). It is noteworthy to mention that large vacuum Rabi couplings $g/2\pi$ on the order of 500 MHz have already been achieved both for flux and charge qubits [144, 347]. We have chosen the qubit to be already detuned from both resonators by 0.5 GHz when biased at the flux degeneracy point. Moving

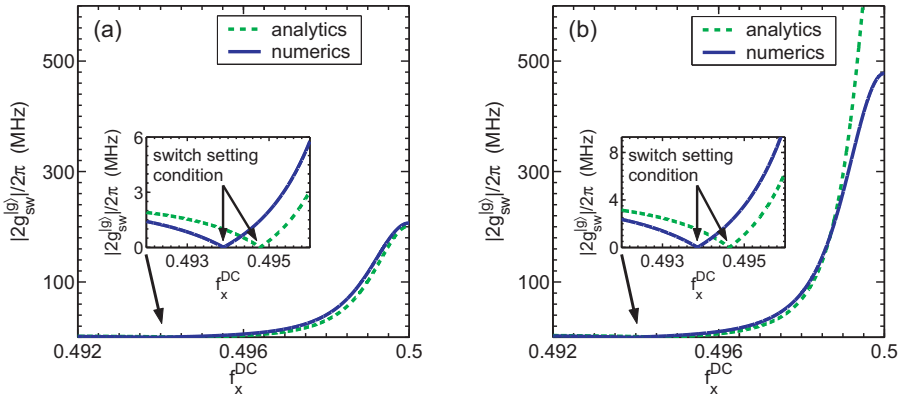

Figure 5.10: Comparison between the $f_{\mathrm{x}}^{\mathrm{DC}}$-dependence of the analytical expression for the coupling coefficient $|2g_{\mathrm{sw}}^{|\mathrm{g}\rangle}|$ obtained from Eq. (5.15a) and the one found by numerically diagonalizing the Hamiltonian of Eq. (5.10). **(a)** We choose a center frequency $f_{\mathrm{A}} = f_{\mathrm{B}} = f = 2.7\,\mathrm{GHz}$ for the two resonators. All the other parameters are the same as those used to obtain the results of Fig. 5.9. The analytical [dashed green (light grey) line] and the numerical [solid blue (dark grey) line] results are in excellent agreement. In the large detuning limit far away from the qubit degeneracy point, $|2g_{\mathrm{sw}}^{|\mathrm{g}\rangle}|$ saturates to the value $|2g_{\mathrm{AB}}| \simeq 2.6\,\mathrm{MHz}$. Inset: close-up of the region near the switch setting condition. **(b)** Here, we choose a center frequency $f_{\mathrm{A}} = f_{\mathrm{B}} = f = 3.5\,\mathrm{GHz}$ for the two resonators. The analytical [dashed green (light grey) line] and numerical [solid blue (dark grey) line] results are in good agreement away from the qubit degeneracy point. Closer to it they diverge (cf. Subsec. 5.2.1 for more details). In the large detuning limit far away from the qubit degeneracy point, $|2g_{\mathrm{sw}}^{|\mathrm{g}\rangle}|$ saturates to the value $|2g_{\mathrm{AB}}| \simeq 4.4\,\mathrm{MHz}$. Inset: close-up of the region near the switch setting condition.

sufficiently far from the degeneracy point enables us to increase the qubit-resonator detuning such that the system can be modeled by the Hamiltonian of Eq. (5.14).

Figure 5.9(a) shows the differences between the first nine excited energy levels of the quantum switch Hamiltonian and the groundstate energy level, $\Delta E_i \equiv E_i - E_0$ with $i = \{1, \ldots, 9\}$, as a function of the frustration $f_{\mathrm{x}} \equiv \Phi_{\mathrm{x}}^{\mathrm{DC}}/\Phi_0$. Here, E_i is the energy level of the i-th excited state and E_0 that of the groundstate. Due to the qubit-resonator detuning, the two lowest energy differences [blue (dark grey) and green (light grey) lines, respectively] correspond to the modified transition frequencies of the two resonators. Owing to the interaction with the qubit these lines are not flat. This effect becomes particularly evident in the region close to the qubit degeneracy point, where dispersivity is reduced. In this region, the third energy difference [hyperbolic shape, magenta (middle grey) line] represents the modified transition frequency of the qubit. When moving away from the qubit degeneracy point, a crossing between the modified resonator lines is encountered, as clearly shown in Fig. 5.9(b) [see, thick blue (dark grey) and thin green (light grey) lines]. This crossing represents the switch setting condition of Eq. (5.16). Figures 5.9(c) and 5.9(d) show the absolute value of the flux-dependent coupling coefficient $|2g_{\mathrm{sw}}^{|\mathrm{g}\rangle}|$ in the flux windows of Figs. 5.9(a) and 5.9(b), respectively. The switch setting

condition $|2g_{\rm sw}^{|{\rm g}\rangle}| = 0$ is reached at $f_{\rm x}^{\rm DC} \simeq 0.4938$.

A comparison between the analytic expression of Eq. (5.15a) with the qubit in $|{\rm g}\rangle$ [dashed green (light grey) lines] and a numerical estimate of the effective coupling coefficient $|2g_{\rm sw}^{|{\rm g}\rangle}|$ [solid blue (dark grey) lines] is shown in Figure 5.10. To clarify similarities and differences between analytical and numerical calculations, we choose two different sets of parameters. In Fig. 5.10(a), the center frequencies of the two resonators are set to be $f_{\rm A} = f_{\rm B} = f = 2.7\,{\rm GHz}$, whereas in Fig. 5.10(b) we choose $f_{\rm A} = f_{\rm B} = f = 3.5\,{\rm GHz}$. All the other parameters are equal to those used to obtain the results of Fig. 5.9. In Fig. 5.10(a), analytics and numerics agree over the entire frustration window. The inset shows that the switch setting condition obtained from the numerical simulation is only slightly shifted with respect to the analytical prediction. Also in Fig. 5.10(b), the agreement between analytical and numerical estimates is good far away from the qubit degeneracy point. However, closer to it the qubit and the two resonators are not detuned enough to guarantee dispersivity. Therefore, analytics and numerics start to deviate, as expected.[6] Again, the inset shows that the switch setting condition can be fulfilled. It is noteworthy to point out that both analytical and numerical estimates converge to the value $|2g_{\rm AB}|$ in the limit of large detuning. We find $|2g_{\rm AB}|/2\pi \simeq 2.6\,{\rm MHz}$ and $|2g_{\rm AB}|/2\pi \simeq 4.4\,{\rm MHz}$ from the simulations that produce Figs. 5.10(a) and 5.10(b), respectively. Additionally, we have two important remarks on the results shown in Figs. 5.10(a) and 5.10(b). First, the change of the coupling constants g and $g_{\rm AB}$ between the two parameter sets is a direct consequence of altering the resonator frequency. Although the mutual inductances remain unaffected, the vacuum (zero-point) currents are changed. Second, the fact that the switch setting condition occurs at almost the same frustration value for both parameter sets is due to our specific choice of these parameters.

Finally, we demonstrate that the quantum switch Hamiltonian is robust to parameter spread due to fabrication inaccuracies. Typically, for a center frequency of 5 GHz the expected spread around this value is approximately $\mp 10\,{\rm MHz}$ for two resonators fabricated on the same chip [351, 352]. Also, the coupling coefficients $g_{\rm A}$ and $g_{\rm B}$ can differ slightly. In this case, a generalized effective Hamiltonian for the quantum switch can be derived [353],

$$\begin{aligned}\widehat{H}_{\rm eff}^{\rm gen} = {} & \hbar\frac{(g_{\rm A}\sin\theta)^2}{\Delta_{\rm A}}\hat{\sigma}_z\hat{a}^\dagger\hat{a} + \hbar\frac{(g_{\rm B}\sin\theta)^2}{\Delta_{\rm B}}\hat{\sigma}_z\hat{b}^\dagger\hat{b} \\ & + \hbar\left[\frac{g_{\rm A}g_{\rm B}\sin^2\theta}{2}\left(\frac{1}{\Delta_{\rm A}}+\frac{1}{\Delta_{\rm B}}\right)\hat{\sigma}_z + g_{\rm AB}\right] \\ & \times\left(\hat{a}^\dagger\hat{b}e^{+j\delta_{\rm AB}t} + \hat{a}\hat{b}^\dagger e^{-j\delta_{\rm AB}t}\right), \end{aligned} \tag{5.17}$$

where $\Delta_{\rm A} \equiv \Omega_{\rm Q} - \omega_{\rm A}$, $\Delta_{\rm B} \equiv \Omega_{\rm Q} - \omega_{\rm B}$, and $\delta_{\rm AB} \equiv \omega_{\rm A} - \omega_{\rm B}$. From Eq. (5.17), we can deduce the generalized coupling coefficient of the switch, $g_{\rm sw}^{|{\rm g}\rangle,|{\rm e}\rangle} \equiv g_{\rm AB} \mp g_{\rm A}g_{\rm B}\sin^2\theta\,(1/2\Delta_{\rm A} + 1/2\Delta_{\rm B})$ for the qubit groundstate $|{\rm g}\rangle$ or excited state $|{\rm e}\rangle$, respectively. As a consequence, the *generalized switch setting condition* becomes

$$\left|\frac{g_{\rm A}g_{\rm B}\sin^2\theta}{2}\left(\frac{1}{\Delta_{\rm A}}+\frac{1}{\Delta_{\rm B}}\right)\right| = |g_{\rm AB}|\,. \tag{5.18}$$

[6] In a recent work, we have found an analytical expression which agrees with the numerical simulations over the entire frustration window of Fig. 5.10(b) [350].

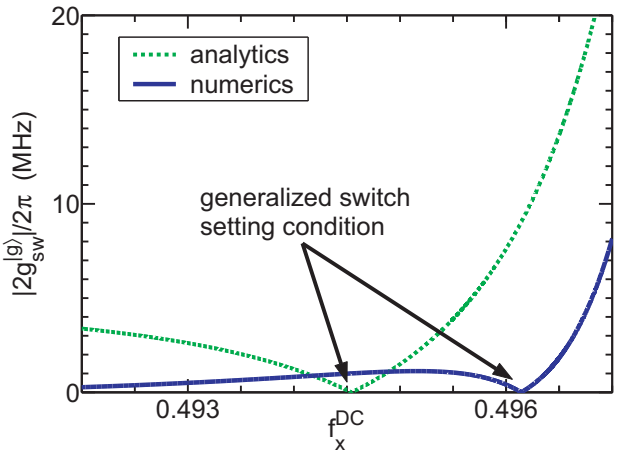

Figure 5.11: Robustness of the quantum switch to fabrication imperfections. Solid blue (dark grey) line: numerical simulation of the quantum switch coupling coefficient $|2g_{\mathrm{sw}}^{|\mathrm{g}\rangle}|$ as a function of the frustration $f_{\mathrm{x}}^{\mathrm{DC}}$. Here, we assume a relatively large spread of 1% for the resonators center frequencies [351, 352] and a difference of approximately 15% between g_{A} and g_{B}. Dashed green (light grey) line: plot of $|2g_{\mathrm{sw}}^{|\mathrm{g}\rangle}|$ extracted from the generalized switch setting condition of Eq. (5.18) for the same parameter spread as in the numerical simulations. For both the analytical and numerical result the switch setting condition is fulfilled (see black arrows).

This condition is displayed in Fig. 5.11 [dashed green (light grey) line] as a function of the external flux. Here, we assume two resonators with center frequencies $f_{\mathrm{A}} = 3.5\,\mathrm{GHz}$ and $f_{\mathrm{B}} = 3.5\,\mathrm{GHz} + 35\,\mathrm{MHz}$. This corresponds to a relatively large center frequency spread of 1% [351, 352].

In addition, we choose the two coupling coefficients $g_{\mathrm{A}}/2\pi = 472\,\mathrm{MHz}$ and $g_{\mathrm{B}}/2\pi = 549\,\mathrm{MHz}$ to differ by approximately 15%. It is remarkable that, also in this more general case, the switch setting condition can be fulfilled easily. We confirm this result by means of numerical simulations [solid blue (dark grey) line in Fig. 5.11] of the full Hamiltonian of Eq. (5.10), assuming fabrication imperfections. Interestingly, in contrast to the case where $\Delta_{\mathrm{A}} = \Delta_{\mathrm{B}}$ and $g_{\mathrm{A}} = g_{\mathrm{B}}$, we observe a different behavior of the analytical and numerical curves of Fig. 5.11 when moving far away from the qubit degeneracy point. The reasons behind this fact rely on the conditions used to obtain the second-order Hamiltonian of Eq. (5.17). If $\delta_{\mathrm{AB}} \gtrsim \max\left\{g_{\mathrm{A}} g_{\mathrm{B}} \sin^2\theta/2\Delta_{\mathrm{A}}, g_{\mathrm{A}} g_{\mathrm{B}} \sin^2\theta/2\Delta_{\mathrm{B}}, g_{\mathrm{AB}}\right\}$, as for the parameters chosen here, this Hamiltonian does not represent an accurate approximation anymore. In this case, as expected, only a partial agreement between analytics and numerics is found. Nevertheless, a clear switch setting condition is obtained in both cases. We notice that the numerical switch setting condition is shifted towards the degeneracy point with respect to the analytical solution. This is due to the detuning δ_{AB} present in Eq. (5.17), which is not accounted for when plotting the analytical solution.

All the above considerations clearly show that the requirements on the sample fabrication are substantially relaxed.

5.2.2 A Quantum Switch Protocol

We now propose a possible switching protocol based on three steps and discuss two different variants to shift from the zero-coupling to a finite-coupling condition characterized by a coupling coefficient $g_{\rm sw}^{\rm on}$. It is important to stress that this protocol is independent of the specific implementation (capacitive or inductive) of the switch. For definiteness, we choose a quantum switch based on a flux qubit in the following.

(i) First, we initialize the qubit in the groundstate $|{\rm g}\rangle$;

(ii) Second, in order to fulfill the switch setting condition, we choose the appropriate detuning Δ by changing the quasi-static bias of the qubit. For the switch operation to be practical, we assume $\Delta = \Delta_1 > 0$. In this way, the sign of the coefficient in front of the $\hat{\sigma}_z$-operator of Eq. (5.14) remains positive and, as a consequence, the switch is off in the groundstate $|{\rm g}\rangle$ (where the eigenvalue of $\hat{\sigma}_z$ is -1), i.e., $g_{\rm sw}^{|{\rm g}\rangle} = 0$;

(iii) Third, the state of the quantum switch can now be changed from off to on in two different ways, (a) or (b):

(a) *Population-inversion.* The qubit is maintained at the bias point preset in (ii). Its population is then inverted from $|{\rm g}\rangle$ to $|{\rm e}\rangle$, e.g., applying a Rabi π-pulse of duration t_π. Such a pulse effectively changes the switch to the on-state, $g_{\rm sw}^{|{\rm e}\rangle} = 2g_{\rm AB}$. In this case, $g_{\rm sw}^{\rm on} = 2g_{\rm AB}$. Under these conditions, the two resonators are effectively coupled and the A-to-B transfer time is $t = \pi/2g_{\rm sw}^{\rm on}$, which also constitutes the required time-scale for most of the operations to be discussed in Subsec. 5.2.3;

(b) *Adiabatic-shift pulse.* We opportunely change the quasi-static bias of the qubit by applying an adiabatic shift pulse [262] (cf. chapter 8, Sec. 8.2). In this way, the qubit transition frequency becomes effectively modified. As a consequence, the detuning Δ is changed from Δ_1 to Δ_2 such that $g_{\rm sw}^{|{\rm g}\rangle} = \widetilde{g}_{\rm sw} = g_{\rm AB} - g^2\sin^2\theta/\Delta_2 \neq 0$. In other words, the geometric and dynamic coupling coefficients are not balanced against each other anymore and the switch is set to the on-state. In this case, $g_{\rm sw}^{\rm on} = \widetilde{g}_{\rm sw}$. The rise time $t_{\rm rise}$ of the shift pulse has to fulfill the condition $2\pi/g_{\rm sw}^{\rm on} \gtrsim t_{\rm rise} \gtrsim \max\left\{2\pi/\delta_{\rm Q}, 2\pi/\omega\right\}$ [141, 262].

Variant (b) strongly benefits from the dependence of $\widetilde{g}_{\rm sw}$ on the external quasi-static bias of the qubit [see Figs. 5.9(c) and 5.9(d)]. We can distinguish between two possible regimes. The first regime is for a flux bias close to the qubit degeneracy point, where the qubit-resonator detuning is reduced and, thus, $\Delta_2 < \Delta_1$. In this case, the dynamic contribution to $\widetilde{g}_{\rm sw}$ dominates over the geometric one. This enables us to achieve very large resonator-resonator coupling strengths, which is a highly desirable condition to perform fast quantum operations (e.g., cf. Sec. 5.2.3). The second regime is for a flux bias far away from the qubit degeneracy point, where the qubit-resonator detuning is increased and, thus, $\Delta_2 > \Delta_1$. In this case, the geometric contribution to $\widetilde{g}_{\rm sw}$ dominates over the dynamic one. Since very far away from the qubit degeneracy point $\widetilde{g}_{\rm sw} \to |2g_{\rm AB}|$ [cf. Subsec. 5.2.1 and Figs. 5.10(a) and 5.10(b)], operating the system in the second regime allows us to probe the pure

geometric coupling between A and B. This would constitute a direct measurement of the geometric second-order coupling when $M_{\mathrm{AQ}}M_{\mathrm{QB}}/M_{\mathrm{QQ}} \gg m$.

5.2.3 Advanced Applications: Nonclassical States and Entanglement

We now provide a few examples showing how the quantum switch architecture can be exploited to create nonclassical states of the microwave radiation as well as entanglement of the resonators and qubit degrees of freedom. In this subsection, when we discuss about *the* qubit we refer to the one used for the quantum switch operation. If the presence of another qubit is required, we refer to it as the auxiliary qubit.

Fock State Transfer and Entanglement between the Resonators

First, we assume the quantum switch to be turned off, e.g., following the protocol outlined in Subsec. 5.2.2 with the qubit in the groundstate $|\mathrm{g}\rangle$. In addition, we assume resonator A to be initially prepared in a Fock state $|1\rangle_{\mathrm{A}}$, while cavity B remains in the vacuum state $|0\rangle_{\mathrm{B}}$. Following the lines of Ref. [150], for example, a Fock state $|1\rangle_{\mathrm{A}}$ can be created in A by means of an auxiliary qubit coupled to it. A population inversion of the auxiliary qubit (via a π-pulse) and its subsequent relaxation suffice to achieve this purpose. Then, we turn on the quantum switch for a certain time t following either one of the two variants (a) or (b) introduced in Subsec. 5.2.2. The initial states are $|\mathrm{e}\rangle|1\rangle_{\mathrm{A}}|0\rangle_{\mathrm{B}}$ and $|\mathrm{g}\rangle|1\rangle_{\mathrm{A}}|0\rangle_{\mathrm{B}}$ for (a) and (b), respectively. The quantum switch is now characterized by an effective coupling $g_{\mathrm{sw}}^{\mathrm{on}}$ and the dynamics associated with the Hamiltonian of Eq. (5.14) is activated for the time t. In this manner, a coherent linear superposition of bipartite states containing a Fock state single photon [141, 150, 151, 289, 354] can be created

$$\cos\left(g_{\mathrm{sw}}^{\mathrm{on}}t\right)|1\rangle_{\mathrm{A}}|0\rangle_{\mathrm{B}} + e^{j\pi/2}\sin\left(g_{\mathrm{sw}}^{\mathrm{on}}t\right)|0\rangle_{\mathrm{A}}|1\rangle_{\mathrm{B}}\ , \tag{5.19}$$

where the qubit state does not change and qubit and resonators remain disentangled. If we choose to wait for a time $t = \pi/2g_{\mathrm{sw}}^{\mathrm{on}}$, we can exploit Eq. (5.19) as a mechanism for the transferring of a Fock state from resonator A to resonator B, $|1\rangle_{\mathrm{A}}|0\rangle_{\mathrm{B}} \rightarrow |0\rangle_{\mathrm{A}}|1\rangle_{\mathrm{B}}$. In this case, also the resonators remain disentangled. It is noteworthy to mention that the controlled transfer of a Fock state between two remote locations constitutes the basis of several quantum information devices [355]. If we choose to wait for a time $t = \pi/4g_{\mathrm{sw}}^{\mathrm{on}}$ instead, we can achieve maximal entanglement between the two remote resonators. This goes beyond the results obtained in atomic systems, where two nondegenerate orthogonally polarized modes of the same cavity have been used to create mode entanglement [345].

Tripartite Entanglement and GHZ States

We follow a modified version of variant (a) of the switching protocol. We start from the same initial conditions as in the previous example. Resonator A is in $|1\rangle_{\mathrm{A}}$ and resonator B is in $|0\rangle_{\mathrm{B}}$. The qubit is in $|\mathrm{g}\rangle$ and the switch setting condition is fulfilled, i.e., the switch is off. We then apply a $\pi/2$-pulse to the qubit bringing it into the symmetric superposition $\left(|\mathrm{g}\rangle + |\mathrm{e}\rangle\right)/\sqrt{2}$ [108]. Then, the state of the system is still

disentangled and can be written as

$$\frac{|\mathrm{g}\rangle\,|1\rangle_{\mathrm{A}}\,|0\rangle_{\mathrm{B}} + |\mathrm{e}\rangle\,|1\rangle_{\mathrm{A}}\,|0\rangle_{\mathrm{B}}}{\sqrt{2}}\,. \tag{5.20}$$

Now, the Hamiltonian of Eq. (5.14) yields the time evolution

$$\begin{aligned}\frac{1}{\sqrt{2}}\big(\,&|\mathrm{g}\rangle\,|1\rangle_{\mathrm{A}}\,|0\rangle_{\mathrm{B}} + \cos\left(g_{\mathrm{sw}}^{\mathrm{on}}t\right)|\mathrm{e}\rangle\,|1\rangle_{\mathrm{A}}\,|0\rangle_{\mathrm{B}}\\ &+ e^{j\pi/2}\sin\left(g_{\mathrm{sw}}^{\mathrm{on}}t\right)|\mathrm{e}\rangle\,|0\rangle_{\mathrm{A}}\,|1\rangle_{\mathrm{B}}\,\big)\end{aligned} \tag{5.21}$$

for the state of the quantum switch. Under these conditions, the dynamics displayed in Eq. (5.21) is characterized by two distinct processes. The first one acts on the $|\mathrm{g}\rangle\,|1\rangle_{\mathrm{A}}\,|0\rangle_{\mathrm{B}}$ part of the initial state of Eq. (5.20). This process is actually frozen because the quantum switch is turned off when the qubit is in $|\mathrm{g}\rangle$. The second process, instead, acts on the $|\mathrm{e}\rangle\,|1\rangle_{\mathrm{A}}\,|0\rangle_{\mathrm{B}}$ part of the initial state, starting the transfer of a single photon from resonator A to resonator B and vice versa. If during such evolution we wait for a time $t = \pi/2g_{\mathrm{sw}}^{\mathrm{on}}$, a tripartite entangled state

$$\frac{|\mathrm{g}\rangle\,|1\rangle_{\mathrm{A}}\,|0\rangle_{\mathrm{B}} + e^{j\pi/2}\,|\mathrm{e}\rangle\,|0\rangle_{\mathrm{A}}\,|1\rangle_{\mathrm{B}}}{\sqrt{2}} \tag{5.22}$$

of the GHZ class [356] is generated. Here, the two resonators can be interpreted as photonic qubits because only the Fock states $|0\rangle_{\mathrm{A,B}}$ and $|1\rangle_{\mathrm{A,B}}$ are involved. Hence, Eq. (5.22) represents a state containing maximal entanglement for a three-qubit system, which consists of two photonic qubits and one superconducting (charge or flux) qubit. The generation of GHZ states is important for the study of the properties of genuine multipartite entanglement. Interestingly, the quantum nature of our switch is embodied in the linear superposition of $|\mathrm{g}\rangle\,|1\rangle_{\mathrm{A}}\,|0\rangle_{\mathrm{B}}$ and $|\mathrm{e}\rangle\,|1\rangle_{\mathrm{A}}\,|0\rangle_{\mathrm{B}}$ of the initial state of Eq. (5.20).

Entanglement of Coherent States

Finally, we show how to produce entangled coherent states of the intracavity microwave fields of the two resonators. These are prototypical examples of the vast class of states referred to as Schrödinger cat states [331, 337, 357–359] (cf. chapter 6, Sec. 6.3). This time, we start with cavity A populated by a coherent state $|\alpha\rangle_{\mathrm{A}}$ instead of a Fock state $|1\rangle_{\mathrm{A}}$. Again, cavity B is in the vacuum state $|0\rangle_{\mathrm{B}}$ and the qubit in the symmetric superposition state $(|\mathrm{g}\rangle + |\mathrm{e}\rangle)/\sqrt{2}$, i.e., a modified version of variant (a) of the switching protocol is again employed. The total disentangled initial state can be written as

$$\frac{|\mathrm{g}\rangle\,|\alpha\rangle_{\mathrm{A}}\,|0\rangle_{\mathrm{B}} + |\mathrm{e}\rangle\,|\alpha\rangle_{\mathrm{A}}\,|0\rangle_{\mathrm{B}}}{\sqrt{2}}\,. \tag{5.23}$$

The resulting dynamics associated with the Hamiltonian of Eq. (5.14) yields a time evolution similar to that shown for Fock states in Eq. (5.21). In this case, the part of the evolution involving $|\mathrm{e}\rangle$ can be calculated either quantum-mechanically or employing a semi-classical model. In both cases, after a waiting time $t = \pi/2g_{\mathrm{sw}}^{\mathrm{on}}$, resonator B is in the state $|\alpha\rangle_{\mathrm{B}}$ and A in the vacuum state $|0\rangle_{\mathrm{A}}$. However, Eq. (5.23)

contains an initial linear superposition of $|\mathrm{g}\rangle\,|\alpha\rangle_{\mathrm{A}}\,|0\rangle_{\mathrm{B}}$ and $|\mathrm{e}\rangle\,|\alpha\rangle_{\mathrm{A}}\,|0\rangle_{\mathrm{B}}$, requiring a quantum-mechanical treatment of the time evolution. From this, one finds that, after the waiting time $t = \pi/2g_{\mathrm{sw}}^{\mathrm{on}}$ the quantum switch operation creates the tripartite GHZ-type entangled state

$$\frac{|\mathrm{g}\rangle\,|\alpha\rangle_{\mathrm{A}}\,|0\rangle_{\mathrm{B}} + e^{j\varphi}\,|\mathrm{e}\rangle\,|0\rangle_{\mathrm{A}}\,|\alpha\rangle_{\mathrm{B}}}{\sqrt{2}}\,, \tag{5.24}$$

where φ is an arbitrary phase. Again, the creation of such states clearly reveals the quantum nature of our switch, showing a departure from standard classical switches [264]. Remarkably, the state of Eq. (5.24) describes the entanglement of coherent ("classical") states in both resonators. This feature is peculiar to our quantum switch and cannot easily be reproduced in atomic systems [345]. In principle, in absence of dissipation the quantum switch dynamics continues transferring back the coherent state to cavity A. In order to stop this evolution, an ultimate measurement of the qubit along the x-axis of the Bloch sphere [150, 360] is necessary. This corresponds to a projection associated with the Pauli operator $\hat{\sigma}_x$, which creates the two-resonator entangled state

$$\frac{|\alpha\rangle_{\mathrm{A}}\,|0\rangle_{\mathrm{B}} + e^{j\varphi}\,|0\rangle_{\mathrm{A}}\,|\alpha\rangle_{\mathrm{B}}}{\sqrt{2}}\,. \tag{5.25}$$

This state is decoupled from the qubit degree of freedom.

Obviously, all the protocols discussed above need suitable measurement schemes to be implemented in reality. For instance, it is desirable to measure the transmitted microwave field through both resonators and, eventually, opportune cross-correlations between them by means of a cross-correlation homodyne detection apparatus as the one described and characterized in chapters 3 and 4. In addition, a direct measurement of the qubit state, e.g., by means of a DC SQUID coupled to it [141, 159] (cf. chapter 8) would allow for the full characterization of the quantum switch device.

In summary, we have shown that a rich landscape of nonclassical and multipartite entangled states can be created and measured by means of our quantum switch in two-resonator circuit QED.

5.3 Treatment of Decoherence

The discussion in the previous sections implicitly assumes pure quantum states. In reality, however, a quantum system gradually decays into an incoherent mixed state during its time evolution. This process, called decoherence, is due to the entanglement of the system with its environment and it is known to be a critical issue for solid-state quantum circuits. Since it is difficult to decouple these circuits from the large number of environmental degrees of freedom to which they are exposed, their typical decoherence rates cannot be easily minimized. Usually, they are in the range from 1 MHz to 1 GHz, depending on the specific implementation. In this section, we discuss the impact of the three most relevant decoherence mechanisms on the quantum switch architecture. These are: First, the population decay of resonators A and B with rates κ_{A} and κ_{B}, respectively; second, the qubit relaxation from the energy excited state to the groundstate at a rate γ_{r} due to high-frequency

noise; third, the qubit dephasing (loss of phase coherence) at a pure dephasing rate γ_φ due to low-frequency noise. We show by means of detailed analytical derivations that, despite decoherence mechanisms, a working quantum switch can be realized with readily available superconducting qubits and resonators.

Decoherence processes are most naturally described in the qubit energy eigenbasis $\{|\mathrm{g}\rangle, |\mathrm{e}\rangle\}$. Under the Markov approximation, the time evolution of the density matrix of the quantum switch Hamiltonian $\widehat{H}$ of Eq. (5.11) is described by the master equation

$$\dot{\hat{\rho}} = \frac{1}{j\hbar}(\widehat{H}\,\hat{\rho} - \hat{\rho}\widehat{H}) + \sum_{n=1}^{4} \hat{\mathcal{L}}_n\,\hat{\rho}\,. \tag{5.26}$$

Here, $\hat{\mathcal{L}}_n$ is the Lindblad superoperator defined as

$$\hat{\mathcal{L}}_n\,\hat{\rho} \equiv \gamma_n(\hat{X}_n\,\hat{\rho}\,\hat{X}_n^\dagger - \hat{X}_n^\dagger\hat{X}_n\,\hat{\rho}/2 - \hat{\rho}\,\hat{X}_n^\dagger\hat{X}_n/2)\,.$$

The indices $n = 1, 2, 3, 4$ label the decay of resonator A, the decay of resonator B, qubit relaxation, and qubit dephasing, respectively. Consequently, the generating operators are $\hat{X}_1 \equiv \hat{a}$, $\hat{X}_1^\dagger \equiv \hat{a}^\dagger$, $\hat{X}_2 \equiv \hat{b}$, $\hat{X}_2^\dagger \equiv \hat{b}^\dagger$, $\hat{X}_3 \equiv \hat{\sigma}^-$, $\hat{X}_3^\dagger \equiv \hat{\sigma}^+$, and $\hat{X}_4 = \hat{X}_4^\dagger \equiv \hat{\sigma}_z$. The corresponding decoherence rates are $\gamma_1 \equiv \kappa_\mathrm{A}$, $\gamma_2 \equiv \kappa_\mathrm{B}$, $\gamma_3 \equiv \gamma_\mathrm{r}$, and $\gamma_4 \equiv \gamma_\varphi/2$. For the resonators, κ_A and κ_B are often expressed in terms of the corresponding loaded quality factors Q_A and Q_B, $\kappa_\mathrm{A} \equiv \omega_\mathrm{A}/Q_\mathrm{A}$ and $\kappa_\mathrm{B} \equiv \omega_\mathrm{B}/Q_\mathrm{B}$, respectively. Although in general all four processes coexist, in most experimental situations one of them dominates over the others. In fact, it is a common experimental scenario that $\gamma_\varphi \gg \gamma_\mathrm{r}$, for example in the special case of a flux qubit operated away from the degeneracy point (see, e.g., Ref. [262]). In this situation, we can extract pessimistic relaxation and dephasing rates from the literature [118, 119, 261, 262], $\gamma_\mathrm{r} \simeq 1\,\mathrm{MHz}$ and $\gamma_\varphi \simeq 200\,\mathrm{MHz}$. In other words, dephasing is the dominating source of qubit decoherence.[7] The decay rates of the resonators can be engineered such that $\kappa_\mathrm{A}, \kappa_\mathrm{B} \lesssim \gamma_\mathrm{r} \ll \gamma_\varphi$ [351, 352]. For these reasons, hereafter we focus on dephasing mechanisms only. Hence, we analyze the following simplified master equation

$$\dot{\hat{\rho}} = \frac{1}{j\hbar}\big(\widehat{H}\,\hat{\rho} - \hat{\rho}\widehat{H}\big) + \hat{\mathcal{L}}_\varphi\,\hat{\rho}\,, \tag{5.27}$$

where $\hat{\mathcal{L}}_\varphi\,\hat{\rho} \equiv \hat{\mathcal{L}}_4\,\hat{\rho} = (\gamma_\varphi/2)(\sigma_z\,\hat{\rho}\hat{\sigma}_z - \hat{\rho})$.

The impact of qubit dephasing on the switch operation depends on the chosen protocol (cf. Subsec. 5.2.2). When employing the population-inversion protocol, qubit dephasing occurs within the duration time t_π of the control π-pulses. The time t_π coincides with the inverse of the qubit Rabi frequency and can be reduced to less than 1 ns using high driving power [361]. In this way, the time window during which the qubit is sensitive to dephasing is substantially shortened. However, it is more favorable to resort to the adiabatic shift pulse protocol. In this case, the qubit always remains in $|\mathrm{g}\rangle$ resulting in a complete elimination of pulse-induced dephasing. The relevant time scale during which dephasing occurs is therefore set

[7] At the qubit degeracy point, the scenario can be quite different and energy relaxation can become the dominating source of decoherence. However, qubit energy relaxation rates are typically $\lesssim 10\,\mathrm{MHz}$ in this situation and, thus, a reasonable operating time for the quantum switch is guaranteed.

by the operation time of the switch between two on-off events. Naturally, this time should be as long as possible if we want to perform many operations.

The effect of dephasing during the switch operation time is better understood by inspecting the effective quantum switch Hamiltonian $\widehat{H}_{\rm eff}$ of Eq. (5.14). In Subsec. 5.2.1, we deduce this effective Hamiltonian by means of a Dyson series expansion. This approach is very powerful and compact when dealing with the analysis of a unitary evolution. However, when treating master equations, we prefer to utilize a variant of the well-known Schrieffer-Wolff unitary transformation [131, 362], $\widehat{U}\,\widehat{H}\,\widehat{U}^{\dagger}$, where

$$\widehat{U} \equiv \exp\left[\frac{g_{\rm A}\sin\theta}{\Delta}(\hat{\sigma}^{-}\hat{a}^{\dagger}-\hat{\sigma}^{+}\hat{a}) + \frac{g_{\rm B}\sin\theta}{\Delta}(\hat{\sigma}^{-}\hat{b}^{\dagger}-\hat{\sigma}^{+}\hat{b})\right] \tag{5.28}$$

and $\widehat{U}^{\dagger}$ is its Hermitian conjugate. In the large-detuning regime, $g_{\rm A}\sin\theta, g_{\rm B}\sin\theta \ll \Delta$, we can neglect all terms of orders $(g_{\rm A}\sin\theta/\Delta)^2$, $(g_{\rm B}\sin\theta/\Delta)^2$, $g_{\rm A}g_{\rm B}\sin^2\theta/\Delta^2$, or higher. After a transformation into an interaction picture with respect to the qubit and both resonators (cf. Subsec. 5.2.1) and performing opportune RWAs, we obtain again $\widehat{H}_{\rm eff}$ of Eq. (5.14). The master equation governing the time evolution of the effective density matrix $\hat{\rho}^{\rm eff} \equiv \widehat{U}\,\hat{\rho}\,\widehat{U}^{\dagger}$ then becomes

$$\dot{\hat{\rho}}^{\rm eff} = \frac{1}{j\hbar}\left(\widehat{H}_{\rm eff}\,\hat{\rho}^{\rm eff} - \hat{\rho}^{\rm eff}\,\widehat{H}_{\rm eff}\right) + \hat{\mathcal{L}}_{\varphi}^{\rm eff}\,\hat{\rho}^{\rm eff}\,. \tag{5.29}$$

The analysis is complicated by the fact that also the Lindblad superoperator $\hat{\mathcal{L}}\hat{\rho}$ has to be transformed. For the sake of simplicity, we can assume $g_{\rm A} = g_{\rm B} \equiv g$ and find

$$\hat{\mathcal{L}}_{\varphi}^{\rm eff}\,\hat{\rho}^{\rm eff} \approx \hat{\mathcal{L}}_{\varphi}\,\hat{\rho}^{\rm eff} + 2\gamma_{\varphi} \times \mathcal{O}\left[\left(\frac{g\sin\theta}{\Delta}\right)^2\right]. \tag{5.30}$$

When deriving this expression, all terms of $\mathcal{O}\left(g\sin\theta/\Delta\right)$ are explicitly neglected by a RWA. This approximation relies on the condition $\left(\gamma_{\varphi}/\Delta\right) g\sin\theta \ll \Delta$, which is well satisfied in the large-detuning regime as long as $\gamma_{\varphi} \lesssim \Delta$. The latter requirement can easily be met by most types of existing superconducting qubits. In the frame of $\widehat{H}_{\rm eff}$, $\hat{\mathcal{L}}_{\varphi}\,\hat{\rho}^{\rm eff}$ has the standard Lindblad dephasing structure and the qubit appears only in the form of $\hat{\sigma}_z$-operators. Since the initial state of the switch operation is characterized by either no (adiabatic shift pulse protocol) or only very small (population-inversion protocol) qubit coherences, the effect of $\hat{\mathcal{L}}_{\varphi}\,\hat{\rho}^{\rm eff}$ on the time evolution of the system is negligible. All other nonvanishing terms are comprised in the expression $2\gamma_{\varphi} \times \mathcal{O}[(g\sin\theta/\Delta)^2]$ of Eq. (5.30) and scale with a factor smaller than $\gamma_{\varphi}^{\rm eff} \equiv 2\gamma_{\varphi}\left(g\sin\theta/\Delta\right)^2$. Hence, the operation of the quantum switch is robust to qubit dephasing on a characteristic time scale $T_{\varphi}^{\rm eff} = 1/\gamma_{\varphi}^{\rm eff} \gg 1/\gamma_{\varphi}$. For completeness, it is important to mention that the higher-order terms of Eq. (5.30) can contain combinations of operators such as $\hat{a}^{\dagger}\hat{a}$ and $\hat{b}^{\dagger}\hat{b}$. In this case, $T_{\varphi}^{\rm eff}$ would be reduced for a large number of photons populating the resonators. Fortunately, this does not constitute a major issue since the most interesting applications of a quantum switch require that the number of photons in the resonators is of the order of one.

In summary, we have shown that for suitably engineered cavities the quantum switch operation time for the adiabatic shift pulse protocol is limited only by the effective qubit dephasing time $T_\varphi^{\rm eff}$. The latter is strongly enhanced with respect to the intrinsic dephasing time $T_\varphi \equiv 1/\gamma_\varphi$. In this sense, the quantum switch is superior to the dual setup, where two qubits are dispersively coupled via one cavity bus [146]. Moreover, the intrinsic dephasing time T_φ and, consequently, $T_\varphi^{\rm eff}$ are further enhanced by choosing a shift pulse which sets the on-state bias near the qubit degeneracy point [262]. As explained in Subsec. 5.2.2, this regime takes place for a qubit-resonator detuning $\Delta_2 < \Delta_1$. In this case, the switch coupling coefficient is also substantially increased because of a dominating dynamic interaction. As a consequence, this option is particularly appealing in the context of the advanced applications discussed in Subsec. 5.2.3. Finally, we notice that for the population-inversion protocol the switch operation time could be limited by the qubit relaxation time $T_{\rm r} \equiv 1/\gamma_{\rm r}$. However, the switch setting condition is typically fulfilled for a bias away from the qubit degeneracy point. There, $T_{\rm r}$ is considerably enhanced by both a reduced $\sin\theta$ [262] and by the Purcell effect due to the presence of the cavities [120, 131].

5.4 An Example of Two-Resonator Circuit QED with a Flux Qubit

In this section, we focus on the geometry sketched in Fig. 5.2(a) and present one specific implementation of two-resonator circuit QED. As a particular case, the described setup can be operated as a superconducting quantum switch. In this example, we consider microstrip resonators. Coplanar wave guide resonators can also be used without significantly affecting our main results. In addition, we choose a flux qubit because this is our main topic of research [159, 261, 262, 289] (cf. chapters 2 and 8). Moreover, as shown in Subsec. 5.2.1, the dynamic properties of the quantum switch are independent of specific implementations. As a consequence, in this section we concentrate on its geometric properties only. It is worth mentioning again that such properties are inherent to circuit QED architectures and constitute a fundamental departure from quantum optical systems.

In Figs. 5.12(a) and 5.12(b), the design of a possible two-resonator circuit QED setup is shown. The overall structure is composed of two superconducting microstrip transmission lines, which are bounded by input and output capacitors, $C_{\rm a,in}$, $C_{\rm b,in}$, $C_{\rm a,out}$, and $C_{\rm b,out}$. This geometrical configuration forms the two resonators A and B. The input and output capacitors also determine the loaded or external quality factors $Q_{\rm A}$ and $Q_{\rm B}$ of the two resonators [363]. Both A and B are characterized by a length $\ell_{\rm m}$, which defines their center frequencies $f_{\rm A}$ and $f_{\rm B}$. We choose $\ell_{\rm m} = \lambda_{\rm m}/2 = 12\,{\rm mm}$, where $\lambda_{\rm m} \equiv \lambda_{\rm A} = \lambda_{\rm B}$ is the full wavelength of the standing waves on the resonators. The superconducting loop of the flux qubit circuit is positioned at the current antinode of the two $\lambda_{\rm m}/2$ resonators.

In Fig. 5.12(c), only the two microstrip resonators A and B are considered. They are chosen to have a width $W_{\rm m} = 10\,\mu{\rm m}$ and a thickness $t_{\rm m} = 100\,{\rm nm}$. The height of the dielectric substrate between each microstrip and the corresponding groundplane is $H_{\rm s} = 12.3\,\mu{\rm m}$. The substrate can opportunely be made of different materials, for example silicon, sapphire, amorphous hydrogenated silicon, or silicon

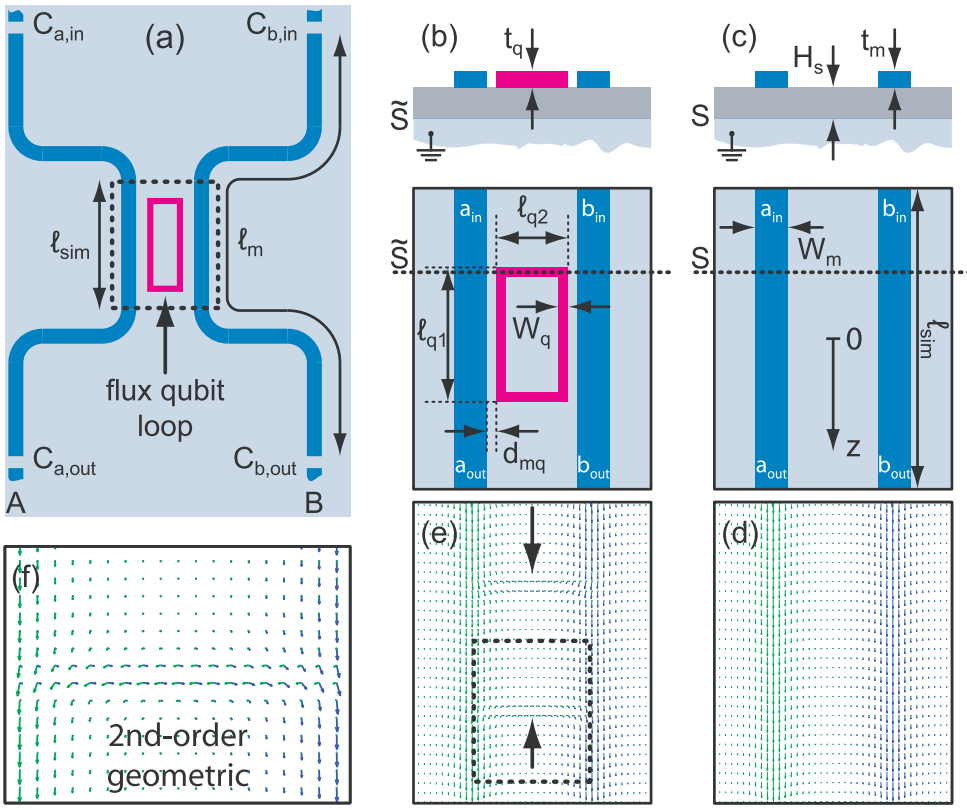

Figure 5.12: A possible setup for two-resonator circuit QED with a flux qubit. **(a)** Overall structure (dimensions not in scale). Two microstrip resonators A and B (thick blue lines) of length ℓ_{m} simultaneously coupled to a flux qubit loop [magenta (middle grey) rectangle]. $C_{\mathrm{a,in}}$, $C_{\mathrm{b,in}}$, $C_{\mathrm{a,out}}$, and $C_{\mathrm{b,out}}$: input and output capacitors for A and B. The dashed black box indicates the region of the close-up shown in **(b)**. ℓ_{sim}: length of the region used for the FASTHENRY [364] simulations. **(b)** Close-up of the region which contains the flux qubit loop in **(a)**. ℓ_{q1} and ℓ_{q2}: qubit loop lateral dimensions. W_{q}: width of the qubit lines. d_{mq}: distance between the qubit and each resonator. The dashed black line denominated as $\widetilde{S}$ marks the cross-section reported on the top part of the panel. t_{q}: thickness of the qubit loop lines. **(c)** As in **(b)**, but without the qubit loop. W_{m} and t_{m}: width and thickness (see cross-section S) of the two microstrip resonators. H_{s}: height of the dielectric substrate. The reference axis $0z$ is also indicated (cf. Appendix E). Both in **(b)** and **(c)**, $\mathrm{a_{in}}$, $\mathrm{a_{out}}$, $\mathrm{b_{in}}$, and $\mathrm{b_{out}}$ represent the input and output probing ports used in the simulations. **(d)** Current density distribution at high frequency (5 GHz) for the structures drawn in **(c)**. The currents are represented by small arrows, green (light grey) for resonator A and blue (dark grey) for resonator B. **(e)** Current density distribution at high frequency (5 GHz) for the structures drawn in **(b)**. The two black arrows indicate two high-current-density channels between the two resonators. The dashed black box marks the close-up area shown in **(f)**. **(f)** Close-up of one of the two geometric second-order interaction channels.

oxide, depending on the experimental necessities. A detailed study on the properties of a variety of dielectrics and on the dissipation processes of superconducting on-chip resonators can be found in Refs. [242, 252, 280–283]. The aspect ratio $W_{\rm m}/H_{\rm s}$ is engineered to guarantee a line characteristic impedance $Z_{\rm c} \simeq 50\,\Omega$, even if this is not a strict requirement for the resonators to function properly.[8] The remaining dimensions of our system are shown in Fig. 5.12(b): the lateral dimensions $\ell_{\rm q1} = 200\,\mu{\rm m}$ and $\ell_{\rm q2} = 87\,\mu{\rm m}$ of the qubit loop, the width $W_{\rm q} = 1\,\mu{\rm m}$ of each line forming the qubit loop, the interspace $d_{\rm mq} = 1\,\mu{\rm m}$ between qubit and resonators, and the thickness $t_{\rm q}(= t_{\rm m}) = 100\,{\rm nm}$ of the qubit lines. The dimensions of the qubit loop are chosen to optimize the qubit-resonator coupling strengths. This geometry results in a relatively large inductance $L_{\rm q} \simeq 780\,{\rm pH}$ (number obtained from FASTHENRY simulations [364]; cf. Table 5.1). Despite the large self-inductance $L_{\rm q}$, reasonable qubit coherence times are expected (see, e.g., Refs. [347] and [365]). Moreover, in the light of Sec. 5.3 these coherence times easily suffice for the operation of a superconducting quantum switch, where the qubit acts as a mere mediator for the exchange of virtual excitations.

In our numerical simulations (cf. Appendix E), we restrict ourselves to the region indicated by the black dashed box in Fig. 5.12(a), the close-up of which is shown in Fig. 5.12(b) and, in the absence of the flux qubit loop, in Fig. 5.12(c). This region is characterized by a length $\ell_{\rm sim} = 500\,\mu{\rm m}$ of the resonators and is centered at a position where the magnetic field reaches a maximum (antinode) and the electric field reaches a minimum (node). We notice that magnetic and electric fields can equivalently be expressed in terms of currents and voltages, respectively. There are two main hypotheses behind the validity of our simulation results for the entire two-resonator-qubit system. These are the uniformity of the electromagnetic field (voltage and current) in the simulated region and the abruptly[9] increasing geometric distance between resonators A and B outside of it [see sketch of Fig. 5.12(a)]. The three main implications of the above assumptions are explained in the following. First, all coupling strengths are dominated by inductive interactions and there are no appreciable capacitive ones. Inside the simulated region, in fact, the voltage is practically characterized by a node, which results in a vanishing coupling coefficient. Outside the simulated region, the effective distance $d_{\rm eff}$ between the cavities strongly increases together with the geometric one [227, 308]. As a consequence, the geometric first-order capacitance $c \propto 1/d_{\rm eff}$ becomes negligible. Second, the coupling coefficients between qubit and resonators can be obtained without integrating over the spatial distribution of the mode. This is because of the uniformity of the field, which, for all practical purposes, is constant over the restricted simulated region. Third, the geometric first-order coupling between the two resonators, which is proportional to their mutual inductance m, is still accurately determined. In fact, outside the simulated region any additional contribution to m becomes negligible. For all the reasons mentioned above, we are allowed to use the FASTHENRY [364] calculation software for our simulations. In this section, we utilize two different versions of FASTHENRY, one for superconducting materials and one for almost

[8] However, in order to avoid unwanted reflections all on-chip transmission lines connected to the resonators via the input and output capacitors have to be properly engineered to be $50\,\Omega$-matched.

[9] Obviously, this does not mean that sharp edges of the microwave on-chip structures are needed (which would imply unwanted radiation effects). It only means that the lines of the two resonators have to rapidly depart from each other.

Table 5.1: Relevant parameters for a possible two-resonator circuit QED setup based on a superconducting flux qubit. The various constants are described in Subsec. 5.4 and reported in Figs. 5.3, 5.4, 5.5, 5.6, 5.7, and 5.8. All inductances are simulated using the version of FASTHENRY for superconducting materials [364]. The capacitances are calculated analytically. All geometric second-order inductances are computed analytically and numerically and then compared to each other for consistency. We find an excellent agreement between the estimates $M_{\rm qa}M_{\rm qb}/L_{\rm q}$ and $\widetilde{m}-m$ for the second-order mutual inductance. Also, the shift inductances $M_{\rm qa}^2/L_{\rm q}$ and $M_{\rm qb}^2/L_{\rm q}$ coincide with their counterparts $L_{\rm sa}\equiv L_{\rm ra}^*-\widetilde{L}_{\rm ra}^*$ and $L_{\rm sb}\equiv L_{\rm rb}^*-\widetilde{L}_{\rm rb}^*$, respectively. These parameters are suitable for the implementation of a superconducting quantum switch.

$L_{\rm ra}^*$ (pH)	$L_{\rm ra}$ (nH)	$C_{\rm ra}$ (pF)	$\lambda_{\rm A}$ (mm)	$i_{\rm A0}\equiv\sqrt{\dfrac{\hbar\omega_{\rm A}}{2L_{\rm ra}}}$ (nA)	$L_{\rm q}$ (pH)	$M_{\rm qa}$ (pH)	$\dfrac{M_{\rm qa}M_{\rm qb}}{L_{\rm q}}$ (pH)	$+L_{\rm sa}\equiv\dfrac{M_{\rm qa}^2}{L_{\rm q}}$ (pH)	$+L_{\rm sb}\equiv\dfrac{M_{\rm qb}^2}{L_{\rm q}}$ (pH)
252.781	6.06697	3.36369	24	13.8249	784.228	61.2387	4.78192	+4.78200	+4.78184

$L_{\rm rb}^*$ (pH)	$L_{\rm rb}$ (nH)	$C_{\rm rb}$ (pF)	$\lambda_{\rm B}$ (mm)	$i_{\rm B0}\equiv\sqrt{\dfrac{\hbar\omega_{\rm B}}{2L_{\rm rb}}}$ (nA)	m (pH)	$\widetilde{m}-m$ (pH)	$-L_{\rm sa}\equiv\widetilde{L}_{\rm ra}^*-L_{\rm ra}^*$ (pH)	$-L_{\rm sb}\equiv\widetilde{L}_{\rm rb}^*-L_{\rm rb}^*$ (pH)
252.778	6.06693	3.36369	24	13.8249	2.90130	4.78192	−4.78100	−4.78100

perfect conducting ones. We use the second version only when we want to obtain current density distributions or the frequency dependence of an inductance. In these cases, due to technical limitations of the software, we cannot use the version valid for superconductors [364].

Figures 5.12(d) and 5.12(e) display the simulated current density distributions at a probing frequency of 5 GHz (high-frequency regime) for the different structures drawn in Fig. 5.12(c) and 5.12(b), respectively. Similar results can be found in a range between 1 GHz and 10 GHz (data not shown). Without loss of generality, these simulations are performed for almost perfect conductors using a FASTHENRY version which does not support superconductivity. The results of Fig. 5.12(d) clearly show that the two microstrip lines are regions characterized by a high current density separated by a region with a low current density in absence of the flux qubit loop. In this case, the geometric interaction between resonators A and B is reduced to a bare first-order coupling, which turns out to be very weak. On the contrary, in Fig. 5.12(e) the presence of the qubit loop clearly opens two new current channels between A and B. These are located at the position of the upper and lower qubit loop segments of Fig. 5.12(b). For clarity, the close-up of one of these channels is shown in Fig. 5.12(f). Notably, the two additional current channels of Fig. 5.12(e) represent the geometric second-order coupling.

We now study in more detail the relationship between geometric first- and second-order inductances for the structures of Fig. 5.12(b) and 5.12(c). The notation is that of Subsec. 5.1.3 and Figs. 5.6, 5.7, and 5.8. All quantities are computed numerically with the aid of FASTHENRY for superconducting materials [364] assuming a London penetration depth $\lambda_{\mathrm{L}} = 180\,\mathrm{nm}$. We notice that, in this case, the simulated inductances are independent of the probing frequency. In a first run of simulations, we calculate pure first-order inductances only (cf. Appendix E). These are the simulated test inductances L^*_{ra} and L^*_{rb} from which we obtain the self-inductances L_{ra} and L_{rb} of resonators A and B (more details in the next paragraph), the first-order mutual inductance m between the two resonators, the self-inductance L_{q} of the qubit loop, and the mutual inductances M_{qa} and M_{qb} between qubit and resonators. In a second run of simulations, we calculate directly (cf. Appendix E) the sum of first- and second-order inductances. These are the renormalized test inductances $\widetilde{L}^*_{\mathrm{ra}}$ and $\widetilde{L}^*_{\mathrm{rb}}$ of the portions of resonators A and B shown in Fig. 5.12(b) and the total mutual inductance $\widetilde{m}$ between the two resonators. The difference $\widetilde{m} - m = 4.78192\,\mathrm{pH}$, i.e., the geometric second-order coupling, coincides up to the sixth significant digit with the quantity $M_{\mathrm{qa}}M_{\mathrm{qb}}/L_{\mathrm{q}}$ expected from our general three-node network approach of Subsec. 5.1.2 and, equivalently, from the three-circuit theory of Subsec. 5.1.3 (cf. Table 5.1). We also find that the dominating geometric coupling between A and B is not the first-order inductance $m = 2.90130\,\mathrm{pH}$, but the second-order one. The ratio between second-order and first-order inductances is $(\widetilde{m} - m)/m \simeq 1.6$. In addition, the numerical simulations yield the two shift test inductances $|\widetilde{L}^*_{\mathrm{ra}} - L^*_{\mathrm{ra}}| = |\widetilde{L}^*_{\mathrm{rb}} - L^*_{\mathrm{rb}}| = 4.78100\,\mathrm{pH}$ (cf. also next paragraph). These shifts renormalize the bare center frequencies f_{A} and f_{B} of resonators A and B, respectively, and are found to be in very good agreement up to several decimal digits with their analytical estimates $L_{\mathrm{sa}} \equiv M^2_{\mathrm{qa}}/L_{\mathrm{q}}$ and $L_{\mathrm{sb}} \equiv M^2_{\mathrm{qb}}/L_{\mathrm{q}}$ of our three-circuit theory of Subsec. 5.1.3 (cf. Table 5.1). We point out that, in our definition, the quantities L_{sa} and L_{sb} are strictly positive. Remarkably, our simulations reveal that $L^*_{\mathrm{ra}} > \widetilde{L}^*_{\mathrm{ra}}$ and $L^*_{\mathrm{rb}} > \widetilde{L}^*_{\mathrm{rb}}$, reproducing the minus sign in the expressions $L_{\mathrm{ra}} - L_{\mathrm{sa}}$

and $L_{\rm rb} - L_{\rm sb}$ of Fig. 5.8. These findings confirm the superiority of the three-circuit theory of Subsec. 5.1.3 over the simple model which results in the Hamiltonian of Eq. (5.9). In the case of purely inductive interactions, the resonators suffer a small blue-shift of their center frequencies, i.e., a shift towards higher values. This is opposite to the redshift, i.e., towards lower frequencies, experienced by the resonators for a pure capacitive coupling [cf. Subsec. 5.1.3 and Fig. 5.5].

The numerical values of all parameters discussed above are listed in Table 5.1. The values of the bare self-inductances of the two resonators are first evaluated for the test length $\ell_{\rm sim}$ in absence of the qubit loop. This yields the simulated test inductances $L^*_{\rm ra}$ and $L^*_{\rm rb}$. Then, $L^*_{\rm ra}$ and $L^*_{\rm rb}$ are extrapolated to the full length $\ell_{\rm m}$ of each microstrip resonator to obtain $L_{\rm ra}$ and $L_{\rm rb}$, respectively. In the presence of the qubit loop, the simulated test inductances $\widetilde{L}^*_{\rm ra}$ and $\widetilde{L}^*_{\rm rb}$ can also be found. The resonator capacitances per unit length, $c_{\rm ra}$ and $c_{\rm rb}$, are calculated analytically by means of a conformal mapping technique [227]:

$$c_{\rm ra} = c_{\rm rb} = 2\pi\epsilon_0\epsilon_r \ln\left(\frac{8H_{\rm s}}{W^{\rm eff}_{\rm m}} + \frac{W^{\rm eff}_{\rm m}}{4H_{\rm s}}\right) . \tag{5.31}$$

Here, $\epsilon_0 = 8.854\times10^{-12}\,{\rm F/m}$ is the permittivity of vacuum (electric constant) [366], $\epsilon_{\rm r} = 11.5$ the relative dielectric constant of the substrate (in our example, sapphire or silicon; other dielectrics could be used), and $W^{\rm eff}_{\rm m} \equiv W_{\rm m}+0.398t_{\rm m}[1+\ln(2H_{\rm s}/t_{\rm m})]$ the effective width of the resonators [227]. As a consequence, the resonator capacitances are $C_{\rm ra} = \ell_{\rm m}c_{\rm ra}$ and $C_{\rm rb} = \ell_{\rm m}c_{\rm rb}$. Finally, from the knowledge of the velocity of the electromagnetic waves inside the two resonators, $\bar{c}_{\rm A} \equiv \ell_{\rm m}/\sqrt{(L_{\rm ra}C_{\rm ra})}$ and $\bar{c}_{\rm b} \equiv \ell_{\rm m}/\sqrt{(L_{\rm rb}C_{\rm rb})}$, one can find the full wavelengths $\lambda_{\rm A} = \bar{c}_{\rm A}/f_{\rm A}$ and $\lambda_{\rm B} = \bar{c}_{\rm B}/f_{\rm B}$ of the two resonators. As before, all these results are summarized in Table 5.1.

We now analyze the frequency dependence of the geometric first- and second-order coupling coefficients, i.e., the first- and second-oder mutual inductances, for a broad frequency span between 1 Hz and 10 GHz. Again, we assume almost perfectly conducting structures and use the FASTHENRY version which does not support superconductivity. The results are plotted in Figs. 5.13 and 5.14. In Fig. 5.13(a), we plot the frequency dependence of the simulated inductances $L_{\rm q}$ (which is renormalized by a factor of 8.5 for clarity) and $M_{\rm qa} = M_{\rm qb}$. From these, we then compute the expression $M_{\rm qa}M_{\rm qb}/L_{\rm q}$ for the second-order mutual inductance as derived in Subsecs. 5.1.2 and 5.1.3. This expression is plotted in Fig. 5.13(b). In Fig. 5.13(c), we plot the bare second-order mutual inductance $\widetilde{m}-m$ as a function of frequency. Remarkably, comparing Fig. 5.13(b) to Fig. 5.13(c), we find $M_{\rm qa}M_{\rm qb}/L_{\rm q} = \widetilde{m} - m$ with very high accuracy over the entire frequency range. In the frequency region of interest for the operation of a quantum switch, i.e., from approximately 1 GHz to 6 GHz, we find $L_{\rm q} \simeq 63.02\,{\rm pH}$, $M_{\rm qa} = M_{\rm qb} \simeq 7.37\,{\rm pH}$, and, consequently, $M_{\rm qa}M_{\rm qb}/L_{\rm q} = \widetilde{m} - m \simeq 7.33\,{\rm pH}$. All these results prove again the general validity of the derivations of Subsecs. 5.1.2 and 5.1.3.

Finally, we study the scattering matrix elements between resonators A and B both without and with flux qubit loop. In absolute value, these elements correspond to the isolation coefficients between A and B. As before, the FASTHENRY simulations are performed within the regions of Figs. 5.12(c) and 5.12(b), respectively. In these figures, we also define the input and output probing ports used in the simulations as $\rm a_{in}$, $\rm a_{out}$, $\rm b_{in}$, and $\rm b_{out}$, respectively. Under these assumptions, the scattering

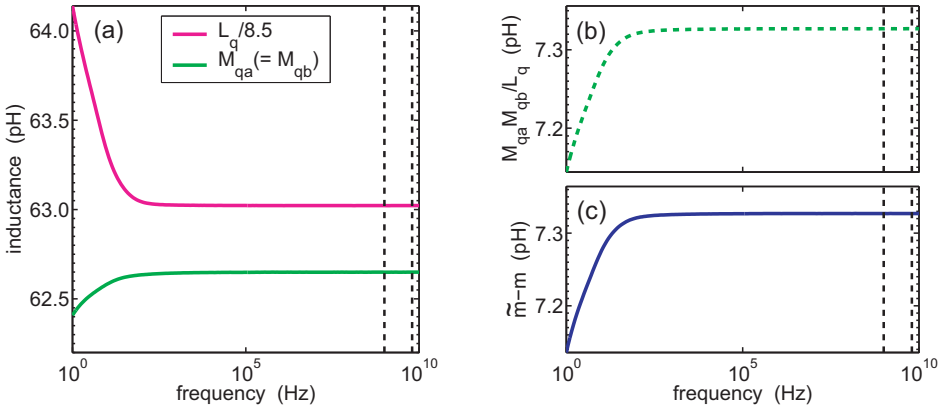

Figure 5.13: FASTHENRY simulation results for the frequency dependence of some relevant first- and second-order inductances relative to our example of two-resonator circuit QED. Vertical dashed black lines: frequency region of interest for the operation of the quantum switch from 1 GHz to 6 GHz. **(a)** Magenta (middle grey) line: qubit loop self-inductance $L_{\rm q}$ renormalized by a factor of 8.5 for clarity. Green (light grey) line: mutual inductance $M_{\rm qa}(=M_{\rm qb})$ between the qubit and resonator A (or B). **(b)** Bare second-order mutual inductance between the two resonators calculated with the results from **(a)** using the expression $M_{\rm qa}M_{\rm qb}/L_{\rm q}$. **(c)** Bare second-order mutual inductance between the two resonators, $\widetilde{m}-m$. The agreement with **(b)** is excellent.

matrix element $S_{\rm ab}=S_{\rm ba}$ in absence of the flux qubit loop is given by [227, 308]

$$S_{\rm ab}\equiv 20\log\left|\frac{-I^-_{\rm a_{in}}}{I^+_{\rm b_{in}}}\right|_{I^+=0}=20\log\frac{m}{L^*_{\rm ra}}\,, \tag{5.32}$$

where $I^+_{\rm b_{in}}$ is a test current wave incident on the input probing port $\rm b_{in}$ of resonator B. The current $-I^-_{\rm a_{in}}$ corresponds to the outgoing wave from the input probing port $\rm a_{in}$ of resonator A. The remaining current waves incident on the ports of the two resonators are $I^+\equiv\left\{I^+_{\rm a_{in}},I^+_{\rm a_{out}},I^+_{\rm b_{out}}\right\}$. In a similar way, the scattering matrix element $\widetilde{S}_{\rm ab}=\widetilde{S}_{\rm ba}$ in presence of the flux qubit loop is given by

$$\widetilde{S}_{\rm ab}=20\log\frac{\widetilde{m}}{\widetilde{L}^*_{\rm ra}}\,. \tag{5.33}$$

We note that the same results as in Eqs. (5.32) and (5.33) are obtained replacing the input probing port $\rm b_{in}$ with the output probing port $\rm b_{out}$ for the incident wave. In this case, the associated current $I^+_{\rm b_{in}}$ has to be exchanged with $I^+_{\rm b_{out}}$. Similar substitutions apply for the probing port and associated current of the outgoing waves. In the literature [227], the outgoing waves are often denominated as reflected waves. Equation (5.32) can be straightforwardly found via the definitions of mutual and self-inductance, $mI^+_{\rm b_{in}}=\Phi_{\rm ba}=L^*_{\rm ra}I^-_{\rm a_{in}}$. There, $\Phi_{\rm ba}$ is the flux generated in the portion of resonator A by the current flowing in the portion of resonator B of Fig. 5.12(c). Similar arguments lead to Eq. (5.33). When considering superconducting materials, the scattering matrix elements between A and B without and with flux qubit

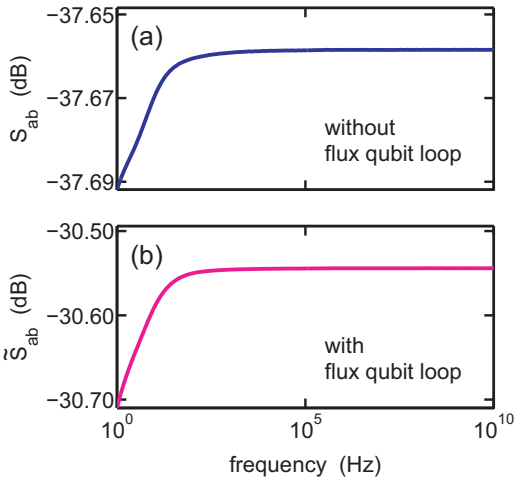

Figure 5.14: FASTHENRY simulation results for the frequency dependence of the scattering matrix elements between resonators A and B considering almost perfect conducting structures. Frequency span: From 1 Hz to 10 GHz. **(a)** Scattering matrix element $S_{\rm ab}$ in absence of the flux qubit loop. **(b)** Scattering matrix element $\widetilde{S}_{\rm ab}$ in presence of the flux qubit loop. Owing to the significant second-order mutual inductance between A and B, we find $|\widetilde{S}_{\rm ab}| < |S_{\rm ab}|$.

loop can be evaluated inserting the opportune numbers reported in Table 5.1 into Eqs. (5.32) and (5.33). This yields $S_{\rm ab} \simeq -38.80\,{\rm dB}$ and $\widetilde{S}_{\rm ab} \simeq -30.18\,{\rm dB}$. If we want to calculate the scattering matrix elements between A and B over a broad frequency span (e.g., from 1 Hz to 10 GHz), we can consider again almost perfect conducting structures.

In this case, the results are plotted in Figs. 5.14(a) and 5.14(b). In the high frequency region from 1 GHz to 6 GHz, we find $S_{\rm ab} \simeq -37.66\,{\rm dB}$ and $\widetilde{S}_{\rm ab} \simeq -30.54\,{\rm dB}$. These numbers are in good agreement with the results obtained for superconducting materials. In addition, it is noteworthy to mention that the scattering matrix elements between A and B calculated here with FASTHENRY for almost perfect conducting structures are in excellent agreement with those evaluated for similar structures by means of more advanced software based on the method of moments [227].

In conclusion, we have studied a detailed setup of two-resonator circuit QED based on a superconducting flux qubit. In this case, we have proven that the geometric second-order inductance found with our three-node network approach agrees well with that obtained from numerical simulations. Moreover, we have given a set of parameters (many sets can easily be found) for which the second-order inductance dominates over the first-order one.

5.5 Summary and Conclusions

In summary, in this chapter we have first introduced the formalism of two-resonator circuit QED, i.e., the interaction between two on-chip microwave cavities and a superconducting qubit circuit. Starting from the Hamiltonian of a generic three-

node network, we have shown that the qubit circuit mediates a geometric second-order coupling between the two resonators. For the case of strong qubit-resonator coupling, the geometric second-order interaction is a fundamental property of the system. In contrast to the geometric first-order coupling between the two resonators, the second-order one cannot be arbitrarily reduced by means of proper engineering.

With the aid of two prototypical examples, we have then highlighted the important role played by circuit topology in two-resonator circuit QED. Our models reveal a clear departure from a less detailed theory based on the Hamiltonian of a charge quantum circuit (e.g., a Cooper-pair box or a transmon) or a flux quantum circuit (e.g., an RF SQUID or a three-Josephson-junction SQUID) coupled to multiple quantized microwave fields. We have demonstrated that this simplified approach easily produces artifacts. We have also shown that our three-node network approach suffices to obtain correct results when including topological details appropriately into the definitions of the nodes.

We have subsequently demonstrated the possibility of balancing a geometric coupling against a dynamic second-order one. In this way, the effective interaction between the two resonators can be controlled by means of an external bias. Based on this mechanism, we have proposed possible protocols for the implementation of a quantum switch and outlined other advanced applications, which exploit the presence of the qubit.

Remarkably, we have found that the quantum switch operation is robust to decoherence processes. In fact, we have been able to show that the qubit acts as a mere mediator of virtual excitations between the two resonators, a condition which substantially relaxes the requirements on the qubit performances.

Finally, we have given detailed parameters for a specific setup of two-resonator circuit QED based on a superconducting flux qubit. We have performed numerical simulations of the geometric coupling coefficients and found an excellent agreement with our analytical predictions. In particular, we have confirmed the existence of a regime where the geometric second-order coupling dominates over the first-order one.

In conclusion, our findings show that, in circuit QED, the circuit properties of the system are crucial to provide a correct picture of the problem and also constitute a major difference with respect to atomic systems. This peculiar aspect of circuit QED makes it a very rich environment for the prediction and experimental implementation of unprecedented phenomena.

In the next chapter, we will study different regimes of two-resonator circuit QED, where, for example, the qubit and both cavities are on resonance. Under opportune conditions this gives rise to JC and anti-JC dynamics, which can be exploited to generate, e.g., Schrödinger cat states. Also, we will consider the case where one cavity is characterized by a high quality factor and the other one by a comparatively low quality factor. In this way, the low quality factor cavity can be used as an efficient readout device, which allows, e.g., for the reconstruction of the Wigner function of nonclassical states of the microwave radiation.

Chapter 6

Two-Resonator Circuit QED: Generation of Schrödinger Cat States and Quantum Tomography

The generation and measurement of nonclassical states of the microwave radiation represent fundamental tasks to understand the interplay between matter and light in solid-state systems. Circuit QED architectures are among the best candidates for the realization of such experiments. However, the lack of microwave single photon detectors and the difficulty in realizing quantum-limited microwave amplifiers make it hard to directly measure the microwave photons emitted by on-chip resonators, extrapolate their full-counting statistics, and perform full-state quantum tomography.[1] This is readily possible in the optical domain, where quantum homodyne tomography has been used to fully characterize squeezed states and Fock states [94, 95, 320, 321].

Recent experiments based on phase qubits capacitively coupled to coplanar waveguide (CPW) resonators have shown that an accurate measurement of the qubit state allows for the reconstruction of the entire Wigner function of intracavity fields. These can be Fock states, arbitrary superposition of Fock states, or even Schrödinger cat states [153]. This technique, which is well-known in quantum optics [367], has reached in circuit QED an extremely high level of precision compared to quantum optical implementations [71, 74]. In the case of phase qubits, the interaction between the qubit and the resonator is used to first generate quantum field states and, then, to encode information on such states into the qubit state. Finally, the qubit is read out with very high efficiency by means of a DC superconducting quantum interference device (SQUID) (cf. chapter 8).

Is it possible to perform similar or even more refined experiments employing only resonators? This is an important question considering that in many implementations of circuit QED [108, 131, 139, 143, 144] it is simpler to use a resonator rather than a DC SQUID [138, 141, 159] or a single-electron transistor (SET) [104, 368] as readout apparatus. Also, DC SQUIDs and SETs can possibly represent an unwanted source of dissipation [262, 369–371], whereas resonators are known to better preserve the qubit coherence [120].

[1] Microwave single photon detectors have been proposed [222–224] and quantum-limited amplifiers are being developed [194–196, 198, 199, 201, 203, 205, 208, 209]. In the near future it could also be possible to directly detect propagating nonclassical microwave fields.

In this chapter, we focus on a different regime of two-resonator circuit QED compared to the case analyzed in the previous chapter. We assume a qubit to be resonantly coupled to one mode of two different resonators, where the first resonator (hereafter also referred to as *quantum bus*) is characterized by a high quality factor and the second resonator (referred to as *leaky cavity*) by a relatively low one. The quantum bus is long lived and can be utilized to perform coherent dynamics and store quantum information, whereas the leaky cavity can be used as a fast independent readout of the qubit state.[2] We present realistic setups for the implementation of this specific case of two-resonator circuit QED. We then show that such setups can be exploited to generate entanglement of coherent states (i.e., Schrödinger cat states [331, 337, 357–359]) with large photon number. This can be realized by means of a strong driving pulse through the leaky cavity, which enables a simultaneous JC and anti-JC dynamics. Other modes of the leaky cavity, dispersively coupled to the qubit, can subsequently be used to switch on and off the quantum-bus–qubit interaction, to project, and, finally, to measure the qubit state. We propose a measurement technique based on a very short interaction time that allows one to obtain all necessary information about relevant observables of the field populating the quantum bus. Due to the short interaction time, our method is naturally robust to qubit dephasing and field relaxation. In addition, we show that the leaky cavity can be utilized to perform full-state quantum tomography of any given nonclassical field.

The regime of two-resonator circuit QED considered here is inherently different from the quantum switch regime analyzed in the previous chapter. In fact, under resonance conditions no quantum switch dynamics can take place. Nevertheless, the geometric first- and second-order coupling between the two resonators cannot be set to zero and must always be accounted for when studying the system Hamiltonian. Another crucial difference compared to the setup described in the previous chapter is represented by the presence of a leaky cavity. This is assumed to be in the so-called overcoupled limit, where the loaded quality factor of the cavity is dominated by the external quality factor (cf. chapter 2 and Refs. [227, 308]). This means that, as for the quantum bus, the leaky cavity is also characterized by very small internal losses. However, its total relaxation rate is enhanced because of a larger coupling to the transmission lines used to read it out. The last main departure from the previous chapter is the use of more than one mode of the same cavity [372]. This feature allows for an advanced control of the circuit QED system. For example, it makes possible to switch on and off the qubit-resonator interaction or to measure the qubit state taking advantage of a mode dispersively coupled to the qubit, while keeping another mode resonantly coupled to it.

The chapter is organized as follows. In Sec. 6.1, we introduce the two main ingredients for the implementation of two-resonator circuit QED in the regime considered here: the quantum bus and the leaky cavity. In the same section, we present the total Hamiltonian of the system. In Sec. 6.2, we show that, when strongly driven, the system under analysis gives rise to a simultaneous JC and anti-JC dynamics. In Sec. 6.3, we show that such dynamics can be exploited, for example, to generate large Schrödinger cat states. In the same section, we propose a method to measure relevant observables of these states. In Sec. 6.4, we study two different alternatives

[2]We remind that the measurement time depends on the quality factor of the resonator used to read out the qubit state [131]. The lower the quality factor, the faster the readout.

for the reconstruction of the Wigner function of any given intracavity field state. Finally, in Sec. 6.6 we summarize our results and draw our conclusions.

The material treated in this chapter, which is totally unpublished, has mainly been developed by the author with a strong support and encouragement from Enrique Solano. The author acknowledges many useful discussions with M. J. Storcz and H. Christ.

6.1 Quantum Bus vs. Leaky Cavity

In this section, we first present two setups for the implementation of two-resonator circuit QED, one suitable for charge and the other for flux qubits. Both setups are optimized to realize two-mode resonant dynamics, to switch on and off the qubit-resonator interaction, and to perform a fast qubit readout (cf. Subsec. 6.1.1). We then introduce the total system Hamiltonian (cf. Subsec. 6.1.2).

6.1.1 The Setup

Figures 6.1(a) and 6.2(a) show a possible implementation of two-resonator circuit QED for charge and flux qubits, respectively. In these implementations, one resonator, the quantum bus, B, is characterized by a high quality factor and the other one, the leaky cavity, L, by a comparatively low quality factor. The two resonators are engineered in an asymmetric T-shape design, where the leaky cavity is orthogonal to the quantum bus. This configuration helps reducing the geometric crosstalk between the two resonators. One end of the quantum bus is positioned nearby the center of the leaky cavity. The latter is a full-wavelength resonator (i.e., its length $\ell_{\rm L} = \lambda$) terminated with input and output capacitors at both edges, $C_{\rm L,in}$ and $C_{\rm L,out}$. These capacitors can be engineered to be large enough in order to operate the leaky cavity in the overcoupled limit. This means that the loaded quality factor of the leaky cavity, $Q_{\rm L}^{\rm load}$, is dominated by the external quality factor $Q_{\rm L,ext}$ instead of the internal quality factor $Q_{\rm L,int}$,

$$\frac{1}{Q_{\rm L}^{\rm load}} \equiv \frac{1}{Q_{\rm L,int}} + \frac{1}{Q_{\rm L,ext}} \approx \frac{1}{Q_{\rm L,ext}} \,. \tag{6.1}$$

In other words, the intrinsic quality of the leaky cavity must be as good as possible in order not to loose radiation through uncontrolled channels. Radiation should be "lost" only through the input and output capacitors that connect the cavity to the transmission lines used to access the cavity from outside and read it out.

In the case of charge qubits (cf. Fig. 6.1), the quantum bus is a $\lambda/2$ resonator (i.e., its length $\ell_{\rm B} = \lambda/2$) capacitively terminated on the end close to the leaky cavity via a stray capacitor $C_{\rm B}$. The other end is left open, i.e., capacitively terminated to infinity via a capacitor $C_{\rm B,\infty}$. This guarantees a very high loaded quality factor for the quantum bus, which, in this geometry, is as decoupled as possible from external networks. In this configuration, the charge qubit can be fabricated in a region of the leaky cavity where it couples well to the first three modes of the voltage [cf. Fig. 6.1(a) and 6.1(b)]. At the same time, the qubit resides close to the capacitive edge $C_{\rm B}$ of the quantum bus, thus being coupled to the voltage antinode of, e.g, the first mode of B [cf. Fig. 6.1(c)]. We notice that the edges of the leaky

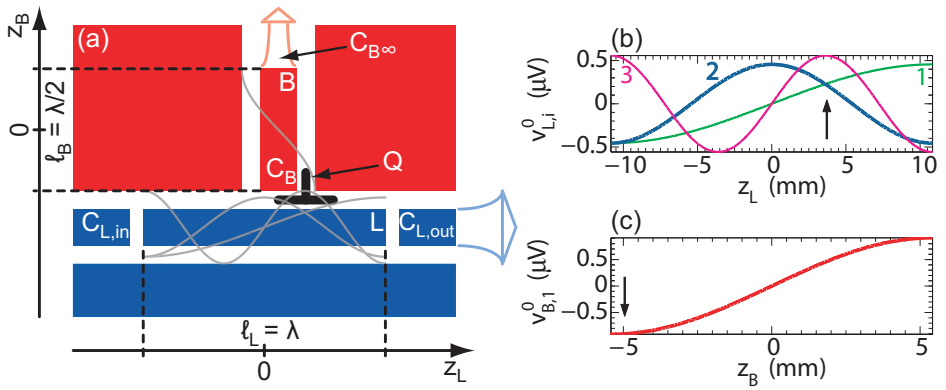

Figure 6.1: Two-resonator circuit QED setup for charge qubits. **(a)** The leaky cavity, L, is represented by the horizontal finite segment of CPW transmission line depicted in blue (dark grey). $C_{\mathrm{L,in}}$ and $C_{\mathrm{L,out}}$: input and output capacitors of L. $\ell_{\mathrm{L}} = \lambda$: total length of L. The reference axis $0z_{\mathrm{L}}$ is also indicated. The big blue arrow next to $C_{\mathrm{L,out}}$ symbolizes the high relaxation rate of L. The quantum bus, B, is represented by the vertical finite segment of CPW transmission line depicted in red (grey). C_{B}: stray capacitor terminating one end of B. $C_{\mathrm{B},\infty}$: open circuit (capacitor to infinity) terminating the other end of B. $\ell_{\mathrm{B}} = \lambda/2$: total length of B. The reference axis $0z_{\mathrm{B}}$ is also indicated. The small red arrow next to $C_{\mathrm{B},\infty}$ symbolizes the low relaxation rate of B compared to L. The qubit, Q, is indicated by the T-shape black line. The mode structures of L and B are shown for clarity (thin light grey lines). **(b)** Distribution of the zero-point fluctuations of the voltage $v^0_{\mathrm{L},i}$ ($i = \{1, 2, 3\}$) for the first three modes of L as a function of the position z_{L}. 1: first mode [light green (light grey) line]; 2: second mode [thick dark blue (dark grey) line]. The qubit is resonantly coupled to this mode; 3: third mode [magenta (middle grey) line]. The black arrow indicates the approximate position of the qubit with respect to z_{L}. The qubit is well coupled to all three modes. **(c)** Distribution of the zero-point fluctuations of the voltage $v^0_{\mathrm{B},1}$ for the first mode of B as a function of the position z_{B} [thick red (grey) line]. The black arrow indicates the approximate position of the qubit with respect to z_{B}.

cavity close to the capacitors $C_{\mathrm{L,in}}$ and $C_{\mathrm{L,out}}$ can also be used to couple the qubit to many voltage modes. In absolute value, the zero-point fluctuations of the voltage $v^0_{\mathrm{L},i}$ ($i = \{1, 2, 3\}$) are even larger at these points. However, their sign changes depending on the specific mode to be used [cf. Fig. 6.1(b)]. This does not have dramatic consequences, but, as shown in Ref. [146], one needs to account for it when designing an experiment.

In the case of flux qubits (cf. Fig. 6.2), the quantum bus is a $\lambda/4$ resonator (i.e., its length $\ell_{\mathrm{B}} = \lambda/4$) terminated with a short on the end close to the leaky cavity. The other end is left open, i.e., capacitively terminated to infinity via a capacitor $C_{\mathrm{B},\infty}$. Again, this guarantees a very high loaded quality factor for the quantum bus. In this configuration, the flux qubit can be fabricated in a region of the leaky cavity where it couples well to the first three modes of the current [cf. Fig. 6.2(a) and 6.2(b)]. At the same time, the qubit resides close to the short-circuited edge of the quantum bus, thus being coupled to the current antinode of, e.g, the first mode of

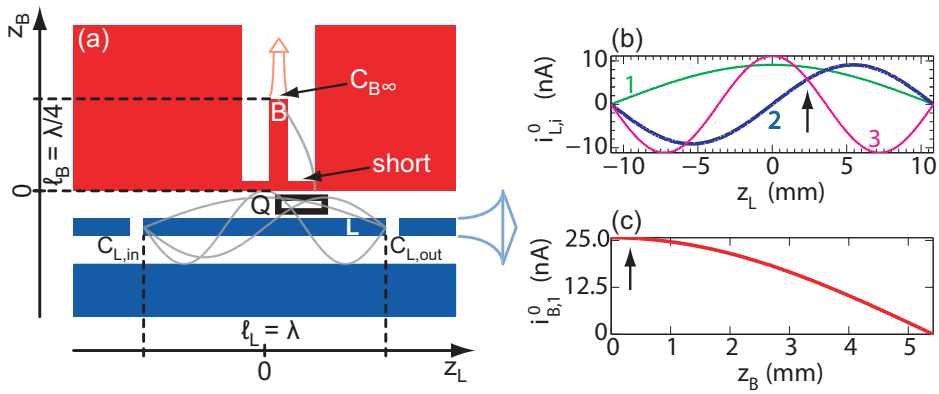

Figure 6.2: Two-resonator circuit QED setup for flux qubits. **(a)** The leaky cavity, L, is represented by the horizontal finite segment of CPW transmission line depicted in blue (dark grey). The quantum bus, B, is represented by the vertical finite segment of CPW transmission line depicted in red (grey). One end of B is short circuited, whereas the opposite end is left open (capacitor to infinity, $C_{\mathrm{B},\infty}$). $\ell_{\mathrm{B}} = \lambda/4$: total length of B. All the other symbols are equal to those used in Fig. 6.1. The qubit, Q, is indicated by the black rectangle. The mode structures of L and B are reported for clarity (light grey thin lines). **(b)** Distribution of the zero-point fluctuations of the current $i^0_{\mathrm{L},i}$ ($i = \{1, 2, 3\}$) for the first three modes of L as a function of the position z_{L}. 1: first mode [light green (light grey) line]; 2: second mode [thick dark blue (dark grey) line]. The qubit is resonantly coupled to this mode; 3: third mode [magenta (middle grey) line]. The black arrow indicates the approximate position of the qubit with respect to z_{L}. The qubit is well coupled to all three modes. **(c)** Distribution of the zero-point fluctuations of the current $i^0_{\mathrm{B},1}$ for the first mode of B as a function of the position z_{B} [thick red (grey) line]. The black arrow indicates the approximate position of the qubit with respect to z_{B}.

B [the current reaches a maximum in the vicinity of a short circuit, cf. Fig. 6.2(c)].

It is worth mentioning that a simplified version of the setups of Figs. 6.1 and 6.2 is realized when the qubit is resonantly or dispersively coupled to B and, at the same time, dispersively coupled to one mode of L (e.g., the first mode). In this case, while the quantum-bus–qubit system undergoes a coherent evolution, the leaky cavity can be used to independently and rapidly read out the qubit state. This would constitute an important improvement on existing experiments [150, 154], where the same cavity is used both for the coherent evolution and the qubit readout. Practically, this can be considered a special case of the general setups analyzed here.

6.1.2 The System Hamiltonian

We consider a superconducting (charge or flux) qubit Q coupled to the first three modes of L and to the first mode of B with coupling coefficients $g_{\mathrm{L},i}$ ($i = \{1, 2, 3\}$) and $g_{\mathrm{B},1}$, respectively. These coefficients already account for the spatial distribution of the zero-point fluctuations of the voltages or currents in the two resonators [cf. Figs. 6.1(b), 6.1(c), 6.2(b), and 6.2(c)]. We assume the second mode of L (with angular frequency $\omega_{\mathrm{L},2}$) and the first mode of B (with angular frequency $\omega_{\mathrm{B},1}$) to

be resonant by construction, $\omega_{\mathrm{L},2} = \omega_{\mathrm{B},1} \equiv \omega \equiv 2\pi f$. We further assume them to be geometrically coupled with a total coupling coefficient g_{LB}. This coefficient is the sum of geometric first- and second-order circuit contributions, as discussed in chapter 5, and simply represents the inevitable crosstalk between the two resonators. Obviously, there are crosstalks between all modes of L and B. Here, we consider only the one between the second mode of L and the first mode of B because these are the only two modes to be resonant.

The first and third modes of L (with angular frequencies $\omega/2$ and $3\omega/2$, respectively) are not drastically affected by the geometric crosstalk with any mode of B (with angular frequencies $\omega, 2\omega, 3\omega, \ldots$) because of the large frequency detunings. An important feature of the first and third modes of L is that they are dispersively coupled to the qubit (i.e., largely detuned by $\omega/2$) and, thus, give rise to second-oder effects such as AC-Stark or -Zeeman shifts. These can efficiently be used to switch on and off the interaction of the qubit with B and L [146] or to read out the qubit state [108, 131]. It is worth mentioning that also the second mode of B is dispersively coupled to the qubit (largely detuned by ω) and could be used for similar purposes. However, the cavity modes of L are more suitable for those tasks because of their lower quality factor (faster readout) and the smaller detuning with respect to the qubit. As a consequence, in the rest of this chapter we do not consider the coupling of the qubit to the second mode of B. Decoherence effects are also not included at this stage.

Before proceeding with our derivations, it is important to make a remark on the possibility to perform rotating-wave approximations (RWAs) and on the applicability of dispersive (large detuning) conditions, all very important for the further development of this chapter. As we will discuss later, in order to generate large Schrödinger cat states it is necessary to have large vacuum Rabi couplings between qubit and resonators. In this case, while RWAs are usually met well enough, dispersive conditions, which are reached when the qubit-resonator detuning is much larger than the corresponding qubit-resonator coupling strength, are often on the edge of applicability due to the large coupling strengths. This means that it is not always completely correct to apply the usual tricks of second-order perturbation theory. However, the order of magnitude and qualitative behavior of our results remain unchanged. We thus prefer to use all standard approximations of quantum optics in order to keep the notation simple and clear. It is also worth mentioning that when the resonators are populated with coherent or Schrödinger cat states, the simple dressed state picture, which is valid only for number states, fails. We can still use such simple picture under the assumption that these states are associated with a photon number distribution very localized around their effective mean photon number.

In the qubit diabatic basis, which consists of the eigenstates $|-\rangle$ and $|+\rangle$ of $\hbar\epsilon\hat{\tilde{\sigma}}_z/2$ (where $\hbar\epsilon/2$ is the qubit energy bias [97–101] (cf. also chapter 2, Sec. 2.2),

the system Hamiltonian can be written as

$$\begin{aligned}\widehat{\widehat{H}} = &\frac{1}{2}\hbar\epsilon\hat{\bar{\sigma}}_z + \frac{1}{2}\hbar\delta_{\mathrm{Q}}\hat{\bar{\sigma}}_x + \sum_{i=1}^{3}\hbar\omega_{\mathrm{L},i}\,\hat{a}_i^\dagger\hat{a}_i + \hbar\omega_{\mathrm{B},1}\,\hat{b}_1^\dagger\hat{b}_1 \\ &+ \sum_{i=1}^{3}\hbar g_{\mathrm{L},i}\,\hat{\bar{\sigma}}_z(\hat{a}_i^\dagger + \hat{a}_i) + \hbar g_{\mathrm{B},1}\,\hat{\bar{\sigma}}_z(\hat{b}_1^\dagger + \hat{b}_1) \\ &+ \hbar g_{\mathrm{LB}}\,(\hat{a}_2^\dagger + \hat{a}_2)(\hat{b}_1^\dagger + \hat{b}_1)\,. \end{aligned} \tag{6.2}$$

Here, all global energy offsets have been neglected since, in experiments, only energy differences are accessible. Also, $\hbar\delta_{\mathrm{Q}}$ is the qubit gap [97–101] (cf. also chapter 2, Sec. 2.2), $\omega_{\mathrm{L},i}$ and $\omega_{\mathrm{B},1}$ are the angular frequencies of the relevant modes of resonators L and B, respectively, $\hat{\bar{\sigma}}_x$ and $\hat{\bar{\sigma}}_z$ are the usual Pauli operators, and $\hat{a}_i^\dagger$, $\hat{a}_i$, $\hat{b}_1^\dagger$, and $\hat{b}_1$ are bosonic creation and annihilation operators for the fields of the various modes of L and B. We notice that the qubit energy bias $\hbar\epsilon$ usually depends on external control parameters such as gate voltage or applied flux for charge and flux qubits, respectively. In general, the coefficients $g_{\mathrm{L},i}$ and $g_{\mathrm{B},1}$ are slightly different because of the different zero-point fields of the corresponding modes and, possibly, because of asymmetries in the geometric couplings (cross-capacitances and/or mutual inductances) between each mode and the qubit [cf. Figs. 6.1(b), 6.1(c), 6.2(b), and 6.2(c)]. This does not constitute an issue for the validity of our derivations. We now rotate the system Hamiltonian of Eq. (6.2) into the qubit energy eigenbasis $\{|\mathrm{g}\rangle, |\mathrm{e}\rangle\}$, obtaining

$$\begin{aligned}\widehat{H} = &\hbar\frac{\Omega_{\mathrm{Q}}}{2}\hat{\sigma}_z + \sum_{i=1}^{3}\hbar\omega_{\mathrm{L},i}\,\hat{a}_i^\dagger\hat{a}_i + \hbar\omega_{\mathrm{B},1}\,\hat{b}_1^\dagger\hat{b}_1 \\ &+ \sum_{i=1}^{3}\hbar g_{\mathrm{L},i}\cos\theta\,\hat{\sigma}_z(\hat{a}_i^\dagger + \hat{a}_i) + \hbar g_{\mathrm{B},1}\cos\theta\,\hat{\sigma}_z(\hat{b}_1^\dagger + \hat{b}_1) \\ &- \sum_{i=1}^{3}\hbar g_{\mathrm{L},i}\sin\theta\,\hat{\sigma}_x(\hat{a}_i^\dagger + \hat{a}_i) - \hbar g_{\mathrm{B},1}\sin\theta\,\hat{\sigma}_x(\hat{b}_1^\dagger + \hat{b}_1) \\ &+ \hbar g_{\mathrm{LB}}(\hat{a}_2^\dagger + \hat{a}_2)(\hat{b}_1^\dagger + \hat{b}_1)\,. \end{aligned} \tag{6.3}$$

Here, $\Omega_{\mathrm{Q}} = \sqrt{\epsilon^2 + \delta_{\mathrm{Q}}^2}$ is the bias-dependent transition angular frequency of the qubit and $\theta = \arctan(\delta_{\mathrm{Q}}/\epsilon)$ is the usual mixing angle. In the Hamiltonian of Eq. (6.3) and in all the following Hamiltonians expressed in the qubit energy eigenbasis, we use the redefined Pauli operators $\hat{\sigma}_x$ and $\hat{\sigma}_z$, where $\hat{\sigma}_x = \hat{\sigma}^+ + \hat{\sigma}^-$, $\hat{\sigma}_z = \hat{\sigma}^+\hat{\sigma}^- - \hat{\sigma}^-\hat{\sigma}^+$, and $\hat{\sigma}^+$ and $\hat{\sigma}^-$ are the lowering and raising operators between the qubit energy groundstate $|\mathrm{g}\rangle$ and excited state $|\mathrm{e}\rangle$, respectively.

Expressing $\widehat{H}$ in an interaction picture with respect to the qubit and all relevant modes of both resonators, $\hat{a}_i^\dagger \to \hat{a}_i^\dagger\exp(+j\omega_{\mathrm{L},i}t)$, $\hat{a}_i \to \hat{a}_i\exp(-j\omega_{\mathrm{L},i}t)$, $\hat{b}_1^\dagger \to \hat{b}_1^\dagger\exp(+j\omega_{\mathrm{B},1}t)$, $\hat{b}_1 \to \hat{b}_1\exp(-j\omega_{\mathrm{B},1}t)$, and $\hat{\sigma}^\mp \to \hat{\sigma}^\mp\exp(\mp j\Omega_{\mathrm{Q}}t)$ (where t is the

time and $j = \sqrt{-1}$), and performing a RWA yields

$$\begin{aligned}\widehat{\widetilde{H}} = &\sum_{i=1}^{3} \hbar g_{\mathrm{L},i} \sin\theta \left(\hat{\sigma}^- \hat{a}_i^\dagger e^{-j\Delta_{\mathrm{L},i}t} + \hat{\sigma}^+ \hat{a}_i e^{+j\Delta_{\mathrm{L},i}t}\right) \\ &+ \hbar g_{\mathrm{B},1} \sin\theta \left(\hat{\sigma}^- \hat{b}_1^\dagger e^{-j\Delta_{\mathrm{B},1}t} + \hat{\sigma}^+ \hat{b}_1 e^{+j\Delta_{\mathrm{B},1}t}\right) \\ &+ \hbar g_{\mathrm{LB}} (\hat{a}_2^\dagger \hat{b}_1 + \hat{a}_2 \hat{b}_1^\dagger) \,. \end{aligned} \tag{6.4}$$

Here, $\Delta_{\mathrm{L},i} \equiv \Omega_{\mathrm{Q}} - \omega_{\mathrm{L},i}$ and $\Delta_{\mathrm{B},1} \equiv \Omega_{\mathrm{Q}} - \omega_{\mathrm{B},1}$ are the qubit-resonator detunings. Under the assumption $\Omega_{\mathrm{Q}} = \omega_{\mathrm{L},2} = \omega_{\mathrm{B},1} \equiv \omega$, the qubit is resonantly coupled to the second mode of L and to the first mode of B, in close analogy to the standard two-mode JC model. The coupling coefficients are $g_{\mathrm{L},2}$ and $g_{\mathrm{B},1}$, respectively.[3] At the same time, the first and third modes of L are largely detuned from the qubit by $\pm\omega/2$, respectively ($\omega_{\mathrm{L},1} = \omega/2$ and $\omega_{\mathrm{L},3} = 3\omega/2$). Assuming $\left|\Delta_{\mathrm{L},1}\right| = \left|\Delta_{\mathrm{L},3}\right| \gg \max\left\{g_{\mathrm{L},i}, g_{\mathrm{B},1}, g_{\mathrm{LB}}\right\}$,[4] it is an easy exercise in second-order perturbation theory to determine the contributions of these modes. To this end, we can define the operators $\hat{\Xi}_1^\dagger \equiv g_{\mathrm{L},1}\hat{\sigma}^+\hat{a}_1$, $\hat{\Xi}_1 \equiv g_{\mathrm{L},1}\hat{\sigma}^-\hat{a}_1^\dagger$, $\hat{\Xi}_3^\dagger \equiv g_{\mathrm{L},3}\hat{\sigma}^+\hat{a}_3$, and $\hat{\Xi}_3 \equiv g_{\mathrm{L},3}\hat{\sigma}^-\hat{a}_3^\dagger$. It can be shown that the Dyson series for the evolution operator associated with the time-dependent Hamiltonian of Eq. (6.4) can be rewritten in the exponential form $\widehat{U} = \exp(-j\widehat{H}_{\mathrm{eff}}t/\hbar)$, where

$$\begin{aligned}\widehat{H}_{\mathrm{eff}} = &\hbar g_{\mathrm{L},2} \sin\theta \left(\hat{\sigma}^- \hat{a}_2^\dagger + \hat{\sigma}^+ \hat{a}_2\right) + \hbar g_{\mathrm{B},1} \sin\theta \left(\hat{\sigma}^- \hat{b}_1^\dagger + \hat{\sigma}^+ \hat{b}_1\right) \\ &+ \hbar \frac{2[\hat{\Xi}_1^\dagger, \hat{\Xi}_1]}{\omega} - \frac{2[\hat{\Xi}_3^\dagger, \hat{\Xi}_3]}{\omega} \\ &+ \hbar g_{\mathrm{LB}} (\hat{a}_2^\dagger \hat{b}_1 + \hat{a}_2 \hat{b}_1^\dagger) \,. \end{aligned} \tag{6.5}$$

For simplicity, we can express this Hamiltonian at the qubit degeneracy point, where $\sin\theta = 1$ and, thus, all coupling coefficients reach their maximum.[5] This represents the best choice also with respect to qubit dephasing, which is highly reduced at the qubit degeneracy point [118, 119, 261, 262]. Under this condition and computing explicitly the commutators of Eq. (6.5), we obtain

$$\begin{aligned}\widehat{H}_{\mathrm{sys}} = &\hbar g_{\mathrm{L},2} (\hat{\sigma}^- \hat{a}_2^\dagger + \hat{\sigma}^+ \hat{a}_2) + \hbar g_{\mathrm{B},1} (\hat{\sigma}^- \hat{b}_1^\dagger + \hat{\sigma}^+ \hat{b}_1) \\ &+ \hbar \frac{2g_{\mathrm{L},1}^2}{\omega} \hat{\sigma}_z \hat{a}_1^\dagger \hat{a}_1 - \frac{2g_{\mathrm{L},3}^2}{\omega} \hat{\sigma}_z \hat{a}_3^\dagger \hat{a}_3 \\ &+ \hbar g_{\mathrm{LB}} (\hat{a}_2^\dagger \hat{b}_1 + \hat{a}_2 \hat{b}_1^\dagger) \,, \end{aligned} \tag{6.6}$$

where all Lamb shifts have been neglected. The terms in the second line of Eq. (6.6) represent AC-Stark or -Zeeman shifts and, when using eigenstates of $\hat{\sigma}_z$ only, they renormalize the transition frequencies of the first and third mode of L. Under driving conditions, these dynamic shifts can be utilized to modify the qubit transition

[3] In reality, the two-mode JC studied here is unbalanced due to the generally different coupling coefficients and, more importantly, the different relaxation rates of the two resonators.

[4] In reality, this condition is only partially met and, strictly speaking, we are in a quasi-dispersive more than a truly dispersive regime of circuit QED (cf. Sec. 6.5 for a set of realistic numbers which help clarifying the quasi-dispersivity of the setup considered here).

[5] In this case, the resonance condition between Q, the second mode of L, and the first mode of B becomes $\delta_{\mathrm{Q}} = \omega_{\mathrm{L},2} = \omega_{\mathrm{B},1} \equiv \omega$.

frequency [146] and/or to measure the qubit state [108, 131] (cf. Subsec. 6.3.1). It is also worth pointing out that quantum switch dynamics similar to those described in chapter 5 cannot take place here due to the fact that the modes of L and B which are dispersively coupled to the qubit are frequency mismatched. The Hamiltonian of Eq. (6.6) constitutes the starting point of our protocol for the generation and measurement of large Schrödinger cat states in two-resonator circuit QED.

6.2 JC and Anti JC Dynamics

An important application of the Hamiltonian of Eq. (6.6) is obtained when the second mode of L is resonantly driven generating an intracavity coherent state $|\alpha\rangle$ with angular frequency $\omega_\alpha = \omega$ and complex amplitude $|\alpha| \exp(j\varphi_\alpha)$. Here $|\alpha|$ is a real amplitude and φ_α a generic phase, which for simplicity, we set to zero, $\varphi_\alpha = 0$. Under this driving condition and assuming the first and third modes of L to be initially in the vacuum state $|0\rangle_{\mathrm{L},1} |0\rangle_{\mathrm{L},3}$,[6] we can rewrite the Hamiltonian of Eq. (6.6) as

$$\begin{aligned}\widehat{H}^\alpha &= \hbar |\alpha| g_{\mathrm{L},2}(\hat{\sigma}^- e^{+j\omega t} + \hat{\sigma}^+ e^{-j\omega t}) \\ &\quad + \hbar g_{\mathrm{B},1}(\hat{\sigma}^- \hat{b}_1^\dagger + \hat{\sigma}^+ \hat{b}_1) \\ &\quad + \hbar |\alpha| g_{\mathrm{LB}}(\hat{b}_1^\dagger e^{-j\omega t} + \hat{b}_1 e^{+j\omega t}) \,. \end{aligned} \tag{6.7}$$

We can now define the effective driving strength of the qubit as $g_{\mathrm{Q}}^\alpha \equiv |\alpha| g_{\mathrm{L},2}$ and the effective driving strength of B as $g_{\mathrm{B}}^\alpha \equiv |\alpha| g_{\mathrm{LB}}$,[7] which, as expected, are larger the larger the amplitude of the coherent state, $|\alpha|$. Following Ref. [373], we describe $\widehat{H}^\alpha$ in a reference frame rotating with the driving field frequency,

$$\begin{aligned}\widehat{H}^{\mathrm{D}} &= \hbar g_{\mathrm{Q}}^\alpha (\hat{\sigma}^- + \hat{\sigma}^+) \\ &\quad + \hbar g_{\mathrm{B},1}(\hat{\sigma}^- \hat{b}_1^\dagger + \hat{\sigma}^+ \hat{b}_1) + \hbar g_{\mathrm{B}}^\alpha (\hat{b}_1^\dagger + \hat{b}_1) \\ &= \widehat{H}_0 + \widehat{H}_{\mathrm{int}} \,, \end{aligned} \tag{6.8}$$

where $\widehat{H}_0 \equiv \hbar g_{\mathrm{Q}}^\alpha (\hat{\sigma}^- + \hat{\sigma}^+)$ plays the role of the unperturbed Hamiltonian and $\widehat{H}_{\mathrm{int}} \equiv \hbar g_{\mathrm{B},1}(\hat{\sigma}^- \hat{b}_1^\dagger + \hat{\sigma}^+ \hat{b}_1) + \hbar g_{\mathrm{B}}^\alpha (\hat{b}_1^\dagger + \hat{b}_1)$ is the interaction Hamiltonian. We notice that the transformation above assumes such a simple form because of the resonance condition between the qubit, the first mode of B, and the driving field. In order to simplify the Hamiltonian of Eq. (6.8), we write the lowering and raising operators as $\hat{\sigma}^- = |\mathrm{g}\rangle \langle \mathrm{e}|$ and $\hat{\sigma}^+ = |\mathrm{e}\rangle \langle \mathrm{g}|$ and, then, perform the substitutions $|\mathrm{g}\rangle = (|+\rangle + |-\rangle)/\sqrt{2}$ and $|\mathrm{e}\rangle = (|+\rangle - |-\rangle)/\sqrt{2}$. We remind that $|+\rangle$ and $|-\rangle$ are eigenstates of $\hat{\sigma}_x$ with eigenvalues ± 1, respectively. Describing now $\widehat{H}^{\mathrm{D}}$ in the interaction picture with

[6] Being these two modes in the vacuum state, the AC-Stark or -Zeeman shifts of Eq. (6.6) do not have any effect. We could transform away those dynamic shifts by means of a unitary transformation similar to the one used to derive Eq. (5.14) in chapter 5. However, we prefer to keep them here given that we make use of them at a later stage of our protocol.

[7] We assume the constant g_{LB} to be real.

respect to $\widehat{H}_0$ (i.e., $|+\rangle \rightarrow \exp\left(+jg_{\mathrm{Q}}^{\alpha}t\right)|+\rangle$ and $|-\rangle \rightarrow \exp\left(-jg_{\mathrm{Q}}^{\alpha}t\right)|-\rangle$), we obtain

$$\begin{aligned}\widehat{H}^{\mathrm{I}} = \hbar\frac{g_{\mathrm{B},1}}{2}[&(|+\rangle\langle+| - |-\rangle\langle-| \\ &+ e^{-j2g_{\mathrm{Q}}^{\alpha}t}|-\rangle\langle+| - e^{+j2g_{\mathrm{Q}}^{\alpha}t}|+\rangle\langle-|)\hat{b}_1^{\dagger} \\ &+ (|+\rangle\langle+| - |-\rangle\langle-| \\ &+ e^{+j2g_{\mathrm{Q}}^{\alpha}t}|+\rangle\langle-| - e^{-j2g_{\mathrm{Q}}^{\alpha}t}|-\rangle\langle+|)\hat{b}_1] \\ &+ \hbar g_{\mathrm{B}}^{\alpha}(\hat{b}_1^{\dagger} + \hat{b}_1)\,. \end{aligned} \tag{6.9}$$

The time evolution of the last term of this Hamiltonian, $\widehat{U}(t) = \exp[-jg_{\mathrm{B}}^{\alpha}t(\hat{b}_1^{\dagger} + \hat{b}_1)]$, after a certain interaction time t_{I} corresponds to the displacement operator

$$\widehat{D}(\beta) = e^{|\beta|(\hat{b}_1^{\dagger} + \hat{b}_1)}\,, \tag{6.10}$$

where $|\beta| \equiv -jg_{\mathrm{B}}^{\alpha}\,t_{\mathrm{I}}$. When applying $\widehat{D}(\beta)$, e.g., to the vacuum state $|0\rangle_{\mathrm{B},1}$ of resonator B, this generates a coherent state, the amplitude of which depends on the interaction time t_{I} and on the driving strength $|\alpha|$. This coherent state can be harmful for the nonclassical states we are interested to generate and store in B. There are two possible strategies to overcome this issue. The first is to engineer the geometric coupling g_{LB} to be as small as possible. In this way, $\widehat{H}^{\mathrm{I}}$ could evolve for a sufficiently long time before any coherent state generated by $\widehat{D}(\beta)$ becomes appreciable. However, as we extensively discuss in chapter 5 it is a hard task to avoid geometric couplings in two-resonator circuit QED. The most elegant strategy is, thus, to implement a calibration technique, which compensates the spurious coherent state generated in B. This can be realized by resonantly driving B with an externally generated coherent state $|\beta_{\mathrm{cal}}\rangle$, characterized by a complex amplitude $|\beta_{\mathrm{cal}}|\exp(j\varphi_{\mathrm{cal}})$. Here, $|\beta_{\mathrm{cal}}|$ is the real amplitude of the calibration state and φ_{cal} its phase. Consequently, $\widehat{H}^{\mathrm{I}}$ (which is already in the rotating frame of the driving field under resonance conditions) becomes

$$\begin{aligned}\widehat{H}_{\mathrm{cal}}^{\mathrm{I}} = \hbar\frac{g_{\mathrm{B},1}}{2}[&(|+\rangle\langle+| - |-\rangle\langle-| \\ &+ e^{-j2g_{\mathrm{Q}}^{\alpha}t}|-\rangle\langle+| - e^{+j2g_{\mathrm{Q}}^{\alpha}t}|+\rangle\langle-|)\hat{b}_1^{\dagger} \\ &+ (|+\rangle\langle+| - |-\rangle\langle-| \\ &+ e^{+j2g_{\mathrm{Q}}^{\alpha}t}|+\rangle\langle-| - e^{-j2g_{\mathrm{Q}}^{\alpha}t}|-\rangle\langle+|)\hat{b}_1] \\ &+ \hbar g_{\mathrm{B}}^{\alpha}(\hat{b}_1^{\dagger} + \hat{b}_1) + \hbar\,|\beta_{\mathrm{cal}}|\,(\hat{b}_1^{\dagger}e^{-j\varphi_{\mathrm{cal}}} + \hat{b}_1 e^{+j\varphi_{\mathrm{cal}}})\,. \end{aligned} \tag{6.11}$$

In order to compensate the spurious coherent state generated by the geometric coupling, we have to choose the externally generated coherent state such that $|\beta_{\mathrm{cal}}| = g_{\mathrm{B}}^{\alpha}$ and $\varphi_{\mathrm{cal}} = \pi$. This can be realized connecting the output port of B, terminated with an open in Figs. 6.1(a) and 6.2(a), to a transmission line and using known feedback methods to calibrate both amplitude and phase of $|\beta_{\mathrm{cal}}\rangle$ [227, 308, 360]. In this way, for any given interaction time the system Hamiltonian is readily reduced

to

$$\begin{aligned}\widehat{H}^{\mathrm{I}} = \hbar\frac{g_{\mathrm{B},1}}{2}[&(|+\rangle\langle+| - |-\rangle\langle-| \\ &+ e^{-j2g_{\mathrm{Q}}^{\alpha}t}|-\rangle\langle+| - e^{+j2g_{\mathrm{Q}}^{\alpha}t}|+\rangle\langle-|)\hat{b}_1^{\dagger} \\ &+ (|+\rangle\langle+| - |-\rangle\langle-| \\ &+ e^{+j2g_{\mathrm{Q}}^{\alpha}t}|+\rangle\langle-| - e^{-j2g_{\mathrm{Q}}^{\alpha}t}|-\rangle\langle+|)\hat{b}_1]\,. \end{aligned} \tag{6.12}$$

This Hamiltonian assumes a particularly useful form when imposing the *strong-driving condition* $g_{\mathrm{Q}}^{\alpha} = |\alpha|\, g_{\mathrm{L},2} \gg g_{\mathrm{B},1}$. This condition is straightforwardly realized inducing a large enough amplitude $|\alpha|$. In this case, we can realize a RWA, eliminate the rapidly oscillating terms, and finally obtain

$$\widehat{H}^{\mathrm{S}} = \hbar\frac{g_{\mathrm{B},1}}{2}(\hat{\sigma}^{-} + \hat{\sigma}^{+})(\hat{b}_1^{\dagger} + \hat{b}_1)\,, \tag{6.13}$$

where $\hat{\sigma}^{-} + \hat{\sigma}^{+} = |+\rangle\langle+| - |-\rangle\langle-|$. The strong-driving limit results in a circuit QED realization of a simultaneous JC and anti-JC dynamics. It is worth mentioning that, under time evolution, there are no Rabi oscillations associated with $\widehat{H}^{\mathrm{S}}$. This is a remarkable aspect of Eq. (6.13), which finds its origin in the exquisite nature of the strong driving regime.

The Hamiltonians of Eqs. (6.6) and (6.13) enable the generation and measurement of mesoscopic superposition states between the qubit and the field in B. This can be accomplished following the protocol here summarized (see also the sketch of Fig. 6.3): *(i)* – The qubit and the quantum bus are initialized in the groundstate. The second mode of L is continuously driven by a strong field in order to keep active the Hamiltonian $\widehat{H}^{\mathrm{S}}$. At the same time, the interaction between the qubit and both resonators is effectively switched off by means of a dynamic shift. This is realized by taking advantage of the dispersive action of the third mode of L under driving conditions. The qubit-resonator interaction can alternatively be switched off tuning the qubit energy gap or its energy bias with pulses. *(ii)* – The qubit-resonator interaction is switched on for a time t_{gen}. A Schrödinger cat state starts being generated in B. *(iii)* – Both the strong driving through L and the qubit-resonator interaction are switched off. *(iv)* – The qubit state is projected by means of a QND dispersive measurement of duration t_{proj} via the first mode of L. *(v)* – A $\pi/2$-pulse is applied to the qubit through L. *(vi)* – The qubit-resonator interaction is switched on and the system is let evolve for a very short pre-measurement time t_{pre}. *(vii)* – The qubit state is measured by means of a QND dispersive readout again via the first mode of L. *(viii)* – The protocol is repeated many times in order to acquire enough statistics for the qubit measurement. In the next section, we delve into the details of this protocol. Additionally, two variants for the reconstruction of the Wigner function of the field in resonator B are given in Sec. 6.4.

6.3 Generation and Measurement of Schrödinger Cat States

In this section, we analyze in detail the protocol outlined above for the generation (cf. Subsec. 6.3.1) and measurement (cf. Subsec. 6.3.2) of large Schrödinger cat states.

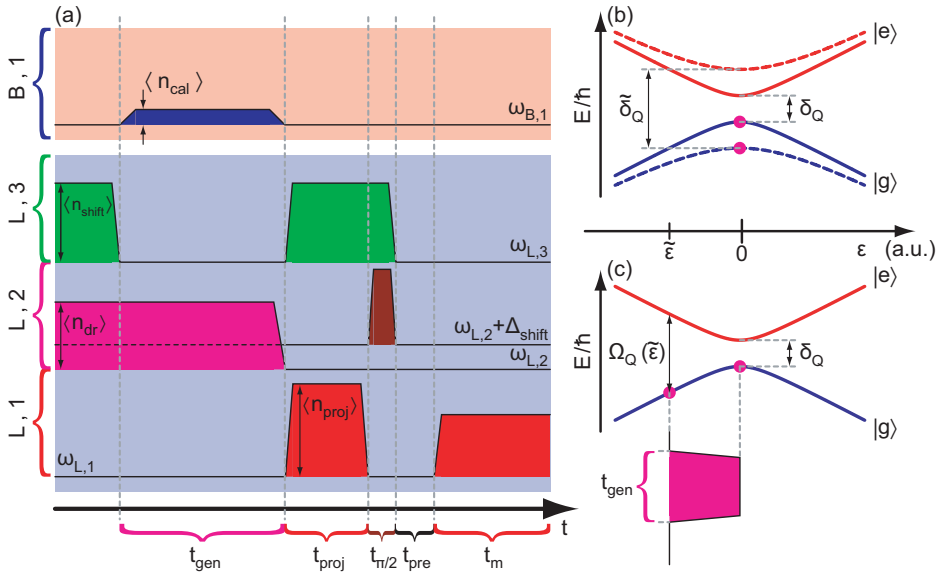

Figure 6.3: Protocol for the generation and measurement of Schrödinger cat states in a two-resonator/multi-mode circuit QED architecture. **(a)** Pulse sequence. L, 1 - L, 2 - L, 3 - B, 1: relevant modes of resonators L and B used in the protocol. The angular frequencies of these modes are $\omega_{\mathrm{L},i}$ ($i = \{1, 2, 3\}$) and $\omega_{\mathrm{B},1}$, respectively. At the qubit degeneracy point, a superconducting qubit is resonant with modes B, 1 and L, 2. Initially, a pulse through mode L, 3 with $\langle n_{\mathrm{shift}} \rangle$ photons [light green (light grey) area] is used to dynamically shift the qubit which, as a result, becomes decoupled from mode L, 2 (AC-Stark or -Zeeman decoupling pulse). The qubit can be shifted also by means of fast DC-Stark or -Zeeman pulses, as indicated in **(b)**, or applying an adiabatic shift pulse through a charge or flux gate, as indicated in **(c)**. The qubit is then set on resonance with both B, 1 and L, 2, while mode L, 2 is strongly driven with $\langle n_{\mathrm{dr}} \rangle$ photons [magenta (middle grey) area]. During the generation time t_{gen}, the spurious crosstalk between modes L, 2 and B, 1 is calibrated out by means of a pulse with $\langle n_{\mathrm{cal}} \rangle$ photons through B, 1 [dark blue (dark grey) area]. As soon as the strong driving is switched off, the qubit is simultaneously decoupled from L, 2, e.g., via a shift pulse through L, 3 [light green (light grey) area], and projected via a projection pulse with $\langle n_{\mathrm{proj}} \rangle$ photons and duration t_{proj} through L, 1 [red (grey) area]. After the projection, a $\pi/2$-pulse of duration $t_{\pi/2}$ (brown area) is applied resonantly to the qubit, which is now at frequency $\omega_{\mathrm{L},2} + \Delta_{\mathrm{shift}}$ due to the decoupling pulse, using L, 2 as a waveguide. All pulses are then switched off and the qubit-resonator system is let to evolve freely for a time t_{pre}, after which the qubit is dispersively measured for a time t_{m} via L, 1 [red (grey) area]. **(b)** $E/\hbar$: qubit energy expressed as an angular frequency. The qubit [magenta (middle grey) dot] is in the groundstate $|\mathrm{g}\rangle$ and biased at its degeneracy point, $\epsilon = 0$. The qubit transition angular frequency can be shifted from δ_{Q} to $\tilde{\delta}_{\mathrm{Q}}$ via AC- or DC-Stark or -Zeeman decoupling pulses [146, 147, 349, 374]. **(c)** Alternatively, the qubit can initially be prepared away from its degeneracy point at $\tilde{\epsilon}$ and, during the generation time t_{gen}, pulsed to the degeneracy point via an adiabatic shift pulse [141, 261, 262] (cf. chapter 8).

6.3.1 Generation of Schrödinger Cat States

We first examine the steps which allow for the generation of Schrödinger cat states.

(i) – System initialization. The first operation of step *(i)* is the initialization of the qubit and the first mode of B in the groundstate

$$|\Psi_0\rangle \;=\; |\mathrm{g}\rangle\,|0\rangle_{\mathrm{B},1} \;=\; \frac{|+\rangle + |-\rangle}{\sqrt{2}}\,|0\rangle_{\mathrm{B},1}\;. \tag{6.14}$$

In order to realize the Hamiltonian $\widehat{H}^{\mathrm{S}}$, the second mode of L must be driven with a strong coherent state $|\alpha\rangle$. Only if the field inside L is in the steady-state regime, we can safely assume $\widehat{H}^{\mathrm{S}}$ as our effective Hamiltonian. For this reason, it is more appropriate to start the protocol with L under a continuous driving, which can be turned off when necessary. In the case of a pulsed driving, in fact, the pulse rise time would be limited by the inverse decay rate of the second mode of L, $t_{\mathrm{pr}} \geqslant 1/\kappa_{\mathrm{L},2}$. This would originate a transient and could ultimately limit the efficiency of our protocol.[8]

While the second mode of L is strongly driven, the qubit-resonator interaction is initially switched off. There are at least three possible ways to achieve this goal. The first is to AC-Stark or -Zeeman shift the qubit with an off-resonance driving pulse [146]. The second is to tune the qubit gap δ_{Q} by means of fast pulses [147, 349, 374]. The third is to apply an adiabatic shift pulse that modifies the qubit bias ϵ [141, 261, 262] (cf. chapter 8). The first two approaches allow one to keep the qubit at the degeneracy point, whereas the third naturally moves it away from it. This high level of flexibility makes possible to choose between a scenario where either the qubit dephasing rate (at the qubit degeneracy point) or its energy relaxation rate (away from the qubit degeneracy point) are best [262].

The first approach can be realized by resonantly driving the third mode of L, thus generating an intracavity coherent state $|\alpha_{\mathrm{shift}}\rangle$. Assuming the amplitude of $|\alpha_{\mathrm{shift}}\rangle$ to be $|\alpha_{\mathrm{shift}}|$, the mean number of photons populating the third mode of L is then $\langle n_{\mathrm{shift}}\rangle = |\alpha_{\mathrm{shift}}|^2$. From Eq. (6.6), in the presence of $|\alpha_{\mathrm{shift}}\rangle$, we obtain the effective qubit shift

$$|\Delta_{\mathrm{shift}}| \;= 4\,\langle n_{\mathrm{shift}}\rangle\,\frac{g_{\mathrm{L},3}^2}{\omega}\,. \tag{6.15}$$

This dynamic (AC-Stark or -Zeeman) shift scales linearly with the mean number of photons of the coherent state and has the effect of "pulling" the qubit out of the cavity. A large shift can be realized by choosing the amplitude $|\alpha_{\mathrm{shift}}|$ to be large enough. In this case, qubit dephasing induced by photon shot noise becomes a severe issue, even when the qubit is biased at its degeneracy point [118, 131, 140]. However, this is not an important limitation for our protocol. In fact, the switch-off pulse is active only before the starting of the cat generation and during the projection pulse (see Fig. 6.3). In the latter case, we are interested in the qubit populations only and the relevant figure of merit is the energy relaxation of the qubit, which is not affected by photon shot noise.

[8] Even if $\kappa_{\mathrm{L},2}$ is here considered to be large, typically $t_{\mathrm{gen}} \approx t_{\mathrm{pr}}$, i.e., it is relatively short (cf. Sec. 6.5). We notice that if it is strictly necessary to apply a pulsed driving from the beginning, this could be realized sending a pulse with larger amplitude, which overcomes the resonator filtering effect. However, heating effects and, possibly, the triggering of nonlinear dynamics could deteriorate our protocol.

Another way to switch off the qubit-resonator interaction is to make use of the high level of tunability of superconducting qubits. In the design of a charge qubit, such as the Cooper-pair box [97] or the transmon [120, 243, 244], is usually included a DC SQUID loop, which can be threaded by an external flux $\Phi_{\rm Z}$. This allows the tuning *in situ* of the qubit gap $\delta_{\rm Q}$, which is a function of $\Phi_{\rm Z}$. In a similar fashion, also flux qubits can be tuned by means of a DC SQUID embedded in their basic loop [189, 349, 374]. In both cases, tuning $\delta_{\rm Q}$ via a magnetic field corresponds to a DC-Zeeman shift of the qubit energy levels, whose final effect is analogous to the dynamic shifts discussed above: It pulls the qubit out of the cavity.

Finally, the third possibility to decouple the qubit-resonator system is to prepare the qubit in its energy groundstate away from the qubit degeneracy point. In the case of charge qubits, the qubit bias ϵ is a function of an external gate charge $n_{\rm g} \equiv C_{\rm g} v_{\rm g}/2e$ [131]. Here, $C_{\rm g}$ is the cross-capacitance between the qubit and the biasing circuit where the voltage $v_{\rm g}$ is applied (e is the electron charge). In the case of flux qubits, ϵ is a function of an external frustration $f_{\rm x} \equiv M_{\rm Q,bias}\, I_{\rm x}/\Phi_0$ [189]. Here, $M_{\rm Q,bias}$ is the mutual inductance between the qubit and the biasing circuit where the current $I_{\rm x}$ is applied (Φ_0 is the flux quantum). In our setup, the qubit is chosen to be on resonance with the second mode of L and with the first mode of B right at the qubit degeneracy point. This is realized for half the charge of a Cooper pair, $n_{\rm g} = 1/2$, or for half a flux quantum, $f_{\rm x} = 1/2$. Consequently, qubit and resonators can be largely detuned by choosing different values of the external gate charge or frustration. This condition corresponds to effectively switch off the qubit-resonator interaction. Notably, the qubit-resonator interaction can be switched off also employing tunable resonators [160, 161]. We do not discuss this obvious option in further detail here.

In order to switch off the qubit-resonator interaction efficiently, one has to make sure that $|\Delta_{\rm shift}| \gg \max\{g_{\rm L,2}, g_{\rm B,1}, g_{\rm LB}\}$ or at least large enough compared to these coupling strengths. Here, $|\Delta_{\rm shift}|$ represents the qubit-resonator detuning induced by any of the three switch-off methods presented above. In this sense, a critical figure of merit for the efficiency of the switch-off pulse is the effective mixing rate of the states of the qubit due to the off-resonance driving $|\alpha\rangle$ [131]

$$\gamma_\alpha^{\rm mix} \approx \langle n_\alpha \rangle \left(\frac{g_{\rm L,2}}{|\Delta_{\rm shift}|} \right)^2 \gamma_{\rm r}\,, \tag{6.16}$$

where $\langle n_\alpha \rangle \equiv |\alpha|^2$ and $\gamma_{\rm r}$ is the energy relaxation rate of the qubit (i.e., the linewidth of the qubit excited state). Equation (6.16) shows that the detuning $|\Delta_{\rm shift}|$ should be large enough to suppress real transitions between the qubit levels, but small enough not to shift the qubit too close to the first and third modes of L, where other pulses could effectively drive the qubit. Finally, given that in this step of the protocol the qubit and resonator B are in a dark state [see Eq. (6.14)], no qubit-resonator dynamics can happen and there are no other conditions on the efficiency of the switch-off pulse.

Our protocol requires to perform the decoupling operations outlined above on a short time scale. In the case of the dynamic shifts, this has already been experimentally realized [146]. The second approach is more challenging, since extra control lines have to be specially dedicated to apply fast DC-Zeeman pulses [137]. Nevertheless, this seems to be feasible and there are already very encouraging experimental results in this direction both for charge and flux qubits [147, 349, 374].

As for the third approach, this can easily be done implementing an adiabatic shift pulse [141, 261, 262]. The rise time $t_{\rm rise}$ of the shift pulse has to fulfill the condition $2\pi/g_{\rm B,1} \gtrsim t_{\rm rise} \gtrsim \max\left\{2\pi/\delta_{\rm Q}, 2\pi/\omega\right\}$ [141, 261, 262]. This condition ensures that the shift pulse is adiabatic with respect to qubit and resonators and nonadiabatic with respect to the interaction between them.

(ii) – Generation pulse. While the second mode of L is continuously driven, the interaction between the qubit, the second mode of L, and the first mode of B is switched on. Depending on the chosen strategy, either the driving which generates $|\alpha_{\rm shift}\rangle$ is turned off or a fast DC-Zeeman pulse or an adiabatic shift pulse are applied. The qubit-resonator interaction is turned on for a time $t_{\rm gen}$. Within this time, the evolution associated with the Hamiltonian of Eq. (6.13) acting on the initial state of Eq. (6.14) yields the following Schrödinger cat state

$$|\Psi_{\rm cat}\rangle = \frac{(|+\rangle\,|\beta_{\rm cat}\rangle + |-\rangle\,|-\beta_{\rm cat}\rangle)}{\sqrt{2}}\,. \tag{6.17}$$

In the expression above,

$$\beta_{\rm cat} = -j\frac{g_{\rm B,1}}{2}t_{\rm gen}\,, \tag{6.18}$$

which is straightforward to find from the definition of the time evolution operator. The state of Eq. (6.17) is in accordance with the original definition given by E. Schrödinger in 1935 of entanglement between a microscopic degree of freedom (in our case, a mesoscopic degree of freedom: a superconducting quantum circuit) and a macroscopic one (the electromagnetic field inside B) [375]. However, for practical purposes it is desirable to separate the two degrees of freedom by means of a projecting (strong) measurement of the qubit state. This will allow us to obtain the so-called *even-* or *odd-cat states* (see below).

(iii) – Switch-off pulse. At the end of the generation pulse, both the strong driving which generates $|\alpha\rangle$ and the interaction between the qubit, the second mode of L, and the first mode of B are switched off. It is necessary to turn off the qubit-resonator interaction, e.g., following similar steps as in *(i)*, in order to prevent a two-mode JC dynamics. This would eventually deteriorate the Schrödinger cat state $|\Psi_{\rm cat}\rangle$.

In this case, the switch-off pulse is efficient when both the effective mixing rate due to the presence of the Schrödinger cat state in B

$$\gamma_{\rm cat}^{\rm mix} \approx n_{\rm cat}\left(\frac{g_{\rm B,1}}{|\Delta_{\rm shift}|}\right)^2 \gamma_{\rm r} \tag{6.19}$$

and the effective decay rate into the second mode of L (now in the vacuum state) due to the fact that the qubit-resonator system is not in a dark state anymore

$$\gamma_{\kappa}^{\rm L,2} \approx \left(\frac{g_{\rm L,2}}{|\Delta_{\rm shift}|}\right)^2 \kappa_{\rm L,2} \tag{6.20}$$

are low. In Eq. (6.19), $n_{\rm cat} \equiv |\beta_{\rm cat}|^2$ represents the size of the cat state, which is considered to behave as an effective driving field.

Before moving to the next step, it is worth gaining further insight into the dissipative dynamics of the first mode of B. B is the quantum bus and its quality factor should be engineered to be as high as possible. The T-shape designs of Figs. 6.1(a)

and 6.2(a) are optimized to achieve this goal. However, there is always an inevitable crosstalk between B and L due to the sum of first- and second-order geometric couplings, g_{LB} (cf. chapter 5). When deriving the Hamiltonian of Eq. (6.12), the field leaking from L to B due to the strong driving of L can be compensated by means of a calibration pulse. The scenario becomes more complex when the strong driving is switched off. In this case, a unitary evolution associated with the Hamiltonian $\widehat{H}_{\mathrm{LB}} \equiv \hbar g_{\mathrm{LB}}(\hat{a}_2^\dagger \hat{b}_1 + \hat{a}_2 \hat{b}_1^\dagger)$ starts taking place. As soon as some field is transferred from B to L, the very large decay rate of L dominates over the unitary dynamics, $\kappa_{\mathrm{L},2} \gg g_{\mathrm{LB}}$, and does not permit the field to go back into B. The field rather leaks out of L, thus making the B $\rightarrow$ L dynamics an effective dissipative evolution. This has the effect to limit the quality factor of B, whose corresponding decay rate, when $|\alpha\rangle$ is turned off, becomes $\kappa_{\mathrm{B},1} \approx g_{\mathrm{LB}}/2\pi$.[9]

(iv) – Projection pulse. As soon as the generation time window is ended, the qubit state must be projected in order to obtain an even- or odd-cat state. The projection can be realized by means of a QND dispersive measurement of duration t_{proj} via the first mode of L [131]. We choose this mode because the conventional linear phase-preserving amplifiers used for such measurements perform better at lower frequencies. As we see from the Hamiltonian of Eq. (6.6), the first mode of L is characterized by an AC-Stark or -Zeeman shift

$$\hbar \frac{2g_{\mathrm{L},1}^2}{\omega} \hat{\sigma}_z \hat{a}_1^\dagger \hat{a}_1 \,.$$

When driving this mode with a classical field which generates an intracavity coherent state $\left|\alpha_{\mathrm{proj}}\right\rangle$ (with complex amplitude $\left|\alpha_{\mathrm{proj}}\right| \exp(j\varphi_{\mathrm{proj}})$), at the output of the resonator the field acquires a qubit-state dependent phase [131, 376]

$$\varphi_{\mathrm{proj}}^{\mp} = \arctan\left(\mp 2 \left\langle n_{\mathrm{proj}} \right\rangle \frac{g_{\mathrm{L},1}^2}{\kappa_{\mathrm{L},1}\omega}\right), \tag{6.21}$$

where $\left\langle n_{\mathrm{proj}} \right\rangle \equiv \left|\alpha_{\mathrm{proj}}\right|^2$ and $\kappa_{\mathrm{L},1}$ is the decay rate of the first mode of L. The phase shift $\varphi_{\mathrm{proj}}^{\mp}$ scales with the coherent state amplitude $\left|\alpha_{\mathrm{proj}}\right|$. Reading out this phase shift[10] corresponds to a QND projective measurement of the qubit, which is then in either the energy groundstate $|\mathrm{g}\rangle$ or excited state $|\mathrm{e}\rangle$.[11] It has been shown experimentally that QND measurements can reach the single-shot limit [108].

There are several conditions that must be met for the projection pulse to accurately perform its function. First, the strong dispersive coupling condition between the qubit and the first mode of L has to be fulfilled

$$\chi_{\mathrm{L},1}^0 = 4\frac{g_{\mathrm{L},1}^2}{\omega\kappa_{\mathrm{L},1}} \geqslant 1 \,. \tag{6.22}$$

[9] A full simulation of the quantum dynamics with and without strong driving should eventually be performed in order to better understand the physics of the bus-leaky cavity system. We believe in fact that the qualitative arguments presented in this thesis are still too speculative.

[10] At the output of the resonator, also the field amplitude is modified by the presence of the qubit and can equivalently be used to monitor the qubit state [131].

[11] Strictly speaking, we should use $|\tilde{\mathrm{g}}\rangle$ and $|\tilde{\mathrm{e}}\rangle$ for the qubit energy groundstate and excited state, respectively. In fact, after the switch-off pulse, the qubit eigenstates are effectively modified. For convenience, we keep using the simplified notation $|\mathrm{g}\rangle$ and $|\mathrm{e}\rangle$ throughout the rest of the chapter.

Here, $\chi^0_{\mathrm{L},1}$ represents the cavity pull per photon due to the off-resonance interaction. If the condition of Eq. (6.22) is fulfilled, it is in principle possible to perfectly distinguish the qubit energy groundstate from the excited state.

Under driving conditions, the cavity pull is enhanced by a quantity $\langle n_{\mathrm{proj}} \rangle$. This enhancement is very important to be able to reach a sufficiently large (at least theoretically) signal-to-noise ratio (SNR), which is given by [131]

$$\mathrm{SNR} \equiv \frac{\langle n_{\mathrm{proj}} \rangle \, \kappa_{\mathrm{L},1}}{\langle n_{\mathrm{amp}} \rangle \, 2\gamma_{\mathrm{r}}} > 1 \,, \tag{6.23}$$

where $\langle n_{\mathrm{amp}} \rangle$ is the noise level of the first amplifier expressed in equivalent photons.[12] It has been shown experimentally that it is hard to reach a very large SNR. This usually saturates to a maximum value smaller than 10 [377]. A theoretical effort has found the origin of this issue in nonlinear effects and intrinsic dephasing mechanisms of the qubit [378, 379]. Nevertheless, from the definition of SNR it appears evident that a low quality factor, i.e., a large decay rate $\kappa_{\mathrm{L},1}$, for the mode used to measure the qubit state and/or a large $\langle n_{\mathrm{proj}} \rangle$ are desirable.

The projection time t_{proj} has to be shorter than the energy relaxation time of the qubit [131]

$$t_{\mathrm{proj}} \equiv 2 \frac{\langle n_{\mathrm{amp}} \rangle}{\kappa_{\mathrm{L},1} \langle n_{\mathrm{proj}} \rangle} \leqslant 1/\gamma_{\mathrm{r}} \,. \tag{6.24}$$

This expression takes into account for the amplifier noise level, which scales up the fundamental time limitation on the resolution of a phase shift in a quantum homodyne measurement [131]. Finally, an upper-bound limit for the readout error is given by the probability for the qubit to relax during the projection time, $P_{\mathrm{r}} \approx t_{\mathrm{proj}} \, \gamma_{\mathrm{r}}$, which limits the projection fidelity [131].

The qubit projection could be realized by means of different techniques. Among those, it is worth mentioning the cavity bifurcation amplifier [110, 216] and the mesoscopic shelving readout [221]. In addition, the development of quantum-limited amplifiers will substantially help improving on the qubit projection speed [194–196, 198, 199, 201, 203, 205, 208, 209].

After the projection pulse, depending on the qubit state $|\mathrm{g}\rangle$ or $|\mathrm{e}\rangle$ the field in B is left in an even or odd coherent state

$$|\Psi_{\mathrm{even}}\rangle = \frac{|\beta_{\mathrm{cat}}\rangle + |-\beta_{\mathrm{cat}}\rangle}{\sqrt{1 + \exp\left(-|\beta_{\mathrm{cat}}|^2\right)}} \tag{6.25}$$

or

$$|\Psi_{\mathrm{odd}}\rangle = \frac{|\beta_{\mathrm{cat}}\rangle - |-\beta_{\mathrm{cat}}\rangle}{\sqrt{1 - \exp\left(-|\beta_{\mathrm{cat}}|^2\right)}} \,, \tag{6.26}$$

respectively.

Before proposing a method for the measurement of the intracavity states $|\Psi_{\mathrm{even}}\rangle$ and $|\Psi_{\mathrm{odd}}\rangle$, we give an upper-bound estimate of their maximum size. The latter is set by the maximum generation time, which is limited by the effective decay rate

[12] If T_{n} is the noise temperature of the amplifier, $\langle n_{\mathrm{amp}} \rangle \equiv k_{\mathrm{B}} T_{\mathrm{n}}/\hbar\omega$, where k_{B} is the Boltzmann constant.

$\kappa_{\mathrm{B},1}^{\mathrm{eff}} \equiv |\beta_{\mathrm{cat}}|^2 \kappa_{\mathrm{B},1}$ of the first mode of B,

$$t_{\mathrm{gen}}^{\max} = \frac{1}{\kappa_{\mathrm{B},1}^{\mathrm{eff}}} . \tag{6.27}$$

This condition means that the larger the cat size, the faster the effective decay rate $\kappa_{\mathrm{B},1}^{\mathrm{eff}}$, and, consequently, the shorter the maximum generation time, which self-consistently limits the cat size. Substituting the definition of β_{cat} given by Eq. (6.18) into Eq. (6.27), we find the maximum amplitude of the Schrödinger cat state to be

$$|\beta_{\mathrm{cat}}^{\max}| = \sqrt[3]{\frac{|g_{\mathrm{B},1}|}{2\kappa_{\mathrm{B},1}}} , \tag{6.28}$$

which also sets the maximum generation time $t_{\mathrm{gen}}^{\max}$.

In reality, the scenario is more complex and we must take into account the projection time t_{proj} for a more accurate estimate of the cat size. We thus make the substitution $t_{\mathrm{gen}}^{\max} \equiv z$, to simplify the notation, and rewrite Eq. (6.27) as

$$t_{\Sigma}^{\max} = \left(\frac{z}{t_{\Sigma}^{\max}} \ \kappa_{\mathrm{B},1} \frac{g_{\mathrm{B},1}^2}{4} z^2 \ + \ \frac{t_{\mathrm{proj}}}{t_{\Sigma}^{\max}} \ g_{\mathrm{LB}} \frac{g_{\mathrm{B},1}^2}{4} z^2 \right)^{-1} , \tag{6.29}$$

where $t_{\Sigma}^{\max} \equiv t_{\mathrm{gen}}^{\max} + t_{\mathrm{proj}} = z + t_{\mathrm{proj}}$. This condition clearly shows that the generation time (and, thus, the cat size) is further reduced compared to the estimate given by Eq. (6.28) because of the time needed to project the qubit state. In Eq. (6.29), the effective decay rate of the quantum bus is the weighted average between the bare decay rate $\kappa_{\mathrm{B},1}$, valid during the time $t_{\mathrm{gen}} \leqslant t_{\mathrm{gen}}^{\max}$, and the enhanced rate $\kappa_{\mathrm{B},1} \approx g_{\mathrm{LB}}$, to be used during the time t_{proj}. The latter is due to the fact that $|\alpha\rangle$ is turned off during the projection time [see explanation in step *(iii)*]. Notably, from Eq. (6.29) it is evident that the best results, i.e., the largest cat states, depend on a trade off between $\kappa_{\mathrm{B},1}$ and $1/t_{\mathrm{proj}} \propto \kappa_{\mathrm{L},1}$ [see Eq. (6.24)] and are obtained when $t_{\mathrm{proj}} \ll t_{\mathrm{gen}}$. From the same equation, it also appears that the effective decay rate of the quantum bus is limited by g_{LB} when $\kappa_{\mathrm{B},1} \to 0$.

After some simple algebra, Eq. (6.29) can be rewritten as

$$z^3 + A_2 z^2 + A_0 = 0 , \tag{6.30}$$

where $A_0 \equiv -4/g_{\mathrm{B},1}^2 \kappa_{\mathrm{B},1}$ and $A_2 \equiv (g_{\mathrm{LB}}/\kappa_{\mathrm{B},1}) t_{\mathrm{proj}}$. The discriminant of this third-order algebraic equation is always larger than zero, $D = A_0^2/4 - A_0 A_2^3/27 > 0$. As a consequence, the equation has one real and two complex conjugate solutions. We are obviously interested in the real (positive) solution only, which is given by

$$z = t_{\mathrm{gen}}^{\max} = -\frac{A_2}{3} + (S + T) , \tag{6.31}$$

where $S \equiv \sqrt[3]{-A_0/2 - A_2^3/27 + \sqrt{D}}$ and $T \equiv \sqrt[3]{-A_0/2 - A_2^3/27 - \sqrt{D}}$. It is now straightforward to calculate the cat size substituting Eq. (6.31) into Eq. (6.18).[13] In Sec. 6.5, we study $|\beta_{\mathrm{cat}}^{\max}|$ as a function of the decay rates of the quantum bus, $\kappa_{\mathrm{B},1}$, and of the leaky cavity, $\kappa_{\mathrm{L},1}$.

[13] It is easy to prove that the result of Eq. (6.31) reduces to that of Eq. (6.27) when setting $t_{\mathrm{proj}} = 0$.

Finally, we notice that the generation time has to be much shorter than the worst qubit coherence time, $t_{\rm gen} \ll \min\{1/\gamma_{\rm r}, 1/\gamma_\varphi\}$, where γ_φ represents the qubit dephasing rate.

The architecture proposed here could directly be applied to implement conventional cavity field measurement. These would consist of an initial qubit-cavity pre-measurement where the qubit acts as the quantum probe with which the cavity field gets entangled, followed by a measurement of the qubit state [380]. In this case, the pre-measurement requires an interaction time sufficiently long (on the order of the inverse interaction frequency) to adequately entangle the cavity field with the qubit. Accordingly, the noisy action of decoherence plays an important role [179, 381]. In contrast to this common approach, in the next subsection we show an alternative method to realize a measurement of the cavity field with a relatively fast qubit-cavity pre-measurement (on the order of a small fraction of the inverse interaction frequency) and, thus, minimal action of decoherence [382]. In this context, we are able to extend the results in Ref. [382] to the case of qubit dephasing. This is an important extension considering that superconducting qubits largely suffer from dephasing mechanisms.

6.3.2 Measurement of Schrödinger Cat States

We now propose a method for the measurement of relevant observables of the Schrödinger cat states generated according to the recipe given in the previous section. Obviously, our method can be applied to other generic intracavity field states.

(v) – $\pi/2$-pulse. For the sake of an example, we now consider the even coherent state $|\Psi_{\rm even}\rangle$ of Eq. (6.25). We then apply a $\pi/2$-pulse of duration $t_{\pi/2}$ on resonance with the qubit.[14] We remind that, at this stage, the interaction between qubit and resonators is still switched off. The $\pi/2$-pulse can be sent through L even if it is detuned from any of its modes (cf., e.g., Refs. [108, 131]). This yields the system density matrix $\hat{\rho}_{\rm sys}(t_\Sigma) = |+^\phi\rangle\langle+^\phi| \otimes \hat{\rho}_{\rm even} \otimes \hat{\rho}_{\rm L,2}$, where $|+^\phi\rangle \equiv [|{\rm g}\rangle + \exp(j\phi)\,|{\rm e}\rangle]/\sqrt{2}$, $\hat{\rho}_{\rm even} \equiv |\Psi_{\rm even}\rangle\langle\Psi_{\rm even}|$, and $\hat{\rho}_{\rm L,2} \equiv |0\rangle_{\rm L,2}\langle 0|_{\rm L,2}$. Here, ϕ is a relative phase and $t_\Sigma \equiv t_{\rm gen} + t_{\rm proj} \leqslant t_\Sigma^{\rm max}$ may be reset to zero, $t_\Sigma = 0$. The $\pi/2$-pulse is used to induce the phase ϕ. This can easily be realized by means of I/Q mixing techniques [360]. As we show in the following, continuously shifting ϕ allows for the measurement of the quadrature of the intracavity field (e.g., $|\Psi_{\rm even}\rangle$) in all possible phase-space directions. The first phase to be used is adopted as reference phase, $\phi_{\rm ref}$.

(vi) – Pre-measurement. The qubit-resonator interaction is switched on. The system, described by the Hamiltonian $\widehat{H}_{\rm sys}$ of Eq. (6.6), is let to evolve for a very short pre-measurement time $t_{\rm pre}$. Since the first and third mode of L are now in the vacuum state, the corresponding dynamic shifts are zero. Under the realistic assumption $g_{\rm L,2} = g_{\rm B,1} \gg g_{\rm LB}$, the state $\hat{\rho}_{\rm sys}(0)$ evolves via a two-mode resonant JC for a dimensionless time $\tau \equiv g_{\rm B,1} t_{\rm pre}$. In the presence of a dispersive bath, producing qubit dephasing, and a thermal bath at zero temperature, inducing field relaxation, the system dynamical equation becomes

$$\dot{\hat{\rho}}_{\rm sys} = \frac{1}{j\hbar}[\hat{H}_{\rm sys}, \hat{\rho}_{\rm sys}] - \sum_k \frac{\gamma_k}{2}(\{\hat{A}_k^\dagger \hat{A}_k, \hat{\rho}_{\rm sys}\} - 2\hat{A}_k \hat{\rho}_{\rm sys} \hat{A}_k^\dagger)\,, \tag{6.32}$$

[14] Depending on the pulse amplitude, the $\pi/2$-pulse can be very fast. We can consequently neglect the time $t_{\pi/2}$ in the rest of the protocol.

where $\dot{\hat{\rho}}_{\rm sys} \equiv (d/d\tau)\hat{\rho}_{\rm sys}$, the braces denote anti-commutators, and the sum runs over two indices corresponding to qubit dephasing ($\hat{A}_1 \equiv \hat{\sigma}_z, \gamma_1 \equiv \gamma_\varphi/2$) and resonator energy relaxation ($\hat{A}_2 \equiv \hat{a}_2, \gamma_2 \equiv \kappa_{\rm L,2}$), respectively. Above, we neglect the energy relaxation rate of the qubit, which is assumed to be small compared to the other decoherence rates [108] (cf. also the discussion in chapter 5, Sec. 5.3),[15] and the field relaxation of B because $\kappa_{\rm B,1} \ll \kappa_{\rm L,2}$. Calculating now $dP_{\rm e}(\tau)/d\tau \equiv d\left\langle |{\rm e}\rangle\left\langle {\rm e}|\right\rangle/d\tau = {\rm Tr}[\dot{\hat{\rho}}_{\rm sys}\left|{\rm e}\right\rangle\left\langle {\rm e}\right|]$ from Eq. (6.32), and after some algebra, we obtain

$$\frac{d}{d\tau}P_{\rm e}(\tau) = \frac{1}{j\hbar}\langle[|{\rm e}\rangle\left\langle {\rm e}\right|, \hat{H}_{\rm sys}]\rangle\,. \tag{6.33}$$

Interestingly, the terms involving qubit dephasing and resonator energy relaxation vanish in this expression. This happens when calculating the expectation value at time τ. Evaluating Eq. (6.33) in the limit $\tau \to 0^+$ yields the important result

$$\frac{d}{d\tau}P_{\rm e}^{|+^\phi\rangle}(\tau)\Big|_{\tau\to 0^+} = (\langle\hat{Y}^\phi_{\rm B,1}\rangle + \langle\hat{Y}^\phi_{\rm L,2}\rangle)\big|_{\tau\to 0^+}\quad, \tag{6.34}$$

where $\hat{Y}^\phi_{\rm B,1} \equiv [\hat{b}_1\exp(-j\phi) - \hat{b}_1^\dagger\exp(j\phi)]/2j$ and $\hat{Y}^\phi_{\rm L,2} \equiv [\hat{a}_2\exp(-j\phi) - \hat{a}_2^\dagger\exp(j\phi)]/2j$ are field quadratures. The conjugated quadratures are $\hat{X}^\phi_{\rm B,1} \equiv [\hat{b}_1\exp(-j\phi) + \hat{b}_1^\dagger\exp(j\phi)]/2$ and $\hat{X}^\phi_{\rm L,2} \equiv [\hat{a}_2\exp(-j\phi) + \hat{a}_2^\dagger\exp(j\phi)]/2$, which are obtained by replacing $\phi \to (\phi - \pi/2)$. Considering that at time $\tau \to 0^+$ the second mode of L is in the vacuum state (or a very small thermal state due to the finite operation temperature of circuit QED experiments), $\langle\hat{Y}^\phi_{\rm L,2}\rangle\big|_{\tau\to 0^+} = 0$. Hence, we obtain

$$\langle\hat{Y}^\phi_{\rm B,1}\rangle\Big|_{\tau\to 0^+} = \frac{d}{d\tau}P_{\rm e}^{|+^\phi\rangle}(\tau)\Big|_{\tau\to 0^+}\,. \tag{6.35}$$

Equation (6.35) shows mathematically that the first derivative of the measured excited-state qubit population, obtained at infinitesimally small interaction time, contains information about resonator-field observables with no influence of decoherence processes.

If the qubit is now prepared in the excited state $|{\rm e}\rangle$,[16] it is also possible to determine the mean photon number of the fields inside resonators B and L, via

$$\begin{aligned}(\langle\hat{n}_{\rm B,1}\rangle + \langle\hat{n}_{\rm L,2}\rangle)\big|_{\tau\to 0^+} &= (\langle\hat{b}_1^\dagger\hat{b}_1\rangle + \langle\hat{a}_2^\dagger\hat{a}_2\rangle)\big|_{\tau\to 0^+}\\ &= -\frac{1}{2}\frac{d^2}{d^2\tau}P_{\rm e}^{|{\rm e}\rangle}(\tau)\Big|_{\tau\to 0^+} - 1\,.\end{aligned} \tag{6.36}$$

Again, the contribution from resonator L is negligible, $\left\langle\hat{n}_{\rm L,2}\right\rangle\big|_{\tau\to 0^+} \approx 0$. Eq. (6.36) thus gives the mean photon number in B (i.e., the size of the Schrödinger cat state). The (-1) on the right hand side of Eq. (6.36) accounts for the vacuum, which is a constant offset.

Although Eqs. (6.35) and (6.36) are exact mathematical expressions, due to their infinitesimal character they do not represent a realistic theoretical description of the

[15] In more recent experimental works, the qubit energy relaxation and dephasing have been largely improved and have now become comparable [118–120, 244, 261]. However, in the present calculations we still prefer to neglect the energy relaxation rate for simplicity.

[16] This can easily be done after the projection pulse. If the qubit is found in the groundstate $|{\rm g}\rangle$, a π-pulse brings it in $|{\rm e}\rangle$. Differently, the qubit is already in $|{\rm e}\rangle$.

measurement process. A more realistic picture is obtained considering an estimator for the derivative, e.g., in Eq. (6.35) over short, but non-zero measurement times $\Delta\tau$ through the Taylor expansion: $P(\tau+\Delta\tau) = P(\tau)+P'(\tau)\Delta\tau+P''(\tau)(\Delta\tau)^2/2!+\mathcal{O}[(\Delta\tau)^3]$. Subsequently, it can be shown that

$$\frac{\Delta P_{\rm e}^{|+^\phi\rangle}(\tau)}{\Delta\tau}\Big|_{\tau=0} \approx \langle\hat{Y}_{\rm B,1}^{\phi}\rangle - \left[1+\frac{(\kappa_{\rm L,2}+\gamma_\varphi)}{4g_{\rm B,1}}\langle\hat{Y}_{\rm B,1}^{\phi}\rangle\right]\Delta\tau\,, \tag{6.37}$$

where the second term on the right hand side is the dominant higher-order contribution to Eq. (6.35). This term, even for ideal ensemble averaging, contains the dominant resonator decay rate $\kappa_{\rm L,2}$ and the qubit dephasing rate γ_φ. Equation (6.37) shows that in the strong-coupling regime, $\{\kappa_{\rm L,2},\gamma_\varphi\} \ll g_{\rm B,1}$, or even in the weak-coupling regime, $\{\kappa_{\rm L,2},\gamma_\varphi\} > g_{\rm B,1}$, it is possible to identify a time $\Delta\tau$ that is long enough to allow the readout of $\langle\hat{Y}_{\rm B,1}^{\phi}\rangle$ and short enough to suppress the effects of decoherence during the pre-measurement. Clearly, a similar discretization can also be done for the case of the mean photon number of Eq. (6.36).

(vii) – Measurement pulse. In order to calculate the probability $P_{\rm e}(\tau)$, the qubit state must be measured, e.g., by means of a QND dispersive readout. This can be performed taking advantage again of the dispersive action of the first mode of L. This measurement pulse has to fulfill similar conditions as those outlined in step *(iv)*. In particular, the measurement time has to be shorter than the energy relaxation time of the qubit, $t_{\rm m} \leqslant 1/\gamma_{\rm r}$.

(viii) – Repetition. Establishing an accurate estimator with the prescribed accuracy for the ensemble averages in Eqs. (6.35) and (6.36) requires, in general, many repetitions of the prescribed protocol. There is a trade-off between the length of the physically implemented $\Delta\tau$, the number of measurement repetitions, and the strength of the qubit-resonator coupling required to achieve a desired degree of noise immunity. In summary, the proposed measurement technique consists of two main steps. First, a fast pre-measurement allows the pointer (qubit) to encode the information about the system (resonator field). This minimizes decoherence processes. Second, the readout of the pointer, happening typically over longer time scales, completes the quantum measurement procedure [380].

6.4 Quantum Tomography in Two-Resonator Circuit QED

In this section, we show that two-resonator circuit QED architectures can be exploited as a quantum-tomography toolbox. We first demonstrate that a variant of the protocol outlined in Sec. 6.3 allows one to reconstruct, in the resonant regime, the Wigner function of any given field (cf. Subsec. 6.4.1). We then consider a simplified configuration of the setups of Figs. 6.1 and 6.2 and show that this can be straightforwardly used to reconstruct, in the dispersive regime this time, the Wigner function of unknown fields (cf. Subsec. 6.4.2).

6.4.1 Wigner Function Reconstruction via JC and Anti-JC Dynamics

The following protocol can be considered as an extension of the protocol of Sec. 6.3.

We assume the first mode of resonator B to be populated with an unknown field state $\hat{\rho}_{\mathrm{B},1} = \left|\Psi_{\mathrm{B},1}\right\rangle\left\langle\Psi_{\mathrm{B},1}\right|$. This, for example, can be the Schrödinger cat state generated following the protocol of Subsec. 6.3.1. It is well known that state $\hat{\rho}_{\mathrm{B},1}$ can equivalently be expressed via its corresponding characteristic function $\chi(\tilde{\beta}) \equiv \mathrm{Tr}[\hat{\rho}_{\mathrm{B},1}\widehat{D}(\tilde{\beta})]$. Here, $\widehat{D}(\tilde{\beta})$ is the usual displacement operator and $\tilde{\beta}$ the complex amplitude in phase space of an arbitrary coherent state [383]. For the sake of simplicity, we consider a pure field state, even though our results remain valid for any arbitrary mixed state. The first step for a full-state quantum tomography is the initialization of the qubit in state $\left|+^{\theta}\right\rangle \equiv [|+\rangle + \exp(j\theta)\,|-\rangle]/\sqrt{2}$, while resonator B, populated with the unknown field $|\Psi_{\mathrm{B},1}\rangle$, stays unperturbed. At this point, the interaction described in Eq. (6.13) must be turned on by driving again the second mode of resonator L strongly. After an interaction time t_{d}, the initial state $\left|+^{\theta}\right\rangle|\Psi_{\mathrm{B},1}\rangle$ evolves to

$$|\Psi(\tilde{\beta},\theta)\rangle = \frac{(|+\rangle\,\widehat{D}(\tilde{\beta})\,|\Psi_{\mathrm{B},1}\rangle + e^{j\theta}\,|-\rangle\,\widehat{D}(-\tilde{\beta})\,|\Psi_{\mathrm{B},1}\rangle)}{\sqrt{2}}\,, \tag{6.38}$$

with $\tilde{\beta} \equiv -jg_{\mathrm{B},1}\,t_{\mathrm{d}}/2$. Notably, the displacement $\widehat{D}(\tilde{\beta})$ is intrinsically realized by the JC–anti-JC dynamics characteristic of our protocol. Such displacement, which usually has to be induced by populating the resonator with a coherent state [71, 153, 367, 384], is necessary to explore the entire phase space via the complex amplitude $\tilde{\beta}$.

By measuring the groundstate qubit population $P_{\mathrm{g}}(\tilde{\beta},\theta)$, given that the initial state is $\left|+^{\theta}\right\rangle$, we can retrieve the characteristic function through

$$\chi(\tilde{\beta}) = \left[P_{\mathrm{g}}\left(\frac{\tilde{\beta}}{2},0\right) - \frac{1}{2}\right] + j\left[P_{\mathrm{g}}\left(\frac{\tilde{\beta}}{2},\frac{\pi}{2}\right) - \frac{1}{2}\right]. \tag{6.39}$$

From the measured function $\chi(\tilde{\beta})$, it is possible to derive $\hat{\rho}_{\mathrm{B},1}$ or its associated Wigner function via a Fourier transform [383, 385], thus achieving a full-state reconstruction.

6.4.2 Wigner Function Reconstruction via Dispersive Interactions

In all protocols studied so far, the qubit, the first mode of B, and the second mode of L are considered to be on resonance. In addition, the qubit is considered to be dispersively coupled to the first and third modes of L. A simplified variant of such setup can be realized assuming the qubit transition angular frequency to be comprised between the transition angular frequencies of the first mode of L and the first mode of B, $\omega_{\mathrm{L},1} < \Omega_{\mathrm{Q}} < \omega_{\mathrm{B},1}$. If the frequency spacing is large enough, the qubit is dispersively coupled to these two modes, which, at the same time, are largely detuned from each other. We also assume the modes of L and B to be suitably spaced in order to avoid resonances between higher harmonics, e.g., $2\omega_{\mathrm{L},1} \neq \omega_{\mathrm{B},1}$, $3\omega_{\mathrm{L},1} \neq \omega_{\mathrm{B},1}$, $3\omega_{\mathrm{L},1} \neq 2\omega_{\mathrm{B},1}$, etc. Being all relevant modes of L and B detuned, the effect of the geometric crosstalk between them is largely minimized and can safely be neglected. Finally, we consider all modes of L besides the first to be in the vacuum state and, as a consequence, disregard their dispersive interaction with the qubit.

Under these assumptions, the Hamiltonian of Eq. (6.3) in an interaction picture with respect to the qubit and the relevant modes of resonators L and B and after a RWA can be written as

$$\begin{aligned}\widehat{\widetilde{H}}^{\text{new}} &= \hbar g_{\text{L},1}\sin\theta\,(\hat{\sigma}^{-}\hat{a}_1^{\dagger}e^{-j\Delta_{\text{L},1}t}+\hat{\sigma}^{+}\hat{a}_1e^{+j\Delta_{\text{L},1}t})\\ &\quad+\hbar g_{\text{B},1}\sin\theta\,(\hat{\sigma}^{-}\hat{b}_1^{\dagger}e^{-j\Delta_{\text{B},1}t}+\hat{\sigma}^{+}\hat{b}_1e^{+j\Delta_{\text{B},1}t})\\ &\quad+\hbar g_{\text{LB}}(\hat{a}_1^{\dagger}\hat{b}_1e^{-j\delta_{\text{LB}}t}+\hat{a}_1\hat{b}_1^{\dagger}e^{j\delta_{\text{LB}}t})\,, \end{aligned} \tag{6.40}$$

where $\delta_{\text{LB}}\equiv\omega_{\text{B},1}-\omega_{\text{L},1}$. If the dispersive conditions $|\Delta_{\text{L},1}|\gg\max\{g_{\text{L},1},g_{\text{B},1},g_{\text{LB}}\}$, $|\Delta_{\text{B},1}|\gg\max\{g_{\text{L},1},g_{\text{B},1},g_{\text{LB}}\}$ are fulfilled, and $\sin\theta=1$ (qubit at the degeneracy point), the following effective Hamiltonian can easily be derived (cf. chapter 5)

$$\begin{aligned}\widehat{\widetilde{H}}_{\text{eff}}^{\text{new}} &= \hbar\frac{g_{\text{L},1}^2}{\Delta_{\text{L},1}}\hat{\sigma}_z\hat{a}_1^{\dagger}\hat{a}_1+\hbar\frac{g_{\text{B},1}}{\Delta_{\text{B},1}}\hat{\sigma}_z\hat{b}_1^{\dagger}\hat{b}_1\\ &\quad+\hbar\left[\frac{g_{\text{L},1}g_{\text{B},1}}{2}\left(\frac{1}{\Delta_{\text{L},1}}+\frac{1}{\Delta_{\text{B},1}}\right)\hat{\sigma}_z+g_{\text{LB}}\right]\\ &\quad\times(\hat{a}_1^{\dagger}\hat{b}_1e^{-j\delta_{\text{LB}}t}+\hat{a}_1\hat{b}_1^{\dagger}e^{+j\delta_{\text{LB}}t})\,. \end{aligned} \tag{6.41}$$

Defining $g_{\text{sw}}\equiv g_{\text{L},1}\,g_{\text{B},1}(\Delta_{\text{L},1}+\Delta_{\text{B},1})\hat{\sigma}_z/(2\Delta_{\text{L},1}\Delta_{\text{B},1})+g_{\text{LB}}$ and assuming $\delta_{\text{LB}}\gg g_{\text{sw}}$, we can estimate the effect of the last term of Eq. (6.41) via second-order perturbation theory. We can define the superoperators $\Lambda^{\dagger}\equiv g_{\text{sw}}\hat{a}_1\hat{b}_1^{\dagger}$ and $\Lambda\equiv g_{\text{sw}}\hat{a}_1^{\dagger}\hat{b}_1$ and, in analogy to the Dyson series derivation of Eq. (6.5), obtain the Hamiltonian

$$\widehat{\widetilde{H}}_{\text{eff}}^{\text{new}}=\hbar\left(\frac{g_{\text{L},1}^2}{\Delta_{\text{L},1}}\hat{\sigma}_z-\frac{g_{\text{sw}}^2}{\delta_{\text{LB}}}\right)\hat{a}_1^{\dagger}\hat{a}_1+\left(\frac{g_{\text{B},1}^2}{\Delta_{\text{B},1}}\hat{\sigma}_z+\frac{g_{\text{sw}}^2}{\delta_{\text{LB}}}\right)\hat{b}_1^{\dagger}\hat{b}_1\,. \tag{6.42}$$

We notice that the coefficient g_{sw} is the balance between a dynamic coupling, which depends on $\hat{\sigma}_z$, and a geometric one, which is qubit-state independent. This is in agreement with the results of chapter 5. In the present setup, though, g_{sw} contributes to the system dynamics only in second-order as $g_{\text{sw}}^2/\delta_{\text{LB}}$. This effective coupling coefficient becomes very small for large δ_{LB} (as in our case) and can be neglected. If necessary, it can be set to zero exactly by choosing a proper qubit-resonator detuning. This can be realized modifying the qubit transition frequency, e.g., as in step *(i)* of the protocol of Subsec. 6.3.1. In the light of these results, the present variant of two-resonator circuit QED does not suffer from any crosstalk between the two resonators and the Hamiltonian can finally be expressed as

$$\widehat{H}_{\text{eff}}^{\text{new}}=\hbar\frac{g_{\text{L},1}^2}{\Delta_{\text{L},1}}\hat{\sigma}_z\hat{a}_1^{\dagger}\hat{a}_1+\frac{g_{\text{B},1}^2}{\Delta_{\text{B},1}}\hat{\sigma}_z\hat{b}_1^{\dagger}\hat{b}_1\,. \tag{6.43}$$

If we now consider resonator B (the quantum bus) to be prepared in an unknown field state $\hat{\rho}_{\text{B},1}$ (e.g., a Fock state, a linear superposition of Fock states, a squeezed state, a Schrödinger cat state, etc.), it is straightforward to utilize the Hamiltonian of Eq. (6.43) to reconstruct the Wigner function of $\hat{\rho}_{\text{B},1}$. This can be realized adapting to our setup the recipes described in Refs. [367, 384]:

(i) The field state $\hat{\rho}_{\mathrm{B},1}$ is displaced by means of a classical driving with strength (angular frequency) η_{dr} and frequency $\omega_{\mathrm{dr}} = \omega_{\mathrm{B},1}$. This frequency must be retuned to compensate for the AC-Stark or -Zeeman shift due to the disperive interaction between the qubit and resonator B (L is now in the vacuum state). The complex amplitude of the displacement field generated in resonator B under the action of η_{dr} grows with the driving time t_{dr}, $\beta_{\mathrm{disp}} = -j\eta_{\mathrm{dr}}t_{\mathrm{dr}}$. This amplitude should be large enough to be able to explore the phase space far from the origin and, thus, resolve with high accuracy the tails of the Wigner function [384]. At the same time, it should be kept low enough in order not to accidentally mix the states of the qubit. As always, the time scale at which the mixing process takes place is $1/\gamma_{\mathrm{disp}}^{\mathrm{mix}}$, where $\gamma_{\mathrm{disp}}^{\mathrm{mix}} \approx n_{\beta}(g_{\mathrm{B},1}/\Delta_{\mathrm{B},1})^2\gamma_{\mathrm{r}}$. Here, $\langle n_{\beta}\rangle$ is the mean number of photons in resonator B, i.e., the mean number of photons of state $\hat{\rho}_{\mathrm{B},1}$ with the addition of the displacement photons $\langle n_{\mathrm{disp}}\rangle \equiv |\beta_{\mathrm{disp}}|^2$. The time $1/\gamma_{\mathrm{disp}}^{\mathrm{mix}}$ should be large compared to the total duration of the measurement;

(ii) A $\pi/2$-pulse with frequency $\omega_{\pi/2} = \Omega_{\mathrm{Q}}$ is applied to the qubit, which is initially prepared, for example, in $|\mathrm{g}\rangle$. The $\pi/2$-pulse is send through resonator L not to disturb state $\hat{\rho}_{\mathrm{B},1}$ and is characterized by a strength with real part (angular frequency) $\eta_{\pi/2}$ and phase $\varphi_{\pi/2}^{(1)}$. The pulse strength must be chosen such that the pulse duration time is $t_{\pi/2} = \pi\Delta_{\mathrm{L},1}/4g_{\mathrm{L},1}\eta_{\pi/2}$. The phase $\varphi_{\pi/2}^{(1)}$ constitutes our reference phase. The $\pi/2$-pulse rotates the qubit and, indirectly, affects the field in resonator B, which is dispersively coupled to the qubit. To keep this effect small, the $\pi/2$-pulse should be fast compared to the dispersive dynamics which takes place between the qubit and resonator B. This can easily be realized increasing the strength of the $\pi/2$-pulse (angular frequency), $\eta_{\pi/2} \gg \Delta_{\mathrm{L},1}\, g_{\mathrm{B},1}^2(\langle n_{\beta}\rangle + 1/2)/\Delta_{\mathrm{B},1}\, g_{\mathrm{L},1}$;

(iii) The driving η_{dr} is switched off. According to Eq. (6.43), qubit and resonator B now evolve under a dispersive interaction with coupling strength $g_{\mathrm{B},1}^2/\Delta_{\mathrm{B},1}$. This evolution, which naturally gives rise to the parity operator necessary for the Wigner function reconstruction [367, 384], has to continue for a time $t_{\mathrm{par}} = \pi\Delta_{\mathrm{B},1}/2g_{\mathrm{B},1}^2$. It is during this time that information about the field state is encoded into the qubit state. It is worth mentioning that the presence of resonator L, also dispersively coupled to the qubit, does not influence the encoding process. This is due to the fact that, at this stage, resonator L is in the vacuum state $|0\rangle_{\mathrm{L},1}$;

(iv) A second $\pi/2$-pulse is applied to the qubit. This pulse is analogous to that of step (ii), the only difference being its phase, which is now $\varphi_{\pi/2}^{(2)}$. This second pulse is crucial to set the effective phase of the system. In fact, the phase difference $\delta_{\varphi} \equiv \varphi_{\pi/2}^{(2)} - \varphi_{\pi/2}^{(1)}$ is the only experimentally accessible quantity and must be set to a precise value in order to reconstruct the Wigner function of $\hat{\rho}_{\mathrm{B},1}$;

(v) Finally, the qubit state must be measured, e.g., by means of a QND dispersive readout via resonator L, as explained in Sec. 6.3. The qubit measurement starts at a time $t_{\mathrm{meas}} = t_{\mathrm{dr}} + t_{\mathrm{par}} + t_{\pi/2}$ and sets the end of the field-qubit encoding process.

Once the qubit populations $P_{\rm g}$ and $P_{\rm e}$ are measured, following the lines of Ref. [384] we can readily compute

$$\langle\hat{\sigma}_z\rangle \equiv P_{\rm e} - P_{\rm g} = {\rm Tr}\left[\sin(\varphi^{(1)}_{\pi/2} - \varphi^{(2)}_{\pi/2})\hat{\rho}_{\rm B,1}\widehat{D}^{-1}(\beta_{\rm disp})e^{-j\pi\hat{a}^\dagger\hat{a}}\widehat{D}(\beta_{\rm disp})\right] . \qquad (6.44)$$

Setting the phase difference $\delta_\varphi = -\pi/2$ allows for the measurement of the Wigner function of $\hat{\rho}_{\rm B,1}$ at the point $-\beta_{\rm disp}$, $W(-\beta_{\rm disp}) = \langle\hat{\sigma}_z\rangle/\pi$. Differently from the case of Ref. [384], in our protocol the $\pi/2$-pulses are applied through resonator L and do not generate any extra displacement of the field in resonator B. Finally, the entire phase space can be explored repeating the experiment for different times $t_{\rm dr}$.

The presence of a leaky cavity represents a key element for the reconstruction of the Wigner function of a generic state $\hat{\rho}_{\rm B,1}$ in circuit QED. Our scheme is particularly useful in those implementations of circuit QED where the qubit is measured by means of a dispersive readout [386] or any other cavity-based readout and constitutes an important extension of the theoretical study reported in Ref. [384]. We notice that there are other qubit-resonator systems where the qubit can be measured independently without the necessity of a second resonator [145, 151]. In those cases, the reconstruction of the Wigner function can be performed straightforwardly [153].

6.5 Experimental Considerations

In this section, we show that for the typical parameter space accessible in circuit QED experiments our protocols can readily be implemented. We first focus on the estimate of the maximum size of the Schrödinger cat states generated according to the recipe of Sec. 6.3. We show that this size depends on a trade-off between the decay rates of the quantum bus B and of the leaky cavity L. We then briefly consider the case of two-resonator circuit QED for the Wigner function reconstruction in the dispersive regime (see Subsec. 6.4.2) and give an estimate of the most relevant parameters for this case. All the numbers used in this section are very close to those reached in existing experiments [144].

In Fig. 6.4, the maximum Schrödinger cat size and generation time are plotted as a function of the decay rates of B and L, $n^{\rm max}_{\rm cat} = n^{\rm max}_{\rm cat}(\kappa_{\rm B,1}, \kappa_{\rm L,1})$ and $t^{\rm max}_{\rm gen} = t^{\rm max}_{\rm gen}(\kappa_{\rm B,1}, \kappa_{\rm L,1})$. Here, $n^{\rm max}_{\rm cat} \equiv |\beta^{\rm max}_{\rm cat}|^2$. These results are obtained for a qubit transition frequency, at the qubit degeneracy point, $\delta_{\rm Q} = \omega = 2\pi \times 5\,{\rm GHz}$. The first mode of resonator B and of resonator L are assumed to have transition frequencies $\omega_{\rm B,1} = \omega = 2\pi \times 5\,{\rm GHz}$ and $\omega_{\rm L,1} = \omega/2 = 2\pi \times 2.5\,{\rm GHz}$, respectively. The coupling coefficient between the qubit and resonator B is considered to be $g_{\rm B,1} = 2\pi \times 500\,{\rm MHz}$ and those between the qubit and the modes of resonator L to be $g_{{\rm L},i} = 2\pi \times 250\,{\rm MHz}$. The couplings with respect to B and L differ by a factor of 2 because of the different zero-point fluctuations of the two resonators.[17] Figs. 6.1(b), 6.1(c), 6.2(b), and 6.2(c) clearly show that for B the maximum zero-point voltage and current are $\bar{v}^0_{\rm B,1} \simeq 1\,\mu{\rm V}$ and $\bar{i}^0_{\rm B,1} \simeq 25\,{\rm nA}$, respectively, whereas for L they are $\bar{v}^0_{{\rm L},i} \simeq 0.5\,\mu{\rm V}$ and $\bar{i}^0_{{\rm L},i} \simeq 10\,{\rm nA}$, respectively. In reality, there is a slight difference also among the zero-point fluctuations of the modes of L, but it is small and we neglect it. A realistic estimate for the geometric coupling between the first mode of B and the second mode of L is $g_{\rm LB} = 1\,{\rm MHz}$ (cf. chapter 5). In Fig. 6.4, we

[17] We remind that the vacuum Rabi coupling is directly proportional to the zero-point field.

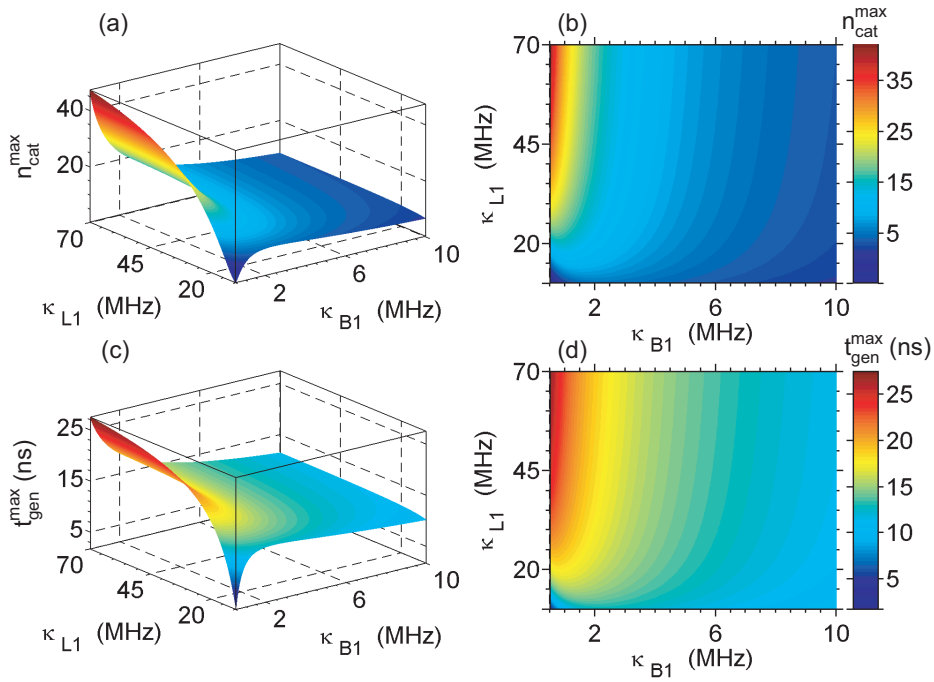

Figure 6.4: Maximum Schrödinger cat size and generation time. **(a)** 3D plot of $n_{\rm cat}^{\rm max}$ as a function of the decay rates of B and L, $\kappa_{\rm B,1}$ and $\kappa_{\rm L,1}$, respectively. **(b)** Top view of the plot in **(a)**. **(c)** 3D plot of $t_{\rm gen}^{\rm max}$ as a function of $\kappa_{\rm B,1}$ and $\kappa_{\rm L,1}$. **(d)** Top view of the plot in **(c)**. We remind to the main text for the complete list of parameters used to obtain these figures and for a more detailed explanation.

also assume $\kappa_{\rm B,1} \in [0.5, 10]\,$MHz, $\kappa_{\rm L,1} \in [10, 70]\,$MHz, $\langle n_{\rm proj}\rangle = 100$, and, finally, $\langle n_{\rm amp}\rangle = 10$, which corresponds to a typical amplifier noise temperature $T_{\rm n} \simeq 2.5\,$K at $\omega = 2\pi \times 5\,$GHz.

The plots of Figs. 6.4(a) and 6.4(b) are based on Eqs. (6.18) and (6.31). They clearly show that the largest cat size is achieved for a very high quality factor quantum bus with decay rate $\kappa_{\rm B,1} \simeq 500\,$kHz and, simultaneously, for a low quality factor resonator L with decay rate $\kappa_{\rm L,1} \simeq 70\,$MHz. In this case, $n_{\rm cat}^{\rm max} \simeq 45$, which represents a remarkable result. Figures 6.4(c) and 6.4(d) reveal that such a cat size is reached within only $t_{\rm gen}^{\rm max} \simeq 27\,$ns, which is much shorter than typical qubit decoherence times [118–120, 244, 261]. In this case, the generation time largely dominates over the projection time, $t_{\Sigma}^{\rm max} \approx t_{\rm gen}^{\rm max} \simeq 27\,{\rm ns} \gg t_{\rm proj} \simeq 2.9\,$ns. Notably, as already pointed out in step *(iv)* of Subsec. 6.3.1, Fig. 6.4(a) shows that it is not sufficient to have a very high quality factor quantum bus to generate large cats, it is also necessary to perform a very fast projection (measurement) of the qubit state. In fact, for $\kappa_{\rm B,1} \simeq 500\,$kHz and $\kappa_{\rm L,1} \simeq 10\,$MHz the cat size $n_{\rm cat}^{\rm max} \to 0$. This is due to the fact that, in this case, the effective decay rate of the quantum bus is limited by $g_{\rm LB}$ and the generation time is dominated by the projection time, $t_{\Sigma}^{\rm max} \approx t_{\rm proj} \simeq 20\,{\rm ns} \gg t_{\rm gen}^{\rm max} \simeq 1.75\,$ns [see Eqs. (6.24) and (6.29)].

Figure 6.5(a), based on Eqs. (6.18) and (6.31), and Fig. 6.5(b), based on Eq. (6.24),

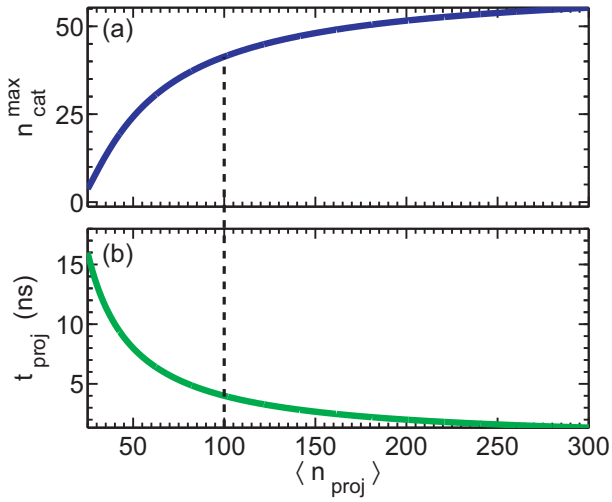

Figure 6.5: The role played by the mean number of photons in the projection pulse, $\langle n_{\rm proj}\rangle$. Parameters: $\kappa_{\rm B,1} = 500\,{\rm kHz}$, $\kappa_{\rm L,1} = 50\,{\rm MHz}$, $\langle n_{\rm proj}\rangle \in [25, 300]$ photons. All other parameters are the same as those used to obtain Fig. 6.4. **(a)** Maximum cat size $n_{\rm cat}^{\rm max}$ as a function of $\langle n_{\rm proj}\rangle$. The calculation is based on Eqs. (6.18) and (6.31). **(b)** Projection time $t_{\rm proj}$ as a function of $\langle n_{\rm proj}\rangle$. The calculation is based on Eq. (6.24). The cat size grows as the projection time decreases. The dashed black line helps to comparing the two plots. This figure clearly shows the main limitation of our protocol for the generation of large cat states: The projection time must be very short. State-of-the-art experiments can hardly realize high fidelity qubit measurements by means of projection pulses on the order of 5 ns or shorter [386]. However, with the advent of quantum-limited amplifiers [110, 194–196, 198, 199, 201, 203, 205, 208, 209, 211–220] and mesoscopic shelving readout [221] this scope might soon become reachable.

show the dependence of $n_{\rm cat}^{\rm max}$ and $t_{\rm proj}$ on the number of photons used for the projection pulse, $\langle n_{\rm proj}\rangle$. In this case, $\kappa_{\rm B,1} = 500\,{\rm kHz}$, $\kappa_{\rm L,1} = 50\,{\rm MHz}$, $\langle n_{\rm proj}\rangle \in [25, 300]$ photons, and all other parameters are the same as those used to obtain Fig. 6.4. The cat size grows as the projection time is reduced by applying a stronger projection pulse and can reach dimensions larger than 50 photons for $\langle n_{\rm proj}\rangle > 200$ photons.

Finally, we show that all conditions necessary for the implementation of the protocol of Sec. 6.3 are readily fulfilled for a realistic set of parameters. In step *(i)* of the protocol, if we assume a moderate $\langle n_{\rm shift}\rangle = 20$ photons, we obtain $|\Delta_{\rm shift}| = 1\,{\rm GHz}$ [Eq. (6.15)] when opting for a dynamic shift pulse [we remind that $|\Delta_{\rm shift}|$ can be induced by means of different switch-off techniques if necessary (cf. Subsec. 6.3.1)]. Hence, a driving through the second mode of resonator L corresponding to $\langle n_\alpha\rangle = 50$ photons starts mixing the states of the qubit after a time on the order of $1/\gamma_\alpha^{\rm mix} \simeq 640\,{\rm ns}$ [Eq. (6.16)]. This time is long enough to reach the steady-state regime, $\exp(-\kappa_{\rm L,2}/10\,\gamma_\alpha^{\rm mix}) \simeq 0.04$. Here, we consider $\kappa_{\rm L,2} = \kappa_{\rm L,1} = 50\,{\rm MHz}$.[18] In step *(iii)* of the protocol, again for $\langle n_{\rm shift}\rangle = 20$ pho-

[18] In reality, the decay rates of different modes of the same resonator are slightly different. They get larger for higher modes.

tons, for $n_{\rm cat} = 45$ photons, and for $\gamma_{\rm r} \simeq 0.5\,{\rm MHz}$ [118–120, 244, 261], we get $1/\gamma_{\kappa}^{\rm L,2} \simeq 320\,{\rm ns} > 1/\gamma_{\rm cat}^{\rm mix} \simeq 178\,{\rm ns} \gg t_{\rm proj} \simeq 2.9\,{\rm ns}$ [Eqs. (6.19) and (6.20)]. This means that $t_{\rm proj} \ll 1/\gamma_{\rm r} \simeq 2\,\mu{\rm s}$, which largely reduces errors due to qubit energy relaxation, $P_{\rm r} \simeq 0.1\,\%$. We also get $\chi_{\rm L,1}^{0} = 1$ [Eq. (6.22)] and a theoretical SNR $= 500$ [Eq. (6.23)].

In the case of two-resonator circuit QED for the Wigner function reconstruction in the dispersive regime, the parameter space has to be adapted to different necessities. In order to minimize the effect of the geometric crosstalk between resonators B and L, we can chose, for example, $\omega_{\rm B,1} \simeq 2\pi \times 7.5\,{\rm GHz}$ and $\omega_{\rm L,1} \simeq 2\pi \times 3\,{\rm GHz}$. In this way, all relevant modes of B and L are detuned. We also choose $\kappa_{\rm B,1} \simeq 100\,{\rm kHz}$ and $\kappa_{\rm L,1} = 1\,{\rm MHz}$. For a qubit transition angular frequency $\Omega_{\rm Q} = \delta_{\rm Q} \simeq 2\pi \times 5\,{\rm GHz}$, we have $|\Delta_{\rm B,1}| \simeq 2\pi \times 2.5\,{\rm GHz}$ and $|\Delta_{\rm L,1}| \simeq 2\pi \times 2\,{\rm GHz}$. In this case, it is also important to choose moderate qubit-resonator coupling coefficients, $g_{\rm B,1} \approx g_{\rm L,1} \simeq 50\,{\rm MHz}$,[19] which corresponds to $\chi_{\rm L,1}^{0} \equiv 2g_{\rm L,1}^{2}/\Delta_{\rm L,1}\kappa_{\rm L,1} = 2.5$. The choice of relatively small coupling coefficients is due to the fact that the condition on the $\pi/2$-pulses, $\eta_{\pi/2} \gg \Delta_{\rm L,1}\, g_{\rm B,1}^{2}(\langle n_{\beta}\rangle + 1/2)/\Delta_{\rm B,1}\, g_{\rm L,1}$, is hard to fulfill for very large couplings and/or very large intracavity fields. In fact, assuming $\langle n_{\beta}\rangle \approx \langle n_{\rm disp}\rangle = 10$ photons, which is obtained for $\eta_{\rm dr} \simeq 32\,{\rm MHz}$ and $t_{\rm dr} = 100\,{\rm ns}$, $\eta_{\pi/2}$ should be much larger than $2\pi \times 0.42\,{\rm GHz}$. This is very easy to realize in contrast to the case when $\langle n_{\beta}\rangle \approx \langle n_{\rm disp}\rangle = 100$ photons, which is obtained for $\eta_{\rm dr} = 100\,{\rm MHz}$ and $t_{\rm dr} = 100\,{\rm ns}$, and $\eta_{\pi/2}$ should be much larger than $2\pi \times 4.02\,{\rm GHz}$. This means that the tails of the Wigner function are harder to resolve, in particular for states $\hat{\rho}_{\rm B,1}$ characterized by large photon numbers (e.g., large Schrödinger cat states). For the parameters chosen here, $t_{\rm par} = 250\,{\rm ns} < \max\{1/\kappa_{\rm B,1}, 1/\gamma_{\rm r}, 1/\gamma_{\varphi}\} \simeq 1\,\mu{\rm s}$ [118–120, 244, 261, 351, 352]. It is also easy to show that, for $\langle n_{\beta}\rangle = 100$ photons, $1/\gamma_{\rm disp}^{\rm mix} = 50\,\mu{\rm s} \gg t_{\rm meas} \approx t_{\rm dr} + t_{\rm par} = 350\,{\rm ns}$.

6.6 Summary and Conclusions

In conclusion, we have presented a two-resonator circuit QED architecture where one resonator, the quantum bus, is characterized by a very high quality factor, and the other resonator, the leaky cavity, by a comparatively low quality factor.

We have shown that this architecture is well suited for the realization of a simultaneous JC and anti-JC dynamics. Such dynamics can be exploited for the generation of large Schrödinger cat states.

Remarkably, we have shown that the interaction between the leaky cavity and the qubit allows for a fast, high-fidelity projection and/or read out of the qubit state. This is due to the low quality factor, which corresponds to a fast measurement time. Taking advantage of this property, we have proposed a complete protocol for the measurement of nonclassical microwave fields trapped inside the quantum bus (e.g., the large Schrödinger cat states mentioned above).

We have analyzed two main techniques to measure such nonclassical states. The first technique is based on a fast qubit pre-measurement and the subsequent estimation of the first and second derivatives of the qubit population. In this way, we have shown that it is possible to obtain information on the first moment of the field

[19] Since we only use the first mode of each resonator, we can now design both B and L to be $\lambda/2$ resonators.

quadratures over the entire phase space and on the mean number of photons of such field. This method has the unique characteristic to be immune to decoherence processes of qubit and resonators.

The second technique is based on the reconstruction of the Wigner function of the intracavity fields and, thus, of their full-state quantum tomography. We have studied two different approaches for the Wigner function reconstruction, the first based on the JC and anti-JC dynamics and the second on an adaptation of the Lutterbach-Davidovich reconstruction method to two-resonator circuit QED.

We have proven by means of numerical simulations and accurate parameter estimation that all tasks enumerated above can readily be realized in circuit QED.

Chapter 7

Two-Dimensional Cavity Grid for Scalable Quantum Computation with Superconducting Circuits

Chapters 5 and 6, clearly show that one of the main strengths of circuit QED setups is the possibility to construct many resonators on one and the same chip. Hence, it is legitimate to pose the question whether it is conceivable to take advantage of this property for the realization of complex architectures based on multi-resonator-multi-qubit systems. The answer to this question constitutes the main subject of this chapter.

Here, we propose a scalable setup for quantum computing where many on-chip microwave resonators are arranged in a two-dimensional grid (hereafter, also referred to as 2D cavity grid) with a qubit at each intersection. The versatility of such a setup allows any two qubits on the grid to be coupled at a swapping overhead independent of their distance. It also yields an optimal balance between reducing the spread of the qubit transition frequencies and spurious cavity-induced couplings. These features make the 2D cavity grid setup unique in its gender and distinct from existing proposals based on ion traps [387, 388], optical lattices [389], semiconductor spins [390], or superconducting qubits [97, 391]. In addition, we demonstrate that our approach encompasses the fundamental elements of a scalable fault-tolerant quantum computing architecture.

The chapter is organized as follows. In Sec. 7.1, we introduce the basic 2D cavity grid architecture and its corresponding Hamiltonian. In Sec. 7.2, we briefly show that one-qubit gates can easily be performed and the qubit state read out with available tools. In Sec. 7.3, we propose a method to perform arbitrary two-qubit gates between any two qubits in the cavity grid. We also study by means of numerical simulations a model including dissipation of qubits and resonators. In Sec. 7.4, we discuss the possibility to perform fast gate operations. In Sec. 7.5, we analyze the scalability properties of our system. In Sec. 7.6, we present a realistic hardware implementation of the 2D cavity grid and address qubit tunability issues. Finally, in Sec. 7.7, we summarize our results.

The material discussed in this chapter is a revised and extended version of article number 7 on the *List of Publications* and is published in *Europhysics Letters* - Ref. [137]. The main contributions of the author are on the development of the hardware implementation of a 2D cavity grid with orthogonal resonators as well

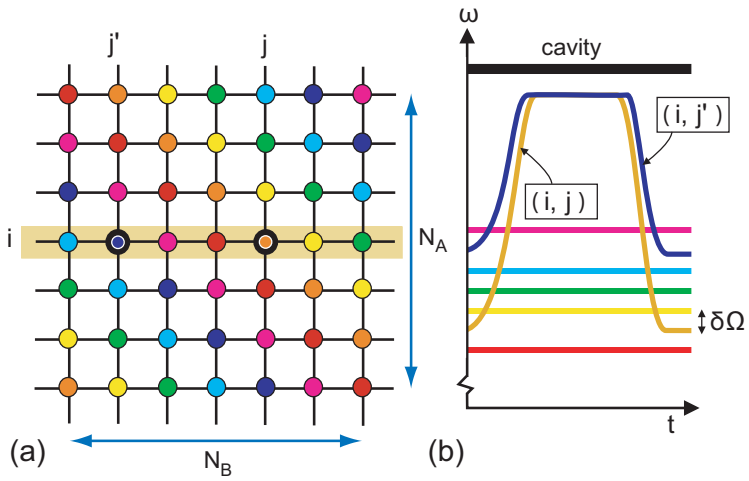

Figure 7.1: Basic architecture for the 2D cavity grid proposal. **(a)** The 2D cavity grid, with qubits depicted as circles and resonators (cavities) shown as lines. The grid is composed by a set of modes belonging to N_A horizontal and N_B vertical resonators. A qubit (i, j) sits at the intersection of resonators i and j. The different colors indicate the transition frequencies of the qubits. In the "idle state," all frequencies are different in any column or row. The coordinates (i, j) and (i, j') denote two different qubits belonging to the same (in this case horizontal) resonator. **(b)** ω: angular frequency. t: time. $\delta\Omega$: angular frequency difference between two qubits. A two-qubit operation can be realized by tuning the transition frequencies of two qubits into resonance near the resonator frequency. This activates a resonator-assisted dispersive coupling between the two qubits [131, 146].

as the discussion on the experimental feasibility of such setup. This project has been led by Florian Marquardt and Enrique Solano, who envisioned the grid as a means for quantum computing. The author expresses his gratitude to both for the possibility of joining such exciting project. The numerical simulations are due to Ferdinand Helmer and the extension to a possible scalable fault-tolerant architecture to Austin G. Fowler and Florian Marquardt. The author thanks Jan von Delft for accepting him in this project and Rudolf Gross for allowing him to be part of the article *solo*.

In addition to the material treated in Ref. [137], in this chapter we consider the possibility to perform fast resonant gates. Also, we give more details on hardware-related issues for the realization of grids with many resonators.

7.1 Basic Architecture

A single superconducting qubit coupled to a microwave on-chip resonator (cavity) has been explored in a series of groundbreaking experiments [108, 138, 139, 141]. More recently, two qubits have been coupled via a resonator which is used to induce a flip-flop (XY) interaction [145, 146], sideband transitions have been exploited to realize two-qubit operations [392], and the Grover search and Deutsch–Jozsa

algorithms have been implemented in a circuit QED architecture [147]. The flip-flop interaction of Refs. [145, 146], in particular, can be exploited to realize two-qubit gates, as outlined, e.g., in Refs. [131]. The natural extension of these experiments is to a scenario where multiple qubits share the same resonator in a linear array configuration [393]. In this case, arbitrary qubit pairs could be coupled selectively. This is advantageous compared to schemes based on sequential nearest-neighbor interactions, which suffer from swapping overhead and disruption by single unusable qubits. However, in the "idle state" of the quantum processor the interactions have to be effectively turned off by detuning all the qubits from each other. For two qubits, this requires a detuning $\delta\Omega$ between them much larger than their coupling strength J in order to avoid spurious two-qubit operations. As a consequence, for N qubits inside one resonator, an angular frequency interval on the order of $N\delta\Omega$ is required, restricting the maximum number of possible qubits.

To overcome this issue, we propose a 2D cavity grid architecture that relaxes the $N\delta\Omega$ requirement and can form the basis for a scalable fault-tolerant scheme. The proposed setup is sketched in Fig. 7.1: Two arrays of parallel resonators are placed orthogonally on top of each other forming an $N_A \times N_B$ grid, where N_A and N_B are the number of horizontal and vertical resonators, respectively. One qubit sits at each intersection between two resonators on the grid. By making sure that within each resonator (column or row) no two qubit angular frequencies are closer than $\delta\Omega$, the required angular frequency range has to be on the order of $\sqrt{N}\delta\Omega$ (where N is the total number of qubits). In this manner, we are able to reduce the necessary frequency spread by a factor $\sqrt{N}$. This readily allows for grids with more than $N = 20 \times 20 = 400$ qubits, for realistic parameters (cf. Sec. 7.6). The constraint on each row and column is similar to the rules of the game of "Sudoku," but without any requirement to choose a prescribed number of different frequencies. Figure 7.1 shows an acceptable frequency distribution. An extension to a fully scalable setup is discussed towards the end of the chapter.

The essential features of our 2D cavity grid are contained in the Hamiltonian

$$\begin{aligned}\widehat{H}_{\text{cgrid}} = &\sum_{i=1}^{N_A} \hbar\omega_i^A \,\hat{a}_i^\dagger \hat{a}_i + \sum_{j=1}^{N_B} \hbar\omega_j^B \,\hat{b}_j^\dagger \hat{b}_j + \frac{1}{2}\sum_{i,j} \Omega_{ij}\,\hat{\sigma}_z \\ &+ \sum_{i,j} \hat{n}_{ij}[g_{ij}^A(\hat{a}_i^\dagger + \hat{a}_i) + g_{ij}^B(\hat{b}_j^\dagger + \hat{b}_j)]\,, \end{aligned} \tag{7.1}$$

where ω_i^A and ω_j^B are the transition angular frequencies of the i-th horizontal and the j-th vertical resonators, respectively, and $\hat{a}_i$, $\hat{a}_i^\dagger$, $\hat{b}_j$, and $\hat{b}_j^\dagger$ are annihilation and creation bosonic operators for the i-th and j-th modes of the horizontal and vertical resonators. In addition, Ω_{ij} represents the transition angular frequency of qubit (i,j), $\hat{\sigma}_z$ the usual Pauli operator, $\hat{n}_{ij}$ the dipole operator of qubit (i,j), and g_{ij}^A and g_{ij}^B the coupling coefficients between the qubit (i,j) and the horizontal or vertical resonator modes, respectively. The qubit-resonator coupling coefficients and the qubit dipole operator depend on the detailed electromagnetic field distribution in the resonators, on the geometry of the qubit, and on its operation point. In the case of charge qubits, the electric-dipole-type operator $\hat{n}_{ij}$ couples to the electric field of the resonators, whereas in the case of flux qubits, it couples to the magnetic field. In general, the form of Eq. (7.1) is independent of the specific hardware implementation

and we can use $\widehat{H}_{\rm cgrid}$ as the starting Hamiltonian for deriving the Jaynes-Cummings model and the resonator-mediated interaction between the qubits [131]. For definiteness, we consider charge (or transmon) qubits, unless noted otherwise.

7.2 One-Qubit Gates and Readout

We briefly review some required features on one-qubit gates that have already been implemented experimentally [108]. $\hat{\sigma}_x$-type operations on a selected qubit can be performed inducing Rabi oscillations of frequency $\Omega_{\rm R}$ by means of a microwave pulse with angular frequency $\Omega_{ij}/\hbar$. This pulse matches the qubit, but is detuned from the resonator mode [108] and all the other qubits in any of the two resonators coupled to the selected qubit, i.e., the peaks of the Mollow triplet $\Omega_{ij}/\hbar$ and $\Omega_{ij}/\hbar \mp \Omega_{\rm Rabi}$ do not overlap with those qubits. $\hat{\sigma}_z$-type operations can be performed by means of strong microwave pulses detuned from the qubit, which induce AC-Stark or -Zeeman shifts [146], or by means of non-adiabatic pulses [104, 394].

We notice that the state of a selected qubit can be measured using the resonators of the grid to perform a high-fidelity dispersive quantum non-demolition readout (cf. chapter 6), a technique which has already been demonstrated in experiments [108]. By tuning only one qubit at the time near the resonator mode used to read out, this method allows for a fast individual qubit addressing (cf. chapter 6). Alternatively, the more sophisticated combinatorial parallel readout (multiplexed readout) suggested in Ref. [131, 146] might be applied.

7.3 Two-Qubit Gates and Treatment of Decoherence

In this section, we study the possibility to perform two-qubit gates in a 2D cavity grid taking advantage of the well-known dispersive qubit-resonator-qubit interaction, which arises from the Hamiltonian of Eq. (7.1) when qubit and resonators are largely detuned from each other [332, 395, 396]. In this case, the resonator acts as a quantum bus which mediates a flip-flop interaction between a pair of qubits α and β. Indicating one of the horizontal or vertical resonators with the index $k = A, B$ and its corresponding transition angular frequency as ω^k, we define the coupling coefficients between each qubit and a resonator as g_α^k and g_β^k, respectively, and the corresponding qubit-resonator detunings as $\Delta_\alpha^k \equiv \Omega_\alpha - \omega^k$ and $\Delta_\beta^k \equiv \Omega_\beta - \omega^k$. Under the dispersive assumption $|\Delta_\alpha^k|, |\Delta_\beta^k| \gg \max\{|g_\alpha^k|, |g_\beta^k|\}$, it is an easy exercise in second-order perturbation theory to obtain the effective Hamiltonian [131, 146]

$$\widehat{H}_{\alpha\beta}^k = \hbar J_{\alpha\beta}^k \left(\hat{\sigma}_\alpha^+ \hat{\sigma}_\beta^- \, e^{+j\delta_{\alpha\beta}t} + \hat{\sigma}_\alpha^- \hat{\sigma}_\beta^+ \, e^{-j\delta_{\alpha\beta}t}\right) , \tag{7.2}$$

where $J_{\alpha\beta}^k \equiv g_\alpha^k \, g_\beta^k (\Delta_\alpha^k + \Delta_\beta^k)/2\Delta_\alpha^k \, \Delta_\beta^k$ is the effective coupling strength between the two qubits α and β, $\hat{\sigma}_\alpha^-$, $\hat{\sigma}_\alpha^+$, $\hat{\sigma}_\beta^-$, and $\hat{\sigma}_\beta^+$ are the usual lowering and rising operators for α and β, and $\delta_{\alpha\beta} \equiv \Omega_\alpha - \Omega_\beta$ is the detuning between the two qubits, which, in general, are nondegenerate.

In the "idle state," the qubit-qubit interaction of the Hamiltonian of Eq. (7.2) must be effectively switched off in order to avoid spurious two-qubit operations. In the "computational state," when the gate is active, the two-qubit interaction must

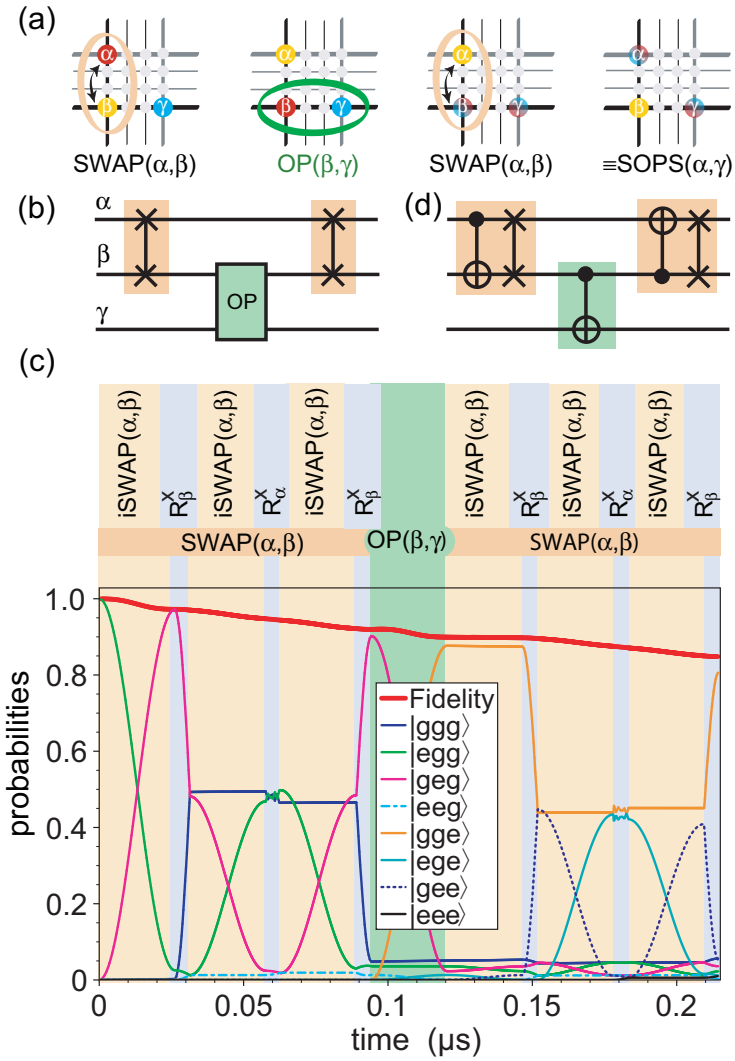

Figure 7.2: Operations between two arbitrary qubits on a 2D cavity grid. **(a)** Sequence of operations for a two-qubit gate between two arbitrary qubits α and γ, which reside in different resonators, via an intermediate qubit β, which is located at the junction of the two orthogonal resonators containing α and γ. **(b)** Quantum circuit associated with the physical implementation described in **(a)**. Every SWAP gate has to be decomposed into three iSWAP gates and local gates. OP: generic operation between qubits β and γ. **(c)** Numerical simulation of the master equation for the sequence of operations in **(a)** and **(b)** assuming OP = iSWAP [cf. Eq. (7.6)]. The probabilities for the groundstate $|g\rangle$ and excited state $|e\rangle$ of qubits α, β, and γ, respectively, are shown together with the overall gate fidelity as a function of time. The parameters used are presently achievable in experiments (cf. Sec. 7.3). **(d)** Quantum circuit for the special cases OP = CNOT or OP = CPHASE. This circuit (faster than the one sketched in **(b)**) exploits the possibility to implement each SWAP-CNOT pair of operations using a single iSWAP gate and local gates [397]. The numerical simulations were performed by F. Helmer [137].

be maximum in order to allow fast operations. This can be realized following a simple *flip-flop protocol*:

(i) In the "idle state," the two qubits α and β are prepared far away from the mode of resonator k, $\Omega_\alpha \to \tilde{\Omega}_\alpha$ and $\Omega_\beta \to \tilde{\Omega}_\beta$. This can be realized employing flux control lines, which are used to DC-Zeeman shift the qubit energy levels (cf. Sec. 7.6), thus creating very large qubit-resonator detunings $\tilde{\Delta}^k_\alpha \equiv \tilde{\Omega}_\alpha - \omega^k$ and $\tilde{\Delta}^k_\beta \equiv \tilde{\Omega}_\beta - \omega^k$. In this manner, the coupling coefficient between the two qubits is drastically reduced to $\tilde{J}^k_{\alpha\beta} = g^k_\alpha\, g^k_\beta(\tilde{\Delta}^k_\alpha + \tilde{\Delta}^k_\beta)/2\tilde{\Delta}^k_\alpha\, \tilde{\Delta}^k_\beta \ll J^k_{\alpha\beta}$;

(ii) At this stage, the qubits are also detuned from each other by a quantity $|\delta_{\alpha\beta}| \gg |\tilde{J}^k_{\alpha\beta}|$, which further reduces their mutual interaction. In this case, it is possible to write an effective second-order Hamiltonian $\widehat{H}^{k,\mathrm{eff}}_{\alpha\beta} = \hbar[\Upsilon^\dagger, \Upsilon]/\delta_{\alpha\beta}$, where $\Upsilon^\dagger \equiv \tilde{J}^k_{\alpha\beta}\hat{\sigma}^+_\alpha\hat{\sigma}^-_\beta$ and $\Upsilon \equiv \tilde{J}^k_{\alpha\beta}\hat{\sigma}^-_\alpha\hat{\sigma}^+_\beta$. A simple calculation shows that $\widehat{H}^{k,\mathrm{eff}}_{\alpha\beta} = 0$ when $|\delta_{\alpha\beta}| \gg |\tilde{J}^k_{\alpha\beta}|$. This condition can easily be fulfilled since $\tilde{J}^k_{\alpha\beta}$ is small due to the very large detuning condition of point (i). Being the qubits largely detuned from each other also minimizes the nearest-neighbor coupling between them, which is independent from the dispersive action of the resonator;

(iii) In the "computational state," the interaction between qubits α and β is switched on by tuning the qubit transition frequencies into mutual resonance near the resonator frequency, $|\tilde{\Delta}^k_\alpha| \to |\Delta|$, $|\tilde{\Delta}^k_\beta| \to |\Delta|$, with $|\Delta| \ll \min\{|\tilde{\Delta}^k_\alpha|, |\tilde{\Delta}^k_\beta|\}$ (cf. Fig. 7.1). The qubit-resonator interaction remains dispersive, but the detuning condition is largely relaxed. In this way, the coupling coefficient between the qubits is increased to $J^k_{\alpha\beta} \gg \tilde{J}^k_{\alpha\beta}$, the qubits are degenerate, and the flip-flop interaction Hamiltonian can finally be expressed as

$$\widehat{H}_{\mathrm{flip-flop}} = \hbar\frac{g^k_\alpha\, g^k_\beta}{\Delta}\left(\hat{\sigma}^+_\alpha\hat{\sigma}^-_\beta + \hat{\sigma}^-_\alpha\hat{\sigma}^+_\beta\right). \tag{7.3}$$

We notice that when the two qubits are degenerate, a nearest-neighbor-type interaction can contribute to their mutual coupling strength. This could possibly generate errors and one has to account for it while designing an experiment.

The time evolution of the Hamiltonian of Eq. (7.3) after a waiting time $t = \pi|\Delta|/(2|g^k_\alpha\, g^k_\beta|)$ realizes a universal two-qubit iSWAP gate (as demonstrated recently in Ref. [146]), which can be used to construct CNOT and SWAP gates. For example, each SWAP(α,β) operation in the protocol [cf. Fig. 7.2(a) and 7.2(b)] can be decomposed into three iSWAP gates between qubits α and β [397]:

$$\mathrm{SWAP}(\alpha,\beta) = \mathrm{iSWAP}(\alpha,\beta)\times \mathrm{R}^x_\beta \times \mathrm{iSWAP}(\alpha,\beta)\times \mathrm{R}^x_\alpha \times \mathrm{iSWAP}(\alpha,\beta)\times \mathrm{R}^x_\beta\,. \tag{7.4}$$

Here, R^x_α and R^x_β represent Rabi pulses (i.e., local qubit rotations) applied via a resonant microwave driving. Such pulses rotate qubits α and β by an angle $-\pi/2$ about the x-axis of the Bloch sphere.

Arbitrary two-qubit gates between any two qubits α and γ residing in different resonators can be implemented using the SWAP gate of Eq. (7.4) and employing an intermediate qubit β located at the junction of the two orthogonal resonators containing α and γ [cf. Fig. 7.2(a)]. The sequence

$$\mathrm{SOPS}(\alpha,\gamma) \equiv \mathrm{SWAP}(\alpha,\beta)\times \mathrm{OP}(\beta,\gamma)\times \mathrm{SWAP}(\alpha,\beta) \tag{7.5}$$

leaves the state of qubit β unchanged and performs the desired operation OP between qubits α and γ.

In order to gain further insight into the physics of the operation of Eq. (7.5) under more realistic assumptions, we model energy relaxation and pure dephasing of each qubit $m = \{\alpha, \beta, \gamma\}$ involved in the operation introducing Lindblad terms in the corresponding master equation. The master equation thus reads

$$\dot{\hat{\rho}} = -\frac{j}{\hbar}[\hat{H}_{\rm SOPS}, \hat{\rho}] + \sum_m (\mathcal{L}_m^{\rm r} + \mathcal{L}_m^{\varphi})\,\hat{\rho}\,, \tag{7.6}$$

where

$$\mathcal{L}_m^{\rm r}\,\hat{\rho} \equiv \Gamma^{\rm r}\left[\hat{\sigma}_m^-\,\hat{\rho}\,\hat{\sigma}_m^+ - \frac{1}{2}\hat{\sigma}_m^+\hat{\sigma}_m^-\hat{\rho} - \frac{1}{2}\hat{\rho}\hat{\sigma}_m^+\hat{\sigma}_m^-\right], \tag{7.7a}$$

$$\mathcal{L}_m^{\varphi}\,\hat{\rho} \equiv \Gamma^{\varphi}\left[2\hat{P}_m\hat{\rho}\hat{P}_m - \hat{P}_m\hat{\rho} - \hat{\rho}\hat{P}_m\right]. \tag{7.7b}$$

In the master equation, $\dot{\hat{\rho}}(t) \equiv (d/dt)\hat{\rho}(t)$, $\hat{H}_{\rm SOPS}$ is the Hamiltonian associated with the entire operation SOPS, where each pair of qubits (α, β) and (β, γ) are coupled via the flip-flop Hamiltonian of Eq. (7.3) and we assume OP = iSWAP, $\Gamma^{\rm r}$ and Γ^{φ} are the energy relaxation and pure dephasing rates equal for all qubits, $\hat{P}_m \equiv |{\rm e}\rangle_m\,{}_m\langle{\rm e}|$ projects onto the excited state of the m-th qubit, and $\hat{\sigma}_m^-$ and $\hat{\sigma}_m^+$ are the usual lowering and rising operators for the m-th qubit. Due to the dispersive condition, the resonators are adiabatically eliminated from the system.[1]

During any two-qubit gate the qubit energy must be ramped. As a consequence, other qubit energies are inevitably crossed [cf. Fig. 7.1(b)]. On one hand, if the ramping process is too slow, it can lead to a spurious population transfer to other qubits. On the other hand, ramping too fast can excite higher qubit energy levels. For a switching time of 10 ns (during which a sweep over $\delta\Omega \simeq 2\pi \times 10\,{\rm GHz}$ has to be typically performed), the probability of an erroneous population transfer during one crossing is estimated to be less than 10^{-2} from the Landau-Zener-Stückelberg tunneling equation. We can therefore safely disregard this effect from our simulations, where we assume the qubit energies to be switched instantaneously. We notice that although several crossings may occur during one single sweep because of the presence of many qubits inside each resonator, the scalable setup to be introduced in Sec. 7.5 keeps this type of error under control by requiring only eight qubits per resonator.

The parameters used for the simulations are: Initial qubit transition angular frequencies $\Omega_m = 2\pi \times 4, 5, 6\,{\rm GHz}$ for qubit $m = \alpha, \beta, \gamma$, respectively; resonator transition angular frequencies $\omega_i^k = \omega_j^k = 2\pi \times 15\,{\rm GHz}$, $\forall i, j, k$; for the local rotations of qubits α and β, R_α^x and R_β^x, a resonant classical microwave driving yielding a Rabi frequency $\Omega^{\rm R} = \Omega_\alpha^{\rm R} = \Omega_\beta^{\rm R} = 150\,{\rm MHz}$;[2] a qubit-resonator vacuum Rabi coupling $g_m^k = 2\pi \times 245\,{\rm MHz}$, $\forall m, k$, and a detuning $\Delta = 2\pi \times 1\,{\rm GHz}$. From these numbers, it is easy to compute the effective coupling coefficient between two

[1] We notice that Eq. (7.6) uses a definition of the Lindblad terms based on the projector $\hat{P}_m$. This is different from the definitions used in the master equations of chapter 5, Sec. 5.3, and chapter 6, Subsec. 6.3.2. For this reason, the rate Γ^{φ} is not divided by two here.

[2] The phase of the driving field already accounts for the qubits phases accumulated during the gate sequence.

qubits, $J^k_{mn} \simeq 60\,\mathrm{MHz}$, with $n = \alpha, \beta, \gamma$ and $m \neq n$. In addition, we assume the pessimistic values for the energy relaxation and pure dephasing rates of the qubits, $\Gamma^{\mathrm{r}} = 0.1\,\mathrm{MHz}$ and $\Gamma^{\varphi} = 2\,\mathrm{MHz}$ (i.e., $T_1 = 10\,\mu\mathrm{s}$ and $T_{\varphi} = 500\,\mathrm{ns}$). It is worth mentioning that longer pure dephasing times have been reported in recent experiments on transmon qubits [120, 244]. Notably, in the "idle state" the actual qubit-qubit coupling strength is largely reduced due to a larger detuning from the resonator. Assuming $|\tilde{\Delta}^k_m| \simeq 10\,\mathrm{GHz}$, $\forall m, k$, we obtain $|\tilde{J}^k_{mn}| \simeq 6\,\mathrm{MHz}$. The effect of this spurious coupling can be further reduced by spacing the qubits, e.g., by $|\delta_{\alpha\beta}| \simeq 500\,\mathrm{MHz}$ ($\gg \tilde{J}^k_{mn} \simeq 6\,\mathrm{MHz}$). As shown in point (ii) of the flip-flop protocol, in this case the resonator-mediated interaction between the two qubits is negligible. The results of our simulations are summarized in Fig. 7.2(c).

The accuracy of the adiabatic elimination of the resonator mode can be verified by performing an additional simulation of an iSWAP operation between two qubits taking fully into account the resonator mode. Such a simple simulation (data not shown) reveals that the spurious population of the resonator mode during the dispersive iSWAP operation stays at all times well below 0.03 and the corresponding error is below the error induced by dissipation. Such errors can be further minimized by optimizing pulse shapes and parameters [398].

A measure of the operation fidelity is obtained by computing $F[\hat{\rho}(t), \hat{\rho}_{\mathrm{ideal}}(t)]$ [399], where $F(\hat{\rho}_1, \hat{\rho}_2) \equiv \mathrm{Tr}(\sqrt{\sqrt{\hat{\rho}_1}\hat{\rho}_2\sqrt{\hat{\rho}_1}})^2$ and $\hat{\rho}_{\mathrm{ideal}}$ denotes the time-evolution in the absence of dissipation. Figure 7.2(c) shows a fidelity of approximately 85% after a gate operation of approximately 210 ns. This result clearly confirms that presently achievable parameters suffice for a first proof-of-principle experiment. We emphasize that the swapping overhead does not grow with the distance between the qubits. Furthermore, multiple operations can run in parallel even if they involve the same resonators, provided that no qubit is affected simultaneously by two operations and the qubit pairs are tuned to different frequencies.

In this section, we have deliberately chosen the comparatively slow dispersive two-qubit gate that relies on proven achievements. Nevertheless, much faster resonant gates might be implemented on a time scale of $1/g^k_m$ instead of $|\Delta|/(g^k_m)^2$. In the next section (Sec. 7.4), we briefly discuss one example of such gates.

7.4 Fast Resonant CPHASE Gates

In this section, we briefly show that the 2D cavity grid architecture can also be exploited to realize resonant gates, which are inherently faster than the dispersive gates analyzed in the previous section (Sec. 7.3). A resonant controlled-phase (CPHASE) gate between two qubits coupled to the same resonator can be implemented if one of the two qubits is characterized by a third energy level $|\mathrm{a}\rangle$ with higher energy compared to its groundstate $|\mathrm{g}\rangle$ and first excited state $|\mathrm{e}\rangle$. The third level $|\mathrm{a}\rangle$ can be regarded as an auxiliary level[3] used to acquire the phase π necessary to perform the CPHASE gate [147, 400, 401]. We assume two qubits α and β coupled to the same resonator. Initially, the qubits are prepared in a linear superposition of energy

[3]It now becomes clear the chosen nomenclature for the third level (cf. chapter 2, Sec. 2.2).

groundstate and excited state

$$|\alpha\rangle = \frac{|\mathrm{g}\rangle_\alpha + |\mathrm{e}\rangle_\alpha}{\sqrt{2}}\,, \tag{7.8a}$$

$$|\beta\rangle = \frac{|\mathrm{g}\rangle_\beta + |\mathrm{e}\rangle_\beta}{\sqrt{2}}\,, \tag{7.8b}$$

where $|\mathrm{g}\rangle_\alpha$, $|\mathrm{e}\rangle_\alpha$, $|\mathrm{g}\rangle_\beta$, $|\mathrm{e}\rangle_\beta$ represent the groundstates and excited states of qubits α and β, respectively. The states of Eqs. (7.8a) and (7.8b) can easily be prepared by means of R^x_α and R^x_β rotations. All qubit transitions $|\mathrm{g}\rangle \leftrightarrow |\mathrm{e}\rangle$, $|\mathrm{e}\rangle \leftrightarrow |\mathrm{a}\rangle$, and $|\mathrm{g}\rangle \leftrightarrow |\mathrm{a}\rangle$ for both qubits are detuned from the resonator transition in order to avoid spurious population transfers. The resonator is prepared in the vacuum state $|0\rangle$. The initial state of the system is thus

$$|\Psi\rangle_0 = (A\,|\mathrm{g}\rangle_\alpha\,|\mathrm{g}\rangle_\beta + B\,|\mathrm{g}\rangle_\alpha\,|\mathrm{e}\rangle_\beta + C\,|\mathrm{e}\rangle_\alpha\,|\mathrm{g}\rangle_\beta + D\,|\mathrm{e}\rangle_\alpha\,|\mathrm{e}\rangle_\beta) \otimes |0\rangle\ , \tag{7.9}$$

where A, B, C, and D are opportune renormalization coefficients.

The state of qubit β is then transferred to the resonator by tuning the transition $|\mathrm{g}\rangle_\beta \leftrightarrow |\mathrm{e}\rangle_\beta$ into resonance with the resonator transition for half a vacuum Rabi oscillation period. This can be realized by applying a fast DC-Zeeman shift pulse to the qubit through opportune control lines [147, 349, 374] (cf. Sec. 7.6). The resonator is thus turned into a photonic qubit and the system state is

$$|\Psi\rangle_1 = (A\,|\mathrm{g}\rangle_\alpha\,|0\rangle + B\,|\mathrm{g}\rangle_\alpha\,|1\rangle + C\,|\mathrm{e}\rangle_\alpha\,|0\rangle + D\,|\mathrm{e}\rangle_\alpha\,|1\rangle) \otimes |\mathrm{g}\rangle_\beta\ , \tag{7.10}$$

where $|1\rangle$ represents a Fock state one in the resonator. The transition $|\mathrm{g}\rangle_\beta \leftrightarrow |\mathrm{e}\rangle_\beta$ is tuned back out of resonance with respect to the resonator transition.

A CPHASE gate between qubit α and the photonic qubit in the resonator can be implemented by tuning the transition $|\mathrm{e}\rangle_\alpha \leftrightarrow |\mathrm{a}\rangle_\alpha$ into resonance with the resonator transition during a full vacuum Rabi period. The process $|\mathrm{e}\rangle_\alpha\,|1\rangle \rightarrow |\mathrm{a}\rangle_\alpha\,|0\rangle \rightarrow -\,|\mathrm{e}\rangle_\alpha\,|1\rangle$ results in a phase factor -1, while all the other initial states only acquire free-evolution phases. The system state becomes

$$|\Psi\rangle_2 = (A\,|\mathrm{g}\rangle_\alpha\,|0\rangle + B\,|\mathrm{g}\rangle_\alpha\,|1\rangle + C\,|\mathrm{e}\rangle_\alpha\,|0\rangle - D\,|\mathrm{e}\rangle_\alpha\,|1\rangle) \otimes |\mathrm{g}\rangle_\beta\ . \tag{7.11}$$

The transition $|\mathrm{e}\rangle_\alpha \leftrightarrow |\mathrm{a}\rangle_\alpha$ is tuned back out of resonance with respect to the resonator transition.

Finally, by mapping back the photonic qubit in the resonator onto qubit β, a CPHASE gate between qubits α and β is implemented. This is realized by tuning once again the transition $|\mathrm{g}\rangle_\beta \leftrightarrow |\mathrm{e}\rangle_\beta$ into resonance with the resonator transition for half a vacuum Rabi oscillation period. The final system state is

$$|\Psi\rangle_3 = (A\,|\mathrm{g}\rangle_\alpha\,|\mathrm{g}\rangle_\beta + B\,|\mathrm{g}\rangle_\alpha\,|\mathrm{e}\rangle_\beta + C\,|\mathrm{e}\rangle_\alpha\,|\mathrm{g}\rangle_\beta - D\,|\mathrm{e}\rangle_\alpha\,|\mathrm{e}\rangle_\beta) \otimes |0\rangle\ . \tag{7.12}$$

In the case of a 2D cavity grid, resonant two-qubit gates can be implemented between qubits located in different resonators if a SWAP gate can efficiently be decomposed into CPHASE gates and local qubit rotations. It can be shown that

$$\begin{aligned}\mathrm{SWAP}(\alpha,\beta) = {} & \mathrm{R}^x_\alpha \times \mathrm{CPHASE}(\alpha,\beta) \times \mathrm{R}^x_\alpha \\ & \times \mathrm{R}^x_\beta \times \mathrm{CPHASE}(\alpha,\beta) \times \mathrm{R}^x_\beta \\ & \times \mathrm{R}^x_\alpha \times \mathrm{CPHASE}(\alpha,\beta) \times \mathrm{R}^x_\alpha\,.\end{aligned} \tag{7.13}$$

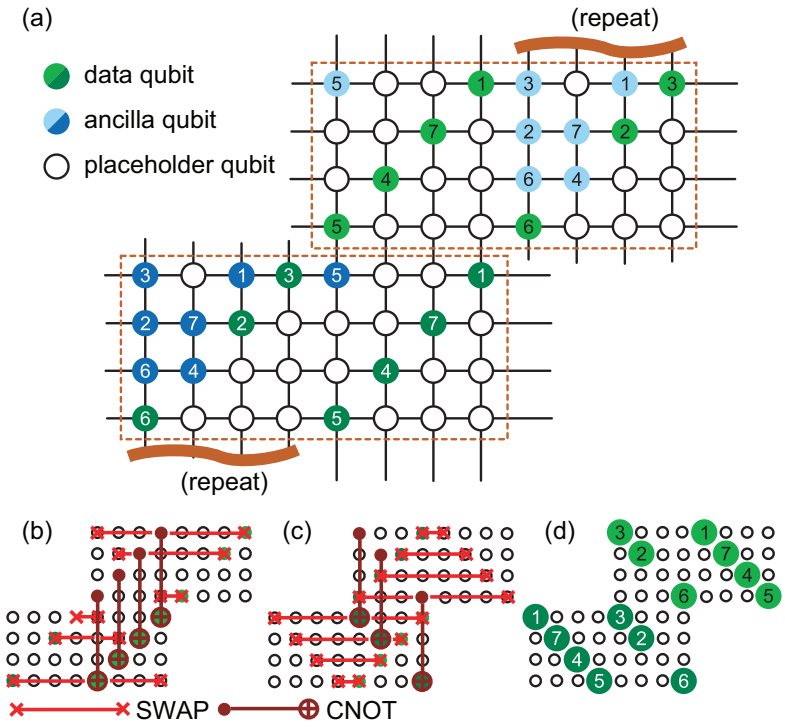

Figure 7.3: A possible fault-tolerant scalable architecture based on the cavity grid. **(a)** The unit cell of the periodic arrangement, with two logical qubits, each made up of seven data qubits (grouping indicated by dashed rectangles), together with ancilla and placeholder qubits. **(b)** First sequence of SWAP and CNOT gates. **(c)** Second sequence of SWAP and CNOT gates. **(d)** Final arrangement produced by the sequence of SWAP and CNOT gates shown in **(b)** and **(c)**, which implements a transversal CNOT between the logical qubits; cf. main text for details.

The resulting two-qubit gate based on the gate of Eq. (7.5) in combination with local qubit rotations can be used for universal quantum computation. It could also be used to directly generate a 1D cluster state [402] sequentially along each row of the grid. Such state can then be extended to a 2D cluster state [403–405] by coupling different rows. We recall that 2D cluster states are fundamental elements for the implementation of the so-called one-way quantum computing [406, 407]. More details on these advanced applications can be found in Ref. [401, 408].

7.5 Scalable Fault-Tolerant Architecture

The 2D cavity grid presented in this chapter has the potential of serving as a building block for a truly scalable, fault-tolerant architecture. Scalability means that, at a minimum, the physics of initialization, readout, single- and two-qubit gates does not depend on the total number of qubits in the system. Figure 7.3 shows a scalable architecture requiring only eight different qubit frequencies to selectively couple a

constant fraction of an arbitrarily large number of qubits in parallel. In each unit cell of 64 physical qubits [cf. Fig. 7.3(a)], we choose 2 arrays of 7 data qubits and use each array to store a single logical qubit following the 7 qubit Steane quantum error correction code [409]. This logical qubit is capable of tolerating an arbitrary single qubit error and may itself be part of a larger logical qubit through concatenation. A logical transversal CNOT gate is illustrated in Figs. 7.3(b), 7.3(c), and 7.3(d). The final arrangement of data qubits [cf. Fig. 7.3(d)] differs from the initial one and could be returned to it by swapping. However, if all logical qubits undergo similar logical gates, explicitly swapping back is not necessary as subsequent logical gates do this automatically. Figure 7.3 also shows 2 additional arrays of 7 ancilla qubits used during error correction.[4] Clean logical states are prepared in these ancilla. Errors in the data are then copied into the ancilla, which are finally measured locating the errors and enabling correction [410]. All unmarked qubits are placeholder qubits and are not used at any given time. The presence of placeholder qubits is crucial to prevent single SWAP gate failures corrupting multiple data qubits in a single logical qubit. If a pair of data qubits need to be interchanged, swapping them directly could corrupt both data qubits in the case of a SWAP gate failure. In fact, this would result in a pair of errors that is not always correctable, since the 7 qubit encoding only copes with a single data or ancilla qubit error in each error correction round. Using a placeholder qubit as a temporary location for one of the data qubits and a sequence of three SWAP gates eliminates this problem by ensuring that each SWAP gate only touches a data and placeholder qubit. We ignore errors on placeholder qubits as they contain no data. A broad range of single logical qubit gates is also possible. Full details of our chosen set of universal fault-tolerant gates and their associated logical circuits including error correction can be found elsewhere [411, 412].

7.6 Experimental Considerations

In this section, we introduce the experimental elements needed for the hardware implementation of a 2D cavity grid. Figure 7.4 shows a possible setup, where the cavities are realized as coplanar wave guide (CPW) resonators and are arranged on two separate layers (layers 2 and 3). As sketched in Fig. 7.4(a), all resonators located on the top layer (layer 3) are parallel with each other and oriented orthogonally with respect to the resonators on the underlying layer (layer 2). Such a design partially reduces the direct crosstalk between the resonators (cf. discussion below for a quantitative analysis) and can easily be implemented with available multilayer technology, which allows for the fabrication of thin films stacked on top of each other. The lowest layer (layer 1) is used for the control lines. These are necessary to tune the qubit energies and to apply fast control pulses. In the case of charge qubits (or transmons), one of such lines for each qubit is dedicated to voltage pulses [charge control line in Fig. 7.4(b)] and another line to flux pulses [flux control line in Fig. 7.4(b)]. In the case of flux qubits, only flux control lines are in principle necessary [349, 374].[5] The qubits are fabricated at the last step above all other layers. This is an important feature of the setup proposed here since it minimizes

[4] We notice that these ancilla qubits move during error correction.

[5] Indeed, the energy of a flux qubit could be tuned via a DC voltage [413], in which case a charge control line would also be required.

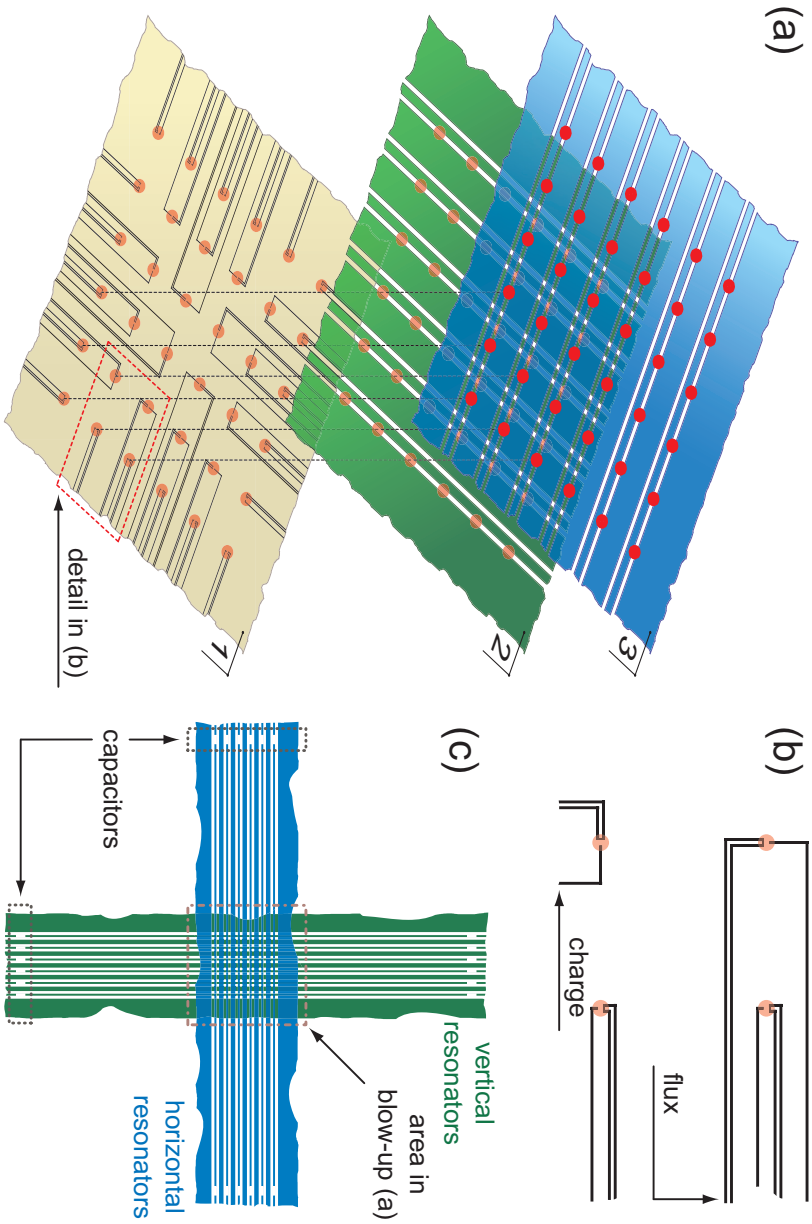

Figure 7.4: Possible multilayer design for a 2D cavity grid setup. **(a)** Layer 1 (bottom, brown): control lines [cf. detail in **(b)**]. Layer 2 (middle, green): portion of vertical CPW resonators. Layer 3 (top, blue): portion of horizontal CPW resonators. The qubits are indicated as red ovals and are resported on each layer for clarity. In reality they are fabricated above layer 3. **(b)** Detail of the charge and flux control lines, which provide individual addressability to each qubit (indicated here as semitransparent red ovals). **(c)** The orthogonal resonators are represented in their entire length. The input and output capacitors as well as the area in **(a)** are indicated.

the possibility of damaging the qubits due to fabrication steps after the qubit fabrication.[6] Another important feature is represented by the small lateral dimensions of the actual grid compared to the total length of the resonators [cf. Fig. 7.4(c)]. This guarantees a homogeneous coupling between all qubits and resonators, the latter being engineered in order to have an antinode of the electromagnetic field right in the center. We emphasize that there is a large flexibility for choosing the components of a 2D cavity grid setup, which can also be realized employing microstrip resonators or even a combination of CPW and microstrip resonators. Here, we focus on the case of CPW resonators for definiteness.

Referring to Fig. 7.5, we now analyze in detail the geometrical dimensions and other experimental parameters of the 2D cavity grid. We consider all metallic structures to be made of Nb or Al, which are in the superconducting state at the typical temperatures of circuit QED experiments. We assume the width of the inner strip of each CPW resonator and the gap between the inner strip and the corresponding groundplanes to be $W_{\rm s} \simeq 19\,\mu$m and $G \simeq 11.5\,\mu$m, respectively. In this case, the aspect ratio $W_{\rm s}/(W_{\rm s}+2G) \simeq 0.45$ guarantees a good 50Ω matching for the CPW structure. In order to reduce unwanted crosstalk between two adjacent resonators we choose the width of the groundplane separating the resonators to be $W_{\rm g} \simeq 72\,\mu$m, which is large enough compared to $W_{\rm s}$. Using these numbers, it is easy to find that the total area of the actual grid [i.e., the region where the qubits are placed; cf. Fig. 7.4(a)] for 10×10 CPW resonators is characterized by a lateral dimension of approximately 1 mm. Since the typical length of the resonators is comprised between 10 and 20 mm, this allows for a homogeneous coupling between the qubits and the electromagnetic field of all resonators. In fact, for the qubits positioned at the edges of the grid the electromagnetic field can easily be estimated to be approximately 99% of the maximum, which is reached in the center of the resonators. The thickness of the dielectric material between the different layers containing resonators and control lines is assumed to be $t \simeq 100\,$nm. Such small separation between the resonator layers compared to the width of the resonator gaps ($G/t \simeq 100$) guarantees a good coupling between qubits and both horizontal and vertical resonators. The dielectric can be made, for example, of amorphous hydrogenated silicon (a-Si:H), a material which has been proven to be optimal with respect to induced decoherence of the qubits [252].

In chapters 5 and 6, we have shown that there is an inevitable crosstalk between two resonators in any two-resonator-qubit setup. This is due to a geometric first- and second-order coupling, which is qubit-state independent, and a dynamic second-order coupling, which is qubit-state dependent and appears when qubit and resonators are detuned from each other (as in the cavity grid architecture). If not opportunely balanced, these two coupling mechanisms sum up giving rise to an effective resonator-resonator interaction dynamics. Such dynamics can constitute a severe issue for the 2D cavity grid architecture, making the model of Eq. (7.1) inadequate for a thorough description of the grid physics. As mentioned in Ref. [331], for the orthogonal design sketched in Figs. 7.4(a), 7.4(c), and 7.5 the geometric first-order coupling between two orthogonal resonators i and j for a resonance frequency of 15 GHz can be estimated to be $g_{ij}^{\rm geom,1} \simeq 2\pi \times 100\,$MHz. The geometric second-order coupling mediated by the presence of a qubit circuit α at the junction

[6] The damaging of a qubit could easily happen when fabricating the qubits between two resonators, in a "sandwich-type" design.

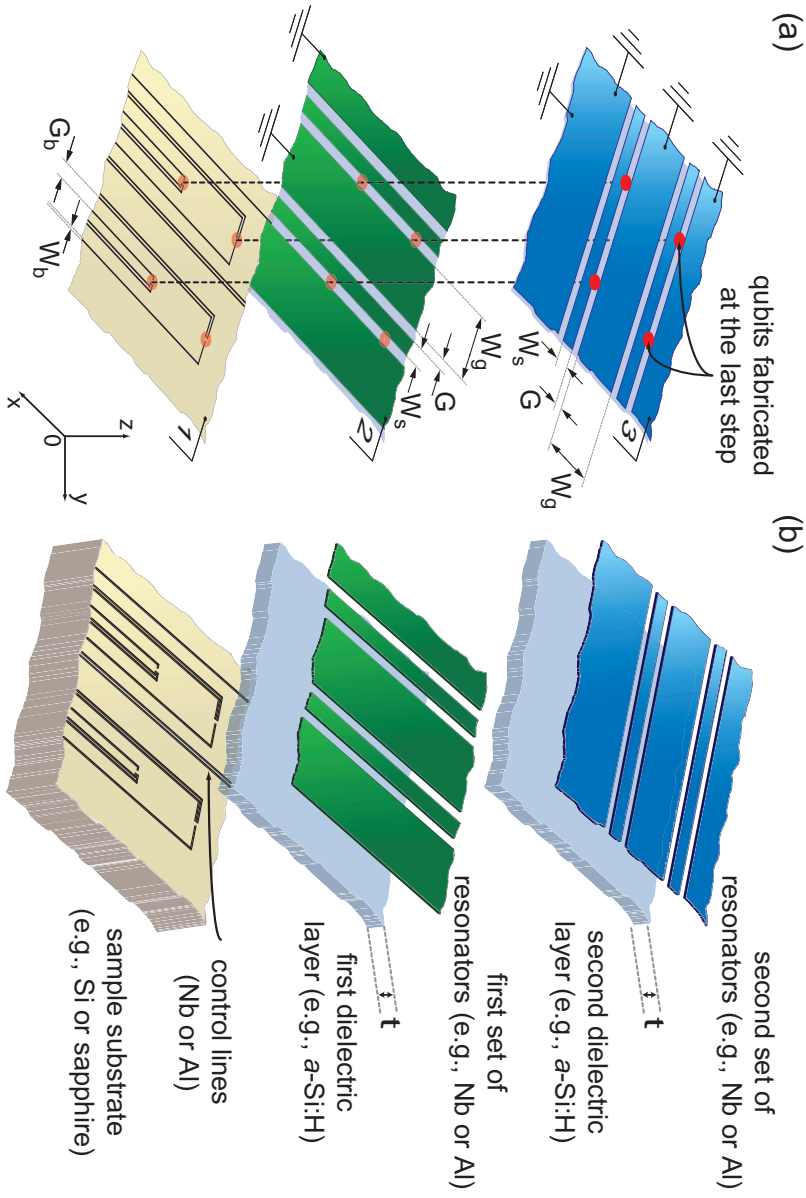

Figure 7.5: Detail of a 2D cavity grid setup. Qubits: red ovals (indicated on all layers for clarity). **(a)** Layer 1 (bottom, brown): control lines. W_{b}: control line width. G_{b}: gap between adjacent lines. Layer 2 (middle, green): two vertical CPW resonators. W_{s}: resonator inner strip width. G: gap between inner strip and groundplanes. W_{g}: groundplane width. Layer 3 (top, blue): two horizontal CPW resonators. The notation is equivalent to that of layer 2. **(b)** The control lines (Nb or Al) are fabricated above a Si or sapphire substrate. A dielectric layer of thickness t (a-Si:H) is fabricated above the control lines and below the first set of CPW resonators (Nb or Al). A second dielectric layer separates the first set of CPW resonators from the second set.

between the two resonators is typically $g_{ij}^{\mathrm{geom},2} \simeq 2\pi \times 1\,\mathrm{MHz}$ (cf. chapters 5 and 6) and we can safely neglect it in the present discussion. In the "idle state," the dynamic second-order coupling mediated by the dispersive action of qubit α is given by (cf. Sec. 5.2)

$$\tilde{g}_{ij}^{\mathrm{dyn}} \equiv \frac{g_\alpha^A \, g_\alpha^B}{\tilde{\Delta}_\alpha} \,, \tag{7.14}$$

where $\tilde{\Delta}_\alpha^A \equiv \Omega_\alpha - \omega_i^A = \tilde{\Delta}_\alpha^B \equiv \Omega_\alpha - \omega_i^B = \tilde{\Delta}_\alpha$. Assuming $g_\alpha^A = g_\alpha^B \simeq 2\pi \times 245\,\mathrm{MHz}$ and $\tilde{\Delta}_\alpha \simeq 2\pi \times 9\,\mathrm{GHz}$,[7] we find a dynamic coupling $\tilde{g}_{ij}^{\mathrm{dyn}} \simeq 2\pi \times 6.7\,\mathrm{MHz}$, which is negligibly small compared to g_{ij}^{geom1}. In the "computational state," however, the dynamic coupling becomes

$$g_{ij}^{\mathrm{dyn}} \equiv \frac{g_\alpha^A \, g_\alpha^B}{\Delta} \,. \tag{7.15}$$

Assuming $\Delta \simeq 2\pi \times 1\,\mathrm{GHz}$, we find $g_{ij}^{\mathrm{dyn}} \simeq 2\pi \times 60\,\mathrm{MHz}$.[8] As a consequence, in the "idle state" the crosstalk between two resonators can be considered to be approximately $g_{\mathrm{cross}} \equiv g_{ij}^{\mathrm{geom},1} \simeq 2\pi \times 100\,\mathrm{MHz}$, whereas in the "computational state," depending on the state of the qubit (cf. chapter 5), such crosstalk varies between $g_{\mathrm{cross}} \equiv g_{ij}^{\mathrm{geom},1} - g_{ij}^{\mathrm{dyn}} \simeq 2\pi \times 40\,\mathrm{MHz}$ (qubit in the groundstate) and $g_{\mathrm{cross}} \equiv g_{ij}^{\mathrm{geom},1} + g_{ij}^{\mathrm{dyn}} \simeq 2\pi \times 160\,\mathrm{MHz}$ (qubit in the excited state). The resonator-resonator crosstalk does not constitute an issue for the operation of the dispersive gates studied in this chapter. In fact, each pair of qubits utilized for the gates exchanges only virtual excitations with the resonators [146], which, thus, remain always in the vacuum state. In this way, the crosstalk dynamics $g_{\mathrm{cross}}(\hat{a}_i^\dagger \hat{b}_j + \hat{a}_i \hat{b}_j^\dagger)$ is effectively inactive. The scenario is different when reading out the state of the qubits. Employing a standard dispersive readout, as suggested in Sec. 7.2, the resonators have to be driven with a resonant coherent field [108]. In this case, the field leakage due to the resonator-resonator crosstalk can spoil the operations between other qubits on the grid. In order to avoid this effect, two possible strategies can be followed. The first strategy is to design the vertical and horizontal resonators with different frequencies, $\omega_i^A \neq \omega_j^B$, $\forall i, j$. Under this assumption, the interaction between a pair of orthogonal resonators can be modeled by a Hamiltonian similar to that of Eqs. (5.17) and (6.41) in chapters 5 and 6, respectively. As shown in chapter 6, Subsec. 6.4.2, if $\omega_i^A - \omega_j^B \gg g_{\mathrm{cross}}$, $\forall i, j$, any dynamics due to the crosstalk is effectively turned off.[9] This approach would also help for the realization of the resonant gates mentioned in Sec. 7.4. The second strategy consists to position an auxiliary qubit at the end of each resonator and operate it as a quantum switch to compensate any resonator-resonator crosstalk (cf. chapter 5).

Following the recipes outlined above, the role played by the resonator-resonator crosstalk in the unitary evolution of the 2D cavity grid gates can be largely minimized. However, we remind that the crosstalk is due to the combination of a stray cross-capacitance and mutual inductance at the junction of each pair of orthogonal

[7] This is the smallest detuning in the "idle state" for the example of our numerical simulations; cf. Sec. 7.3.

[8] It is worth mentioning that for the case of the "computational state" the dispersive condition $\Delta \gg \{g_\alpha^A, g_\alpha^B\}$ is not well satisfied. It is more appropriate to use numerical simulations analogous to those of chapter 5, Sec. 5.2. In this way, it is possible to estimate the true dynamic coupling coefficient without the dispersive assumption. This gives $g_{ij}^{\mathrm{dyn}} \simeq 62.5\,\mathrm{MHz}$, which is nevertheless very similar to the simple analytical estimate based on Eq. (7.15).

[9] $\omega_i^A - \omega_j^B \simeq 2\pi \times 1\,\mathrm{GHz}$, $\forall i, j$ would be sufficient.

resonators. The presence of such stray elements imposes a set of extra boundary conditions on each resonator besides the conditions already imposed by the input and output capacitors, which define the length of the resonators [cf. Fig. 7.4(c)]. As a consequence, each resonator on the grid behaves as a periodic structure with a modified mode function due to the extra boundary conditions. In addition, the quality factor of each resonator is degraded by the leakage owing to the crosstalk to other resonators (this is similar to the effect already discussed in chapter 6, Sec. 6.3.1). It is a very hard task to properly simulate a grid structure as the one depicted in Fig. 7.4 and verify mode-function distortions and quality factor degradation. For the work of Ref. [331], we have simulated two transmission lines crossing each other. In such a simplified design, we have found that the presence of the crossing affects only marginally the transmission through the lines. This is an encouraging result, but not an ultimate prove. In the case of many crossings, the total effect could be much more pronounced and experimental investigations are needed to further clarify the physics of the 2D cavity grid.

The control lines [cf. Figs. 7.4(b) and 7.6], can be used to adjust the quasi-static charge or flux bias of the qubits and/or to apply fast pulses. The quasi-static bias is necessary to set the qubits right at the degeneracy point, thereby ensuring maximum dephasing times through a weak coupling to $1/f$ noise [118, 119, 261, 262].[10] For charge qubits a charge control line is used and for flux qubits a flux control line. It is desirable to keep such lines weakly coupled to the qubits in order to minimize noise backaction. In the case of charge qubits, we suggest to use a very small cross-capacitance between charge gate and qubit, e.g., $C_{\rm g} \simeq 0.01\,{\rm fF}$ [104, 112]. The dimensions of $C_{\rm g}$ can be tuned by adjusting the gate-qubit separation distance. Considering a Cooper-pair box [97] or transmon [120, 243, 244] of total capacitance C_Σ biased at the degeneracy point, the energy relaxation rate induced by the presence of the control line can be estimated as $2(C_{\rm g}/C_\Sigma)^2 e^2 \Omega_{ij}\, \Re[Z_{\rm env}(\Omega_{ij})]/\hbar$, where e is the electron charge and $Z(\Omega_{ij})$ the control line environmental impedance at the qubit transition angular frequency. If we assume $C_\Sigma \simeq 67\,{\rm pF}$ [146] and $\Re[Z(\Omega_{ij})] \simeq 100\Omega$, we find a relaxation rate on the order of approximately 0.43 MHz, which is similar to the rate $\Gamma_{\rm r}$ of our simulations and, thus, does not pose a major limitation to the fidelity of the gates. In the case of flux qubits, the mutual inductance between flux control line and qubit can be engineered to be small enough not to induce any appreciable noise backaction on the qubit (see below).

Fast pulses need to be applied via flux control lines (microcoils [147, 349, 374]) both for charge and flux qubits [cf. Fig. 7.6(b)].[11] Such pulses allow one to DC-Zeeman shift the qubit energies Ω_{ij} on a short time scale maintaining the qubits at the degeneracy point (cf. chapter 6, Sec. 6.3.1 for more details). Good choices for the inductance and capacitance per unit length of the microcoils are $l_{\rm b} \simeq 0.9\,\mu{\rm H/m}$ and $c_{\rm b} \simeq 1.4\,{\rm nF/m}$, respectively, which guarantee a microcoil characteristic impedance $Z_{\rm c} \simeq 25\,\Omega$. Assuming a microcoil length $\ell \simeq 10\,{\rm mm}$ ensures a frequency cut-off at about 3 GHz for any excitation applied through the microcoils. This allows for pulses with a bandwidth of at least 100 MHz, corresponding to pulse rise times on the order of 10 ns or less. The microcoils are coupled to the qubits via a mutual inductance,

[10] We notice that this requirement is not strictly necessary for transmon qubits [120, 244].

[11] It is worth mentioning that in the case of flux qubits two similar flux control lines are needed: one for the quasi-static control and one for the fast control. In Fig. 7.6, this means substituting the charge control line with another flux control line.

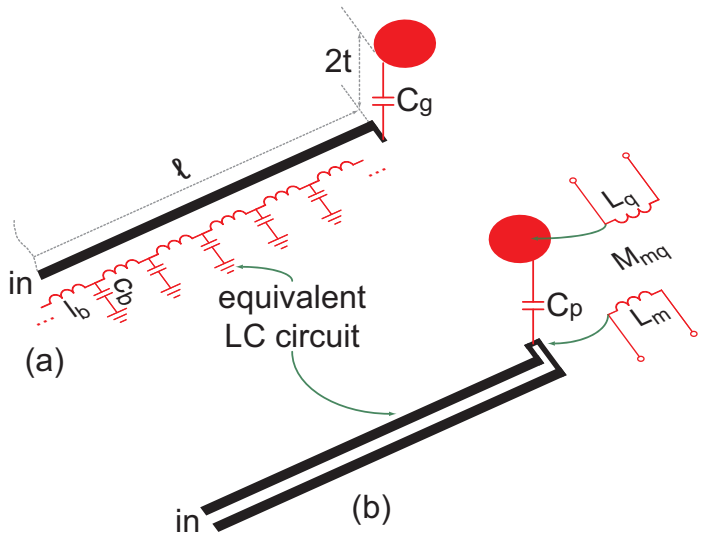

Figure 7.6: Equivalent circuit model for the charge and flux 2D cavity grid control lines [cf. Fig. 7.4(b)]. **(a)** A generic charge control (bias) line is depicted. The equivalent LC lumped-parameter circuit is sketched in red. The quantities $l_{\rm b}$ and $c_{\rm b}$ represent the line inductance and capacitance per unit length, respectively, and set the line characteristic impedance. The length ℓ of the line, which sets the line cut-off frequency, is also indicated. A qubit (red oval) is positioned $2t$ [corresponding to the combined thickness of two dielectric layers; cf. Fig. 7.5(b)] above the charge bias line. The cross-capacitance $C_{\rm g}$ between line and qubit is reported. **(b)** A generic flux control line is depicted. This line can be represented by an LC lumped-parameter equivalent circuit similar to the one sketched in **(a)**. The quantity $L_{\rm m}$ indicates the flux line (microcoil) self-inductance. $M_{\rm mq}$ indicates the microcoil-qubit mutual inductance. $L_{\rm q}$ indicates the qubit self-inductance. $C_{\rm p}$ is the parasitic microcoil-qubit cross-capacitance, which should be minimized (cf. main text for details). Signals are applied through the input ports, which are indicated as "in," via $50\,\Omega$ transmission lines and/or coaxial cables.

which can easily be estimated by means of FASTHENRY simulations [364]. In order to obtain a large enough mutual inductance, the qubit design must include control loops with area in the range between $2\times2\,\mu{\rm m}^2$ and $2\times6\,\mu{\rm m}^2$. These areas correspond to self-inductances $L_{\rm q}\simeq$ 20-40 pH and allow for mutual inductances $M_{\rm mq}\simeq$ 0.1-1 pH. Such mutual inductances are large enough to permit a good control of the qubit and small enough to minimize flux noise backaction. The microcoils can also be used to apply a quasi-static flux bias, which can help compensating the inevitable spread of the qubit energies due to fabrication inaccuracy. It is worth mentioning that, in order not to screen the pulses and other signals applied through the control lines, the gap G of the resonators has to be designed to be large enough. For example, $G\simeq 11.5\,\mu$m should suffice for this purpose.

Although individual addressability by means of extra control lines introduces some hardware overhead, it is an essential feature for the entire operation of any large scale architecture.

7.7 Summary and Conclusions

In conclusion, we have proposed a new kind of flexible architecture for quantum computation using a grid of superconducting qubits coupled to an orthogonal array of microwave transmission line resonators: a 2D cavity grid.

We have shown that a "Sudoku"-type arrangement of qubit transition frequencies permits global coupling of a large number of qubits with strongly suppressed spurious interactions.

We have proven by means of numerical simulations based on the parameters reached in standard circuit QED experiments that high-fidelity gates can be implemented on the 2D cavity grid. In addition, we have analyzed in detail the experimental issues related to the hardware realization of 2D grids in circuit QED, showing that such grids could possibly be realized with available technology.

Elementary operations within this scheme could be demonstrated in the near future on small grids, while the setup has the potential to form the basis for truly scalable fault-tolerant architectures or for the implementation of one-way quantum computing.

Chapter 8

Circuit QED Experiments with Superconducting Flux Qubits

In all previous chapters, we have considered qubit-cavity systems where the cavity is assumed to be either a coplanar wave guide (CPW) or a microstrip transmission line resonator. Moreover, we have mostly dealt with systems where the microwave radiation emitted by the resonator is used to infer information about the qubit-resonator interaction. Also, such interaction has been typically assumed to be in the strong coupling limit, which means the loss rates of both qubit and resonator are small compared to the qubit-resonator coupling strength. These are not the only conditions under which circuit QED experiments can be performed.

In this chapter, we experimentally study a superconducting flux qubit [189, 245] coupled to the resonant mode of a lumped-parameter LC-resonator with low quality factor [141]. Instead of the radiation from the resonator, the state of the qubit is utilized to characterize the qubit-resonator interaction. Even if such interaction is associated with a large coupling coefficient, due to the low quality factor of the resonator we cannot reach the strong coupling regime of circuit QED. Nevertheless, we are able to observe the key signatures of a two-photon driven Jaynes-Cummings model, which unveils the upconversion dynamics of the qubit-resonator system. Our experiment and theoretical analysis show clear evidence for the coexistence of one- and two-photon driven level anticrossings in such a system. This results from the controlled symmetry breaking of the system Hamiltonian, causing parity to become a not well-defined property [414]. Our study provides deep insight into the interplay of multiphoton processes and symmetries in circuit QED.

The chapter is organized as follows. In Sec. 8.1, we compare our experiment to cavity QED experiments in quantum optics and the state-of-the-art experiments in circuit QED. In Sec. 8.2, we introduce the main elements of the setup and explain the qubit manipulation and readout processes. In Sec. 8.3, we present our experimental results on the two-photon probing of the Jaynes-Cummings (JC) model. In Sec. 8.4, we theoretically analyze the role played by selection rules and symmetry breaking in circuit QED reserving special attention to the case of superconducting flux quantum circuits. In Sec. 8.5, we discuss the impact of spurious fluctuators [spurious resonators or two-level systems (TLSs)] on circuit QED experiments. Finally, in Sec. 8.6, we summarize our results and draw our conclusions.

The material discussed in this chapter is an extension of article number 4 on the *List of Publications* and is published in *Nature Physics* - Ref. [159]. Frank

Deppe and the author contributed equally to this work. In particular, the author has largely contributed in the interpretation of the data suggesting the concepts of selection rules, symmetry breaking in circuit QED, and two-photon upconversion dynamics as explanation of the experimental results. Moreover, the author has extensively helped in the development of the numerical simulations used to clarify the experimental data, in the critical discussion of the results, and in the writing of the manuscript. The experiments were carried out by Frank Deppe at the NTT corporation, Japan.

In addition to the material treated in Ref. [159], in this chapter we delve into the details of the concept of selection rules in circuit QED experiments based on supeconducting flux quantum circuits. Also, we discuss more extensively the role played by spurious fluctuators in time-resolved experiments summarizing part of the results described in article number 3 on the *List of Publications*, which is published in *Physical Review B* - Ref. [262]. The main contributions of the author to this article are on the development of the theoretical model utilized to explain the time-resolved experimental data, on the critical discussion of the results, and on the writing of the manuscript. Once again, the experiments were carried out by Frank Deppe at the NTT corporation, Japan.

8.1 Introduction

In cavity QED, a two-level atom interacts with the quantized modes of an optical or microwave cavity. The information on the coupled system is encoded both in the atom and in the cavity states. The latter can be accessed spectroscopically by measuring the transmission properties of the cavity [52], whereas the former can be read out by suitable detectors [180, 185]. In circuit QED, the solid-state counterpart of cavity QED, the first category of experiments has been implemented by measuring the microwave radiation emitted by a resonator (acting as a cavity) strongly coupled to a superconducting charge qubit [139]. In a dual experiment, the state of a superconducting flux qubit has been detected with a DC SQUID and vacuum Rabi oscillations have been observed [141]. More recently, both approaches have been exploited to extend the toolbox of quantum optics on a chip [108, 142–158, 160, 161]. Whereas all these experiments employ one-photon driving of the coupled qubit-resonator system, multi-photon studies are available only for sideband transitions [142] or bare qubits [361, 415–419]. Only very recently, the nonlinear dynamics of the JC model both in quantum-optical cavity QED [57] and in circuit QED have been studied experimentally [151, 157, 158]. Differently from those works, which focus on higher-level excitations of the JC ladder, the experiments discussed in this chapter explore the physics of the two-photon driven JC dynamics in circuit QED. In this context, we show that the dispersive interaction between the qubit and the two-photon driving enables real level transitions. The nature of our experiment can be understood as an upconversion mechanism, which transforms the two-photon coherent driving into single photons of the JC dynamics. This process requires energy conservation and a not well-defined parity [414] of the interaction Hamiltonian due to the symmetry breaking of the qubit potential. Our experimental findings reveal that such symmetry breaking can be obtained either in a controlled way by choosing a suitable qubit operation point or by the presence of additional TLSs or spurious fluctuators [249].

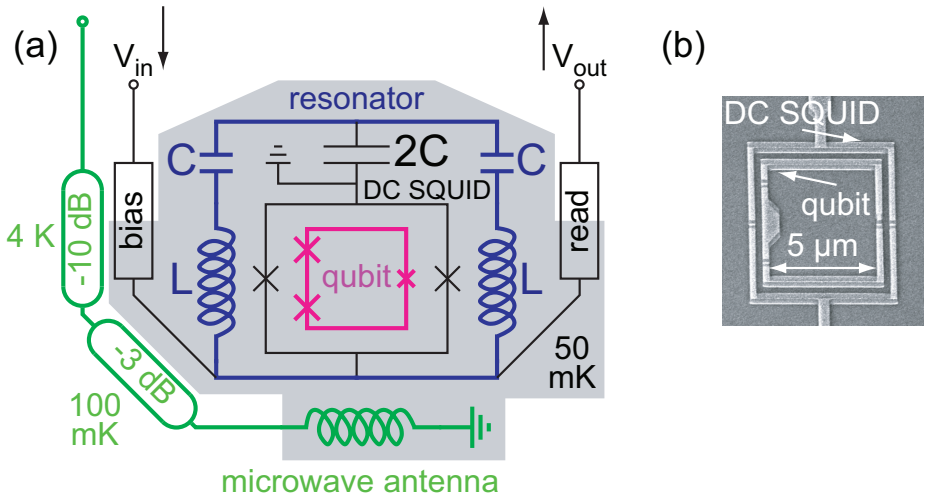

Figure 8.1: Circuit QED with superconducting flux qubits: experimental architecture. **(a)** The flux qubit [magenta (middle grey) square, junctions marked by crosses] is inductively coupled to the readout DC SQUID (black rectangle), which is shunted by an LC-circuit acting as a quantized resonator [dark blue (dark grey) square] [141]. The DC SQUID is biased with a voltage pulse $V_{\rm in}$ and its response, which encodes information on the qubit state, is read out as a voltage $V_{\rm out}$ [cf. also Figs. 8.2(a) and 8.3]. All elements within the shaded area are at a temperature $T \simeq 50\,{\rm mK}$. Microwave signals and flux-shift pulses are applied via an on-chip antenna [light green (light grey) line]. The signal-to-noise ratio is improved by cold attenuators (10 dB at 4 K and 3 dB at 100 mK). C and L are the capacitor and inductor forming both the LC-resonator and DC SQUID shunting circuit. **(b)** Scanning electron microscopy micrograph of flux qubit (inner square) and readout DC SQUID (outer square).

8.2 Setup

The main elements of our setup, shown in Figs. 8.1(a) and 8.1(b), are a superconducting flux qubit based on a three-Josephson-junction SQUID, an LC-resonator, a readout DC SQUID, and a microwave antenna [261, 262]. The investigated sample was fabricated on a $3.5 \times 3.5\,{\rm mm}^2$ SiO_2-covered Si substrate. Standard electron beam lithography and aluminum thin film technology were used. The sample chip is surrounded by a T-shaped printed circuit board (PCB). Both sample chip and PCB are placed inside a gold-plated copper box, which is connected to the mixing chamber stage of a dilution refrigerator. All experiments were performed at the base temperature of the cryostat, which is approximately 50 mK. In the following, we briefly describe the main components of the sample and summarize their characteristic parameters and function. A sketch of the sample layout is shown in Fig. 8.1(a). The superconducting flux qubit [189, 245] consists of a square-shaped superconducting aluminum loop interrupted by three nano scale $Al/AlO_x/Al$ Josephson tunnel junctions. The size of two of these junctions is chosen to be the same, $0.03\,\mu{\rm m}^2$, whereas the third one is designed to be smaller by a factor $\alpha = 0.7$. The qubit (and DC SQUID) junctions are fabricated using the shadow evaporation

technique. The Josephson junctions are characterized by their Josephson coupling energy $E_\mathrm{J} \equiv I_{c0}\Phi_0/2\pi$ and their charging energy $E_\mathrm{c} \equiv e^2/2C_\mathrm{j}$. Here, Φ_0 is the flux quantum, e the electron charge, and I_{c0} and C_j are the critical current and capacitance of the junction, respectively. The specific capacitance of our junctions was determined to be $C_\mathrm{s} = 100 \mp 25\,\mathrm{fF/\mu m^2}$ [420]. When the ratio $E_\mathrm{J}/E_\mathrm{c}$ is approximately 50, the device is expected to behave as an effective quantum two-level system (qubit).

As already described in chapter 2, Sec. 2.2.3, the qubit can be described by the effective Hamiltonian [97, 189, 229, 245]

$$\widehat{\widehat{H}}_\mathrm{Q} = \frac{1}{2}\left[\epsilon\left(\Phi_\mathrm{x}^\mathrm{DC}\right)\hat{\hat{\sigma}}_z + \delta_\mathrm{Q}\hat{\hat{\sigma}}_x\right], \tag{8.1}$$

where $\hat{\hat{\sigma}}_x$ and $\hat{\hat{\sigma}}_z$ are the usual Pauli operators, $\epsilon(\Phi_\mathrm{x}^\mathrm{DC})$ is the so-called qubit energy bias, which depends on an externally applied quasi-static flux $\Phi_\mathrm{x}^\mathrm{DC}$, and δ_Q is the qubit energy gap (tunnel coupling). For vanishing tunnel coupling ($\delta_\mathrm{Q} = 0$) the two qubit states correspond to the classical states $|+\rangle$ and $|-\rangle$ with counterclockwise and clockwise persistent currents $I_\mathrm{p} = \pm I_{c0}\sqrt{1-(2\alpha)^{-2}}$ circulating in the loop [189, 245]. These two states are eigenstates of $\epsilon\hat{\hat{\sigma}}_z$ and are separated by the flux-dependent qubit energy bias $\epsilon = 2|I_\mathrm{p}|(\Phi_\mathrm{x}^\mathrm{DC} - 1.5\Phi_0)$. Our sample is designed to be operated in the vicinity of the flux bias $\Phi_\mathrm{x}^\mathrm{DC} = 1.5\Phi_0$ instead of the usual $\Phi_\mathrm{x}^\mathrm{DC} = 0.5\Phi_0$ [189, 245]. For finite tunnel coupling ($\delta_\mathrm{Q} > 0$), we obtain superpositions of $|+\rangle$ and $|-\rangle$ states. This results in new qubit eigenstates $|\mathrm{g}\rangle$ and $|\mathrm{e}\rangle$, whose energy difference $E_\mathrm{Q} \equiv \hbar\Omega_\mathrm{Q}(\Phi_\mathrm{x}^\mathrm{DC}) \equiv h\nu_\mathrm{Q}(\Phi_\mathrm{x}^\mathrm{DC}) \equiv \sqrt{\delta_\mathrm{Q}^2 + \epsilon(\Phi_\mathrm{x}^\mathrm{DC})^2} = \sqrt{\delta_\mathrm{Q}^2 + [2I_\mathrm{p}(\Phi_\mathrm{x}^\mathrm{DC} - 1.5\Phi_0)]^2}$ has a hyperbolic flux dependence (ν_Q is the qubit transition frequency). At the qubit degeneracy point ($\Phi_\mathrm{x}^\mathrm{DC} = 1.5\Phi_0$, $\epsilon(\Phi_\mathrm{x}^\mathrm{DC}) = 0$) the qubit is protected from dephasing because $\Omega_\mathrm{Q}(\Phi_\mathrm{x}^\mathrm{DC})$ is stationary with respect to small variations of the control parameter $\Phi_\mathrm{x}^\mathrm{DC}$. Therefore, this point represents the optimal point for the coherent manipulation of the qubit. Note that at the qubit degeneracy point the qubit eigenstate is an equal superposition of $|+\rangle$ and $|-\rangle$ states, i.e., the expectation value of the persistent current vanishes. Far away from the qubit degeneracy point ($\epsilon(\Phi_\mathrm{x}^\mathrm{DC}) \gg \delta_\mathrm{Q}$) the qubit behaves as a classical two-level system and the eigenstates $|\mathrm{g}\rangle$ and $|\mathrm{e}\rangle$ correspond to the classical states $|\pm\rangle$ of $\widehat{\widehat{H}}_\mathrm{Q}$. From low-level microwave spectroscopy (see below), we estimate a qubit gap $\delta_\mathrm{Q}/\hbar = 2\pi \times 3.89\,\mathrm{GHz}$, $E_\mathrm{J}/E_\mathrm{c} \simeq 50$, and a critical current density $J_\mathrm{c} \simeq 1300\,\mathrm{A/cm^2}$. This means that at an operation temperature $T \simeq 50\,\mathrm{mK}$ the condition $k_\mathrm{B}T \ll \delta_\mathrm{Q}$ required for the observation of quantum effects is well satisfied.

When describing the influence of fluctuations $\delta\vec{\Omega}$ on the qubit, it is convenient to express the Hamiltonian of Eq. (8.1) in a two-dimensional Bloch vector representation: $\widehat{\widehat{H}}_\mathrm{Q} = \hbar\vec{\Omega}\,\vec{\hat{\sigma}}/2$. Here, $\vec{\hat{\sigma}} \equiv (\hat{\sigma}_\perp, \hat{\sigma}_\parallel) \equiv (\hat{\hat{\sigma}}_x, \hat{\hat{\sigma}}_z)$ and $\vec{\Omega} \equiv (\Omega_\perp, \Omega_\parallel) \equiv \left[\delta_\mathrm{Q}, \epsilon(\Phi_\mathrm{x}^\mathrm{DC})\right]/\hbar$. The representation of the Bloch vector $\vec{\Omega}$ in the qubit energy eigenbasis ($|\mathrm{g}\rangle$ and $|\mathrm{e}\rangle$) is obtained by multiplying $\vec{\Omega}$ with the rotation matrix

$$D \equiv \begin{bmatrix} \cos\theta & -\sin\theta \\ \sin\theta & \cos\theta \end{bmatrix} \tag{8.2}$$

from the left. The angle θ is defined via $\tan\theta \equiv \delta_\mathrm{Q}/\epsilon(\Phi_\mathrm{x}^\mathrm{DC})$ [229]. This results in $\sin\theta = \delta_\mathrm{Q}/E_\mathrm{Q}$ and $\cos\theta = \epsilon(\Phi_\mathrm{x}^\mathrm{DC})/E_\mathrm{Q}$. In the qubit energy eigenbasis, for simplicity we redefine the Pauli operators as $\hat{\sigma}_x$, $\hat{\sigma}_y$, and $\hat{\sigma}_z$.

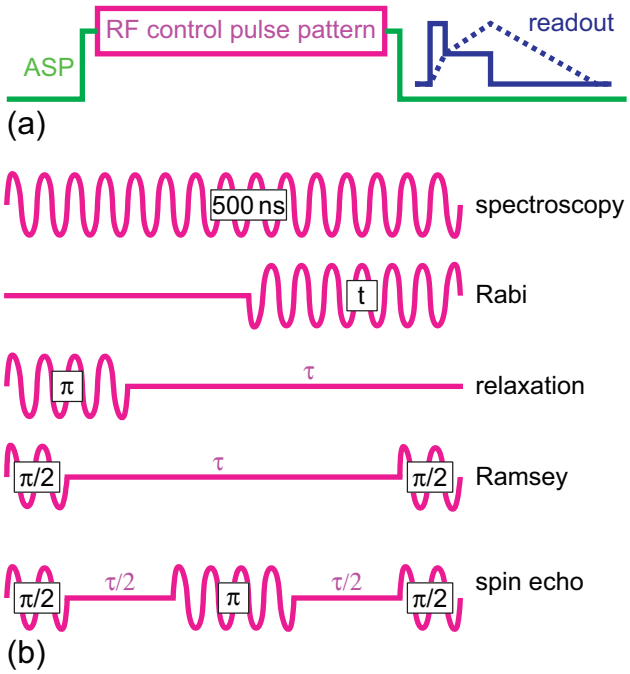

Figure 8.2: Flux qubit manipulation and readout sequences. **(a)** Adiabatic shift pulse (ASP) readout. Adiabatic shift pulse: light green (light grey) rectangle. RF control pulse pattern: magenta (middle grey) box [cf. **(b)**]. Readout sequence: dark blue (dark grey) rectangles. **(b)** Five possible RF control pulse patterns. The boxed values denote either the pulse duration t or the corresponding rotation angle of the qubit state vector on the Bloch sphere. Free evolution times are denoted by the symbol τ.

The qubit control is achieved by varying the control parameter $\Phi_{\rm x}^{\rm DC}$ and, simultaneously, applying a suitable sequence of microwave pulses $A\cos(\omega t+\varphi) = A\cos(2\pi\nu t+\varphi)$ with frequency $\nu \approx \nu_{\rm Q}$. A single microwave pulse results in a rotation of the qubit state vector by an angle $\Omega = 2\pi\nu_{\rm R}t\sqrt{1+(\delta/\nu_{\rm R})^2}$ on the Bloch sphere, where t is the pulse duration and the Rabi frequency $\nu_{\rm R} \equiv \nu_{\rm R}(A)$ is a function of the pulse amplitude A. The relative phase φ of the pulse and the detuning $\delta \equiv \nu - \nu_{\rm Q}$ determine the rotation axis $\vec{v} \equiv (v_1, v_2, v_3) = (\nu_{\rm R}\cos\varphi, \nu_{\rm R}\sin\varphi, \delta)/\sqrt{\nu_{\rm R}^2+\delta^2}$. Mathematically, we can describe this rotation with the matrix

$$\tilde{R}_{\varphi,\delta}(\Omega) \equiv \tilde{R}_{\mathbf{v}}(\Omega) = \begin{bmatrix} \cos\Omega + v_1^2(1-\cos\Omega) & v_1v_2(1-\cos\Omega) - v_3\sin\Omega & v_1v_3(1-\cos\Omega) + v_2\sin\Omega \\ v_2v_1(1-\cos\Omega) + v_3\sin\Omega & \cos\Omega + v_2^2(1-\cos\Omega) & v_2v_3(1-\cos\Omega) - v_1\sin\Omega \\ v_3v_1(1-\cos\Omega) - v_2\sin\Omega & v_3v_2(1-\cos\Omega) + v_1\sin\Omega & \cos\Omega + v_3^2(1-\cos\Omega) \end{bmatrix}. \tag{8.3}$$

For the case $\varphi = 0$ and $\delta = 0$, Eq. (8.3) describes a rotation by an angle $2\pi\nu_{\rm R}t$ about the x-axis. When introducing a finite relative phase φ the orientation of the rotation axis within the x,y-plane changes. Finite detuning results in a change of the rotation angle and a tilt of the rotation axis out of the x,y-plane. In the absence of any microwave radiation ($\nu_{\rm R} = 0$) the qubit evolves freely, i.e., its state vector rotates about the z-axis of the Bloch sphere with a frequency $\Omega_{\rm free} = 2\pi\delta\cdot t$ (since we work in a frame rotating with the frequency ν). The corresponding rotation matrix $\tilde{R}_z(\Omega_{\rm free})$ is obtained from Eq. (8.3) by choosing $\vec{v} = \vec{v}_z \equiv (0,0,1)$.

Finally, the qubit-resonator system can be controlled and excited by means of microwave pulses applied through an on-chip antenna. The antenna, which is inductively coupled to the qubit, is implemented as a CPW transmission line shorted

at one end [cf. Fig. 8.1(a)]. From a FASTHENRY [364] simulation, the mutual inductance between the antenna and the qubit is determined to be $M_{\mathrm{QA}} \simeq 73\,\mathrm{fH}$. The applied microwave radiation is cooled by means of a 10 dB and a 3 dB attenuator, which are thermally anchored at a temperature of 4 K and 100 mK, respectively [cf. Fig. 8.1(a)]. The initial qubit state, which in our measurements is always the groundstate, is prepared by waiting for a time $t \simeq 300\,\mu\mathrm{s}$ much longer than the energy relaxation time T_1 of the system. For the time and frequency domain experiments, the pulse sequences shown graphically in Figs. 8.2(a) and 8.2(b) are used for the qubit manipulation. For the measurements in the frequency domain (microwave spectroscopy) the qubit is saturated to an equilibrium mixed state by means of a sufficiently long microwave pulse, followed by the readout [cf. Fig. 8.2(b) - spectroscopy]. In the time domain, driven Rabi oscillations are recorded by measuring the qubit state as a function of the duration of a single microwave pulse of fixed amplitude A [cf. Fig. 8.2(b) - Rabi]. From the measured Rabi frequency ν_{R} of these oscillations we determine the duration t_π and $t_{\pi/2}$ of the π- and $\pi/2$-pulses, which rotate the qubit state vector by the corresponding angles. In our experiments, we typically choose the microwave amplitude such that $t_\pi = 2t_{\pi/2} = 1/2\nu_{\mathrm{R}} \simeq 8\,\mathrm{ns}$. Then, the energy relaxation time is determined by exciting the qubit with a π-pulse and, subsequently, recording the decay of $\langle\hat{\sigma}_z\rangle$ as a function of the waiting time [cf. Fig. 8.2(b) - relaxation]. Finally, the evolution of $\langle\hat{\sigma}_{x,y}\rangle$ is probed by the sequence $\pi/2$-pulse–wait–$\pi/2$-pulse–readout [cf. Fig. 8.2(b) - Ramsey] or the sequence $\pi/2$-pulse–wait–π-pulse–wait–$\pi/2$-pulse–readout [cf. Fig. 8.2(b) - spin-echo]. In the case of a spin-echo sequence, low-frequency phase fluctuations are canceled because of the refocusing effect of the intermediate π-pulse.

In order to read out the qubit state, the qubit is surrounded by a slightly larger square-shaped aluminum loop containing two Al/AlO$_x$/Al Josephson tunnel junctions, a so-called DC SQUID [cf. Figs. 8.1(a) and 8.1(b)]. The DC SQUID is sensitive to the flux difference generated by the persistent currents flowing in the qubit loop. In our design the DC SQUID is coupled to the qubit via a purely geometric mutual inductance $M_{\mathrm{SQ}} = 6.7\,\mathrm{pH}$. Different from other flux qubit designs [118, 119], in our sample there is no galvanic connection between qubit and DC SQUID. This is expected to reduce the effect of asymmetry-related issues as well as the detector backaction on the qubit. In fact, we do not find any measurable bias current dependence of the qubit decay time, as reported recently for shared-edge designs [118, 119]. The lines used for biasing and reading out the DC SQUID detector are heavily filtered against noise in the gigahertz range using a combination of copper powder filters and stainless steel ultra-thin coax cables at the mixing chamber temperature level (see below and cf. Fig. 8.3).

The detection of the qubit state ($|\mathrm{g}\rangle$ or $|\mathrm{e}\rangle$) is straightforward far away from the qubit degeneracy point. In this region, the energy eigenstates coincide with the states $|+\rangle$ and $|-\rangle$, which correspond to counterclockwise and clockwise persistent currents in the qubit loop, respectively. The flux generated by these currents is then detected by the DC SQUID. However, in the vicinity of the qubit degeneracy point the qubit eigenstates $|\mathrm{g}\rangle$ and $|\mathrm{e}\rangle$ cannot be distinguished in this way because they become nearly equal superpositions of $|+\rangle$ and $|-\rangle$. This means that the expectation value $\langle I_{\mathrm{p}}\hat{\sigma}_z\rangle$ of the persistent current circulating in the qubit loop vanishes. To circumvent this problem we employ the adiabatic shift pulse method [cf. Fig. 8.2(a)]. This method exploits the possibility to perform the readout process sufficiently far

away from the qubit degeneracy point by applying a control pulse, which adiabatically shifts the qubit in and out of the region around the degeneracy point. In contrast to the quasi-static flux bias at the readout point, which is generated by a superconducting coil located in the helium bath of a dilution refrigerator, the shift pulse is applied to the qubit through the on-chip microwave antenna sketched in Fig. 8.1(a). The total control sequence (cf. Fig. 8.2) for initialization, manipulation, and readout of the qubit can be summarized as follows: First, the qubit is initialized in the groundstate at the readout point far away from the degeneracy point by waiting for a sufficiently long time. Second, a rectangular (0.8 ns rise time) adiabatic shift pulse together with the microwave control sequence is applied to the qubit via the microwave antenna. In this way, the qubit is adiabatically shifted to the desired operation point, where the qubit operation is performed according to the chosen microwave pulse sequence. Finally, immediately after the ending of the microwave pulse sequence, the qubit is adiabatically shifted back to the readout point, where the state detection is performed. Note that, in order to avoid qubit state transitions, the rise and fall times of the shift pulse have to be long enough to fulfill the adiabatic condition, but also short enough to avoid unwanted relaxation processes.

In the readout process performed right after shifting the qubit back to the readout point, the DC SQUID is biased with a current pulse of amplitude just between the two switching currents corresponding to the qubit states. Depending on the actual qubit state, the DC SQUID detector either remains in the zero-voltage state or switches to the running-phase state. Only in the latter case a voltage response pulse can be detected from the readout line. The DC SQUID voltage signal is amplified by means of a room temperature differential amplifier with an input impedance of 1 MΩ against a cold ground taken from the mixing chamber temperature level.

The DC SQUID is shunted with an $\mathrm{Al/AlO}_x\mathrm{/Al}$ on-chip capacitance $C = 6.3 \mp 0.5\,\mathrm{pF}$. This capacitance also behaves as a filter and, in combination with the other biasing elements (either a resistor or a resistor-capacitor combination), creates the electromagnetic environment of the qubit. The environmental noise should be reduced as much as possible in order not to deteriorate the qubit coherence times. The resistive part of the biasing circuit helps damping away modes formed by the shunted DC SQUID and the parasitic inductance/capacitance of its leads. Ideally, it should be placed as close as possible to the shunted DC SQUID.

Finally, after a typical "single-shot" measurement sequence as described above, the response signal of the DC SQUID is binary (zero or finite voltage state), depending on the qubit state. In the experiments, we measure the switching probability P_{sw}, which is the average over several thousands of single-shot measurements. For a proper bias current pulse height the qubit state is encoded in the value of the switching probability. In the best case, the groundstate would correspond to $P_{\mathrm{sw}}^{\mathrm{min}} = 0\%$ and the excited state to $P_{\mathrm{sw}}^{\mathrm{max}} = 100\%$, or vice versa. In reality, however, due to noise issues the actual visibility $P_{\mathrm{sw}}^{\mathrm{max}} - P_{\mathrm{sw}}^{\mathrm{min}}$ is usually significantly smaller than 100%.

The readout of the qubit is performed by means of a switch&hold measurement technique, which makes use of the hysteretic current-voltage characteristic of the DC SQUID detector. In the so-called resistive-bias detection scheme, a voltage pulse is generated at room temperature, fed into the DC SQUID bias line, and then transformed into a current pulse via a cold 1.25 kΩ bias resistor (cf. Fig. 8.3). According to Ohm's law, the voltage pulse must have the same shape as the desired

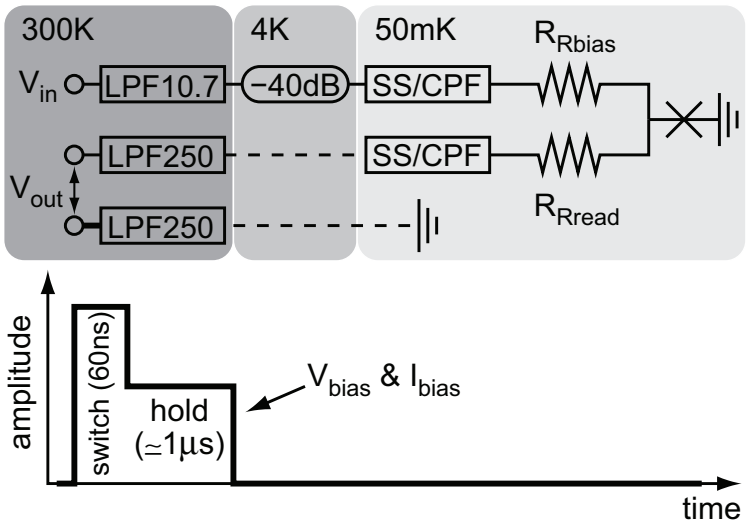

Figure 8.3: Resistive bias setup. Top part. LPF10.7 and LPF250: commercial low-pass filters with 10.7 and 250 MHz cutoff frequency, respectively. SS/CPF: combination of 1 m of ultra-thin (⌀0.33 mm) stainless steel coaxial cable and copper powder filter (bias line: 25 cm wire length; readout line: 100 cm wire length). Qubit, DC SQUID, and shunting capacitor C are indicated with a single cross (×). Solid and broken lines represent high-bandwidth semirigid ⌀1.2 mm CuNi/Nb and narrower bandwidth stainless steel braided flexible coaxial cables, respectively. The bias voltage pulse is attenuated by 40 dB at 4 K. The bias resistors are $R_{\mathrm{Rbias}} = 250\,\Omega + 1\,\mathrm{k}\Omega$ and $R_{\mathrm{Rread}} = 2.25\,\mathrm{k}\Omega + 3\,\mathrm{k}\Omega$ (on-chip + off-chip). V_{in} and V_{out} refer to the same voltages indicated in Fig. 8.1(a). Bottom part. Switch&hold readout pulses for the resistive-bias setup. Note that the 60 ns-segment is the portion of the switching pulse which exceeds the $\simeq 1$ μs-long hold level. Only there switching events can be induced. V_{bias} and I_{bias}: voltage and current bias pulses sent through the line indicated by V_{in} in the top part. The voltage and current bias pulses have the same shape because of Ohm's law.

bias current pulse. The latter is composed of a short rectangular switching pulse (of duration $\simeq 60$ ns) immediately followed by a much longer hold pulse ($\simeq 1$ μs) of smaller amplitude, as shown in Fig. 8.3. The switching pulse height is chosen such that the DC SQUID either switches to the voltage state or stays in the zero voltage state, depending on the state of the qubit. Therefore, the length of the switching pulse determines the time resolution for the switching event detection. The hold pulse level is chosen to be just above the value of the DC SQUID retrapping current. Consequently, if the DC SQUID switches to the voltage state during the switching pulse, it does not switch back to the zero voltage state during the hold pulse. In this way, the voltage is sustained for a sufficiently long time interval allowing one to use a room temperature amplifier with reduced bandwidth. At the same time, quasiparticle generation is minimized.

In the resistive-bias experiments the bias lines of the readout DC SQUID are strongly low-pass filtered (cf. Fig. 8.3). This is required to reduce the high-frequency

noise $S_\omega(\omega = \Omega_\mathrm{Q})$, which is responsible for the qubit energy relaxation. Here, $\omega \equiv 2\pi f \in [0, \infty)$ is a generic angular frequency. In addition, filtering is necessary to eliminate part of the low-frequency noise. Here, the term low-frequency noise refers to noise which has a large spectral density at frequencies much smaller than the qubit level splitting $\Omega_\mathrm{Q} \simeq 2\pi \times 3.89\,\mathrm{GHz}$. The dephasing time T_φ of the qubit is mainly determined by this low-frequency environmental noise spectral density $S_\omega(\omega \to 0)$. Consequently, the cut-off frequency for the low-pass filter should be chosen as low as possible in order to strongly attenuate low-frequency noise. However, a lower limit is set by the requirement that the readout pulse has to be sufficiently short to avoid any deterioration of visibility. For this reason, the filter cutoff cannot be chosen smaller than approximately 10 MHz.

The shunting circuit of the readout DC SQUID, including the inductance of its leads, constitutes an effective lumped-parameter LC-resonator [141] [cf. Fig. 8.1(a)], which is inductively coupled to the qubit. This resonator can be represented by a quantum harmonic oscillator,

$$\widehat{H}_\mathrm{R} = \hbar\omega_\mathrm{R}\left(\hat{a}^\dagger\hat{a} + \frac{1}{2}\right) , \tag{8.4}$$

with photon number states $|0\rangle$, $|1\rangle$, $|2\rangle, \ldots$ and boson creation and annihilation operators $\hat{a}^\dagger$ and $\hat{a}$, respectively. The photon number operator is defined as $\hat{N} \equiv \hat{a}^\dagger\hat{a}$. In our experiments, the resonator is designed such that its angular frequency, $\omega_\mathrm{R} = 2\pi \times 6.16\,\mathrm{GHz}$, is largely detuned from $\Delta/\hbar$. In the rest of the chapter, we base our arguments on the assumption that our LC-resonator is characterized by a purely harmonic behavior. This means that a classical driving with half the resonator fundamental angular frequency, $\omega_\mathrm{R}/2$ (two-photon driving), cannot directly populate the resonator. An anharmonic response would allow such two-photon driving to populate the resonator. However, in the case of strong driving, anharmonicities only arise when the maximum induced current density J^max in the LC-resonator approaches the critical current density of the resonator lines. For lines made of aluminum, as in our case, the critical current density is $J_\mathrm{c} \simeq 10^7\,\mathrm{Acm}^{-2}$. From qubit Rabi oscillation measurements (data not shown), we can determine the current flowing through the microwave antenna to be $I_\mathrm{A} \lesssim 1\,\mu\mathrm{A}$. This results in a maximum resonator current $I^\mathrm{max} = M_\mathrm{AR} I_\mathrm{A}/L \simeq 25\,\mathrm{nA}$. Here, $L \simeq 200\,\mathrm{pH}$ is the resonator self-inductance and $M_\mathrm{AR} \simeq 5\,\mathrm{pH}$ the antenna-resonator mutual inductance. Assuming that the supercurrent flows only within the London penetration depth $\lambda_\mathrm{L} \simeq 50\,\mathrm{nm}$, we obtain $J^\mathrm{max} \simeq 2.5 \times 10^2\,\mathrm{Acm}^{-2}$ for a thin film of 100 nm thickness. Since $J^\mathrm{max}/J_\mathrm{c} < 10^{-4}$, anharmonicities can be neglected safely.

Finally, the qubit-resonator interaction Hamiltonian is

$$\widehat{\bar{H}}_\mathrm{QR} = \hbar g\hat{\bar{\sigma}}_z\left(\hat{a}^\dagger + \hat{a}\right) , \tag{8.5}$$

where $g = 2\pi \times 115\,\mathrm{MHz}$ (cf. Sec. 8.3 for details) is the qubit-resonator coupling strength. This interaction Hamiltonian is expressed in the qubit diabatic basis, which consists of the eigenstates $|+\rangle$ and $|-\rangle$ of $\hbar\epsilon\hat{\bar{\sigma}}_z$.

8.3 Two-Photon Driven Jaynes-Cummings

In order to probe the basic properties of our system, we perform qubit microwave spectroscopy using the adiabatic shift pulse technique explained in Sec. 8.2 and

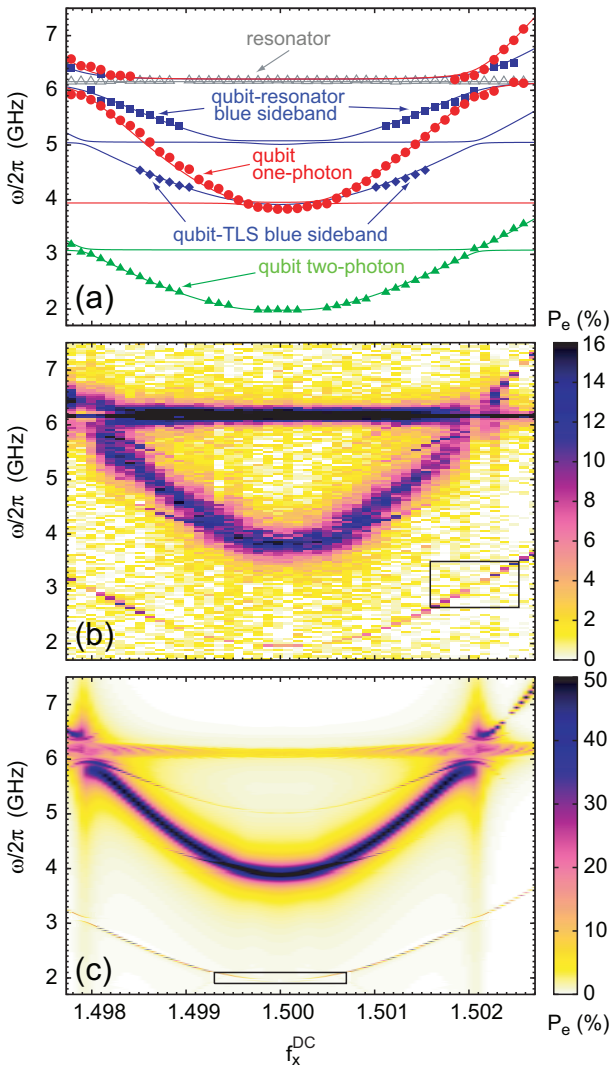

Figure 8.4: Qubit microwave spectroscopy: data and simulations. **(a)** Center frequency of the measured absorption peaks (symbols) plotted versus the flux bias $f_{\rm x}^{\rm DC}$. The lines are fits to the data based on $\widehat{H}_{\rm U}$. The presence of a large ($\omega \approx \omega_{\rm R}$) and small ($2\omega \approx \omega_{\rm R}$) anticrossing constitutes direct evidence that two-photon spectroscopy selectively drives the qubit, but not the resonator. This allows us to extrapolate the bare vacuum Rabi coupling g. On the contrary, the one-photon driving populates the cavity resulting in an enhanced coupling $g\sqrt{\langle \hat{N} \rangle}$. **(b)** Measured probability $P_{\rm e}$ to find the qubit in the excited state plotted versus flux bias and driving frequency [black box: area shown in Fig. 8.5(a)]. **(c)** Simulated probability $P_{\rm e}$ obtained with the time-trace-averaging method for $\widehat{H}_{\rm D}$ (black box: area shown in Fig. 8.10). We start with the qubit in $|{\rm g}\rangle$ and take $P_{\rm e}$ as the average over a full 100 ns time trace consisting of 10000 discrete time points. This simple method gives excellent agreement with the experimental data reported in **(b)**.

Fig. 8.2(a) (cf. also Refs. [261, 262]). The main results are shown in Figs. 8.4(a) and 8.4(b). First, we notice a flux-independent feature at approximately 6 GHz due to the resonator. Second, we observe two hyperbolas with minima near 4 GHz $\simeq \delta_{\rm Q}/h$ and 2 GHz $\simeq \delta_{\rm Q}/2h$, one with a broad and the other with a narrow linewidth. They correspond to the one-photon ($\omega = \Omega_{\rm Q}$) and two-photon ($2\omega = \Omega_{\rm Q}$) resonance condition between the qubit and the external microwave driving field. Additionally, the signatures of two-photon driven blue sideband transitions are partially visible. One of these sidebands can be attributed to the resonator, $|{\rm g}\rangle\,|0\rangle \rightarrow |{\rm e}\rangle\,|1\rangle$, and the other to a spurious fluctuator [249]. We remind that the presence of spurious fluctuators in qubits based on Josephson tunnel junctions is a well-known issue [249]. In

principle, such fluctuators can either be resonators or TLSs [421]. Since our experimental data do not allow us to distinguish between these two cases, for simplicity, we assume a TLS represented by the flux-independent Hamiltonian

$$\widehat{H}_{\mathrm{TLS}} = \frac{1}{2}\left(\epsilon^{\star}\hat{\sigma}_z^{\star} + \delta^{\star}\hat{\sigma}_x^{\star}\right) , \tag{8.6}$$

which is coupled to the qubit via the interaction Hamiltonian

$$\widehat{H}_{\mathrm{Q-TLS}} = \hbar g^{\star}\hat{\sigma}_z\hat{\sigma}_z^{\star} . \tag{8.7}$$

Here, $\hat{\sigma}_x^{\star}$ and $\hat{\sigma}_z^{\star}$ are Pauli operators, $\epsilon^{\star}$ and $\delta^{\star}$ are the TLS characteristic energies, and $g^{\star}$ is the qubit-TLS coupling coefficient. Exploiting the different response of the system in the anticrossing region under one- and two-photon driving, as explained in Fig. 8.4(a), the center frequencies of the spectroscopic peaks can accurately be fitted to the undriven Hamiltonian $\widehat{H}_{\mathrm{U}} = \widehat{\widehat{H}}_{\mathrm{Q}} + \widehat{H}_{\mathrm{R}} + \widehat{H}_{\mathrm{TLS}} + \widehat{\widehat{H}}_{\mathrm{QR}} + \widehat{H}_{\mathrm{Q-TLS}}$. In the numerical fit shown in Fig. 8.4(a), we choose $\epsilon^{\star} = 0$ due to the limited experimental resolution. We thus obtain $g = 2\pi \times 115\,\mathrm{MHz}$,[1] $\langle\hat{N}\rangle \simeq 10$, $I_{\mathrm{p}} = 367\,\mathrm{nA}$, $\omega_{\mathrm{TLS}} \equiv \sqrt{\epsilon^{\star 2} + \delta^{\star 2}}/\hbar = 2\pi \times 3.94\,\mathrm{GHz}$, and $g^{\star}\sin\theta^{\star} = 37\,\mathrm{MHz}$, where $\sin\theta^{\star} \equiv \delta^{\star}/\hbar\omega_{\mathrm{TLS}}$. Consequently, the coupling constant estimated from the undriven fit is not $g^{\star}$, but $g^{\star}\sin\theta^{\star}$. Away from the qubit degeneracy point, in particular near the qubit-resonator anticrossings, the effect of the observed TLS can be neglected within the scope of this study. However, near the qubit degenercy point, its effect can have important consequences on the symmetry properties of the system (cf. Sec. 8.5). We notice that, differently from $\sin\theta$ and $\cos\theta$, the TLS parameters $\sin\theta^{\star}$ and $\cos\theta^{\star}$ are constants, i.e., they do not depend on the quasi-static frustration bias $f_{\mathrm{x}}^{\mathrm{DC}}$. Another important feature emerging from the spectroscopy data of Figs. 8.4(a) and 8.4(b) is the presence of a pronounced flux-independent one-photon excitation signal of the resonator. On the contrary, two-photon excitation peaks exclusively occur when the qubit is two-photon driven. In other words, the data unambiguously show that there is no direct two-photon excitation of our resonator, thus confirming our theoretical estimate on resonator anharmonicities discussed toward the end of Sec. 8.2.

Further insight into our experimental results can be gained by numerical spectroscopy simulations based on the driven Hamiltonian $\widehat{H}_{\mathrm{D}} = \widehat{H}_{\mathrm{U}} + \widehat{H}_{\mathrm{MQ}} + \widehat{H}_{\mathrm{MR}} + \widehat{H}_{\mathrm{M-TLS}}$. Here, $\widehat{H}_{\mathrm{MQ}} \equiv (\Omega_{\mathrm{D}}/2)\hat{\sigma}_z\cos\omega t$, $\widehat{H}_{\mathrm{MR}} \equiv \eta\left(\hat{a}^{\dagger} + \hat{a}\right)\cos\omega t$, and $\widehat{H}_{\mathrm{M-TLS}} \equiv (\Omega_{\mathrm{D}}^{\star}/2)\hat{\sigma}_z^{\star}\cos\omega t$ represent the driving of the qubit, resonator, and fluctuator, respectively. We approximate the reaching of the steady state condition of the qubit evolution with the time average of the probability P_{e} to find the qubit in $|\mathrm{e}\rangle$ (time-trace-averaging method). By inspecting Fig. 8.4(c), we find that for the driving strengths $\Omega_{\mathrm{D}} = 2\pi \times 244\,\mathrm{MHz}$, $\eta = 2\pi \times 655\,\mathrm{MHz}$, and $\Omega_{\mathrm{D}}^{\star} = 0$ our simulations match well all the experimental features discussed above. Using η and the relation $\langle\hat{N}\rangle = (\eta/\kappa)^2$ for the steady-state mean number of photons of a driven dissipative

[1] We remind that $g \equiv M_{\mathrm{QR}} I_{\mathrm{p}} I_{\mathrm{R}}^0$ (cf. chapter 2, Sec. 2.3 for an exhaustive explanation), where M_{QR} is the mutual inductance between qubit and resonator and $I_{\mathrm{R}}^0 \equiv \sqrt{\hbar\omega_{\mathrm{R}}/2L}$ is the zero-point (vacuum) current of the resonator. Thus, from the knowledge of g and computing $I_{\mathrm{R}}^0 \simeq 101\,\mathrm{nA}$ we find $M_{\mathrm{QR}} \simeq 0.327\,\mathrm{pH}$. This simple estimate reveals that the origin of such a large qubit-resonator coupling g is due to the very high zero-point current of our LC-resonator. This current is approximately one order of magnitude larger than the typical currents achieved in a CPW resonator design [e.g., cf. chapter 6, Figs. 6.2(b) and 6.2(c)].

resonator, we estimate a resonator decay rate $\kappa \simeq 210\,\mathrm{MHz}$. This result is of the same order as $\kappa \simeq 400\,\mathrm{MHz}$ estimated directly from the experimental linewidth of the resonator peak. The large κ (corresponding to a poor quality factor) is due to the galvanic connection of the resonator to the DC SQUID measurement lines [cf. Fig. 8.1(a)].

To elucidate the two-photon driving physics of the qubit-resonator system we consider the spectroscopy data near the corresponding anticrossing, as shown in Fig. 8.5(a). For $2\omega = \Omega_\mathrm{Q} = \omega_\mathrm{R}$, the split peaks cannot be observed directly because the spectroscopy signal is decreased below the experimental noise floor $\delta P_\mathrm{e} \simeq 1-2\%$. This results from the fact that the resonator cannot absorb a two-photon driving and its excitation energy is rapidly lost to the environment ($\kappa > g/2\pi$). In contrast, for the one-photon case ($\omega = \Omega_\mathrm{Q} = \omega_\mathrm{R}$), there is a driving-induced steady-state population of $\langle \hat{N} \rangle \simeq 10$ photons in the resonator. Accordingly, the one-photon peak height shows a reduction by a factor of approximately two, whereas the two-photon peak almost vanishes [cf. Fig. 8.5(b)]. To support this interpretation, we compare the simulation results from the time-trace-averaging method to those obtained with the standard Lindblad dissipative-bath approach [cf. Figs. 8.5(c)-(f)]. In the latter case, the role of qubit decoherence and resonator decay can be studied explicitly solving a master equation [131]. The simulation results of Figs. 8.5(c)-(f) prove that the two-photon peak indeed vanishes because of the rapid resonator decay, but not because of qubit decoherence. Altogether, our experimental data and numerical simulations constitute clear evidence for the presence of a qubit-resonator anticrossing under two-photon driving.

The effective second-order Hamiltonian under two-photon driving can be derived using our usual Dyson-series approach to perturbation theory (cf. chapter 5, Subsec. 5.2.1 and chapter 6, Subsec. 6.1.2). We start from the first-order Hamiltonian in the basis $|\pm\rangle$,

$$\begin{aligned} \widehat{H} = \frac{1}{2}\left(\epsilon\hat{\tilde{\sigma}}_z + \delta_\mathrm{Q}\hat{\tilde{\sigma}}_x\right) + \hbar\omega_\mathrm{R}\left(\hat{a}^\dagger\hat{a} + \frac{1}{2}\right) \\ + \hbar g\,\hat{\tilde{\sigma}}_z\left(\hat{a}^\dagger + \hat{a}\right) + \frac{\Omega_\mathrm{D}}{2}\hat{\tilde{\sigma}}_z\cos\omega t\,. \end{aligned} \tag{8.8}$$

Here, in comparison to $\widehat{H}_\mathrm{D}$, the terms associated with the TLS are not included ($\epsilon^* = \delta^* = \Omega_\mathrm{D}^* = 0$) since the important features are contained in the driven qubit-resonator system. Additionally, we focus on the two-photon resonance condition $\omega_\mathrm{R} = \Omega_\mathrm{Q} = 2\omega$. Thus, the driving angular frequency ω is largely detuned from ω_R and the corresponding term in $\widehat{H}_\mathrm{D}$ can be neglected ($\eta = 0$). Next, we transform the qubit into its energy eigenframe. As already mentioned, in this frame the Pauli operators are defined as $\hat{\tilde{\sigma}}_x \to \hat{\sigma}_x$ and $\hat{\tilde{\sigma}}_z \to \hat{\sigma}_z$. We then move to an interaction picture with respect to qubit and resonator, $\hat{\sigma}^\pm \to \hat{\sigma}^\pm \exp(\pm j\Omega_\mathrm{Q}t)$ (where, $\hat{\sigma}^+$ and $\hat{\sigma}^-$ are the qubit raising and lowering operators, respectively), $\hat{a}^\dagger \to \hat{a}^\dagger \exp(+j\omega_\mathrm{R}t)$, and $\hat{a} \to \hat{a}\exp(-j\omega_\mathrm{R}t)$. After a rotating-wave approximation (RWA), we identify the expression $\hat{S}^\dagger \exp(+j\omega t) + \hat{S}\exp(-j\omega t)$, where the superoperator $\hat{S} \equiv \Omega_\mathrm{D}(\cos\theta\,\hat{\sigma}_z - \sin\theta\,\hat{\sigma}^-)/4$ and its Hermitian conjugate $\hat{S}^\dagger \equiv \Omega_\mathrm{D}(\cos\theta\,\hat{\sigma}_z - \sin\theta\,\hat{\sigma}^+)/4$. In our experiments the two-photon driving of the qubit is weak, i.e., the large-detuning condition $\Omega_\mathrm{Q} - \omega = \omega \gg (\Omega_\mathrm{D}/2)\sin\theta$ is fulfilled. In such a situation, it can be shown that the Dyson series for the evolution operator associated with the

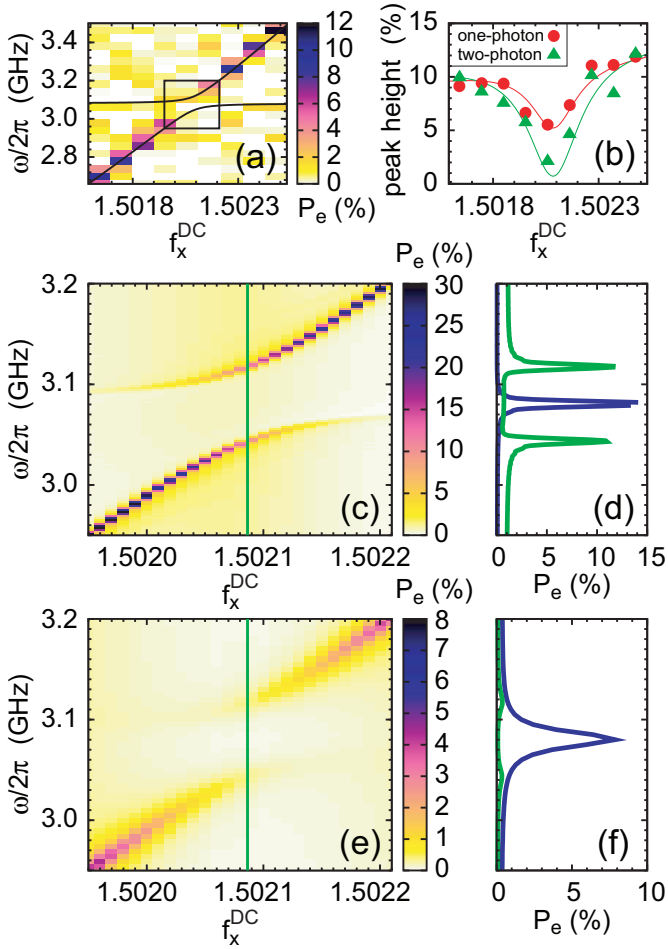

Figure 8.5: Qubit microwave spectroscopy close to the qubit-resonator anticrossing under two-photon driving: data and simulations. **(a)** Measured probability P_e to find the qubit in $|e\rangle$ plotted versus flux bias and driving frequency (black rectangle: area of simulations in **(c)** and **(e)**; solid lines: fit to $\widehat{H}_U$). **(b)** Maximum height of the spectroscopy peaks under one-photon and two-photon driving plotted versus the flux bias (solid lines: guides to the eye). **(c)** Simulated probability P_e [time-trace-averaging method, no dissipation, parameters as in Fig. 8.4(c)], revealing an anticrossing signature. **(d)** Light green (light grey) curve: split-peak profile of P_e along the vertical line in **(c)**. Dark blue (dark grey) curve: single-peak result obtained for the same flux bias and $g = 0$. **(e)** Simulated probability P_e using the Lindblad formalism [131] neglecting the TLS (dissipation: qubit relaxation rate $\gamma_r = 3.3\,\mathrm{MHz}$, qubit dephasing rate $\gamma_\varphi = 67\,\mathrm{MHz}$, resonator quality factor $Q \equiv \omega_R/\kappa = 2\pi \times 6.16\,\mathrm{GHz}/400\,\mathrm{MHz} \simeq 100$). When qubit and resonator become degenerate, the spectroscopy signal fades away. **(f)** Light green (light grey) curve: split-peak profile of P_e along the vertical line in **(e)**. Dark blue (dark grey) line: single-peak result obtained for the same flux bias and $g = 0$. Differently from the nondissipative case [**(c)** and **(d)**], the split peak amplitudes are reduced by a factor of 10 compared to the single peak. This demonstrates that the vanishing two-photon spectroscopy signal observed in the experimental data [cf. **(a)**, **(b)**, and **(e)**] is not caused by qubit decoherence.

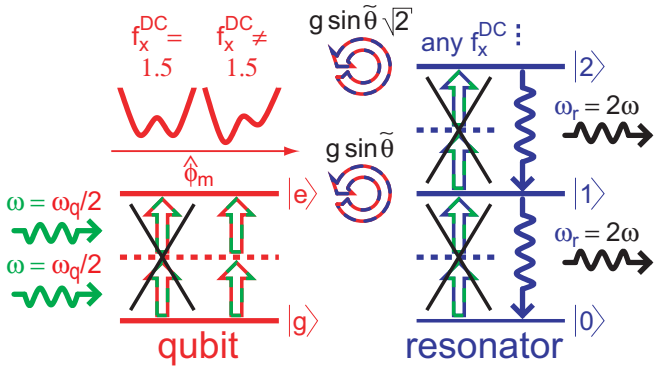

Figure 8.6: Upconversion dynamics describing the physics governing our experiments [cf. Eq. (8.10)]. The qubit (red) level splitting is $\hbar\Omega_{\rm Q}$ and the resonator (blue) angular frequency is $\omega_{\rm R}$. In the relevant case of two-photon driving with frequency $\omega=\Omega_{\rm Q}/2$ (green), the system predominantly decays via the resonator at frequency $\omega_{\rm R}=2\omega$. The qubit-resonator coupling strength is $g\sin\tilde{\theta}=g\delta_{\rm Q}/\omega_{\rm R}\simeq 0.63\,g$. For $f_{\rm x}^{\rm DC}=1.5$ the qubit potential (red double well; x-axis: phase variable $\hat{\phi}_{\rm m}$) is symmetric and two-photon transitions are forbidden. For $f_{\rm x}^{\rm DC}\neq 1.5$ the mirror symmetry of the qubit potential is broken allowing for two-photon transitions.

time-dependent Hamiltonian $-\hbar g\sin\theta(\hat{\sigma}^-\hat{a}^\dagger+\hat{\sigma}^+\hat{a})+[\hat{S}^\dagger\exp(+j\omega t)+\hat{S}\exp(-j\omega t)]$ can be rewritten in an exponential form $\widehat{U}=\exp(-j\widehat{H}_{\rm eff}t/\hbar)$, where

$$\begin{aligned}\widehat{H}_{\rm eff} &= -\hbar g\sin\theta\left(\hat{\sigma}^-\hat{a}^\dagger e^{-j\Delta t}+\hat{\sigma}^+\hat{a}e^{+j\Delta t}\right)+\frac{\left[\hat{S}^\dagger,\hat{S}\right]}{\hbar\omega}\\ &= -\hbar g\sin\theta\left(\hat{\sigma}^-\hat{a}^\dagger e^{-j\Delta t}+\hat{\sigma}^+\hat{a}e^{+j\Delta t}\right)\\ &\quad+\frac{\Omega_{\rm D}^2}{4\delta_{\rm Q}}\left(\sin^2\theta\cos\theta\,\hat{\sigma}_x+\frac{1}{2}\sin^3\theta\,\hat{\sigma}_z\right).\end{aligned}\tag{8.9}$$

Here, $\Delta\equiv\Omega_{\rm Q}-\omega_{\rm R}$ is the qubit-resonator detuning. In Eq. (8.9), the dispersive shift $\Omega_{\rm D}^2\sin^3\theta\,\hat{\sigma}_z/8\delta_{\rm Q}$ is a reminiscence of the full second-order $\hat{\sigma}_z$-component of the interaction Hamiltonian, $\Omega_{\rm D}^2\sin^3\theta\,\hat{\sigma}_z[\exp(+j2\omega t)+\exp(-j2\omega t)+1]/8\delta_{\rm Q}$. The terms proportional to $\hat{\sigma}_z\exp(\pm j2\omega t)$ are neglected implicitly by a RWA when deriving the effective Hamiltonian $\widehat{H}_{\rm eff}$ of Eq. (8.9). In this equation, the $\hat{\sigma}_z$-term renormalizes the qubit transition frequency, and, in the vicinity of the anticrossing ($|\Delta|\lesssim g\sin\tilde{\theta}$, $\sin\tilde{\theta}=\delta_{\rm Q}/\omega_{\rm R}\simeq 0.63$), the Hamiltonian $\widehat{H}_{\rm eff}$ can be considered equivalent to

$$\begin{aligned}\widehat{H}^{(2)} &= \frac{\hbar\Omega_{\rm Q}}{2}\hat{\sigma}_z+\frac{\Omega_{\rm D}^2}{4\delta_{\rm Q}}\sin^2\theta\cos\theta\left(\sigma^-e^{+j2\omega t}+\sigma^+e^{-j2\omega t}\right)\\ &\quad-\hbar g\sin\theta\left(\hat{\sigma}^-\hat{a}^\dagger+\hat{\sigma}^+\hat{a}\right)+\hbar\omega_{\rm R}\left(\hat{a}^\dagger\hat{a}+\frac{1}{2}\right).\end{aligned}\tag{8.10}$$

The upconversion dynamics sketched in Fig. 8.6 is clearly described by Eq. (8.10). The first two terms represent the qubit and its coherent two-photon driving with angular frequency ω. The last two terms show the population transfer via the JC

interaction to the resonator. As discussed before, the resonator then decays emitting radiation of angular frequency 2ω.

8.4 Selection Rules and Controlled Symmetry Breaking

In this section, we first analyze in detail the theory governing the selections rules and controlled symmetry breaking in circuit QED within a simple two-level/two-photon approximation (cf. Subsec. 8.4.1). We then extend our scope to the more general case of superconducting flux quantum circuits, where many quantized states have to be considered in the theoretical model. This allows us to study the coupling coefficients between one such circuit and an electromagnetic field for many circuit levels and higher photon transitions (cf. Subsec. 8.4.2). A comparison between the results obtained using the flux quantum circuit approach and the two-level approximation in the case of one- and two-photon transitions is given.

8.4.1 Two-Level/Two-Photon Approximation

The model outlined above allows us to unveil the symmetry properties of our system. Even though the two-photon coherent driving is largely detuned, $\Omega_\mathrm{Q}/2 = \omega \gg \Omega_\mathrm{D}/2 \sin\theta$, a not well-defined symmetry of the qubit potential permits level transitions away from the optimal point. Because of energy conservation, i.e., frequency matching, these transitions are real and can be used to probe the qubit-resonator anticrossing. The effective two-photon qubit driving strength, $(\Omega^2 \sin^2\theta/4\delta_\mathrm{Q})\cos\theta$, has the typical structure of a second-order dispersive interaction with the extra factor $\cos\theta$. The latter causes this coupling to disappear at the qubit degeneracy point (optimal point). There, the qubit potential is symmetric and the parity of the interaction operator is well defined. Consequently, selection rules similar to those governing electric dipole transitions hold [414]. This is best understood in our analytical two-level model, where the first-order Hamiltonian for the driven diagonalized qubit becomes

$$\widehat{H}_\mathrm{OP}^{(1)} = \frac{\delta_\mathrm{Q}}{2}\hat{\sigma}_z + \frac{\Omega_\mathrm{D}}{4}\hat{\sigma}_x\left(e^{+j\omega t} + e^{-j\omega t}\right) \tag{8.11}$$

at the qubit degeneracy point (optimal point). In this case, one-photon transitions are allowed because the driving couples to the qubit via the odd-parity operator $\hat{\sigma}_x$. In contrast, the two-photon driving effectively couples via the second-order Hamiltonian

$$\widehat{H}_\mathrm{OP}^{(2)} = \frac{\delta_\mathrm{Q}}{2}\hat{\sigma}_z + \frac{\Omega_\mathrm{D}^2}{8\delta_\mathrm{Q}}\hat{\sigma}_z\left(e^{+2j\omega t} + e^{-2j\omega t} + 1\right) . \tag{8.12}$$

Since $\hat{\sigma}_z$ is an even-parity operator, real level transitions are forbidden. We note that the second $\hat{\sigma}_z$-term of $\widehat{H}_\mathrm{OP}^{(2)}$ only slightly renormalizes the qubit transition frequency and, thus, can be neglected in Eq. (8.10), which describes the real level transitions corresponding to our spectroscopy peaks. The intimate nature of the symmetry breaking resides in the coexistence of $\hat{\sigma}_x$- and $\hat{\sigma}_z$-operators in the first-order Hamiltonian $\widehat{H}_\mathrm{D}$, which produces a nonvanishing $\hat{\sigma}_x$-term in the second-order Hamiltonian $\widehat{H}^{(2)}$ of Eq. (8.10).

The role of selection rules and symmetry breaking in circuit QED systems can be fully explained in terms of qubit parity operators. The two lowest energy eigenstates $|\mathrm{g}\rangle$ and $|\mathrm{e}\rangle$ are, respectively, symmetric and antisymmetric superpositions of $|+\rangle$ and $|-\rangle$. Thus, $|\mathrm{g}\rangle$ has even parity and $|\mathrm{e}\rangle$ is odd. In this situation, the parity operator $\widehat{\Pi}$ can be defined via the relations

$$\begin{aligned} \widehat{\Pi}\,|\mathrm{g}\rangle &= +\,|\mathrm{g}\rangle \\ \widehat{\Pi}\,|\mathrm{e}\rangle &= -\,|\mathrm{e}\rangle \end{aligned} \quad . \tag{8.13}$$

The Hamiltonian of the classically driven qubit at the qubit degeneracy point is

$$\widehat{H}_{\mathrm{DQ}} = \frac{\delta_{\mathrm{Q}}}{2}\hat{\sigma}_z - \frac{\Omega_{\mathrm{D}}}{2}\cos\omega t\,\hat{\sigma}_x\,. \tag{8.14}$$

For a one-photon driving, $\omega = \delta_{\mathrm{Q}}/\hbar$ (energy conservation), after a RWA, and moving into the uniformly rotating frame of the external driving field, the Hamiltonian becomes $-\Omega_{\mathrm{D}}\hat{\sigma}_x/4$, where $\hat{\sigma}_x \equiv |\mathrm{g}\rangle\langle\mathrm{e}| + |\mathrm{e}\rangle\langle\mathrm{g}|$. This is an odd-parity operator because the anticommutator $\{\widehat{\Pi}, \hat{\sigma}_x\} = 0$ and, consequently, one-photon transitions are allowed. For a two-photon driving, $\omega = \delta_{\mathrm{Q}}/2\hbar$ (energy conservation), the effective interaction Hamiltonian becomes $\Omega_{\mathrm{D}}^2\hat{\sigma}_z/8\delta_{\mathrm{Q}}$, where $\hat{\sigma}_z \equiv |\mathrm{e}\rangle\langle\mathrm{e}| - |\mathrm{g}\rangle\langle\mathrm{g}|$. Since the commutator $[\widehat{\Pi}, \hat{\sigma}_z] = 0$, this is an even-parity operator and two-photon transitions are forbidden [229]. These selection rules are analogous to those governing electric dipole transitions in quantum optics. The major departure from this simple behavior is that in circuit QED the qubit can be biased away from its degeneracy point. In this case, the symmetry of the system is broken in a *controlled* way and the discussed strict selection rules do not hold. Instead, we find the finite transition matrix elements $\Omega_{\mathrm{D}}\sin\theta/2$ and $\Omega_{\mathrm{D}}^2\sin^2\theta\cos\theta/2\delta_{\mathrm{Q}}$ for the one- and two-photon process, respectively.[2] These elements allow for real level transitions between the qubit levels as demonstrated by our experimental data.

8.4.2 Selection Rules and Flux Quantum Circuits

In the search for a more intimate relationship between selection rules, broken symmetries, and quantum circuits, we now attempt to go beyond the two-level (qubit) approximation considered so far and analyze the complete Hamiltonian of a flux quantum circuit (cf. also chapter 2, Sec. 2.2). Such a circuit is made by three Josephson tunnel junctions interrupting a superconducting loop [189]. Under special conditions, e.g., in all experiments described above, the flux quantum circuit can be used as a flux qubit and the properties of the Pauli operators adequately describe its interaction with external classical and/or quantum fields. The aim of this subsection is to give a hint that there might be a more general way to describe such interaction and, eventually, to reveal different phenomena. Before delving into the details of the analytical derivations, we remind that the shape of the potential of a flux quantum circuit is governed by the Josephson-junction potential. This is

[2] We remind that, depending on which picture the interaction Hamiltonian between driving and qubit is represented, the transition matrix elements are sometimes renormalized by an extra factor of 2. This is due to the Euler expansion of the sine or cosine driving term. We prefer to use the definition without renormalization because it refers to the complete driven Hamiltonian before moving into the interaction picture and performing the RWA.

a transcendental (combination of cosine functions) function of the gauge-invariant phases across the junctions as well as of an external control parameter, a control flux acting as a field (see below). Inspired by Ref. [414], we can regard the control flux as a perturbative field and perform a quantum small-signal analysis of the transcendental potential. In other words, we can expand the potential with respect to the external control parameter and compute the corresponding matrix elements for the circuit-field interaction. First-order processes correspond to one-photon transitions, second-order processes to two-photon transitions, and so on and so forth. As expected, we find that everything works well up to first order and we can show that all results obtained from the expansion of the flux quantum circuit Hamiltonian converge with those derived within the two-level approximation. However, already in second order we find that, for example, the two-photon transition matrix element of Eq. (8.10) is characterized by a drastically different behavior than that obtained in the flux quantum circuit case.

There are several possible explanations for this unexpected result. When expanding the flux quantum circuit potential to higher order with respect to the external field (e.g., with respect to a $\cos\omega t$ driving), we are exploring the intrinsic nonlinearity of the circuit. In this case, such nonlinearity gives rise to two-photon (multiphoton) transitions, since the potential is a $\cos(\cos\omega t)$-function, which can be expanded in a Bessel series.[3] This is in perfect analogy to the generation of higher harmonics in a nonlinear classical circuit [422]. When deriving the two-photon Hamiltonian of Eq. (8.10), we do not rely on the specific nature of the qubit. This can be any type of qubit, flux- or charge-based. It is the time evolution of the driven qubit[4] $\propto \exp(\cos\omega t)$, which can also be expanded in a Bessel series, to give rise to two-photon (multiphoton) transitions. If this explanation were true, we would face a scenario where two distinguished mechanisms allow for multiphoton transitions: one based on the nonlinear response of the flux quantum circuit and the other on its time evolution. The global effect would be the sum or a combination of both of them. However, we could argue that any two-level system is inherently the most nonlinear system there is and in any case we are studying its nonlinear response with respect to external fields. If this were true, it could be that the different results arise from the wrong use of the quantum small-signal formalism applied to the flux quantum circuit. In fact, it is well-known that, due to gauge-invariance arguments, one can place the field associated with the external control parameter in different terms of the circuit potential, paying back this arbitrariness with an opportune choice of the quantum variables of the circuit. Oftentimes, such choice can be counterintuitive and not a trivial task. Last but not least, it could be that the simple two-level approximation fails in explaining multi-photon transitions, in particular away from the qubit degeneracy point. Understanding this conundrum[5] goes far beyond the focus of this thesis, where the message we want to give is that further investigations are needed in order to straighten up so many outstanding issues.

We can now start a more quantitative study of the problem. The basic Hamiltonian of a flux quantum circuit has already been derived in chapter 2. Here, we

[3] We notice that a Taylor expansion can also be employed yielding similar results.

[4] Here, we omit all qubit-related operators for simplicity.

[5] The author has enjoyed many discussions with the most eminent experts in the field of superconducting quantum circuits to find out that the mechanisms at the base of the circuit-field interaction are not well-understood and properly studied yet.

summarize only the key points of that derivation. In general, the flux quantum circuit is based on the quantization of the gauge-invariant phases across the three junctions, $\hat{\phi}_1$, $\hat{\phi}_2$, and $\hat{\phi}_3$ (cf. chapter 2, Fig. 2.10). The superconducting loop is characterized by a geometric self-inductance $L_{\rm F}$, whose dimension is small enough to allow us to neglect the magnetic energy term associated with it in the final Hamiltonian [189]. Nevertheless, the presence of $L_{\rm F}$ is necessary for any classical or quantum external circuit to be inductively coupled to the flux quantum circuit. This coupling is mediated by the mutual inductance $M_{\rm FX}$, which is a function of $L_{\rm F}$, between the external circuit and the flux quantum circuit. The coupling also depends on the driving level or the zero-point (vacuum) fluctuations of the external circuit. As already mentioned in Sec. 8.2, in a flux quantum circuit two of the three tunnel junctions, e.g., those characterized by the phases $\hat{\phi}_1$ and $\hat{\phi}_2$, have equal Josephson coupling energy $E_{\rm J} \equiv I_{\rm c0}\Phi_0/2\pi$ and same charging energy $E_{\rm c} \equiv e^2/2C_{\rm j}$. Here, $I_{\rm c0}$ and $C_{\rm j}$ are again the critical current and capacitance of each junction, respectively, and Φ_0 is the flux quantum. The third junction, characterized by a phase $\hat{\phi}_3$, is made α-times smaller than the other two, where α is a parameter chosen during the design of the device. Since the three Josephson tunnel junctions are embedded in a superconduting loop, due to flux quantization only two of the three phases associated with them are independent. For example, we can choose $\hat{\phi}_1$ and $\hat{\phi}_2$ to be the independent phases and rewrite them as $\hat{\phi}_{\rm p} \equiv (\hat{\phi}_1 + \hat{\phi}_2)/2$ and $\hat{\phi}_{\rm m} \equiv (\hat{\phi}_1 - \hat{\phi}_2)/2$. Following Ref. [189] (cf. also chapter 2, Sec. 2.2), the Hamiltonian associated with the flux quantum circuit can be written as

$$\widehat{H}_{\rm F} = \frac{1}{2}\frac{\widehat{P}_{\rm p}^2}{M_{\rm p}} + \frac{1}{2}\frac{\hat{P}_{\rm m}^2}{M_{\rm m}} + E_{\rm J}[2 + \alpha - 2\cos\hat{\phi}_{\rm p}\cos\hat{\phi}_{\rm m} - \alpha\cos(2\pi f_{\rm x} + 2\hat{\phi}_{\rm m})]\,, \tag{8.15}$$

where $\hat{P}_{\rm p} \equiv -j\hbar\partial/\partial\hat{\phi}_{\rm p}$ and $\hat{P}_{\rm m} \equiv -j\hbar\partial/\partial\hat{\phi}_{\rm m}$, $M_{\rm p} \equiv (\Phi_0/2\pi)^2\, 2C_{\rm j}\left(1+\gamma_{\rm g}\right)$ and $M_{\rm m} \equiv (\Phi_0/2\pi)^2\, 2C_{\rm j}\left(1+2\alpha+\gamma_{\rm g}\right)$ ($\gamma_{\rm g}$ is a parameter that accounts for external gate capacitances and/or parasitic capacitances to ground), and, as always, $f_{\rm x}^{\rm DC} = \Phi_{\rm x}^{\rm DC}/\Phi_0$ is a normalized externally applied flux bias (frustration).

The presence of $f_{\rm x}^{\rm DC}$ in Eq. (8.15) shows that this Hamiltonian contains already an effective interaction with external circuits. In general, the frustration can be written as

$$f_{\rm x} = f_{\rm x}^{\rm DC} + f_{\rm x}^{\rm AC}\,, \tag{8.16}$$

where the first term of the sum represents a DC or quasi-static flux bias and the second term an AC flux excitation, typically in the radio-frequency or microwave range. The AC flux excitation can either be a classical signal

$$f_{\rm x}^{\rm AC} = \frac{M_{\rm FX} I_{\rm x}}{\Phi_0}\sin(\omega t + \phi) \equiv \tilde{f}_{\rm Q}\sin(\omega t + \phi) \tag{8.17}$$

due to an AC current of amplitude $I_{\rm x}$ driving the external circuit or a quantum signal. In the latter case, the classical AC flux excitation is promoted to its quantum-mechanical counterpart, $f_{\rm x}^{\rm AC} \rightarrow \hat{f}_{\rm x}^{\rm AC}$. The quantum flux excitation

$$\hat{f}_{\rm x}^{\rm AC} = \int_0^{+\infty} d\omega\, \frac{M_{\rm FX}(\omega)\, I_{\rm x}^0(\omega)}{\Phi_0}\left[\hat{a}^\dagger(\omega) + \hat{a}(\omega)\right] \tag{8.18}$$

is due to the interaction with, in general, a multi-mode quantized current characterized by a frequency-dependent zero-point fluctuation $I_{\rm x}^0(\omega)$ and bosonic creation and annihilation operators $\hat{a}^\dagger(\omega)$ and $\hat{a}(\omega)$, respectively. In our experiments, where the flux quantum circuit is operated as a qubit (cf. Sec. 8.2), the classical signal is represented by the antenna driving with amplitude $I_{\rm x} = I_{\rm A}$. This signal couples to the qubit via the antenna-qubit mutual inductance $M_{\rm FX} = M_{\rm QA}$. The quantum signal instead is associated with the single mode of a quantized LC-resonator with resonance frequency $\omega_{\rm R}$, zero-point current $I_{\rm x}^0(\omega) \to I_{\rm R}^0$, inductively coupled to the flux quantum circuit (qubit) via a mutual inductance $M_{\rm FX}(\omega) \to M_{\rm QR}$, and characterized by single-mode bosonic operators $\hat{a}^\dagger(\omega) \to \hat{a}^\dagger$ and $\hat{a}(\omega) \to \hat{a}$. Hereafter, for the sake of simplicity, we focus on the classical signal case only. This can easily be extended to the case of quantum signals via a canonical quantization.

We now split the Hamiltonian of Eq. (8.15) into the sum of two components, $\widehat{H}_{\rm F} \equiv \widehat{H}_{\rm A} + \widehat{H}_{\rm B}$, where

$$\widehat{H}_{\rm A} = \frac{1}{2}\frac{\hat{P}_{\rm p}^2}{M_{\rm p}} + \frac{1}{2}\frac{\hat{P}_{\rm m}^2}{M_{\rm m}} + E_{\rm J}(2 + \alpha - 2\cos\hat{\phi}_{\rm p}\cos\hat{\phi}_{\rm m})\,, \tag{8.19a}$$

$$\widehat{H}_{\rm B} = -\alpha E_{\rm J}\cos(2\pi f_{\rm x} + 2\hat{\phi}_{\rm m})\,. \tag{8.19b}$$

Among these two Hamiltonians, $\widehat{H}_{\rm A}$ is independent of any external classical or quantum signal, whereas $\widehat{H}_{\rm B}$ explicitly depends on $f_{\rm x}$. Inserting the general expression for $f_{\rm x}$ given in Eq. (8.16) into $\widehat{H}_{\rm B}$ and using the expression of Eq. (8.17) for $f_{\rm x}^{\rm AC}$, we obtain

$$\widehat{H}_{\rm B} = -\alpha E_{\rm J}\cos[(2\pi f_{\rm x}^{\rm DC} + 2\hat{\phi}_{\rm m}) + 2\pi\tilde{f}_{\rm Q}\sin(\omega t + \varphi)]\,. \tag{8.20}$$

Hereafter, without loosing generality, we assume the signal phase $\varphi = 0$. Under this condition and after some easy trigonometry, the Hamiltonian of Eq. (8.20) can readily be written as

$$\begin{aligned}\widehat{H}_{\rm B} = -\alpha E_{\rm J}[&\cos(2\pi f_{\rm x}^{\rm DC} + 2\hat{\phi}_{\rm m})\cos(2\pi\tilde{f}_{\rm Q}\sin\omega t) \\ &- \sin(2\pi f_{\rm x}^{\rm DC} + 2\hat{\phi}_{\rm m})\sin(2\pi\tilde{f}_{\rm Q}\sin\omega t)]\,.\end{aligned} \tag{8.21}$$

This Hamiltonian contains two nested trigonometric functions that can easily be expanded in a Jacobi-Anger series [423], which ultimately results in a Bessel-Fourier structure of Hamiltonian $\widehat{H}_{\rm B}$:

$$\begin{aligned}\widehat{H}_{\rm B} = -\alpha E_{\rm J}\Bigg\{ &\cos(2\pi f_{\rm x}^{\rm DC} + 2\hat{\phi}_{\rm m})\left[J_0(2\pi\tilde{f}_{\rm Q}) + 2\sum_{k=1}^{\infty} J_{2k}(2\pi\tilde{f}_{\rm Q})\cos 2k\omega t\right] \\ &- \sin(2\pi f_{\rm x}^{\rm DC} + 2\hat{\phi}_{\rm m})\left[2\sum_{k=0}^{\infty} J_{(2k+1)}(2\pi\tilde{f}_{\rm Q})\sin(2k+1)\omega t\right]\Bigg\}\,,\end{aligned} \tag{8.22}$$

where $J_n(\,\cdot\,)$ are nth-order Bessel functions of the first kind and $k \in \mathbb{N}$. In typical applications, even under the strong driving conditions of our experiments, we can

assume $\tilde{f}_{\mathrm{Q}} \ll 1$ and approximate $\widehat{H}_{\mathrm{B}}$ as

$$\begin{aligned}\widehat{H}_{\mathrm{B}} \approx -\alpha E_{\mathrm{J}} \Bigg\{ & \cos(2\pi f_{\mathrm{x}}^{\mathrm{DC}} + 2\hat{\phi}_{\mathrm{m}}) \\ & + 2\cos(2\pi \tilde{f}_{\mathrm{Q}} + 2\hat{\phi}_{\mathrm{m}}) \sum_{k=1}^{\infty} (2\pi \tilde{f}_{\mathrm{Q}})^{2k} \left[\Gamma(2k+1)\right]^{-1} \cos 2k\omega t \\ & - 2\sin(2\pi f_{\mathrm{x}}^{\mathrm{DC}} + 2\hat{\phi}_{\mathrm{m}}) \sum_{k=0}^{\infty} (2\pi \tilde{f}_{\mathrm{Q}})^{2k+1} \left[\Gamma(2k+2)\right]^{-1} \sin(2k+1)\omega t \Bigg\},\end{aligned} \tag{8.23}$$

where $\Gamma(\,\cdot\,)$ is the gamma function. We can now isolate the term of Eq. (8.23) interacting only with the DC (or quasi-static) flux bias, i.e., the term in the flux quantum circuit Hamiltonian enabling DC Zeeman shifts,

$$\widehat{H}_{\mathrm{Z}} = -\alpha E_{\mathrm{J}} \cos(2\pi f_{\mathrm{x}}^{\mathrm{DC}} + 2\hat{\phi}_{\mathrm{m}}) \,. \tag{8.24}$$

Together with $\widehat{H}_{\mathrm{A}}$, the Hamiltonian of Eq. (8.24) allows us to define the free energy term of the flux quantum circuit Hamiltonian, $\widehat{H}_{\mathrm{F}}^{0} \equiv \widehat{H}_{\mathrm{A}} + \widehat{H}_{\mathrm{Z}}$. The Hamiltonian $\widehat{H}_{\mathrm{F}}^{0}$ resumes the Hamiltonian studied in Ref. [189]. Diagonalizing $\widehat{H}_{\mathrm{F}}^{0}$ gives the flux quantum circuit energy eigenstates $\{|i\rangle\} = \{|\mathrm{g}\rangle, |\mathrm{e}\rangle, |\mathrm{a}\rangle, \ldots\}$ and the corresponding eigenvalues $\hbar\Omega_i$, with $i = \mathrm{g}, \mathrm{e}, \mathrm{a}, \ldots$. Finally, applying the closure theorem ($\sum_i |i\rangle \langle i| = \mathbf{I}$, where $\mathbf{I}$ is the $i \times i$ identity matrix) twice, the flux quantum circuit free energy Hamiltonian can be expressed in the energy eigenbasis as

$$\widehat{H}_{\mathrm{F}}^{0} = \sum_i \hbar\Omega_i \, |i\rangle \langle i| \,. \tag{8.25}$$

The diagonalization of $\widehat{H}_{\mathrm{F}}^{0}$ has to be carried out by means of a numerical simulation. For the flux quantum circuit parameters of our experiments, the results are shown in chapter 2, Fig. 2.10. There, the energy levels for the six lowest states of the Hamiltonian $\widehat{H}_{\mathrm{F}}^{0}$ are plotted as a function of the DC frustration bias $f_{\mathrm{x}}^{\mathrm{DC}}$. Figure 2.11 shows the wavefunctions for the three lowest states of $\widehat{H}_{\mathrm{F}}^{0}$, $|\mathrm{g}\rangle$, $|\mathrm{e}\rangle$, and $|\mathrm{a}\rangle$, respectively.

We now focus on the remaining terms in the Hamiltonian of Eq. (8.23) besides $\widehat{H}_{\mathrm{Z}}$. Those terms define the interaction Hamiltonian between the flux quantum circuit and external microwave fields,

$$\begin{aligned}\widehat{H}_{\mathrm{I}} = -\alpha E_{\mathrm{J}} \Bigg\{ & 2\cos(2\pi f_{\mathrm{x}}^{\mathrm{DC}} + 2\hat{\phi}_{\mathrm{m}}) \\ & \times \sum_{k=1}^{\infty} (2\pi \tilde{f}_{\mathrm{Q}})^{2k} \left[\Gamma(2k+1)\right]^{-1} \cos 2k\omega t \\ & - 2\sin(2\pi f_{\mathrm{x}}^{\mathrm{DC}} + 2\hat{\phi}_{\mathrm{m}}) \\ & \times \sum_{k=0}^{\infty} (2\pi \tilde{f}_{\mathrm{Q}})^{2k+1} \left[\Gamma(2k+2)\right]^{-1} \sin(2k+1)\omega t \Bigg\}.\end{aligned} \tag{8.26}$$

This interaction Hamiltonian can be rewritten invoking again the closure theorem for the energy eigenstates of $\widehat{H}_{\rm F}^0$ twice, obtaining

$$\begin{aligned}\widehat{H}_{\rm I} = -\alpha E_{\rm J} \sum_{i,j} \Bigg\{ & \left|i\right\rangle \left\langle i\right| \cos(2\pi f_{\rm x}^{\rm DC} + 2\hat{\phi}_{\rm m}) \left|j\right\rangle \left\langle j\right| \\ & \times \sum_{k=1}^{\infty} (2\pi \tilde{f}_{\rm Q})^{2k} \left[\Gamma(2k+1)\right]^{-1} \cos 2k\omega t \\ & - \left|i\right\rangle \left\langle i\right| \sin(2\pi f_{\rm x}^{\rm DC} + 2\hat{\phi}_{\rm m}) \left|j\right\rangle \left\langle j\right| \\ & \times \sum_{k=0}^{\infty} (2\pi \tilde{f}_{\rm Q})^{2k+1} \left[\Gamma(2k+2)\right]^{-1} \sin(2k+1)\omega t \Bigg\}, \end{aligned} \tag{8.27}$$

where $i, j = \{{\rm g}, {\rm e}, {\rm a}, \ldots\}$. The total Hamiltonian of the driven flux quantum circuit is thus $\widehat{H}_{\rm T} = \widehat{H}_{\rm F}^0 + \widehat{H}_{\rm I}$. We remind that in the case of a quantized external field, e.g., of a resonator coupled to the flux quantum circuit, also the resonator free energy Hamiltonian [cf. Eq.(8.4)] has to be added to the total system Hamiltonian.

The coupling coefficients between the flux quantum circuit and the external microwave field can be evaluated by inspecting the Hamiltonian of Eq. (8.27). Expressing the coefficients as angular frequencies, this gives

$$g_{ij}^{(2k+1)}(f_{\rm x}^{\rm DC}) = \frac{\alpha E_{\rm J} (2\pi \tilde{f}_{\rm Q})^{2k+1}}{\hbar} \left[\Gamma(2k+2)\right]^{-1} \left\langle i\right| \sin(2\pi f_{\rm x}^{\rm DC} + 2\hat{\phi}_{\rm m}) \left|j\right\rangle, \tag{8.28a}$$

$$g_{ij}^{(2k)}(f_{\rm x}^{\rm DC}) = -\frac{\alpha E_{\rm J} (2\pi \tilde{f}_{\rm Q})^{2k}}{\hbar} \left[\Gamma(2k+1)\right]^{-1} \left\langle i\right| \cos(2\pi f_{\rm x}^{\rm DC} + 2\hat{\phi}_{\rm m}) \left|j\right\rangle. \tag{8.28b}$$

These coefficients are formed by the product of two terms: The first term is a constant factor, which depends on $\tilde{f}_{\rm Q}$ and, thus, on the driving strength $I_{\rm x}$ of the external circuit (e.g., in our experiments, the current on the antenna, $I_{\rm A}$) and on the mutual inductance $M_{\rm FX}$ between external and flux quantum circuit ($M_{\rm QA}$ in the case of the antenna); the second term is one of the matrix elements $\langle i| \cdot |j\rangle$ of the flux quantum circuit. Such matrix elements are different from those characteristic of the electric-dipole moment operator $\widehat{\mathbf{D}}_{\rm E}$ of atoms [91]. In atomic physics, $\widehat{\mathbf{D}}_{\rm E}$ is typically an odd-parity operator where all diagonal terms of the kind $\langle i| \widehat{\mathbf{D}}_{\rm E} |i\rangle$ are zero. This is different in the case of flux quantum circuits (or superconducting quantum circuits in general), where both diagonal and off-diagonal matrix elements can exist. In addition, for quantum circuits all matrix elements depend on the externally applied frustration bias $f_{\rm x}^{\rm DC}$. If $i = j$, the matrix elements represent the expectation value to find the circuit in an eigenstate $|i\rangle$. For $i \neq j$, they represent the overlap between the wavefunctions of two different eigenstates $|i\rangle$ and $|j\rangle$ (transition matrix elements). The $f_{\rm x}^{\rm DC}$-dependence of the absolute value $|g_{ij}^{(1)}|$ and $|g_{ij}^{(2)}|$ for the three lowest states $|{\rm g}\rangle$, $|{\rm e}\rangle$, and $|{\rm a}\rangle$ is plotted in Fig. 8.7.

(i) – When $f_{\rm x}^{\rm DC} = 0.5$ (or, equivalently, $= 1.5$ as in our experiments),[6] the potential landscape of chapter 2, Fig. 2.11(a) associated with the flux quantum circuit is characterized by a well-defined *symmetry* with respect to the quantum variables $\hat{\phi}_{\rm p}$ and $\hat{\phi}_{\rm m}$. In particular, the two-dimensional potential can be reduced

[6] In this theoretical section, we use $f_{\rm x}^{\rm DC} = 0.5$ instead of $f_{\rm x}^{\rm DC} = 1.5$ for simplicity.

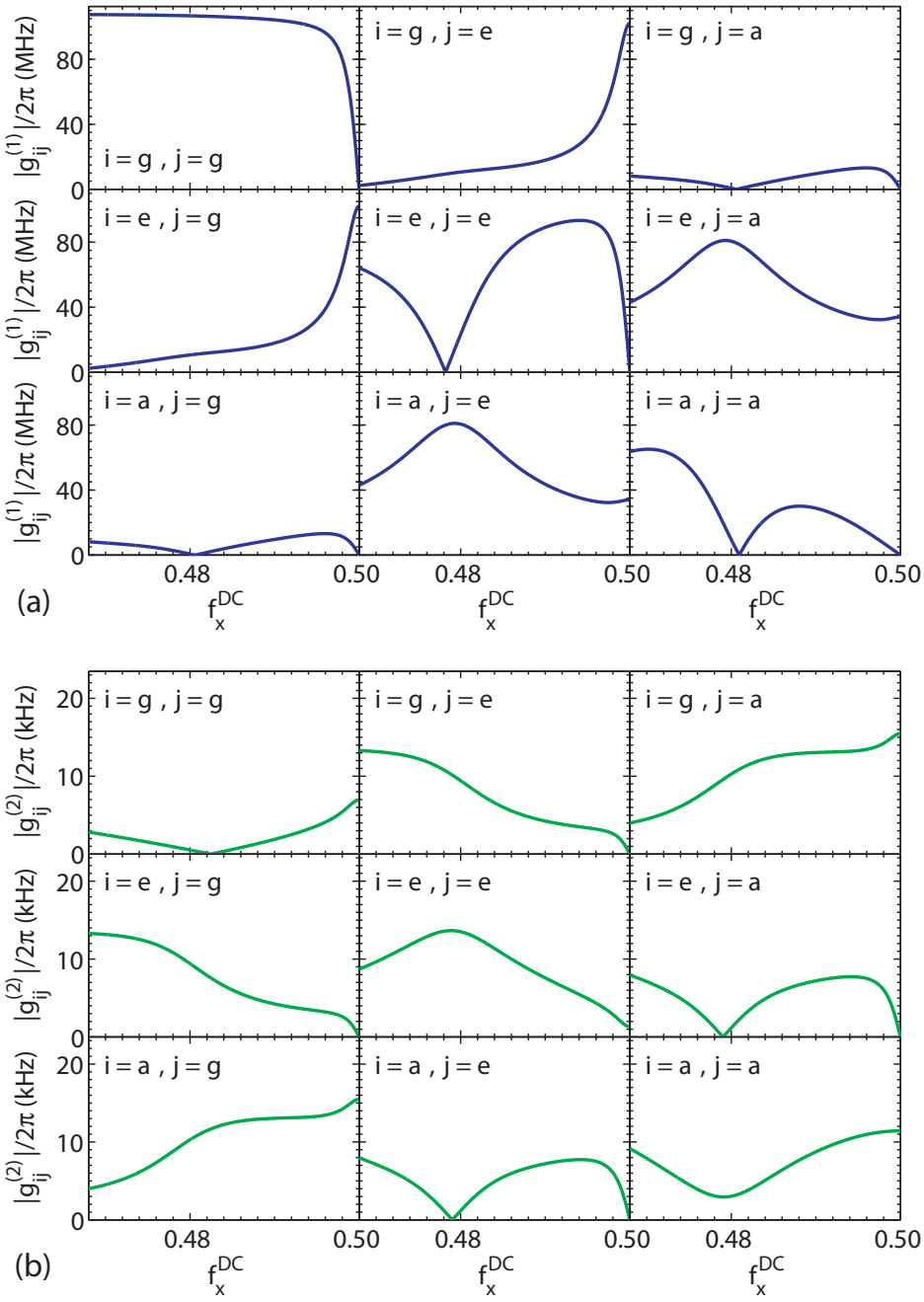

Figure 8.7: Absolute value for the coupling coefficients between the flux quantum circuit and the external microwave field as a function of $f_{\mathrm{x}}^{\mathrm{DC}}$. The elements of the full matrix for the first three states $|\mathrm{g}\rangle$, $|\mathrm{e}\rangle$, and $|\mathrm{a}\rangle$ are plotted ($i, j = \{\mathrm{g}, \mathrm{e}, \mathrm{a}\}$). **(a)** One-photon coupling coefficients expressed in unit Hz, $|g_{ij}^{(1)}|$, for $f_{\mathrm{x}}^{\mathrm{DC}} \in [0.468, 0.5]$ [dark blue (dark grey) lines]. **(b)** Two-photon coupling coefficients expressed in unit Hz, $|g_{ij}^{(2)}|$, for $f_{\mathrm{x}}^{\mathrm{DC}} \in [0.468, 0.5]$ [light green (light grey) lines].

to a symmetric one-dimensional double well with respect to the phase variable $\hat{\phi}_{\rm m}$ [cf. chapter 2, Fig. 2.11(b); cf. also the red well on the left-hand side of Fig. 8.6]. Under these conditions, the transition matrix elements of Eqs. (8.28a) and (8.28b) constitute a well-defined set of selection rules, in analogy with the electric-dipole selection rules of atomic systems.

In order to compare the results of this subsection to those of Subsec. 8.4.1, we now restrict ourselves to the subspace of the two lowest eigenstates of the flux quantum circuit, $\{|{\rm g}\rangle, |{\rm e}\rangle\}$. In this case, from the symmetry of the interaction Hamiltonian or, equivalently, from the symmetry of the wavefunctions of $|{\rm g}\rangle$ and $|{\rm e}\rangle$, it is easy to decide whether an n-photon transition is allowed or not. We first consider one-photon transitions, which, for a bias $f_{\rm x}^{\rm DC} = 0.5$, are governed by the total Hamiltonian

$$\begin{aligned}\widehat{H}_{\rm T}^{(1)} &= \hbar(\Omega_{\rm g}\,|{\rm g}\rangle\langle{\rm g}| + \Omega_{\rm e}\,|{\rm e}\rangle\langle{\rm e}|) \\ &\quad + \alpha E_{\rm J}[|{\rm g}\rangle\langle{\rm g}|\sin(\pi + 2\hat{\phi}_{\rm m})\,|{\rm g}\rangle\langle{\rm g}| + |{\rm g}\rangle\langle{\rm g}|\sin(\pi + 2\hat{\phi}_{\rm m})\,|{\rm e}\rangle\langle{\rm e}| \\ &\quad + |{\rm e}\rangle\langle{\rm e}|\sin(\pi + 2\hat{\phi}_{\rm m})\,|{\rm g}\rangle\langle{\rm g}| + |{\rm e}\rangle\langle{\rm e}|\sin(\pi + 2\hat{\phi}_{\rm m})\,|{\rm e}\rangle\langle{\rm e}|] \\ &\quad \times (2\pi\tilde{f}_{\rm Q})\sin\omega t \\ &= \hbar\frac{\Omega_{\rm ge}}{2}(|{\rm e}\rangle\langle{\rm e}| - |{\rm g}\rangle\langle{\rm g}|) + \hbar\frac{g_{\rm ge}^{(1)}}{2j}(|{\rm g}\rangle\langle{\rm e}| + |{\rm e}\rangle\langle{\rm g}|)\,(\mathrm{e}^{+j\omega t} - \mathrm{e}^{-j\omega t})\,, \end{aligned} \tag{8.29}$$

where $\Omega_{\rm ge} \equiv \Omega_{\rm e} - \Omega_{\rm g}$, the zero of energy is taken at the middle level between the groundstate $|{\rm g}\rangle$ and excited state $|{\rm e}\rangle$, and the definition of Eq. (8.28a) is evaluated at $f_{\rm x}^{\rm DC} = 0.5$, which gives the conditions $g_{\rm gg}^{(1)} = g_{\rm ee}^{(1)} = 0$ and $g_{\rm eg}^{(1)} = g_{\rm ge}^{(1)}$ [cf. Fig. 8.7(a)]. After a RWA, moving into the uniformly rotating frame of the external driving field, and assuming angular frequency matching, $\omega = \Omega_{\rm ge}$ (energy conservation), we obtain the effective interaction Hamiltonian $\widehat{\widetilde{H}}_{\rm I}^{(1)} = -\hbar j g_{\rm ge}^{(1)}(|{\rm g}\rangle\langle{\rm e}| - |{\rm e}\rangle\langle{\rm g}|)/2$. As in Subsec. 8.4.1, this Hamiltonian is an odd-parity operator because the anticommutator $\{\widehat{\Pi}, \widehat{\widetilde{H}}_{\rm I}^{(1)}\} = 0$ and, consequently, one-photon transitions are allowed. In the case of two-photon transitions, the total Hamiltonian becomes

$$\begin{aligned}\widehat{H}_{\rm T}^{(2)} &= \hbar(\Omega_{\rm g}\,|{\rm g}\rangle\langle{\rm g}| + \Omega_{\rm e}\,|{\rm e}\rangle\langle{\rm e}|) \\ &\quad - \alpha E_{\rm J}[|{\rm g}\rangle\langle{\rm g}|\cos(\pi + 2\hat{\phi}_{\rm m})\,|{\rm g}\rangle\langle{\rm g}| + |{\rm g}\rangle\langle{\rm g}|\cos(\pi + 2\hat{\phi}_{\rm m})\,|{\rm e}\rangle\langle{\rm e}| \\ &\quad + |{\rm e}\rangle\langle{\rm e}|\cos(\pi + 2\hat{\phi}_{\rm m})\,|{\rm g}\rangle\langle{\rm g}| + |{\rm e}\rangle\langle{\rm e}|\cos(\pi + 2\hat{\phi}_{\rm m})\,|{\rm e}\rangle\langle{\rm e}|] \\ &\quad \times \frac{(2\pi\tilde{f}_{\rm Q})^2}{2}\cos 2\omega t \\ &= \hbar\frac{\Omega_{\rm ge}}{2}(|{\rm e}\rangle\langle{\rm e}| - |{\rm g}\rangle\langle{\rm g}|) + \hbar\left(\frac{g_{\rm gg}^{(2)}}{2}\,|{\rm g}\rangle\langle{\rm g}| + \frac{g_{\rm ee}^{(2)}}{2}\,|{\rm e}\rangle\langle{\rm e}|\right)(\mathrm{e}^{+j2\omega t} + \mathrm{e}^{-j2\omega t})\,, \end{aligned} \tag{8.30}$$

where the definition of Eq. (8.28b), evaluated at $f_{\rm x}^{\rm DC} = 0.5$, gives the condition $g_{\rm ge}^{(2)} = g_{\rm eg}^{(2)} = 0$ [cf. Fig. 8.7(b)]. Assuming angular frequency matching, $2\omega = \Omega_{\rm ge}$ (energy conservation), we obtain the effective interaction Hamiltonian $\widehat{\widetilde{H}}_{\rm I}^{(2)} = \hbar(g_{\rm gg}^{(2)}\,|{\rm g}\rangle\langle{\rm g}| + g_{\rm ee}^{(2)}\,|{\rm e}\rangle\langle{\rm e}|)/2$. As in Subsec. 8.4.1, this Hamiltonian is an even-parity operator because the commutator $[\widehat{\Pi}, \widehat{\widetilde{H}}_{\rm I}^{(2)}] = 0$ and, consequently, two-photon

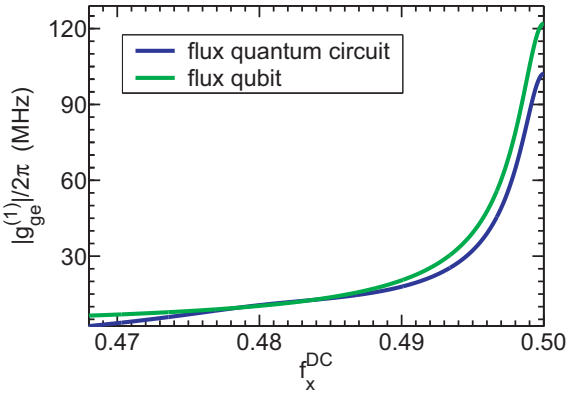

Figure 8.8: Comparison between the models based on the flux quantum circuit and on the simple two-level approximation: one-photon transitions. Dark blue (dark grey) line: $|g_{ge}^{(1)}|$ in unit Hz for $f_x^{DC} \in [0.468, 0.5]$ obtained from Eq. (8.28a). Light green (light grey) line: $|g_{ge}^{(1)}| = \Omega_D \sin\theta/2$ in unit Hz for $f_x^{DC} \in [0.468, 0.5]$ obtained within the two-level approximation. The agreement between the two curves is excellent. The reduction in the absolute value of the maximum amplitude at the degeneracy point for the flux quantum circuit curve is due to the presence of higher energy levels compared to the two-level approximation.

transitions are forbidden. More in general, for the $|g\rangle \rightarrow |e\rangle$ transition, which goes from a state with a symmetric to one with an antisymmetric wavefunction [cf. chapter 2, Figs. 2.14(a) and 2.14(b), respectively], all processes involving an odd number of photons are allowed, whereas processes with an even number of photons are forbidden [229].

(ii) – When $f_x^{DC} \neq 0.5$ (or, equivalently, $\neq 1.5$), the symmetry of the potential landscape is *broken* [cf. chapter 2, Fig. 2.12(a) and, for the cut along the $\hat{\phi}_m$-direction, chapter 2, Fig. 2.12(b) as well as the red well on the right-hand side of Fig. 8.6], the selection rules are not well-defined anymore, and level transitions, which are usually forbidden in the atomic case, are allowed. We can use Eqs. (8.28a) and (8.28b) to compute the coefficients for the various transitions as a function of the frustration f_x^{DC}. In Figs. 8.7(a) and 8.7(b), such coefficients are plotted for the three lowest levels of a flux quantum circuit in the case of one- and two-photon processes.

We can now make a quantitative comparison between these results and those obtained within the two-level approximation in some cases of interest. The first case is for the transition matrix element between $|g\rangle$ and $|e\rangle$ and one-photon transitions. As found in Subsec. 8.4.1, within a two-level approximation this element is $\hbar\Omega_D \sin\theta/2$ (before representing the interaction Hamiltonian in the rotating frame of the driving). Figure 8.8 shows a plot of this quantity together with the more general result $g_{ge}^{(1)}$ computed with the aid of Eq. (8.28a) for an extended range of the externally applied frustration bias f_x^{DC}. Remarkably, the agreement between the two curves is excellent. The reduction by approximately 19 % in the absolute value of the maximum amplitude at the degeneracy point ($f_x^{DC} = 0.5$) for the flux quantum circuit result is due to the presence of higher energy levels compared to the

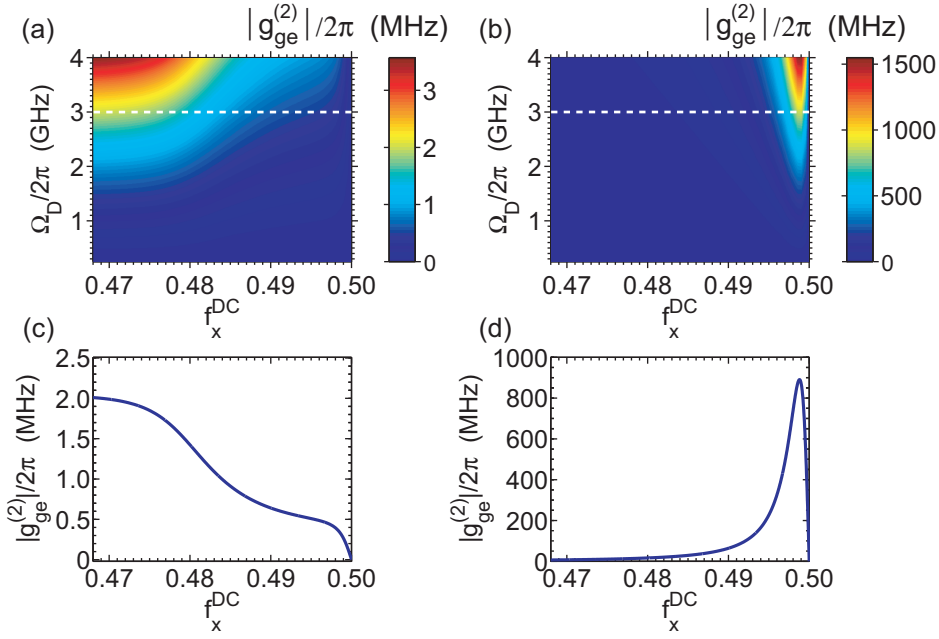

Figure 8.9: Comparison between the models based on the flux quantum circuit and on the simple two-level approximation: two-photon transitions. **(a)** Color code plot of $|g_{ge}^{(2)}|$ in unit Hz for $f_x^{DC} \in [0.468, 0.5]$ and a driving strength $\Omega_D \in [300\,\text{MHz}, 4\,\text{GHz}]$ obtained from Eq. (8.28b). **(b)** Color code plot of $|g_{ge}^{(2)}| = \Omega_D^2 \sin^2\theta \cos\theta/4\delta_Q$ in unit Hz for $f_x^{DC} \in [0.468, 0.5]$ and a driving strength $\Omega_D \in [300\,\text{MHz}, 4\,\text{GHz}]$ obtained within the two-level approximation. **(c)** Cut along the dashed white line in **(a)** for a driving strength $\Omega_D = 3\,\text{GHz}$. **(d)** Cut along the dashed white line in **(b)** for a driving strength $\Omega_D = 3\,\text{GHz}$. The departure between the curves in **(c)** and **(d)** is drastic. We notice that, in experiments, the maximum applied driving strength is typically not larger than approximately 1 GHz. Here, we plotted a more extended driving strength range for a better comparison.

simple two-level approximation.[7] Such agreement ensures that we are not making trivial mistakes in computing the tricky prefactors of the different matrix elements.

The second case is for the transition matrix element between $|g\rangle$ and $|e\rangle$ and two-photon transitions. The two-level approximation result is represented by the coefficient of the second term of Eq. (8.10), $\Omega_D^2 \sin^2\theta \cos\theta/4\delta_Q$. Figure 8.9(b) shows a plot of this quantity for the same range of f_x^{DC} as in Fig. 8.8 and also as function of the driving strength Ω_D. The reason for plotting the driving strength dependence is to analyze a broader range of regimes of two-photon processes and permit a more thorough comparison between two-level approximation and flux quantum circuit approach. In fact, we find a drastic departure between the two approaches as it appears evident from Figs. 8.9(a) and 8.9(b), which are obtained using the flux quantum circuit approach and the simple two-level approximation, respectively. The

[7]We have double checked the numerical calculations using two codes based on a different approach to the quantization of the flux quantum circuit finding the same reduction factor.

departure is true for the entire $f_{\mathrm{x}}^{\mathrm{DC}} - \Omega_{\mathrm{D}}$ parameter space and it is twofold. Not only the absolute values of the matrix elements in Figs. 8.9(a) and 8.9(b) differ by several orders of magnitude, at least in the close vicinity of the degeneracy point, but also their $f_{\mathrm{x}}^{\mathrm{DC}}$-dependence is totally different. This is more easily noticeable in Figs. 8.9(c) and 8.9(d), where the transition matrix elements for the flux quantum circuit approach and the two-level approximation, respectively, are plotted for a fixed driving strength $\Omega_{\mathrm{D}} = 3\,\mathrm{GHz}$.

As already pointed out in the beginning of this subsection, such an unexpected behavior in the case of two-photon transitions can be due to the fact that the quantum small-signal analysis of the driven flux quantum circuit inherently explores the nonlinear response of the circuit. It could also be due to artifacts arising from a wrong choice of the quantum variables involved in the dynamics. In our quantum small-signal analysis we only focus on the potential energy term of the Hamiltonian, factoring out the kinetic energy contribution. A more opportune choice of the gauge conditions could possibly unify the two approaches. However, the quantum small-signal formalism has already been employed by other authors successfully[8] [414] and we find striking the agreement between the two different theories for one-photon processes. Finally, it could be that the simple two-level approach fails away from the trivial degeneracy point (where the system symmetries help hiding the differences giving zero transition matrix elements) when considering multi-photon transitions. In fact, as studied in Refs. [63, 351, 424] two-photon (multi-photon) processes can be explained with the aid of virtual intermediate levels. It might be that the two-level approximation is not the most adequate way to account for such *multi*-level scenarios. Nevertheless, the notion to be learnt from this subsection is that the physics behind multi-level/multi-photon transitions in circuit QED is far from being a closed subject and deeper theoretical and experimental investigations must be carried out in order to shed new light on such an intriguing topic of research.

8.5 Spurious Fluctuators

In this section, we discuss the impact of two-level systems (TLSs) or, more in general, spurious fluctuators on circuit QED experiments. We first show that the presence of a TLS can indeed break the symmetry properties of superconducting qubits even at the qubit degeneracy point (cf. Subsec. 8.5.1). We then characterize the interaction between a flux qubit and a generic spurious fluctuator[9] by means of numerical simulations that qualitatively explain certain beatings in a Ramsey-type experiment (cf. Subsec. 8.5.2). The main point of this subsection is to show that the time evolution of the interaction between a superconducting flux qubit and a spurious fluctuator can give rise to a so-called collapse and revival of the system dynamics. This phenomenon has been first studied in the realm of atomic physics, which con-

[8] Indeed, some of the plots in Fig. 8.7(a) reproduce accurately the findings of Fig. 1(c) of Ref. [414].

[9] We notice that in this subsection we prefer to use the more generic expression "spurious fluctuator" instead of TLS. A spurious fluctuator could either be a TLS or some other kind of impurity/defect behaving as a resonator [421] and located in the vicinity of the qubit [249, 262]. There are two reasons behind this choice. First, we find no major difference assuming a TLS or a point-like resonator to explain our data. Second, our experimental findings do not allow us to distinguish between these two scenarios. In any case, this does affect our results.

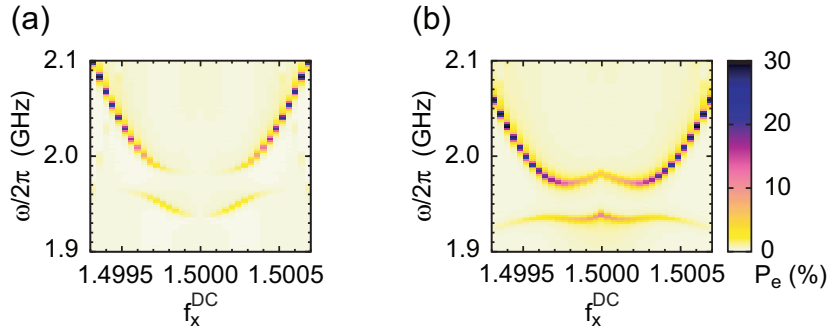

Figure 8.10: Two-photon spectroscopy simulations close to the qubit degeneracy point using the time-trace-averaging method. **(a)** Probability P_e to find the qubit in $|e\rangle$ plotted versus driving angular frequency and frustration bias [parameters as in Fig. 8.4(c); in particular, the TLS parameters are $\epsilon^* = 0 \leftrightarrow \sin\theta^* = 1$ and $\Omega^* = 0$]. The spectroscopy signal vanishes completely at the denegeracy point, $f_x^{DC} = 1.5$, because of the specific selection rules associated with the symmetry properties of the Hamiltonian [414]. **(b)** Same as in **(a)**, however, for $\sin\theta^* = 0.3$ and $\Omega^* = 280\,\mathrm{MHz}$.

stitutes the inspiration for our analysis [425, 426]. A more detailed study of such effects in associations with superconducting flux qubits can be found in our article Ref. [262], where we also explain in ample length the experimental data only briefly mentioned here. We remind the interested reader to this reference for a complete enumeration of all fitting parameters used to characterize our system and to perform the corresponding numerical simulations.

8.5.1 Symmetry Breaking via TLSs

As explained in Subsec. 8.4.1, symmetries can be broken in a controlled way in circuit QED because of the coexistence of $\hat{\sigma}_x$- and $\hat{\sigma}_z$-operators in the first-order Hamiltonian $\widehat{H}_D$, which produces a nonvanishing $\hat{\sigma}_x$-term in the second-order Hamiltonian $\widehat{H}^{(2)}$ of Eq. (8.10). As illustrated by the simulation results shown in Fig. 8.10, this scenario can also be realized at the qubit degeneracy point when considering the terms due to the TLS, $\hat{\sigma}_x^*$ and $\hat{\sigma}_z^*$. The coexistence of these flux-independent first-order terms gives rise to a nonvanishing second-order $\hat{\sigma}_x^*$-term even at the qubit degeneracy point. As a consequence, the symmetry of the total system is broken and, again, parity becomes a not well defined property. Hence, the discussed strict selection rules no longer apply and the spectroscopy two-photon signal is partially revived. Due to this very phenomenon we observe only a reduction instead of a complete suppression of the two-photon peaks near the qubit degeneracy point in the experimental data of Fig. 8.4(b). In reality, an ensemble of TLSs with some distribution of frequencies and coupling strengths rather than a single TLS is expected to contribute to the symmetry breaking. Furthermore, when the experimental resolution is limited, a single peak is detected instead of the detailed structure of Fig. 8.10(b). This is the case in our measurements [cf. Fig. 8.4(b)].

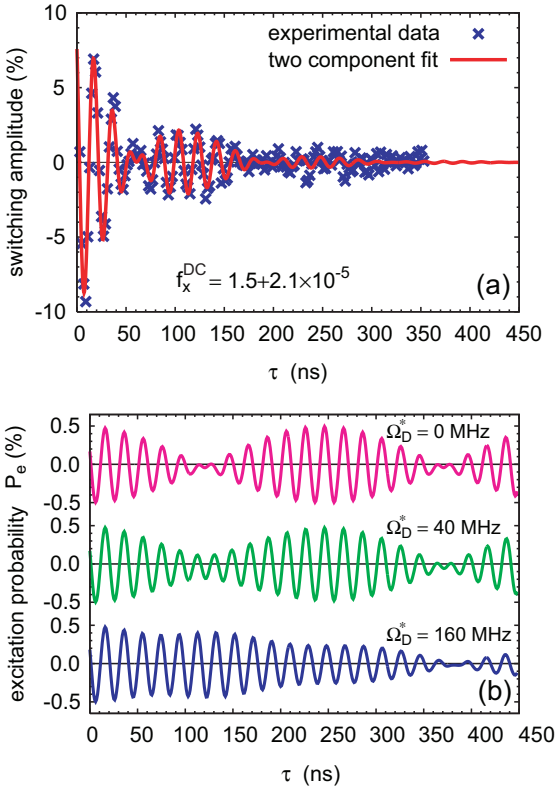

Figure 8.11: Ramsey decay beatings: experimental data and simulations. **(a)** Ramsey decay trace measured for $f_x^{DC} \simeq 1.5$. τ is the free evolution time (cf. Fig. 8.2). The red lines are fits to the data (blue crosses) using a split-peak model in combination with an exponentially decaying envelope (for details cf. [262]). The observed decay time is $T_{2R} = 75 \mp 4$ ns. **(b)** Simulated periodic Ramsey beatings due to a qubit-fluctuator interaction. The system parameters are chosen to be similar to those found in the experiment (cf. Secs. 8.2 and 8.3). The qubit and fluctuator are assumed to be on resonance. The maximum free evolution time τ is 450 ns. The microwave excitation frequency is slightly detuned from that of the fluctuator by $\simeq 1\%$. The coupling constants are chosen in a way that the results resemble our experimental data. Three simulated Ramsey traces are shown for increasing driving strengths Ω_D^*. The other parameters are a qubit-fluctuator coupling of 2 MHz and a qubit driving of 80 MHz for the displayed traces.

8.5.2 Collapse and Revival

Figure 8.11(a) shows a Ramsey decay trace obtained applying the corresponding pulse sequence of Fig. 8.2. The experimental data clearly reveal a beating structure, which, as carefully explained in Ref. [262], cannot be due to trivial reasons such as imperfect pulse sequences or spurious resonance modes of the packaging/chip environment. Therefore, we suggest a different explanation for the origin of the observed beatings in analogy to cavity QED, where the coupling between an atom and a photonic mode can give rise to beating signals [425, 426]. In our case, the

qubit acts as an "artificial atom" and the photonic mode is represented by a spurious fluctuator. We stress one more time that such fluctuator could either be a TLS (e.g., as modeled in Sec. 8.3) or a resonator-like center. This distinction does not affect our general arguments. Since the coupling strength between qubit and fluctuator is larger than the characteristic decay rates of both qubit and fluctuator, the system has to be treated as a single quantum entity (cf. also Ref. [427]). This argument can be supported by numerical simulations, which reproduce the main experimental features of Figure 8.11(a) qualitatively.

As already pointed out in Sec. 8.3, the fluctuator is characterized by a transition angular frequency $\omega_{\mathrm{TLS}} = 2\pi \times 3.94\,\mathrm{GHz}$. This is very close to the qubit transition angular frequency at the degeneracy point. As a consequence, we can restrict ourselves to the region in the close vicinity of the qubit degeneracy point (approximately 4 GHz). Based on the driven Hamiltonian[10] $\widehat{H}_{\mathrm{D}}$ and adiabatically eliminating the resonator degree of freedom (located at approximately 6 GHz) because largely detuned from the qubit in the region of interest, we simulate the Ramsey sequence choosing similar parameters to those found in the experiments. The effects of decoherence are neglected for simplicity. The driving terms are only present within the duration of the control pulses and are switched off during the free evolution periods (cf. Fig. 8.2). The time traces are obtained by numerically solving the Schrödinger equation for the Ramsey pulse sequence. The initial state is the energy ground-state of the qubit-fluctuator system in absence of driving. The results are shown in Fig. 8.11(b). Already at a first glance, it is evident that the simulations can reproduce the main feature of the experimental data, i.e., periodic Ramsey beatings due to an on-resonance qubit-fluctuator interaction. Energy is coherently exchanged between the two systems resulting in a typical collapse and revival effect. On closer inspection, we find that the resonance condition is very important for our simulation results. This might seem controversial, given that we observe the beatings over a considerable frequency range around the degeneracy point. However, we have to recall that we neglect decoherence here. As a consequence, in the simulations we have much sharper resonance peaks than in the experiments. Furthermore, we only account for a single fluctuator. In reality, there is probably an ensemble of fluctuators with slightly different frequencies close to 4 GHz and with different coupling constants. It is noteworthy to mention that there is no fundamental restriction for these fluctuators to be present only in the frequency range around 4 GHz. However, only there the qubit coherence time is long enough to allow for a clear observation of beatings or splittings.

8.6 Summary and Outlook

In summary, in this chapter we have introduced the main ingredients to perform circuit QED experiments with superconducting flux qubits: the three-Josephson-junction qubit, the lumped-parameter LC-resonator, the on-chip microwave antenna, and the DC SQUID readout circuitry. In addition, we have shown how to perform advanced manipulation and readout of the qubit state. We have then

[10] Strictly speaking, for the numerical simulations of Fig. 8.11(b) the fluctuator is assumed to be a resonator-like center. This has later been double checked with a true TLS without noticing a major difference. However, we prefer to keep the original simulations for consistency with our published article Ref. [262].

demonstrated that it is possible to use two-photon qubit spectroscopy to study the qubit-resonator interaction. Our experimental findings are evidence for the presence of an anticrossing under two-photon driving, which permits us to estimate the bare vacuum Rabi coupling. Furthermore, our experiments and theoretical analysis shed new light on the fundamental symmetry properties of quantum circuits and the nonlinear dynamics inherent to circuit QED. Finally, we have developed a theoretical model to explain the role played by spurious fluctuators in connection to symmetry breaking and the phenomenon of collapse and revival of Ramsey decay experiments.

As an outlook, we notice that multi-photon transitions in circuit QED can be exploited in a wide range of applications such as parametric up-conversion, generation of microwave single photons on demand [150, 289, 354] or squeezing [428]. Moreover, it will be exciting to repeat and extend the experimental results of this chapter to the case of circuit QED with flux qubits in the strong coupling limit. This would allow for example to resolve the two-photon vacuum Rabi splitting with very high accuracy. At last, a deeper theoretical understanding of multi-photon processes in the case of flux quantum circuits beyond the simple two-level approximation will be another important milestone on the circuit QED road map.

Chapter 9

Summary and Outlook

In this chapter, we summarize our main theoretical and experimental results, emphasizing a set of possible future applications. In addition, we point out the main steps which we think have to be followed in order to further develop the field of research of circuit QED.

In this thesis work, we have proposed a novel circuit QED architecture based on two resonators coupled to a superconducting qubit. We have defined this subfield of circuit QED as *two-resonator circuit QED*. In order to properly describe two-resonator circuit QED architectures, we have developed a theoretical formalism where the circuit properties of the resonators and qubit help finding the correct Hamiltonian of the system. When the resonators and qubit are largely detuned from each other, which means the resonance frequencies of the resonators, assumed here to be the same, and the transition frequency of the qubit are different, two interaction channels are established between the resonators.

The first channel owns its origin to a first- and second-order geometric interaction between the resonators and qubit circuit components. The second channel, instead, is due to a dynamic interaction originating from the presence of a detuned qubit. The first-order geometric interaction is present even in the absence of the qubit circuit and simply represents a finite cross-talk between the two resonators. The second-order geometric interaction is mediated by the presence of the circuit associated with the qubit. This circuit is made of capacitors and inductors where electric and magnetic energy can be stored. Via the cross-capacitances and/or mutual inductances between each resonator and the qubit circuit, energy can be transferred from one resonator to the other. Remarkably, while the first-order geometric interaction can largely be reduced by proper engineering, we have shown that the second-order interaction is a fundamental property of the system and is inevitably present in the total Hamiltonian.

The dynamic interaction is due to a second-order perturbative coupling between the resonators, which arises when a qubit is dispersively (large detuning condition) coupled to two resonators. This interaction depends on the state of the qubit.

Since the geometric and dynamic interactions are characterized by coupling coefficients with similar strength, it is possible to balance them one against the other and, thus, realize a superconducting quantum switch. The switch tunability resides in the possibility to bias the qubit at different operation points or to apply fast pulses which rapidly change the qubit population. As a result, the bosonic fields in the two resonators can be made to interact strongly or weakly depending on the

biasing/pulsing conditions. This has the important consequence that entanglement of bosonic fields between two distinguished resonators can be realized.

How to measure such entanglement? The natural answer to this question is by means of a cross-correlation measurement apparatus, where the output signals of the two resonators can be measured independently or can be correlated. This possibility has given us a strong motivation in developing a *cross-correlation homodyne detection* setup at microwave frequencies.

In order to thoroughly characterize such a setup at the quantum level, we have performed a complete set of experiments where thermal and vacuum states were measured for a wide range of parameters. In particular, we have been able to quantify *how close it is possible to observe the variance of vacuum fluctuations at microwave frequencies* by using noisy amplifiers. Moreover, we have measured the temperature and frequency dependence of the thermal-to-vacuum state cross-over by recording a large set of Planck distributions. We have called this measurement technique *Planck spectroscopy*.

Planck spectroscopy can be used for the characterization of quantum microwave devices. This can be realized as follows. Let us assume that a microwave device (a black box) is cooled in a dilution refrigerator and its temperature suitably controlled. The device is then connected to a transmission line and its emission monitored. By measuring the temperature and frequency dependence of the emitted signals we obtain a Planck spectroscopy diagram. Along the temperature axis, the diagram encodes information on the state populating the device. Below a certain temperature, when the Planck distribution flattens, we can assure that the device is in the vacuum state. The frequency dependence of the diagram encodes information on a relevant subset of scattering matrix parameters of the device. For example, if the device were an electromagnetic resonator, it should be possible to observe the typical Lorentzian peak characteristic of a resonator. This would allow us to state beyond any doubt that a resonator, for example in a circuit QED experiment, is prepared in the vacuum state. The scenario becomes more intriguing when the electromagnetic resonator is substituted by a nanomechanical resonator with resonance frequency in the microwave range, such as the dilatational disk resonators proposed and realized in Refs. [429, 430]. In this case, Planck spectroscopy would allow us to demonstrate the vacuum state of a nanomechanical system, which represents one of the holy grail of the physics research in the past few years.

While characterizing our cross-correlation setup, we have also been able to study the *quantum properties of microwave beam splitters*. First, we have developed a theoretical model for the three-port beam splitter known as Wilkinson power divider. We have shown that such a divider effectively behaves as if it were a four-port device. We have shown that an input resistive impedance and the internal resistance of the divider constitute two effective noise sources with amplitude A and B, respectively. These amplitudes are linearly superposed by the splitter and, thus, at the splitter output ports we find the sum and difference $A + B$ and $A - B$. When correlating the output signals, $A + B$ and $A - B$, we simply obtain $A^2 - B^2$: The amplitude squared associated with the first noise source cancels with the amplitude squared associated with the second noise source. Because of a slight temperature difference between the two noise sources, we effectively obtain a nonvanishing correlation, $A^2 - B^2 \neq 0$. By measuring such a correlation and fitting the results with our theoretical model for the Wilkinson power divider, we have experimentally proven

the validity of the model. We have repeated similar experiments using four-port beam splitters obtaining analogous results. These experiments reveal that in any beam splitter, including so-called three-port dividers, there are always two intrinsic noise sources at the input. In this sense, it is impossible, at least for the splitters tested in our experiments, to realize a true three-port quantum-mechanical beam splitter.

Note added in Fall 2010. We find remarkable that our work on cross-correlation measurements has already prompted several other theoretical [431] and experimental investigations [432].

Among the other results presented in this thesis, it is worth mentioning the theoretical development of another class of two-resonator circuit QED applications. In this class, one resonator (the quantum bus) is characterized by a high quality factor and allows the realization of cavity QED experiments in the strong coupling regime. The other resonator (the leaky cavity) has, instead, a low quality factor and can be used to perform an independent dispersive read out of the qubit population. A low quality factor, in fact, results in a fast measurement time, which constitutes a highly desirable feature for quantum computing applications. In addition, the low quality factor resonator can be used to perform full-state tomography of nonclassical microwave fields prepared in the quantum bus.

Note added in Fall 2010. After the first submission of this thesis, two experimental works on the coupling of a high and a low quality factor mode of the same resonator [433] and of two distinct resonators have been reported [434].

We have also proposed an extension from a two-resonator to a multi-resonator architecture, where the resonators form a two-dimensional pattern defined as cavity grid. Such a grid has the advantage over linear implementations of circuit QED for quantum computing purposes because it allows to scale the number of qubits with $\sqrt{N}$ instead of N. Hence, a large number of qubits can be positioned at the crossing between two resonators on the grid. We have shown that all basic operations for quantum computing can be realized on the grid and that the grid encompasses all fundamental elements of a scalable fault-tolerant architecture.

Finally, we have studied theoretically and experimentally the two-photon driven Jaynes-Cummings interaction in a circuit QED setup based on a flux qubit read out by means of a DC SQUID. At the basis of such an interaction stands an upconversion dynamics, where two incoming classical photons with half the qubit transition frequency are transformed into a single quantum output photon at the qubit frequency. This process, which has allowed us to prove experimentally the selection rules and symmetry properties of a superconducting qubit, can serve as a means to generate microwave single photons and squeezed states.

What Next?

We conclude this chapter with a "todo-list" of circuit QED, opening a window on what we think are the next steps that should be pursued in the field:

1. A single photon detector at microwave frequencies has to be experimentally developed. Such a photodetector is a necessary tool in most quantum computing architectures based on photonic qubits. Also, it is indispensable to have a single photon detector for a deeper understanding of the quantum nature of propagating microwave fields, which still represents a totally open topic;

2. The work on phase-preserving and phase-sensitive (parametric) linear amplifiers has to continue. This will allow us to further improve the readout of superconducting qubits in circuit QED. The combination of quantum-limited amplifiers and nonlinear readout based on bifurcation amplifiers will eventually permit to reach qubit readout fidelities above 99 %;

3. The coherence properties of superconducting qubits must be largely improved. This is one of the weakest point of circuit QED. Increasing the qubit-resonator coupling strength will help to realize many more quantum operations within the same time. However, we truly believe that a novel qubit design is needed in order to bring circuit QED to the next level of complexity;

4. The realization of multi-resonator architectures has to be pursued in order to create an independent field of research with respect to quantum-optical cavity QED;

5. The coupling of qubits to transmission lines instead of resonators also constitute and intriguing path to follow.

We hope this thesis has served its purpose to show that circuit QED is an extremely interesting and highly interdisciplinary field of research, where a number of doors is still open for further ground-breaking developments.

Appendix A

The Noise Contribution of the Cryogenic Circulators

In this Appendix, we show two set of experimental data on the noise contribution of the cryogenic circulators to the measurement of the quantum-mechanical variance of thermal/vacuum states as a function of temperature T (i.e., of the Planck distribution). We focus on the case of a Wilkinson power divider used as a microwave beam splitter.

The role played by the circulators in terms of added noise has already been explained in detail in chapter 3, Subsec. 3.2.1. In summary, the terminations $Z_{\rm Lc}$ at port C of each circulator are heat sunk to the still stage of the dilution refrigerator. Hereafter, we will assume $Z_{\rm Lc} = Z_0$. As indicated in the bottom part of Fig. 3.10, the temperature $T_{\rm Lc}$ of the terminations $Z_{\rm Lc}$, which is equivalent to the still temperature, varies between approximately 450 and 500 mK during the experiment. Such a variation depends on the temperature T of the mixing chamber stage of the dilution refrigerator according to a nontrivial function which accounts for the heat flow between the mixing chamber and the still stage,

$$T_{\rm Lc} = f_{\rm flow}(T)\,. \tag{A.1}$$

During the experiments, we monitor both T and $T_{\rm Lc}$ at all times. This allows us to obtain experimentally the function $f_{\rm flow}$.

In the classical limit, the resistive terminations $Z_{\rm Lc}$ at temperature $T_{\rm Lc}$ generate an RMS thermal noise voltage

$$v_{ck} = \sqrt{4k_{\rm B}T_{\rm Lc}Z_{\rm Lc}{\rm BW}_k}\,, \tag{A.2}$$

which, recalling Eq. (A.1), corresponds to an available power

$$\begin{aligned}\Pi_{ck} &= \frac{v_{ck}^2}{4Z_0} = k_{\rm B}T_{\rm Lc}{\rm BW}_k \\ &= k_{\rm B}f_{\rm flow}(T){\rm BW}_k\,.\end{aligned} \tag{A.3}$$

The power Π_{ck} generated by one of the two circulators follows, for example, the path indicated by the solid red arrow in the bottom part of Fig. 3.10 until it gets reflected by one of the output ports of the Wilkinson power divider [in this case, port $1 \equiv$ B; cf. also Fig. 3.1(a)]. At the same time, the power generated by the other circulator follows the path indicated by the solid magenta arrow in the bottom

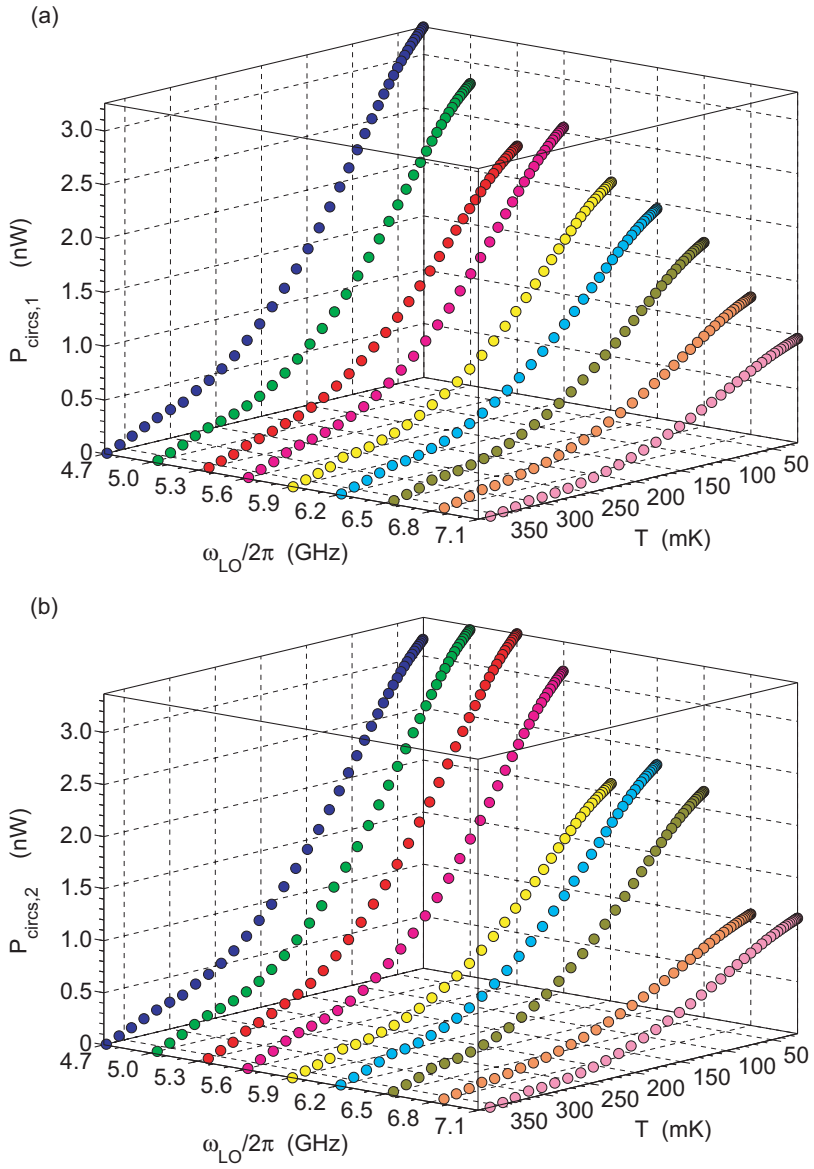

Figure A.1: Temperature and frequency dependence of the noise power due to the circulators obtained according to Eq. (A.6). Each face color of the full circles is associated with a different LO frequency. The temperature dependence is plotted backwards for a better visualization of the data. **(a)** Noise power $P_{\mathrm{circs},1}$ added to the signals on the first channel of the detection chain. **(b)** Noise power $P_{\mathrm{circs},2}$ added to the signals on the second channel of the detection chain.

part of Fig. 3.10. Once it reaches the output port of the divider [in this case, port 2 ≡ C; cf. also Fig. 3.1(a)], the power gets partially transmitted through the divider into port B ≡ 1. In the bottom part of Fig. 3.10, the noise from the first circulator reflected by the divider is indicated by a broken red arrow and the noise from the second circulator transmitted through the divider is indicated by a broken magenta arrow. Both these noise contributions go back into channel 1 of the detection chain (similar arguments apply for channel 2). The effect of the reflection and transmission[1] coefficients of the divider is to diminish significantly the power Π_{ck} initially generated by the two circulators. As a consequence, we define a coefficient δ_{ck} which accounts for the effective contribution of the noise voltage due to the circulators. At the output of either one of the two circulators we are left with a power

$$\Pi_{ck}^{\text{out}} = \delta_{ck}^2 \, \Pi_{ck} \, , \tag{A.4}$$

which is then amplified along one of the two channels of the detection chain resulting in a power $G_k \, \Pi_{ck}^{\text{out}}$ at the input ports of the acquisition card.

Since we are dealing with thermal/vacuum states, the power Π_{ck} is a good approximation of the quantum-mechanical variance associated with the circulator noise voltage [cf. Eq. (4.49) in chapter 4],

$$\Pi_{ck} \approx \tilde{\sigma}_{ck}^2 = \text{BW}_k \, \bar{\sigma}_{ck}^2 = \text{BW}_k \, \varsigma(T_{\text{Lc}}) \, , \tag{A.5}$$

where $\bar{\sigma}_{ck}^2$ is given by Eq. (4.59). The effective noise power generated by the circulators after amplification can finally be written as

$$P_{\text{circs},k} = G_k \delta_{ck}^2 \Pi_{ck} \, . \tag{A.6}$$

Figures A.1(a) and A.1(b) show a set of experimental data for the noise power due to the circulators obtained according to Eq. (A.6). The noise power is plotted as a function of the temperature of the primary noise source and of the LO frequency. The primary noise source is represented by the resistive load at the input of the Wilkinson power divider [cf. Fig. 3.1(b)]. Since such a load is thermalized to the mixing chamber stage, in first approximation we can assume its temperature to be the same as the mixing chamber temperature. Each face color of the full circles in the figures is associated with a different frequency [same color coding as in Figs. 4.7(a) and 4.7(c) of chapter 4]. The temperature dependence is plotted backwards for a better visualization of the data. The frequency-dependent gains for each channel, $G_1(\omega_{\text{LO}})$ and $G_2(\omega_{\text{LO}})$, are taken from Figs. 4.11(a) and 4.11(b), respectively. The attenuation coefficient has been estimated in chapter 3, Subsec. 3.2.1 to be $\delta_{ck} \simeq 0.36$ for the case of a Wilkinson power divider. It is worth comparing the results for the effective noise power added by the circulators to the corresponding power due solely to the thermal/vacuum states generated by the primary and secondary noise sources at the divider input, which are reported in chapter 4, Figs. 4.7(a) and 4.7(c). Notably, the difference between the maximum and minimum noise power due to the circulators ranges between approximately 1 and 3.3 nW depending on the chosen LO frequency. In the case of the power due to the primary and secondary noise sources, such a difference ranges between approximately 60 and 240 nW. This clearly indicates that the temperature-dependent noise contribution originating from

[1] We remind that the transmission is equivalent to the isolation between the output channels C and B of the divider.

the circulators does not constitute an issue for our experiments, being the average circulators noise power much smaller than the power we are interested in measuring. In this sense, the approximation performed when deriving Eq. (4.90) is now justified by experimental evidence.

In the experiments, the physics modeled by Eq. (4.90) can be obtained by subtracting the noise power contribution due to the circulators from the raw variance data expressed in units W. All data plotted and analyzed in chapter 4 have been obtained in this way.

Appendix B

The Polynomial Fitting Model

In chapter 4, Subsec. 4.3.2 we have mentioned that extracting the thermal-to-vacuum state cross-over temperature by means of a simple polynomial fitting model is inadequate because of the ambiguity associated with such a simple fitting. An example of polynomial fitting is shown in Fig. 4.6(a), where the horizontal and oblique dashed red lines give the asymptotic behavior of a Planck distribution in the limits of low and high temperature, respectively. The statement we have made in chapter 4 was that the number of data points used to obtain the dashed red lines is totally arbitrary. In other words, we can choose as many points as we want in order to fit such lines resulting in an arbitrary level for the horizontal line and in an arbitrary slope for the oblique line. The horizontal line is fitted by means of a zero-order polynomial fitting based on the first N_{low} data points of the Planck distribution (i.e., the first N_{low} points from the left), whereas the oblique line is fitted by means of a first-order polynomial fitting based on the last N_{up} data points of the Planck distribution (i.e., the first N_{up} points from the right). Hereafter, we assume $N_{\text{low}} = N_{\text{up}} = N_{\text{poly}}$ and we refer to them as fitting points.

In this Appendix, we motivate the statement of arbitrariness of the polynomial fitting model by investigating the dependence of the cross-over temperature extracted from the crossing between the horizontal and oblique lines as in Fig. 4.6(a), but for three different sets of fitting points. Figures B.1(a), B.1(b), and B.1(c) show three Planck spectroscopy measurements, where the fitted cross-over temperatures indicated by open brown-red diamonds connected by a brown-red line are compared to the theoretical cross-over temperature represented by a dashed white line. The fitted cross-over temperatures of Figs. B.1(a), B.1(b), and B.1(c) are obtained for $N_{\text{poly}} = 4, 8, 12$, respectively. The three figures clearly show that the fitted cross-over temperatures vary arbitrarily as a function of the fitting points. The measurements refer to channel 1. Similar results hold for channel 2 (data not shown). As a consequence, we can conclude that the simple polynomial fitting model is an improper method for analyzing our experimental results.

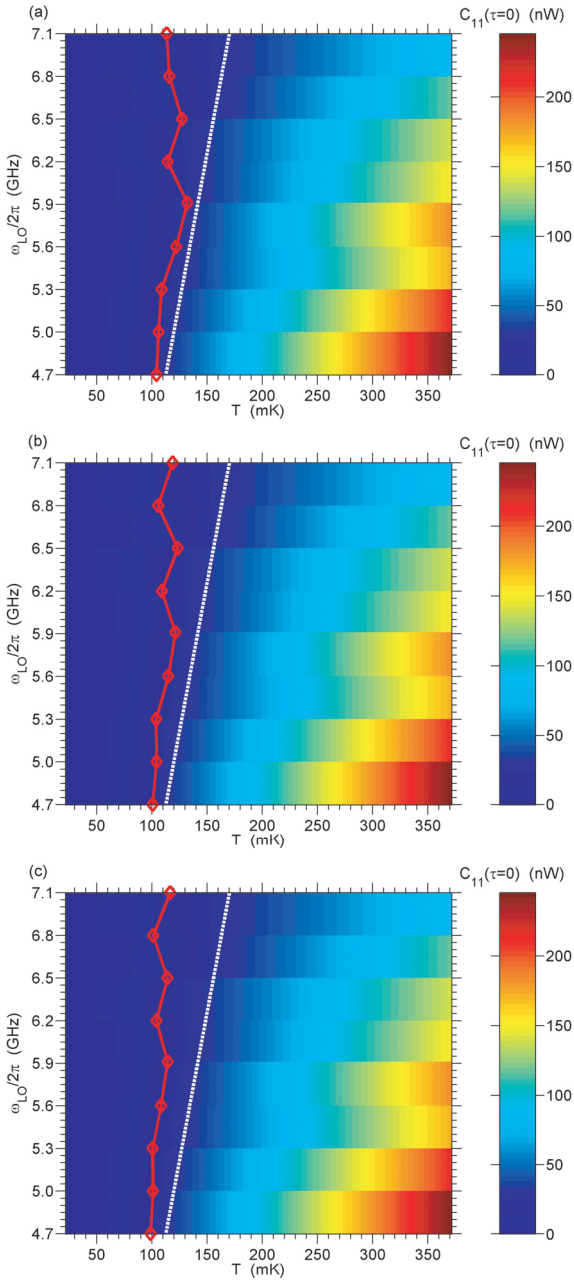

Figure B.1: Planck spectroscopy: the arbitrariness of the polynomial fitting model. Color-code plots of the red curves in Fig. 4.7(b). **(a)** Polynomial fitting for $N_{\rm poly} = 4$, **(b)** for $N_{\rm poly} = 8$, and **(c)** for $N_{\rm poly} = 12$.

Appendix C

The Bin Average

In chapter 4, Subsec. 4.3.2, within the analysis of the Planck spectroscopy data, we have described in detail the averaging method which leads to the results of Figs. 4.7(a) and 4.7(c). Such results were obtained employing a so-called moving average. The moving average allows us to average together many different traces associated with the same LO frequency minimizing the temperature inhomogeneity between the points of the different traces.[1] This inhomogeneity owns its origin to the time lag between the recording of such traces.

In this Appendix, we show an alternative method for the averaging of the different traces of the Planck spectroscopy data: the bin average method. We make use of a similar notation as in chapter 4, Subsec. 4.3.2. The bin average method is realized as follows:

1. We first consider one LO frequency, (h). The Planck distribution associated with such a frequency is measured p times. Henceforth, we assume the maximum number of measured traces to be $p^{\max}$;

2. The minimum and maximum temperatures for the p-th trace are evaluated. These are defined as $T_p^{\min}$ and $T_p^{\max}$, respectively;

3. The total minimum and maximum temperatures for the set of measurements associated with the h-th LO frequency are calculated as

$$T_{(h)}^{\min} = \min\{T_p^{\min}\}\,, \tag{C.1}$$

and

$$T_{(h)}^{\max} = \max\{T_p^{\max}\}\,, \tag{C.2}$$

for $p = 1, 2, \ldots, p^{\max}$;

[1] More in general, there are two different issues connected to the so-called downsweep measurements. First, within each measured trace the temperature spacing is uneven due to the different response of the cooling power of the cryostat at different temperatures. Second, the temperatures are inhomogeneously distributed between traces measured at different times. All averaging methods explained in this thesis try to cope with both issues. In the experiments, we have tried to perform so-called upsweep measurements (data not shown), where the Planck distribution is measured for a limited set of temperatures which are well stabilized. The drawback of this method is that is very slow and, thus, does not allow to measure many temperature points.

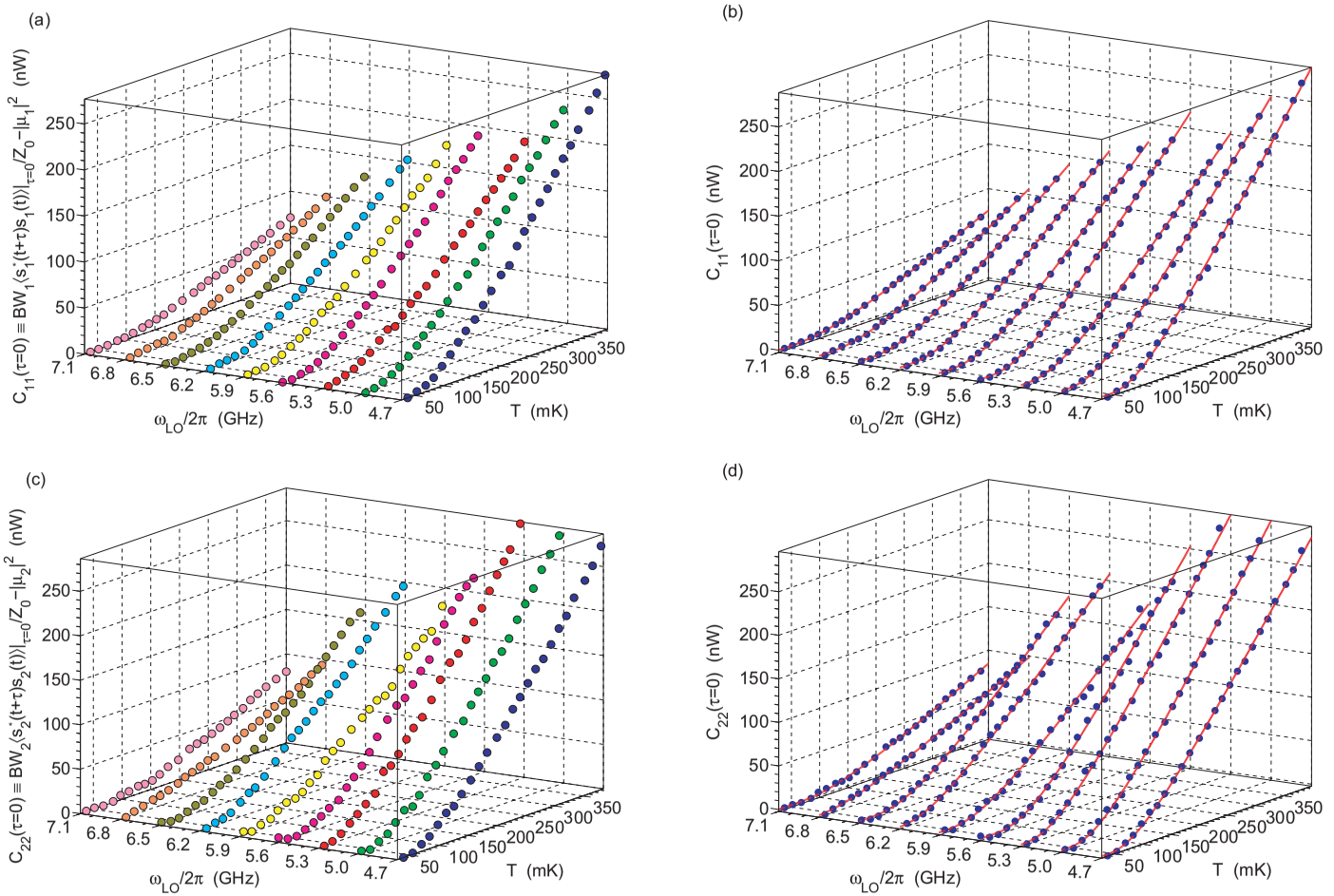

Figure C.1: Planck spectroscopy: raw data and fitting. **(a)** Experimental data associated with 9 Planck distributions measured at 9 different $\omega_{\rm LO}$ for channel 1. Each face color for a set of full circles represents a different angular frequency. **(b)** Open dark blue circles: same experimental data as in **(a)**. Red lines: fitted curves obtained from the three-parameter fitting model [cf. Eq. (4.98)]. **(c)** As in **(a)** for channel 2. **(d)** as in **(b)** for channel 2. The experimental data are the result of a bin average.

4. The width $\Delta T_{\rm bin}$ of one temperature bin is set. This represents the desired temperature spacing of the final trace resulting from the averaging method. The number of bins for the h-th LO frequency is obtained as

$$N_{\rm bin} = \left\lfloor \frac{T^{\rm max}_{(h)} - T^{\rm min}_{(h)}}{\Delta T_{\rm bin}} \right\rfloor ; \tag{C.3}$$

5. For every trace p, the temperature corresponding to each point $x_i^{(h)}$ of the trace is compared to the lower, $T^{\rm low}_{{\rm bin}j}$, and upper, $T^{\rm up}_{{\rm bin}j}$, temperatures of the j-th temperature bin. The upper and lower temperatures are given by

$$T^{\rm low}_{{\rm bin}j} = T^{\rm max}_{(h)} - j\Delta T_{\rm bin} , \tag{C.4}$$

and

$$T^{\rm up}_{{\rm bin}j} = T^{\rm max}_{(h)} - (j-1)\Delta T_{\rm bin} , \tag{C.5}$$

where $j = 1, 2, \ldots, N_{\rm bin}$. All points $x_i^{(h)}$ the temperature of which lies within the range comprised between $T^{\rm low}_{{\rm bin}j}$ and $T^{\rm up}_{{\rm bin}j}$ are averaged together resulting in one single point

$$y_j^{(h)} . \tag{C.6}$$

The effective temperature associated with this point is simply the average temperature of the j-th temperature bin,

$$\overline{T}_{{\rm bin}j} = \frac{T^{\rm low}_{{\rm bin}j} + T^{\rm up}_{{\rm bin}j}}{2} . \tag{C.7}$$

In this way, each trace $\{x_i^{(h)}\}_p$ is reduced to a new trace $\{y_j^{(h)}\}_p$ with fewer data points, which are now *equally spaced in temperature*;

6. This procedure is repeated for all traces p, until $p^{\rm max}$. The so-obtained $\{y_j^{(h)}\}_p$ traces are all equally spaced in temperatures and can homogeneously be averaged together,

$$\{y_j^{(h)}\} = \frac{1}{p} \sum_{p=1}^{p^{\rm max}} \{y_j^{(h)}\}_p . \tag{C.8}$$

All traces displayed in Figs. C.1(a) and C.1(c) are obtained following the recipe given above. In this case, $p^{\rm max} = 4$ and $\Delta T_{\rm bin} = 15\,{\rm mK}$. The exact number of temperature bins, $N_{\rm bin}$, varies depending on which LO frequency is considered. In the case of Fig. C.1, $N_{\rm bin}$ varies between 25 and 27. Figures C.1(b) and C.1(d) show the same data as in Figs. C.1(a) and C.1(c). The red lines overlaid to the data are fitted curves obtained from the three-parameter fitting model (cf. chapter 4, Subsec. 4.3.2). The fitting allows us to extract for each channel k of the detection chain an η_k as a function of the LO angular frequency $\omega_{\rm LO}$.[2] From the knowledge of η_k we can then compute the corresponding measured cross-over temperature by means of Eq. (4.96). Figures C.2(a) and C.2(b) show the frequency dependence of

[2]We remind that the η_k are obtained by substituting $\eta \to \eta_k$ in Eq. (4.98), where the η were initially assumed to be channel-independent, an assumption that turned out not to be experimentally confirmed.

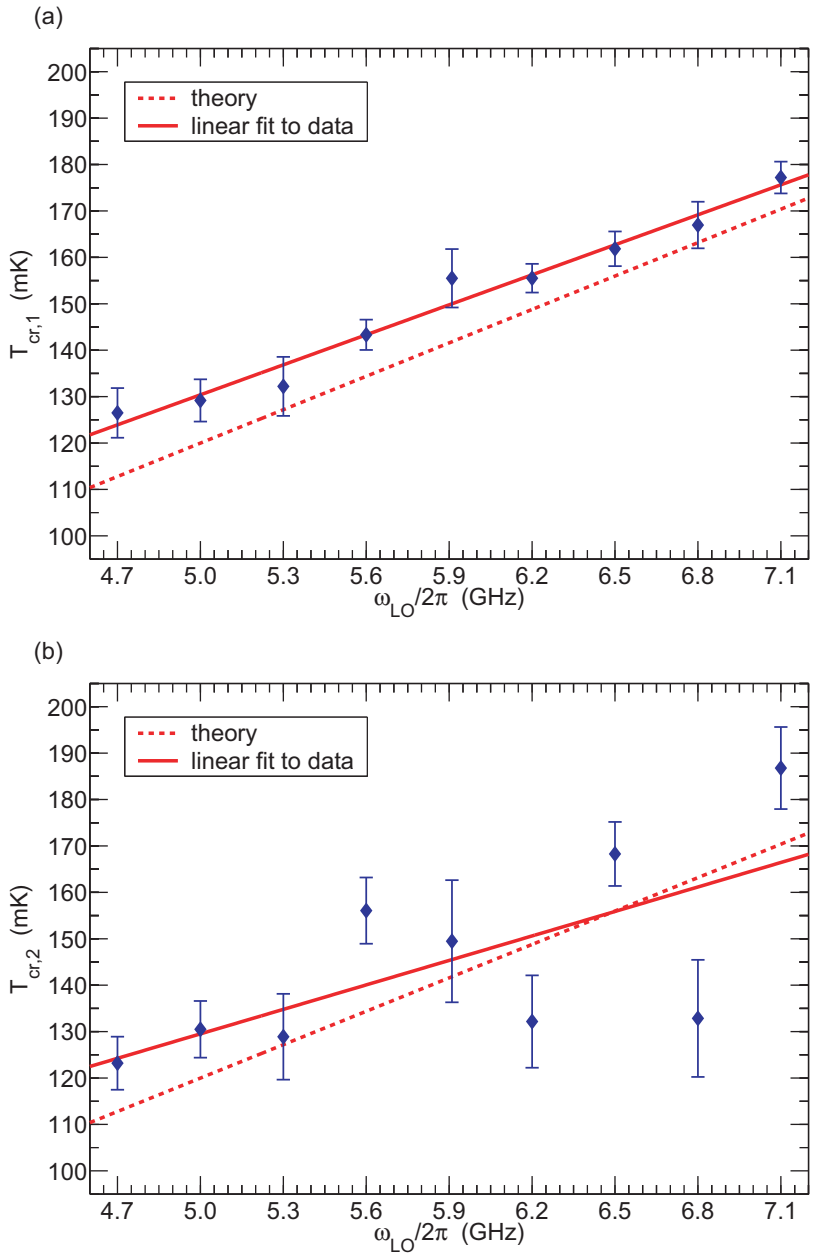

Figure C.2: Summary of the cross-over temperatures estimated from the three-parameter fitting model [cf. Eq. (4.98)] for channels 1 and 2 as a function of the LO angular frequency $\omega_{\rm LO}$. Dark blue diamonds: data points for the cross-over temperatures obtained from Eq. (4.96) using the channel-dependent η_k (here, $\eta \to \eta_k$) fitted from Eq. (4.98). The confidence bounds are indicated. Solid red lines: linear fits to data. Dashed red lines: frequency dependence of the theoretical cross-over temperature associated with the vacuum. **(a)** Results for channel 1. **(b)** Results for channel 2. The data used for the fittings were obtained employing the bin average method.

the measured cross-over temperature (dark blue diamonds) for the two channels of the detection chain, respectively. The solid red lines are obtained by means of a linear fit to the data, while the dashed red lines represent the theoretical cross-over temperature. It is worth comparing these results with those shown in chapter 4, Figs. 4.12(a) and 4.12(b). Focusing on the results for channel 1 only (similar arguments are valid for channel 2), we notice that in the case of the bin average method the measured cross-over temperatures deviate from the theory more than in the case of the moving average method. The reason behind this difference is due to the larger loss of data points when performing the bin average as compared to the moving average. However, according to the bin average method the fitted η is always positive (at least for channel 1) and it is visibly less dependent on frequency, as expected from our model.

In summary, we find a slight dependence of the downsweep measurements on the averaging method employed to analyze the data. This fact reveals that further studies should be made in order to more clearly understand the validity of our three-parameter fitting model. However, it seems that in general our model can explain reasonably well the basic features of the Planck spectroscopy data.

Appendix D

Higher-Order Corrections to the Capacitance and Inductance Matrices

In chapter 5, Subsec. 5.1.2, we have accounted for corrections up to second-order capacitive and inductive interactions between the elements of a three-node network. We have shown that for a three-node network the geometric second-order coupling coefficients can dominate over the first-order ones. For this reason, in the following we can safely assume vanishing first-order coupling coefficients, $c = m = 0$. Nevertheless, we notice that our results would not be qualitatively affected even in the presence of appreciable first-order couplings.

In this Appendix, we demonstrate that third- and fourth-order capacitances and inductances are negligible. We start with the case of third-order corrections. There are two possible excitation pathways giving rise to third-order coupling coefficients. These pathways are between resonator A and qubit Q, A-Q-B-Q, or between resonator B and qubit Q, B-Q-A-Q. Assuming the two resonators to have identical properties, we only study the A-Q-B-Q pathway. In this case, from the knowledge of the electromagnetic energy we can derive

$$\begin{aligned}\widehat{H}^{(3)}_{\mathrm{AQ}} = \hat{V}_{\mathrm{A}} C_{\mathrm{AQ}} \hat{V}_{\mathrm{Q}} + \hat{I}_{\mathrm{A}} M_{\mathrm{AQ}} \hat{I}_{\mathrm{Q}} \\ + \hat{V}_{\mathrm{A}} C_{\mathrm{AQ}} \frac{1}{C_{\mathrm{QQ}}} C_{\mathrm{QB}} \frac{1}{C_{\mathrm{BB}}} C_{\mathrm{BQ}} \hat{V}_{\mathrm{Q}} \\ + \hat{I}_{\mathrm{A}} M_{\mathrm{AQ}} \frac{1}{M_{\mathrm{QQ}}} M_{\mathrm{QB}} \frac{1}{M_{\mathrm{BB}}} M_{\mathrm{BQ}} \hat{I}_{\mathrm{Q}} \,, \end{aligned} \tag{D.1}$$

where the inverse paths Q-A and Q-B-Q-A are already included. In the equation above, resonator B is only virtually excited. In the same equation, we identify the capacitance and inductance matrix elements up to third order

$$C^{(3)}_{\mathrm{AQ}} \equiv C_{\mathrm{AQ}} \left(1 + \frac{C^2_{\mathrm{QB}}}{C_{\mathrm{QQ}} C_{\mathrm{BB}}} \right) \tag{D.2}$$

and

$$M^{(3)}_{\mathrm{AQ}} \equiv M_{\mathrm{AQ}} \left(1 + \frac{M^2_{\mathrm{QB}}}{M_{\mathrm{QQ}} M_{\mathrm{BB}}} \right) . \tag{D.3}$$

In circuit theory, it is well-known that the squares of the electromagnetic coupling coefficients are $C_{\mathrm{QB}}^2/C_{\mathrm{QQ}}C_{\mathrm{BB}} < 1$ and $M_{\mathrm{QB}}^2/M_{\mathrm{QQ}}M_{\mathrm{BB}} < 1$ [264]. This implies that the pure third-order capacitance and inductance are always smaller than the first-order ones, $C_{\mathrm{AQ}}^{(3)} - C_{\mathrm{AQ}} < C_{\mathrm{AQ}}$ and $M_{\mathrm{AQ}}^{(3)} - M_{\mathrm{AQ}} < M_{\mathrm{AQ}}$. For typical experimental parameters, we find third-order processes to be negligible, $C_{\mathrm{AQ}}^{(3)} - C_{\mathrm{AQ}} \ll C_{\mathrm{AQ}}$ and $M_{\mathrm{AQ}}^{(3)} - M_{\mathrm{AQ}} \ll M_{\mathrm{AQ}}$. For example, using the parameters given in chapter 5, Sec. 5.4 yields $M_{\mathrm{QB}}^2/M_{\mathrm{QQ}}M_{\mathrm{BB}} \simeq 7.88 \times 10^{-4} \ll 1$.

In a similar way, the fourth-order coupling coefficients for the excitation pathways A-Q-B-Q-B and, equivalently, B-Q-A-Q-A can easily be found. In this case, it is the qubit to be only virtually excited. The capacitance and inductance matrix elements up to fourth order become

$$C_{\mathrm{AB}}^{(4)} \equiv \frac{C_{\mathrm{AQ}}C_{\mathrm{QB}}}{C_{\mathrm{QQ}}} \left(1 + \frac{C_{\mathrm{QB}}^2}{C_{\mathrm{QQ}}C_{\mathrm{BB}}}\right) \tag{D.4}$$

and

$$M_{\mathrm{AQ}}^{(4)} \equiv \frac{M_{\mathrm{AQ}}M_{\mathrm{QB}}}{M_{\mathrm{QQ}}} \left(1 + \frac{M_{\mathrm{QB}}^2}{M_{\mathrm{QQ}}M_{\mathrm{BB}}}\right) . \tag{D.5}$$

When comparing the above equations to Eqs. (D.2) and (D.3), respectively, we find that fourth-order processes are negligible for typical experimental parameters.

In the light of all these considerations, all higher-order coupling coefficients can safely be ignored in two-resonator circuit QED.

Appendix E

Details of the FASTHENRY Simulations

In this Appendix, we discuss the details of our FASTHENRY simulations [364]. First, we verify our hypothesis on the uniformity of the AC currents (corresponding to the magnetic fields) flowing on the resonators in the regions of Figs. 5.12(b) and 5.12(c) in chapter 5. To this end, we derive the quantized current on one of the two resonators (e.g., A) following similar calculations as in Refs. [131] and [289]

$$\hat{I}_{\rm ra}\left(z,t\right) \equiv i_{\rm A0}\cos\left(\frac{\pi z}{\ell_{\rm m}}\right)\, j\left[\hat{a}^{\dagger}\left(t\right)-\hat{a}\left(t\right)\right]\,, \tag{E.1}$$

where z represents a coordinate along the longitudinal direction of the resonator [see Fig. 5.12(c)] and t is the time. In Eq. (E.1), the bosonic field operators are expressed in the Heisenberg picture. We notice that Eq. (E.1) is valid for the first mode of the $\lambda/2$ resonator(s) considered in our example. The contribution from the second mode is negligible for two main reasons. First, the current is characterized by a node at the flux qubit loop position chosen here. Second, the qubit-resonator detuning becomes substantially larger, hence resulting in a correspondingly reduced coupling. The contribution form higher modes can also be neglected because of the increasing detuning.

Substituting the numbers of Table 5.1 into Eq. (E.1) and setting $z=\mp\ell_{\rm sim}/2$, we find that the two currents at the boundaries $\mp\ell_{\rm sim}/2$ are about $0.998i_{\rm A0}$, where $i_{\rm A0}$ is the maximum amplitude of the quantized current in Eq. (E.1). This maximum is obtained at the position $z=0$ of the mode antinode. The main implications of current uniformity over $\ell_{\rm sim}$ are explained in detail in Sec. 5.4. In a similar way, we can also estimate the voltage contribution for the first mode at the boundaries $\mp\ell_{\rm sim}/2$. In this case, we must replace the cosine function of Eq. (E.1) with a sine function, owing to the conjugation of quantized currents and voltages. The maximum vacuum voltage of, e.g., resonator A is given by $v_{\rm A0}\equiv\sqrt{\hbar\omega_{\rm A}/2C_{\rm ra}}\simeq 0.5871\,\mu{\rm V}$ for the realistic parameters of Table 5.1. At $\mp\ell_{\rm sim}/2$, we then obtain the maximum voltages in the simulated regions, which are approximately $\mp 0.065v_{\rm A0}$. Towards the center of the simulated regions the voltage reduces to zero because its corresponding first mode is characterized by a node. Also, higher modes do not contribute for the same detuning arguments outlined above. Therefore, we can safely neglect all capacitive couplings in our simulations.

Second, we notice that $\ell_{\rm sim}=500\,\mu{\rm m}$ is chosen to be large enough compared to the lateral dimension $l_{\rm q1}=200\,\mu{\rm m}$ of the flux qubit loop [see Figs. 5.12(a)-(c)].

This avoids errors due to fringing effects when simulating the coupling coefficients between qubit and resonators. For consistency, we have also performed several simulations assuming larger values of ℓ_{sim}, up to 1-1.5 mm (data not shown). We have not found any appreciable deviation in the resulting inductances.

Third, we stress that special care has to be taken when using FASTHENRY to simulate the second-order inductances of our three-circuit network. In order to compute the inductance matrix, test currents must be applied to the involved structures at specific probing ports. However, when applying test currents to all three circuits simultaneously, only first-order inductances are calculated. This is due to the boundary conditions that must be fulfilled at the probing ports. This fact has important implications for the calculation of the mutual inductance $\widetilde{m}$, which is the sum of first- and second-order mutual inductances between resonators A and B. In this case, it is crucial to apply test currents only to the two resonators, but not to the qubit circuit. On the contrary, the pure first-order mutual inductance m between A and B can be simulated in two equivalent ways: Either the qubit circuit is completely removed from the network or test currents are applied to all three structures. We do not notice any difference between these two approaches. The above arguments also apply to the calculation of the renormalized self-inductances $\widetilde{L}^*_{\mathrm{ra}}$ and $\widetilde{L}^*_{\mathrm{rb}}$ of the two resonators and their pure counterparts L^*_{ra} and L^*_{rb}.

Bibliography

[1] D. O. Hall and K. K. Rao, *Photosynthesis*, 6th ed., (Cambridge University Press, Cambridge, 1999).

[2] I. Thomas, *Greek Mathematical Works: Volume II, From Aristarchus to Pappus*, p. 19, (Loeb Classical Library, Harvard University Press, Cambridge, 1941).

[3] I. Newton, *Opticks*, (Prometheus Books, New York, 2003).

[4] J. C. Maxwell, On Physical Lines of Force, Philosophical Magazine 4th series, 161 (1861).

[5] J. C. Maxwell, A Dynamical Theory of the Electromagnetic Field, Phil. Trans. R. Soc. London **155**, 459 (1865).

[6] J. C. Maxwell, *A Treatise on Electricity and Magnetism*, (Dover Publications, Inc., Mineola - New York, 1954).

[7] H. R. Hertz, Über sehr schnelle electrische Schwingungen, Ann. Phys. (Leipzig) **267**, 421 (1887).

[8] H. R. Hertz, Über einen Einfluss des ultravioletten Lichtes auf die electrische Entladung, Ann. Phys. (Leipzig) **267**, 983 (1887).

[9] H. R. Hertz, Über die Einwirkung einer geradlinigen electrischen Schwingung auf eine benachbarte Strombahn, Ann. Phys. (Leipzig) **270**, 155 (1888).

[10] H. R. Hertz, Über die Ausbreitungsgeschwindigkeit der electrodynamischen Wirkungen, Ann. Phys. (Leipzig) **270**, 551 (1888).

[11] O. Heaviside, Electromagnetic Waves, the Propagation of Potential, and the Electromagnetic Effects of a Moving Charge, Electrical Papers **2**, 490 (1894).

[12] J. Pietzsch, X-Ray's Identity Becomes Crystal Clear, on http://nobelprize.org/nobel_prizes/physics/laureates/1914/perspectives.html .

[13] M. Planck, Über das Gesetz der Energieverteilung im Normalspectrum, Ann. Phys. (Leipzig) **4**, 553 (1901).

[14] A. Einstein, Über einen die Erzeugung und Verwandlung des Lichtes betreffenden heuristischen Gesichtspunkt, Ann. Phys. (Leipzig) **17**, 132 (1905).

[15] M. von Laue, Röntgenstrahlinterferenzen, Phys. Z. **14** 1075 (1913).

[16] H. K. Onnes, The Superconductivity of Mercury, Leiden Comm., **120b**, **122b**, and **124c** (1911).

[17] A. Einstein, Zur Quantentheorie der Strahlung, Phys. Z. **18**, 121 (1917).

[18] W. E. Lamb, Jr. and R. C. Retherford, Fine Structure of the Hydrogen Atom by a Microwave Method, Phys. Rev. **72**, 241 (1947).

[19] H. A. Bethe, The Electromagnetic Shift of Energy Levels, Phys. Rev. **72**, 339 (1947).

[20] S. Tomonaga, On a Relativistically Invariant Formulation of the Quantum Theory of Wave Fields, Prog. Theor. Phys. **1**, 27 (1946).

[21] S. Tomonaga, On Infinite Field Reactions in Quantum Field Theory, Phys. Rev. **74**, 224 (1948).

[22] J. Schwinger, On Quantum-Electrodynamics and the Magnetic Moment of the Electron, Phys. Rev. **73**, 416 (1948).

[23] J. Schwinger, The Theory of Quantized Fields, I, Phys. Rev. **82**, 914 (1951).

[24] J. Schwinger, The Theory of Quantized Fields, II, Phys. Rev. **91**, 713 (1953).

[25] R. P. Feynman, Space-Time Approach to Quantum Electrodynamics, Phys. Rev. **76**, 769 (1949).

[26] R. P. Feynman, Mathematical Formulation of the Quantum Theory of Electromagnetic Interaction, Phys. Rev. **80**, 440 (1950).

[27] F. J. Dyson, The Radiation Theories of Tomonaga, Schwinger, and Feynman, Phys. Rev. **75** 486 (1949).

[28] V. L. Ginzburg and L. D. Landau, On the Theory of Superconductivity, Zh. Eksp. Theor. Fiz. [Sov. Phys. JETP] **20**, 1064 (1950).

[29] J. Bardeen, L. N. Cooper, and J. R. Schrieffer, Theory of Superconductivity, Phys. Rev. **108**, 1175 (1957).

[30] A. L. Schawlow and C. H. Townes, Infrared and Optical Masers, Phys. Rev. **112**, 1940 (1958).

[31] T. H. Maiman, Ruby Laser Systems, Patent number 3353115, inventor: T. H. Maiman - assignee: Hughes Aircraft Company, filing: 1961, issue: 1967. Available at http://www.google.com/patents?vid=3353115 .

[32] R. J. Glauber, The Quantum Theory of Optical Coherence, Phys. Rev. **130**, 2529 (1963).

[33] R. J. Glauber, Coherent and Incoherent States of the Radiation Field, Phys. Rev. **131**, 2766 (1963).

[34] E. M. Purcell, The Question of Correlation between Photons in Coherent Light Rays, Nature (London) **178**, 1449 (1956).

[35] L. Mandel, Fluctuations of Photon Beams and their Correlations, Proc. Phys. Soc. London **72**, 1037 (1958).

[36] L. Mandel, Fluctuations of Photon Beams: The Distribution of the Photo-Electrons, Proc. Phys. Soc. London **74**, 233 (1959).

[37] B. S. Deaver, Jr. and W. M. Fairbank, Experimental Evidence for Quantized Flux in Superconducting Cylinders, Phys. Rev. Lett. **7**, 43 (1961).

[38] R. Doll and M. Näbauer, Experimental Proof of Magnetic Flux Quantization in a Superconducting Ring, Phys. Rev. Lett. **7**, 51 (1961).

[39] B. D. Josephson, Possible New Effects in Superconductive Tunnelling, Phys. Lett. **1**, 251 (1962).

[40] B. D. Josephson, Supercurrents Through Barriers, Adv. Phys. **14**, 419 (1965).

[41] P. W. Anderson and J. M. Rowell, Probable Observation of the Josephson Superconducting Tunneling Effect, Phys. Rev. Lett. **10**, 230 (1963).

[42] R. C. Jaklevic, J. Lambe, A. H. Silver, and J. E. Mercereau, Quantum Interference Effects in Josephson Tunneling, Phys. Rev. Lett. **12**, 159 (1964).

[43] A. H. Silver and J. E. Zimmerman, Quantum States and Transitions in Weakly Connected Superconducting Rings, Phys. Rev. **157**, 317 (1967).

[44] H. J. Kimble, M. Dagenais, and L. Mandel, Photon Antibunching in Resonance Fluorescence, Phys. Rev. Lett. **39**, 691 (1977).

[45] R. F. Voss and R. A. Webb, Macroscopic Quantum Tunneling in 1-μm Nb Josephson Junctions, Phys. Rev. Lett. **47**, 265 (1981).

[46] L. D. Jackel, J. P. Gordon, E. L. Hu, R. E. Howard, L. A. Fetter, D. M. Tennant, R. W. Epworth, and J. Kurkijärvi, Decay of the Zero-Voltage State in Small-Area, High-Current-Density Josephson Junctions, Phys. Rev. Lett. **47**, 697 (1981).

[47] M. H. Devoret, J. M. Martinis, D. Esteve, and J. Clarke, Resonant Activation from the Zero-Voltage State of a Current-Biased Josephson Junction, Phys. Rev. Lett. **53**, 1260 (1984).

[48] J. M. Martinis, M. H. Devoret, and J. Clarke, Energy-Level Quantization in the Zero-Voltage State of a Current-Biased Josephson Junction, Phys. Rev. Lett. **55**, 1543 (1985).

[49] M. H. Devoret, J. M. Martinis, and J. Clarke, Measurements of Macroscopic Quantum Tunneling out of the Zero-Voltage State of a Current-Biased Josephson Junction, Phys. Rev. Lett. **55**, 1908 (1985).

[50] T. A. Fulton and G. J. Dolan, Observation of Single-Electron Charging Effects in Small Tunnel Junctions, Phys. Rev. Lett. **59**, 109 (1987).

[51] More details can be found browsing http://www.mpq.mpg.de/cms/mpq/en/departments/quanten/homepage_cms/projects/index.html .

[52] R. J. Thompson, G. Rempe, and H. J. Kimble, Observation of Normal-Mode Splitting for an Atom in an Optical Cavity, Phys. Rev. Lett. **68**, 1132 (1992).

[53] J. McKeever, A. Boca, A. D. Boozer, J. R. Buck, and H. J. Kimble, Experimental Realization of a One-Atom Laser in the Regime of Strong Coupling, Nature (London) **425**, 268 (2003).

[54] S. Nußmann, K. Murr, M. Hijlkema, B. Weber, A. Kuhn, and G. Rempe, Vacuum-Stimulated Cooling of Single Atoms in Three Dimensions, Nature Phys. **1**, 122 (2005).

[55] M. Hijlkema, B. Weber, H. P. Specht, S. C. Webster, A. Kuhn, and G. Rempe, A Single-Photon Server with just one Atom, Nature Phys. **3**, 253 (2007).

[56] K. M. Birnbaum, A. Boca, R. Miller, A. D. Boozer, T. E. Northup, and H. J. Kimble, Photon Blockade in an Optical Cavity with one Trapped Atom, Nature (London) **436**, 87 (2005).

[57] I. Schuster, A. Kubanek, A. Fuhrmanek, T. Puppe, P. W. H. Pinkse, K. Murr, and G. Rempe, Nonlinear Spectroscopy of Photons Bound to one Atom, Nature Phys. **4**, 382 (2008).

[58] A. Kubanek, A. Ourjoumtsev, I. Schuster, M. Koch, P. W. H. Pinkse, K. Murr, and G. Rempe, Two-Photon Gateway in One-Atom Cavity Quantum Electrodynamics, Phys. Rev. Lett. **101**, 203602 (2008).

[59] J. Bochmann, private communications. Cf. also the website: http://www.mpq.mpg.de/cms/mpq/en/departments/quanten/homepage_cms/projects/qip/qip_details/index.html .

[60] More details can be found browsing http://www.cqed.org/spip.php .

[61] C. Fabre, S. Haroche, J. M. Raimond, P. Goy, M. Gross, L. Moi, Rydberg Atoms and Radiation in a Resonant Cavity: II Experiments, J. de Phys. Coll. C2 **43**, 275 (1982).

[62] Y. Kaluzny, P. Goy, M. Gross, J. M. Raimond, and S. Haroche, Observation of Self-Induced Rabi Oscillations in Two-Level Atoms Excited Inside a Resonant Cavity: The Ringing Regime of Superradiance, Phys. Rev. Lett. **51**, 1175 (1983).

[63] M. Brune, J. M. Raimond, P. Goy, L. Davidovich, and S. Haroche, Realization of a Two-Photon Maser Oscillator, Phys. Rev. Lett. **59**, 1899 (1987).

[64] Observation of Sub-Poissonian Photon Statistics in a Micromaser, G. Rempe, F. Schmidt-Kaler, and H. Walther, Phys. Rev. Lett. **64**, 2783 (1990).

[65] M. Brune, S. Haroche, V. Lefevre, J. M. Raimond, and N. Zagury, Quantum Nondemolition Measurement of Small Photon Numbers by Rydberg-Atom Phase-Sensitive Detection, Phys. Rev. Lett. **65**, 976 (1990).

[66] O. Benson, G. Raithel, and H. Walther, Quantum Jumps of the Micromaser Field: Dynamic Behavior Close to Phase Transition Points, Phys. Rev. Lett. **72**, 3506 (1994).

[67] M. Brune, F. Schmidt-Kaler, A. Maali, J. Dreyer, E. Hagley, J. M. Raimond, and S. Haroche, Quantum Rabi Oscillation: A Direct Test of Field Quantization in a Cavity, Phys. Rev. Lett. **76**, 1800 (1996).

[68] E. Hagley, X. Maître, G. Nogues, C. Wunderlich, M. Brune, J. M. Raimond, and S. Haroche, Generation of Einstein-Podolsky-Rosen Pairs of Atoms, Phys. Rev. Lett. **79**, 1 (1997).

[69] G. Nogues, A. Rauschenbeutel, S. Osnaghi, M. Brune, J. M. Raimond, and S. Haroche, Seeing a Single Photon Without Destroying it, Nature (London) **400**, 239 (1999).

[70] B. T. H. Varcoe, S. Brattke, M. Weidinger, and H. Walther, Preparing Pure Photon Number States of the Radiation Field, Nature (London) **403**, 743 (2000).

[71] P. Bertet, A. Auffeves, P. Maioli, S. Osnaghi, T. Meunier, M. Brune, J. M. Raimond, and S. Haroche, Direct Measurement of the Wigner Function of a One-Photon Fock State in a Cavity, Phys. Rev. Lett. **89**, 200402 (2002).

[72] A. Auffeves, P. Maioli, T. Meunier, S. Gleyzes, G. Nogues, M. Brune, J. M. Raimond, and S. Haroche, Entanglement of a Mesoscopic Field with an Atom Induced by Photon Graininess in a Cavity, Phys. Rev. Lett. **91**, 230405 (2003).

[73] S. Gleyzes, S. Kuhr, C. Guerlin, J. Bernu, S. Deléglise, U. Busk Hoff, M. Brune, J.-M. Raimond, and S. Haroche, Quantum Jumps of Light Recording the Birth and Death of a Photon in a Cavity, Nature (London) **446**, 297 (2007).

[74] S. Deléglise, I. Dotsenko, C. Sayrin, J. Bernu, M. Brune, J.-M. Raimond, and S. Haroche, Reconstruction of Non-Classical Cavity Field States with Snapshots of their Decoherence, Nature (London) **455**, 510 (2008).

[75] U. Hartmann, *Decoherence and Measurement of Charge Qubits in Double Quantum Dots*, (Ph.D. thesis, Ludwig-Maximilians-Universität, Munich, 2009).

[76] For example, cf. the website http://en.wikipedia.org/wiki/Quantum_dot .

[77] L. P. Kouwenhoven and C. M. Marcus, Quantum Dots, Physics World **11** no. 6, 35 (1998).

[78] L. P. Kouwenhoven, D. G. Austing, and S. Tarucha, Few-Electron Quantum Dots, Rep. Prog. Phys. **64**, 701 (2001).

[79] R. Hanson, L. P. Kouwenhoven, J. R. Petta, S. Tarucha, and L. M. K. Vandersypen, Spins in Few-Electron Quantum Dots, Rev. Mod. Phys. **79**, 1217 (2007).

[80] D. D. Awschalom, R. Epstein, and R. Hanson, The Diamond Age of Spintronics, Sci. Am. **297(4)**, 84 (2007).

[81] More details can be found browsing http://www.wsi.tum.de/Research/FinleygroupE24/ResearchAreas/NanoPhotonics/tabid/197/Default.aspx .

[82] J. Kim, O. Benson, H. Kan, and Y. Yamamoto, A Single-Photon Turnstile Device, Nature (London) **397**, 500 (1999).

[83] M. Pelton, C. Santori, J. Vuckovic, B. Zhang, G. S. Solomon, J. Plant, and Y. Yamamoto, An Efficient Source of Single Photons: a Single Quantum Dot in a Micropost Microcavity, Phys. Rev. Lett. **89**, 233602 (2002).

[84] M. Kaniber, A. Laucht, T. Hürlimann, M. Bichler, R. Meyer, M. C. Amann, and J. J. Finley, Highly Efficient Single-Photon Emission from Single Quantum Dots within a Two-Dimensional Photonic Band-Gap, Phys. Rev. B **77**, 073312 (2008).

[85] M. Kaniber, A. Neumann, A. Laucht, M. Huck, M. Bichler, M. C. Amann, and J. Finley, Efficient and Selective Cavity-Resonant Excitation for Single Photon Generation, New J. Phys. **11**, 013031 (2009).

[86] J. P. Reithmaier, G. Sęk, A. Löffler, C. Hofmann, S. Kuhn, S. Reitzenstein, L. V. Keldysh, V. D. Kulakovskii, T. L. Reinecke, and A. Forchel, Strong Coupling in a Single Quantum Dot-Semiconductor Microcavity System, Nature (London) **432**, 197 (2004).

[87] A. Badolato, K. Hennessy, M. Atatüre, J. Dreiser, E. Hu, P. M. Petroff, A. Imamoğlu, Deterministic Coupling of Single Quantum Dots to Single Nanocavity Modes, Science **308**, 1158 (2005).

[88] K. Hennessy, A. Badolato, M. Winger, D. Gerace, M. Atatüre, S. Gulde, S. Fält, E. Hu, and A. Imamoğlu, Quantum Nature of a Strongly Coupled Single Quantum Dot-Cavity System, Nature (London) **445**, 896 (2007).

[89] M. Kaniber, A. Laucht, A. Neumann, J. M. Villas-Boas, M. Bichler, M. C. Amann, J. Finley, Investigation of the Nonresonant Dot-Cavity Coupling in Two-Dimensional Photonic Crystal Nanocavities, Phys. Rev. B **77**, 161303(R) (2008).

[90] A. Laucht, F. Hofbauer, N. Hauke, J. Angele, S. Stobbe, M. Kaniber, G. Boehm, P. Lodahl, M. C. Amann, and J. Finley, Electrical Control of Spontaneous Emission and Strong Coupling for a Single Quantum Dot, New J. Phys. **11**, 023034 (2009).

[91] R. Loudon, *The Quantum Theory of Light*, 3rd ed., (Oxford Univ. Press Inc., New York, 2000).

[92] J. Gabelli, L.-H. Reydellet, G. Fève, J.-M. Berroir, B. Plaçais, P. Roche, and D. C. Glattli, Hanbury Brown-Twiss Correlations to Probe the Population Statistics of GHz Photons Emitted by Conductors, Phys. Rev. Lett. **93**, 056801 (2004).

[93] U. Leonhardt, *Measuring the Quantum State of Light*, (Cambridge University Press, Cambridge, 1997).

[94] G. Breitenbach, S. Schiller, and J. Mlynek, Measurement of the Quantum States of Squeezed Light, Nature (London) **387**, 471 (1997).

[95] A. I. Lvovsky, H. Hansen, T. Aichele, O. Benson, J. Mlynek, and S. Schiller, Quantum State Reconstruction of the Single-Photon Fock State, Phys. Rev. Lett. **87**, 050402 (2001).

[96] M. Tinkham, *Introduction to Superconductivity*, 2nd ed., (McGraw-Hill Book Co., New York, 1996).

[97] Yu. Makhlin, G. Schön, and A. Shnirman, Quantum-State Engineering with Josephson-Junction Devices, Rev. Mod. Phys. **73**, 357 (2001).

[98] M. H. Devoret, A. Wallraff, and J. M. Martinis, Superconducting Qubits: A Short Review, eprint arXiv:cond-mat/0411174 (unpublished).

[99] G. Wendin, V. S. Shumeiko, Quantum Bits with Josephson Junctions, Low. Temp. Phys. **33**, 724 (2007).

[100] J. Q. You and F. Nori, Phys. Today **58**, 42 (2005).

[101] J. Clarke and F. K. Wilhelm, Superconducting Quantum Bits, Nature (London) **453**, 1031 (2008).

[102] V. Bouchiat, *Quantum Fluctuations of the Charge in Single Electron and Single Cooper Pair Devices*, (Ph.D. thesis, Université Paris VI, Paris, 1997).

[103] Y. Nakamura, C. D. Chen, and J. S. Tsai, Spectroscopy of Energy-Level Splitting between Two Macroscopic Quantum States of Charge Coherently Superposed by Josephson Coupling, Phys. Rev. Lett. **79**, 2328 (1997).

[104] Y. Nakamura, Yu. A. Pashkin, and J. S. Tsai, Coherent Control of Macroscopic Quantum States in a Single-Cooper-Pair Box, Nature (London) **398**, 786 (1999).

[105] D. Vion, A. Aassime, A. Cottet, P. Joyez, H. Pothier, C. Urbina, D. Esteve, M. H. Devoret, Manipulating the Quantum State of an Electrical Circuit, Science **296**, 886 (2002).

[106] J. M. Martinis, S. Nam, J. Aumentado, C. Urbina, Rabi Oscillations in a Large Josephson-Junction Qubit, Phys. Rev. Lett. **89**, 117901 (2002).

[107] I. Chiorescu, Y. Nakamura, C. J. P. M. Harmans, J. E. Mooij, Coherent Quantum Dynamics of a Superconducting Flux Qubit, Science **299**, 1869 (2003).

[108] A. Wallraff, D. I. Schuster, A. Blais, L. Frunzio, J. Majer, M. H. Devoret, S. M. Girvin, and R. J. Schoelkopf, Approaching Unit Visibility for Control of a Superconducting Qubit with Dispersive Readout, Phys. Rev. Lett. **95**, 060501 (2005).

[109] E. Lucero, M. Hofheinz, M. Ansmann, R. C. Bialczak, N. Katz, M. Neeley, A. D. O'Connell, H. Wang, A. N. Cleland, and J. M. Martinis, High-Fidelity Gates in a Josephson Qubit, Phys. Rev. Lett. **100**, 247001 (2008).

[110] F. Mallet, F. R. Ong, A. Palacios-Laloy, F. Nguyen, P. Bertet, D. Vion, and D. Esteve, Single-Shot Qubit Readout in Circuit Quantum Electrodynamics, Nature Phys. **5**, 791 (2009).

[111] M. D. Reed, L. DiCarlo, B. R. Johnson, L. Sun, D. I. Schuster, L. Frunzio, and R. J. Schoelkopf, High Fidelity Readout in Circuit Quantum Electrodynamics Using the Jaynes-Cummings Nonlinearity, eprint arXiv:1004.4323 (unpublished).

[112] T. Yamamoto, Yu. A. Pashkin, O. Astafiev, Y. Nakamura, and J. S. Tsai, Demonstration of Conditional Gate Operation Using Superconducting Charge Qubits, Nature (London) **425**, 941 (2003).

[113] J. H. Plantenberg, P. C. de Groot, C. J. P. M. Harmans, and J. E. Mooij, Demonstration of Controlled-NOT Quantum Gates on a Pair of Superconducting Quantum Bits, Nature (London) **447**, 836 (2007).

[114] T. Hime, P. A. Reichardt, B. L. T. Plourde, T. L. Robertson, C.-E. Wu, A. V. Ustinov, and J. Clarke, Solid-State Qubits with Current-Controlled Coupling, Science **314**, 1427 (2006).

[115] A. O. Niskanen, K. Harrabi, F. Yoshihara, Y. Nakamura, S. Lloyd, J. S. Tsai, Quantum Coherent Tunable Coupling of Superconducting Qubits, Science **316**, 723 (2007).

[116] M. S. Allman, F. Altomare, J. D. Whittaker, K. Cicak, D. Li, A. Sirois, J. Strong, J. D. Teufel, and R. W. Simmonds, RF-SQUID-Mediated Coherent Tunable Coupling between a Superconducting Phase Qubit and a Lumped-Element Resonator, Phys. Rev. Lett. **104**, 177004 (2010).

[117] R. C. Bialczak, M. Ansmann, M. Hofheinz, M. Lenander, E. Lucero, M. Neeley, A. D. O'Connell, D. Sank, H. Wang, M. Weides, J. Wenner, T. Yamamoto, A. N. Cleland, and J. M. Martinis, Demonstration of a Tuneable Coupler for Superconducting Qubits Using Coherent, Time Domain, Two-Qubit Operations, arXiv:1007.2219 (unpublished).

[118] P. Bertet, I. Chiorescu, G. Burkard, K. Semba, C. J. P. M. Harmans, D. P. DiVincenzo, and J. E. Mooij, Dephasing of a Superconducting Qubit Induced by Photon Noise, Phys. Rev. Lett. **95**, 257002 (2005).

[119] F. Yoshihara, K. Harrabi, A. O. Niskanen, Y. Nakamura, and J. S. Tsai, Decoherence of Flux Qubits due to $1/f$ Flux Noise, Phys. Rev. Lett. **97**, 167001 (2006).

[120] A. A. Houck, J. A. Schreier, B. R. Johnson, J. M. Chow, J. Koch, J. M. Gambetta, D. I. Schuster, L. Frunzio, M. H. Devoret, S. M. Girvin, and R. J. Schoelkopf, Controlling the Spontaneous Emission of a Superconducting Transmon Qubit, Phys. Rev. Lett. **101**, 080502 (2008).

[121] F. Marquardt and C. Bruder, Superposition of Two Mesoscopically Distinct Quantum States: Coupling a Cooper-Pair Box to a Large Superconducting Island, Phys. Rev. B **63**, 054514 (2001).

[122] O. Buisson and F. W. J. Hekking, Entangled States in a Josephson Charge Qubit Coupled to a Superconducting Resonator, in Macroscopic Quantum Coherence and Computing, edited by D. V. Averin, B. Ruggiero, and P. Silvestrini (Kluwer Academic Publishers, New York, 2001), pp. 137-146.

[123] W. A. Al-Saidi and D. Stroud, Eigenstates of a Small Josephson Junction Coupled to a Resonant Cavity, Phys. Rev. B **65**, 014512 (2001).

[124] R. Migliore and A. Messina, Quantum Superpositions of Clockwise and Counterclockwise Supercurrent States in the Dynamics of an RF-SQUID Exposed to a Quantized Electromagnetic Field, Phys. Rev. B **67**, 134505 (2003).

[125] C.-P. Yang, S.-I Chu, and S. Han, Possible Realization of Entanglement, Logical Gates, and Quantum-Information Transfer with Superconducting-Quantum-Interference-Device Qubits in Cavity QED, Phys. Rev. A **67**, 042311 (2003).

[126] R. Migliore and A. Messina, Rabi Oscillations in the Dynamics of a Fully Quantized SQUID Ring-Electromagnetic Field System, Opt. Spectrosc. (USSR) **94**, 817 (2003).

[127] F. Plastina and G. Falci, Communicating Josephson Qubits, Phys. Rev. B **67**, 224514 (2003).

[128] J. Q. You and F. Nori, Quantum Information Processing with Superconducting Qubits in a Microwave Field, Phys. Rev. B **68**, 064509 (2003).

[129] C.-P. Yang, S.-I Chu, and S. Han, Quantum Information Transfer and Entanglement with SQUID Qubits in Cavity QED: A Dark-State Scheme with Tolerance for Nonuniform Device Parameter, Phys. Rev. Lett. **92**, 117902 (2004).

[130] M. Paternostro, G. Falci, M. Kim, and G. M. Palma, Entanglement Between Two Superconducting Qubits Via Interaction with Nonclassical Radiation, Phys. Rev. B **69**, 214502 (2004).

[131] A. Blais, R.-S. Huang, A. Wallraff, S. M. Girvin, and R. J. Schoelkopf, Cavity Quantum Electrodynamics for Superconducting Electrical Circuits: An Architecture for Quantum Computation, Phys. Rev. A **69**, 062320 (2004).

[132] S. M. Girvin, R.-S. Huang, A. Blais, A. Wallraff, and R. J. Schoelkopf, Prospects of Strong Cavity Quantum Electrodynamics with Superconducting Circuits, in Quantum Entanglement and Information Processing, Proceedings of the Les Houches Summer School 2003 (Les Houches, Volume Session LXXIX) (D. Esteve, J.-M. Raimond, J. Dalibard Eds.), ISBN 0-444-51728-6, Elsevier Science (2004), also avalibale as eprint arXiv:cond-mat/0310670.

[133] C.-P. Yang and S. Han, Preparation of Greenberger-Horne-Zeilinger Entangled States with Multiple Superconducting Quantum-Interference Device Qubits or Atoms in Cavity QED, Phys. Rev. A **70**, 062323 (2004).

[134] T. Lindström, C. H. Webster, J. E. Healey, M. S. Colclough, C. M. Muirhead, and A. Ya. Tzalenchuk, Circuit QED with a Flux Qubit Strongly Coupled to a Coplanar Transmission Line Resonator, Supercond. Sci. Technol. **20** 814 (2007).

[135] M. Devoret, S. Girvin, and R. Schoelkopf, Circuit-QED: How Strong can the Coupling Between a Josephson Junction Atom and a Transmission Line Resonator be? Ann. Phys. (Leipzig) **16**, No. 1011, 767 (2007).

[136] M. Mariantoni, F. Deppe, A. Marx, R. Gross, F. K. Wilhelm, and E. Solano, Two-Resonator Circuit Quantum Electrodynamics: a Superconducting Quantum Switch, Phys. Rev. B **78**, 104508 (2008).

[137] F. Helmer, M. Mariantoni, A. G. Fowler, J. von Delft, E. Solano, and F. Marquardt, Cavity Grid for Scalable Quantum Computation with Superconducting Circuits, Europhys. Lett. **85**, 50007 (2009).

[138] I. Chiorescu, P. Bertet, K. Semba, Y. Nakamura, C. J. P. M. Harmans, and J. E. Mooij, Coherent Dynamics of a Flux Qubit Coupled to a Harmonic Oscillator, Nature (London) **431**, 159 (2004).

[139] A. Wallraff, D. I. Schuster, A. Blais, L. Frunzio, R.-S. Huang, J. Majer, S. Kumar, S. M. Girvin, and R. J. Schoelkopf, Strong Coupling of a Single Photon to a Superconducting Qubit Using Circuit Quantum Electrodynamics, Nature (London) **431**, 162 (2004).

[140] D. I. Schuster, A. Wallraff, A. Blais, L. Frunzio, R.-S. Huang, J. Majer, S. M. Girvin, and R. J. Schoelkopf, AC Stark Shift and Dephasing of a Superconducting Qubit Strongly Coupled to a Cavity Field, Phys. Rev. Lett. **94**, 123602 (2005).

[141] J. Johansson, S. Saito, T. Meno, H. Nakano, M. Ueda, K. Semba, and H. Takayanagi, Vacuum Rabi Oscillations in a Macroscopic Superconducting Qubit LC Oscillator System, Phys. Rev. Lett. **96**, 127006 (2006).

[142] A. Wallraff, D. I. Schuster, A. Blais, J. M. Gambetta, J. Schreier, L. Frunzio, M. H. Devoret, S. M. Girvin, and R. J. Schoelkopf, Sideband Transitions and Two-Tone Spectroscopy of a Superconducting Qubit Strongly Coupled to an On-Chip Cavity, Phys. Rev. Lett. **99**, 050501 (2007).

[143] A. A. Abdumalikov, Jr., O. Astafiev, Y. Nakamura, Yu. A. Pashkin, and J. S. Tsai, Vacuum Rabi Splitting due to Strong Coupling of a Flux Qubit and a Coplanar-Waveguide Resonator, Phys. Rev. B **78**, 180502(R) (2008).

[144] R. J. Schoelkopf and S. M. Girvin, Wiring up Quantum Systems, Nature (London) **451**, 664 (2008).

[145] M. A. Sillanpää, J. I. Park, and R. W. Simmonds, Coherent Quantum State Storage and Transfer Between Two Phase Qubits via a Resonant Cavity, Nature (London) **449**, 438 (2007).

[146] J. Majer, J. M. Chow, J. M. Gambetta, J. Koch, B. R. Johnson, J. A. Schreier, L. Frunzio, D. I. Schuster, A. A. Houck, A. Wallraff, A. Blais, M. H. Devoret, S. M. Girvin, and R. J. Schoelkopf, Coupling Superconducting Qubits via a Cavity Bus, Nature (London) **449**, 443 (2007).

[147] L. DiCarlo, J. M. Chow, J. M. Gambetta, L. S. Bishop, B. R. Johnson, D. I. Schuster, J. Majer, A. Blais, L. Frunzio, S. M. Girvin, and R. J. Schoelkopf, Demonstration of Two-Qubit Algorithms with a Superconducting Quantum Processor, Nature (London) **460**, 240 (2009).

[148] M. Ansmann, *Benchmarking the Superconducting Josephson Phase Qubit - The Violation of Bell's Inequality*, (Ph.D. thesis, University of California at Santa Barbara, Santa Barbara, 2009).

[149] J. M. Chow, L. DiCarlo, J. M. Gambetta, A. Nunnenkamp, L. S. Bishop, L. Frunzio, M. H. Devoret, S. M. Girvin, and R. J. Schoelkopf, Entanglement Metrology Using a Joint Readout of Superconducting Qubits, eprint arXiv:0908.1955 (unpublished).

[150] A. A. Houck, D. I. Schuster, J. M. Gambetta, J. A. Schreier, B. R. Johnson, J. M. Chow, L. Frunzio, J. Majer, M. H. Devoret, S. M. Girvin, and R. J. Schoelkopf, Generating Single Microwave Photons in a Circuit, Nature (London) **449**, 328 (2007).

[151] M. Hofheinz, E. M. Weig, M. Ansmann, R. C. Bialczak, E. Lucero, M. Neeley, A. D. O'Connell, H. Wang, J. M. Martinis, and A. N. Cleland, Generation of Fock States in a Superconducting Quantum Circuit, Nature (London) **454**, 310 (2008).

[152] H. Wang, M. Hofheinz, M. Ansmann, R. C. Bialczak, E. Lucero, M. Neeley, A. D. O'Connell, D. Sank, J. Wenner, A. N. Cleland, and J. M. Martinis, Measurement of the Decay of Fock States in a Superconducting Quantum Circuit, Phys. Rev. Lett. **101**, 240401 (2008).

[153] M. Hofheinz, H. Wang, M. Ansmann, R. C. Bialczak, E. Lucero, M. Neeley, A. D. O'Connell, D. Sank, J. Wenner, J. M. Martinis, and A. N. Cleland, Synthesizing Arbitrary Quantum States in a Superconducting Resonator, Nature (London) **459**, 546 (2009).

[154] D. I. Schuster, A. A. Houck, J. A. Schreier, A. Wallraff, J. M. Gambetta, A. Blais, L. Frunzio, J. Majer, B. Johnson, M. H. Devoret, S. M. Girvin, and R. J. Schoelkopf, Resolving Photon Number States in a Superconducting Circuit, Nature (London) **445**, 515 (2007).

[155] A. Fragner, M. Goeppl, J. M. Fink, M. Baur, R. Bianchetti, P. J. Leek, A. Blais, and A. Wallraff, Resolving Vacuum Fluctuations in an Electrical Circuit by Measuring the Lamb Shift, Science **322**, 1357 (2008).

[156] O. Astafiev, K. Inomata, A. O. Niskanen, T. Yamamoto, Yu. A. Pashkin, Y. Nakamura, and J. S. Tsai, Single Artificial-Atom Lasing, Nature (London) **449**, 588 (2007).

[157] J. M. Fink, M. Göppl, M. Baur, R. Bianchetti, P. J. Leek, A. Blais, and A. Wallraff, Climbing the Jaynes-Cummings Ladder and Observing its $\sqrt{n}$ Nonlinearity in a Cavity QED System, Nature (London) **454**, 315 (2008).

[158] L. S. Bishop, J. M. Chow, J. Koch, A. A. Houck, M. H. Devoret, E. Thuneberg, S. M. Girvin, and R. J. Schoelkopf, Nonlinear Response of the Vacuum Rabi Resonance, Nature Phys. **5**, 105 (2009).

[159] F. Deppe, M. Mariantoni, E. P. Menzel, A. Marx, S. Saito, K. Kakuyanagi, H. Tanaka, T. Meno, K. Semba, H. Takayanagi, E. Solano, and R. Gross, Two-Photon probe of The Jaynes-Cummings Model and Controlled Symmetry Breaking in Circuit QED, Nature Phys. **4**, 686 (2008).

[160] A. Palacios-Laloy, F. Nguyen, F. Mallet, P. Bertet, D. Vion, and D. Esteve, Tunable Resonators for Quantum Circuits, J. Low Temp. Phys. **151**, 1034 (2008).

[161] M. Sandberg, C. M. Wilson, F. Persson, G. Johansson, V. Shumeiko, T. Duty, and P. Delsing, Tuning the Field in a Microwave Resonator Faster than the Photon Lifetime, Appl. Phys. Lett. **92**, 203501 (2008).

[162] M. Mariantoni *et al.*, Planck Spectroscopy and Quantum Noise of Microwave Beam Splitters, Phys. Rev. Lett. **105**, 133601 (2010).

[163] P. W. H. Pinkse, T. Fischer, P. Maunz, and G. Rempe, Trapping an Atom with Single Photons, Nature (London) **404**, 365 (2000).

[164] P. Maunz, T. Puppe, I. Schuster, N. Syassen, P. W. H. Pinkse, and G. Rempe, Cavity Cooling of a Single Atom, Nature (London) **428**, 50 (2004).

[165] P. Maunz, T. Puppe, I. Schuster, N. Syassen, P. W. H. Pinkse, and G. Rempe, Normal-Mode Spectroscopy of a Single-Bound-Atom-Cavity System, Phys. Rev. Lett. **94**, 033002 (2005).

[166] A. Kuhn, M. Hennrich, and G. Rempe, Deterministic Single-Photon Source for Distributed Quantum Networking, Phys. Rev. Lett. **89**, 067901 (2002).

[167] H. J. Kimble, Comment on "Deterministic Single-Photon Source for Distributed Quantum Networking," Phys. Rev. Lett. **90**, 249801 (2003).

[168] A. Kuhn, M. Hennrich, and G. Rempe, A Reply to the Comment by H. J. Kimble, Phys. Rev. Lett. **90**, 249802 (2003).

[169] T. Wilk, S. C. Webster, A. Kuhn, and G. Rempe, Single-Atom Single-Photon Quantum Interface, Science **317**, 488 (2007).

[170] J. Bochmann, M. Mücke, G. Langfahl-Klabes, C. Erbel, B. Weber, H. P. Specht, D. L. Moehring, and G. Rempe, Fast Excitation and Photon Emission of a Single-Atom-Cavity System, Phys. Rev. Lett. **101**, 223601 (2008).

[171] B. Weber, H. P. Specht, T. Müller, J. Bochmann, M. Mücke, D. L. Moehring, and G. Rempe, Photon-Photon Entanglement with a Single Trapped Atom, Phys. Rev. Lett. **102**, 030501 (2009).

[172] H. P. Specht, J. Bochmann, M. Mücke, B. Weber, E. Figueroa, D. L. Moehring, and G. Rempe, Phase Shaping of Single-Photon Wave Packets, Nature Phot. **3**, 469 (2009).

[173] H. Mabuchi, M. Armen, B. Lev, M. Loncar, J. Vuckovic, H. J. Kimble, J. Preskill, M. Roukes, and A. Scherer, Quantum Networks Based on Cavity QED, Quantum Information and Computation **1**, Special Issue on Implementation of Quantum Computation, 7 (2001).

[174] H. Mabuchi and A. C. Doherty, Cavity Quantum Electrodynamics: Coherence in Context, Science **298**, 1372 (2002).

[175] J. McKeever, A. Boca, A. D. Boozer, R. Miller, J. R. Buck, A. Kuzmich, and H. J. Kimble, Deterministic Generation of Single Photons from one Atom Trapped in a Cavity, Science **303**, 1992 (2004).

[176] A. Boca, R. Miller, K. M. Birnbaum, A. D. Boozer, J. McKeever, and H. J. Kimble, Observation of the Vacuum Rabi Spectrum for one Trapped Atom, Phys. Rev. Lett. **93**, 233603 (2004).

[177] C. J. Hood, M. S. Chapman, T. W. Lynn, and H. J. Kimble, Real-Time Cavity QED with Single Atoms, Phys. Rev. Lett. **80**, 4157 (1998).

[178] C. J. Hood, T. W. Lynn, A. C. Doherty, A. S. Parkins, and H. J. Kimble, The Atom-Cavity Microscope: Single Atoms Bound in Orbit by Single Photons, Science **287**, 1457 (2000).

[179] J. M. Raimond, M. Brune, and S. Haroche, Manipulating Quantum Entanglement with Atoms and Photons in a Cavity, Rev. Mod. Phys. **73**, 565 (2001).

[180] S. Haroche and J.-M. Raimond, *Exploring the Quantum*, (Oxford University Press Inc., New York, 2006).

[181] J. Bernu, S. Deléglise, C. Sayrin, S. Kuhr, I. Dotsenko, M. Brune, J. M. Raimond, and S. Haroche, Freezing Coherent Field Growth in a Cavity by the Quantum Zeno Effect, Phys. Rev. Lett. **101**, 180402 (2008).

[182] M. Brune, J. Bernu, C. Guerlin, S. Deléglise, C. Sayrin, S. Gleyzes, S. Kuhr, I. Dotsenko, J. M. Raimond, and S. Haroche, Process Tomography of Field Damping and Measurement of Fock State Lifetimes by Quantum Nondemolition Photon Counting in a Cavity, Phys. Rev. Lett. **101**, 240402 (2008).

[183] M. Keller, B. Lange, K. Hayasaka, W. Lange, and H. Walther, Continuous Generation of Single Photons with Controlled Waveform in an Ion-Trap Cavity System, Nature (London) **431**, 1075 (2004).

[184] M. Weidinger, B. T. H. Varcoe, R. Heerlein, and H. Walther, Trapping States in the Micromaser, Phys. Rev. Lett. **82**, 3795 (1999).

[185] H. Walther, B. T. H. Varcoe, B. G. Englert, and T. Becker, Cavity Quantum Electrodynamics, Rep. Prog. Phys. **69**, 1325 (2006).

[186] E. Turlot, D. Esteve, C. Urbina, J. M. Martinis, M. H. Devoret, S. Linkwitz, and H. Grabert, Escape Oscillations of a Josephson Junction Switching out of the Zero-Voltage State, Phys. Rev. Lett. **62**, 1788 (1989).

[187] D. P. DiVincenzo, Fault Tolerant Architectures for Superconducting Qubits, eprint arXiv:0905.4839 (unpublished).

[188] B. Yurke and J. S. Denker, Quantum Network Theory, Phys. Rev. A **29**, 1419 (1984).

[189] T. P. Orlando, J. E. Mooij, L. Tian, C. H. van der Wal, L. S. Levitov, S. Lloyd, and J. J. Mazo, Superconducting Persistent-Current Qubit, Phys. Rev. B **60**, 15398 (1999).

[190] G. Burkard, R. H. Koch, and D. P. DiVincenzo, Multilevel Quantum Description of Decoherence in Superconducting Qubits, Phys. Rev. B **69**, 064503 (2004).

[191] G. Burkard, Circuit Theory for Decoherence in Superconducting Charge Qubits, Phys. Rev. B **71**, 144511 (2005).

[192] G. Burkard, in *Handbook of Theoretical and Computational Nanotechnology*, edited by M. Rieth and W. Schommers (American Sscientific Publishers, New York, 2005), see aslo arXiv:cond-mat/0409626.

[193] R. Movshovich, B. Yurke, P. G. Kaminsky, A. D. Smith, A. H. Silver, R. W. Simon, and M. V. Schneider, Observation of Zero-Point Noise Squeezing via a Josephson-Parametric Amplifier, Phys. Rev. Lett. **65**, 1419 (1990).

[194] T. Yamamoto, K. Inomata, M. Watanabe, K. Matsuba, T. Miyazaki, W. D. Oliver, Y. Nakamura, and J. S. Tsai, Flux-Driven Josephson Parametric Amplifier, Appl. Phys. Lett. **93**, 042510 (2008).

[195] K. W. Lehnert, K. D. Irwin, M. A. Castellanos-Beltran, J. A. B. Mates, and L. R. Vale, Evaluation of a Microwave SQUID Multiplexer Prototype, IEEE Trans. Applied Superconductivity **17**, 705 (2007).

[196] M. A. Castellanos-Beltran and K. W. Lehnert, Widely Tunable Parametric Amplifier Based on a Superconducting Quantum Interference Device Array Resonator, Appl. Phys. Lett. **91**, 083509 (2007).

[197] J. A. B. Mates, G. C. Hilton, K. D. Irwin, L. R. Vale, and K. W. Lehnert, Demonstration of a Multiplexer of Dissipationless Superconducting Quantum Interference Devices, Appl. Phys. Lett. **92**, 023514 (2008).

[198] M. A. Castellanos-Beltran, K. D. Irwin, G. C. Hilton, L. R. Vale, and K. W. Lehnert, Amplification and Squeezing of Quantum Noise with a Tunable Josephson Metamaterial, Nature Phys. **4**, 929 (2008).

[199] M. A. Castellanos-Beltran, K. D. Iwin, L. R. Vale, G. C. Hilton, and K. W. Lehnert, Bandwidth and Dynamic Range of a Widely Tunable Josephson Parametric Amplifier, IEEE Trans. Appl. Superconductivity **19**, 944 (2009).

[200] J. D. Teufel, T. Donner, M. A. Castellanos-Beltran, J. W. Harlow, and K. W. Lehnert, Nanomechanical Motion Measured with an Imprecision Below that at the Standard Quantum Limit, Nature Nanotech. **4**, 820 (2009).

[201] A. Kamal, A. Marblestone, and M. H. Devoret, Signal-To-Pump Backaction and Self-Oscillation in Double Pump Josephson Parametric Amplifier, Phys. Rev. B **79**, 184301 (2009).

[202] J. Clarke, M. Mück, M.-O. André, J. Gail, and C. Heiden, The Microstrip DC SQUID Amplifier, in Microwave Superconductivity p. 473, edited by H. Weinstock and M. Nisenoff (Kluwer Academic Publishers, Norwell; NATO Science Series: E Vol. **375**, 2002).

[203] M. Mück, C. Welzel, and J. Clarke, Superconducting Quantum Interference Device Amplifiers at Gigahertz Frequencies, Appl. Phys. Lett. **82**, 3266 (2003).

[204] D. Kinion and J. Clarke, Microstrip Superconducting Quantum Interference Device Radio-Frequency Amplifier: Scattering Parameters and Input Coupling, Appl. Phys. Lett. **92**, 172503 (2008).

[205] L. Spietz, K. Irwin, and J. Aumentado, Input Impedance and Gain of a Gigahertz Amplifier Using a DC Superconducting Quantum Interference Device in a Quarter Wave Resonator, Appl. Phys. Lett. **93**, 082506 (2008).

[206] M. Mück, D. Hover, S. Sendelbach, and R. McDermott, Microstrip Superconducting Quantum Interference Device Radio-Frequency Amplifier: Effects of Negative Feedback on Input Impedance, Appl. Phys. Lett. **94**, 132509 (2009).

[207] I. Serban, B. L. T. Plourde, and F. K. Wilhelm, Quantum Nondemolition-Like Fast Measurement Scheme for a Superconducting Qubit, Phys. Rev. B **78**, 054507 (2008).

[208] N. Bergeal, R. Vijay, V. E. Manucharyan, I. Siddiqi, R. J. Schoelkopf, S. M. Girvin, and M. H. Devoret, Analog Information Processing at the Quantum Limit with a Josephson Ring Modulator, Nature Phys. **6**, 296 (2010).

[209] N. Bergeal, F. Schackert, M. Metcalfe, R. Vijay, V. E. Manucharyan, L. Frunzio, D. E. Prober, R. J. Schoelkopf, S. M. Girvin, and M. H. Devoret, Phase-Preserving Amplification near the Quantum Limit with a Josephson Ring Modulator, Nature (London) **465**, 64 (2010).

[210] O. V. Astafiev, A. A. Abdumalikov Jr., A. M. Zagoskin, Yu. A. Pashkin, Y. Nakamura, and J. S. Tsai, Ultimate On-Chip Quantum Amplifier, Phys. Rev. Lett. **104**, 183603 (2010).

[211] I. Siddiqi, R. Vijay, F. Pierre, C. M. Wilson, M. Metcalfe, C. Rigetti, L. Frunzio, and M. H. Devoret, RF-Driven Josephson Bifurcation Amplifier for Quantum Measurement, Phys. Rev. Lett. **93**, 207002 (2004).

[212] I. Siddiqi, R. Vijay, F. Pierre, C. M. Wilson, L. Frunzio, M. Metcalfe, C. Rigetti, R. J. Schoelkopf, and M. H. Devoret, Direct Observation of Dynamical Bifurcation between Two Driven Oscillation States of a Josephson Junction, Phys. Rev. Lett. **94**, 027005 (2005).

[213] I. Siddiqi, R. Vijay, M. Metcalfe, E. Boaknin, L. Frunzio, R. J. Schoelkopf, and M. H. Devoret, Dispersive Measurements of Superconducting Qubit Coherence with a Fast Latching Readout, Phys. Rev. B **73**, 054510 (2006).

[214] V. E. Manucharyan, E. Boaknin, M. Metcalfe, R. Vijay, I. Siddiqi, and M. Devoret, Microwave Bifurcation of a Josephson Junction: Embedding-Circuit Requirements, Phys. Rev. B **76**, 014524 (2007).

[215] N. Boulant, G. Ithier, P. Meeson, F. Nguyen, D. Vion, D. Esteve, I. Siddiqi, R. Vijay, C. Rigetti, F. Pierre, and M. Devoret, Quantum Nondemolition Readout Using a Josephson Bifurcation Amplifier, Phys. Rev. B **76**, 014525 (2007).

[216] M. Metcalfe, E. Boaknin, V. E. Manucharyan, R. Vijay, I. Siddiqi, C. Rigetti, L. Frunzio, R. J. Schoelkopf, and M. H. Devoret, Measuring the Decoherence of a Quantronium Qubit with the Cavity Bifurcation Amplifier, Phys. Rev. B **76**, 174516 (2007).

[217] O. Naaman, J. Aumentado, L. Friedland, J. S. Wurtele, and I. Siddiqi, Phase-Locking Transition in a Chirped Superconducting Josephson Resonator, Phys. Rev. Lett. **101**, 117005 (2008).

[218] A. Lupaşcu, C. J. M. Verwijs, R. N. Schouten, C. J. P. M. Harmans, and J. E. Mooij, Nondestructive Readout for a Superconducting Flux Qubit, Phys. Rev. Lett. **93**, 177006 (2004).

[219] A. Lupaşcu, E. F. C. Driessen, L. Roschier, C. J. P. M. Harmans, and J. E. Mooij, High-Contrast Dispersive Readout of a Superconducting Flux Qubit Using a Nonlinear Resonator, Phys. Rev. Lett. **96**, 127003 (2006).

[220] A. Lupaşcu, S. Saito, T. Picot, P. C. de Groot, C. J. P. M. Harmans, and J. E. Mooij, Quantum Non-Demolition Measurement of a Superconducting Two-Level System, Nature Phys. **3**, 119 (2007).

[221] B. G. U. Englert, G. Mangano, M. Mariantoni, R. Gross, J. Siewert, and E. Solano, Mesoscopic Shelving Readout of Superconducting Qubits in Circuit Quantum Electrodynamics, Phys. Rev. B **81**, 134514 (2010).

[222] G. Romero, J. J. García-Ripoll, and E. Solano, Microwave Photon Detector in Circuit QED, Phys. Rev. Lett. **102**, 173602 (2009).

[223] G. Romero, J. J. García-Ripoll, and E. Solano, Photodetection of Propagating Quantum Microwaves in Circuit QED, Phys. Scr. T **137**, 014004 (2009).

[224] B. Osberg, J. Gambetta, and F. Wilhelm, The Josephson Microwave Photomultiplier, http://meetings.aps.org/link/BAPS.2009.MAR.Y34.13 (unpublished).

[225] C. W. Gardiner and M. J. Collett, Input and Output in Damped Quantum Systems: Quantum Stochastic Differential Equations and The Master Equation, Phys. Rev. A **31**, 3761 (1985).

[226] C. W. Gardiner, A. S. Parkins, and M. J. Collett, Input and Output in Damped Quantum Systems. II. Methods in Non-White-Noise Situations and Application to Inhibition of Atomic Phase Decays, J. Opt. Soc. Am. B **4**, 1683 (1987).

[227] R. E. Collin, *Foundations for Microwave Engineering*, 2nd ed., (Wiley-IEEE Press, New Jersey, 2001).

[228] R. Paschotta, *Encyclopedia of Laser Physics and Technology*, (Wiley-VCH, Berlin, 2008).

[229] C. Cohen-Tannoudji, B. Diu, and F. Laloë, *Quantum Mechanics - Vol. I*, (Wiley-Interscience, New York, 1977).

[230] B. D. Josephson, Coupled Superconductors, Rev. Mod. Phys. **36**, 216 (1964).

[231] B. D. Josephson, The Discovery of Tunnelling Supercurrents, Rev. Mod. Phys. **46**, 251 (1974).

[232] A. Barone and G. Paterno, *Physics and Applications of the Josephson Effect*, (Wiley-VCH, New York, 1982).

[233] K. M. Lang, D. A. Hite, R. W. Simmonds, R. McDermott, D. P. Pappas, and J. M. Martinis, Conducting Atomic Force Microscopy for Nanoscale Tunnel Barrier Characterizaton, Rev. Sci. Instrum. **75**, 2726 (2004).

[234] S. Oh, K. Cicak, R. McDermott, K. B. Cooper, K. D. Osborn, R. W. Simmonds, M. Steffen, J. M. Martinis, and D. P. Pappas, Low-Leakage Superconducting Tunnel Junctions with a Single-Crystal Al_2O_3 Barrier, Superconductor Science and Technology **18**, 1396 (2005).

[235] R. W. Simmonds, D. A. Hite, R. McDermott, M. Steffen, K. B. Cooper, K. M. Lang, J. M. Martinis, and D. P. Pappas, Junction Materials Research using Phase Qubits, in *Quantum Computing in Solid State Systems* edited by P. Delsing, C. Granata, Yu. Pashkin, B. Ruggiero, and P. Silvestrini, (Springer, New York, 2005).

[236] J. S. Kline, H. Wang, S. Oh, J. M. Martinis, and D. P. Pappas, Josephson Phase Qubit Circuit for the Evaluation of Advanced Tunnel Barrier Materials, Superconductor Science and Technology **22**, 015004 (2009).

[237] J. M. Martinis, Superconducting Phase Qubits, Quantum Information Processing **8**, 81 (2009).

[238] P. G. De Gennes, *Superconductivity Of Metals And Alloys* (Advanced Book Program, Perseus Books, Reading, 1999).

[239] J. Clarke and A. I. Braginski (Eds.), *The SQUID Handbook - Vol. I Fundamentals and Technology of SQUIDs and SQUID Systems*, (Wiley-VCH Verlag, GmbH & Co. KGaA, Weinheim, 2004).

[240] J. R. Friedman, V. Patel, W. Chen, S. K. Tolpygo, and J. E. Lukens, Quantum Superposition of Distinct Macroscopic States, Nature (London) **406**, 43 (2000).

[241] K. W. Lehnert, B. A. Turek, K. Bladh, L. F. Spietz, D. Gunnarsson, P. Delsing, and R. J. Schoelkopf, Quantum Charge Fluctuations and the Polarizability of the Single-Electron Box, Phys. Rev. Lett. **91**, 106801 (2003).

[242] J. M. Martinis, K. B. Cooper, R. McDermott, M. Steffen, M. Ansmann, K. Osborn, K. Cicak, S. Oh, D. P. Pappas, R. W. Simmonds, and C. C. Yu, Decoherence in Josephson Qubits from Dielectric Loss, Phys. Rev. Lett. **95**, 210503 (2005).

[243] J. Koch, T. M. Yu, J. M. Gambetta, A. A. Houck, D. I. Schuster, J. Majer, A. Blais, M. H. Devoret, S. M. Girvin, and R. J. Schoelkopf, Charge Insensitive Qubit Design from Optimizing the Cooper-Pair Box, Phys. Rev. A **76**, 042319 (2007).

[244] J. A. Schreier, A. A. Houck, J. Koch, D. I. Schuster, B. R. Johnson, J. M. Chow, J. M. Gambetta, J. Majer, L. Frunzio, M. H. Devoret, S. M. Girvin, and R. J. Schoelkopf, Suppressing Charge Noise Decoherence in Superconducting Charge Qubits, Phys. Rev. B **77**, 180502(R) (2008).

[245] J. E. Mooij, T. P. Orlando, L. Levitov, L. Tian, C. H. van der Wal, and S. Lloyd, Josephson Persistent-Current Qubit, Science **285**, 1036 (1999).

[246] S. Sendelbach, D. Hover, A. Kittel, M. Mueck, J. M. Martinis, and R. McDermott, Magnetism in SQUIDs at Millikelvin Temperatures, Phys. Rev. Lett. **100**, 227006 (2008).

[247] R. H. Koch, D. P. DiVincenzo, and J. Clarke, Model for $1/f$ Flux Noise in SQUIDs and Qubits, Phys. Rev. Lett. **98**, 267003 (2007).

[248] J. M. Martinis, S. Nam, J. Aumentado, K. M. Lang, and C. Urbina, Decoherence of a Superconducting Qubit from Bias Noise, Phys. Rev. B **67**, 094510 (2003).

[249] R. W. Simmonds, K. M. Lang, D. A. Hite, D. P. Pappas, and J. M. Martinis, Decoherence in Josephson Phase Qubits from Junction Resonators, Phys. Rev. Lett. **93**, 077003 (2004).

[250] R. C. Bialczak, R. McDermott, M. Ansmann, M. Hofheinz, N. Katz, E. Lucero, M. Neeley, A. D. O'Connell, H. Wang, A. N. Cleland, and J. M. Martinis, $1/f$ Flux Noise in Josephson Phase Qubits, Phys. Rev. Lett. **99**, 187006 (2007).

[251] M. Neeley, M. Ansmann, R. C. Bialczak, M. Hofheinz, N. Katz, E. Lucero, A. O'Connell, H. Wang, A. N. Cleland, and J. M. Martinis, Transformed Dissipation in Superconducting Quantum Circuits, Phys. Rev. B **77**, 180508(R) (2008).

[252] A. D. O'Connell, M. Ansmann, R. C. Bialczak, M. Hofheinz, N. Katz, E. Lucero, C. McKenney, M. Neeley, H. Wang, E. M. Weig, A. N. Cleland,

and J. M. Martinis, Microwave Dielectric Loss at Single Photon Energies and milliKelvin Temperatures, Appl. Phys. Lett. **92**, 112903 (2008).

[253] J. M. Martinis, M. Ansmann, and J. Aumentado, Energy Decay in Josephson Qubits from Non-Equilibrium Quasiparticles, Phys. Rev. Lett. **103**, 097002 (2009). Cf. also the eprint supplement arXiv:0904.2035 or http://ftp.aip.org/epaps/phys_rev_lett/E-PRLTAO-103-051936/QPtheoryPE3.pdf .

[254] J. Lisenfeld, A. Lukashenko, M. Ansmann, J. M. Martinis, and A. V. Ustinov, Temperature Dependence of Coherent Oscillations in Josephson Phase Qubits, Phys. Rev. Lett. **99**, 170504 (2007).

[255] C. Song, T. W. Heitmann, M. P. DeFeo, K. Yu, R. McDermott, M. Neeley, J. M. Martinis, and B. L. T. Plourde, Microwave Response of Vortices in Superconducting Thin Films of Re and Al, Phys. Rev. B **79**, 174512 (2009).

[256] D. J. Van Harlingen, B. L. T. Plourde, T. L. Robertson, P. A. Reichardt, and J. Clarke, in *Quantum Computing and Quantum Bits in Mesoscopic Systems*, edited by A. Leggett, B. Ruggiero, and P. Silvestrini, p. 171, Proceedings of the 3rd International Workshop on Quantum Computing, June 3-7 2002 Città della Scienza, Napoli, Italy, (Springer, New York, 2003).

[257] D. J. Van Harlingen, T. L. Robertson, B. L. T. Plourde, P. A. Reichardt, T. A. Crane, and J. Clarke, Decoherence in Josephson-Junction Qubits due to Critical-Current Fluctuations, Phys. Rev. B **70**, 064517 (2004).

[258] M. Mück, M. Korn, C. G. A. Mugford, J. B. Kycia, and J. Clarke, Measurements of $1/f$ Noise in Josephson Junctions at Zero Voltage: Implications for Decoherence in Superconducting Quantum Bits, Appl. Phys. Lett. **86**, 012510 (2005).

[259] K. W. Lehnert, K. Bladh, L. F. Spietz, D. Gunnarsson, D. I. Schuster, P. Delsing, and R. J. Schoelkopf, Measurement of the Excited-State Lifetime of a Microelectronic Circuit, Phys. Rev. Lett. **90**, 027002 (2003).

[260] O. Astafiev, Yu. A. Pashkin, Y. Nakamura, T. Yamamoto, and J. S. Tsai, Temperature Square Dependence of the Low Frequency $1/f$ Charge Noise in the Josephson Junction Qubits, Phys. Rev. Lett. **96**, 137001 (2006).

[261] K. Kakuyanagi, T. Meno, S. Saito, H. Nakano, K. Semba, H. Takayanagi, F. Deppe, and A. Shnirman, Dephasing of a Superconducting Flux Qubit, Phys. Rev. Lett. **98**, 047004 (2007).

[262] F. Deppe, M. Mariantoni, E. P. Menzel, S. Saito, K. Kakuyanagi, H. Tanaka, T. Meno, K. Semba, H. Takayanagi, and R. Gross, Phase Coherent Dynamics of a Superconducting Flux Qubit with Capacitive Bias Readout, Phys. Rev. B **76**, 214503 (2007).

[263] D. A. Wells, *Theory and Problems of Lagrangian Dynamics*, Chap. 15, (McGraw-Hill, New York, 1967).

[264] L. O. Chua, C. A. Desoer, and E. S. Kuh, *Linear and Non-Linear Circuits*, (McGraw-Hill C., New York, 1987).

[265] M. H. Devoret, in *Quantum Fluctuations*, Chap. 10, edited by S. Reymaud, E. Giacobino, and J. Zinn-Justin, (Elsevier, New York, 1997).

[266] J. J. Sakurai, *Modern Quantum Mechanics*, Revised Edt., (Addison-Wesley Pub. Comp., Inc., Reading, 1994).

[267] A. Garg, Tunnel Splittings for One-Dimensional Potential Wells Revisited, Am. J. Phys. **68** (5), 430, (2000).

[268] G. Burkard, D. P. DiVincenzo, P. Bertet, I. Chiorescu, and J. E. Mooij, Asymmetry and Decoherence in a Double-Layer Persistent-Current Qubit, Phys. Rev. B **71**, 134504 (2005).

[269] T. L. Robertson, B. L. T. Plourde, P. A. Reichardt, T. Hime, C.-E. Wu, and J. Clarke, Quantum Theory of Three-Junction Flux Qubit with Non-Negligible Loop Inductance: Towards Scalability, Phys. Rev. B **73**, 174526 (2006).

[270] J. Bourassa, J. M. Gambetta, A. A. Abdumalikov Jr., O. Astafiev, Y. Nakamura, and A. Blais, Ultrastrong Coupling Regime of Cavity QED with Phase-Biased Flux Qubits, Phys. Rev. A **80**, 032109 (2009).

[271] P. Forn-Díaz, private communications.

[272] B. Peropadre, P. Forn-Díaz, E. Solano, and J. J. García-Ripoll, Switchable Ultrastrong Coupling in Circuit QED, Phys. Rev. Lett. **105**, 023601 (2010).

[273] I. Lizuain, J. Casanova, J. J. García-Ripoll, J. G. Muga, and E. Solano, Zeno Physics in Ultrastrong-Coupling Circuit QED, Phys. Rev. A **81**, 062131 (2010).

[274] Q.-H. Chen, L. Li, T. Liu, K.-L. Wang, Theory of Spectrum in Qubit-Oscillator Systems in the Ultrastrong Coupling Regime, eprint arXiv:1007.1747 (unpublished).

[275] J Hausinger and M. Grifoni, The Qubit-Oscillator System: An Analytical Treatment of the Ultra-Strong Coupling Regime, eprint arXiv:1007.5437, (unpublished).

[276] J. Casanova, G. Romero, I. Lizuain, J. J. Garcia-Ripoll, and E. Solano, Deep Ultrastrong Coupling Regime of the Jaynes-Cummings Model, eprint arXiv:1008.1240 (unpublished).

[277] T. Niemczyk, F. Deppe, H. Huebl, E. P. Menzel, F. Hocke, M. J. Schwarz, J. J. García-Ripoll, D. Zueco, T. Hümmer, E. Solano, A. Marx, and R. Gross, Beyond the Jaynes-Cummings Model: Circuit QED in the Ultrastrong Coupling Regime, eprint arXiv:1003.2376 (unpublished).

[278] P. Forn-Díaz, J. Lisenfeld, D. Marcos, J. J. García-Ripoll, E. Solano, C. J. P. M. Harmans, and J. E. Mooij, Observation of the Bloch-Siegert Shift in a Qubit-Oscillator System in the Ultrastrong Coupling Regime, eprint arXiv:1005.1559 (unpublished).

[279] D. F. Walls and G. J. Milburn, *Quantum Optics*, 2nd ed., (Springer-Verlag, Berlin-Heidelberg, 2008).

[280] J. Gao, *The Physics of Superconducting Microwave Resonators*, Ph.D. thesis (2008).

[281] J. Gao, M. Daal, A. Vayonakis, S. Kumar, J. Zmuidzinas, B. Sadoulet, B. A. Mazin, P. K. Day, and H. G. Leduc, Experimental Evidence for a Surface Distribution of Two-Level Systems in Superconducting Lithographed Microwave Resonators, Appl. Phys. Lett. **92**, 152505 (2008).

[282] J. Gao, M. Daal, J. M. Martinis, A. Vayonakis, J. Zmuidzinas, B. Sadoulet, B. A. Mazin, P. K. Day, and H. G. Leduc, A Semiempirical Model for Two-Level System Noise in Superconducting Microresonators, Appl. Phys. Lett. **92**, 212504 (2008).

[283] R. Barends, H. L. Hortensius, T. Zijlstra, J. J. A. Baselmans, S. J. C. Yates, J. R. Gao, and T. M. Klapwijk, Contribution of Dielectrics to Frequency and Noise of NbTiN Superconducting Resonators, Appl. Phys. Lett. **92**, 223502 (2008).

[284] H. Wang, M. Hofheinz, M. Ansmann, R. C. Bialczak, E. Lucero, M. Neeley, A. D. O'Connell, D. Sank, M. Weides, J. Wenner, A. N. Cleland, and J. M. Martinis, Phys. Rev. Lett. **103**, 200404 (2009).

[285] D. I. Shuster, *Circuit Quantum Electrodynamics*, Ph.D. thesis (2007). Available at http://www.eng.yale.edu/rslab/papers/SchusterThesis.pdf .

[286] J. M. Martinis, M. H. Devoret, and J. Clarke, Experimental Tests for the Quantum Behavior of a Macroscopic Degree of Freedom: The Phase Difference Across a Josephson Junction, Phys. Rev. B **35**, 4682 (1987).

[287] R. J. Schoelkopf, P. Wahlgren, A. A. Kozhevnikov, P. Delsing, and D. E. Prober, The Radio-Frequency Single-Electron Transistor (RF-SET): A Fast and Ultrasensitive Electrometer, Science **280** (1998).

[288] M. Mück, M.-O. André, J. Clarke, J. Gail, and C. Heiden, Radio-Frequency Amplifier Based on a Niobium DC Superconducting Quantum Interference Device with Microstrip Input Coupling, Appl. Phys. Lett. **72**, 2885 (1998).

[289] M. Mariantoni, M. J. Storcz, F. K. Wilhelm, W. D. Oliver, A. Emmert, A. Marx, R. Gross, H. Christ, and E. Solano, On-Chip Microwave Fock States and Quantum Homodyne Measurements, eprint arXiv:cond-mat/0509737 (unpublished).

[290] C. G. Montgomery, R. H. Dicke, and E. M. Purcell, Eds., *Principles of Microwave Circuits*, (IEE Electromagnetic Waves Series 25, Institution of Engineering and Technology, London, 1987).

[291] E. Wilkinson, An N-Way Hybrid Power Divider, IEEE Trans. Microwave Theory Tech. **8**, 116, 1960.

[292] S. B. Cohn, A Class of Broadband 3-Port TEM Hybrids, IEEE Trans. Microwave Theory Tech. **16**, 110, 1968.

[293] J. Stiles, The Wilkinson Power Divider, available at http://www.ittc.ku.edu/∼jstiles/723/handouts/The%20Wilkinson%20Power%20Divider%20723.pdf (unpublished).

[294] Cf. datasheet at http://amps.miteq.com/Amps2007/viewmodel.php?model=PD2-2000/18000-30S .

[295] Cf. the website http://www.hubersuhner.com/de/ie60/hs-index.htm for more information on microwave terminations and connectors.

[296] A. Premoli, *Fondamenti di Circuiti Elettr(on)ici - Vols. I/II*, (Cazzamali, Milano, 1998).

[297] H. Nyquist, Thermal Agitation of Electric Charge in Conductors, Phys. Rev. **32**, 110 (1928).

[298] A. M. Mood, F. A. Graybill, and D. C. Boes, *Introduction to the Theory of Statistics*, 3rd ed., (McGraw-Hill, Inc., New York, 1974).

[299] P. Baldi, *Calcolo delle Probabilità e Statistica*, 2nd ed., (McGraw-Hill Libri Italia srl, Milano, 1998).

[300] P. Z. Peebles, Jr., *Probabilty, Random Variables, and Random Signal Principles*, 2nd ed., (McGraw-Hill, Inc., New York, 1987).

[301] C. Prati, *Teoria dei Segnali*, (Edizioni CUSL, Milano, 1997).

[302] Sh. Kogan, *Electronic Noise and Fluctuations in Solids*, (Cambridge University Press, Cambridge, 2008).

[303] L. Mandel and E. Wolf, *Optical Coherence and Quantum Optics*, (Cambridge University Press, Cambridge, 1995).

[304] H. J. Carlin, Principles of Gyrator Networks, Polytech. Inst. Brooklyn, Microwave Res. Inst. Symp. Ser. **4**, 175 (1955).

[305] Cf. the website http://www.aspen-electronics.com/page.asp?page=Pamtech for more information on PAMTECH cryogenic circulators and isolators.

[306] For example, cf. the website http://www.microwaves101.com/encyclopedia/vswr.cfm .

[307] C. M. Caves, Quantum Limits on Noise in Linear Amplifiers, Phys. Rev. D **26**, 1817 (1982).

[308] D. M. Pozar, *Microwave Engineering*, 3rd ed., (J. Wiley & Sons Inc., New Jersey, 2005).

[309] A. A. Clerk, M. H. Devoret, S. M. Girvin, F. Marquardt, and R. J. Schoelkopf, Introduction to Quantum Noise, Measurement, and Amplification, Rev. Mod. Phys. **82**, 1155 (2010).

[310] L. Angelov, N. Wadefalk, J. Stenarson, E. L. Kollberg, P. Starski, and H. Zirath, On the Performance of Low-Noise Low-DC-Power-Consumption Cryogenic Amplifiers, IEEE Trans. Microwave Theory Tech. **50**, 1480 (2002).

[311] C. Risacher, E. Sundin, V. P. Robles, M. Pantaleev, and V. Belitsky, Low Noise and Low Power Consumption Cryogenic Amplifiers for Onsala and Apex Telescopes, 12th GAAS Symposium - Amsterdam (2004). Excellent reference, available at http://amsacta.cib.unibo.it/1081/1/GA043201.PDF .

[312] M. Á. Araque Caballero, *A Setup for Quantum Signal Detection in a Circuit QED Architecture*, Master/Diploma thesis (2008). Available at http://www.wmi.badw-muenchen.de/publications/theses/Araque%20Caballero_Diplomarbeit_2008.pdf .

[313] An excellent reference for details on microwave connectors is the ANRITSU *Catalog - Precision RF and Microwave Components*, which is avaliable at http://www.eu.anritsu.com/files/11410-00235.pdf .

[314] J. Majer, private communications.

[315] Cf. the website http://www.keycom.co.jp/eproducts/upj/top.htm for more information on KEYCOM microwave cables.

[316] S. A. Maas, *Microwave Mixers*, (Artech House Books, Norwood, Mass., 1986).

[317] V. B. Braginsky and F. Ya. Khalili, *Quantum Measurement*, (Cambridge University Press, Cambridge, 1992).

[318] O. Astafiev, S. Komiyama, T. Kutsuwa, V. Antonov, Y. Kawaguchi, and K. Hirakawa, Single-Photon Detector in the Microwave Range, Appl. Phys. Lett. **80**, 4250 (2002).

[319] O. Astafiev, T. Kutsuwa, V. Antonov, and S. Komiyama, FIR and Microwave Photon Detection by Quantum Dots, J. Phys. Soc. Jpn. **72** - Suppl. A, 102 (2003).

[320] A. I. Lvovsky and M. G. Raymer, Continuous-Variable Quantum-State Tomography of Optical Field and Photons, in *Quantum Information with Continuous Variables of Atoms and Light* p. 409, edited by N. J. Cerf, G. Leuchs, and E. S. Polzik, (World Scientific Publishing Co., Pte. Ltd., Singapore, 2007).

[321] A. I. Lvovsky and M. G. Raymer, Continuous-Variable Optical Quantum-State Tomography, Rev. Mod. Phys. **81**, 299 (2009).

[322] J. S. Lundeen, A. Feito, H. Coldenstrodt-Ronge, K. L. Pregnell, Ch. Silberhorn, T. C. Ralph, J. Eisert, M. B. Plenio, and I. A. Walmsley, Tomography of Quantum Detectors, Nature Phys. **5**, 27 (2008).

[323] E. P. Menzel, F. Deppe, M. Mariantoni, M. Á. Araque Caballero, A. Baust, T. Niemczyk, E. Hoffmann, A. Marx, E. Solano, and R. Gross, Dual-Path State Reconstruction Scheme for Propagating Quantum Microwaves and Detector Noise Tomography, Phys. Rev. Lett. **105**, 100401 (2010).

[324] B. Yurke, L. R. Corruccini, P. G. Kaminsky, L. W. Rupp, A. D. Smith, A. H. Silver, R. W. Simon, and E. A. Whittaker, Observation of Parametric Amplification and Deamplification in a Josephson Parametric Amplifier, Phys. Rev. A **39**, 2519 (1989).

[325] C. W. J. Beenakker and H. Schomerus, Counting Statistics of Photons Produced by Electronic Shot Noise, Phys. Rev. Lett. **86**, 700 (2001).

[326] C. W. J. Beenakker and H. Schomerus, Antibunched Photons Emitted by a Quantum Point Contact out of Equilibrium, Phys. Rev. Lett. **93**, 096801 (2004).

[327] P. W. Milonni, *The Quantum Vacuum - An Introduction to Quantum Electrodynamics*, (Academic Press, Inc., San Diego, 1994).

[328] I. Kant, *Critique of Pure Reason*, rev. ed., (Penguin Books, Ltd., London, 2008).

[329] C. P. Sun, L. F. Wei, Y. X. Liu, and F. Nori, Quantum Transducers: Integrating Transmission Lines and Nanomechanical Resonators via Charge Qubits, Phys. Rev. A **73**, 022318 (2006).

[330] F. L. Semião, K. Furuya, and G. J. Milburn, Kerr Nonlinearities and Nonclassical States with Superconducting Qubits and Nanomechanical Resonators, Phys. Rev. A **79**, 063811 (2009).

[331] M. J. Storcz, M. Mariantoni, H. Christ, A. Emmert, A. Marx, W. D. Oliver, R. Gross, F. K. Wilhelm, and E. Solano, Orthogonally-Driven Superconducting Qubit in Circuit QED, eprint arXiv:cond-mat/0612226 (unpublished).

[332] A. Blais, J. M. Gambetta, C. Cheung, A. Wallraff, D. I. Schuster, S. M. Girvin, and R. J. Schoelkopf, Single Microwave Photon Source Using Circuit QED, http://meetings.aps.org/link/BAPS.2007.MAR.H33.5 (unpublished).

[333] M. Wubs, S. Kohler, and P. Hänggi, Entanglement Creation in Circuit QED via Landau-Zener Sweeps, Physica E (Amsterdam) **40**, 187 (2007).

[334] F. Helmer, M. Mariantoni, E. Solano, and F. Marquardt, Quantum Nondemolition Photon Detection in Circuit QED and the Quantum Zeno Effect, Phys. Rev. A **79**, 052115 (2009).

[335] P. Xue, B. C. Sanders, A. Blais, and K. Lalumière, Quantum Walks on Circles in Phase Space via Superconducting Circuit Quantum Electrodynamics, Phys. Rev. A **78**, 042334 (2008).

[336] L. Zhou, Z. R. Gong, Yu-xi Liu, C. P. Sun, and F. Nori, Controllable Scattering of a Single Photon inside a One-Dimensional Resonator Waveguide, Phys. Rev. Lett. **101**, 100501 (2008).

[337] L. Davidovich, A. Maali, M. Brune, J. M. Raimond, and S. Haroche, Quantum Switches and Nonlocal Microwave Fields, Phys. Rev. Lett. **71**, 2360 (1993).

[338] D. V. Averin and C. Bruder, Variable Electrostatic Transformer: Controllable Coupling of Two Charge Qubits, Phys. Rev. Lett. **91**, 057003 (2003).

[339] E. Il'ichev, N. Oukhanski, A. Izmalkov, Th. Wagner, M. Grajcar, H.-G. Meyer, A. Yu. Smirnov, Alec Maassen van den Brink, M. H. Amin, and A. M. Zagoskin, Continuous Monitoring of Rabi Oscillations in a Josephson Flux Qubit, Phys. Rev. Lett. **91**, 097906 (2003).

[340] B. L. T. Plourde, J. Zhang, K. B. Whaley, F. K. Wilhelm, T. L. Robertson, T. Hime, S. Linzen, P. A. Reichardt, C.-E. Wu, and J. Clarke, Entangling Flux Qubits with a Bipolar Dynamic Inductance, Phys. Rev. B **70**, 140501(R) (2004).

[341] M. A. Sillanpää, T. Lehtinen, A. Paila, Yu. Makhlin, L. Roschier, and P. J. Hakonen, Direct Observation of Josephson Capacitance, Phys. Rev. Lett. **95**, 206806 (2005).

[342] T. Duty, G. Johansson, K. Bladh, D. Gunnarsson, C. Wilson, and P. Delsing, Observation of Quantum Capacitance in the Cooper-Pair Transistor, Phys. Rev. Lett. **95**, 206807 (2005).

[343] G. Johansson, L. Tornberg, V. S. Shumeiko, and G. Wendin, Readout Methods and Devices for Josephson-Junction-Based Solid-State Qubits, J. Phys.: Condens. Matter **18**, S901 (2006).

[344] J. Könemann, H. Zangerle, B. Mackrodt, R. Dolata, and A. B. Zorin, Quasiparticle Transitions in Charge-Phase Qubits Probed by RF Oscillations, Phys. Rev. B **76**, 134507 (2007).

[345] A. Rauschenbeutel, P. Bertet, S. Osnaghi, G. Nogues, M. Brune, J. M. Raimond, and S. Haroche, Controlled Entanglement of Two Field Modes in a Cavity Quantum Electrodynamics Experiment, Phys. Rev. A **64**, 050301(R) (2001).

[346] A. Messina, S. Maniscalco, and A. Napoli, Interaction of Bimodal Fields with Few-Level Atoms in Cavities and Traps, J. of Modern Opt. **50**, 1 (2003).

[347] R. H. Koch, G. A. Keefe, F. P. Milliken, J. R. Rozen, C. C. Tsuei, J. R. Kirtley, and D. P. DiVincenzo, Experimental Demonstration of an Oscillator Stabilized Josephson Flux Qubit, Phys. Rev. Lett. **96**, 127001 (2006).

[348] C. Wildfeuer and D. H. Schiller, Generation of Entangled N-Photon States in a Two-Mode Jaynes-Cummings Model, Phys. Rev. A **67**, 053801 (2003).

[349] F. G. Paauw, A. Fedorov, C. J. P. M. Harmans, and J. E. Mooij, Tuning the Gap of a Superconducting Flux Qubit, Phys. Rev. Lett. **102**, 090501 (2009).

[350] G. M. Reuther *et al.*, unpublished.

[351] T. Niemczyk, F. Deppe, M. Mariantoni, E. P. Menzel, E. Hoffmann, G. Wild, L. Eggenstein, A. Marx, and R. Gross, Fabrication Technology of and Symmetry Breaking in Superconducting Quantum Circuits, Supercond. Sci. Technol. **22**, 034009 (2009).

[352] T. Niemczyk, private communications.

[353] M. Mariantoni and F. Deppe, unpublished.

[354] Yu-xi Liu, L. F. Wei, and F. Nori, Generation of Nonclassical Photon States Using a Superconducting Qubit in a Microcavity, Europhys. Lett. **67**, 941 (2004).

[355] N. Kiesel, C. Schmid, G. Tóth, E. Solano, and H. Weinfurter, Experimental Observation of Four-Photon Entangled Dicke State with High Fidelity, Phys. Rev. Lett. **98**, 063604 (2007).

[356] L. F. Wei, Yu-Xi Liu, and F. Nori, Generation and Control of Greenberger-Horne-Zeilinger Entanglement in Superconducting Circuits, Phys. Rev. Lett. **96**, 246803 (2006).

[357] E. Solano, R. L. de Matos Filho, and N. Zagury, Mesoscopic Superpositions of Vibronic Collective States of N Trapped Ions, Phys. Rev. Lett. **87**, 060402 (2001).

[358] E. Solano, R. L. de Matos Filho, and N. Zagury, Entangled Coherent States and Squeezing in N Trapped Ions, J. Opt. B: Quantum Semiclass. Opt. **4**, S324 (2002).

[359] Yu-xi Liu, L. F. Wei, and F. Nori, Preparation of Macroscopic Quantum Superposition States of a Cavity Field via Coupling to a Superconducting Charge Qubit, Phys. Rev. A **71**, 063820 (2005).

[360] M. Steffen, M. Ansmann, R. McDermott, N. Katz, R. C. Bialczak, E. Lucero, M. Neeley, E. M. Weig, A. N. Cleland, and J. M. Martinis, State Tomography of Capacitively Shunted Phase Qubits with High Fidelity, Phys. Rev. Lett. **97**, 050502 (2006). We also suggest to browse: http://www.physics.ucsb.edu/∼martinisgroup/electronics.shtml and http://www.physics.ucsb.edu/∼martinisgroup/tutorials.shtml .

[361] S. Saito, T. Meno, M. Ueda, H. Tanaka, K. Semba, and H. Takayanagi, Parametric Control of a Superconducting Flux Qubit, Phys. Rev. Lett. **96**, 107001 (2006).

[362] J. Hauss, A. Fedorov, C. Hutter, A. Shnirman, and G. Schön, Single-Qubit Lasing and Cooling at the Rabi Frequency, Phys. Rev. Lett. **100**, 037003 (2008).

[363] L. Frunzio, A. Wallraff, D. Schuster, J. Majer, and R. Schoelkopf, Fabrication and Characterization of Superconducting Circuit QED Devices for Quantum Computation, IEEE Trans. Applied Supercond. **15**, 860 (2005).

[364] FASTHENRY, Inductance Analysis Program, RLE Computational Prototyping Group, Boston; M. Kamon, M. J. Tsuk, and J. K. White, FASTHENRY: a Multipole-Accelerated 3-D Inductance Extraction Program, IEEE Trans. Microwave Theory Tech. **42**, 1750 (1994); see also http://www.fastfieldsolvers.com and http://www.wrcad.com/freestuff.html .

[365] B. L. T. Plourde, T. L. Robertson, P. A. Reichardt, T. Hime, S. Linzen, C.-E. Wu, and J. Clarke, Flux Qubits and Readout Device With Two Independent Flux Lines, Phys. Rev. B **72**, 060506(R) (2005).

[366] In all our calculations and simulations, for the permittivity of vacuum we use the standard value provided by the National Institute of Standards and Technology (NIST), retaining all given decimal digits. The same applies for all other fundamental physical constants, which can be found at http://physics.nist.gov/cuu/Constants/ .

[367] L. G. Lutterbach and L. Davidovich, Method for Direct Measurement of the Wigner Function in Cavity QED and Ion Traps, Phys. Rev. Lett. **78**, 2547 (1997).

[368] A. Aassime, G. Johansson, G. Wendin, R. J. Schoelkopf, and P. Delsing, Radio-Frequency Single-Electron Transistor as Readout Device for Qubits: Charge Sensitivity and Backaction, Phys. Rev. Lett. **86**, 3376 (2001).

[369] C. H. van der Wal, F. K. Wilhelm, C. J. P. M. Harmans, and J. E. Mooij, Engineering Decoherence in Josephson Persistent-Current Qubits - Measurement Apparatus and Other Electromagnetic Environments, Eur. Phys. J. B **31**, 111 (2003).

[370] T. L. Robertson, B. L. T. Plourde, T. Hime, S. Linzen, P. A. Reichardt, F. K. Wilhelm, and J. Clarke, Superconducting Quantum Interference Device with Frequency-Dependent Damping: Readout of Flux Qubits, Phys. Rev. B **72**, 024513 (2005).

[371] B. A. Turek, K. W. Lehnert, A. Clerk, D. Gunnarsson, K. Bladh, P. Delsing, and R. J. Schoelkopf, Single-Electron Transistor Backaction on the Single-Electron Box, Phys. Rev. B **71**, 193304 (2005).

[372] F. Marquardt, Efficient On-Chip Source of Microwave Photon Pairs in Superconducting Circuit QED, Phys. Rev. B **76**, 205416 (2007).

[373] E. Solano, G. S. Agarwal, and H. Walther, Strong-Driving-Assisted Multipartite Entanglement in Cavity QED, Phys. Rev. Lett. **90**, 027903 (2003).

[374] F. G. Pauuw, *Superconducting Flux Qubits - Quantum Chains and Tunable Qubits*, Ph.D. thesis (2009).

[375] E. Schrödinger, Die gegenwärtige Situation in der Quantenmechanik, Naturwissenschaften **23**, 807 (1935).

[376] M. Sarovar, H.-S. Goan, T. P. Spiller, and G. J. Milburn, High-Fidelity Measurement and Quantum Feedback Control in Circuit QED, Phys. Rev. A **72**, 062327 (2005).

[377] R. J. Schoelkopf and R. Bianchetti, private communications.

[378] M. Boissonneault, J. Gambetta, and A. Blais, Non-Linear Dispersive Regime of Cavity QED: the Dressed Dephasing Model, Phys. Rev. A **77**, 060305(R) (2008).

[379] M. Boissonneault, J. M. Gambetta, and A. Blais, Dispersive Regime of Circuit QED: Photon-Dependent Qubit Dephasing and Relaxation Rates, Phys. Rev. A **79**, 013819 (2009).

[380] W. H. Zurek, Decoherence, Einselection, and the Quantum Origins of the Classical, Rev. Mod. Phys. **75**, 715 (2003).

[381] D. Leibfried, R. Blatt, C. Monroe, and D. Wineland, Quantum Dynamics of Single Trapped Ions, Rev. Mod. Phys. **75**, 281 (2003).

[382] P. Lougovski, H. Walther, and E. Solano, Instantaneous Measurement of Field Quadrature Moments and Entanglement, Eur. Phys. J. D **38**, 423 (2006).

[383] K. E. Cahill and R. J. Glauber, Ordered Expansions in Boson Amplitude Operators, Phys. Rev. **177**, 1857 (1969).

[384] F. de Melo, L. Aolita, F. Toscano, and L. Davidovich, Direct Measurement of the Quantum State of the Electromagnetic Field in a Superconducting Transmission Line, Phys. Rev. A **73**, 030303(R) (2006).

[385] XuBo Zou, K. Pahlke, and W. Mathis, Scheme for Direct Measurement of the Wigner Characteristic Function in Cavity QED, Phys. Rev. A **69**, 015802 (2004).

[386] R. Bianchetti, S. Filipp, M. Baur, J. M. Fink, M. Göppl, P. J. Leek, L. Steffen, A. Blais, and A. Wallraff, Dynamics of Dispersive Single-Qubit Readout in Circuit Quantum Electrodynamics, Phys. Rev. A **80**, 043840 (2009).

[387] J. I. Cirac and P. Zoller, A Scalable Quantum Computer with Ions in an Array of Microtraps, Nature (London) **404**, 579 (2000).

[388] D. Kielpinski, C. Monroe, and D. J. Wineland, Architecture for a Large-Scale Ion-Trap Quantum Computer, Nature (London) **417**, 709 (2002).

[389] D. Jaksch, J. I. Cirac, P. Zoller, S. L. Rolston, R. Côté, and M. D. Lukin, Fast Quantum Gates for Neutral Atoms, Phys. Rev. Lett. **85**, 2208 (2000).

[390] J. M. Taylor, H.-A. Engel, W. Dür, A. Yacoby, C. M. Marcus, P. Zoller, and M. D. Lukin, Fault-Tolerant Architecture for Quantum Computation Using Electrically Controlled Semiconductor Spins, Nature Phys. **1**, 177 (2005).

[391] M. Wallquist, J. Lantz, V. S. Shumeiko, and G. Wendin, Superconducting Qubit Network with Controllable Nearest-Neighbour Coupling, New J. Phys. **7**, 178 (2005).

[392] P. J. Leek, S. Filipp, P. Maurer, M. Baur, R. Bianchetti, J. M. Fink, M. Göppl, L. Steffen, and A. Wallraff, Using Sideband Transitions for Two-Qubit Operations in Superconducting Circuits, Phys. Rev. B **79**, 180511(R) (2009).

[393] M. Wallquist, V. S. Shumeiko, and G. Wendin, Selective Coupling of Superconducting Charge Qubits Mediated by a Tunable Stripline Cavity, Phys. Rev. B **74**, 224506 (2006).

[394] S. Poletto, F. Chiarello, M. G. Castellano, J. Lisenfeld, A. Lukashenko, C. Cosmelli, G. Torrioli, P. Carelli, and A. V. Ustinov, Coherent Oscillations in a Superconducting Tunable Flux Qubit Manipulated without Microwaves, New J. Phys. **11**, 013009 (2009).

[395] A. Imamoğlu, D. D. Awschalom, G. Burkard, D. P. DiVincenzo, D. Loss, M. Sherwin, and A. Small, Quantum Information Processing Using Quantum Dot Spins and Cavity QED, Phys. Rev. Lett. **83**, 4204 (1999).

[396] S. Osnaghi, P. Bertet, A. Auffeves, P. Maioli, M. Brune, J. M. Raimond, and S. Haroche, Coherent Control of an Atomic Collision in a Cavity, Phys. Rev. Lett. **87**, 037902 (2001).

[397] N. Schuch and J. Siewert, Natural Two-Qubit Gate for Quantum Computation Using the XY Interaction, Phys. Rev. A **67**, 032301 (2003).

[398] A. Spörl, T. Schulte-Herbrüggen, S. J. Glaser, V. Bergholm, M. J. Storcz, J. Ferber, and F. K. Wilhelm, Optimal Control of Coupled Josephson Qubits, Phys. Rev. A **75**, 012302 (2007).

[399] A. Gilchrist, N. K. Langford, and M. A. Nielsen, Distance Measures to Compare Real and Ideal Quantum Processes, Phys. Rev. A **71**, 062310 (2005).

[400] A. Rauschenbeutel, G. Nogues, S. Osnaghi, P. Bertet, M. Brune, J. M. Raimond, and S. Haroche, Coherent Operation of a Tunable Quantum Phase Gate in Cavity QED, Phys. Rev. Lett. **83**, 5166 (1999).

[401] G. Haack, F. Helmer, M. Mariantoni, F. Marquardt, and E. Solano, Toolbox of Resonant Quantum Gates in Circuit QED, eprint arXiv:0908.3673 (unpublished).

[402] H. J. Briegel and R. Raussendorf, Persistent Entanglement in Arrays of Interacting Particles, Phys. Rev. Lett. **86**, 910 (2001).

[403] R. Raussendorf, D. E. Browne, and H. J. Briegel, Measurement-Based Quantum Computation on Cluster States, Phys. Rev. A **68**, 022312 (2003).

[404] L.-M. Duan and R. Raussendorf, Efficient Quantum Computation with Probabilistic Quantum Gates, Phys. Rev. Lett. **95**, 080503 (2005).

[405] M. Van den Nest, A. Miyake, W. Dür, and H. J. Briegel, Universal Resources for Measurement-Based Quantum Computation, Phys. Rev. Lett. **97**, 150504 (2006).

[406] R. Raussendorf and H. J. Briegel, A One-Way Quantum Computer, Phys. Rev. Lett. **86**, 5188 (2001).

[407] T. Tanamoto, Yu-xi Liu, X. Hu, and F. Nori, Efficient Quantum Circuits for One-Way Quantum Computing, Phys. Rev. Lett. **102**, 100501 (2009).

[408] G. Haack, *Faster Gates for Quantum Computing and Simulation in Circuit QED*, Master/Diploma thesis (2008). Available at http://www.theorie.physik.uni-muenchen.de/lsvondelft/publications/pdf/20080201_haack.pdf .

[409] A. Steane, Multiple-Particle Interference and Quantum Error Correction, Proc. R. Soc. A **452**, 2551 (1996).

[410] D. P. DiVincenzo and P. Aliferis, Effective Fault-Tolerant Quantum Computation with Slow Measurements, Phys. Rev. Lett. **98**, 020501 (2007).

[411] A. G. Fowler, W. F. Thompson, Z. Yan, A. M. Stephens, B. L. T. Plourde, and F. K. Wilhelm, Long-Range Coupling and Scalable Architecture for Superconducting Flux Qubits, Phys. Rev. B **76**, 174507 (2007).

[412] A. M. Stephens, A. G. Fowler, and L. C. L. Hollenberg, Universal Fault Tolerant Quantum Computation on Bilinear Nearest Neighbor Arrays, Quant. Inf. Comp. **8**, 330 (2008).

[413] L. Chirolli and G. Burkard, Full Control of Qubit Rotations in a Voltage-Biased Superconducting Flux Qubit, Phys. Rev. B **74**, 174510 (2006).

[414] Yu-xi Liu, J. Q. You, L. F. Wei, C. P. Sun, and F. Nori, Optical Selection Rules and Phase-Dependent Adiabatic State Control in a Superconducting Quantum Circuit, Phys. Rev. Lett. **95**, 087001 (2005).

[415] Y. Nakamura, Yu. A. Pashkin, and J. S. Tsai, Rabi Oscillations in a Josephson-Junction Charge Two-Level System, Phys. Rev. Lett. **87**, 246601 (2001).

[416] W. D. Oliver, Y. Yu, J. C. Lee, K. K. Berggren, L. S. Levitov, and T. P. Orlando, Mach-Zehnder Interferometry in a Strongly Driven Superconducting Qubit, Science **310**, 1653 (2005).

[417] M. Sillanpää, T. Lehtinen, A. Paila, Yu. Makhlin, and P. Hakonen, Continuous-Time Monitoring of Landau-Zener Interference in a Cooper-Pair Box, Phys. Rev. Lett. **96**, 187002 (2006).

[418] C. M. Wilson, T. Duty, F. Persson, M. Sandberg, G. Johansson, and P. Delsing, Coherence Times of Dressed States of a Superconducting Qubit under Extreme Driving, Phys. Rev. Lett. **98**, 257003 (2007).

[419] D. M. Berns, M. S. Rudner, S. O. Valenzuela, K. K. Berggren, W. D. Oliver, L. S. Levitov, and T. P. Orlando, Amplitude Spectroscopy of a Solid-State Artificial Atom, Nature (London) **455**, 51 (2008).

[420] F. Deppe, S. Saito, H. Tanaka, and H. Takayanagi, Determination of the Capacitance of nm Scale Josephson Junctions, J. Appl. Phys. **95**, 2607 (2004).

[421] A. Lupaşcu, P. Bertet, E. F. C. Driessen, C. J. P. M. Harmans, and J. E. Mooij, One- and Two-Photon Spectroscopy of a Flux Qubit Coupled to a Microscopic Defect, Phys. Rev. B **80**, 172506 (2009).

[422] R. P. Feynman, R. B. Leighton, and M. Sands, *The Feynman Lectures on Physics including Feynman's Tips on Physics: the Definitive and Extended Edition*, 2nd ed., (Addison-Wesley Pub. Comp., Inc., Reading, 2005).

[423] M. Abramowitz and I. A. Stegun, *Handbook of Mathematical Functions: with Formulas, Graphs, and Mathematical Tables*, 9th ed., (Dover Publications, Inc., Mineola - New York, 1964).

[424] M. Brune, J. M. Raimond, and S. Haroche, Theory of the Rydberg-Atom Two-Photon Micromaser, Phys. Rev. A **35**, 154 (1987).

[425] G. Morigi, E. Solano, B. -G. Englert, and H. Walther, Measuring Irreversible Dynamics of a Quantum Harmonic Oscillator, Phys. Rev. A **65**, 040102(R) (2002).

[426] T. Meunier, S. Gleyzes, P. Maioli, A. Auffeves, G. Nogues, M. Brune, J. M. Raimond, and S. Haroche, Rabi Oscillations Revival Induced by Time Reversal: a Test of Mesoscopic Quantum Coherence, Phys. Rev. Lett. **94**, 010401 (2005).

[427] M. Neeley, M. Ansmann, R. C. Bialczak, M. Hofheinz, N. Katz, E. Lucero, A. O'Connell, H. Wang, A. N. Cleland, and J. M. Martinis, Process Tomography of Quantum Memory in a Josephson-Phase Qubit Coupled to a Two-Level State, Nature Phys. **4**, 523 (2008).

[428] K. Moon and S. M. Girvin, Theory of Microwave Parametric Down-Conversion and Squeezing Using Circuit QED, Phys. Rev. Lett. **95**, 140504 (2005).

[429] A. N. Cleland and M. R. Geller, Superconducting Qubit Storage and Entanglement with Nanomechanical Resonators, Phys. Rev. Lett. **93**, 070501 (2004).

[430] A. D. O'Connell, M. Hofheinz, M. Ansmann, R. C. Bialczak, M. Lenander, E. Lucero, M. Neeley, D. Sank, H. Wang, M. Weides, J. Wenner, J. M. Martinis, and A. N. Cleland, Quantum Ground State and Single-Phonon Control of a Mechanical Resonator, Nature (London) **464**, 697 (2010).

[431] M. P. da Silva, D. Bozyigit, A. Wallraff, and A. Blais, Schemes for the Observation of Photon Correlation Functions in Circuit QED with Linear Detectors, eprint arXiv:1004.3987 (unpublished).

[432] D. Bozyigit, C. Lang, L. Steffen, J. M. Fink, M. Baur, R. Bianchetti, P. J. Leek, S. Filipp, M. P. da Silva, A. Blais, and A. Wallraff, Measurements of the Correlation Function of a Microwave Frequency Single Photon Source, eprint arXiv:1002.3738 (unpublished).

[433] P. J. Leek, M. Baur, J. M. Fink, R. Bianchetti, L. Steffen, S. Filipp, and A. Wallraff, Cavity Quantum Electrodynamics with Separate Photon Storage and Qubit Readout Modes, Phys. Rev. Lett. **104**, 100504 (2010).

[434] B. R. Johnson, M. D. Reed, A. A. Houck, D. I. Schuster, L. S. Bishop, E. Ginossar, J. M. Gambetta, L. DiCarlo, L. Frunzio, S. M. Girvin, and R. J. Schoelkopf, Quantum Non-Demolition Detection of Single Microwave Photons in a Circuit, Nature Phys. **6**, 663 (2010).

List of Publications

The following list of publications includes accepted articles as well as all eprints submitted to the arXiv server. In addition, two manuscripts which are in preparation are listed. The articles are enumerated in chronological order:

1. M. Mariantoni, M. J. Storcz, F. K. Wilhelm, W. D. Oliver, A. Emmert, A. Marx, R. Gross, H. Christ, and E. Solano, On-Chip Microwave Fock States and Quantum Homodyne Measurements, eprint arXiv:cond-mat/0509737 (unpublished);

2. M. J. Storcz, M. Mariantoni, H. Christ, A. Emmert, A. Marx, W. D. Oliver, R. Gross, F. K. Wilhelm, and E. Solano, Orthogonally-Driven Superconducting Qubit in Circuit QED, eprint arXiv:cond-mat/0612226 (unpublished).

   Markus J. Storcz and Matteo Mariantoni contributed equally to this work;

3. F. Deppe, M. Mariantoni, E. P. Menzel, S. Saito, K. Kakuyanagi, H. Tanaka, T. Meno, K. Semba, H. Takayanagi, and R. Gross, Phase Coherent Dynamics of a Superconducting Flux Qubit with Capacitive Bias Readout, Phys. Rev. B **76**, 214503 (2007);

4. F. Deppe, M. Mariantoni, E. P. Menzel, A. Marx, S. Saito, K. Kakuyanagi, H. Tanaka, T. Meno, K. Semba, H. Takayanagi, E. Solano, and R. Gross, Two-Photon probe of The Jaynes-Cummings Model and Controlled Symmetry Breaking in Circuit QED, Nature Phys. **4**, 686 (2008).

   Frank Deppe and Matteo Mariantoni contributed equally to this work;

5. M. Mariantoni, F. Deppe, A. Marx, R. Gross, F. K. Wilhelm, and E. Solano, Two-Resonator Circuit Quantum Electrodynamics: a Superconducting Quantum Switch, Phys. Rev. B **78**, 104508 (2008);

6. T. Niemczyk, F. Deppe, M. Mariantoni, E. P. Menzel, E. Hoffmann, G. Wild, L. Eggenstein, A. Marx, and R. Gross, Fabrication Technology of and Symmetry Breaking in Superconducting Quantum Circuits, Supercond. Sci. Technol. **22**, 034009 (2009);

7. F. Helmer, M. Mariantoni, A. G. Fowler, J. von Delft, E. Solano, and F. Marquardt, Cavity Grid for Scalable Quantum Computation with Superconducting Circuits, Europhys. Lett. **85**, 50007 (2009);

8. F. Helmer, M. Mariantoni, E. Solano, and F. Marquardt, Quantum Nondemolition Photon Detection in Circuit QED and the Quantum Zeno Effect, Phys. Rev. A **79**, 052115 (2009);

9. B. G. U. Englert, G. Mangano, M. Mariantoni, R. Gross, J. Siewert, and E. Solano, Mesoscopic Shelving Readout of Superconducting Qubits in Circuit Quantum Electrodynamics, Phys. Rev. B **81**, 134514 (2010);

10. G. M. Reuther, D. Zueco, F. Deppe, E. Hoffmann, E. P. Menzel, T. Weißl, M. Mariantoni, S. Kohler, A. Marx, E. Solano, R. Gross, and P. Hänggi, Two-Resonator Circuit Quantum Electrodynamics: Dissipative Theory, Phys. Rev. B **81**, 144510 (2010);

11. G. Haack, F. Helmer, M. Mariantoni, F. Marquardt, and E. Solano, Resonant Quantum Gates in Circuit Quantum Electrodynamics, Phys. Rev. B **82**, 024514 (2010);

12. E. P. Menzel, F. Deppe, M. Mariantoni, M. Á. Araque Caballero, A. Baust, T. Niemczyk, E. Hoffmann, A. Marx, E. Solano, and R. Gross, Dual-Path State Reconstruction Scheme for Propagating Quantum Microwaves and Detector Noise Tomography, Phys. Rev. Lett. **105**, 100401 (2010);

13. M. Mariantoni, E. P. Menzel, F. Deppe, M. Á. Araque Caballero, A. Baust, T. Niemczyk, E. Hoffmann, E. Solano, A. Marx, and R. Gross, Planck Spectroscopy and Quantum Noise of Microwave Beam Splitters, Phys. Rev. Lett. **105**, 133601 (2010);

14. M. Mariantoni *et al.*, Two-Resonator Circuit QED: Generation of Schrödinger Cat States and Quantum Tomography, in preparation.

Acknowledgments

The work which has been presented in this thesis would have not been possible without the financial support by the German Science Foundation via the Sonderforschungsbereich (SFB) 631 (Collaborative Research Centre 631) and the German Excellence Initiative via the Nanosystems Initiative Munich (NIM).

In particular, the SFB meetings have been a great occasion for me to start new collaborations and to meet researchers working in other subfields of quantum computing. I am very grateful to all my collaborators within the SFB 631 and to Prof. Dr. Rudolf Gross and Dr. Achim Marx for making me part of it.